Universidade de Brasília
Instituto de Geociências
Programa de Pós-graduação em Geologia

Integrated remote sensing and geophysical analysis of confirmed impact structures in Brazil: Towards a guide to evaluate other circular structures of potential impact origin

Análise integrada de sensoriamento remoto e geofísico de estruturas de impacto confirmadas no Brasil: Rumo a um guia para avaliar outras estruturas circulares de potencial origem por impacto.

ADOLFO BARBOSA DA SILVA

Dissertação de Mestrado Nº 541

Orientador: Prof. Dr. Wolf Uwe Reimold

Brasília, 29/10/2025

Universidade de Brasília
Instituto de Geociências
Programa de Pós-graduação em Geologia

Integrated remote sensing and geophysical analysis of confirmed impact structures in Brazil: Towards a guide to evaluate other circular structures of potential impact origin

Análise integrada de sensoriamento remoto e geofísico de estruturas de impacto confirmadas no Brasil: Rumo a um guia para avaliar outras estruturas circulares de potencial origem por impacto.

ADOLFO BARBOSA DA SILVA

Dissertação apresentada ao Programa de Pós-Graduação em Geologia – Instituto de Geociências – IG da Universidade de Brasília – UnB como requisito parcial obrigatório para a obtenção do título de Mestre em Geologia.

Área de concentração: Geologia Regional

Orientador: Prof. Dr. Wolf Uwe Reimold

Comissão Examinadora:

Prof. Dr. Elder Yokoyama (Titular Interno) (IG/UnB);

Prof. Dr. Jüri Plado (Titular Externo) (University of Tartu);

Prof. Dra. Roberta Mary Vidotti (Suplente Interno) (IG/UnB);

Prof. Dr. Robert Luther (Suplente Externo) (Museum fuer Naturkunde Berlin);

Prof. Dra. Julia Curto Ma (Suplente Interno) (IG/UnB);

Prof. Dr. Marcos A. R. Vasconcelos (Suplente Externo) (Universidade Federal da Bahia)

Brasília, 29/10/2025

Barbosa da Silva, Adolfo
BS586a Análise integrada de sensoriamento remoto e geofísico de estruturas de impacto confirmadas no Brasil: Rumo a um guia para avaliar outras estruturas circulares de potencial origem por impacto / Adolfo Barbosa da Silva; orientador Wolf Uwe Reimold. Brasília, 2025.
343 p.

Dissertação(Mestrado em Geologia) Universidade de Brasília, 2025.

1. Imagens multiespectrais. 2. Magnetometria aérea. 3. Gamaespectrometria aérea. 4. Radar de Abertura Sintética. 5. Estruturas circulares. I. Uwe Reimold, Wolf, orient. II. Título.

ACKNOWLEDGMENTS

This study was made possible thanks to a support network of individuals and institutions to whom the author would like to express his gratitude. I express my gratitude to the Institute of Geosciences of the University of Brasília, and its Programa de Pós-Graduação em Geologia, and the Geological Survey of Brazil for providing the necessary infrastructure for this research. I am grateful to my advisor, collaborator, and friend, Prof. Dr. Wolf Uwe Reimold, for his advice, collaboration, corrections, and numerous productive discussions that contributed not only to the development of this project but also to my career as a researcher. I also extend my gratitude to Prof. Dr. Natalia Hauser, who also contributed to the discussions throughout the development of this work.

To the members of the Geological Survey of Brazil, I thank for the invaluable support and encouragement of the Chief of the Remote Sensing and Geophysics Division, Mr. Iago Sousa Lima Costa, and the Mineral Resources Manager of the Goiânia Branch, Mr. Jonatas de Sale Macedo Carneiro. I would also like to thank my geophysicist colleagues Felipe da Mota Alves and Éderson Ribeiro da Silva for their understanding, which was essential for me to dedicate more time to my master's project. I would also like to express my gratitude to geologist Ivan Pereira Marques, who not only kindly shared information about a geological target studied in this project, but also for his expertise. Similarly, I would like to thank Prof. Sérgio Luís Araújo Brenha (Federal University of Maranhão) for sharing some of his data and wish him success in his research.

On a family level, I would like to thank my wife, Catharina Kaly Pereira Bispo dos Santos. Besides being my love, my companion, and my friend, she has been a great supporter of my personal and professional growth. I am privileged to be surrounded by wonderful people who have contributed directly and indirectly to this project. They are: Renato Borges (a PhD student at IG-UNB), my brothers and sisters (Angélica, Marília, Rafael, and Anderson), Ana Elisa (my friend and English teacher), my friends Diogo Silva (no less than 20 years of friendship) and Gabi (she loves dinosaurs), and my psychologist Marcos Matias. Finally, I thank my mother Rosana de Oliveira for giving me life and the determination to face life's challenges. I dedicate this work to my grandmother and godmother Benedita (Dona Lurde), who passed away in October 2024.

This study was financed in part by the Coordenação de Aperfeiçoamento de Pessoal de Nível Superior - Brasil (CAPES) - Finance Code 001

RESUMO

O estudo de crateras de impacto na Terra é um campo multidisciplinar que integra vários ramos da geociência para o mapeamento e análise de estruturas de impacto. Estas podem ser resumidamente definidas como formas de relevo formadas quando corpos extraterrestres colidem com a superfície da Terra em hipervelocidade (> 11 km/s), liberando imensa quantidade de energia e causando deformação permanente na rocha alvo. Apesar do notável progresso no estudo de estruturas de impacto brasileiras nos últimos anos, o número de estruturas de impacto confirmadas no Brasil permanece relativamente baixo. Isso se deve a vários fatores, incluindo o número limitado de pesquisadores dedicados a essa linha de pesquisa na América do Sul, a ausência geral do ensino de crateras de impacto nos currículos de geociências, a extensa cobertura do território brasileiro por espessos estratos sedimentares e/ou vulcânicos e vegetação densa. Para enfrentar esses desafios, imagens de sensoriamento remoto (SR) de vários sensores — como multiespectrais, radar de abertura sintética, magnetométricos e radiométricos — podem ser empregadas para identificar formas de relevo circulares potencialmente formadas por eventos de impacto. Tais identificações preliminares podem orientar os esforços de verificação em campo. A principal motivação para este estudo advém da comprovada utilidade de dados de SR, incluindo levantamentos geofísicos aerotransportados (especialmente magnetometria e espectrometria de raios gama), na descoberta de inúmeras estruturas circulares com potenciais origens de impacto em outros países. Além disso, dados de SR têm sido utilizados com sucesso para identificar formações e padrões circulares, contribuindo para o mapeamento de diversas estruturas de impacto brasileiras, como Araguainha, Serra da Cangalha, Riachão e, mais recentemente, a estrutura de impacto de Nova Colinas. Apesar desses sucessos, ainda há escassez de publicações que interpretem dados de SR integrados no contexto de potenciais estruturas de impacto no Brasil. Este estudo visa preencher essa lacuna. Seu objetivo principal é avaliar dados de SR e registros geofísicos de estruturas de impacto brasileiras confirmadas, com o objetivo de desenvolver um conjunto de ferramentas para identificar locais potenciais adicionais para investigação de campo. Ao aplicar diversas técnicas de processamento e interpretar os resultados utilizando o conhecimento geológico existente, este estudo avaliou com sucesso outras estruturas circulares com potenciais origens de impacto, estabelecendo uma estrutura de priorização para futuras investigações de campo. Entre os alvos no terreno cristalinos, a estrutura Colônia continua sendo a principal candidata para origem de impacto. Dois outros sítios — Bom Jardim e Inajáh — apresentam características promissoras que podem sugerir derivação por evento de impacto meteorítico. No entanto, como ambos estão localizados em ambientes vulcânicos antigos do Cráton Amazônico, processos geológicos endógenos não podem ser descartados neste tempo. No domínio sedimentar, as estruturas circulares de São Francisco do Maranhão e Caraíbas são priorizadas para verificação de campo para avaliar suas potenciais origens de impacto. As características dos alvos circulares restantes examinadas neste estudo (Cardoso, Itiquira, Brejões e o Domo de Sucunduri) parecem menos promissoras para pesquisa de impacto meteorítico, mas podem ser de grande interesse para

exploração mineral. Espera-se que os resultados aqui apresentados sejam considerados uma motivação para o desenvolvimento de pesquisas contínuas no campo de estudo de estruturas de impacto confirmadas e propostas no Brasil.

Palavras-chave: Imagens multiespectrais; Magnetometria aérea; Gamaespectrometria aérea; Radar de Abertura Sintética; Estruturas circulares; Pesquisa de impacto meteorítico.

ABSTRACT

The study of the geological record of impact cratering on Earth is a multidisciplinary field that integrates various branches of geoscience for the mapping and analysis of impact structures. These can be, in short, defined as relief landforms formed when extraterrestrial bodies collide with Earth's surface at hypervelocity (>11 km/s), releasing immense energy and causing permanent deformation in the target rock. Although notable progress has been made in the study of Brazilian impact structures, the number of confirmed sites within Brazil remains relatively low. This is due to several factors, including the limited number of dedicated researchers in South America, the general absence of impact cratering in geoscience curricula, and the extensive coverage of Brazil's territory by thick sedimentary and/or volcanic strata and dense vegetation. To address these challenges, remote sensing (RS) imagery from various sensors—such as multispectral, synthetic aperture radar, magnetic, and radiometric—can be employed to identify circular landforms potentially formed by impact events. These preliminary identifications can guide ground-truthing efforts. The primary motivation for this study stems from the proven utility of RS data, including airborne geophysical surveys (especially magnetics and gamma-ray spectrometry), in discovering numerous circular structures with potential impact origins in other countries. Furthermore, RS data have been successfully used to identify circular formations and patterns, contributing to the mapping of several Brazilian impact structures, such as Araguainha, Serra da Cangalha, Riachão, and, more recently, the Nova Colinas impact structure. Despite these successes, there remains a scarcity of publications interpreting integrated RS data in the context of potential impact structures in Brazil. This study is aimed at filling ths gap. Its primary objective is to evaluate RS data and geophysical records of confirmed Brazilian impact structures, with the goal of developing a toolkit for identifying additional potential sites for ground-truth surveys. By applying various processing techniques and interpreting the results using existing geological knowledge, it was possible to successfully assess other circular structures of potential impact origin, establishing a prioritization framework for future field investigations. Among crystalline targets, the Colônia structure remains a prime candidate for impact origin. Two other sites – Bom Jardim and Inajáh – exhibit promising features that may suggest impact derivation. However, as both are located within ancient volcanic environments of the Amazonian Craton, endogenous geological processes cannot be ruled out. For targets in sedimentary terrane, the São Francisco do Maranhão and Caraíbas circular structures are prioritized for ground-truthing to assess their potential impact origin. The remaining circular features examined in this study (Cardoso, Itiquira, Brejões, and Sucunduri Dome) appear less promising for impact research, but they could be of prime interest for mineral exploration. It is hoped that the results presented here will be considered motivation for the development of continuing research in the field of study of confirmed and proposed impact structures in Brazil.

Keywords: Multispectral imagery; airborne magnetic; airborne gamma-ray spectrometry; Synthetic Aperture Radar; Circular structures; Impact cratering research

LIST OF ILLUSTRATIONS

LIST OF TABLES

TABLE OF CONTENT

CHAPTER 1
INTRODUCTION

1. INTRODUCTION

The geological record of impact cratering on Earth is based on mapping and studying terrestrial impact structures (Schmieder and Kring, 2021; Gottwald et al, 2021; Kenkmann, 2021; Osinski et al. 2022; and references therein). Such structures can, in short, be defined as relief landforms built when extraterrestrial bodies hit Earth's surface at hypervelocity (> 11 km/s, Melosh, 1989; French, 1998), resulting in huge energy release and causing permanent deformation in target rock (e.g., Osinski and Pierazzo, 2012; Osinski et al., 2022). Such studies have contributed to a better understanding of numerous planetary issues, such as formation of the Moon (Canup, 2012), delivery of metals to Earth (Korenaga and Marchi, 2023), assessment of future impacts on Earth (Pierazzo and Artemieva, 2012), and asteroid deflection tests for planetary defense (e.g. Michael et al., 2022).

To date some 210 impact structures are confirmed on Earth, but only eight impact structures have been confirmed so far in Brazil, with another (São Miguel do Tapuio) having essentially been confirmed as well but not been published properly yet (Crósta et al., 2019a; Reimold et al., 2022; Crósta, 2024). One of the main current research problems is the relatively low number of impact structures known in the Brazilian, in fact in the South American, territory. This is because of several factors, including: there are few dedicated researchers in this field in South America, and impact cratering is not generally taught in geoscience curricula. Consequently, the knowledge about the recognition criteria of impact structures is limited; there is only limited detailed geological mapping carried out with impact in mind, and large parts of the country´s territory are covered with thick sequences of sedimentary and/or volcanic strata (Crósta 1989; Crósta et al., 2019a). Moreover, dense vegetation cover is hindering remote sensing investigations (especially investigations based on optical instruments) in wide regions of the continent. The huge size of Brazil and the lack of infrastructure in rural areas also make field surveys, which are essential for identifying impact diagnostic features (see below, Chapter 4), difficult and expensive. To overcome these challenges, remote sensing imagery with different sensors such as multispectral, synthetic aperture radar, magnetic, and radiometric data can be used to map circular landforms potentially formed

by impact cratering to predetermine possible targets for ground truthing (see also Gottwald et al., 2021).

The main motivation for the present study is based on the fact that remote sensing data have been useful for discovering a significant number of circular structures potentially formed by impact in Australia (e.g., the Tonami East, Camooweal, and Mount Ashmore circular structures - Glikson, 2018), in Mauritania (e.g., Temimichat-Ghallaman, Rachid, and or in Tichit circular structures) (Navee et al., 2024), and other regions of North and West Africa (e.g., Anefis, Temimichat, and Velingara circular structures) (Theilen-Willige, 2023a and b; Niang et al., 2025). In Brazil, remote sensing (RS), including airborne geophysical mapping (especially magnetics and gamma-ray spectrometry), has been successfully employed for the recognition of circular formations and patterns and for further mapping of several impact structures, such as Araguainha, Serra da Cangalha, Riachão, and most recently, the Nova Colinas impact structures (e.g., Crósta et al. 2019a; Reimold et al. 2022; Leite et al., 2022; this work). However, there are only a few publications about the interpretation of integrated RS data that address the study of structures of potential impact origin in Brazil (e.g., Acevedo et al., 2015; Crósta et al., 2019b). The present work is designed to fill this knowledge gap.

The prime objective of this present research project is to evaluate the remote sensing and geophysical record of impact structures in Brazil, with the aim to screening of potential other impact sites that may become targets for ground-truth surveys. Towards these goals, this work starts with an overview of impact structure research. This overview was organized into several chapters where a short review of impact cratering related processes, the types of rocks affected by shock metamorphism (impactites), and main shock diagnostic features, and the morphology and the main structural elements in impact structures are presented in chapters 2 - 5. The geophysical signatures of impact structures (gravity, magnetic, seismic, gamma-ray spectrometry, electromagnetic and eletroresistivity, and petrophysics) are presented in Chapter 6, whereas the main characteristics of impact structures seen in spaceborne imagery (optical and radar sensors) are presented in Chapter 7. The bibliographic review organized in these chapters will serve as a guide to understanding the context of impact structures.

The regional and local geological settings of Brazilian impact structures and potential targets are presented in chapters 8 and 9, respectively. These impact structures were divided into two groups: impact structures in the Paraná Basin and impact structures in the Parnaiba Basin. A similar grouping is made for potential targets, but they are grouped into circular structures in sedimentary targets and circular structures on crystalline targets. This distincton was done to facilitate the recognition of overall features of such structures. Chapter 10 is dedicated to a summary of the methodology followed in this research. Basically, this study was divided into two steps. In the first, images derived from different sensors (geophysics, multispectral, radar, etc.) and geological information are used to analyze main features (morphological aspects, geophysical anomalies with circular or part-circular pattern, relief disruption, fragmented/interrupted geophysical patterns, drainage controls, local versus regional deformation, etc.) related to all known Brazilian impact structures (i.e., Araguainha, Vista Alegre, Vergeão Dome, Cerro do Jarau, Serra da Cangalha, Riachão Ring, Nova Colinas, Santa Marta, and São Miguel do Tapuio). In the second step, the same approach for data capture is applied for several near-circular target structures (i.e., Colônia, Brejões, Itiquira, Cardoso, Carnaíba, São Francisco do Maranhão, Inajah, Sucunduri Dome, and Bom Jardim), for some of which a potential origin by impact has already been suggested (e.g., Colônia and Inajá; Riccomoni et al., 2011; Velázquez et al., 2013; Prado et al., 2019; Martini and Liu, 1997 apud Acevedo et al., 2015). Some of these targets have been noted with well-defined circular shape on regional maps, but an origin by impact has not been assessed for them yet (e.g., Brejões, Itiquira, and Cardoso, São Francisco do Maranhão, Sucunduri Dome, and Bom Jardim). Finally, the combined findings for, on the one hand, known Brazilian impact structures and, on the other, potential targets are compared. The described methodology has produced a large number of results, a part of which has been published in a research article (Chapter 11) and in the form of two conference abstracts (Chapter 12). A second research paper (Chapter 13) is currently in an advanced stage of preparation. The remaining results are organized in Chapter 14 and discussed in Chapter 15.

Regarding the main objective of this study, it is concluded that this work was successful to evaluate other circular structures of potential impact origin,

such that a priorization for future ground-truth surveys has been established. On crystalline target, the Colônia circular target remains the prime candidate for impact origin. In addition, this study has revealed that two targets (Bom Jardim and Inajáh) may show promising results that could be interpreted as indications of derivation from impact. However, because these two targets occur in ancient volcanic environments of the Amazonian Craton, endogenous processes cannot be ruled out for these structures either. On sedimentary rocks, São Francisco do Maranhão and Caraíbas seem to be potential priority targets for ground-truthing. The remainng circular tagets (e.g., Cardoso, Itiquira, Brejões, and Sucunduri Dome) show less potential for impact research, but they could be of prime interest for mineral exploration.

It is hoped that the results presented here will be considered as motivation for the development of continuing research in the field of study of confirmed and proposed impact structures in Brazil.

CHAPTER 2

A SHORT REVIEW OF THE IMPACT CRATERING PROCESS

2. A SHORT REVIEW OF THE IMPACT CRATERING PROCESS

The dynamics of impact structure formation involves several complex physico-chemical interactions. Based on some 60 years of planetary impact studies and extensive numerical modelling, the process has been historically separated into three phases: contact and compression; excavation, and modification (Melosh, 1989). A detailed description of these stages can be found in textbooks (e.g., Melosh, 1989; French, 1998; Osinski and Pierazzo, 2012) or review papers (e.g., Reimold and Koeberl, 2014; Kenkmann et al., 2014; Kenkmann, 2021; Osinski et al., 2022).

The contact/compression stage begins when the projectile comes into contact with a target surface, such as Earth´s surface (Fig. 1). As the impactor collides at hypervelocity (> 11 km/s in the case of Earth), it becomes compressed against the target, instantly increasing the pressure at the point of impact. Additionally, part of the kinetic energy is immediately transferred to the target, raising its internal energy and temperature. Such sudden disturbances in pressure, temperature, and density generate a shock wave that travels back into the projectile and forward the target at supersonic velocity (e.g., Melosh, 1989; Collins et al., 2012). When this shock wave reaches the projectile's rear free surface, it is reflected towards the target as a so-called rarefaction/release wave. The release wave promotes the decompression of the projectile and, as the temperatures are high, the projectile may vaporize, thus marking the end of the contact/compression stage (Fig. 1) (Melosh, 1989; Melosh and Ivanov, 1999).

During the passage of the shock wave into the target rocks, there is a considerable amount of stress that surpasses the rock strength, making the target material reach a limit (Hugoniot Elastic Limit) beyond which plastic or irreversible distortions occur in the target materials. During the excavation stage (Fig. 1), the shock wave expands and hemispherically propagates through the target rock. As the center of this hemisphere lies below the original surface, the part of the shock wave that travels upward is reflected back from the surface, downwards as release waves (French, 1998; Melosh and Ivanov, 1999). The mutual action of the release waves and the inertia of the initial movement resulting from the passage of the shock waves results in a curved path that

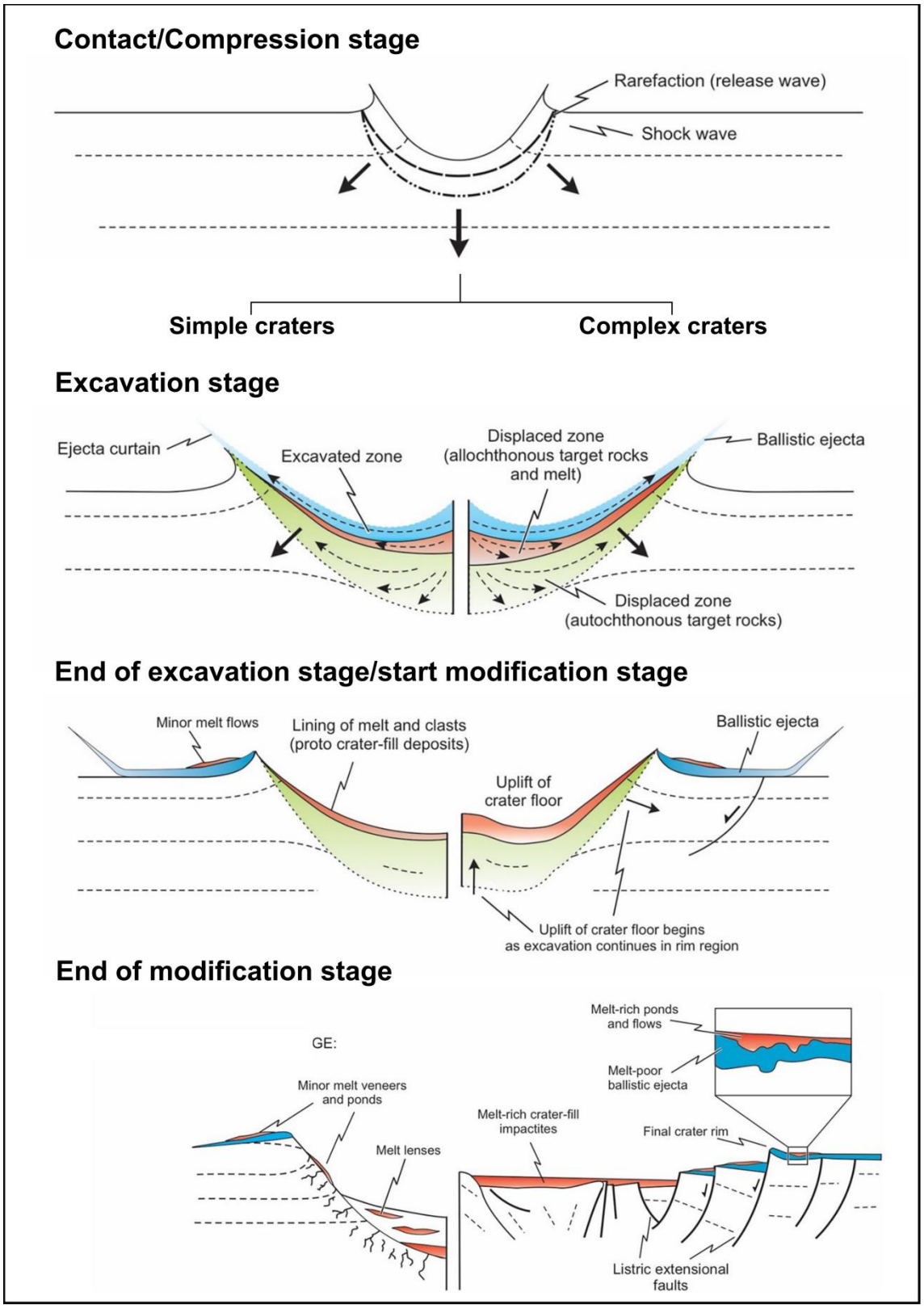

Figure 1: Stages of formation of impact structures. Modified from Osinski et al. (2022).

displaces the particles of the target rock, thus allowing the opening and growth of a cavity known as a "transient crater" (French, 1998; Melosh and Ivanov, 1999). Although the transient cavity does not exist as a physical entity, it helps

to understand the displacement processes of particles during impact events. Depending on trajectory, target rock materials, rock fragments and melt can be ejected beyond the transient cavity rim, forming a continuous, and further out, discontinuous ejecta blanket (Fig. 1). Depending on the scale of an impact event, ejected materials can be thrown outward for several kilometers from the impact point, forming strewn fields (ejecta blankets and perhaps even global ejecta deposits; e.g., Glass and Simonson, 2012). On the other hand, target rock and melt fragments derived from below the point of impact can be displaced upward and outward parallel to the base of the transient cavity, without being ejected from the structure. In this process, ground hugging material flows can be formed and breccia dikes can be injected into the crater floor (Fig. 1). As the shock wave begins to lose energy, the materials are no longer ejected or displaced. Thus, the transient crater stops expanding, which marks the end of the excavation stage and the beginning of the modification stage (Fig. 1).

The modification stage is characterized by rather conventional mechanisms driven by gravity and rock mechanics (French, 1998; Melosh and Ivanov, 1999). These mechanisms modify the geometry of the transient crater to a more stable configuration under a given planetary gravitational field. In the case of a complex impact structure, which is the case for all Brazilian impact structures, the transient crater is immediately modified as rocks from the deepest zone below the transient crater ascend/rebound to form a central uplift (Fig. 1). This begins at the same time when the rocks on the periphery of the transient crater collapse downward and inward along concentric faults to form one or more depressed rings (ring graben structures) (Fig. 1), and terraces form along the outer rim of the final structure (French, 1998; Melosh and Ivanov, 1999; Osinski et al., 2022).

Regarding the impact processes described above, it is worth mentioning two points: first, the three stages of impact crater formation are extremely dynamic and their duration is extremely short. For instance, even in the formation of large impact structures, for example a structure of 160-180 km diameter such as the Chicxulub structure (Mexico), the duration of formation of the structure has been estimated to last just a few minutes (e.g., Gulick et al., 2013; Osinski et al., 2022). Second, after impact structure formation, other

mechanisms can play an important role in the further modification of shape and geometry of a structure, such as anisotropy of the target, post-impact tectonism, hydrothermal alteration, erosion, and others (Naumov, 2005; Pirajno, 2005; Osinski et al., 2013, 2020). If erosion levels are significant, the entire “crater” geometry may become erased. Therefore, the term “impact structure” is preferred, rather than “impact crater”, in all those where the original crater form is no longer present. Naturally, erosion can also affect geophysical signatures (e.g., Plado et al., 1999), but on the other hand, erosive processes may also reveal structural elements buried at deeper levels in impact structures (Kenkmann et al., 2014).

CHAPTER 3
IMPACT PRODUCTS (IMPACTITES)

3. IMPACT PRODUCTS (IMPACTITES)

A characteristic suite of different impact generated rocks (i.e., impactites) is generated in the dynamic impact process (Stoeffler and Grieve, 2007; Stoeffler et al., 2018). An updated classification system of impactites was proposed by Stoeffler et al. (2018).

Impactites can be classified based on two approaches: based on their textural characteristics or based on the degree to which impact-affected materials were moved from the original pre-impact location (ibid). In the first approach, impactites are divided into: shocked rocks - a rock that shows unambiguous evidence of shock metamorphism; impact breccias - can be subdivided into lithic impact breccias and impact melt-bearing breccias (also referred as suevite) - depending on the presence of only lithic clasts or of lithic clasts plus impact melt fragments in these breccias, respectively. When there are no melt fragments and the lithic clasts are dominated by only one lithotype, the breccias are referred to as monomict impact breccias, and when lithic clasts come from more than one lithotype, breccias are polymict (Fig. 2). Finally, there are impact melt rocks - formed due to impact generated heat during decompression from initial shock pressure. When such melt rocks have high clast content, they are also referred as impact melt breccias (ibid).

Based on the second approach, impactites can be divided into: autochthonous or authigenic types, that is these impactites are formed in situ, with their pre-impact stratigraphic relationships still recognizable; parautochthonous impactites - can be represented by shocked rocks or monomict impact breccias with angular clasts that suffered some displacement within the crater; allochthonous impactites have been significantly transported from the true formation position (e.g., occurring in the form of dike injections into the crater floor). Allochthonous impactites may occur as *proximal* (up to 5 crater radii from the crater) or *distal* deposits. Commonly observed dikes can be meter wide and of varied length, and they can be composed of impact melt rocks, impact melt-bearing breccias, or lithic impact breccias. There are also aphanitic to fine-grained crystalline formations that resemble pseudotachylite (friction melt rock), and have been called such in abundance in past decades. As they, however, can represent a number of phases of different genesis (e.g., friction melt or shock melt, decompression melt, or pre- or post-impact tectonic

veining), it has been proposed (e.g., Reimold, 1998) to term these formations “pseudotachylitic breccias”, in a non-genetic sense, until the true mode of origin has been established.

The proximal ejecta deposits consist of materials that are transported and deposited beyond the crater rim to a distance up to 5 times of the transient cavity radius (e.g., Glass and Simonson, 2012; Kenkmann et al., 2014). These deposits can form a blanket (continuous deposit) around impact structures, but they tend to become more discontinuous as radial distance increases (Kenkmann et al., 2014). Distal ejecta deposits consist of material that were transported and deposited further out than 5 times the transient cavity radius. These deposits represent tektite/microtektite strewn fields of melt particles that were ballistically ejected (Glass and Simonson, 2012). In Archean terranes so-called spherule layers have been observed, the spherule components of which formed either by ejection from within-crater melt, or by sublimation/precipitation from ejecta plumes (Koeberl et al., 2024 and references therein).

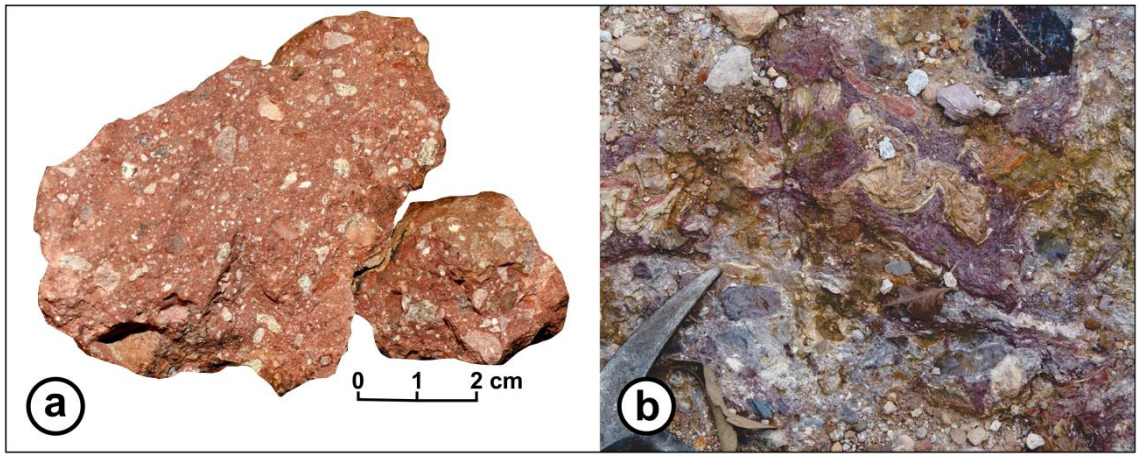

Figure 2: Some examples of impactites. Polymict breccia from the center of the Vargeão Dome impact structure (a) and from the northern part of the Araguainha central uplift (b). Modified after Crósta et al. (2019a).

CHAPTER 4

MAIN SHOCK DEFORMATION FEATURES

4. MAIN SHOCK DEFORMATION FEATURES

After the passage of the shock wave during an impact event, a set of irreversible plastic deformations can be observed in the target rock (e.g., Langenhorst, 2002; Stöffler et al., 2018). Such permanent deformation is known as shock metamorphism and is characterized by features of high pressure (2 to hundreds of GPa) and temperatures (>> 1000°C) that affect target rock during the impact event (e.g., Deutsch et al., 2015; Stöffler et al., 2018). Because typical crustal metamorphic processes are characterized by comparatively much lower pressures (< 2 Ga) and lower temperatures (commonly < 1000 °C) (Fig. 3), shock deformation features are considered bona fide evidence for impact events/presence of impact structures (e.g., Grieve, 1990; Stöffler and Langenhorst, 1994; Stöffler et al., 2018; various contributions to Reimold and Jourdan, 2012).

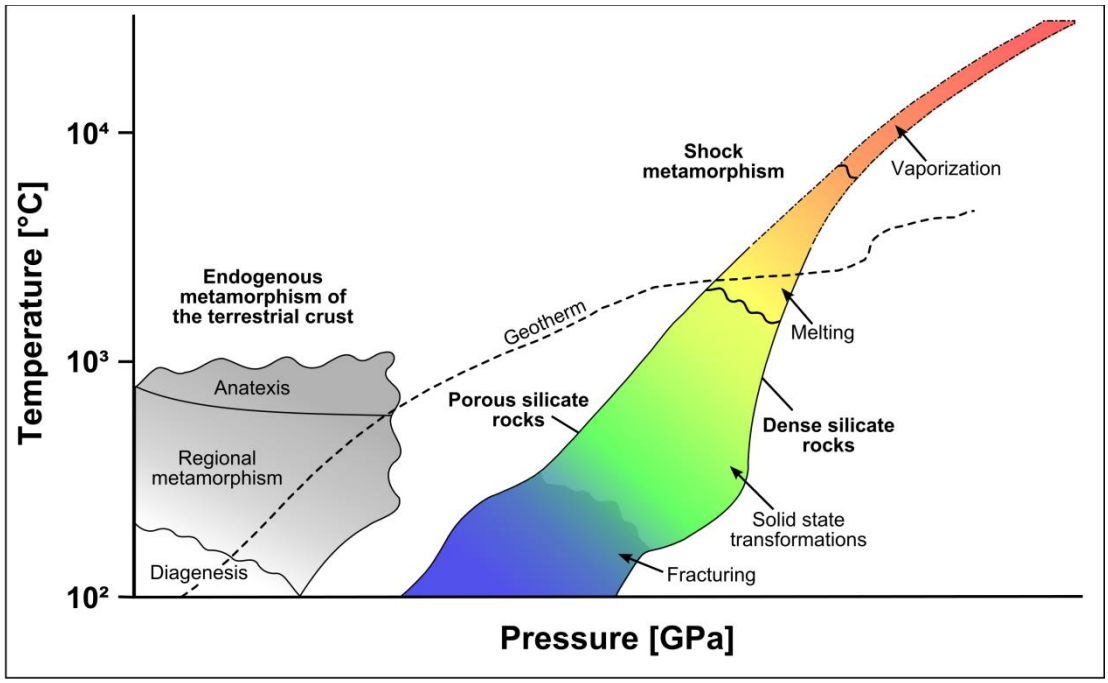

Figure 3: Pressure–temperature fields for shock metamorphism of porous (sedimentary) and crystalline rocks in comparison with endogenous metamorphism of the terrestrial crust. The upper and lower curves are the fields for shock metamorphism for porous and dense crystalline silicate rocks. Detail about the temperature estimates for the slightly dashed boundaries of the P-T field of shock metamorphism (upper part of “melting” and “vaporization”; yellow to orange) and for the geotherm for continental crust can be found in Stöffler et al. (2018). Modified after Stöffler and Langenhorst (1994) and Stöffler et al. (2018).

Shock deformation features can be divided into two groups: macroscopic and microscopic features. The former group is represented only by shatter cones, whereas the latter is represented by mechanical deformation features and transformations (e.g., Planar Features - PF, Feather Features - FF, Planar Deformation Features - PDF), formation of diaplectic glass (formed without fusion), high-pressure phase transformation (e.g., transformation of SiO_2 into coesite or stishovite; of zircon to reidite, inter alia), and mineral or bulk rock melting. These effects created in the shock regime represent diagnostic evidence of impact deformation. Isotopic or chemical traces of extraterrestrial projectiles can also provide bona fide evidence for impact events (e.g., Stöffler and Langenhorst, 1994; Reimold and Jourdan, 2012 and papers therein; Reimold and Koeberl, 2014; Koeberl, 2014; Deutsch et al., 2015; Stöffler et al., 2018, inter alia).

Although shatter cones can also form after the passage of shock waves in a nuclear weapons test, in the natural environment shatter cones have only ever been observed in confirmed impact structures (e.g., Dietz, 1960; Melosh, 1989; Baratoux and Reimold, 2016). In a rock affected by impact, shatter cones can be recognized by showing a set of striations and grooves that radiate from an apex in a divergent and pervasive shape, forming a cone (ibid, and references therein) (Fig. 4a). Although such conical features can be formed in different lithologies, they are best developed in fine-grained materials such as fine limestone. Shatter cones can be formed in the shock pressure range from ca. 2 to 45 GPa, and they are more likely found in rocks of a central uplift. They are sometimes also found in clasts of crater fill impact breccias or even in ejected target rock clasts embedded within impact ejecta (Baratoux and Reimold, 2016).

For shock pressures from ca. 5 - 20 GPa, mechanical shock deformation features include Planar Fractures (PF) and Feather Features (FF) (Fig. 4b). The former are a set of open, subparallel micro-fissures spaced at ~20 – 30 micrometers and with widths greater than 3 micrometers, whereas the latter form sets of finely spaced lamellar branches (like a comb) developed mainly on only one side of a PF (Poelchau and Kenkmann, 2011; Tada et al., 2024). The angle between PF’s and associated FF’s commonly exceeds 35°, and their

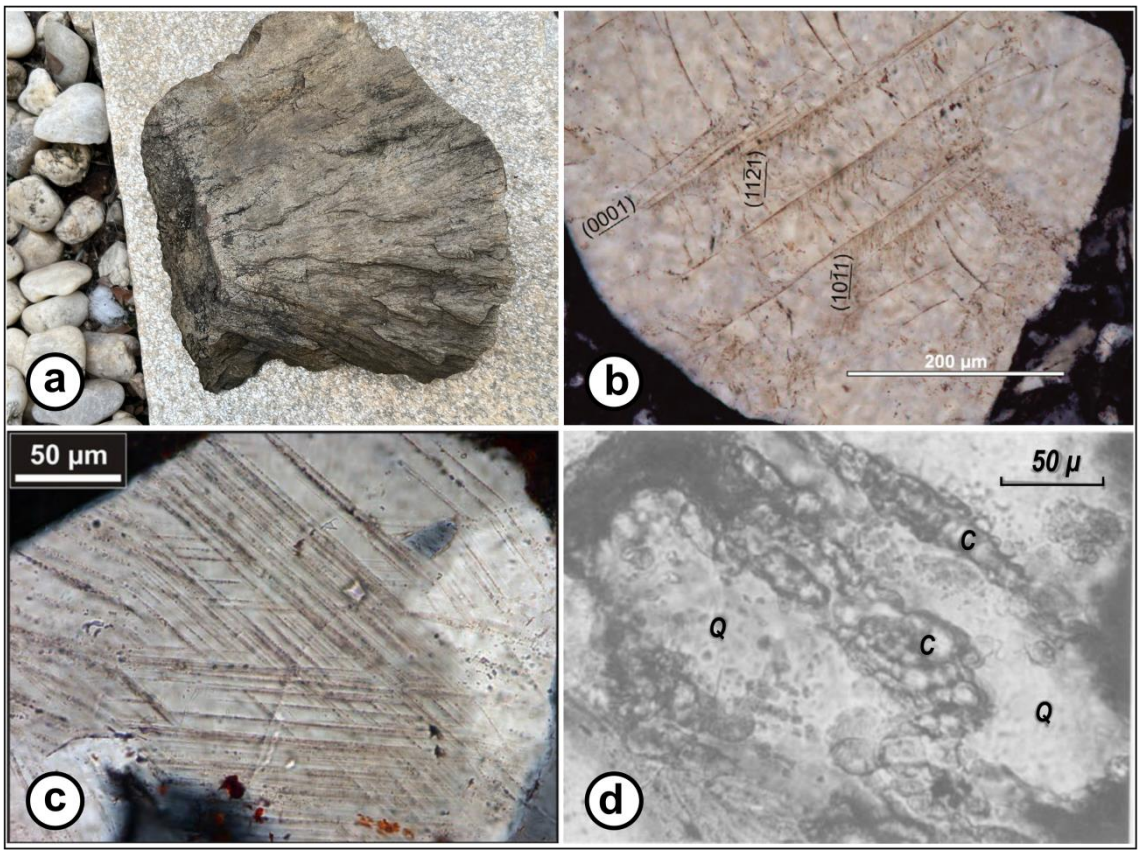

Figure 4: Examples of shock deformation features. a) Shatter cone in meta-sandstone of the northern central uplift of the Araguainha impact structure. Note the apex area of polygonal shape. From the base to the apex area, the specimen measures 12 cm in length. Image courtesy of W.U. Reimold. b) Quartz grain with feather features (FFs) from the Cerro do Jarau central uplift. The planar fractures on these features are oriented parallel to the basal plane (0001), whereas the microfeatures branching off the planar fractures under oblique angles are oriented parallel to $\{10\bar{1}1\}$ and $\{11\bar{2}1\}$. The scale bar measures 200 µm in total width. Modified after Reimold et al. (2018). c) Quartz grain with two sets of PDFs (sample from the Nicholson impact structure, Canada). Modified after Reimold et al. (2014). d) Example of high-pressure quartz polymorphs. Here, coesite (C) occurs within diaplectic glass (Q) of a shocked granitic clast in suevite from the Ries impact structure, Germany. Modified after Stöffler and Langenhorst (1994).

crystallographic orientations in quartz are commonly (0001), $\{10\bar{1}1\}$, and $\{11\bar{2}1\}$ (ibid). FF's form in quartz grains at shock pressure up to 16 – 18 GPa from experimentally shocked granites may show angles ranging from 80° to 90° regarding to their PF and show other crystallographic orientations like $\{10\bar{1}4\}$ / $\{10\bar{1}3\}$ (Tada et al., 2024). It is worth mentioning that PF's only can be considered a shock feature when they occur in abundance and together with other shock features (Reimold et al., 2018).

Solid-state deformations and phase transitions begin to develop at pressures above 10 and up to 60 GPa (Stöeffer et al., 2018). In the ca. 5 - 30 GPa range, narrow (less than 5 micrometers thick), individual planes of amorphous or high-dislocation density materials can be formed under strict crystallographic control in the major rock-forming minerals such as quartz and feldspars (Stöffler and Langenhorst, 1994; Langenhorst, 2002; Reimold et al., 2014). When visualized together, such planes comprise straight, parallel sets of features that are spaced 2–10 micrometers apart. These parallel features are known as Planar Deformation Features (PDF) (Fig. 4c) and are arguably one of the most important shock diagnostic features (Langenhorst and Stöffler, 1994; Stöffler et al., 2018) because they occur in many silicate minerals including quartz and feldspars that are so abundant in the Earth´s crust. The PDFs generally occur as one or multiple sets per host grain with the most common crystallographic orientations being $\{10\bar{1}3\}$, $\{10\bar{1}2\}$, $\{10\bar{1}1\}$, (0001), $\{11\bar{2}1\}$, $\{11\bar{2}2\}$, $\{21\bar{3}1\}$, and $\{51\bar{6}1\}$. The PF, FF, and PDF can occur in crater fill deposits, ejected deposits, or in situ in target rock.

Under high pressure conditions, the crystal lattice of minerals can collapse to form diaplectic glass without fusion (Fig. 4d) (e.g., Deutsch et al., 2015). In the ~25 - 45 GPa pressure range, diaplectic glasses from quartz and feldspar can form. High pressure polymorphs, such as coesite and stishovite (polymorphs of SiO_2) (Fig. 4d), result from shock compression but may also crystallize directly from impact melt when the pressure release path passes through the stability field of such polymorphs (Stöffler and Langenhorst, 1994; Langenhorst and Deutsch, 2012; Deutsch et al., 2015). As coesite formation is also known from kimberlites and ultrahigh metamorphic terranes, it is mandatory to carefully screen the geological setting if this mineral can be considered an impact indicator. In recent years the high-pressure polymorph reidite after zircon has also become very important in the analysis of shock metamorphism (e.g., Timms et al., 2017; Cavosie et al., 2018). In so-called shock veins of many different types of meteorites, a range of high-pressure polymorphs after major rock-forming minerals (olivine, pyroxenes, and feldspar minerals) has been discovered and provided essential information on these transformation processes, besides giving much information about possible

phase transitions in Earth´s deep mantle (e.g., Langenhorst and Deutsch, 2012; Deutsch et al., 2015).

Individual target minerals may begin to melt under high shock pressures > 45 GPa and associated post-shock temperatures. At even higher shock pressures/post-shock temperatures, bulk rock melt (impact melt) can be formed, sometimes assisted by shear heating. Impact melt may provide essential geochronological information to determine the age of an impact event or may contain chemical traces from meteoritic components of the projectile (e.g., Koeberl, 2014). When meteoritic components are present in sufficient amount, isotope analysis (Re-Os, Cr, or Ru) may indicate the meteoritic type of the impactor (ibid). For instance, isotopic analysis of ruthenium from K-Pg boundary samples (i.e., sedimentary strata related to the Chicxulub impact event) suggested that the Chicxulub impactor was derived from the impact of a carbonaceous chondrite projectile that had been derived from the outer Solar System (Fischer-Gödde et al., 2024).

Finally, under extremely high temperature and pressure (near to 10^4 °C and 100 GPa), the rocks (impactor and part of the target) may be vaporized (Fig. 3). Because vaporization is a process that depends on several factors (e.g., temperature, pressure, oxidizing-reducing conditions, acid-base features of the melt being evaporized), the vaporization of chemical components occurs selectively (e.g., Parfenova and Yakovlev, 1977). According to these and other authors, the selective vaporization could be responsible for increasing K_2O/Na_2O ratios observed in some impact melt from known impact structures (e.g., Brent, East Clearwater, and Ries) (ibid).

Vaporization processes have also been studied with stable isotope analysis of tektites. Previous work has demonstrated that vaporization may be responsible for the enrichment of heavier isotopes of Zn, Cu, and Sn in tektites (Moynier et al., 2009, 2010; Creech et al., 2019). According to the model proposed by Moynier et al. (2009), the relative isotopic fractionation of Zn, Cu, and Sn is controlled by the diffusivity of these elements. Moreover, isotopic fractionation is also dependent on the time-operation regime, so that the more proximal tektites are less isotopically fractionated for Zn, Cu, and Sn than more distally deposited ones (Moynier et al., 2009, 2010; Creech et al., 2019).

CHAPTER 5

MORPHOLOGY AND MAIN STRUCTURAL ELEMENTS OF IMPACT STRUCTURES

5. MORPHOLOGY AND MAIN STRUCTURAL ELEMENTS OF IMPACT STRUCTURES

Shock deformation features described in the previous section are very important to confirm the impact event. However, depending on the impact energy, only a fraction of the target rock volume is affected by shock metamorphism which is concentrated in the center of the structure and decreases in strength radially outwards (Kenkmann et al., 2014). Most of the target rock volume has no shock deformation, but can show several deformation features dominated by sub-shock pressure mechanisms, such as ductile and brittle deformation which can produce structural elements such as folds and faults (ibid). A brief description of the main structural elements found in impact structures will be presented here. A more comprehensive discussion of structural geology and morphologies of impact structures can be found in Melosh (1989) or Kenkmann et al. (2014).

Morphological and structural diversity depend on impact scale. Small impact structures have simple, bowl-shaped forms, whereas larger impact structures show complex morphological and structural patterns (e.g., Melosh, 1989; Kenkmann et al., 2014; Kenkmann, 2021). Overall, simple impact structures are morphologically bowl-shaped with a raised rim and an inner rim slope that is steepest near the rim and gently decreases toward the crater center. Because they are formed from the direct collapse of the transient crater rim, simple impact structures have few interior topographic features; crater fill consists of a mixture of impact breccias, sometimes interbedded with lenses of impact melt rock or suevite. Due to their small diameter, simple impact structures are rapidly modified by erosion (Melosh, 1989). Despite their susceptibility to rapid degradation, it has been estimated that maybe as many as 250 impact structures with diameters varying from 0.25 to 1 km could still be discovered on Earth (Hergarten and Kenkmann, 2015).

The transition diameter from simple to complex impact structure geometries is approximately inversely proportional to planetary gravity, but it also depends on target rock properties (Melosh, 1989). Previous studies (e.g., Grieve, 1987) suggested that complex impact structures begin to appear with diameters above 2 km in sedimentary targets and above 4 km in crystalline targets. More recent studies (e.g., Osinski et a., 2022), however, suggest that the transition diameter

between simple and complex structures in crystalline targets is more likely in a range of 3.2 to 5 km, whereas in sedimentary targets, complex structures begin to appear at diameters greater than 2.8 km. This is, however, in stark contrast to observation at the BP crater in Libya, which with a diameter of merely 2 km has a well-defined, although small central uplift (Koeberl et al., 2005).

One of the most important differences between simple and complex impact structures is that the latter show a central area of stratigraphic uplift, which, in turn, results from uplift of the base of the transient cavity during the modification stage (Melosh and Ivanov, 1999; Kenkmann et al., 2014). It is important to keep in mind that this uplift is taking place at the same time as collapse of the crater rim. This collapse creates a flow of material into the cavity. As the diameter of the structure increases, the central uplift becomes unstable and collapses under its own weight, resulting in a flow directed downward and outward from the elevation. The interaction between both outward and inward flow can favor the development of various structural features, such as a ring syncline and/or local anticlines, rotated blocks, or even overturned layers, and reverse or thrust faults (Kenkmann, 2002; Kenkmann et al., 2014). Complex impact structures may thus have a central peak or central uplift, a peak ring from the collapse of the over-steepened peak, and multiple ring structures that at even larger diameters may form so-called multi-ring basins (Spudis, 1993).

According to Kenkmman (2002), considering typical diameters from 5 to 15 km, the most common structural features in complex impact structures can be divided into (compare Fig. 5): First order features - a set of features (e.g., crater-rim faults or crater-rim monocline, ring syncline, and central uplift) that trend from the crater rim toward the crater center (Fig. 5). The central uplift commonly has an outer zone of mega-breccias surrounded by steep to vertically arranged layers and folds with steep axes and fault traces. Complex impact structures may show at least three morphological compartments: central uplift, annular basin, and crater-rim zone. Second-order features can be thought of as features developed into the domains of first-order features. For instance: listric normal faults can occur at different positions along the crater rim and extend into the ring syncline; detachments with subtle dip can occur in the crater-rim/ring syncline zones, and apparent thickening of masses, folding, stacking of thrust slices can be present in the intermediate zone between

inward and outward flow (Kenkmann et al., 2014). Because of this diversity of structural features, it is expected that there will be a diversity of topographic features in the inner zone of complex impact structures, naturally also dependent on degree of erosion.

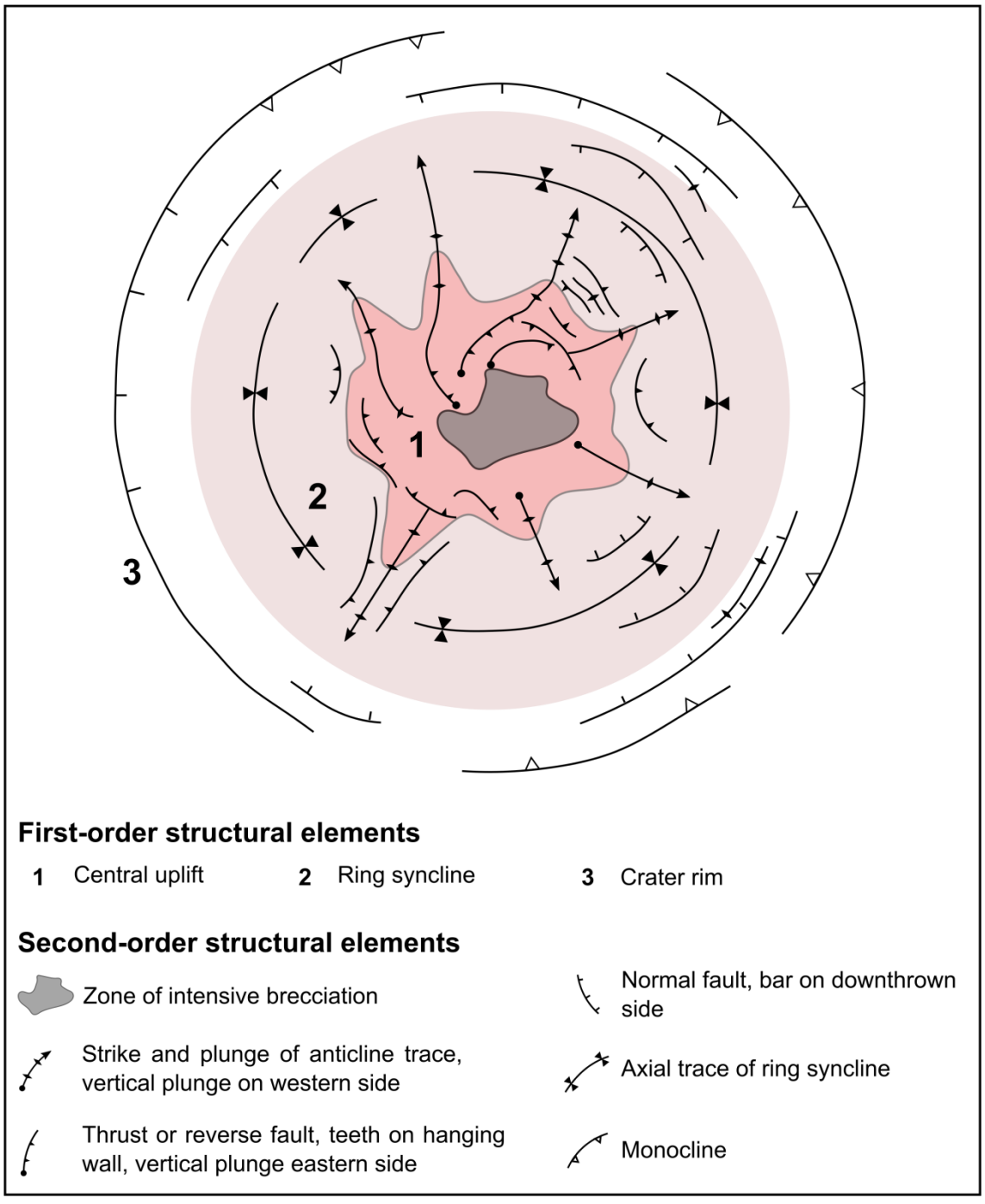

Figure 5: Schematic view of the main structural elements in complex impact structures. Modified after Kenkmann (2002).

CHAPTER 6

MAIN GEOPHYSICAL SIGNATURES OF IMPACT STRUCTURES

6. MAIN GEOPHYSICAL SIGNATURES OF IMPACT STRUCTURES

An impact event results in a huge disturbance of the target rock volume, such that the physical properties of target rocks can also be expected to change (e.g., Morgan and Robolledo–Vieyra, 2013). These changes may create new contrasts between rock masses, which commonly are the source of geophysical signatures in impact structures. Main geophysical signatures of impact structures have been discussed, for example, by Pilkington and Grieve (1992), Grieve and Pilkington (1996), and Morgan and Rebolledo–Vieyra (2013). Gravity and magnetic data have been most commonly used in impact structure studies, mainly due to their relatively low-cost acquisition. Seismic methods have also been used and can yield good results for mapping structural elements, especially in buried impact structures (Stewart, 2003) and stratigraphic sequences. Structural elements and damage zones also can be mapped by using electromagnetic and resistivity methods (Henkel, 1992; Pilkington and Grieve, 1992; Morgan and Rebolledo–Vieyra, 2013), and, more recently, gamma-ray spectrometry data have been used to aid in constructing geological maps of impact structures or to reveal post-impact processes (e.g., hydrothermal alteration, erosion, weathering, etc.) (e.g., Niang et al., 2021 and references therein). Whilst geophysical studies can provide important information about geology and structure of impact settings, these results cannot be applied to confirm the presence of an impact structure by themselves. In any case, ground-truthing, sampling, and subsequent petrographic/geochemical analysis must be carried out (e.g., French and Koeberl, 2010; Reimold and Koeberl, 2014).

6.1 **Gravity studies**

Among the geophysical methods, the gravity (mainly ground-based) method has been commonly used to investigate possible or confirmed impact structures. Several works have reported impact structures commonly associated with negative anomalies in residual Bougher maps (e.g., Sierra Madera, Lake Mien, Gosses Bluff, Iso-Naakkima; Lake Saarijärvi, Shoemaker, Dellen, Keurusselkä, Holleford, and Lake Summanen) (Van Lopik and Geyer, 1963; Henkel, 1992; Milton et al., 1996; Pesonen et al., 1996 and 1998; Pirajno et al., 2003; Henkel et al., 2022; Hietala et al., 2022; Armour et al., 2023;

Hietala et al., 2023, and others). There is a well-known relationship between amplitude of this negative anomaly and impact structure diameter (Pilkington and Grieve, 1992) The decrease in target rock densities driven by fracturing induced by impact events has been pointed out as a main cause of such negative anomalies (Pilkington and Grieve, 1992), but low-density impact breccias and sedimentary crater fill may also contribute to such negative gravity signature (Morgan and Rebolledo–Vieyra, 2013). However, when impact crater diameters are larger than 20 - 30 km, the negative anomaly amplitude tends to reach a limit of ~30 mGal because the fracturing in target rocks tends to become closed due to lithostatic pressures (Grieve and Pesonen, 1992). Moreover, depending on some factors (impact scale, target rock properties, melt production), denser target rock in the crater interior may contrast with less dense rock further out and may produce a central positive anomaly, as has been reported, for example, for Karla, Jebel Waqf as Suwwan, Connolly Basin, Yallalie, and Chesapeake Bay (Pilkington and Grieve, 1992; Quesnel et al., 2022, and references therein). In large impact structures, such as Mjølnir, Chicxulub, and Vredefort, positive Bouguer anomalies can be surrounded by circular negative Bouguer anomalies (Tsikalas, 2005; Pilkington and Grieve, 1992; Morgan and Rebolledo – Vieyra, 2013), but the reverse has also been observed, that is, a circular gravity high surrounding a central gravity low (Vargeão, Vista Alegre, and Cerro do Jarau impact structures) – which has been related to the pre-impact stratigraphic sequence of strata of different densities in the target (e.g., Henkel and Reimold, 1999 – the central positive Bouguer anomaly in the central uplift structure of the Vredefort impact structure was related to relatively denser mid-crustal rock uplifted in the central part of the central uplift). Gravity lows at Vargeão, Vista Alegre, and Cerro do Jarau (Ferreira et al., 2015, 2017; Giacomini et al. 2017; Vasconcelos et al., 2019) have been interpreted to be derived from lesser density and strongly fractured sandstones that outcrop in the central uplifts of these structures. The gravity highs are thought to be derived from the density contrast between a thickened basalt layer and these sandstones (ibid).

Gravity signatures of impact structures may be used to estimate the deficit of mass below the surface (Innes, 1961; Campos-Enriquez et al., 1998; Morgan and Rebolledo–Vieyra, 2013). More recently, gravimetric signatures

have been derived from three-dimensional modeling of the evolution of the morphology of impact craters (Oufella et al., 2024). The preliminary results from such modelling have suggested that, for some cases, the amplitude of the gravity low can become increased as a consequence of erosion and depositional processes (ibid). On the other hand, erosion tends to erase the overall gravity signatures, but the positive Bouguer anomaly might still be detected in eroded complex impact craters, such as most notable in the Vredefort impact structure (Antoine et al., 1992; Henkel and Reimold, 1999; Gibson and Reimold, 2008; see also Plado et al., 1999).

6.2 **Magnetic studies**

The magnetization of rocks in impact events depends on several factors such as composition and physical properties of target rocks, melt and heat production, shock demagnetization/magnetization due to mineral transformations, or hydrothermal activity (e.g., Henkel and Reimold, 2002; Henkel et al., 2022; Cowan and Cooper, 2012). Such factors result in a great variation of magnetic signatures, so that there is no intrinsic magnetic anomaly/anomaly pattern that can be related to different morphotypes of impact structures (ibid; also Gilder et al., 2018). However, a magnetic low with strongly subdued anomaly amplitudes and gradients has been observed in several impact structures, especially for relatively small structures < 10 km diameter (e.g., Lake Saarijärvi, Johnsonville, Lake Karikkoselkä, and Målingen impact structures - Pesonen et al., 1998, 1999; Talwani et al., 2003; Melero-Asensio et al., 2018). This low magnetic pattern can be caused by shock demagnetization, dissociation of Si and Fe in magnetic minerals, or by oxidation of magnetite in the fractured target rocks, promoting a contrast with undeformed/less shocked surrounding terrain (Henkel, 1997; Henkel and Pesonen, 1992; Henkel and Guzman, 1977; Henkel and Reimold, 2002; Gilder et al., 2018). In large/mid-size complex structures (>15-20 km diameter), impact melt or target rock fragments heated in the central uplift sector may acquire remanent magnetization and contribute to the magnetic signal of the central part of a structure, including central uplift (e.g., Dellen, Manicouagan, and Acraman impact structures) (Cowan and Cooper, 2012; Gilder et al., 2018; Henkel et al, 2002). It has been reported that magnetic anomalies derived from remanent

magnetization in impact structures commonly have short-wavelength, high-gradient, and generally highly irregular forms, and can show magnetization which has a different direction from the present geomagnetic field and/or from the expected magnetization of the target rocks (e.g., Suvasvesi, Ries, and Chicxulub impact structures, Pesonen et al., 1996; Gilder et al., 2018, Gulick et al., 2013). However, long wavelength and relatively wide magnetic anomalies in central uplifts can also be related to basement uplifts (e.g., Karla impact structure, Cowan and Cooper, 2012; Quesnel et al., 2022). Additionally, magnetic anomalies of impact structures may have other shapes depending on regional geological context (Hawke, 2003). For instance, in the Glikson and Foelsche structures of Australia, the impact events may have deformed (or even upturned) pre-impact horizontal magnetic layers, causing dip changes and/or thickening of these layers. In this way, the undeformed flat-magnetized layer did not show any magnetic anomaly, but in the impact-induced thicker zones, the magnetic contrast can generate a magnetic anomaly with ring-shape over part of the structure´s rim (Hawke, 2003; Haines and Rawlings, 2002; MacDonald et al., 2005). Hydrothermal activity also may result in concentric magnetic anomalies (e.g., Yallalie and Haughton impact structures - Hawke et al., 2006; Quesnel et al., 2013).

The shapes of magnetic anomalies over impact structures also depend on magnetic latitude and remanent magnetization (Beard, 2012). For example: in the absence of remanent magnetization or when the direction of the remanence vector is similar to the induced magnetization vector, magnetic anomalies in high magnetic latitudes (e.g., inclinations > 60°) are expected to show approximately a bell-shape, with magnetic peak values coinciding with magnetic source center (Reid, 2010; Dentith and Mudge, 2014). At the magnetic equator (inclination < 10°), magnetic anomalies are expected to show a U-shape with positive parts surrounding a minimum value which, in turn, coincides with the magnetic source center (Reid, 2010; Dentith and Mudge, 2014). More complex shapes in magnetic anomalies may occur at mid-latitudes (inclination ~45°) where magnetic anomalies may have a dipole shape, with positive and negative parts.

Even so, in the southern hemisphere, the negative and positive parts are expected to face toward the south and north, respectively, and the opposite

should occur in the northern hemisphere (Jessel, 2002; Reid, 2010; Isles and Rankin, 2013; Dentith and Mudge, 2014). When strong remanence is present and/or depending on the orientation (strike/dip/plunge) of magnetic sources with respect to the orientation of the Earth´s magnetic field, the magnetic anomaly can show asymmetries, such that the expected shape of magnetic anomalies described before may be different (Jessel, 2002; Reid, 2010; Isles and Rankin, 2013). In some cases, these asymmetries can invert the dipoles, making negative and positive parts change their places. Instances of magnetic anomalies in impact structures with such asymmetries include Gosses Bluff (Young, 1972), Chicxulub (Gulick et al., 2013), Manicouagan (Roest and Pilkington, 1993), and Bosumtwi (Plado et al., 2000; Kuzmicheva and Ivanov, 2021).

It is worth noting that in addition to the variation of the form of magnetic anomalies, their amplitudes can be attenuated or even erased by erosion (Plado et al., 1999). Despite all this variety, magnetic anomalies in impact structures often tend to be circular reflecting the magnetization contrasts in crater rim and/or central uplift zones, or remagnetization in central uplift areas (Henkel, 1992). Moreover, circular patterns of magnetic anomalies that disrupt a regional pattern may be considered good targets for impact structure research (Pilkington and Grieve, 1992; Morgan and Rebolledo-Veyra, 2013).

6.3 **Application of seismic methods**

Impact events can also induce contrast in acoustic impedance (which can be thought of as resistance that a rock shows against seismic wave propagation) (e.g., Dentith and Mudge, 2014), such that this contrast can be detected by seismic methods. Depending on the elastic properties of rocks (e.g., density, elastic moduli, shear modulus, etc), a seismic wave (e.g., P-wave) propagating into two rock layers with different acoustic impedance will be partitioned into refracted and reflected waves at the interface of two layers (Kearey et al., 2002; Dentith and Mudge, 2014). In this way, the seismic method can be divided into refraction and reflection seismic methods (Kearey et al., 2002; Dentith and Mudge, 2014). The former can provide a velocity structure of the subsurface, whereas the latter can provide an image of the subsurface structure (Kearey et al., 2002; Dentith and Mudge, 2014).

Acoustic impedance depends on the density of the material, and this density, in turn, is influenced by the amount of pores or fracturing (Kearey et al., 2002). As an impact event induces a reduction of the density of target rock by brecciation and fracture (Pilkington and Grieve, 1992; Morgan and Rebolledo-Vieyra, 2013), a corresponding reduction in seismic velocity has been observed in refraction seismic data for impact structures (e.g., Barringer, Lake Saarijärvi, and Middlesboro impact structures - Ackermann et al., 1975; Pesonen et al., 1998; Wihanto and Kenkmann, 2023). As these low-velocity zones can be due to brecciated materials, crater fill sediments, or rock fracture, refraction seismic data can be used to delineate the depth and horizontal extent of such geologic units (Pilkington and Grieve, 1992; Morgan and Rebolledo, 2013). On the other hand, high velocity zones have also been observed, especially in large impact structures. For instance, in velocity models proposed for 160-180 km sized Chicxulub, the structural uplift shows high velocity zones (~6.3 - 6.4 km/s) that can be observed at 4.5 - 5.0 km depth over 35 - 40 km width (Gulick et al., 2013 and references therein). According to them, these high velocity zones can be related to an upwarped Moho. Similarly, high velocity zones probably due to uplifted lower crustal basement also have been reported in the Vredefort Dome impact structure (Green and Chetty, 1990). Even in relatively smaller impact structures (diameter < 20 km), high velocity zones in the central uplifts can be related to brecciated bedrock (e.g., El'gygytgyn impact structure, Gebhardt et al., 2013) or to inverted stratigraphy of a slump block (e.g., Steen River, Hladiuk et al., 2002). In some cases, first and second order structural elements (e.g., uplifted rim, slump blocks, collapsed disrupted cavity edge, central uplift, and overturned layers) can be identified from refraction seismic data (e.g., Steen River, ibid).

Although refraction seismic data can provide information about structural elements in impact structures, the reflection seismic method commonly provides a more detailed structural mapping tool, allowing identifying several aspects related to crater geometry (Pilkington and Grieve, 1992; Morgan and Rebolledo, 2013). Reflectors related to thrust faulting, down-faulting, and/or loss of coherence of seismic energy in impact-induced chaotically disrupted zones are some features that can be observed in the central uplift of complex impact structures (e.g., Woodleigh, Montagnais, Chicxulub, Siljan impact structures -

Juhlin and Pedersen, 1987; Pilkington and Grieve, 1992; Morgan et al., 2000; Glikson and Uysal, 2013; Gulick et al., 2013). When good marker seismic horizons are present in the seismic section, the base of the disrupted zone in the central uplift is marked by reappearance of undisturbed reflectors and then the amount of structural uplift can be estimated (e.g., Red Wing Creek and Siljan impact structures - Juhlin and Pedersen, 1987; Pilkington and Grieve, 1992). Moreover, if there is clear termination of good marker seismic horizons toward the center, the coherent and incoherent transition can provide an approximate measure of the extension of the transient cavity (e.g., Siljan or Vredefort - Juhlin and Pedersen, 1987; Henkel and Reimold, 1998). In the Chicxulub impact structure, the top of the impact melt sheet has been mapped as a low-frequency reflector, whereas its borders show high velocity zones strongly correlated with low-frequency reflectors (Gulick et al., 2013). Gulick et al. (2013) used these results to estimate the horizontal dimensions of the impact melt sheet in this structure.

The central uplift also can show other reflection patterns. In the Manson impact structure, the contact zones between the central peak of uplifted Proterozoic crystalline rocks and younger sedimentary rocks have been characterized by a pronounced double reflector pattern (Anderson and Hartung, 1991). Similarly, strong pairs of reflections were reported in the central uplift of the Siljan impact structure, although several diffraction effects may have obstructed seismic sections in this case (Juhlin and Pedersen, 1987). In the Ries impact structure, higher-amplitude reflections (named facies B) have been interpreted as being derived from melt-rich suevite deposits (McCall et al., 2024). Some reflections show truncations and narrowing within facies B, which has been interpreted as indicating multiple directions of suevite emplacement in the inner basin (ibid).

Seismic markers also can be used to interpret processes related to the modification stage in cases of complex impact structures (e.g., extension within the ring syncline and inward collapse of the crater rim - Glikson and Uysal, 2013; Osinski et al., 2022). As materials are mildly deformed in annular basin or outer rim region settings, the seismic marker horizons in these regions can be well-traced, allowing to identify dipping reflectors which can be used to estimate the morphology of peak ring craters (e.g., Chicxulub - Morgan et al., 2000;

Gulick et al., 2013), diameters (e.g., Sudbury and Red Wing Creek - Moon and Jiao, 1998; Pilkington and Grieve, 1992), or morphology asymmetries (e.g. Mjølnir - Tsikalas, 2005).

Finally, seismic data can play an essential role in mapping buried impact structures. When excellent three-dimensional tomographic seismic images are available but rock specimens are not, Steward (2003) proposed to discuss that geometrical characterizations (e.g., craterform, central peak within crater, overturned peripheral strata, etc) could identify an impact structure in three dimensional seismic data with high resolution. In fact, three (or even two) dimensional seismic data did provide excellent buried targets possibly formed by impact such as: Praia Grande (Correia et al., 2005), Silverpit (Stewart and Allen, 2002), and, most recently, an alleged Nadir Crater (Nicholson et al., 2022). Then, there is still the Saqqar structure as well, a 34 km-diameter circular subsurface structure that was identified based on a 2-D reflection seismic profile and magnetic and gravity data (Kenkmann et al., 2015). Bona fide shock features proving an impact origin have not been reported for three of these targets yet, only from drill core studies of Saqqar (Kenkmann et al., 2015).

6.4 **Gamma-ray spectrometry**

Gamma-ray spectrometry data allow to measure gamma-ray intensity naturally occurring at the Earth's surface. This method estimates percent of total potassium (%K), and part per million of equivalent thorium (eTh) and uranium (eU) concentrations, and total counts in wide areas (Dentith and Mudge, 2014; Killeen et al., 2015). Similar to magnetic signatures, there are no specific gamma-ray spectrometry signatures for impact structures because such signatures depend on several factors. Compared to other geophysical methods (e.g., gravity, magnetic, seismic), there are relatively few studies in which gamma-ray spectrometry has been used in impact structure research.

The most complete study about airborne gamma-ray spectrometry on impact structures was carried out by Niang et al. (2021, and references therein). They proposed that impact-induced K volatilization, impact melt differentiation, hydrothermal alteration, structural deformation, and post-impact alteration (including erosion and weathering) could be main factors to affect the K, eTh, and eU distributions over actual or suspected impact structures. In a given

impact structure, such factors can play an important role, to increase or decrease K, eTh, and/or eU values. This, coupled with differential erosion, may result in the development of complete or partially circular features (Niang et al., 2021 and 2022). In fact, concentric and/or circular airborne gamma-ray spectrometry signatures have been reported for Lawn Hill and Mount Toondina (Niang et al., 2022), Strangways (Zumsprekel and Bischoff, 2005), Shoemaker (Pirajno et al., 2003), Serra da Cangalha (Vasconcelos et al., 2012; Silva et al., 2024), Riachão Ring (Maziviero et al., 2013), and Araguainha (Leite et al., 2022). These examples show that circular radiometric signatures that disrupt a regional pattern may be good indicators of potential targets for impact structure research.

The utility of ground-based gamma-ray spectrometry data has been exemplified by previous works (e.g., Vasconcelos et al., 2012; Leite et al., 2022; Niang et al., 2022; Garcia et al., 2024). In Araguainha, Cerro Jarau, and Serra da Cangalha impact structures, K-rich zones have been interpreted as indications of element remobilization processes or hydrothermal alterations. However, no petrographic evidence supporting these hypotheses has been reported yet. In Bosumtwi, K-rich zones in the crater rim and in outer ejecta are thought to be derived from current erosion of metasedimentary substrate and impact breccias, whereas K-poor areas (in the annular moat of this impact structure) represent metasedimentary rocks, from which K was leached by fluids (Niang et al., 2022).

Gamma-ray data acquired in wells may be useful to identify markers related to induced-impact widespread events. For instance, Mercher and Schultz (1997) argued that dark grey laminated dolomudstone layers in the Ames impact structure contain unusual detrital quartz particles, with some quartz grains showing supposed shock lamellae (PDFs) and siliceous particles representing former lechatelierite. These layers also contain basement-derived potassium feldspar which is regarded the source of gamma-ray signatures. As this signature has a regional significance and considering stratigraphic and regional geological aspects (e.g., a sharp erosion boundary, basement fragments, faunal extinctions, and other), Mercher and Schultz (1997) suggested these sedimentary rocks in the gamma-ray marker interval

correspond in part to tsunami deposits associated with the impact event that formed the Ames impact structure.

6.5 **Electromagnetic (EM) and Electroresistivity (ER) data**

Other geophysical methods sensitive to electrical properties of materials also have been useful in impact studies. Electrical and electromagnetic methods have been used to estimate the ease (i.e., conductivity) or difficulty (i.e., resistivity) with which an electrical current may flow at the subsurface (Dentith and Mudge, 2014). In short, resistivity measurements in the electroresistivity (ER) method are estimated from the potential difference recorded in electrodes placed in the ground, whereas in the electromagnetic (EM) method, conductivity is estimated from the recording of the electromagnetic field induced in coils (Dentith and Mudge, 2014). Despite of their similarities regarding the physical parameters measured (i.e. electrical properties), EM methods respond to the distribution of absolute conductivity in the ground and the dimension of this distribution, such that EM surveys are more sensitive to map conductive targets. The ER methods, on the other hand, tend to work well in regions where the electrical current flow is inhibited, such that a lateral or vertical contrast in electrical properties can be mapped (e.g., Henkel, 1992; Kearey et al., 2002; Dentith and Mudge, 2014). As electrical properties respond primarily to porosity and pore space rather than mineral composition, and considering that impact events induce brecciation and fracturing in target rocks, the porosities of impact breccias and fractured rocks can increase electric conductivity (or decrease resistivity) in impact structures, such that these damaged materials can potentially be mapped by EM and ER methods (Pilkington and Grieve, 1992; Henkel and Pesonen, 1992; Henkel, 1992; Morgan and Rebolledo-Vieyra, 2012). However, the central uplifts in large impact structures can contain a central portion of normal or relatively higher resistivity (e.g., Siljan impact structure - Henkel, 1992). It must also be observed that considerable flow of hot fluids may be induced by impact events, so that initial pore space may become recemented (e.g., resilicified) thereafter (e.g., observed widely in the interior of Nova Colinas, this work).

In EM methods, electromagnetic waves are attenuated as they travel into the ground (skin effect - Kearey et al., 2002; Dentith and Mudge, 2014).

Effective depth of penetration of electromagnetic waves is inversely dependent on frequency of the electromagnetic field and the conductivity of the ground. Higher frequencies provide good resolution but are confined to shallow depths due to strong attenuation. On the other hand, lower frequencies provide information from deeper layers but with lower resolution (Kearey et al., 2002; Dentith and Mudge, 2014). The possibility of adjusting the frequency of the electromagnetic wave to investigate a desired depth range in any particular medium allows EM to be applied with different variants such as Very Low Frequency (VLF), Time-Domain Electromagnetic (TDEM), and Ground-Penetrating Radar (GPR) surveys (Kearey et al., 2002; Dentith and Mudge, 2014).

In impact structure studies, GPR surveys have been more utilized in relatively small impact craters, mainly simple impact structures (Pilkington and Grieve, 1992; Grant et al., 1997). This method is sensitive to dielectric properties, which means it is strongly influenced by water within pore space (Pilkington and Grieve, 1992). The contrast of dielectric properties generates reflections of electromagnetic waves, such that the interpretation of GPR images shows similarities with seismic sections. In Kamil crater, Egypt, GPR investigations were useful to map the crater floor, transient cavity, and breccia lenses (Urbini et al., 2012).

Very low frequency (VLF) techniques also have been useful in impact crater studies. An excellent characterization of geophysical signatures in terms of electrical properties was given by Henkel (1992), who investigated three impact structures (Björkö, Siljan, and Dellen) by VLF (airborne and/or ground-based) and in-situ resistivity measurements. He highlighted that i) the entire Björkö central uplift is dominated by low bedrock resistivities and the resulting resistivities for brecciated rocks are as low as 500 ohm m, whereas undeformed crystalline rocks show values around 15,000 ohm m. ii) The airborne VLF survey of the Siljan impact structure showed closely spaced fracture zones with smaller resistivity contrast than found in the surrounding region. According to Henkel (1992), this low contrast is because these fractures occur within a brecciated rock mass (see also Henkel and Aaro, 2005). iii) At the ca. 20 km wide Dellen impact structure, from the outer rim along a 16 km inward profile, resistivity drops to the lowest values around 100 ohm m, which was interpreted

to represent electrical properties of breccias. Near the central region, the resistivities are slightly higher (200 ohm m), probably because they reflect the upper part of the impact melt sheet (Dellenite). Besides Björkö, Siljan, and Dellen, low resistivity has also been reported from other impact structures, such as Lake Summanen (Hietala et al., 2020), Lake Karikkoselkä (Pesonen et al., 1999b), and from the northeastern and southern parts of the granitic core of the Araguainha central uplift (Tong et al., 2010). In this latter case, Tong et al. (2010) also mapped high-resistivity blocks near the granitic inner core - metasedimentary outer core boundary (in the central uplift), which they interpreted as representing possible occurrences of impact melt rock .

Another variant of EM methodology is known as Magnetotellurics (MT). Differently from the aforementioned EM variant, where the frequency can be tuned, the electrical currents (also called telluric currents) measured in MT are naturally induced by electromagnetic waves (magnetotelluric fields). These, in turn, are believed to result from the flow of charged particles in the ionosphere, as fluctuations in the magnetotelluric fields correlate with diurnal variations in the geomagnetic field caused by solar emissions (Kearey et al., 2002). These waves travel toward the Earth's surface and penetrate into the ground, where they are able to reach great depths (Kearey et al., 2002). In MT surveys, telluric currents and their associated magnetic fields can be used to compute an apparent resistivity. As frequency is the inverse of period and, considering electromagnetic waves tend to be attenuated with increase of depth, large depth can only be investigated over long periods of time (i.e., with extremely low frequencies). Resulting MT data consist of temporal series, where after applying some corrections, an apparent resistivity curve can be produced in function of the periods. Short periods provide information for the shallowest electrical layers, whereas long periods provide information for deeper electric layers.

Regarding the application of the MT method in the study of impact craters, Masero et al. (1994) identified a rapid increase of the basement depth inside an area around the center of the Araguainha impact structure at a radius of 9 km from the structure´s center. Outside of this 9 km area, the basement lies, on average, at a depth of 1000 m. Still in Araguainha, the central region can be modeled as a disk-shaped zone that exhibited resistivities (20 - 500 ohm m) significantly below the bulk resistivity of the surrounding basement rocks of

the upper crust. This zone was interpreted to result from impact-induced fracturing (ibid). The authors also identified an anomalous anisotropic layer in the lower crust (at 15-30 km depth in the Araguainha region. Although the origin of this layer is unclear, the Transbrasiliano Lineament has been proposed for the origin of this lower crustal anomaly (ibid).

As at the Araguainha impact structure, impact-induced low resistivity zones were reported from central Siljan (Zhang et al., 1988; Henkel and Aaro, 2005) and at the Serra da Cangalha (Adepelumi et al., 2005) impact structures. A decrease in apparent resistivity was also reported at the Santa Marta impact structure (Ferreira et al., 2019), but it remained unclear whether these latter results can be related to the impact.

6.6 **Petrophysical studies**

Petrophysics measurements (e.g., density, magnetic susceptibility, conductivity, porosity, permeability, P-wave velocity, thermal conductivity, and others) play an essential role in the interpretation of the geophysical anomalies determined by the methods discussed in the previous subsections, and can be used to constrain geophysical or numerical modelling (Morgan and Rebolledo, 2013; Popov et al., 2014; Le Ber et al., 2022). As described throughout this chapter, an impact event produces brecciation and fracturing in the target rock, increasing its porosity and affecting its physical properties. For instance, an increase in porosity may lead to a decrease in density that is the main contributor for low gravity in impact structures. In crystalline targets, unaffected rocks commonly show higher densities than impact breccias (e.g., Mien, Dellen, Lappajärvi, Jänisjärvi, Karikkoselkä, and Målingen impact structures - Henkel, 1992; Pesonen et al., 2012; Melero-Asensio et al., 2018). Similarly, the resistivity of impact breccias is also reduced compared to surrounding terrain because the pore space can be filled by fluid, which leads to a decrease in resistivity (e.g., Björkö, Siljan, and Dellen impact structures - Henkel, 1992).

Regarding magnetic susceptibility, impact melt, impact melt-bearing breccias (suevites), brecciated basement rocks, or post-impact new magnetic carrier phases can show high magnetic suscetibilities (Henkel and Reimold, 2002). Some examples include: melt-rich suevites in the Chesapeake Bay and Bosumtwi impact structures (Plado et al., 2000; Elbra et al., 2009), impact melt

rocks of the Mien and Dellen impact structures (Henkel, 1992), and impact melt rock (Granophyre) of the Vredefort impact structure (Henkel and Reimold, 2002; Salminen et al., 2009).

In some cases, the acquired magnetization in such lithotypes may record the environmental magnetic field, thus acquiring a remanent magnetization (Henkel, 1997; Henkel and Reimold, 2002; Gilder et al., 2018). The intensity of this remanent magnetization may be higher than induced magnetization, such that the Koenigsberger ratio (Q) (i.e., the ratio between remanent and induced magnetizations) is greater than one for impactites with remanent magnetization (e.g., impact melt rocks of Mien and Dellen impact structures - Henkel, 1992; or at Vredefort: Salminen et al., 2009 and references therein). Moreover, by applying paleomagnetism techniques, it is possible to recover the Characteristic Remanent Magnetization (ChRM) (i.e., the most stable primary magnetization acquired by rock during its formation), which can provide valuable information about Earth's magnetic field at that time (Lower, 2007). Such information can be used to provide data for paleoreconstructions of continental drifts (e.g., Salminen et al., 2009; Yokoyama et al., 2014). Additionally, paleomagnetic data from impact structures can also provide a constraint of the age of the impact event. For instance: Yokoyama et al. (2014) revealed that magnetite and hematite from granites and impact melt rock in the Araguainha impact structure carried a ChRM with normal polarity. The author noted that normal polarity of Earth's magnetic field was predominant in a short interval between 252 and 256 Ma, whereas the Permo-Carboniferous Reversed Superchron which reversed normal polarity of the Earth's magnetic field ended at 269 Ma. Since these magnetic carriers (magnetite and hematite) were formed instantly at the beginning of the cratering process, their magnetization direction could be used to constrain the age of the Araguainha impact event to < 256 Ma (Yokoyama et al., 2014). Since then, the age of this impact event has been constrained by different geochronological methods to 254-259 Ma (Tohver et al., 2012; Erickson et al., 2017; Hauser et al., 2019).

CHAPTER 7

SPACEBORNE IMAGERY OF IMPACT STRUCTURES

7. SPACEBORNE IMAGERY OF IMPACT STRUCTURES

The basic principle of generating spaceborne images involves the detection of electromagnetic waves that arrive in instruments onboard artificial satellites after these waves interact with terrestrial materials (e.g., rocks or surfaces – Goetz and Rowan, 1981; Wright et al., 2012; Bishop, 2019). The present work will focus on images derived from multispectral optical and Synthetic Aperture Radar (SAR) instruments.

Multispectral instruments are passive systems that record the radiation reflected by or emitted from Earth's surfaces (Goetz and Rowan, 1981; Meneses, 2012). Because the solar radiation incident on Earth can be absorbed by some mineral constituents in specific regions of the electromagnetic spectrum (commonly from visible to short-wave infrared), the reflected radiation that is recorded with multispectral instruments, and that can be represented by images, can provide information about the composition of terrestrial materials (Goetz and Rowan, 1981; Meneses, 2012; Rossman and Ehlmann, 2015). For instance: ferric minerals can show absorption features (that is, a drop in radiation recorded) in the visible regions, whereas OH-bearing minerals, such as several types of phyllosilicates, commonly show absorption features in short-wave infrared regions (Hunt, 1977, 1979; Rossman and Ehlmann, 2015; Bishop, 2019).

Synthetic Aperture Radar (SAR) instruments are active systems based on Radio Detection and Ranging (RADAR), in which electromagnetic waves are transmitted toward the Earth's surface, interact with terrestrial material, and then their echos (or backscattering) are recorded by receivers that also make up SAR instruments (Meneses and Sano, 2012; van Zyl et al., 2015). In a conventional RADAR system, higher resolution images commonly require a large antenna transmitter for a given wavelength, whereas in a SAR system, a sequence of acquisitions from a shorter antenna are combined to simulate a much larger antenna, thus providing higher resolution data (van Zyl et al., 2015). SAR images can offer important information about surface roughness or dielectric properties of terrestrial materials (Meneses and Sano, 2012). Moreover, electromagnetic waves transmitted/received by SAR instruments commonly are linearly polarized, that is, they can be vertically transmitted/received (VV); horizontally transmitted/received (HH); vertically

transmitted and horizontally received (VH); or horizontally transmitted and vertically received (HV). By analyzing the strength of these different polarizations, information about the structure of the surface image can be obtained (Meneses and Sano, 2012; van Zyl et al., 2015).

In the context of terrestrial impact structure mapping, multispectral and SAR images can be useful for different purposes, mainly to study confirmed impact structures (e.g., Garvin et al., 1992; Wright et al., 2013; Dunster et al., 2014; Gottwald et al., 2021) or investigate circular targets potentially formed by impact (e.g., Emmanuel et al., 2023; Theilen - Willige, 2023; Navee et al., 2024).

When studying confirmed impact structures, multispectral and SAR images can offer a plan view, allowing identifying the circular characteristics of the structure as a whole. For instance: several impact structures (e.g., Meteor Crater, Deep Bay, Clearwater Lakes, Manicouagan, Lonar, Oasis, Vredefort, Spider, Acraman, Gosses Bluff) listed in the Astronaut's Guide to Terrestrial Impact Craters (Grieve et al., 1988) and all confirmed Brazilian impact structures (Crósta et al., 2019, Reimold et al., 2022) show circular patterns that often disrupt a pre-existing regional pattern. In fact, multispectral and SAR (or derived products such as a Digital Elevation Model - DEM) images have been useful to identify first order (e.g., crater-rim faults or crater-rim monocline, ring syncline, and central uplift) or second order (e.g., listric normal faults, folds and thrusts, etc) structural elements in complex impact structures, including Araguainha (e.g., Theilen - Willige, 1982, 1987; Lana et al., 2008), Gosses Bluff (Abels et al., 2005; Dunster et al., 2014); Serra da Cangalha (Almeida-Filho et al., 2005; Reimold et al., 2006; Silva et al., 2024), BP and Oasis (McHone et al., 2002; Koeberl et al., 2005; van Gasselt et al., 2017), Spider (McHone et al., 2002); Bosumtwi (Theilen - Willige, 2021); and Manicouagan (Smith et al., 1999). Even in simple impact structures, for example at the Talemzane impact structure (Algeria), high spatial resolution Digital Terrain Model imagery derived from modern instruments (e.g., TanDEM-X) has allowed the mapping of detailed features, such as ravines and small drainage channels terminating in the crater interior (Gottwald et al., 2021).

Spaceborne images also can be used to derive topographic parameters (e.g., elevation, slope, hillshade) that can be useful to highlight

geomorphological aspects (e.g., elevated rim, central uplift, bowl-shaped depression, etc) of impact structures (Emmanuel et al., 2023). When impact structures are well-preserved, topographic and other parameters derived from spaceborne images can be used as object attributes to train machine learning algorithms to explore undiscovered terrestrial impact craters (ibid). However, such approaches may yield limited results in strongly vegetated areas or where impact structures are severely eroded.

In hot desert regions, such as the Sahara Desert of Africa, SAR images can be useful in mapping confirmed or candidate impact structures. Depending on water content in the sands, the electromagnetic wave emitted by SAR instruments can penetrate into the ground and aid to estimate crater diameter or define associated features, like ejecta deposits, or impact-generated fracture zones (e.g., Aorounga, BP, and Roter Kamm - McHone et al., 1996, 2002). On the other hand, flat-surface trench zones (e.g., Spider impact structure) or fine-grained sediments of post-impact crater fill (e.g., Connolly Basin crater) may decrease the backscattering on SAR images (McHone et al., 2002). Moreover, by analyzing the strength of backscattering on each polarimetric component, van Gasselt et al. (2017) attempted to distinguish bed rock from unconsolidated cover strata in the Oasis impact structure.

Spectral signatures of target rocks also can be used for geological mapping in impact structures. At Meteor Crater, Ramsey (2002) demonstrated that image-derived spectra from thermal infrared multispectral scanner (TIMS) instruments can be used to map ejecta distribution patterns. In a similar way, Tornabene et al. (2005) used several remote sensing techniques (e.g., minimum noise fraction transformation, band rationing, decorrelation stretching, image-derived spectra by Pure Pixel Index, etc) applied to ETM+ and ASTER scenes, and their results show several geological units can be mapped in Canada´s Haughton impact structure, including polymict breccia composed predominantly of carbonate with a quartz-rich component.

Analysis of spectra in the visible - near-infrared (~380 – 2500 nm) and thermal infrared (3 - 14 µm) regions of experimentally shocked minerals/rocks (e.g. albite, anorthite, labradorite/basalts and andesites) (e.g. Bruckenthal and Pieters, 1984; Johnson et al., 2003, 2007) or naturally shocked samples from terrestrial impact structures (e.g., basalts and impact melt from Lonar impact

crater, vein-forming hydrothermal alteration from Vargeão Dome and Vista Alegre impact structures - Wright et al., 2004, 2006; Dieperink et al., 2024) have also been studied. These works demonstrated an overall degradation in the spectral detail and position of absorption features with increasing shock pressure, mainly in the thermal infrared region (e.g., Bruckenthal and Pieters, 1984; Williams and Jeanloz, 1988; Johnson et al., 2003, 2007; Johnson and Christensen, 2004; Wright et al., 2006).

In the thermal infrared region (3 - 14 μm), as shock pressure increases, the mutual existence of crystalline and amorphous phases and proportions of diaplectic glass in feldspar weaken the tetrahedral coordination bonds of Si and Al, depolymerizing octahedral coordination, such that the typical spectral absorption features of unshocked feldspar coalescence into two broad bands (Williams and Jeanloz, 1988; Johnson et al., 2003, 2007). In the visible - near-infrared regions, experimentally shocked albite and anorthite rich rocks revealed an overall decrease of reflectance values resulting from greater internal scattering as the proportion of fractured and disaggregated crystals increases with pressure (Johnson and Hörz, 2003). However, increases of reflectance in the pressure range from 22 to 28 GPa (for anorthosite) and 28 to 35 GPa (for albite) can occur due to diaplectic glass formation (ibid).

The spectral changes can be used to infer or map shocked material in surface-near materials on other terrestrial bodies. Johnson and Christensen (2004) reported that the ST2 Martian surface and impact glass from Lonar Crater had a similar thermal infrared spectral signature, suggesting that impact glass might be present on ST2. In a similar context, Dieperink et al. (2024) collected short wave infrared spectra from vein-forming hydrothermal alteration in the Vista Alegre and Vargeão Dome impact structures, and they used a machine learning approach (decision tree) to map the spatial distribution of minerals in Martian craters. They found that some mineral types observed in the white veins at Vargeão Dome could be present in the Martian Toro crater.

All the examples listed in this subsection demonstrate that the use of spaceborne images can play an important role in the mapping and interpretation of terrestrial and other impact structures.

CHAPTER 8

GEOLOGICAL SETTING OF BRAZILIAN IMPACT STRUCTURES

8. GEOLOGICAL SETTING OF BRAZILIAN IMPACT STRUCTURES

To date eight impact structures have been confirmed in Brazil through the identification of bona fide shock deformation features (Fig. 6). These eight impact structures are Araguainha Dome (AGD), Cerro do Jarau (CJU), Vista Alegre (VTA), Vergeão Dome (VGD), Serra da Cangalha (SdC), Riachão Ring (RR), Nova Colinas (NVC), and Santa Marta (SM). Another circular structure referred as São Miguel do Tapuio (SMT) is not officially listed as a confirmed impact structure yet, but as evidence for an impact origin has been published already in abstract form (e.g., Crósta et al., 2019c), this structure is considered of impact origin here as well.

The confirmed Brazilian impact structures are located in Paleozoic intracratonic sedimentary basins (Fig. 6), with five impact structures known in the Parnaíba (formerly called Maranhão) Basin and four in the Paraná Basin (Fig. 6). The origin of the Parnaíba and Paraná basins can be attributed to thermal contraction of the lithosphere, which triggered extensional processes that, turn in, reactivated ancient brittle structures commonly inherited from the Brazilian cycle (i.e., a set of transcontinental suture zones that is characterized by a system of NE-SW strike-slip faults collectively known as the Transbrasilian Lineament – Schobbenhaus et al., 1975; Brito-Neves et al., 2014) (Fig. 6). These zones formed a set of rift basins that would later become aborted and suffered slow thermal subsidence and isostatic adjustment (e.g., Brito Neves et al., 1984; Milani and Thomas- Filho, 2000; Brito Neves, 2002). The basement to both the Paraná and Parnaíba basins is formed by parts of cratonic blocks, but materials from the Brasiliano orogenic belts and syn-Brasiliano blocks are also present, mainly at the margins of these basins which commonly are delimited by structural arches and lineaments (Brito Neves et al., 1984; Silva et al., 2003; Mantovani and Brito Neves, 2009; Daly et al., 2014; Castro et al., 2016; Soares et al., 2018).

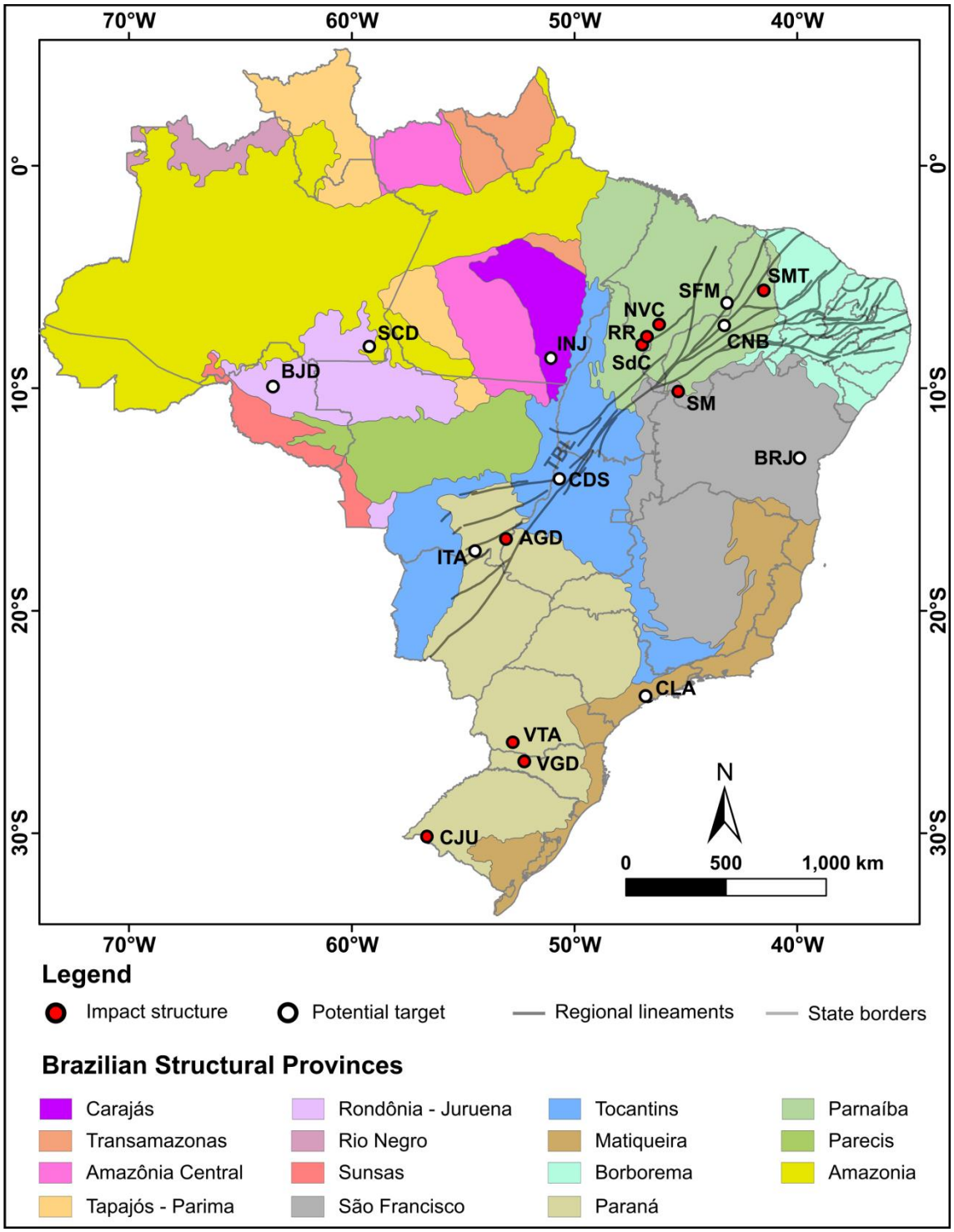

Figure 6: Locations of confirmed Brazilian impact structures and potential targets within the Brazilian structural provinces (provinces after Santos, 2003). TBL = Transbrasiliano Lineament. Abrreviations: AGD – Araguainha Dome; CJU – Cerro do Jarau; VGD – Vargeão Dome; VTA – Vista Alegre; SdC – Serra da Cangalha; RR – Riachão Ring; NVC – Nova Colinas; SM – Santa Marta; - SMT – São Miguel do Tapuio; ITA – Itiquira; CDS – Cardoso; CNB – Caraíbas; SFM – São Francisco do Maranhão; CLA – Colônia; BRJ – Brejões; INJ – Inajáh; SCD – Sucunduri Dome; BJD – Bom Jardim.

The sedimentary records of the Parnaíba and Paraná basins have been studied in terms of sedimentary sequences (or supersequences) (Milani and Zalán, 1999). These sedimentary sequences were formed by major tectono-sedimentary cycles (e.g., late Palaeozoic Gondwana glaciation, opening of the equatorial and South Atlantic Ocean, etc), and they are separated from each other by inter-regional unconformities (Silva et al., 2003; Milani and Zalán, 1999). The stratigraphic column of the Paraná Basin has six supersequences (namely the Ordovician - Silurian Rio Ivaí, Permian - Devonian Paraná, Carboniferous - Early Triassic Gondwana I, Middle to Upper Triassic Gondwana II, Jurassic - Early Cretaceous Gondwana III, and Middle to Lower Bauru), of which three correspond to Paleozoic transgressive-regressive cycles and the remaining supersequences represent Mesozoic continental deposits with associated igneous rocks (Milani and Zalán, 1999; Milani and Thomas-Filho, 2000). Tthe stratigraphic of the Parnaíba Basin is represented by five sequences (Silurian, Mesodevonian – Eocarboniferous, Neocarbonifera – Eotriassica, Jurassic, and Cretaceous) (after Vaz et al., 2007), with the first three related to Paleozoic transgressive-regressive cycles and the latter two to Mesozoic continental deposits including igneous rocks (Góis and Feijó, 1994; Vaz et al., 2007).

8.1 **Impact structures of the Paraná Basin**

In the Paraná basin, four impact structures have been confirmed: Araguainha Dome (AGD), Cerro do Jarau (CJU), Vargeão Dome (VGD), and Vista Alegre (VTA). In the AGD, the impact event affected lithotypes of the first three Paraná Basin supersequences, whereas the impacts of the remaining structures (VGD, VTA, and CJU) affected essentially only Bauru Group strata (Crósta et al., 2019a, 2024).

8.1.1 Araguainha impact structure (AGD)

The Araguainha Dome (AGD) is centered at 16°48’45’’S and 52°59’02’’W, near the Goiás and Mato Grosso state border, in Central-Western Brazil (Fig. 7). The diameter of the structure is estimated at 40 km, such that it is the largest impact structure currently known in South America (Crósta et al., 2019a; Crósta, 2024, Bernardes et al., 2025). Initially, the AGD impact structure

was regarded as an alkaline intrusion, but after several shock deformation and impact-characteristic structural features had been reported (e.g., Dietz and French, 1973; Theilen-Willige, 1982; Engelhardt et al., 1985; Engelhardt et al., 1992; Crósta et al., 1981; Lana et al. 2008; and others), origin by impact became widely accepted.

The geological map of the AGD impact structure has been the subject of several revisions (e.g., Correia Filho et al., 1981; Crósta, 1982). In the most recent geological map proposed by Sousa et al. (2024) (Fig. 7), the basement of the AGD structure is represented by Neoproterozoic - Cambrian Serra Negra Suite porphyritic alkali granite and Cuiabá Group metasediments, which includes phyllites, metasandstones, and schists at the base and a cover of diamictites (Puga Formation) and carbonates (Araras Group) at the top (Lacerda-Filho et al., 2007; Sousa et al., 2024). In addition to the basement, the rocks of the Paraná Basin affected by the impact include: Ordovician Rio Ivaí Group sandstones, diamictites, and conglomerate; as well as the Furnas and Ponta Grossa formation sandstones and pelites; both these latter formations are grouped into the Devonian Paraná Group; Carboniferous sandstones of the Aquidauana Formation (Tubarão Group); and Permian Passa Dois Group rocks which include shales and limestones with minor evaporites (Irati Formation) and clayey siltstone, and massive or laminated siltstone and shale (Corumbataí Formation) (Milani and Zalán, 1999; Silva et al., 2003; Horn et al., 2022; Sousa et al., 2024). Polymict impact breccia deposits (referred as the Araguainha unit) were emplaced on the top of the Permian sequence (Lacerda-Filho et al., 2004; Sousa et al., 2024).

In terms of structural and morphological aspects, previous works (e.g. Lana et al., 2007 and 2008) divided the AGD impact structure in concentric sectors, including a 4 – 5 km wide porphyritic alkali granite core, which, in turn, is surrounded by polymict breccias and by strongly deformed Furnas Formation rocks. Both sectors would form the 10 - 12 km diameter central peak of the structure. More recent workers (Miyazaki et al., 2022) prefered a somewhat wider central uplift structure of 16 km width. Then, this central peak is surrounded by an annular basin where the geology is dominated by Aquidauana sandstones and strata of the Ponta Grossa Formation. Alleged alignments of hills within the surrounding annular basin suggested the existence of two

concentric ring structures at 10 - 12 km and 14 - 18 km from the center of the structure (Lana et al., 2007 and 2008) but this has recently been questioned by Bernades et al. (2025). Finally, the annular basin is surrounded by the crater rim, which was regarded as the AGD limit and is composed of kilometer-wide blocks of Passa Dois Group and Aquidauana Formation rocks with variable deformation. These units are cut by radial faults (Sousa et al., 2024).

A recent study (Bernardes et al., 2025) has pointed out that the AGD impact structure can be though in terms of 20 km diameter central region (i.e. central uplift) sourrounded by another 20 km circular region that, turn in, can be subdivided into intermediate section and outer rim zone (Bernardes et al., 2025) (Fig. 7). According to Bernardes et al., (2025), besides granitic core, polymict breccias, Cuiabá Group metasediments and Furnas Fm., the central uplift also encompasses the Aquidauana Fm, which was uplifted during central uplift formation and worked as a barrier against inward-moving Passa Dois Group volumes. In the annular basin (i.e. the region between central uplift and outer rim), the authors did not find evidence for presence of concentric inner rings. They argued that the structural elements in the annular basin resulted from the inward movement of rock volumes during the crater collapse as a consequence of rheological contrasts in the sedimentary target sequences. Finally, the structural style of the Passa Dois Group in the outer rim region may be related to gravity-driven mass transport during the collapse of the transient crater (ibid).

The main shock deformation features found in the rocks of the AGD's central uplift include shatter cones in Cuiabá Group metasedimentary strata (Crósta et al., 1982), kink bands in biotite and muscovite (Engelhardt et al., 1992; Crósta et al., 1981), planar fracrures (PF) and planar deformation features (PDF) in K-feldspar and quartz in the central granite and in quartz and feldspar clasts of impact melt rocks (Dietz and French, 1973; Engelhardt et al., 1992; Souza et al., 2024), and shock deformation in zircon (Hauser et al., 2019). Many of these shock diagnostic features basically come from two main kinds of impactites: polymict impact breccias – both lithic and suevitic breccias, and impact melt rocks. The polymict impact breccias are generally poorly to moderately sorted, matrix supported, and the groudmass is composed of fine-grained material derived from sandy to pelitic clastic material. Larger clasts are

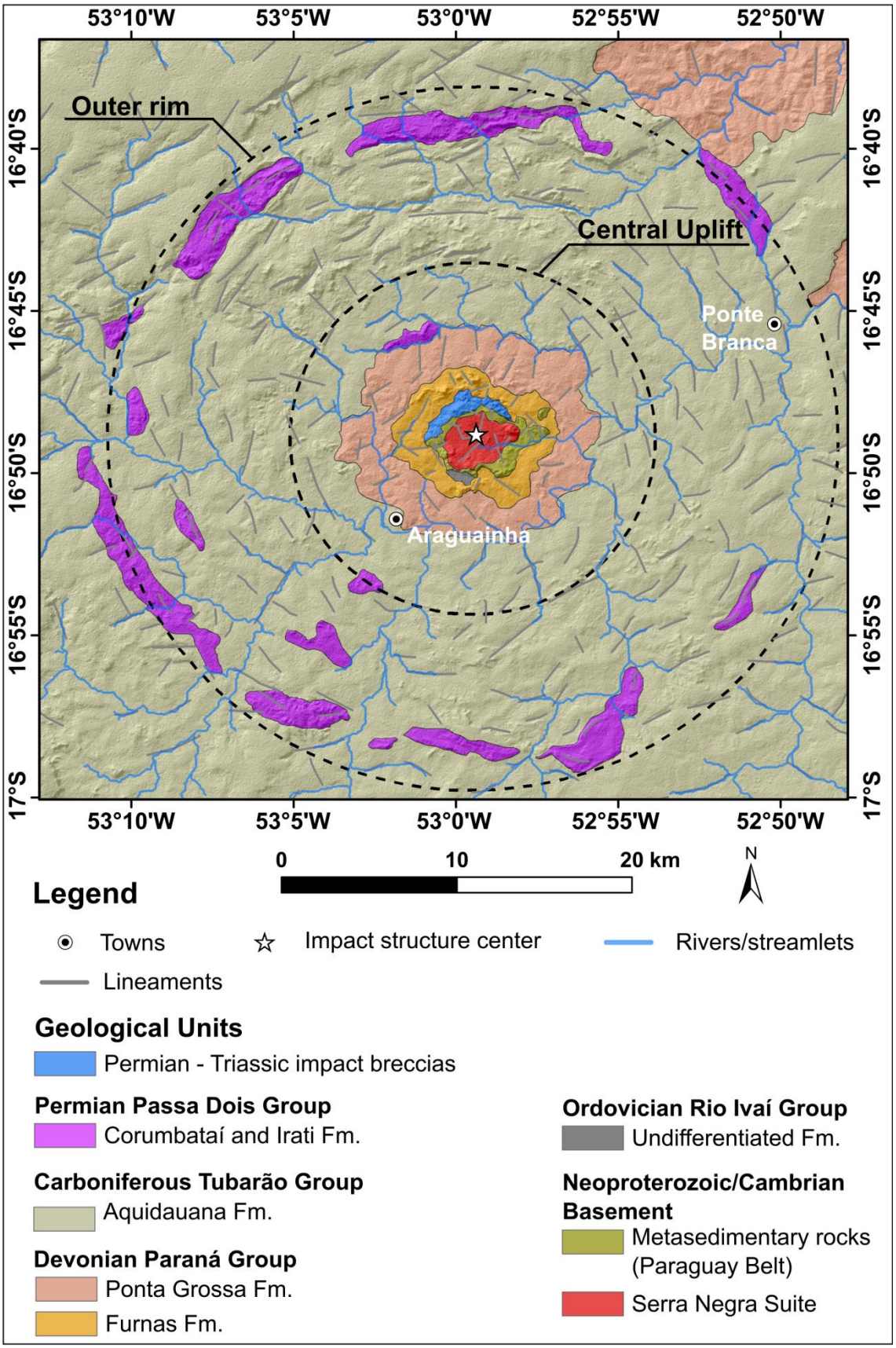

Figure 7: Geological map of the Araguainha impact structure after Sousa et al. (2024) and Berbardes et al. (2025).

derived from metasedimentary and sedimentary sources; there is litte evidence for significant contribution from granite (Sousa et al., 2024).

Regarding impact melt rocks, Sousa et al. (2024) proposed that 3 types of impact melt rocks can be distinguished: Type-I occurs as dikes, veins or pods with granitic composition and porphyroblastic, aphanitic, or spherulitic textures; Type-II occurs as clasts of polymict breccias that are plastically deformed and have highly silicious composition; this suggests that they are deived from arenitic, sedimentary precursor; Type-III occurs as irregular blocks dominantly composed of silicate materials in an annulus just inside of the basement (metasedimentary rocks) collar, shows fluidal structure, sometimes spherulitic texture, and granular texture in zircon grains. In this last type, one zircon grain analyzed by Hauser et al. (2019) shows a domain of neoblastic zircon interspersed within a lamellar-habit relict domain. They interpreted such neoblastic domains as former reidite (a high pressure-temperature polymorph of zircon) in granular neoblastic zircon (FRIGN zircon), that is, reidite lamellae that reverted back to zircon. From zircon grains derived from Type-III impact melt rock, Hauser et al. (2019) estimated the age of the impact event at Araguainha to 251.5 ± 2.9 Ma, which is very similar to the age proposed by Tohver et al. (2012) of 254.7±2.5 Ma.

Beyond the magnetotelluric, electroresistivity, gamma-ray and paleomagnetism studies mentioned in Chapter 6, the Araguainha impact structure has also been studied by ground-based gravity and magnetic (airborne and ground surveys) data. Initially, a circular negative Bouguer anomaly (-4 mGal) was reported in the Araguainha granitic core (Vasconcelos, 2007; Marangoni et al., 2007). Granite with very low density (~2.15 g/cm^3) was proposed to explain this low gravity (Marangoni et al., 2007). Later, Miyazaki et al. (2021) collected data from 300 new gravity stations in the central Araguainha area. Unlike Vasconcelos (2007) and Marangoni et al. (2007), Miyazaki et al. (2021) did not find a circular negative Bouguer anomaly, but their results show a gravity field with local highs and lows in the Araguainha central uplift. By using a 3D gravity model and numerical modeling, they argued that the highs can be related to massive porphyritic granite, whereas fractured granites, breccias and even sandstones are responsible for low gravity areas. Regarding magnetic data, linear magnetic anomalies with NE – SW trend seen in an airborne survey

were associated with the Transbrasiliano Lineament, whereas the modeling of a ground-based magnetic survey revealed that the breccia/granite contact zone in the central uplift has strong remanent magnetization (Vasconcelos, 2007). No seismic survey has been carried out by the time of writing.

8.1.2 Cerro do Jarau impact structure (CJU)

The Cerro do Jarau impact structure is located close to Quaraí town, in the south of Rio Grande do Sul state, near the border between Brazil and Uruguay (Fig. 8). The structure is centered at 30°12'S and 56°32'W. Its diameter has been estimated at 13.5 km based on drainage patterns seen on satellite images (ASTER sensor and Digital Elevation Model from Shuttle Radar Topography Mission) (Crósta et al., 2010a). Despite the circular landform character of CJU having been noticed since the 1970's, the origin by impact was promoted only in 2010 (Crósta et al., 2010a), and, even more recently, bona fide evidence for shock metamorphism was published by Reimold et al. (2019). According to a geological map and outcrop descriptions (Crósta et al., 2010a; Sánchez et al, 2014) (Fig. 8), the target rocks at CJU are Jurassic-Early Cretaceous São Bento Group (Gondwana III Supersequence) rocks, which include basalts (Serra Geral Formation) and sandstones (Guará and Botucatu formations).

Sandstones occur in the central part of the structure, whereas basalts occur in the environs (Crósta et al., 2010a). Guará Formation fluvial sandstones can be found in direct contact with basalts in the structure's central parts. These sandstones are composed of quartz (50%), feldspar (10%), lithic grains (5%), and accessory minerals (e.g., zircon, magnetite, apatites), all of which is supported by a strongly oxidized, fine-grained matrix (Crósta et al., 2010a). The Botucatu Formation aeolian sandstones are mostly composed of quartz (86%) and can be strongly silicified in some areas, supporting high elevations in the NE sector of the CJU central area (Crósta et al., 2010a). In some places close to the central zone, these sandstones show subvertical dip and tectonic contacts with basalts, or even stratigraphic inversion, with sandstones overlying basalts. These basalts, in turn, show intense fracturing and abundant joints. Basaltic monomict breccias, sandstone monomict breccias, and lithic polymict breccias have been found at CJU (Reimold et al., 2019).

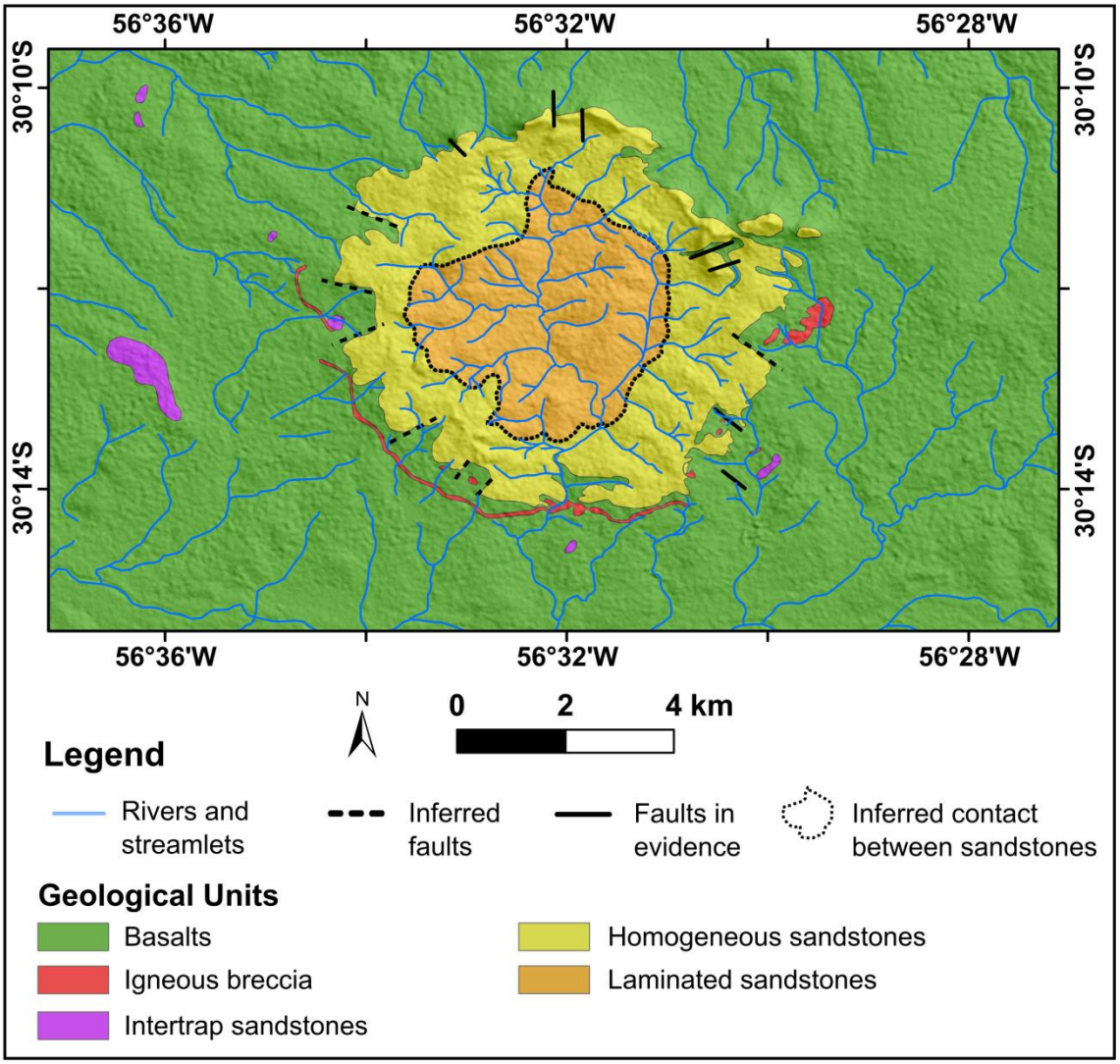

Figure 8: Geological map of the Cerro do Jarau impact structure. Modified after Sánchez (2014).

Several quartz grains of sandstone samples from CJU have shown bona fide evidence of shock diagnostic features such as FF, PF, and PDF. According to the spatial distribution of these diagnostic shock features, Reimold et al. (2019) estimated that the shock level of the currently exposed rocks was less than 10 GPa, even for samples taken from the innermost part of the impact structure.

Ground based gravity surveys have been carried out at CJU by Giacomini et al. (2017). Based on 3D density models derived from residual Bouguer data, they identified a 9-10 km diameter semicircular gravity high (> 6 mGal) surrounding a 5 km diameter low-gravity zone lacated in CJU's central uplift. This low gravity has been related to sandstones uplifted around the CJU

center, whereas the semicircular gravity high could be related to emplacement of basalts below the sandstones (Giacomini et al., 2017). In another study based on ground-based gamma spectrometry and numerical modelling, Garcia et al. (2024) claimed that high potassium concentrations in the CJU central uplift were consistent with remobilization of this element by impact. However, no petrographic or geochemical evidence to support these claims has been presented yet.

8.1.3 Vargeão Dome impact structure (VGD)

Like at the CJU impact structure, target rocks at Vargeão Dome (VGD) are composed of Jurassic-Cretaceous sandstones (Pirambóia and Botucatu formations) and Early Cretaceous Serra Geral Formation basalts (Crósta et al., 2012). Both the Pirambóia and Botucatu formations comprise fine- to medium-grained sandstones with large scale cross-stratification, but they are separated by regional discordance, differ in color, and have different dimensions of their cross-strata (Assine et al., 2004). The Serra Geral Formation rocks are predominantly composed of tholeiitic basalts, but rocks of intermediate compositions (e.g., Paranapanema and Palmas basaltic-andesites) and andesites, and even acid types (e.g., Chapecó Formation rhyodacites) also occur, but at lower (< 7 %) proportions (Luchetti et al., 2018; Horn et al., 2022).

The VGD structure is centered at 26°49’S and 52°10’W near Vargeão town, in Santa Catarina State, southern Brazil (Crósta et al., 2019a). Its diameter has been estimated at 12.4 km (Crósta et al., 2012, 2019a). Although the circular aspect of VGD had already been known since the end of the 1970s, shock deformation diagnostic for impact was reported only in the 2000's (Crósta et al., 2005; Crósta et al., 2012). The main shock deformation features at VGD include shatter cones developed in sandstones and basalts, and rare PF and FF in monomict sandstone breccias (Crósta et al., 2006, 2012, 2019a). In addition to monomict sandstone breccias, polymict impact breccias are present at VGD (Crósta et al., 2012).

Polymict breccias occur in meter-scale outcrops near the center of the structure (Crósta et al., 2012). They are composed of angular, volcanic clasts, with smaller amounts of sandstone and calcite supported by red, fine-grained,

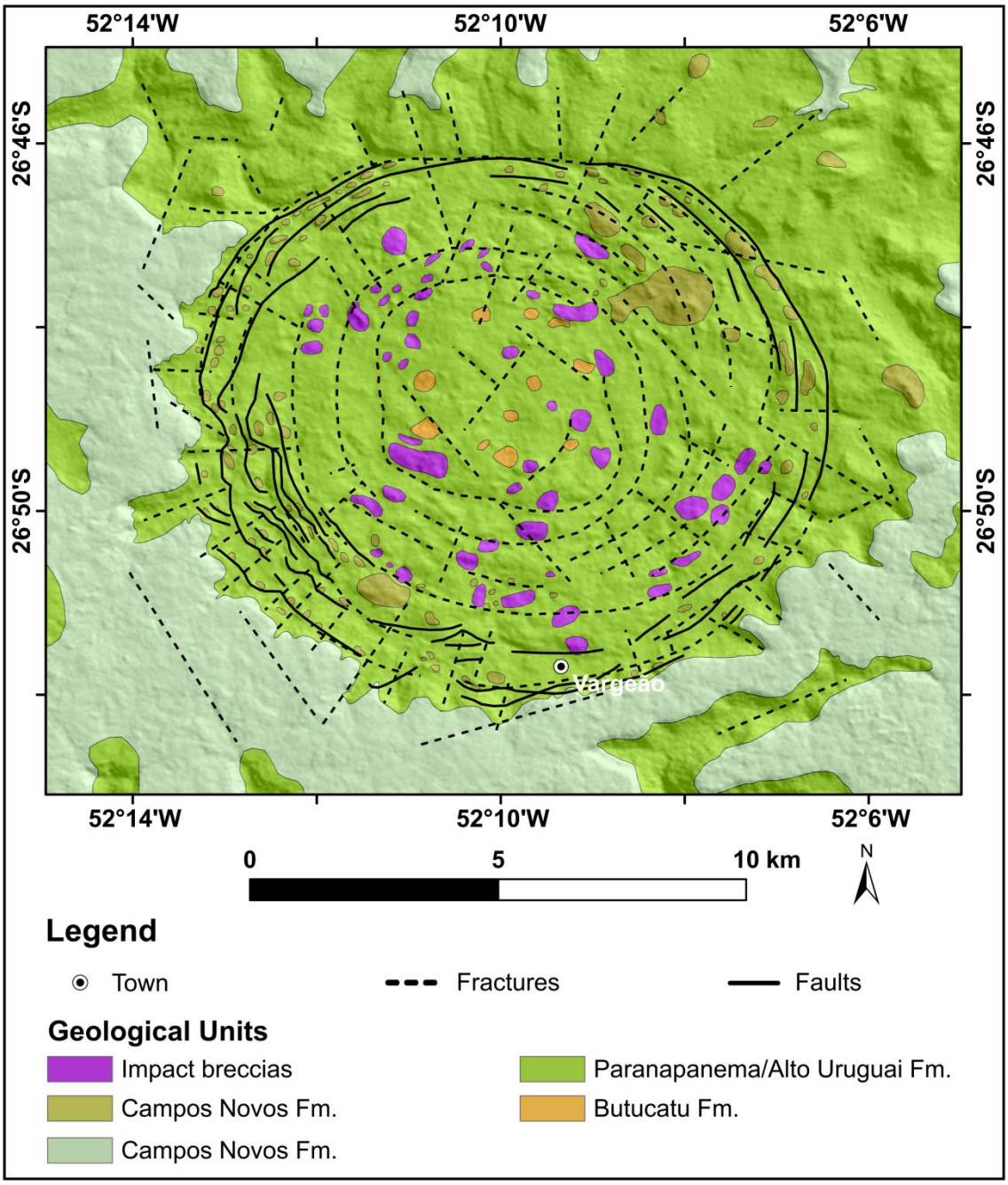

Figure 9: Geological map of the Vargeão Dome impact structure. Modified after Yokoyama et al. (2015) and Alsemgeest (2024).

strongly oxidized groundmass that is composed of comminuted basalt and rhyodacite, quartz, and calcite (Crósta et al., 2012, 2019a). Geochronology on zircon grains from brecciated rhyodacite suggested an age of 123.0±1.4 Ma for the impact event (Nédélec et al., 2013) but this result is strongly debatable, as it is based on samples from the crater rim where a significant shock overprint to reset zircon can not be expected (Crósta et al., 2019a).

Regarding its morphological aspect, the VGD impact structure is markedly circular with several concentric and radial features (Kazzuo-Vieira et al., 2009). These structures are readily visible in spaceborne images, such as ASTER scenes and C-band Radarsat images and a 90m-resolution Digital Elevation Model derived from Shuttle Radar Topography Mission (SRTM) (Kazzuo-Vieira et al., 2009; Crósta et al., 2012). At the rim, the concentric features have been related to listric faults which, in turn, disrupt ENE - WSW and E - W linear trends related to regional geological background (Kazzuo-Vieira et al., 2009). Undeformed or slightly deformed large volcanic (Chapecó and Alto Uruguai Formation) blocks occur near the rim, with some blocks being seemingly rotated. Towards the center of the structure, the rocks (basalts, rhyolites, and sandstones) become more intensely brecciated, fractured, and locally possibly fused (Crósta et al., 2012). On the central uplift, sandstones show strong deformation that hinders distinguishing between Botucatu or Pirambóia formation strata (Crósta et al., 2012).

Kazzuo-Vieira et al. (2009) suggested that the magnetic signatures of the ENE - WSW linear trends mentioned above were interrupted by the VGD impact structure and those them, therefore, represented pre-impact features probably related to the Lacinha-Cubatão fault zone. Moreover, based on Analytical Signal Amplitude (that is, a filter that enhances the magnetic contrasts and simplifies the dipolar nature of magnetic anomalies – e.g. Roest et al., 1992), Kazzuo-Vieira et al. (2009) also identified a peculiar circular magnetic signature near the VGD center, with low magnetic zones surrounding it - mainly in the northern portion of the VGD impact structure. According to these authors, circular magnetic signatures near the center could be related to presence of impact breccias, whereas low magnetic zones could be related to Chapecó acid volcanic rocks.

Discontinuities of amplitudes of the seismic signals at VGD's rim have been interpreted as listric faults, whereas VGD's center shows a conical uplifted structure characterized by high disturbance of seismic signals, which suggests the presence of strongly deformed rocks (Crósta et al., 2012). In ground-based gravity surveys, VGD showed a negative residual Bouguer anomaly (- 2.8 mGal) surrounded by a ring-shaped positive residual Bouguer anomaly (1.4 - 2.8 mGal) (Ferreira et al., 2015). Based on a 3D subsurface model, these

authors claimed that this low gravity arises from less dense Pirambóia/Botucatu sandstones uplifted during the modification stage. The origin of a ring-shaped high gravity anomaly, however, has not been effectively clarified. Finally, it is worth mentioning that average density values of impact breccias (2.39 g/cm^{-3}) are lower than values for sandstones (2.43 g/cm^{-3}), basalts (2.88), rhyodacite (2.56), and fractured basalts (2.74).

8.1.4 Vista Alegre impact structure (VTA)

The third impact structure in basalt in southern Brazil is Vista Alegre (VTA) (Fig. 10). It is centered at 25°57'S and 52°41'W, near Vista Alegre town, in Santa Catarina state. Based on a DEM derived from SRTM data, the diameter of the VTA impact structure has been estimated at 9.5 km (Crósta et al., 2010b). Morphologically, the rim is a circular ring up to 150 m high and with steep slopes, which that separates terrains with different morphologies, in the internal and external portions. The internal portion of VTA is dominated by gentle hills with low topographic gradients, commonly less than 50 m high. In contrast, the surrounding terrain around the VTA impact structure is characterized by high topographic gradients (> 200 m) and hilly landforms (Crósta et al., 2010b, 2019). The central zone in the VTA impact structure is not well defined, but it has been supposed to be present based on deformed sandstone blocks in a similar geological context as seen at Cerro do Jarau and Vargeão Dome (Crósta et al., 2010a, b, 2012).

From the rim to one third towards the center of the structure, fractured basalts with no shock deformation features are dominant. In the northeast sector of the central area, hydrothermal alteration, veins predominantly composed of calcite) and melt veinlets were identified by Alsemgeest et al. (2021). According to these authors, the lack of dendritic growth or amorphous phases in these melt veinlets suggests that they are more likely unrelated to the impact event and should be related to an earlier process. Similarly, thermodynamic modeling has suggested to them that calcite veins should probably be related to regular geo-processes.

Another type of hydrothermal alteration (type 2) was reported by Alsemgeest et al. (2021) in fractured basalt and samples from two polymict

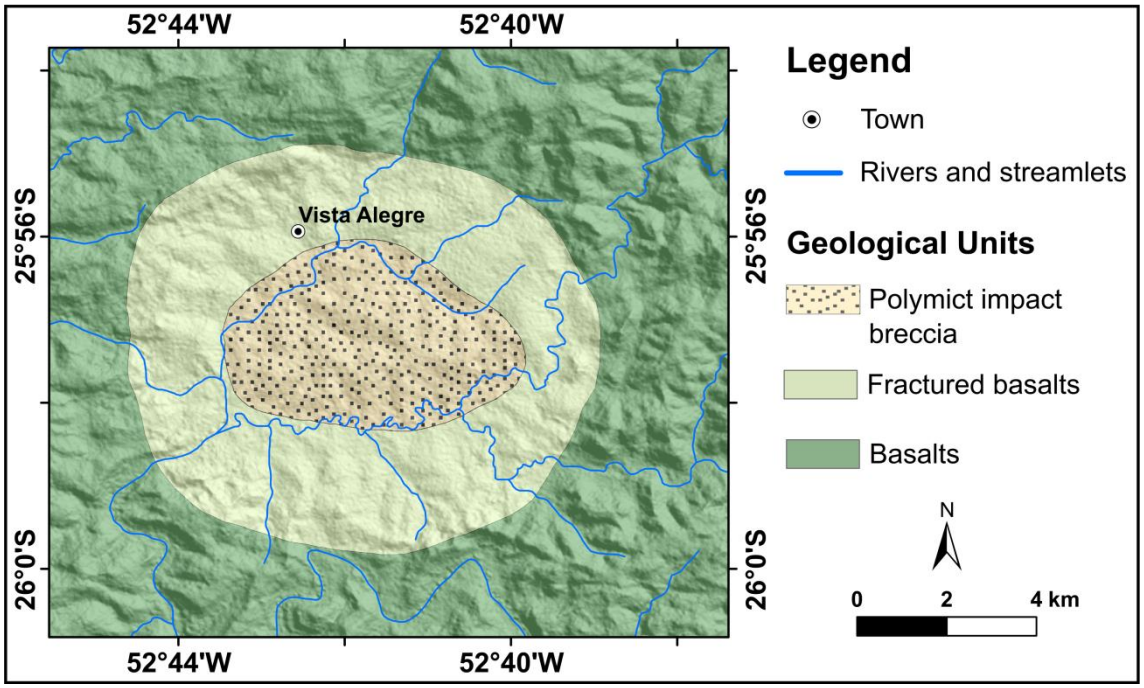

Figure 10: Geological map of the Vista Alegre impact structure. Modified from Alsemgeest et al. (2021).

impact breccia outcrops. This type is characterized by chabazite veins, with other zeolites, calcite, and phyllosilicates. Thermodynamic modeling suggested zeolite-bearing veins were formed before the impact and were exposed due to crater excavation processes (ibid).

In the central zone, polymict impact breccias containing quartz grains with PDFs and shatter cones in basaltic clasts were identified (Crósta et al., 2010b, 2019a). Shatter cones in these polymict breccias were formed in fine-grained tholeiitic basalt fragments, and have sizes from 0.5 to 20 cm (Pittarello et al., 2015). According to these authors, parallel fractures filled by fine-grained cataclasite crosscut the striated surfaces of these shatter cones.

Ground-based gravity surveys revealed a negative residual Bouguer anomaly in the central portion that, in turn, is surrounded by a positive residual Bougher anomaly in the VTA impact structure (Ferreira et al., 2017; Vasconcelos et al., 2019). Results from the 3D gravity inversion modeling and iSale Numerical Modeling suggest that low gravity in the central area of VTA is due to less dense and strongly deformed sandstones that were uplifted during the modification stage (ibid). Moreover, the best-fit numerical model shows warping/folding of sedimentary strata downward, which could have led to local thickening of the basalt layers, causing a positive contrast in density

(Vasconcelos et al., 2019). Finally, these modeling results were used to justify the absence of a pronounced central uplift at VTA, possibly related to the greater resistance of basalts to deformation in comparison to sandstones. Erosion estimated at 320 m (Vasconcelos et al., 2019) could also explain the lack of a pronounced central uplift.

8.2 **Impact structures of the Parnaíba Basin**

To date, four impact structures have been confirmed in the Parnaíba Basin: Serra da Cangalha (SdC), Riachão Ring (RR), Santa Marta (SM) and Nova Colinas (NVC) (see Fig. 6). A fifth structure, São Miguel do Tapuio (SMT) still need to be published properly, but preliminary results have been promising, gave some petrographic results that point to an impact origin (Crósta et al., 2019b). Overall, target rocks affected by these impact events are dominantly composed of siliciclastic material, but for the NVC impact structure shatter cones formed in Mosquito Formation basalt have been reported (Oliveira et al., 2014).

8.2.1 Serra da Cangalha impact structure (SdC)

Serra da Cangalha is a ~13.4 km diameter complex impact structure centered at 8°05'S / 46°52'W (Fig. 11) (Crósta et al., 2019a). An origin by impact for SdC had been proposed since the 1970's (Dietz and French, 1973), but bona fide evidence (e.g., shatter cones, Planar Deformation Features (PDF), Planar Fractures (PF) and Feather Features) was only reported by Kenkmann et al. (2011) and Vasconcelos et al. (2013).

Morphologically, SdC comprises a set of concentric rings, and the innermost part is characterized by a 2.2-km-wide depressed zone with rare outcrops of Longá Formation black shales and siltstones. This zone is surrounded by a prominent (up to 350 m high) collar (which gave the structure its name) of Poti Formation silicified sandstones (Fig. 11). Both these zones form the central area that has been interpreted as a differentially eroded central uplift structure (ibid). Rare monomict and polymict impact breccias have been found in the central depression and at the periphery of the central uplift. In the central-northwestern sector of SdC's central uplift, polymict lithic breccias occur as well.

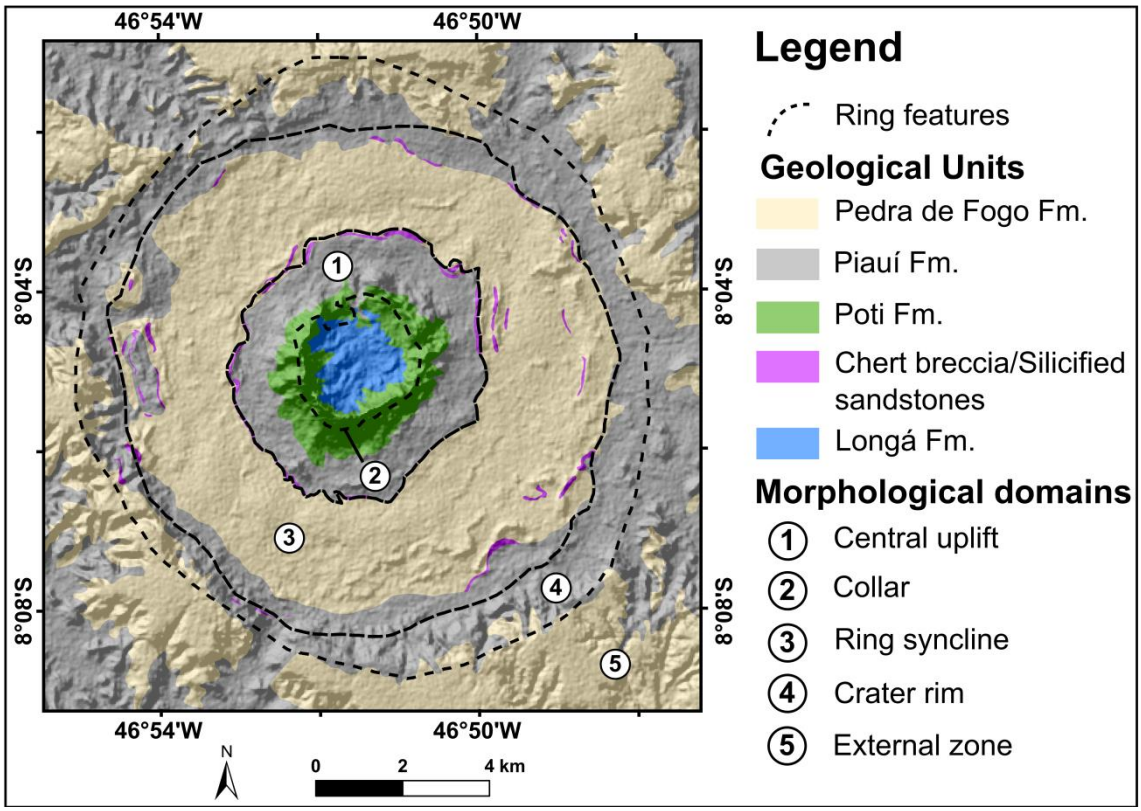

Figure 11: Geological map of the Serra da Cangalha impact structure. Modified after Kenkmann et al. (2010) and Vasconcelos et al. (2013).

The central part is surrounded by a 6 km diameter, intermediate ring feature (first ring) composed of Pedra de Fogo brecciated chert and quartzite, and then by an 11 km diameter second intermediate ring that comprises Pedra de Fogo Formation silicified chert and sandstones (Reimold et al., 2006; Vasconcelos et al., 2013) (Fig. 11). The outer, apparent size of the SdC structure is constrained by a 13.4 km diameter outer ring composed of Pedra de Fogo rocks (mainly sandstones; Vasconcelos et al., 2013). Because impact-generated and possibly datable lithologies have not been found at SdC, the maximum age for this structure is constrained by the age of the youngest strata affected by impact, which in this case corresponds to the Pedra de Fogo Formation of ca. 250 Ma age (Vaz et al., 2007). Moreover, structural aspects have suggested that SdC has been significantly eroded since its formation, possibly by as much as some 500 m (Kenkmann et al., 2011).

The geophysical surveys at SdC utilized different methods, such as airborne radiometric (Vasconcelos et al., 2012a), magnetotelluric (MT) (Adepelumi et al., 2005), airborne and ground based magnetic (Vasconcelos et al., 2010, 2012b), and ground-based gravity surveys (Vasconcelos et al.,

2012b). The SdC impact structure shows a noticeable concentric gamma-ray signature which has been thought to be derived from differential resistance to erosion of the exposed lithologies (Kenkmann et al., 2011; Vasconcelos et al., 2012a). In addition, previous workers have argued that hydrothermally driven K enrichment could be in evidence in the airbore radiometric data, mainly in the southwestern portion of SdC (Vasconcelos et al., 2012a). However, impact-induced hydrothermal alteration at SdC has not been extensively reported yet.

Part of the results of the airborne gamma-ray spectrometry data processing in the SdC impact structure derived from this dissertation were published by me in the Brazilian Journal of Geophysics (Chapter 11, Silva et al., 2024). By using radiometric ratios (e.g., K/eTh, eU/eTh, eU/K), it was possible to highlight other processes that had not been reported in previous studies. For instance: relative eU enrichment zones seems to be related to Piaui and Pedra de Fogo contact zones, such that these elevated eU concentrations may come from brecciated chert layers or silicified sandstones (Silva et al., 2024).

Regarding other geophysical signatures, a significant reduction in the basement resistivity around the center of the SdC was suggested by 3D models from MT data (Adepelumi et al., 2005). Moreover, based on 2D MT inversion and downward continuation of the reduced to pole residual magnetic map, Adepelumi et al. (2005) claimed that the top of the basement below SdC was located at 1.1 km depth. They suggested that the oval-shape magnetic anomaly detected by them at the center of SdC could be related to the impact event and result from shock remagnetization. In the same way, based on airborne and ground-based magnetic and gravity data, and numerical modeling, Vasconcelos et al. (2012b) argued that the basement to the central area was uplifted during the modification stage. In contrast to Adepelumi et al. (2005) and Vasconcelos et al. (2012b) suggested an average depth to basement of 1900 m for the entire structure, and a depth of approximately 500 m at the center.

8.2.2 Riachão Ring impact structure (RR)

Like the SdC structure, the Riachão (RR) impact structure is also a complex impact structure, but its apparent diameter (~4 km) is much smaller than that of SdC (Crósta et al., 2019). The RR structure is centered at 7°42’S and 46°38’W in the southern part of Maranhão State (Fig. 13). The impact origin

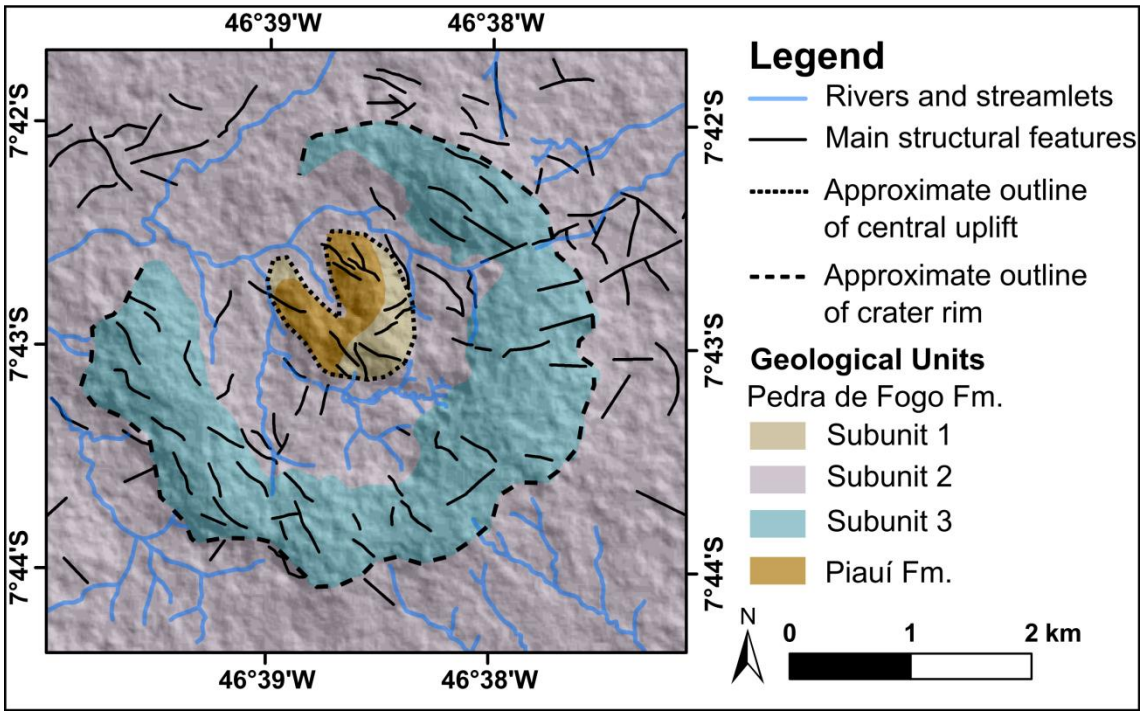

Figure 12: Geological map of the Riachão Ring impact structure. Modified after Maziviero et al. (2013).

for RR had also been proposed in the 1970's (McHone, 1979; McHone, 1981), but the only quartz grain from Piaui sandstone in RR that exhibited a Planar Deformation Feature was reported as bona fide evidence for impact only in 2013 (Maziviero et al., 2013) (Fig. 12). The local stratigraphy proposed by Maziviero et al. (2013) for the RR impact structure includes basically two strata with dominantly siliciclastic sedimentary rocks: the Pedra de Fogo and Piaui formations (Fig. 12). Piauí Formation strata crop out only in the RR central zone. These strata are composed of sandstones with a high proportion of comminuted and sharp-edged quartz grains. Such strata are exposed as chaotically arranged blocks and folded beds in the small, apparent central uplift area (Maziviero et al., 2012 and 2013). The Pedra de Fogo Formation has been informally subdivided into three subunits: Unit 1 - chert layers, strongly fractured; Unit 2 - carbonates with pelitic contributions and locally concretionary chert nodules, and Unit 3 - composed of breccias and lithic sandstones supposed to have been lithified before the impact event. These strata were tilted (dip angles in primary sedimentary structures ranging from 40° to subvertical, mainly toward NW) during the impact event. Because the Pedra de Fogo Formation is the youngest unit affected by this impact, the age for the impact event has been estimated at < 250 Ma.

Based on spaceborne images (Landsat 7 ETM+, CBERS-2B/HRC, DEM from stereoscopic ASTER), Maziviero et al. (2013) divided the RR impact structure into three morpho-structural zones (Fig. 12): central uplift, annular depression, and elevated rim. The central uplift at RR is a 1.4 km diameter, approximately circular structure that comprises massive Piauí Formation sandstones that dip at 55 to 80 degrees into several directions (Maziviero et al., 2012) (Fig. 12). The sandstones are dominantly (~75 vol %) composed of monocrystalline quartz grains, with lithic particles (sericitic shale) (< 25 vol %) and heavy minerals (3 - 5 vol %) such as zircon, tourmaline, rutile, and others (Maziviero et al., 2013). The central uplift is surrounded by an annular depression where outcrops are represented by siltstones and calcilutite (Subunit 2) (Fig. 12). Brecciated cherts occur at the transition central-uplift/annular depression (Subunit 1). These breccias show microcrystalline silica commonly crosscut by silica and/or iron oxide hydroxide veins (Maziviero et al., 2013). The apparent outer diameter is marked by a 4 km diameter elevated rim that is open in the NW sector (Fig. 12). This morphostructural zone has been severely affected by erosion, such that there are few outcrops available. The outcrops are composed of sedimentary breccias and lithic sandstones. The former occur mainly in the northern portion of the rim and show a massive texture, with quartz sandstone clasts poorly to moderately sorted and with rounded to angular shapes, all embedded in a sand and silt grain-size matrix. The latter occurs in the eastern portion of the RR rim. The lithic sandstones are composed of quartz grains, possess small-scale cross-bedding, and contain local concentration of sandstone clasts which, in turn, are supported by a matrix that shows similar characteristics as the sedimentary breccia matrix (Maziviero et al., 2013).

Like the SdC impact structure, RR shows a noticeable circular pattern in airborne gamma-ray signature. This pattern has been interpreted to suggest high K concentration in the central part, possibly associated with phyllosilicate in the cement of Piauí sandstone, whereas low K, eTh, and eU concentrations in the crater rim area could be due to weathering-driven remobilization of radioelements (Maziviero et al., 2013). Regarding potential field data, these authors reported a positive Bouguer anomaly coinciding with the outermost limit of the RR impact structure, whereas a slightly NW - SE elongated weak

magnetic anomaly occurs near the structure´s center. The high gravity has been interpreted as a result of erosion perhaps to or below the original crater floor, whereas the magnetic anomaly could be related to oblique impact, as the elongated magnetic anomaly direction coincides with the shape of the structure that is open in the same direction, to the NW (ibid).

8.2.3 Nova Colinas impact structure (NVC)

Nova Colinas (NVC) is the most recently confirmed impact structure in Brazil (Reimold et al., 2022). It is also a complex impact structure, with a 7 km diameter. NVC is centered at 7°09'33''S / 46°06'30''W (ibid). An impact origin for NVC had been suggested by previous workers (e.g., Silva, 2020), but bona fide shock diagnostic evidence (planar features, feather features, and planar deformation features) was only reported by Reimold et al. (2022). A geological map for NVC has been proposed by Avona et al. (2025), but in the present work the morphological unit map proposed by Reimold et al. (2022) and regional geological maps are considered, because: i) outcrop points visited by Avona et al. (2025) are not available in their map; ii) Avona et al. (2025) proposed that NVC's rim is composed of a continuum of basalt units, whereas it will be shown below, such units occur only discontinuously along the rim, and iii) silicification and laterite units are not shown in Avona's geological map.

In regional geological maps, the northern part of the NVC structure is covered by Mosquito Formation basalt and some Corda Formation sandstone (Fig. 13). The central and southern parts of the NVC structure are dominated by siliciclastic units (e.g., Sambaíba sandstones, Pedra de Fogo Formaton sandstone, and fine-grained Motuca Formation sandstones), with the Motuca Formation possibly containing some evaporites and the Pedra de Fogo Formation some chert (Fig. 13). The northern and southern areas are well-defined in a color composite map of multitemporal thermal infrared from ASTER scenes and residual magnetic maps (Silva, 2020; Reimold et al., 2022; Pereira et al., 2024). Morphological analysis reported in Reimold et al. (2022) indicates that the relief pattern is essentially moderate within the NVC structure, with dissected relief of moderate and low slopes (Fig. 13). Greater elevation occurs

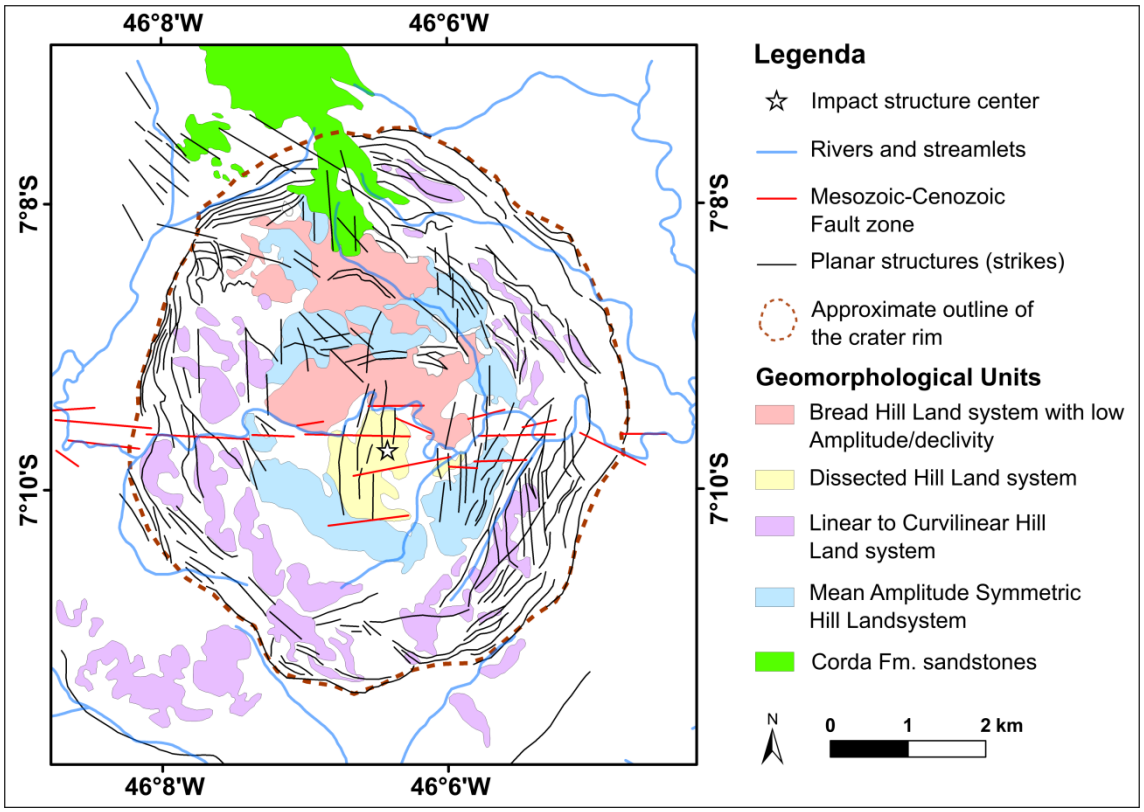

Figure 13: Geomorphological map of the Nova Colinas impact structure. Modified after Reimold et al. (2022).

along the perimeter of the structure and in a small area (up to 0.8 km wide) in the central part of NVC. In this central part, the strata are strongly fractured and display variable bedding orientation, from locally subhorizontal to steeply upturned (Reimold et al., 2022).

Monomict sandstone breccia, a few samples of which contain quartz with PDF and FF, are the main impactite facies reported until now from the NVC. These monomict breccias consist of very fine-grained, pure quartz sandstone with large rounded grains embedded in a fine-grained groundmass of crushed, splintery fragments (see Table SM-1 in Reimold et al., 2022). Many other sandstone samples from the NVC impact structure also are strongly cataclased and/or fractured, but they do not show shock features. For instance: near the southeast of the central zone, strongly silicified sedimentary breccia with variably rounded to angular sedimentary clasts has been mapped, but none of these samples display any diagnostic shock evidence.

Airborne magnetic and gamma-ray data for NVC have been analyzed by different workers (e.g., Silva, 2020; Reimold et al., 2022; Pereira et al., 2024) and all of them show a ring-shaped magnetic anomaly that approximately

coincides with NVC's rim. According to numerical modeling, magnetic inversion models, and reflection seismic analysis, the ring-shaped magnetic anomaly has been interpreted to be due to magnetic contrast between a Mosquito Formation basaltic layer and clastic sequences in the surroundings (Pereira et al., 2024; Avona et al., 2025). Moreover, a regional magnetic map derived from radially averaged power spectrum analysis is suggestive of a conspicuous dipolar anomaly over the center of the NVC impact structure and may arise from diabase sills that could have been uplifted during the impact (Pereira et al., 2024; Avona et al., 2025). As these diabase sills are denser than the siliciclastic rocks, they are regarded as the main cause of a positive residual Bouguer anomaly that was reported by Avona et al. (2025) in the central uplift area. Regarding the basement, seismic data show that its top occurs at 2200 m depth. As the seismic horizon associated with the basement does not shows any discontinuities, it has been regarded as unaffected by impact (Pereira et al., 2024).

Regarding gamma-ray signatures, high K concentration in the northern sector may reflect near-surface materials overlying Mosquito Formation basalts, whereas high-K concentration in the central area could be related to the radiometric signature of a lower stratigraphic unit that was uplifted during collapse and modification of the impact structure (Reimold et al., 2022).

Like at SdC and RR, the lack of any impact melt rock or suevite with impact melt clasts has not allowed to determine the age of impact, such that the age suggested by Avona et al. (2024), on stratigraphic grounds, is poorly constrained to the interval from ~199 to 130 Ma, where the upper limit represents the age of the pre-impact basalt layer of the Mosquito Formation (e.g., Merly et al., 2011), and the lower limit represents the depositional interval of the Corda Fm. sandstones, which occur undeformed within the northern NVC rim (Fig. 13) (Avona et al., 2024 and my own observations during the present work).

8.2.4 Santa Marta impact structure (SM)

Santa Marta (SM) is an impact structure of approximately 10 km diameter centered at 10°10'S and 45°14'W, in southern Piauí State, near the borders between

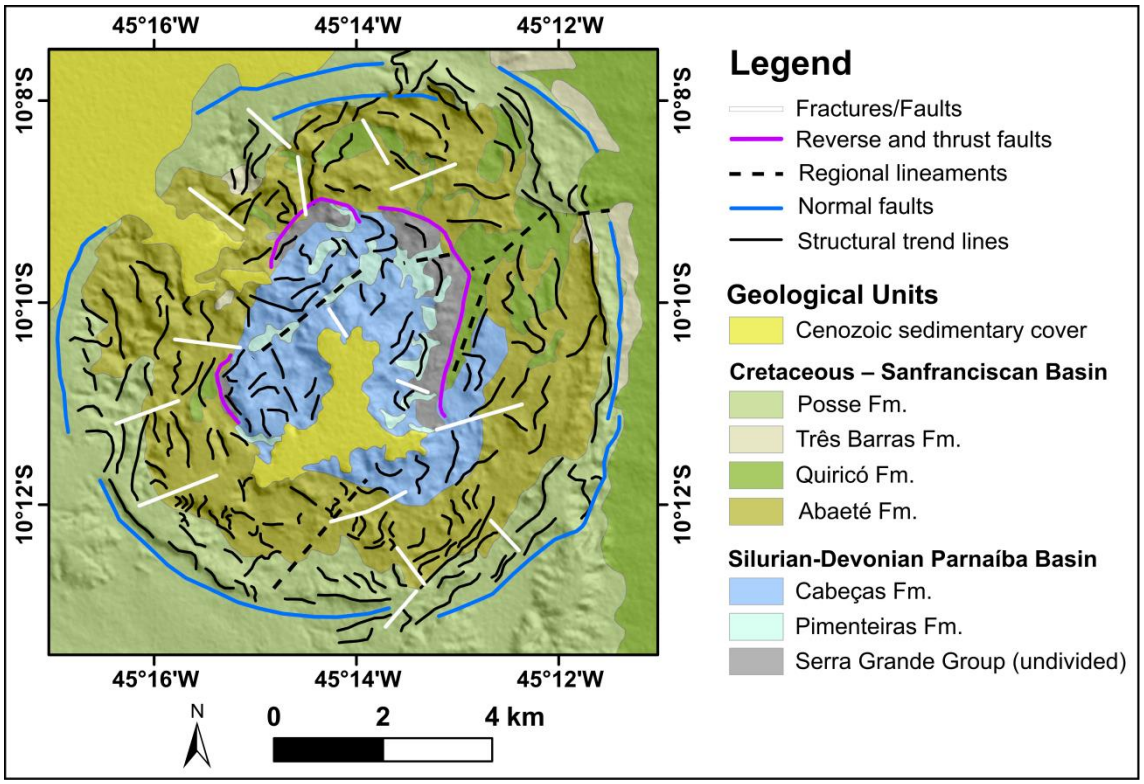

Figure 14: Geological map of the Santa Marta impact structure. Modified after Oliveira (2014).

Maranhão, Tocantins, and Bahia states (Fig. 14). The structure occurs in predominantly siliciclastic sediments of the Silurian-Mesodevonian-Eocarboniferous Parnaíba and Cretaceous Sanfranciscan basins (Fig. 14). From bottom to top, the local stratigraphic record comprises, after Oliveira et al. (2014, 2017), Silurian Serra Grande Group conglomerates and sandstones; Pimenteiras Formation shales and sandstones, and Cabeças Formation sandstones and conglomerates of the Mesodevonian-Eocarboniferous Canindé Group; Early Cretaceous Areado Group aeolian sandstones, and Middle-Late Cretaceous Urucuia Group fluvial-aeolian sandstones (Campos and Dardenne, 1997a; Campos and Dardenne, 1997b). The three lowermost packages belong to the Parnaíba basin, and the two uppermost to the Sanfranciscan Basin stratigraphy (Oliveira et al., 2017). In the western central parts of SM, Cenozoic cover supposedly coeval to the Chapadão Formation (unconsolidated, predominantly sandy cover composed of alluvial, colluvial, and eluvial deposits) (Campos and Dardenne, 1997b) occurs.

Using remote sensing images (e.g., ASTER scenes, WorldView-2, and stereoscopic ASTER DEM), Oliveira et al. (2014) identified three morpho-structural compartments in the SM impact structure: a Central Elevated Plateau

(CEP); Intermediate Annular Basin with inner rings, and an Outer Zone (Fig. 14). The CEP is characterized by a 3.2 km wide elevated area around the center of the Santa Marta structure and has been interpreted as a remaining part of the central uplift (Oliveira et al., 2014). Whereas the top of the CEP is a flat surface composed of undeformed materials (probably coeval to Chapadão Formation), the central uplift zone is represented by strongly deformed Devonian sandstones and pelites of the Pimenteiras and Cabeças formations that crop out concentrically and discontinuously in a region between the edge of the CEP and the inner rings. In the southern portion of the CEP (locally known as Sinésio's hill), impact breccias are represented by monomict sandstone breccias and polymict lithic breccias (Uchôa et al., 2013). The monomict breccia consists of clasts of coarse-grained, poorly sorted sandstones, with some samples exhibiting shock deformation features, such as PDF in quartz fragments. Polymict lithic breccias show clasts with mostly angular shapes, coarse-grained and poorly sorted sedimentary rocks within a silty-to-sandy groundmass (Uchôa et al., 2013; Oliveira et al., 2017). A few quartz grains from polymict lithic breccia also show PDFs (Oliveira et al., 2017). On the slopes of the CEP, polymict breccias also can occur as injected bodies (called intra/inter-strata polymict breccia) and, differently to polymict lithic breccias at the top of the CEP, such intra-/inter-strata polymict breccia shows fluidal structures and is intensely silicified (Oliveira et al., 2017). Structurally, several second-order structural elements were identified in the SM central uplift, such as drag and recumbent folds, overturned bedding, reverse faults, radial folds, antiform and synform axial traces (Oliveira et al., 2017).

The inner rings that emerge from the periphery of the central uplift to the outer zone have been thought to be sustained by rudaceous and coarse-grained psammitic facies that tend to be more resistant to erosive action (Oilveira et al., 2017). A good example is the Serra Grande Group of rudaceous rocks, which support the tops of elevations and separate Paleozoic units from Mesozoic units (e.g., Areado Group and Posse Formation). In some places, this separation can be represented by tectonically induced juxtaposition of units with different origins and ages (e.g., Serra Grande and Abaeté formations) (Oliveira et al., 2017).

Shatter cones are developed in fractured quartzite boulders from Quiricó Formation conglomeratic sandstone, and in chert breccias (Oliveira et al., 2017). In both morpho-structural compartments, primary sedimentary structures such as bedding and laminations are tilted and deformed, such that some strata show dips with high angles or even overturning. Concentric normal faults, fracture zones, synthetic faults, and lateral thrust ramps are some of the structural features that have been mapped in the SM impact structure (Oilveira et al., 2014, 2017).

Regarding geophysical data, a ground-gravity survey (Oliveira et al., 2014) revealed a large wavelength NE-SW trend of negative Bouguer anomalies that partially coincide with the CEP and shorter wavelength positive Bouguer anomalies in the central part and at the northwestern rim. According to Oliveira et al. (2014), part of the negative gravity signatures at SM may be related to the basement, but they also can be related to structural deformation undergone by target rocks due to the impact, whereas positive signatures probably are related to structural uplift. Oliveira et al. (2019) acquired additional gravity data and carried out forward modeling based on density values for sedimentary strata available in the literature. The results suggested the depth to basement was slightly shallower (700 m) in the northern portion of the CEP than directly below the CEP (850 m).

The large wavelength NE - SW trending negative Bouguer anomalies have also been identified by airborne gravity data (Vasconcelos et al., 2010), but these data also suggest the presence of a slightly circular 2 mGal positive Bouguer anomaly with a diameter at least twice the size of SM. This circular anomaly seems to be affected by a regional 1 mGal Bouguer anomaly (Vasconcelos et al., 2010). Additionally, this prominent NE-SW trend has been identified in magnetic data processed by Vasconcelos et al. (2010), who also identified an approximately circular -10nT low magnetic field slightly coinciding with SM's center. Because the origin by impact of SM was still under investigation in 2010, Vasconcelos et al. (2010) claimed that this low magnetic field could have resulted from impact, as impact structures with similar size to SM commonly showed such magnetic signatures. Vasconcelos et al. (2010) interpreted the strong Bouguer anomaly in SM as an indication that this structure could be an eroded impact structure because a positive Bouguer

anomaly may be present in such eroded impact structures (Pilkington and Grieve, 1992).

Magnetotelluric data acquired at SM showed complex geophysical signatures. On the one hand, Vasconcelos et al. (2019) suggested that the significant increase in the conductivity (or reduction in resistivity) starting at ~1 km depth might be interpreted as the depth to basement of the basin, but on the other the authors seem to attribute this increase to shale lithologies, not to crystalline basement. Whatever the case, Vasconcelos et al. (2019) claimed that the top of the basement was located at 1 km depth, consistent with the earlier estimation derived from low resolution magnetic data (~1 km) (Vasconcelos et al., 2010).

8.2.5 The São Miguel do Tapúio (likely) impact structure (SMT)

Like at other Brazilian impact structures, circular characteristics at São Miguel do Tapuio (SMT) had been noted since the 1970's (Lima and Leite, 1977; Crósta, 1987; Torquato, 1981; Crósta et al., 2019a), but shock deformation features were reported only since 2019 (Crósta et al., 2019c). The proposed SMT impact structure is located in the eastern portion of Piauí State (Fig. 15). It is centered at 5°37.6'S and 41°23.3'W, and its diameter has been estimated at 20-21 km (Torquato, 1981). Although bona fide shock evidence is still sparse, the existing findings suggest an impact origin for SMT, such that it can be considered the second largest impact structure in South America (Crósta et al., 2024). However, it should be noted that this shock evidence has only been presented in abstract form and that a full publication is still outstanding. These alleged shock features include FF, PF, and PDF features that have been found in sandstone and monomict sandstone breccia collected ca. 1 km from the center of the structure (Crósta et al., 2019c). SMT shows other features that would be consistent with an origin by impact but, by themselves, are not impact-diagnostic. This includes a rugged inner morphology contrasting with the surrounding terrain; annular and radial drainage; elevated rim and central ring; strongly deformed sandstones (sometimes even recrystallized/silicified) in the central zone with some strongly fractured quartz grains (Martins, 2016; Martins et al., 2016a, b; Crósta et al., 2019b).

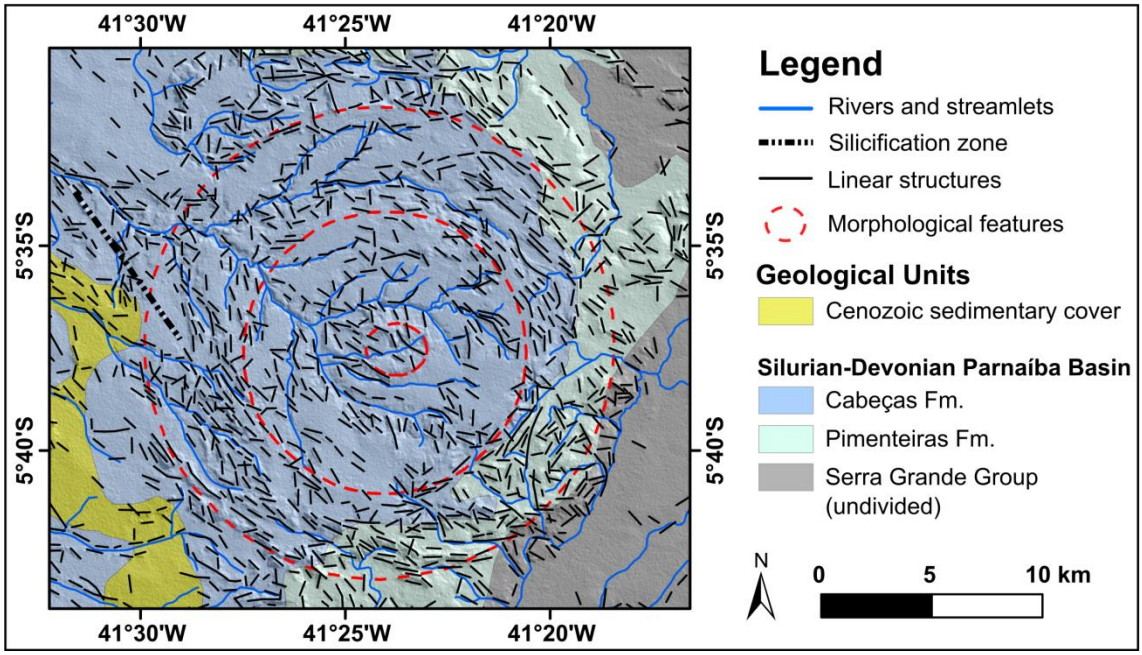

Figure 15: Geological map of the São Miguel do Tapuio (impact) structure. Modified after Martins (2016).

According to a geological map proposed for SMT, the affected country rocks consist of Silurian Serra Grande Group sandstones, conglomerate, siltstones and shales, and strata of the Mesodevonian-Eocarboniferous Canindé Group which are represented by Cabeças Formation sandstones, siltstones, and diamictites and Pimenteiras Formation sandstones (Martins et al., 2016b).

Based on remote sensing images (Landsat scenes and DEM from ASTER/GDEM), Martins et al. (2016b) proposed that SMT can be subdivided into the following morphostructural compartments (from periphery to center) (Fig. 15): outer rim - 20.5 km diameter and with elevated escarpment; intermediate ring – consists of circular elevated lineaments at 15.6 km diameter; annular rings - depressed zones between intermediate ring and central high, and central high - central zone - slightly elliptical with 3.8 km diameter. According to these authors, the strength of deformation increases from outer rim to central high, such that: i) the dip of strata becomes steeper toward the center; ii) sandstones become intensely deformed toward the central high, such that comminution of quartz grains, recrystallization, and presence of fractures are more evident towards the central zone.

Low-resolution airborne magnetic data for SMT were interpreted by previous workers (e.g., Mariano et al., 2004; Vasconcelos et al., 2010; Martins,

2016). Mariano et al. (2004) claimed that a semi-circular magnetic pattern is evident at SMT with spatial distribution of magnetic highs coinciding with morphologic characteristics of SMT. They suggested that this pattern reflects the iron-rich sandstone beds of the Cabeças Formation. Using these same low resolution airborne magnetic data, Martins (2016) suggested that the long wavelength magnetic signatures at SMT show a NE-SW trend compatible with the general tectonic framework of the Precambrian basement to the Parnaíba Basin, such that this trend can be related to the Transbrasiliano Lineament. Moreover, they noted that magnetic patterns at SMT were not compatible with mafic-alkaline igneous bodies at depth. Vasconcelos et al. (2010) carried out a profile analysis of magnetic data acquired at SMT, but their data was of a much lower resolution than the magnetic data used by Mariano et al. (2004) and Martins (2016). Even so, Vasconcelos et al. (2010) argued that magnetic signatures at SMT were very complex, with a positive and negative anomaly near the center and at the northern rim, respectively, and these interacted with a second positive anomaly between the center and rim.

A complex pattern has also been observed in gravity data acquired for the SMT impact structure. Vasconcelos et al. (2010) suggested that the gravity signatures are characterized by a positive anomaly at the southern rim, whereas the northern rim showed a negative one. On the other hand, Martins (2016) acquired ground-based gravity data and claimed to observe a gradual increase in the values of residual Bouguer gravity towards the internal and central rings of SMT. According to them, this would be in agreement with density variations. By Euler Deconvolution techniques, Martins (2016) suggested that the sources of gravity signatures at SMT are shallow (to a depth of 1.5 km), and some of them could be related to major faults in internal sectors of SMT.

CHAPTER 9

GEOLOGICAL SETTING OF POTENTIAL TARGETS

9. GEOLOGICAL SETTING OF POTENTIAL TARGETS

A series of possible targets as potential impact structures has been divided into two groups: potential targets in sedimentary rocks and potential targets in crystalline rocks. The first group includes the circular features named Itiquira (ITA), Cardoso (CDS), Carnaíbas (CNB), and São Francisco do Maranhão (SFM), whereas the second group includes the Bom Jardim (BJD), Sucunduri Dome (SCD), Inajá (INJ), Brejões (BRJ), and Colônia (CLA) targets (compare Fig. 6). Origin by impact has already been proposed for CLA and INJ, but no shock deformation features have been confirmed yet (Crósta et al., 2019a). The circular patterns of the SFM, BJD, SDC, and BRJ structures were already recognized in previous works (e.g., Lima and Leite, 1977; Romanini, 1982; Iwanuch, 1981; Barbosa et al. 1998), but the origin of these structures has been considered so far only as results from endogenous processes. The ITA and CDS structures can be seen in airborne magnetic regional maps (e.g., Brazil's Magnetic Map and Mato Grosso Aerogeophysical Atlas) (Correia, 2019; Silva and Alves, 2023), but their origin, whether by endogenous or exogenous processes, has not been discussed at the time of writing. Similarly, the formation of the CNB structure is unknown and, according to the available literature, this structure has not been identified in previous works, such that its characterization is described here for the first time. It is worth mentioning that the names for ITA, CDS and CNB were proposed based on the proximity of these structures to closest towns or villages. For the remaining targets, we use the names that were already referred in the literature. Finally, the center positions and sizes (e.g. diameter) of all targets are based on spaceborne or geophysical images, as will be introduced in the next sections. A brief description of local geologic settings for each target will be given.

9.1 Potential targets in sedimentary rocks

The CDS, ITA, CNB, and SFM structures occur in terrains covered by sedimentary rocks (Fig. 16). Like the confirmed Brazilian impact structures, ITA, CNB, and SFM occur in the Paraná and Parnaíba basins, whereas the CDS circular structure occurs in Tocantins Province where basement is covered by sedimentary strata of the Bananal Basin (Moreira et al., 2008).

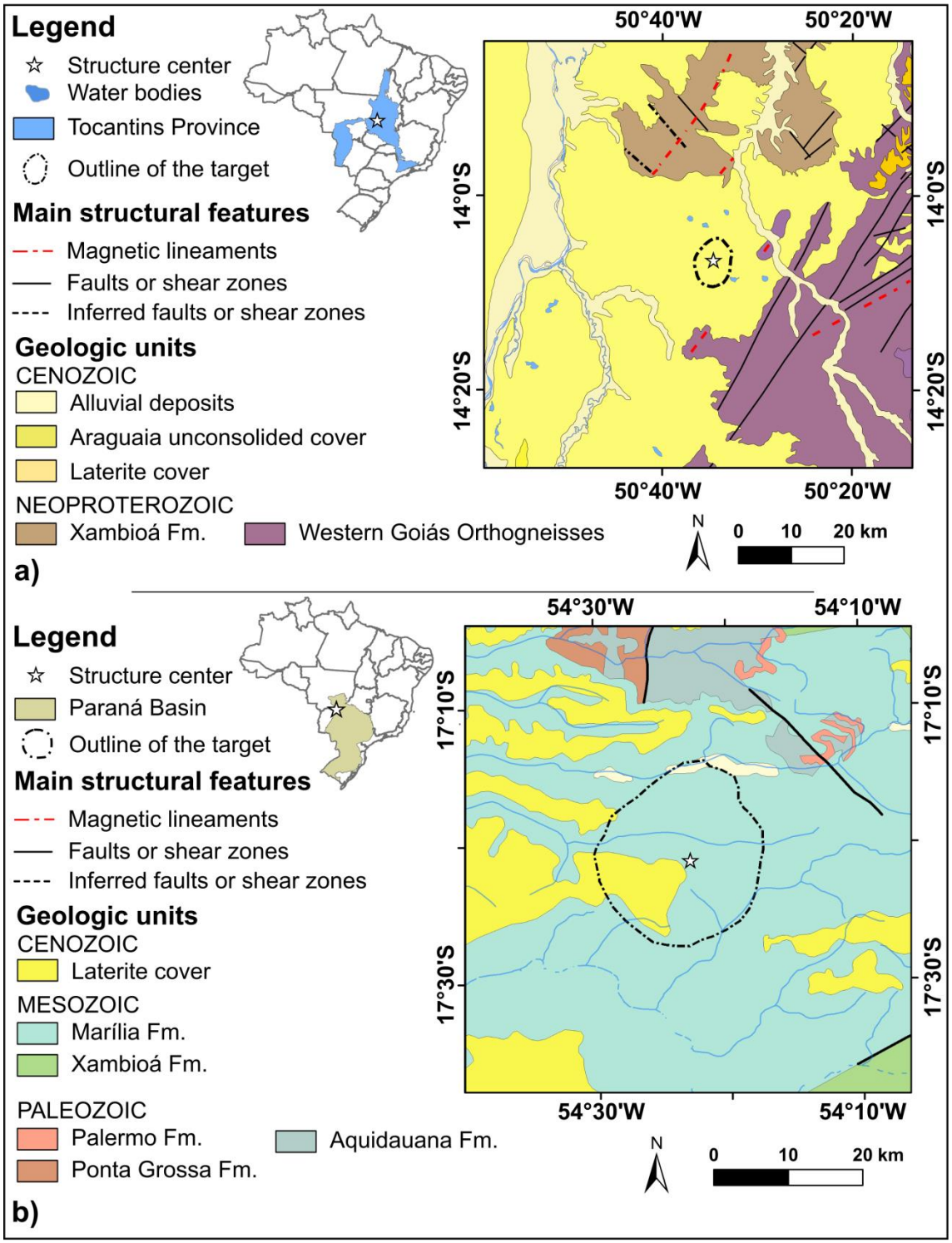

Figure 16: Simplified geological map of potential targets in the Bananal and Paraná basins. a) Geological map of the Cardoso structure. Modified after Moreira et al. (2008). b) Geological map of the Itiquira circular structure. Modified from Horn et al. (2022).

The CDS structure is centered at 50°34'W and 14°06'S, approximately 26 km to the west of the town of Nova Crixás in the northwest portion of Goiás State (Fig. 16a). Based on magnetic maps (this work, Chapter 14), the structure´s shape is slightly elliptical with a major axis estimated at ~5.25 km

trending in north-south direction. According to a regional geological map proposed by Moreira et al. (2008), the basement is composed of Neoproterozoic Western Goiás Orthogneisses (e.g., tonalitic orthogneiss) that occur mainly in the eastern portion of the CDS structure. Neoproterozoic metasedimentary rocks (aluminous schists, graphite schists, ferruginous quartzites, metaconglomerate) belonging to the Xambioá Formation have been mapped in the northern portion of the CDS structure, whereas the remaining areas, including the center of CDS, are covered by Cenozoic deposits (alluvial, laterites, and other unconsolidated materials – such as sand, silt, clay). The main structural features (magnetic lineaments, faults, shear zones) in the area are oriented along NE - SW and have been related to the Transbrasiliano Lineament (ibid).

The ITA circular target occurs near Itiquira town, in the southeast of Mato Grosso State (Fig. 16b). This structure is centered at 54°22'W and 17°21'S, approximately 160 km to the southwest of the Araguainha impact structure. Based on magnetic maps (this work), a ~17.5 km diameter is estimated for ITA. According to the regional geological map available for the Paraná Basin (Horn et al., 2022), the ITA region is predominantly formed by Upper Cretaceous Marilia Formation, fine-to coarse-grained sandstones and Cenozoic laterite cover, whereas in the north and northeast portions, Devonian-Permian strata are more abundant (e.g., Ponta Grossa Formation shales, Aquidauana Formation sandstones with shales or diamictites, Palermo Formation shales and siltstones) (Milani and Zalán, 1999; Horn et al., 2022). Late Jurassic to Early Cretaceous Botucatu Formation sandstones occur at the southeastern edge of the ITA structure.

The SFM and CNB circular structures are located in western Piauí State (Fig. 17). Initially, SFM was named "Amarante" by Lima et al. (1990), who were the first to recognize the circular pattern of this structure by analyzing radar images (SLAR X-band and Landsat - TM 4 - band). According to them, the "Amarante" structure shows circular features related to Mesozoic magmatism (probably Sardinha Formation basalts, see the geological map shown in Fig. 17). They also point out a set of NE-SW fractures within the area of circular

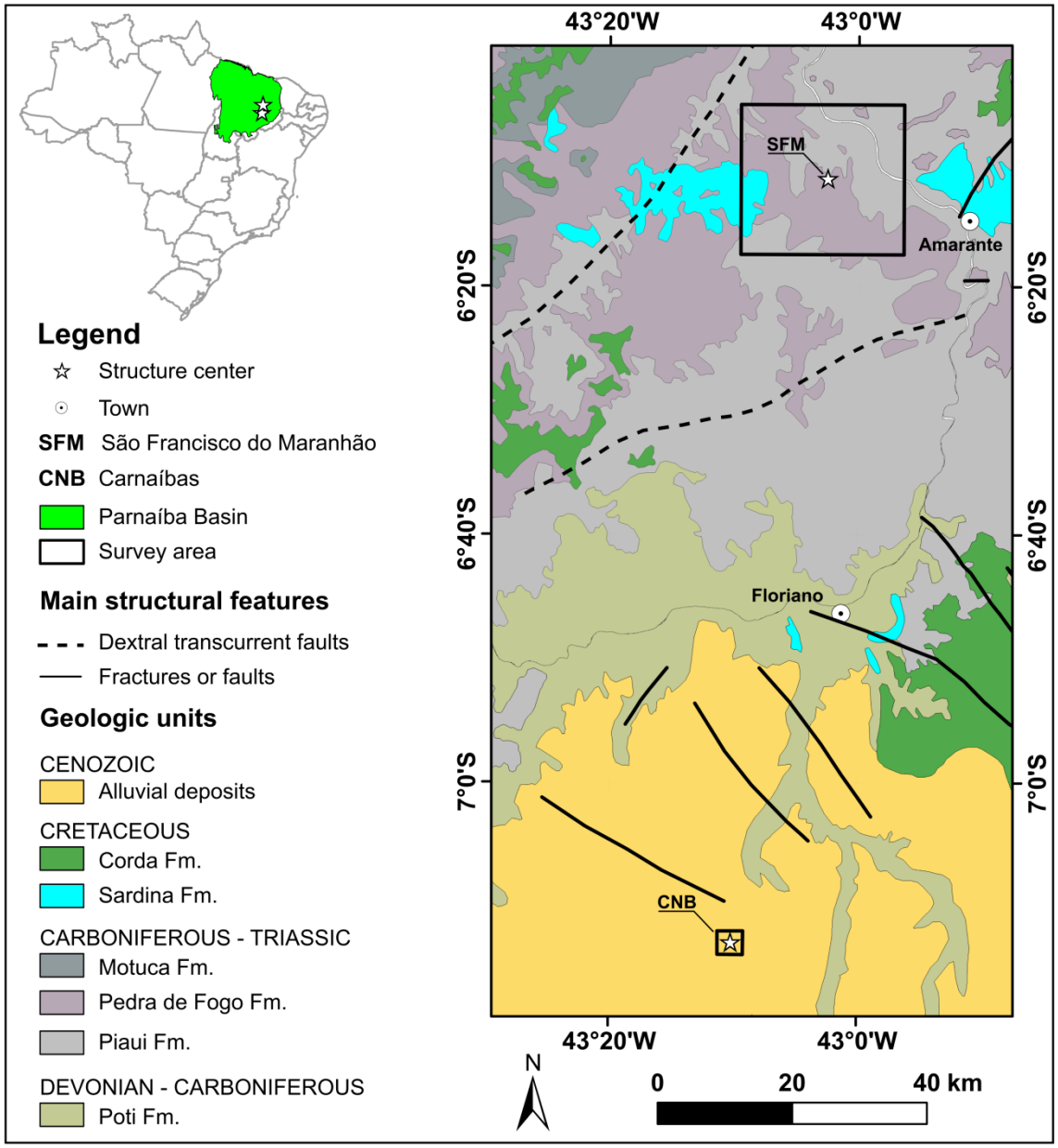

Figure 17: Simplified geological map of the potential targets in the Parnaíba Basin. Modified after Klein and Sousa (2012).

features (Lima et al., 1990). In 2015, a research team from the Maranhão Astronomy Society and Astrobiology Laboratory of the Federal University of Maranhão State (pers. comm. S.L.A. Brenha, São Luis) carried out fieldwork on the "Amarante" structure. Because most of the circular features of the "Amarante" structure are located relatively near to São Francisco do Maranhão town, this team decided to rename the circular feature from "Amarante" to "São Francisco do Maranhão".

The SFM structure is centered at 43°02'W and 6°11'S; its diameter has been estimated at 8.5 km. The structure occurs approximately 21 km from the

NW part of São Francisco do Maranhão town that, in turn, is located approximately 130 km from the state capital, Teresina. Although a set of uncommon rocks has been found within the SFM circular structure (e.g., supposedly fractured and brecciated sandstones), no shock deformation features have been reported from SFM yet. The regional geological map by Klein and Sousa (2012) shows that rocks probably represent mainly Pennsylvanian Piauí Formation sandstones, mudstones, and siltstones, and Permian Pedra de Fogo sandstones, shales, and siltstones (Fig. 17), whereas Middle Cretaceous Sardinha Formation gabbroic rocks seem to occur in the western portion of SFM.

The CNB circular structure is located approximately 115 km to the south of the SFM structure (Fig. 17). The nearest town from the CNB structure is Floriano, which is 52 km to the north. This circular structure is centred at 43°10'W and 7°12'S, and its diameter has been estimated at 650-700 m (this work). According to the geological map (Fig. 17), CNB seems to be located in a large area predominantly formed by unconsolidated material (e.g., sand, clay, gravel). In the northern portion of the CNB structure, NW-SE trending structural features (fractures or faults) occur at a distance of 6-10 km from the circular structure.

9.2 **Potential targets in crystalline rocks**

Three of these five targets occur on the Amazonian Craton and two on the São Francisco Craton and in the Mantiqueira Belt, respectively (see Fig. 6). The Amazonian Craton has been traditionally subdivided into structural provinces based on geochronological data (e.g., Santos, 2003), such that the three potential targets there are located in the Rondônia - Juruena and Carajás provinces (see Fig. 6) (after Santos, 2003).

The Carajás Province has been interpreted as a dominantly Neoarchean province with a WNW – ESE structural trend, practically covering the SW portion of Pará State. This province can be divided into two domains, named Carajás and Rio Maria. The Inajah potential target studied here occurs in the Rio Maria domain, more precisely in its southernmost portion that has also been referred as the Santana do Araguaía Domain (Silva et al., 2021). In this domain, the oldest geologic units near INJ are Mesoarchean tonalite-trondhjemite-

granodiorite terrains and migmatites and gneisses of the Arco Verde Complex, and metavolcanosedimentary facies (e.g., Mesoarchean Quixadá Formation metamafic/meta-ultramafic rocks, Morada da Prata metasandstones, shales, and metasiltstones, and banded iron formation, and Neoarchean metagranites - Alto Rio Inajá) (Silva et al., 2021) (Fig. 18).

The Inajah (INJ) circular structure is centered approximately at 50°58'W and 8°40'S, and its diameter has been estimated at 6-8 km (Cunha et al., 1981, p. 111; Cicco and Zucoloto, 2002; Crósta et al., 2019a; Silva et al., 2021). Although a possible origin by impact has been suggested to explain the formation of INJ (Martini and Liu, 1997 apud Acevedo et al., 2015; Cicco and Zucoloto, 2002), no shock deformation has so far been found. Alternatively, INJ has also been interpreted as a magmatic intrusion similar to other 2-4.5 km sized circular bodies in the southernmost portion of the Rio Maria Domain (Cunha et al., 1981, p. 111; Silva et al., 2021) (Fig. 18). Such circular bodies and the INJ structure belong to the Orosirian Tarumã Suite (Cunha et al., 1981; Silva et al., 2021).

According to Cunha et al. (1981, p.111), the Tarumã Suite encompasses biotite-granites, monzonite, alkali granites, hornblende-biotite granite, granodiorite, and tonalite. In its type section, which corresponds to the location of the INJ circular structure, Tarumã Suite rocks intrude the Paleoproterozoic Mururé Formation metapsammite facies (medium- to coarse-grained meta-sandstones, which are stratified and sometimes feldspathic, with levels of conglomeratic metasandstones and oligomict metaconglomerates (Silva et al., 2021) (Fig. 18). In the contact zone between INJ and the metapsammites, contact metamorphism has generated strongly silicified rocks and alumosilicate para-hornfels, where the granular minerals (quartz, feldspars and/or cordierite) are associated with elongated poikiloblastic andalusite, biotite, muscovite, and fibrous sillimanite (Cunha et al., 1981, pg. 111; Silva et al., 2021).

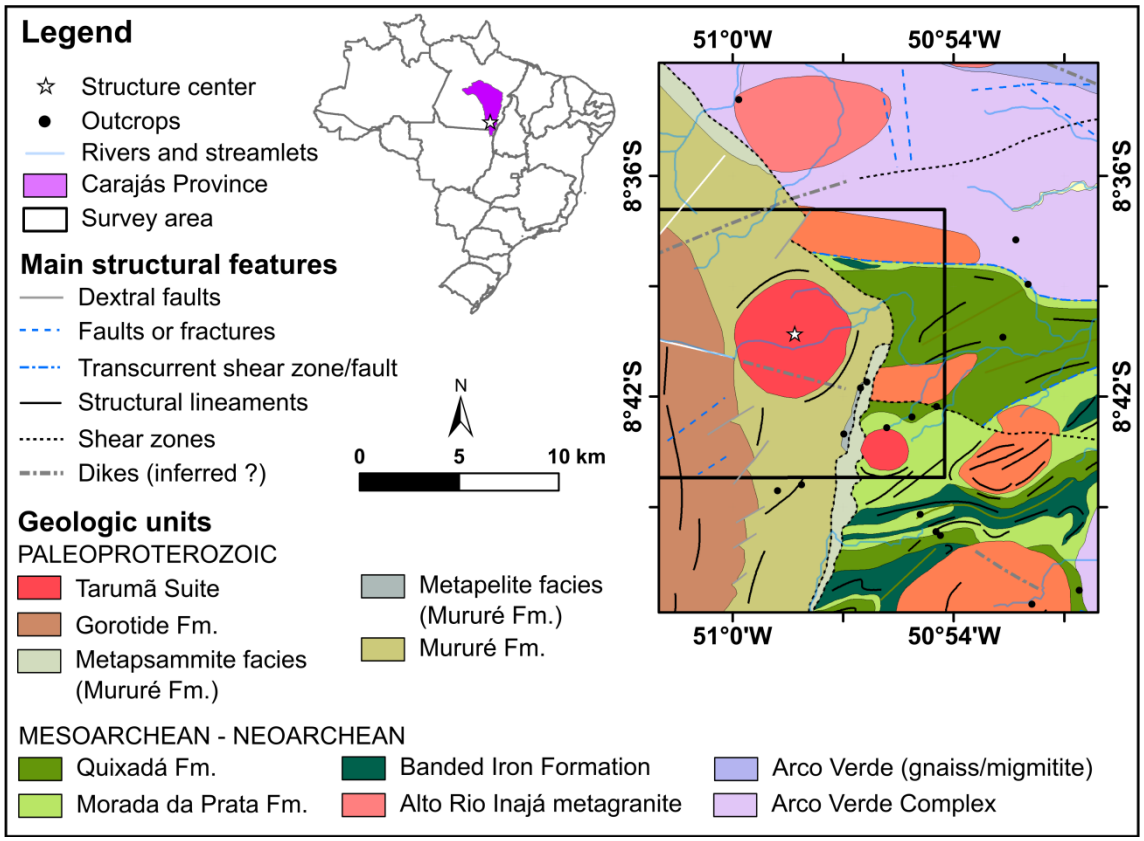

Figure 18: Simplified geological map of the Inajáh potential target. Modified after Silva et al. (2021).

Morphologically, INJ is characterized by a depressed circular basin surrounded by a strongly weathered ring (Cicco and Zucoloto, 2002; Acevedo et al., 2015). Dikes inferred from magnetic data seem to occur in the southern INJ. According to the geological map of the Rio Inajá sheet (Silva et al., 2020), vertical fractures and vertical quartz veins occur within INJ. The INJ border is well defined in the magnetic map, but radiometric signatures are subdued over INJ (Almeida et al., 2020; Silva et al., 2020). Unregulated gold mining has been reported from the southern INJ structure by Silva et al. (2020).

The other two circular features in the Amazonian Craton studied here occur in the Rondonia-Juruena Province. This province is younger than Carajás, and its evolution has been linked to a system of magmatic arcs (Santos, 2003). The Rondonia-Juruena Province can be divided into three domains, namely the Alta Floresta, Jamari, and Juruena domains. The Sucunduri Dome circular structure occurs in the Juruena Domain, whereas Bom Jardim occurs in the Jamari Domain.

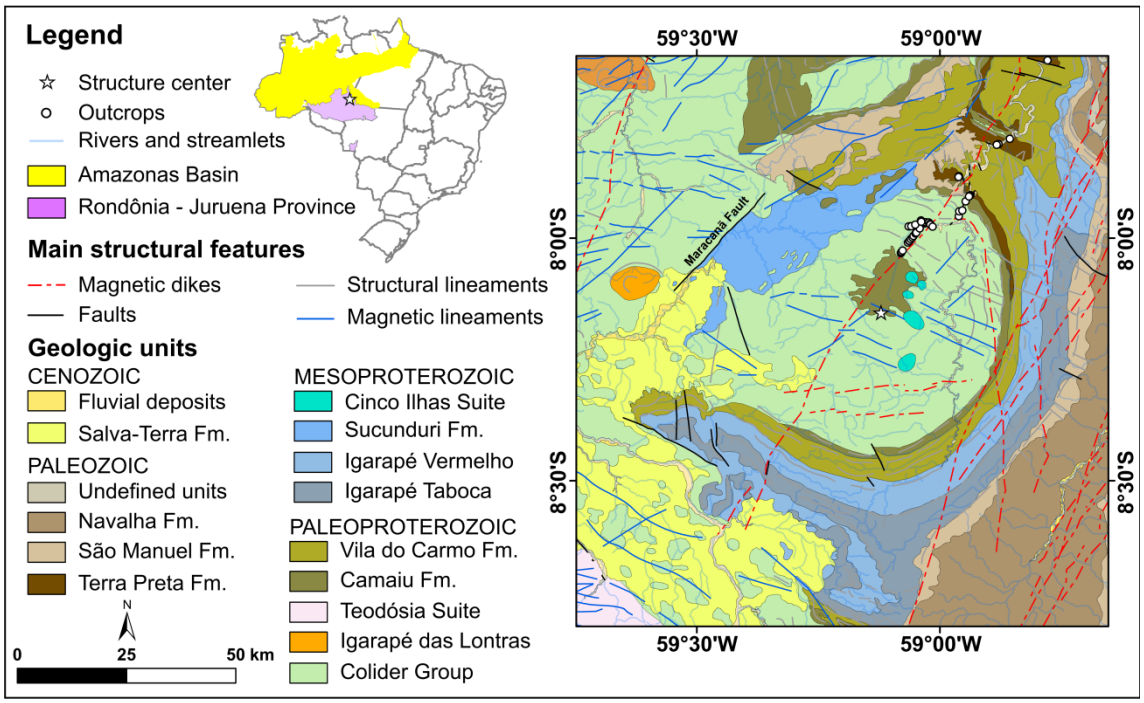

Figure 19: Simplified geological map of the Sucunduri Dome potential target. Modified after Meloni et al. (2021). The outcrop places were visited by I.P. Marques (Geological Survey of Brazil), who kindly shared information in 2024/2025 for the present research.

The Sucunduri Dome (SCD) is an impressive semi-circular feature with an estimated diameter of over 75 km (Iwanuch, 1981). This domal structure is centered at 59°07'W and 8°07'S, in the northwestern Juruena Domain, southeastern Amazonas State (Fig. 19). According to a geological map by Meloni et al. (2021), felsic volcanic rocks with subordinate mafic and intermediate rocks belonging to the Orosirian-Statherian Colíder Group occur in the inner portion of SDC and over the entire western portion of this structure (Fig. 19). Other Statherian units (e.g., Igarapé das Lontras Suite syenogranitos, monzogranites, quartz syenites, and Teodosia Suite monzogranites, granites, tonalites and orthogneiss) also occur in the study area, but they are outside of Sucunduri Dome (Fig. 19).

In the innermost portion of SDC, Orosirian-Statherian Camaiú Formation volcanic rocks and rocks of the Calymmian Cinco Ilhas Alkaline Suite occur (Fig. 19) (Iwanuch, 1981; Teixeira, 1990; Meloni et al., 2021). The sequence can be summarized as a sequence of conglomerates, sandstones, and volcanic tuffs, whose transport occurred at a high base level gradient, and sedimentation was concomitant with volcanism (Meloni et al., 2021). However, the type section of the Camaiú Formation described by Meloni et al. (2021) is outside of the

SDC circular structure. Within SDC, fieldwork carried out within the scope of the Geology of Rio Acari sheet Project, Geological Survey of Brazil geologists found volcanic and primary volcaniclastic rocks (see the outcrop points on the geological map in Fig. 19) (I.P. Marques, pers. commun). Near the northcentral SDC, where Meloni et al. (2021) proposed the occurrence of Camaiú Formation (Fig. 19), these geologists found alkaline volcanic rocks, some of which are hematite-bearing (I.P. Marques, pers. commun). These findings suggest that the volcanic rocks near the northern part of SDC may be related to the Cinco Ilhas Alkaline Suite rather than the Camaiú Formation. Other volcanic products such as tuffs, basalts, breccias (pyroclastic - with rhyolite fragments; and epiclastic - e.g. tuffo-psamite), rhyolites, quartzites, and ignimbrite have been reported from the eastern inner portion of the SDC structure (Iwanuch, 1981; I.P. Marques, pers. commun.), whereas quartzites and meta-arenites were mapped on the outside of the NE sector of SDC.

Morphologicaly, the circular pattern of SDC is well-defined in the NE, E, SE, S, and SW sectors, but the structure is open in the NW and N sectors. In the western portion of the SDC structure, Colíder Group volcanic rocks are covered by Mesoproterozoic Sucunduri Formation sandstones that, in turn, are covered by Cenozoic cover (Fig. 19) (Meloni et al., 2021). Long magnetic dikes trending NE-SW cut the eastern rim and inner southern portion of the SDC structure, whereas magnetic lineaments trending NW-SE cut the inner portion of SDC and the NW sector of the survey area (Fig. 19). Other NW-SE trending structural features (e.g., morphological lineaments) also cut SDC, whereas some NNW-SSE faults seem to be present in the southern rim of SDC. The northwestern rim seems to be marked by a large NE-SW trending fault known as the Maracanã Fault (Iwanuch, 1981).

Finally, the SDC structure shows impressive semi-circular and concentric radiometric signatures in regional maps (Correia et al., 2019b; Meloni et al., 2021). The circular shape of the SDC structure is not so well-developed in the magnetic anomaly maps as suggested by the radiometrics, but it is still possible to identify circular magnetic anomalies that apparently follow the morphology of the structure (Correia, 2019a).

The third potential target on the Amazonian Craton is located in the western portion of the Rondônia-Juruena Province, in the Jamari Domain. This

domain is composed of Paleoproterozoic metamorphic complexes, Mesoproterozoic metavolcanosedimentary rocks, and several rapakivi type granitic intrusions with associated charnockites (Santos et al., 2000; Santos, 2003). Rapakivi magmatism has been thought to have occurred in successive episodes, of which the youngest (995 to 974 Ma) resulted in the formation of the Rondônia Intrusive Suite, also known as Younger Granites of Rondônia (Bettencourt et al., 1997; 1999; Palmeira and Carvalho, 2018).

Among several granite massifs of the Younger Granites of Rondônia, this study focuses on the Tonian Massangana granites. These granites intruded the metamorphic complex forming an ellipsoidal intrusion with a major axis along NE-SW. These rocks are mainly composed of tabular and ovoid megacrysts of K-feldspar with biotite (Romanini, 1982; Bettencourt et al., 1997) (Fig. 20). Besides the Massangana granite itself, this massif shows three other granite facies known as São Domingos, Tabocas, and Bom Jardim. The potential target Bom Jardim (BJD) studied here occurs precisely in this latter facies (Fig. 20).

The Bom Jardim (BJD) target is centered at 63°27'W and 9°57'S, approximately 47 km to the west of Ariquemes town, which is southwest of Porto Velho, the capital of Rondônia State (Fig. 20). The BJD structure has been interpreted as an elliptical stock with a diameter estimated at 8-10 km (Romanini, 1982). According to this author, the Bom Jardim/Massangana facies contact zones are abrupt with numerous enclaves of Massangana facies of up to meter-size in Bom Jardim facies. In the southeastern part of the rim of BJD, Bettencourt et al. (1997) reported that fine-grained Bom Jardim biotite granite intruded the Massangana coarse-grained porphyritic biotite granite. The contact zone is sharp and blocky, with many fragments of the Massangana granite in the Bom Jardim granite, up to 50 m from the contact. According to Romanini (1981), Bom Jardim granite injection overprinted intense fracturing of the Massangana facies.

The Bom Jardim granites show textural variation towards the center, changing from coarse-grained to medium- or even fine-grained. This textural variation has been interpreted as resulting from uneven cooling of the magma, or melting with uneven distribution of water in the magma chamber (Romanini,

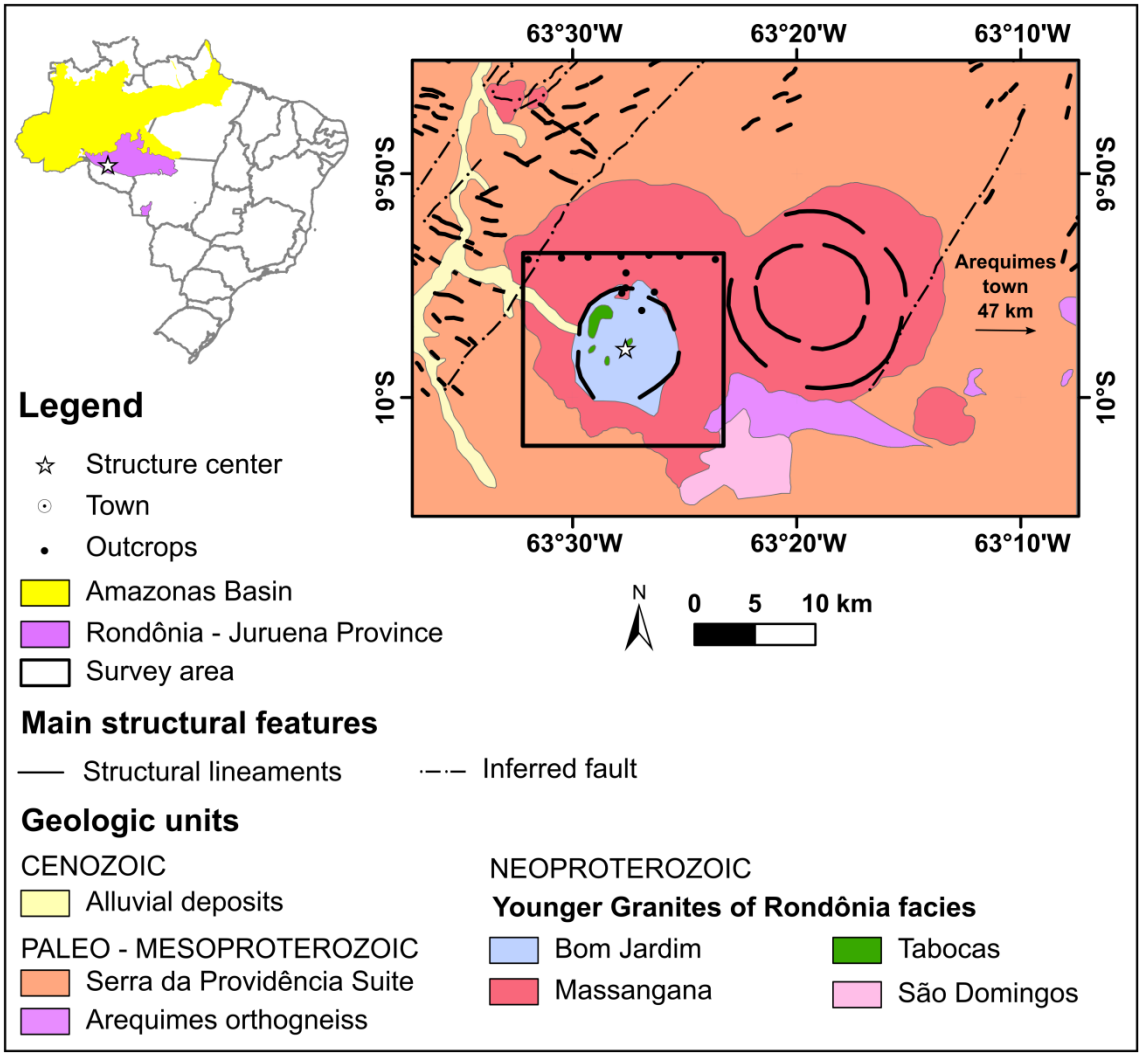

Figure 20: Simplified geological map of the Bom Jardim potential target. Modified after Romanini (1982), Bettencourt et al. (1997,1999), and Palmeira and Carvalho (2018).

1981). Microgranite dykes of 20 cm width trending NW and NE are common near the central zone of the stock. In thin sections, perthitic orthoclase seems be dominant in the Bom Jardim facies, with biotite, quartz, and plagioclase the most common inclusions. These minerals are commonly surrounded by finer-grained quartz, biotite, plagioclase, fluorite, and biotite halos. Quartz occurs in idiomorphic crystals and mainly as a constituent of finer-grained masses in the interstices between larger crystals (mainly orthoclase) (ibid).

The São Domingos facies has also been affected by intense fracturing of the Massangana facies, and the contact zones between the São Domingos and Massangana facies are also abrupt. From one of these contact zones, Bettencourt et al. (1997) reported that the São Domingos granite contains angular decimetric to metric xenoliths of different types of rocks, including a

prominent biotite augen gneiss (probably from the Jamari Complex). Still according to these authors, the xenoliths are dislocated from their original positions and show sharp contacts with the host granite. The São Domingos granites apparently show less textural variation compared to those of the Bom Jardim facies.

The northwestern part of the BJD structure seems to be intruded by hornblende syenites and quartz-syenites of the Tabocas facies (Fig. 20). The contact zones between the Tabocas and Bom Jardim facies are marked by a number of granite enclaves of up to several meter size (Romanini, 1981). Similarly to the Bom Jardim facies, Tobocas syenites also show textural variation with granular, microgranular, and porphyritic types.

In terms of geophysical signatures, Buch et al. (2019) reported that granitic intrusions related to the Younger Granites of Rondônia commonly are demagnetized, showing anomalies of low amplitudes and frequencies. On the other hands, such granites show strong radiometric signals, mainly regarding K, such that these granites show red shades in RGB composite color of a radioelement map.

Like the potential targets of the Amazonian Craton, Brejões (BRJ) (also known as the Brejões Dome) occurs in a cratonic terrain, but on the São Francisco Craton (Fig. 21). The BRJ circular structure is centered at 39°46'W and 13°07'S, approximately 8 km from the southern end of Brejões town and approximately 200 km to the west of Salvador, the capital of Bahia State. The BJR structure occurs in the Jequié Block of enderbite to charnockite suites (2.7-2.8 Ga), with heterogeneous granulites with migmatites and supracrustal rocks (Barbosa et al. 1998, 2004, 2006). According to the Geological Map of the Amargosa sheet (Cruz et al., 2009) and previous studies carried out by Barbosa et al. (1998 and 2004), the nearest exposures of country rocks at the BRJ structure are supracrustal formations and heterogeneous granulites, whereas inside the BRJ structure occur the Brejões charnockites (Fig. 21). The western portion of BRJ is covered by Cenozoic sediments (Fig. 21).

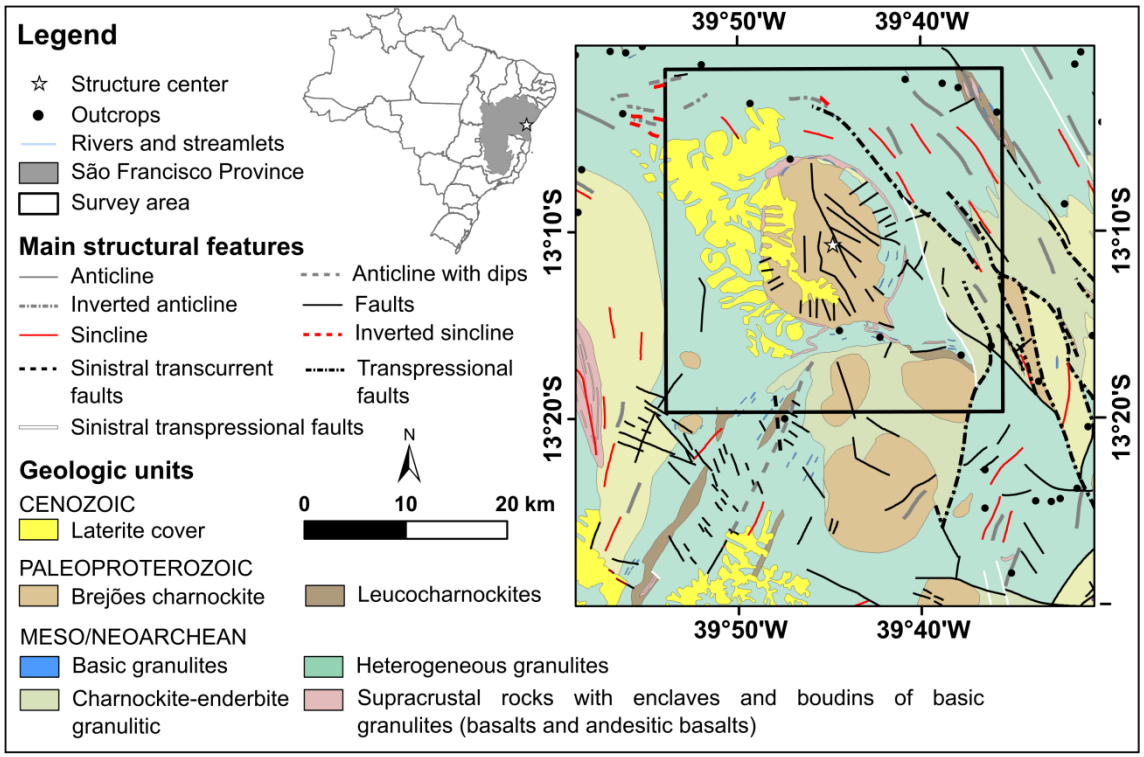

Figure 21: Simplified geological map of the Brejões potential target. Modified after Barbosa et al. (1998, 2004) and Cruz et al. (2009).

The heterogeneous granulites and supracrustal rocks seem to be the oldest rocks of the Jequié Block (Barbosa et al., 2004). The former mainly consist of dark green granulites with charnockite characteristics and the latter include aluminous kinzigite gneisses, metabasalts/andesitic metabasalts, iron formation, quartzites, and garnet bearing quartzites, graphite, quartz, feldspathic bands, intrusive metagrabbros and charnockites with garnet and cordierite (Barbosa et al., 1998, 2004). The heterogeneous granulites occur mainly outside of the BJR structure, but they are also found in BRJ's eastern sector (Fig. 21) (Cruz et al., 2009). The rim of BRJ is well-defined by the supracrustal rocks that occur continuously in the northern, northeastern and southeastern sectors of the BRJ structure (Fig. 21) (Barbosa et al., 1998; Cruz et al., 2009).

Inside of the BRJ structure, the charnockite intrusive bodies are heterogeneously deformed and include angular xenoliths of the country rocks (e.g., heterogeneous granulites) (Barbosa et al., 2004). These charnockites are composed of mesoperthite and antiperthite alkali feldspar, quartz, hornblende, orthopyroxene, clinopyroxene, opaque minerals (ilmenite, magnetite, pyrite), and accessory minerals (apatite and zircon). Near the Brejões charnockite

contact zone, Barbosa et al. (2006) reported porphyroblasts (2.0 - 4.3 mm) and xenomorphic (0.3 - 1.2 mm) quartz crystals with undulatory extinction, deformation bands, development of sub-grains with serrated to lobate boundaries to other quartz grains, and microstructures that bulge into neighbouring, deformed (elongate and almond-shaped) garnet porphyroblasts. Moreover, thermobarometry, chemical and mineral assemblage analyses suggest the conditions at BRJ emplacement were high temperature (900-1000°C) and low and intermediate pressures (5-8 kbar) (Barbosa et al., 2006). Because this temperature is higher than the temperature of the regional metamorphic peak recorded outside of the BRJ, Barbosa et al. (2006) suggested that this temperature rise could have been caused by underplating of lower crust by magmas that provoked partial melting of the Brejões charnockite.

Structurally, the rocks in the BRJ structure show foliations dipping outwards in the east, west, and north sectors, but their dips change towards the center in the southern portion (Barbosa et al., 2004; Cruz et al., 2009). According to Barbosa et al. (2004), the BRJ structure is widely deformed, with the rim showing high strain with typically vertical structures, whereas the central portion displays more homogeneous rocks with subhorizontal dips. Radial faults are abundant in the rim, whereas the core seems to be characterized by an approximately N-S trending fault. In terms of geophysical signatures, the BRJ structure shows high eU and eTh concentrations that have been related to laterite cover (Iza et al., 2020). Although a well-defined circular magnetic anomaly can be seen in the regional magnetic map (e.g. Cruz et al., 2009; Correa, 2019a), the origin of this magnetic anomaly has not been studied yet in detail.

The last potential target located in a crystalline domain is the well-known Colônia (CLA) structure. The CLA occurs within Neoproterozoic - Early Paleozoic Mantiqueira Province strata, which form an overall NNE-SSW trending tectonic entity with several remnants of Precambrian rocks that were involved in the Brasiliano orogenic cycle (Delgado et al., 2003). According to most recent geological maps (Perrota et al., 2005; Riccomini et al., 2011; Almeida et al., 2019), the northern portion of the Precambrian basement in the CLA structure is represented by metasedimentary rocks (amphibolite, biotite quartz-muscovite schist, mica schist, quartzite and intercalations of amphibolite

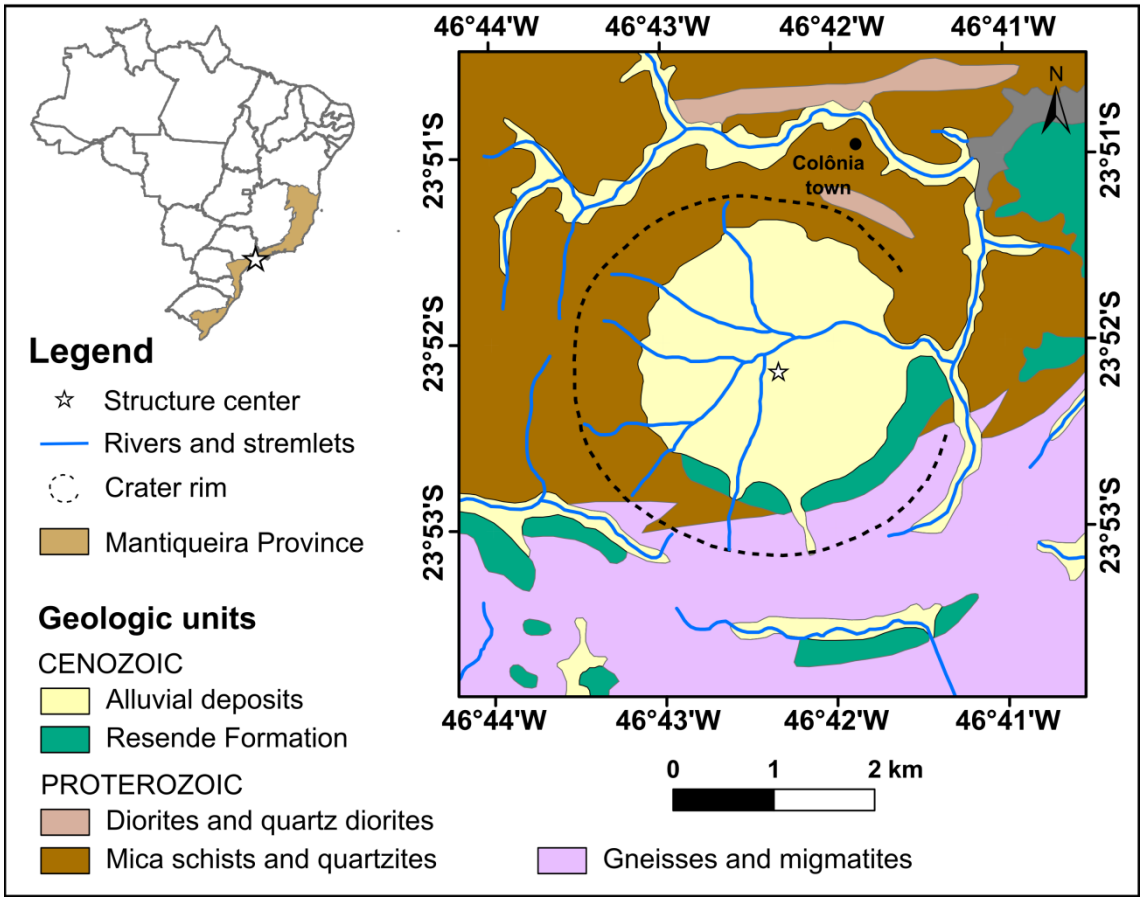

Figure 22: Simplified geological map of the Colônia potential target. Modified after Riccomini et al. (2011).

and calc-silicate), whereas the southern portion is composed of gneisses and migmatites.

According to the geological map proposed by Riccomini et al. (1991, 2011) (Fig. 22), the southern sector of the CLA structure is covered by Resende Formation mudstones that occur tectonically imbricated with gneiss along a WNW - ESE-oriented thrust fault zone. The CLA crater structure is filled by organic matter-rich alluvial deposits (Riccomini et al., 1991).

The CLA structure is centered at 46°42'20'' and 23°52'S and is located approximately 35 km south of São Paulo city center (Riccomoni et al., 1991, 2011) (Fig. 22). The CLA has an almost perfectly circular shape of 3.6 km diameter, and its elevated rim reaches up to 125 m above the inner depression (ibid; Crósta et al., 2019b). Although this structure has been listed as a confirmed impact structure in the Impact Earth Database (https://impact.uwo.ca) (Osinski et al., 2022), bona fide shock diagnostic features have not been reported from the CLA structure yet. This apparent contradiction is due to the

poor publication and documentation of supposed shock deformation (e.g., Velázquez et al., 2013, 2018). From chip samples recovered from two boreholes drilled inside the CLA crater for groundwater exploration, Velázquez et al. (2013, 2018) claimed to have identified impact products (e.g., impact melt-bearing breccia, impact melt rock) and shock deformation (PDF). Whilst a few of their images show interesting features, these presentations are not sufficient to clarify whether this is diagnostic impact deformation (see Reimold et al., 2014). Unfortunately, the samples analyzed by Velázquez et al. have not been made available to the scientific community, so the origin of CLA will still remain under discussion.

The CLA structure has also been studied by geophysical methods. Overall, all previous geophysical studies carried out at the CLA structure were aimed at the identification of basement depth and thickness of the sedimentary fill (e.g., Kollert et al., 1961; Motta and Flexor, 1991; Passos and Shukowsky, 1997; Masero and Fontes, 1991; Neves, 1998, Miura et al., 2015, and Riccomini et al., 2011). The basement depth estimated in these studies, which applied different geophysical methods, varied from 285 m (by using Vertical Electrical Sounding - Koller et al., 1961) to 380 - 450 m (using P-wave refraction seismic – Neves, 1998).

The most recent geophysical investigation at CLA was carried out by Prado et al. (2019). By integrating different results from different geophysical methods (e.g., 3D inversion of ground-gravity and geoeletrical pseudo-sections, interpretations of stacked seismic reflaction sections, and inversions of surface wave data), they suggested that they found a depth to basement of approximately 400 m. Moreover, they also found a seismic interface (named SS5) that could represent the top of a potential breccia layer in the structure. According to Prado et al. (2019), their results were significant achievements toward the planning of a deep borehole, which was proposed under the auspices of ICDP, but unfortunately this project has been on hold for several years.

CHAPTER 10
METHODOLOGY

10. METHODOLOGY

In order to compile the main features of the Brazilian impact structures and then compare with those of potential targets, three types of information were analyzed: geological; geophysical, and spaceborne optical and radar data. The Oasis Montaj (version 2022) software from Seequent was used to process airborne geophysical data, whereas Sentinel Application Platform (SNAP) from the European Space Agency (ESA) and Environment for Visualization Images (ENVI) (version 5.6) from NV5 Geospatial softwares were used for processing spaceborne images. The geological, geophysical, and spaceborne images were organized into maps by using ArcMap environment from ArcGis software from Esri. Some statistical analysis applied on gamma-ray spectrometry data was carried out by using the interface RStudio for R software (R Core Team, 2024; RStudio Team, 2024). Figure 23 schematically summarizes the overall framework of methodology adopted in this work. In the following subsections, some detail of how each kind of information was obtained will be given.

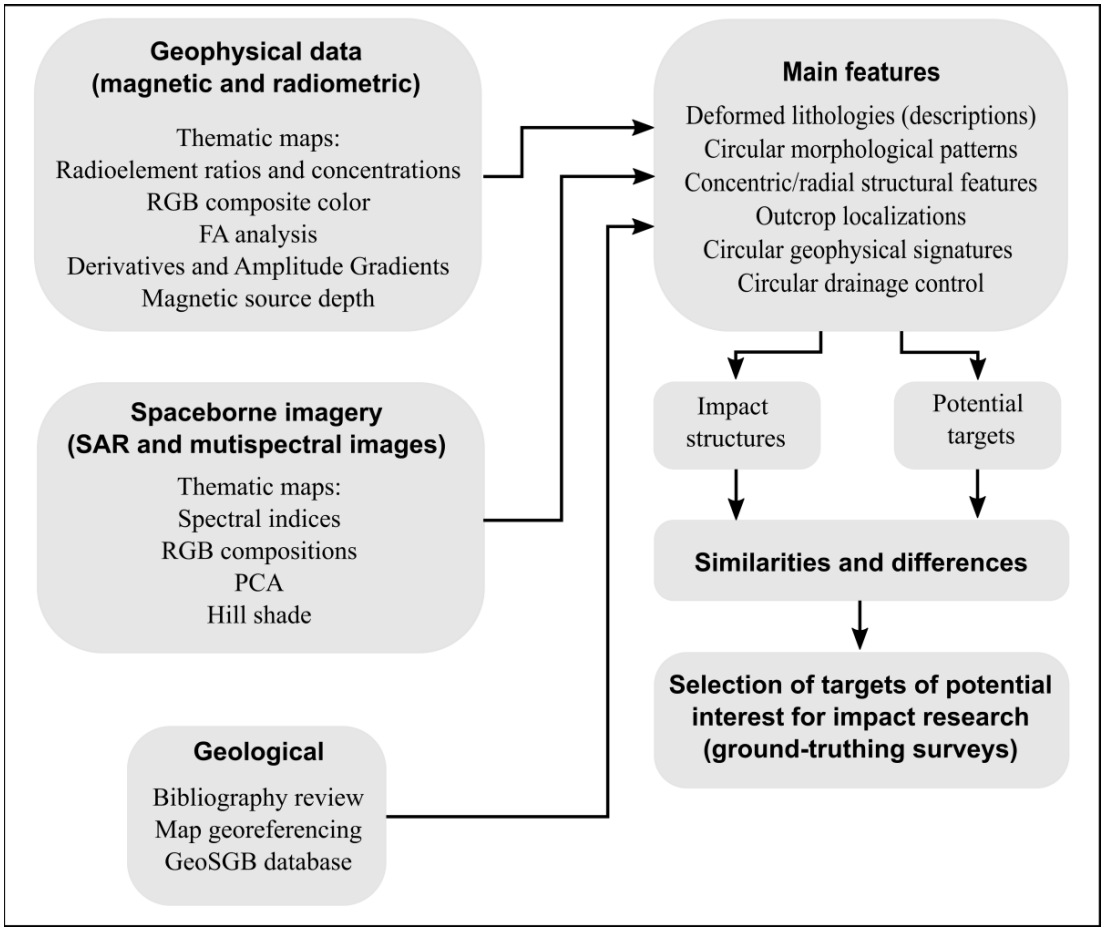

Figure 23: Overall framework of methodology adopted in this work.

10.1 **Geological information and maps**

In order to obtain comprehensive information about the impact structures, several types of geological information (e.g., lithologies, morphological limits, shock deformation, structural features, etc) were compiled from the literature and by digitalization of geological maps that had been published previously (see Table 1).

Although each Brazilian impact structure shows particularities, this work has looked for characteristics that are common to all or most of them, mainly regarding features related to deformation (e.g., faulting, brecciation, folding). In order to do this, the geological information was categorized into three classes: information about shock diagnostic features; information about presence of different types of impactites, including their textural and/or compositional aspects; information about the presence of first (central uplift, annular basin, crater rim) or second (listric faults, thrusting, isoclinal folds, sinclines, anticlines, etc) order structural elements. The relationship between undeformed and deformed zones has also been analyzed to verify how impact events disturbed regional geological patterns. The main objective of this approach was to understand the overall context of Brazilian impact structures.

Regarding potential targets, the main geological information (e.g., lithologies, outcrop localization, structural features, etc) was obtained from Geological Survey of Brazil final reports or geological maps, and other publications (e.g., dissertations, theses, expanded abstracts, and articles). The geological maps of potential targets were derived from several vectorial files available on the GeoSGB database website (Table 1). For each potential target, a geological map was prepared according to the scale available on the GeoSGB website. Additionally, information on mining activity (requirements) derived from the Mining Geographic Information System website (SIGMINE in Portuguese) was also researched, because it may provide useful information for the interpretation of the origin of potential targets.

Table 1: List of Brazilian impact structures and potential targets that were studied in this work.

Structure		References
Impact structure	Araguainha (AGD)	Engelhardt et al. (1985, 1992), Crósta et al. (1981, 1982, 2019a), Lana et al. (2007, 2008), Sousa et al. (2024), Borgest et al. (2025)
	Cerro do Jarau (CJU)	Sánchez (2014), Crósta et al. (2010b, 2019a), Reimold et al. (2019)
	Vargeão Dome (VGD)	Crósta et al. (2005, 2012, 2019a), Alsemgeest et al. (2024)
	Vista Alegre (VTA)	Crósta et al. (2010b, 2019a)
	Serra da Cangalha (SdC)	Reimold et al. (2006), Kenkmann et al. (2011), Vasconcelos et al. (2013)
	Riachão Ring (RR)	McHone (1981), Maziviero et al. (2012, 2013), Crósta et al. (2019a)
	Nova Colinas (NVC)	Reimold et al. (2022), Avona et al. (2025)
	Santa Marta (SM)	Uchôa et al. (2013), Oliveira et al. (2014, 2015, 2017), Crósta et al. (2019a)
	São Miguel do Tapuio (SMT)	Torquato (1981), Crósta (1987), Crósta et al. (2019b and c), Martins et al. (2016a and b)
Potential target	Itiquira (ITA)	Horn et al., 2022
	Cradoso (CDS)	Moreira et al. (2008)
	São Francisco do Maranhão (SFM)	Lima et al. (1990), Klein and Sousa (2012)
	Caraíbas (CNB)	
	Bom Jardim (BJD)	Romanini (1982), Bettencourt et al.(1997), Bettencourt et al. (1999), Palmeira and Carvalho (2018)
	Sucunduri Dome (SCD)	Iwanuch (1981), Meloni et al. (2021)
	Inajáh (INJ)	Cunha et al. (1981), Silva et al. (2020), Silva et al. (2021)
	Brejões (BRJ)	Barbosa et al. (1998, 2004, 2006), Cruz et al. (2009)
	Colônia (CLA)	Riccomini et al. (1991, 2011), Perrota et al. (2005), Velázquez et al. (2013, 2018), Crósta et al. (2019b), Prado et al. (2019)

The geological features of potential targets are also categorized into classes similar to what was done for impact structures, but with significant changes. For instance, instead of searching for information about shock diagnostic features, which obviously are not available for potential targets, this work focused on searching for petrographic descriptions that could suggest the presence of deformation features in minerals in general. Similarly, instead of searching for information about possible types of impactites, this work focused on investigating whether brecciated or deformed rocks had been described in outcrops in internal zones, mainly in central parts, of potential targets and if these descriptions could be similar to impact breccias described in confirmed impact structures. Furthermore, the lineaments in potential targets were considered as generic lineaments, without genetic or displacement relationships. Finally, the surrounding terrain and its potential relationship to the target has been investigated to understand whether the formation process of potential targets has changed a regional geological pattern in a similar way as an impact might have.

The results regarding geological information about the impact structures and potential targets were organized into tables and maps (see Chapter 14).

10.2 **Geophysical information – databases and processing**

The compiled geophysical information has been limited to airborne magnetic and gamma-ray spectrometry data. This choice was made because such data are freely available and accessible on websites (e.g., GeoSGB and REATE). Based on nominal clearance terrain height, the airborne data were subdivided into three groups: high resolution (100m); mid-resolution (150m); lower-resolution (300-500m). Airborne gamma-ray measurements were available only for the first two groups (Table 2).

High resolution surveys are available for three impact structures (SdC, RR, and NVC) and five potential targets (BJD, CDS, ITA, INJ, and SCD), whereas mid-resolution surveys are available for the AGD and SM impact structures and only one potential target (CLA). Although mid-resolution data were collected over the CJU impact structure, it has not been possible to recover these data from analog files. Finally, lower resolution surveys contain magnetic data only and they cover three impact structures (VTA, VGD, and

SMT) and only one potential target (SFM). Table 2 summarizes the main characteristics for each kind of survey.

10.2.1 Airborne gamma-ray data processing

The airborne gamma-ray spectrometry data of high-resolution data sets correspond to the percent of total potassium (%K), part per million of equivalent thorium concentration (eTh), and part per million of equivalent uranium concentration (eU) and the total count data (TC). These measurements already have been corrected for dead time, background removal (aircraft, cosmic and radon), height, Compton Effect, and conversion to elemental concentration for gamma-ray spectrometric data, leveling and micro-levelling (Marques et al. 2006). Similarly, several of these corrections were applied to mid-resolution data (see reports in Table 2). However, gamma-ray spectrometry data of mid-resolution surveys are not calibrated, such that radiometric measurements are expressed in count per one (cps) or two (cp2s) seconds. Moreover, mid-resolution data commonly are barely leveled, so when such data are interpolated into a regular grid, several flight-line artifacts become noticeable. Finally, because the analog radiometric data of the AGD impact structure have been lost, it has not been possible to produce these K, eTh, and eU concentration maps. Nonetheless, Total Count (TC) measurements have been manually recovered by J. Lambert (compare Leite et al., 2022). He digitized ~34000 data points from a contour map published by CPRM in 1972 (CPRM, 1972; Leite et al., 2022). All these data were kindly shared by J. Lambert for this work, and it was possible to produce a digital TC map for the AGD impact structure. As will be detailed in the next lines, the processing of airborne gamma-ray spectrometry data follows two approaches: one based on conventional techniques and another based on statistical analysis techniques.

Table 2: Main characteristics of high, medium, and low resolution airborne surveys acquired for Brazilian impact structures and the chosen potential targets. Abbreviations: AGD – Araguainha; CJU – Cerro do Jarau; VGD – Vargeão Dome; VTA – Vista Alegre; SdC – Serra da Cangalha; RR – Riachão Ring; NVC – Nova Colinas; SM – Santa Marta; SMT – São Miguel do Tapuio; ITA – Itiquira; CDS – Cardoso; BJD – Bom Jardim; SCD – Sucunduri Dome; INJ – Inajáh; BRJ – Brejões; SFM – São Francisco do Maranhão; CNB – Caraíbas; CLA – Colônia.

Structure		Aerogeophysical Project Name (code)	Spacing flight lines (m)	Flight height (m)	Year	Report	Group
Impact structure	SdC, RR, and NVC	Parnaíba Basin (0050_MAGGAMA002)	500	100	2006	Marques et al. (2006)	High-resolution
	SM	Borda Sul da Bacia do Parnaíba (1027)	2000	150	1976	Prospec (1978)	Mid-resolution
	AGD	Alto Garças (2009)	1000	150	1971	Prospec (1972)	Mid-resolution
	VTA and VGD	Rio Iguaçu (4023)	2000	500	1981	Uncompleted	Lower-resolution
	SMT	Bacia do Maranhão (Bloco Este) (4048)	3000	500	1988	Uncompleted	Lower-resolution
Potential targets	ITA	Rondonopolis – Dom Aquino (1111)	500	100	2012	Lasa Prospecções (2012)	High-resolution
	CDS	Sudeste do Mato Grosso (1113)	500	100	2011	Lasa Prospecções (2012)	High-resolution
	BJD	Rondônia Central (1094)	500	100	2009	Lasa Prospecções (2010)	High-resolution
	SCD	Sucunduri (1098)	500	100	2009	Prospectors (2010)	High-resolution
	INJ	Conceição do Araguaia (1110)	500	100	2011	Lasa Prospecções (2015a)	High-resolution
		Oeste de Carajás (1125)	500	100	2013	Lasa Prospecções (2015b)	High-resolution
	BRJ	Ipirá – Ilhéus (3089)	500	100	2010	Microsurvey (2011)	High-resolution
	CLA	São Paulo – Rio de Janeiro (1039)	1000	150	1978	CPRM (1988)	Mid-resolution
	SFM	Bacia do Parnaíba (4031)	2500	300	1981	Uncompleted	Lower-resolution

10.2.1.1 Processing based on conventional techniques

The first approach consists of computing basic grids (e.g. TC, K, eTh, eU) for five impact structures (SdC, RR, NVC, SM, and AGD) and six potential targets (BJD, CDS, ITA, INJ, SCD, and CLA) by interpolation of the radiometric data points into a regular grid using the Inverse Distance Weighted (IDW) method (Shepard, 1968). The IDW interpolation method was chosen because previous work had demonstrated that it provides better results than other methods, such as the minimum curvature method (Grant, 1998; Silva et al., 2023). Except for AGD, the cell size used in the interpolation was equivalent to one-fourth of flight line spacing. For the AGD impact structure, cell size was chosen by trial and error. This was done because the spatial georeference of TC data points did not agree with the survey area of the AGD structure, even after several attempts of reprojection. To overcome this limitation, the data were first interpolated and then the gridded image was georeferenced. The flight-line artifacts on the grids from mid-resolution data were suppressed by applying the directional cosine filter, which is commonly used to remove or isolate signals in the specified azimuth direction in magnetic data (Reeves, 2005; Betts et al., 2024). Here, this filter was used considering azimuth equal to zero (direction along flight lines) and degree of cosine function equal to one. Indeed, a Hanning filter (Reeves, 2005) with three passes was also applied after the directional cosine filter to suppress spurious spikes. These filters were applied on radiometric basic grids from the SM and AGD impact structure and CLA potential target.

Radiometric ratio (e.g., eTh/K, eU/eTh, eU/K) grids were produced from the basic grids. Such ratios are very useful because they suppress several effects, such as soil mixture and geometry detecting, and highlight subtle variations, providing a measurement of relative enrichment between radioelements, so that this enrichment may be indicative of mineralization, rock alteration, or lithological discrimination (Killeen et al., 2015). These ratios were computed for three impact structures (SdC, RR, and NVC) and one potential target (CLA). Radiometric ratios for the SM impact structure did not yield stable grids, so that these results are not presented here. No radiometric grids have been computed for the AGD impact structure, because only TC grids were recovered. This grid,

in turn, was later georeferenced by using a first-order polynomial function and ground control points extracted from the Digital Elevation Model (see next section) and from contours of geological units (Silva et al., 2024). The Root Mean Square (RMS) obtained was less than 0.1 %. Finally, radiometric basic and ratio grids were superimposed onto a hill shaded (computed from the aforementioned DEM) map with 40 % transparency, and then these sets of images were organized into maps. For each impact structure or potential target, the centers of each structure were draped onto each of these maps. In some cases, additional geological information (e.g., outcrops, linear features, geologic unit contours, etc.) was also draped onto the maps to aid further interpretation.

10.2.1.2 Processing based on statistical analysis techniques

The second approach was carried out only on impact structures in an attempt to enhance the radiometric signatures to obtain new interpretative insights. For this task, two statistical techniques were applied on airborne gamma ray spectrometry data: Principal Component Analysis (PCA) and Factorial Analysis (FA). The first is a dimensionality reduction technique, whereas the second can be defined as a correlation structure modeling technique (Suhr, 2005). The mathematical details can be found, for example, in a textbook (Fabrigar and Wegener, 2012) and various articles (Fabrigar et al., 1999; Jolliffe and Cadima, 2016).

In short, in the PCA transformation, the radiometric variables (i.e., K, eTh, eU, and their ratios) are linearly combined to form a few new variables (i.e., the Principal Components - PC) that can represent the main part of total variance of original variables, or in other words, without significant loss of information (Suhr, 2005). For instance, it is known that eTh and eU are commonly correlated variables (e.g., Pires de Lima and Mafurt, 2018). In the PCA approach, eTh and eU can be linearly combined into a PC, such that this new component can represent the total variance that comes from eTh and eU variables. So, as the eTh and eU variables were combined into a single variable (PC), the dimensionality here was reduced from two to one. Previous work suggested that PCA applied to airborne radiometric data can be useful to highlight lithological or mineralization contributions (Ford et al., 2008; Pires de Lima and Mafurt, 2018; Silva et al., 2023). Here, it was hoped that this approach

could enhance the contrast of radiometric signatures for four Brazilian impact structures (SdC, RR, NVC and SM).

Regarding Factorial Analysis (FA), although it also can be used for dimensionality reduction, the main objective of this technique is to model the correlation structure by assumption that the original variables (i.e., K, eTh, eU, TC, etc) in a given study are, in fact, resulting from linearly combined latent variables, or factors. Such factors cannot be directly observed, but they influence the original variables (or observable variables), causing them to covary (Fabrigar and Wegener, 2012). Again, the well-known correlation of eTh and eU suggests that both variables have a common variance. This common variance, in turn, can be thought *a priori* to be due to the same factor. It is possible to create a map for this factor and interpret it in terms of geology. For example, Asfahani et al. (2005) found that TC, eU, eU/eTh, and eU/K are variables with a common factor, in this case, the first factor (F1). By analyzing F1 score maps, these authors found that the high F1 scores were related with U presence in phosphate deposits in the Al-Awabed study area of Syria. For this reason, they termed F1 the uranium phosphate factor. In another study, F1 was interpreted as the common factor that leads TC, K, eTh, eU variables to covary (Hussein et al., 1995). In this case, F1 scores reflected the presence of radioelements hosted in acid rocks, such that F1 was termed the integrated radioactivity factor. Still in this same study, the authors termed a second factor (F2) a ^{40}K index, whereas a third factor (F3) was interpreted as intra-rock unit differentiation factor. For this present work, the FA approach was applied on high resolution airborne gamma-ray spectrometry data acquired for three impact structures (SdC, RR, and NVC) in an attempt to understand the main factors that control the distribution of radioelements in these structures.

Finally, PCA and FA approaches were applied using several R packages that provide a set of script-based routines or functions in the R language (R Core Team, 2024) (see the R script given in Appendix I). In the PCA approach, the basic and ratio grids were imported into R software and were stacked into a single raster file. Then, this raster was standardized and PCA was carried out. Tables and chart plots of the amount of explained total variance and cumulative total variance were produced. In the FA approach, all procedure was carried out considering the data points along the flight line instead of using grid files. This

choice was made to improve the performance of the FA approach. More details about FA can be found in the output paper (in final preparation) related to this dissertation (Chapter 13). The PC and Factor maps were produced in a similar way as done for maps derived from conventional approaches and their interpretations were guided by geological information.

10.2.2 Processing of airborne magnetic data

For impact structures and potential targets, Anomalous Magnetic Field (AMF) grids were obtained using essentially two interpolation methods: Bi-Directional and Minimum Curvature (Reeves, 2005). The former was used to interpolate high-resolution magnetic data, whereas the second was used to interpolate lower resolution magnetic data. In order to assess mid-resolution magnetic data, the interpolation method chosen was based on comparative visual analysis between the outcomes of the Bi-Directional and Minimum Curvature applications. A cell size equivalent to one-fourth of flight line spacing was considered, irrespective of which method was used.

The magnetic signature of impact structures, especially for small to medium sized structures, is commonly associated with shallow sources. For this reason, it is necessary to perform a separation of regional and residual components of the Anomalous Magnetic Field (AMF). Although this can be done by several methods (spectral analysis, polynomial-fitting, filtering), in this work the residual contributions of AMF grids were separated by using an upward continuation, because this technique yields more stable results (Milligan and Gunn, 1997). Here, all the AMF grids (from high, mid, and lower resolution) were continued to a height of 5000 m and then the resulting continued grids were subtracted from their respective AMF original grids. The resulting grids after this operation were termed residual AMF grids.

In order to highlight the magnetization contrast, the Total Horizontal Derivative Amplitude (THDR) (Grauch and Cordell, 1987) and Total Gradient Amplitude (TGA) (formerly known as Analytical Signal Amplitude - ASA) (Roest et al., 1992; Li, 2006, Li and Nabighian, 2015) were computed from residual AMF grids. Both transformations are useful to estimate the borders of magnetic sources and, as such transformations are based on amplitudes, the dipolar nature of a magnetic anomaly can be simplified in THDR and TGA output maps

(Betts et al., 2024). Moreover, magnetic signatures of the shallowest sources tend to be highlighted in such transformations because THDR and TGA are computed from the derivatives of AMF (Li and Nabighian, 2015; Betts et al., 2024).

Finally, the magnetic source depth of these magnetic anomalies has been estimated based on two approaches: Standard Euler Deconvolution Solutions (SEDS) (Reid et al., 1990; Thompson, 1982) and Analytical Signal-Euler Solutions (ANEULS) (Salem and Ravat, 2003). In both approaches, the magnetic source depths are estimated without prior knowledge about magnetic susceptibility contrasts (Li, 2003; Salem and Ravat, 2003). However, the magnetic source shape is a priori information that must be given in the SEDS approach, but in the ANEULS approach, both magnetic shape and depth are directly and independently estimated (Salem and Ravat, 2003).

In the SEDS approach, each magnetic anomaly is assumed to have simple ideal geometries according to its structural index which, in turn, can be regarded as the rate at which the magnetic signal decays with source–sensor distance (Reid et al., 1990; Thompson, 1982; Barbosa and Silva, 2005). For simple geometries such as a straight contact, vertical dike, or sill, vertical or horizontal cylinder, or sphere, the structural index values are 0, 1, 2, and 3, respectively (Barbosa and Silva, 2005; Reid et al., 1990; Thompson, 1982). Once structural index and the size of the data moving window are defined, the SEDS are calculated by linear inversion (Li, 2003). In other variations of the SEDS approach, the solutions are computed only over magnetic peaks selected from TGA grids, such that no moving window is necessary. The main advantage in computing solutions only for magnetic peaks is that the solutions occur localized, unlike the solution clouds that appear in traditional SEDS. Such clouds can make it difficult or even misleading to interpret the solutions.

Unlike the SEDS approach, the depth estimation by ANEULS does not require any a priori information. The ANEULS approach consists of a combination of the Analytical Signal (or TGA) with Euler Deconvolution. This combination was proposed by Salem and Ravat (2003) who demonstrated that, by applying derivatives to the homogeneous Euler equation, the depth and structural index of a magnetic anomaly can be estimated independently based on the higher-order derivatives of the Analytical Signal. The main advantage of

ANEULS over SEDS is that the latter assumes simple geometries for magnetic sources, such that only integer numbers can be considered, whereas in the former the structural index can be a non-integer number that means the magnetic source can have more complex shapes. On the other hand, ANEULS is more susceptible to noise, so that sometimes, after successive derivatives applied to data, the level of noise becomes significant and ANEULS cannot yield solutions.

In this work, magnetic source depths were preferably estimated with the ANEULS approach, for five impact structures (AGD, SdC, RR, NVC, and SM) and six potential targets (BJD, BRJ, ITA, CDS, INJ, and SCD). Initially, magnetic peaks were selected from the TGA grid by using the peak selection algorithm proposed by Blakely and Simpson (1986). Basically, this algorithm compares the cell value of a given pixel with its nearest neighbor in previously defined directions. Here, this algorithm was run considering the highest restrictive selection level, which is that a peak was only selected if its value in the grid cell was greater than the values of the grid cells in the four adjacent directions. The remaining parameters were: number of smoothing filter passes equal to 3, flight height equal to 100 m, and no cutoff value of TGA. Next, over each peak previously selected, magnetic source depths and structural indexes were calculated according to Salem and Ravat´s (2003) equations. For the VGD impact structure, ANEULS did not yield solutions and the magnetic source depths were computed by SEDS approaches. Note that the solutions estimated by SEDS were also computed over TGA's magnetic peaks. Here, the structural index, flight height, and maximum error in depth estimation parameters were equal to 1.00, 100 m, and 5 %, respectively. For the SMT impact structure, TGA grids were very noisy, so that TGA magnetic peaks could not be selected. In this case, the magnetic source depths were estimated by SEDS approaches but now a solution cloud was generated. The SEDS parameters used for the SMT structure were the same as for the VGD structure, but a window size with 20 times the cell size was considered. Additionally, the solution cloud was reduced by considering only solutions near the SMT impact structure. Because the noise level in airborne magnetic data acquired on the VTA and SFM structures were significant, no magnetic source depth estimation was possible for these structures.

Finally, the magnetic grids (i.e., regional and residual AMF, THDR, TGA) of impact structures and potential targets were organized into several maps. Similarly to the radiometric maps, the center of each structure and additional geological information (e.g., outcrops, linear features, geological unit contours, etc.) were draped onto the maps to aid further interpretation.

10.3 **Spaceborne Information – Database and processing**

The spaceborne optical and radar images used in this work are from four sensors: a Dual-polarization C-band Synthetic Aperture Radar (SAR) instrument onboard the Sentinel-1A/B satellites; MultiSpectral instrument (MSI) onboard the Sentinel-2A/B satellites; Advanced Spaceborne Thermal Emission and Reflection Radiometer (ASTER) instrument onboard the Terra satellite, and a Digital Elevation Model (DEM) derived from the Shuttle Radar Topography Mission (SRTM) and resampled to 12.5 m available in radiometric terrain corrected (RTC) ALOS PALSAR products. All images of these sensors were downloaded considering the local dry season period for each impact structure or potential target. The image processing performed in this work was divided into three classes: i) processing of optical images (Sentinel - 2 MSI and ASTER scenes); ii) processing of SAR images (Sentinel-1 scenes), and iii) processing of Digital Elevation Model and associated products. For this study, the spaceborne images were used for basically two main reasons: to make a lithologic discrimination and generate a map of morphostructural elements of Brazilian impact structures and potential targets. A detailed description of processing performed with respect to each sensor will be provided in the next section.

10.3.1 Processing of optical images

The Sentinel-2 mission is composed of two satellites (namely 2A and 2B) operating simultaneously, phased at 180° to each other, in a sun-synchronous orbit at a mean altitude of 786 km (ESA, 2025a). Each satellite carries a Multi-Spectral Instrument (MSI) sensor (MSI) that records the radiance reflected by Earth in thirteen spectral bands (ibid). Among these thirteen spectral bands, four (B2, B3, B4, and B8) have 10 m spatial resolution and range from the Visible to the Near Infrared (VNIR) spectral region (from ~493 to ~833 nm), and

the other six bands have 20 m spatial resolution and encompass the narrow VNIR vegetation red edge spectral domain (from ~704 to ~865 nm) (B5, B6, B7, and B8A) plus a wider Short-Wave Infrared (~1610 and 2190 nm) (B11 and B12). The remaining three bands are devoted to cloud screening and atmospheric correction studies at 60 m spatial resolution (B1, B9, and B10) (ESA, 2025a). The orbital swath width is 290 km.

The Sentinel-2 images used here were acquired mainly during dry seasons and with a cloud cover of less than 3 %. They were previously preprocessed by ESA Copernicus Space Component Ground Segment and lodged in the public domain through Copernicus Data Space Ecosystem (ESA, 2025a). The scenes processed here correspond to the L1C level that includes radiometric and geometric corrections and conversion to reflectance, such that each pixel in Sentinel-2 L1C images denoted the Top Of Atmospheric (TOA) reflectance (ESA, 2025a). For all structures (confirmed impact and potential targets), the processing carried out in this work started from Sentinel-2 L1C images. Because B1, B9, B10, and B8 are essentially used for cloud screening, atmospheric correction, and vegetation studies, such bands were ruled out of the processing flow described below.

Initially, the atmospheric effects on Sentinel-2 L1C images were corrected by applying QUick Atmospheric Correction tools integrated into ENVI software. Next, 10 m bands were resampled to 20 m and stacked with other 20 m bands to build a single multiband raster file. Then, the reflectance values of this multiband raster file were adjusted from zero to one range in order to avoid spurious values. From this final multiband raster, two kinds of RGB visualizations were produced: one based on RGB composite color by using B12, B11, and B4 in red, green, and blue bands, respectively, and another based on band rationing. In this latter case, the B11/B8A, B4/B3, and B12/B11 band ratios were computed and combined into RGB visualization with the first, second, and third ratio into red, green, and blue bands, respectively. Note that such bands can also be used as proxies for mineralogy. For instance, the B11/B8A band ratio can be used to map ferric oxides, whereas the B4/B3 and B12/B11 band ratios can be used for mapping ferric iron ($Fe3^{3+}$) and ferrous silicates (biotite, chloride, amphibole), respectively (Van der Meer et al., 2014). Both RGB visualizations of each impact structure or potential targets were

superimposed onto hill shade and then organized into maps and integrated with geological information.

The ASTER sensor comprises a set of three radiometers (visible and near infrared radiometer – VNIR, shortwave infrared radiometer – SWIR, and thermal infrared radiometer - TIR) that, together, detect the solar radiation reflected and emitted by the Earth's surface in three regions of the electromagnetic spectrum (Yamaguchi et al., 1998). These regions are divided into 14 spectral bands with spatial resolutions of 15 m, 30 m, and 90 m for the VNIR, SWIR and TIR bands, respectively (ibid). The ASTER scenes were previously preprocessed by Land Processes Distributed Active Archive Center (LP DAAC) and made available through the EARTHDATA SEARCH website. The ASTER scenes processed here correspond to the AST L1T product that includes radiometric, geometric, cross-talking, terrain accuracy, and north rotation corrections (Duda et al., 2015). Each pixel of AST L1T scene data contains sensor calibrated radiance. The AST L1T images were downloaded with cloud cover of less than 3 %. Unfortunately, it was not possible to download good ASTER images for several potential targets, so that the results derived from these images in this study are focused on confirmed impact structures only. The ASTER images were processed in two steps where VNIR and SWIR bands were processed in the first step and TIR images were processed in the second step.

The data from the VNIR and SWIR bands were radiometrically calibrated and atmospherically (by using QUick tools) corrected and then stacked into a multi-layer raster file with 30 m spatial resolution. The reflectances of this multi-layer raster were also adjusted from zero to one and then PCA transformation was applied to a multi-layer raster to enhance the spectral contrasts (Crósta et al., 2003; Kalinowski and Oliver, 2004). Because three first principal components account for the total amount of total variance (commonly more than 99.9 %), these three first components were matched into a RGB visualization with PC3, PC2, and PC1 in red, green, and blue bands, respectively. The RGB composite color of PC's was superimposed onto a hill shade with 40 % transparency, and then these images were organized into a map and integrated with geological information.

In the second step, the TIR bands were also radiometrically calibrated and then atmospherically corrected by using Thermal Atmospheric Correction tools integrated into ENVI software. Subsequently, the Decorrelation Stretch tool also integrated into the ENVI software was used to reduce the strong correlation among TIR bands. Basically, this tool stretched each TIR band such that areas of the spectrum where the bands are not correlated are highlighted, producing a more colorful color composite image (Kalinowski and Oliver, 2004). As this tool input requires three bands, it was applied for Decorrelation Stretch to the B13, B12, and B10 bands. This band combination can be useful for lithology discrimination (Kalinowski and Oliver, 2004; Ninomiya and Fu, 2018). After applying Decorrelation Stretch, the output image consists of a 90 m spatial resolution RGB image with B13, B12, and B10 uncorrelated bands in the red, green, and blue bands. Again, this RGB image was organized into a map, dropped onto a hill shade with 40 % transparency, and then integrated with geological information.

10.3.2 Processing of SAR images

Similar to the Sentinel-2 satellite mission, the Sentinel-1 mission also comprised two satellites (named 1A and 1B) operating simultaneously, phased at 180° to each other, in a sun-synchronous orbit at a mean altitude of 693 km (ESA, 2025b). Each satellite carries a C-band instrument at a frequency of 5.405 GHz, corresponding to a wavelength of 5.55 cm that operates in dual-polarization capacity (ibid). In this study, Sentinel-1 SAR images with VV and VH polarization were used. These polarizations were chosen because previous work had suggested that such polarizations can be useful for lithology discrimination (ibid).

Sentinel-1 images capture backscattering of radiation reflected by the Earth's surface (ESA, 2025b). The images used in this study were acquired during the dry season in Interferometric Wide Swath mode and were pre-processed by ESA's Copernicus Space Component Ground Segment before having been made publicly available through the Copernicus Data Space Ecosystem. The datasets correspond to Level-1 Ground Range Detected (GRD) images, which undergo multi-look processing and are projected to ground level, resulting in a final spatial resolution of 12.5 m (ibid).

In this work, the processing of Sentinel-1 SAR Level-1 GRD images was carried out following the procedure described by Theilen-Willige (2021). This includes: i) convert the Level-1 GRD image pixel values to radar backscattering by applying radiometric calibration; ii) mitigation of speckle noise (i.e., the noise caused by the random interference effect between coherent returns from scatters on the Earth's surface) by using a Refined Lee filter (Yommy et al., 2015); iii) compensate for geometric distortion by applying terrain correction, and iv) converting backscattering values to linear dB format to enhance visualization and analysis. After this processing, the following additional bands were created from the original VV and VH bands: Ratio Pol - computed from dividing VV by VH components; Multi Pol - computed from absolute values of product of VV by VH components; and Diff Pol - computed from absolute values of difference between VV and VH components. The original and derived bands were combined into RGB composite color visualizations. Again, such RGB visualizations were organized into maps and integrated with geological information.

10.3.3 Processing of Digital Elevation Models

The Digital Elevation Models (DEM's) used in this study are part of the set of the radiometric terrain corrected SAR images that are processed and made available by the Alaska Satellite Facility's Distributed Active Archive Center (ASF-DAAC, 2014). This DEM was originally derived from Shuttle Radar Topography Mission (SRTM) with a 30 m resolution, and then it was reprocessed as a DEM with 12.5 m resolution to correct the ALOS PALSAR SAR images (Laurencelle et al., 2015). The DEMs for all structures (impact structures and potential targets) were downloaded from the Vertex - ASF Data Search platform and then the shaded relief (lightsource with a 45 ° elevation and a 0 ° azimuth) and slope maps were computed for each structure studied here. Topographic profiles derived from DEM images were also computed for some circular targets.

CHAPTER 11
RESEARCH ARTICLE 1

11. RESEARCH ARTICLE 1 - THE AEROGEOPHYSICAL ATLAS OF TOCANTINS STATE: SYNTHESIS OF MAGNETIC ANOMALY AND RADIOELEMENT MAPS WITH EMPHASIS ON REGIONAL SIGNATURES AND THE SERRA DA CANGALHA IMPACT STRUCTURE

This first paper has been published as an original research paper in the Brazilian Journal of Geophysics (BJGf). Bacause a final version has not been published yet in print by BJGf, only an online first version has been available for download on BJGf's website. This version also can be found in the next pages. The full citable reference is shown here:

Silva, A.B., Silva, M. F., Reimold, W. U., Alves, F. M., Lago, A. L., Couto Jr, M. Frasca, A.A.S., & Ribeiro, P.S.E. (2024). The aerogeophysical atlas of Tocantins state: synthesis of magnetic anomaly and radioelement maps with emphasys on regional signatures and the Serra da Cangalha impact structure. Brazilian Journal of Geophysics, 42(2), 1 – 29. http://dx.doi.org/10.22564/brjg.v42i2.2316

Brazilian Journal of Geophysics, **42** (2024), 2, 1–25
Brazilian Geophysical Society
ISSN 2764-8044
DOI 10.22564/brjg.v42i2.2316

THE AEROGEOPHYSICAL ATLAS OF TOCANTINS STATE: SYNTHESIS OF MAGNETIC ANOMALY AND RADIOELEMENT MAPS WITH EMPHASIS ON REGIONAL SIGNATURES AND THE SERRA DA CANGALHA IMPACT STRUCTURE

Adolfo Barbosa da Silva [1,2*], Marcelo Ferreira da Silva [3], Wolf Uwe Reimold [2], Felipe da Mota Alves [1], Alexandre Lisboa Lago [4], Marco Antônio Couto Jr [5], Antônio Augusto Soares Frasca [1], and Pedro Sérgio Estevam Ribeiro

[1]Serviço Geológico do Brasil - SGB, Goiânia, GO, Brazil
[2]Universidade de Brasília - UnB, Campus Darcy Ribeiro, Brasília, DF, Brazil
[3]Serviço Geológico do Brasil - SGB, Plano Diretor Norte, Palmas, TO, Brazil
[4]Serviço Geológico do Brasil - SGB, Rio de Janeiro, RJ, Brazil
[5]Vale S/A, Nova Lima, MG, Brazil

*Corresponding author: adolfo.barbosa@sgb.gov.br

11.1 ABSTRACT:

The Tocantins State Aerogeophysical Atlas (TSAA) is an institutional product of the Geological Survey of Brazil. It is aimed at promoting the use of airborne magnetic and gamma-ray spectrometry data to support geophysical and geological research at state level. Here, we present a synthesis of the TSAA with special emphasis on the interpretation of the magnetic (Anomalous Magnetic Field, First Vertical Derivative [FVD], and Total Gradient Amplitude [TGA] images) and radiometric (RGB composite color map of concentrations, Inverse Images of K, eTh and eU, and Normalized eU enhancement) map. In particular, the radiometric data for the Serra da Cangalha impact structure in northeast Tocantins are discussed. For Tocantins State, the results show that the radiometric and/or magnetic signatures of geological units (e.g., Mosquito Formation basalts; granite- gneiss/migmatite terrains) and structural features (e.g., dykes and lineaments), or related exogenous deposits (Serra Geral do Tocantins quartzose soils; alluvial deposits of main drainage channels) can be visualized well on regional-scale maps. Analysis of radiometric ratios for the area of the Serra da Cangalha impact structure indicates that eU concentrations are enriched in the annular basin around the central uplift structure and in the zone straddling the contact between the Piauí and Pedra de Fogo formations. In the latter case, the elevated eU concentrations could be related to brecciated chert layers or silicified sandstones.

Keywords: Tocantins state aerogeophysical data; gamma-ray spectrometry; magnetometry; geological- geophysical integration; Serra da Cangalha impact structure.

11.2 INTRODUCTION

In order to contribute to the improvement of geological knowledge and the discovery of mineral resources in Brazil, the federal government, through the Geological Survey of Brazil (SGB), has made important investments over the last two decades in acquisition of airborne geophysical data, such as airborne magnetics and gamma-ray spectrometry data (Pinto, 2022).An area of ca. 3,726,364 km² (or 92 % of the outcropping basement) of the Brazilian territory was covered by high-density airborne surveys, with a line spacing of 500 m and a flight height of 100 m (Oliveira and Rodrigues, 2019; Pinto, 2022).

With the aim to improve the dissemination of knowledge and the availability of aerogeophysical data to the technical-scientific community, the SGB has published a series of State Aerogeophysical At-

lases (e.g., Pernambuco, Rondônia, Ceará, Goiás, Roraima and others; Sousa, 2021; Alves et al., 2022; Oliveira, 2022). In these atlases, airborne geophysical data are integrated and correlated with geology, according to Brazilian state limits. This compartmentalization is aimed at facilitating the management and use of the geophysical data according to the preferences and priorities of the public and/or private entities and in relation to geological characteristics and local mineral potential. It is expected that the information contained in these atlases can help in the planning and execution of public policies, as well as decision-making by private entities.

This article provides a synthesis of the Tocantins State Aerogeophysical Atlas (TSAA), as published by the SGB (Silva and Alves, 2021). In the TSAA, magnetic and gamma-ray spectrometry signatures were interpreted taking into account geological units that had been mapped in the state of Tocantins. Additionally, airborne geophysical data were used in three case studies, whereby the magnetic and/or gamma-ray spectrometry signatures of two known mineral deposits (the Palmeirópolis polymetallic and Alecrim/Campos Belos uranium deposits) and the Serra da Cangalha impact structure are analyzed in greater detail than before.

Some of the main interpretations of magnetic (Anomalous Magnetic Field, First Vertical Derivative and Total Gradient Amplitude) and radiometric (RGB color composite of concentrations and ratios) signature maps are emphasized. These maps were chosen because they are amongst the most common products used in geological-geophysical interpretation. From the selected case studies, only the radiometric signatures of the Serra da Cangalha impact structure are presented here. This work can contribute to a better understanding of airborne geophysics over Tocantins State and may encourage the development of new research approaches.

11.3 GEOLOGICAL SETTING

11.3.1 Geology of Tocantins State

A large portion of the Tocantins territory, namely the part not covered by consolidated and unconsolidated sediments, is composed of rocks of the Tocantins Province (Almeida et al., 1981, Figure 1a). This geological province comprises three fold belts of Neoproterozoic age, which are known as the Araguaia, Paraguay and Brasília Belt. The latter is located at the western margin of the São Francisco Craton (Figure 1a). There are also several other cratonic blocks (the Parnaíba, Paranapanema and Goiás Massif), which were part of the amalgamation of western Gondwana (e.g., Brito Neves and Cordani, 1991; Pimentel and Fuck, 1992; Delgado et al., 2003; Mantovani and Brito Neves, 2009; Soares et al., 2018). The geotectonic compartmentalization of Tocantins State, as based on previous works (Pimentel et al., 2000; Frasca, 2015), can be summarized as follows: Archean-Paleoproterozoic TTG domes; basement of the Tocantins Structural Province; Paleo-proterozoic Rift Basins (Araí, Serra da Mesa and Natividade); remnants of Mesoproterozoic oceanic crust (Palmeirópolis Complex); Neoproterozoic orogens (Araguaia and Brasilia); Neoproterozoic passive margin basins (Paranoá Group) and platforms of the São Francisco Craton (Bambuí Group); the Paleozoic Parnaíba and Cretaceous (Urucuia Group) Sanfranciscana intracratonic basins, the Silurian-Devonian Água Bonita graben and the Cenozoic Bananal sedimentary basin (Figure 1b).

The TTG domes (Colméia, Lontra, Grota Rica and Cocalândia) crop out in the northern part of Tocantins State and form the basement of the northern Araguaia Orogen (Figure 1b). These domes are correlated with rocks from the SW part of the Amazonian Craton (Moura and Gaudette, 1999). In the southern portion of the Araguaia orogen, basement is composed of ortho- and para-derived metamorphic rocks of the Porto Nacional and Rio dos Mangues complexes, and granites and cogenetic volcanic rocks of the Ipueiras Suite (Ribeiro and Alves, 2017, Figure 1b). The southeastern portion of the basement in Tocantins State is represented by the Natividade-Cavalcante Block. This block is a Paleoproterozoic core that represents an extension of the São Francisco Paleocontinent. The block was deformed in the Brasiliano Orogeny (Fuck et al., 2014; Martins-Ferreira et al., 2020). This geotectonic unit is composed of greenstone belts (Riachão do Ouro Group), granite-gneiss (Almas-Cavalcante Complex), TTGs (Serra do Boqueirão Suite), deformed granitic rocks (Aurumina Suite) and mafic-ultramafic intrusions (Frasca et al., 2010, 2018; Abdallah and Meneghini, 2017) (Figure 1b).The basement in the southeastern Tocantins State is composed of geotectonic units that can be re- lated to divergent tectonics (Figure 1b). These terranes comprise a Paleoproterozoic rift basin and remnants of Mesoproterozoic oceanic crust. The former involves metasedimentary and metavolcano-sedimentary sequences of the Araí, Serra da Mesa and Natividade groups (Figure 1b). The latter is represented by metavolcano-sedimentary sequences of the Palmeirópolis Complex (Oliveira, 2000; Martins-Ferreira et al., 2018b,a). This complex has considerable deposits of Cu, Pb and Zn. The shales and graphite phyllites of the Água Suja Group and the Ticunzal Formation represent a portion of the Goiás Massif located in Tocantins State. This massif has been interpreted as an exotic and allochthonous continental block of a long and complex crustal

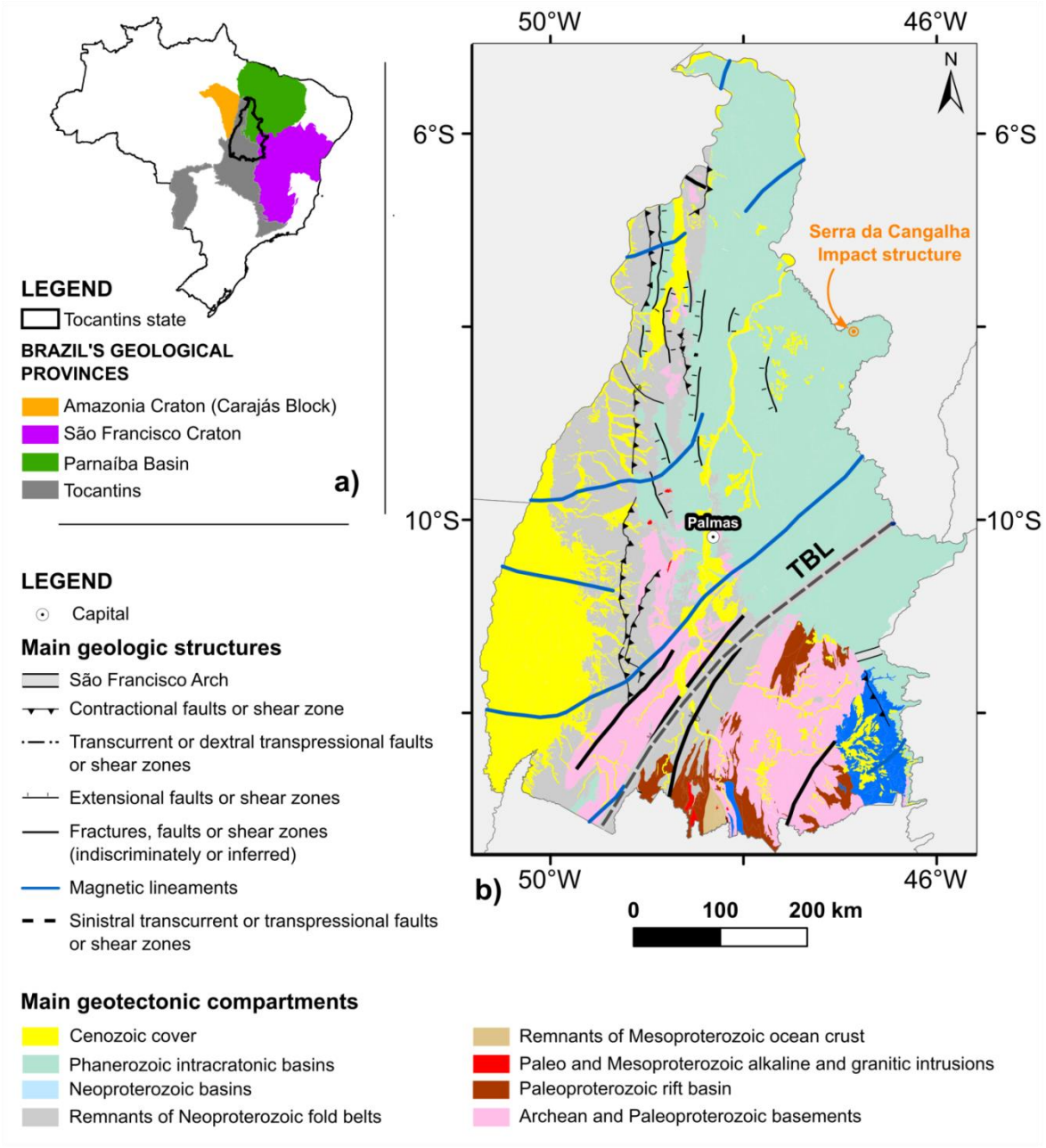

Figure 1: Simplified geology of Tocantins State. a) Position of the Tocantins State in relation to Brazil's geological provinces (after Santos, 2003). b) Simplified geotectonic compartment map for the state. TBL = Transbrasiliano Lineament. The main lithologies within these compartments are described in the text. The vectorial files of geological units were modified after Ribeiro et al. (2022).

evolution, which collided against the western margin of the São Francisco craton in the Neoproterozoic, during the final stages of the Brasiliano Orogeny (Jost et al., 2010, 2013).

In southern Tocantins State, a number of Paleo- to Mesoproterozoic granitic intrusions of the Tocantins River Stanniferous Subprovince have been mapped (Figure 1b). These bodies are in intrusive and tectonic contact with the host metasedimentary rocks of the Serra da Mesa and Araí groups (Marini and Botelho, 1986). The most prominent of these bodies of this subprovince is the Serra Dourada Granite.

The strata of the Serra da Mesa Group are also intruded by syenites and monzonites that makes up the Peixe Alkaline Suite (Frasca et al., 2018). Alkaline rocks (Monte Santo-Serra da Estrela Suite) also oc- cur in the central-west portion of the state. It has been suggested that these rocks could have been associated with the beginning of fragmentation of theRodinia supercontinent (Arcanjo et al., 2001). This episode triggered the formation of the "Araguaia Rift", with subsequent deposition of sediments into the pre- cursor basin

(Baixo Araguaia Group; Arcanjo et al., 2013).

The Baixo Araguaia Group is the main lithostratigraphic unit of the Araguaia orogen that constitutes a large geotectonic province of preferential N-S direction of more than 1,000 km length and 150 km width (Figure 1b). The Araguaia orogen is covered by Phanerozoic sedimentary rocks of the Parnaíba Basin to the north and east, and shows a tectonic relationship with aforedescribed Paleoproterozoic basement rocks. From base to top, the Baixo Araguaia Group is composed of the Morro do Campo, Xambioá, Canto da Vazante, Pequizeiro and Couto Magalhães formations (Herz et al., 1989). Except for the Morro do Campo quartzites, the other formations are composed of pelitic rocks of varied metamorphic degrees (Gorayeb, 1981). The highest-grade metasedimentary rocks of the Baixo Araguaia Group host some granitic intrusions of syn- to late-orogenic origin, notably the Santa Luzia, Barrolândia, Presidente Kennedy and Ramal do Lontra granites (Alves et al., 2019).

Serpentinized mafic-ultramafic bodies (Quatipuru Complex) also occur within Baixo Araguaia Group metasedimentary rocks (Paixão et al., 2008; Barros and Gorayeb, 2019). These bodies are believed to have been obducted during the agglomeration of West Gondwana, which would make the Araguaia Orogen a possible suture zone (Hodel et al., 2018). Metavolcano-sedimentary rocks of the Rio do Coco Group have been included in this complex as well (**?**). Thick, magnetite-rich dykes have been mapped in the Araguaia orogen (Hasui et al., 1980; Figueiredo et al., 2001).

Other Neoproterozoic tectonic units with prominent geophysical expressions in Tocantins State are the Goiás Magmatic Arc and the Brasília orogen. The former is mainly represented by orthogneisses occurring in the central-southern part of Tocantins and the latter comprises passive margin related to metasedimentary and metavolcano-sedimentary rocks (e.g., Paranoá Group) that partially cover the basement inthe southern part of Tocantins State (Marini et al., 1984; Fuck, 1994; Dardenne, 2000).

In eastern Tocantins, the extreme southeastern part of the sedimentary domain is composed of Neoproterozoic sequences of the Bambuí Group (Figure 1b). This includes several stratigraphic units such as diamictites, dolomites, clayey limestones, shale, siltstones, limestones, calcarenites, arkoses, quartz sandstones and conglomerates (Martins-Neto et al., 2001; Alvarenga et al., 2007; Martins-Neto, 2009). The sedimentary domain in the eastern portion of the state is composed of sedimentary strata that were deposited in Phanerozoic intracratonic basins. Of these, the Parnaíba Basin is the largest and its strata cover almost half of the state. The Parnaíba sedimentary column is predominantly siliciclastic, with subordinate limestone, anhydrite and flint, in addition to injections of diabase and basalt that have been related to the Mosquito (Early Triassic) and Sardinha formations (Early Cretaceous), respectively (Góes and Feijó, 1994; Vaz et al., 2007; Oliveira et al., 2018). At the Tocantins and Bahia state border, Parnaíba Basin rocks are covered by eolian sandstones of the Posse and Serra das Araras formations (Campos and Dard- enne, 1997a), which make up the Urucuia Group that, in turn, is part of the sedimentary succession of the Sanfranciscana Basin (Campos and Dardenne, 1997b; Sgarbi et al., 2001). Unconsolidated cover (Cenozoic Cover) rocks occur predominantly in the region bordering Pará State (Bananal Basin; Figure 1b). These deposits essentially consist of alluvial sand, clay and silt of the Araguaia Formation (Ribeiro and Alves, 2017). Such alluvial deposits, mainly sand and gravel, also occur along the Tocantins River. The Cenozoic cover also includes detrital crust formations (ferruginous laterite) that are distributed throughout the Tocantins territory (Sousa et al., 2012).

The structural framework within the limits of Tocantins State is essentially determined by the Trans- brasiliano Lineament (TBL) (Schobbenhaus et al., 1975, Figure 1b). The TBL has been interpreted as a transcontinental suture zone that is characterized by a system of NE-SW strike-slip faults stretching for more than 4000 km and extending as far as Africa and Argentina (Ramos et al., 2010; Cordani et al., 2013; Brito Neves et al., 2014). The system shows evidence of predominantly dextral kinematics (Brito Neves and Cordani, 1991; Brito Neves et al., 2014).

11.3.2 The Serra da Cangalha impact structure

The Serra da Cangalha (SdC) structure in the northeasternmost part of Tocantins State (Figures 1b and 2a) is a 12 km diameter impact structure of complex morphology. It is located some 10 km from the small town of Campos Lindos, close to the border between Tocantins and Maranhão states (see Crósta et al., 2019 for a recent review; Figure 2a and b). Since the 1970s, an impact origin had been suggested for SdC (Dietz and French, 1973; Reimold et al., 2006). However, robust evidence to support this hypothesis was only presented by Kenkmann et al. (2011) and Vasconcelos et al. (2013).

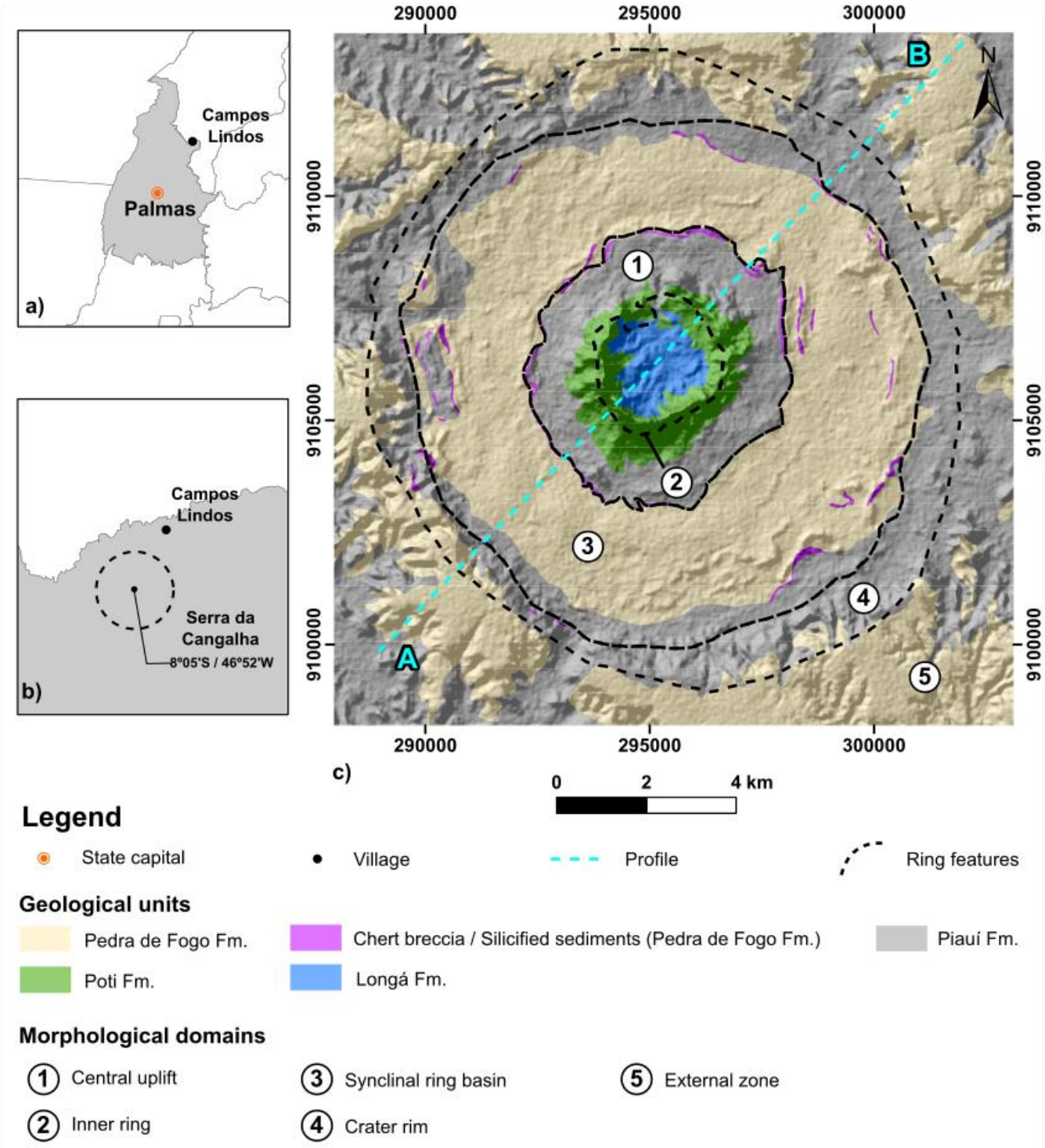

Figure 2: Survey area of the Serra da Cangalha (SdC) impact structure overlaid on elevation data (see Digital Elevation Model description in next section). The blue line corresponds to the A - B profile from which the radiometric ratios were extracted. a) Location of the town of Campos Lindos in relation to Palmas city, the capital of Tocantins state. b) Proximity between Campos Lindos and the SdC impact structure. c) Simplified geological map of the SdC impact structure. Modified after Kenkmann et al. (2011) and Vasconcelos et al. (2013).

The SdC structure is entirely formed in sedimentary strata of the Parnaíba Basin. The local stratigraphic column involves, from base to top, shales, siltstones and sandstones of the Longá and Poti formations (Mesodevonian Sequence – Eocarboniferous / Canindé Group), andsandstones, claystones, carbonates and chert of the Piauí and Pedra de Fogo for- mations (Neocarboniferous – Early Triassic Sequence/ Balsas Group) (Vaz et al., 2007; Kenkmann et al., 2011; Figure 2c). The SdC morphology can be divided into four domains: central, annular basin; inner ring (collar of the central uplift); synclinal ring basin; and crater rim and external zone (Figure 2c; Reimold et al., 2006; Kenkmann et al., 2011; Vascon- celos et al., 2013). It has been estimated that the structure has been significantly eroded since its formation, at least by some 500 m (Kenkmann et al., 2011). In the absence of datable impact-generated lithologies, the impact age has remained ill-defined. A maximum age is constrained only by the age of the youngest strata affected by the impact event. Thus, the age of the Pedra de Fogo Formation of ca. 250 Ma (Vaz et al., 2007) serves as the upper limit for the SdC impact age.

The central domain of the structure corresponds to a nearly circular region of 5.8 km diameter, which represents the central uplift complex of the structure (Figure 2c). This zone comprises an innermost depression where Longa Formation has been drilled. This depression is surrounded by a prominent collar of up to 300 m elevation and 3.4 km diameter (Reimold et al., 2006). This collar is composed of massive, strongly folded and silicified Poti Formation sandstones, and has given the name to this impact structure (Figure 2c). Impact-diagnostic shock metamorphic microdeformation features, shatter cones and evidence of intense macrodeformation (folding, faulting) have been described from rocks of this central domain (Kenkmann et al., 2011; Crósta et al., 2019). The central domain can also be subdivided lithologically into three zones: 1) an outer periphery, where red and sometimes white sandstones predominate, with fine to coarse granulometry, sub-rounded to rounded grains and moderate sorting; these rocks have been mapped as Piauí Formation; 2) an inner collar that consists of a set of sub-vertical ridges formed by silicified sandstones of the Poti Formation; and 3) the innermost depression of smooth topographic relief, where only very limited outcrop of medium- to coarse-grained sandstone, shale and schist of the Longá Formation could be observed (Reimold et al., 2006; Vasconcelos et al., 2013). Locally, these innermost rocks have been found to contain shatter cones.

The Annular Basin domain is a topographically low region in which the main drainage channels occur (Reimold et al., 2006). Outcrops are scarce due to intense erosion and weathering. Such outcrops are, for the most part, formed by rocks of the Pedra de Fogo Formation, with additional subsidiary, local occurrences of rocks from the Piauí Formation. The main features of the annular basin domain are two sets of well-developed concentric ridges (Vasconcelos et al., 2013). The first set occurs at about 2.8 km from the center of the structure. It not only marks the Piauí / Pedra de Fogo Formation contact zone, but also the outer margin of the central domain (central uplift structure). This first set is formed by brecciated chert layers and by silicified sandstones with minor claystone intercalations. The second set of chert ridges occurs at about 6 km from the center of the structure and involves deformed strata of the Pedra de Fogo Formation (Vasconcelos et al., 2013).

The crater rim domain marks the boundary of the SdC structure with the surrounding terrain (external domain). The crater rim is marked by a plateau with flat relief that is composed of rocks from the Pedra de Fogo Formation. The relatively flat external terrain shows very little evidence of deformation and is relatively flat. In this domain, Piauí Formation occurs at low altitude and the Pedra de Fogo Formation at comparatively higher stratigraphic and topographic levels (Vasconcelos et al., 2013). Kenkmann et al. (2011) provided a detailed description of the monocline structure that dips at moderate angles - along the inner slope of the crater rim - into the crater.

The principal domains of the SdC impact structure can also be recognized based on radiometric signatures, which was already proposed by Vasconcelos et al. (2012). In the innermost zone of the central domain (the inner depression), high K values were linked to high Al2O3 levels that suggested enhanced presence of muscovite in Longá Formation schist, whereas shales of the same formation would be related to high eU and eTh concentrations. On the other hand, products of erosion and weathering processes were implicated by those authors as main factors that could have contributed to comparatively low radiometric values observed over the area of the annular basin. Finally, the external zone is characterized by low K but high eU and eTh values, and this character could be related to the occurrence of lateritic soils (ibid).

11.4 METHODS

11.4.1 Processing of airborne geophysical data

The airborne geophysical data acquired over Tocantins State are derived from 6 aerogeophysical projects carried out by contracted companies between 2005 and 2016 (Figure 3). The main characteristics of these projects (e.g., spacing and direction of lines, sensors, interval sampling, preprocessing corrections) are given in Table 1 of the Supplementary Material. The average spacing of flight lines was 500 m and flight height was 100 m, for all projects.

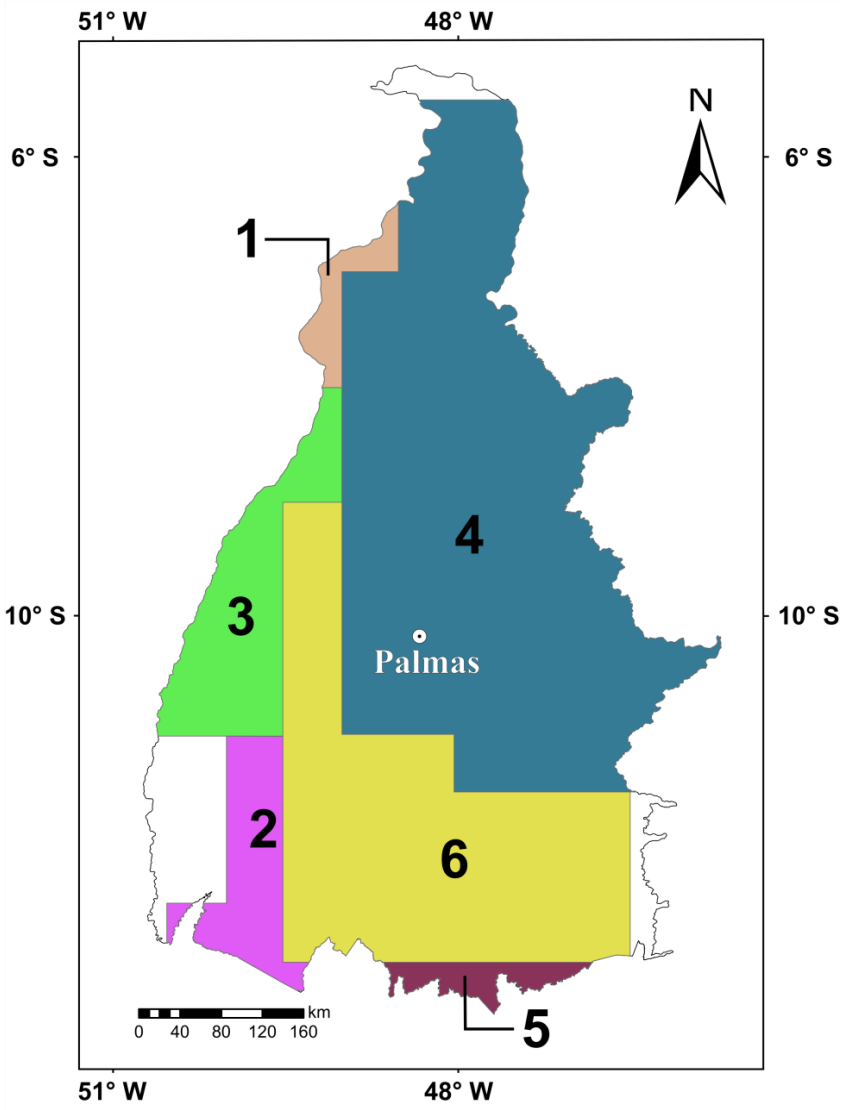

Figure 3: Aerogeophysical projects executed over Tocantins State. 1 – Rio Maria; 2 – Rio Formoso; 3 – Conceição do Araguaia; 4 – Parnaíba Basin; 5 – Tocantins Complement; 6 – Tocantins (compare with the table in the Supplementary Material for further information about these projects).

The Oasis Montaj version 9.8.1 software was used to produce the Anomalous Magnetic Field (AMF) and the K, eTh and eU concentration grids. These grids were obtained from data interpolation by Bi-Directional (magnetic data) and Inverse Distance Weighted (radiometric data) methods with a 125 m cell size. Grid merging for the data sets of the different aerogeophysical projects was carried out using the Grid Knitting extension integrated into the Oasis software. The AMF grid was merged by using the suture method, whereas K, eTh, and eU concentration grids were merged by using the Blend method (Cheesman et al., 1998; Johnson et al., 1999).

From the AMF grid, the First Vertical Derivative of AMF (FVD-AMF) and Total Gradient Amplitude (TGA) were computed, and the radioelement concentration grids were matched using the RGB composite color triangular system. These maps were chosen because they are the most commonly used ones in geological-geophysical interpretation (e.g. Airo, 2002; Dentith and Mudge, 2014).

The FVD-AMF is a type of transformation whereby the short wavelength magnetic signatures from shallow magnetic sources are enhanced, whilst the magnetic signal derived from deep sources is attenuated (Milligan and Gunn, 1997). For this reason, the FVD-AMF map is very useful in identifying and defining structural features generated by near-surface sources (e.g. Dentith and Mudge, 2014). The TGA - AMF, formerly known as Analytical Signal Amplitude (ASA) (Nabighian, 1972; Roest et al., 1992), is also a type of transformation that highlights the short wavelength magnetic signatures from shallow magnetic sources, but different from FVD, the TGA simplifies the magnetic anomaly shape, and, for 1D or 2D geometries, TGA centralizes the magnetic anomaly

on causative bodies (Li, 2006). In this work, we follow the recommendation of previous studies (e.g. Reid, 2012; Li and Nabighian, 2015) and decided to use the TGA nomenclature instead of the ASA terminology.

The RGB radioelement mapping facilitates the identification of areas relatively enriched/depleted in one or more elements by their respective, specific shades (Ford et al., 2008). Commonly, an RGB radioelement map is produced by placing the K grid into the red component (Red), the eTh grid into the green (Green) and the eU grid into the blue (Blue). Thus, bright shades denote areas enriched in the three radioelements, whereas dark areas denote relative depletion. Similarly, other RGB radioelement maps can be produced from the K, eTh, eU and their ratios. For instance, Duval (1983) proposed a RGB composite color scheme named Inverse Image of K, eTh, or eU. Such images match a given concentration grid of one element with their ratios in relation to the other two elements. For example: the K inverse image can be produced by placing the K grid into the red component (Red) and placing the K/eTh and K/eU ratio grids into the green (Green) and blue (Blue) components, respectively. In the K Inverse Image composition, areas with high K concentration and with K enrichment relative to eTh and eU are expected to be seen in bright tones, whereas dark areas denote low K concentration in conjunction with relative enrichment of eTh and eU to K (Duval, 1983; Dentith and Mudge, 2014). The same idea can be expanded to get eTh or eU Inverse Images by matching eTh, eTh/eU and eTh/K or eU, eU/K and eU/eTh grids with RGB compositions, respectively.

For this work, we computed the radiometric ratios and produced K, eTh, and eU Inverse Image maps. In order to avoid only one of the radioelements having a small spread of concentration estimates relative to its mean, which makes it difficult to see its contribution to the ratio map, we have normalized all radiometric grids before ratioing (Minty, 2011). This process was carried out to ensure that both radioelements in numerator and denominator can contribute equally to the enhancement of the differences between them across the study area (Minty, 2011).

In order to normalize the radiometric concentration, we use the MIN – MAX normalization according to this equation:

$$R_{norm} = \frac{R - Min_R}{Max_R - Min_R} \qquad (1)$$

where R is a radiometric variable (that is, K, eTh, or eU) and Min and Max are the minimum and maximum values of the radiometric variable. We verified that this does not change the distribution of radiometric on centrations significantly.Whenradiometric variables are normalized by equation 1, their values range from 0 to 1, and this ensures that both radioelements in the numerator and denominator can contribute equally to ratios. Moreover, possible nega- tive values can also be suppressed, making the ratios more stable. Normalizing radiometric values has been essential for the method to highlight ratios (Minty, 2011) or as a pre-step for unsupervised clustering and machine learning methods (e.g. O'Leary et al., 2022). After normalizing the radioelements, we computed the ratios and produced the Inverse Images for K, eTh and eU. It is worth mentioning that such Inverse Image maps were specially produced for this work and, therefore, they are not included in TSAA.

From visual analysis of magnetic, radiometric and geological maps, some of the main aerogeophysical signatures were correlated with some of the geological units mapped in the territory of Tocantins State.

11.4.2 Processing of the airborne gamma-ray spectrometry data for the Serra da Cangalha impact structure

In order to facilitate the visualization of the correlation between the respective SdC domains and their radiometric signatures, a profile view of the radioelement concentration curves with a 3D view of the RGB map is superposed onto a digital terrain model (DEM). This DEM was derived from Shuttle Radar Topography Mission data acquired at 30 m resolution. Besides concentration curves of the main channels (K, eTh and eU), eTh/K, eU/eTh and eU/K ratio curves also were computed. The ratio curves highlight the differences in the geochemical behavior of the radioelements, thus allowing further interpretation (International Atomic Energy Agency (IAEA), 2003).

During the visual analysis of the profile of SdC radioelement curves, two points with relative eU enrichment were observed on the profile. In order to investigate the spatial context of this enrichment, we used the eU Inverse Image described in the previous subsection and a second map referred here as a normalized eU enhancement. This second map is an attempt to combine various elements into a single term to highlight one element of interest (Dentith and Mudge, 2014). Here, we used the eU/eTh and eU/K normalized ratios to derive the eU enhancement map by using the following equation:

$$NeU_E = \frac{eU}{eTh} \cdot \frac{eU}{K} = \frac{eU^2}{eTh \cdot K} \qquad (2)$$

where NeU_E is the normalized eU enhancement and K, eTh and eU are normalized radiometric variables. Based on equation 2, areas with relative eU enrichment compared to eTh and K would be expected to have NeU_E

high values. In the visual analysis, the geological map of SdC and the two points with eU enrichment seen in the profile were dropped onto the eU Inverse Image and the NeU_E.

11.5 RESULTS AND DISCUSSION

11.5.1 Significant correlations between airborne magnetic and radiometric data for the region of Tocantins State

In the Tocantins State Aerogeophysical Atlas (TSAA), results and discussion are presented in different sections dealing with correlations between main geological units and magnetic and gamma-ray spectrometry products. These correlations may suggest probable sources for the airborne geophysical signatures observed on the thematic maps. However, only dedicated studies of such possible sources can confirm, or not, the association between these proposed sources and the aerogeophysical signatures.In this work, features whose magnetic and radiometric signals provide a regional expression have been analyzed. This form of analysis was chosen as such aerogeophysical signals can be easily visualized on regional maps, such as the magnetic and radiometric maps that are discussed here. Furthermore, although it is possible to identify several features on the regional maps, only 5 magnetic features (denoted M1 to M5 in Figures 4, 5 and 6) and 5 radiometric features (G1 to G5 in Figures 7, 8 and 9) will be described and related to geological information. Because the eU Inverse Image yields a noisy representation of Tocantins State, we decided to show it only for the SdC impact structure in the next subsection. Finally, it is important to underline that magnetic and/or radiometric signals of chosen features can be related to one or more lithostratigraphic unit(s).

The features in areas M1 and G1 show that most of the granitic/gneissic/migmatite rocks that make up the Natividade-Cavalcante Block correlate with magnetic lows (low values on the AMF, FVD-AMF and TGA - AMF maps; Figures 4, 5 and 6) and high radioelement abundances, mainly of K, which gives a reddish hue in the RGB radiometric concentration map (Figure 7) and a bright hue in the K Inverse Image (Figure 8). Comparing the Inverse Images (Figures 8 and 9), it seems that the K Inverse Image yields better results in order to define the contours of granitic/gneissic/migmatite rocks, whereas the eTh Inverse Image shows such contours in a more diffuse way. As these terrains were affected by several types of metamorphism, it is possible that magnetite alteration and deformation could have contributed to the formation of the observed low magnetism (Airo, 2002; Clark, 1997; Reeves, 2005). On the other hand, the radiometric pattern observed over these terrains may be associated with compositional aspects, as the rocks of the Almas-Cavalcante Complex and the Aurominas Suite are commonly enriched in radioelements, mainly in K.

Among the magnetic signatures in the M1 area there is a set of short wavelength magnetic anomalies (indicated by white arrows in Figures 4, 5 and 6) close to the Natividade-Cavalcante granitic/gneiss/migmatite rocks. Many of these anomalies appear to coincide with dark areas in the three RGB radiometric maps (RGB concentrations and K and eTh Inverse Images; Figures 7, 8 and 9). This is suggestive of low concentrations of K, eTh and eU (white arrows in Figure 7).

The zones of strong magnetization within the Natividade-Cavalcante Block may be associated with ferrimagnetic minerals in volcanosedimentary units, such as the metavolcanics of the Córrego do Paiol Formation at the base of the Riachão Group, the suite of Barra do Gameleira mafic intrusions, or even in Cretaceous mafic dykes (Sabóia and Meneghini, 2019; Martins-Ferreira et al., 2020). The low concentration of these radioelements in such rocks may also be a plausible explanation for the radiometric signatures observed as dark areas in the G1 region of Figures 7, 8 and 9 (Galbraith and Saunders, 1983; Airo, 2002).

The maps for areas M2 and G2 (compare Figures 4, 5 and 6 with 7, 8 and 9) show a set of magnetic anomalies and radiometric patterns with linear shapes. The spatial locations of M2 and G2 signatures suggest that they could be related to the lithostratigraphic units that were affected by the Transbrasiliano Lineament. The cause of these magnetic anomalies and radioelement concentrations could be related to several factors, such as the juxtaposition of lithologies with contents of ferrimagnetic minerals and radioisotopes, and the deposition and accumulation of such minerals in fault troughs (Henkel and Guzmán, 1977; Airo, 2002). Similarly, magnetic signatures in area M3 (Figures 4, 5 and 6) indicate linear shapes of great extensions. Such linear magnetic anomalies are well defined in FVD – AMF and TGA – AMF maps, suggesting that such anomalies come from near-surface sources. As has been suggested by Cruz and Gorayeb (2020), many of these anomalies may have been generated by mafic dykes, but others could also be due to the juxtaposition of units in thrust zones or along faults, or they could represent slivers of oceanic crust (ophiolites, Paixão et al., 2008). Weak radioelement concentrations also occur over the sedimentary domain. Such radiometric signatures are represented by the character of areas G3 and G4 (Figures 7, 8 and 9). In the former case, such low concentration areas may be due to the low natural concentrations of K, eTh and eU in Mosquito Forma- tion basalts. The magnetic minerals in the subvol- canic lithotypes of this unit may be one of the main sources of high-intensity magnetic anomalies observed on magnetic anomaly maps, mainly on FVD – AMD and TGA – AMF maps,

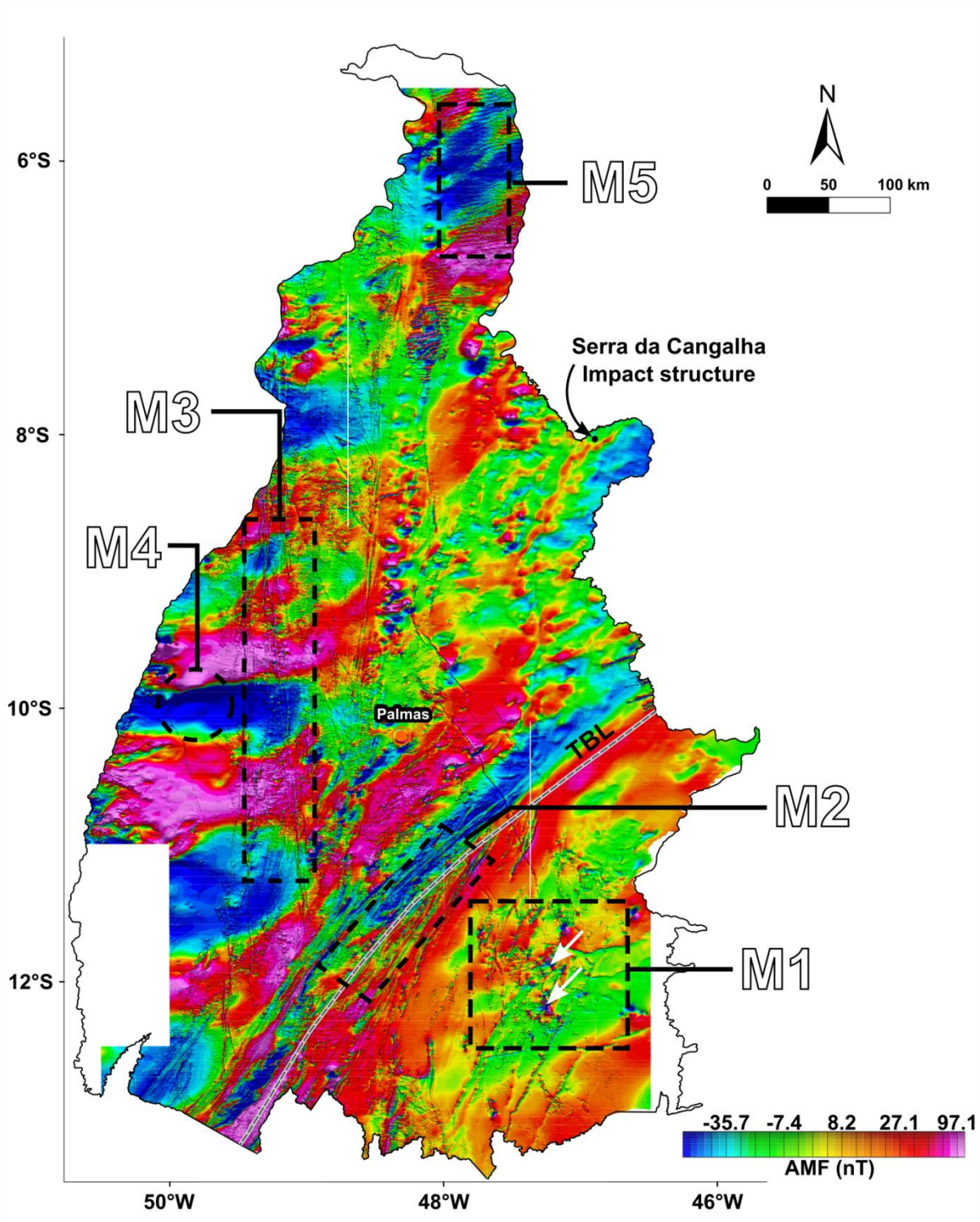

Figure 4: Anomalous Magnetic Field (AMF) map of Tocantins State. M1–M5 corresponds to features whose magnetic signatures can be visualized at regional scales. M1 - magnetic lows of granitic/gneiss/migmatite rocks. The white arrows highlight high-amplitude magnetic anomalies related to the Córrego do Paiol Formation metavolcanics or the Barra do Gameleira mafic intrusions; M2 - linear magnetic anomalies associated with the Transbrasiliano Lineament (TBL); M3 - linear magnetic anomalies associated with dikes and ophiolitic bodies; M4 - unknown circular magnetic anomaly; M5 - Magnetic signatures associated with Mosquito Formation basalts.

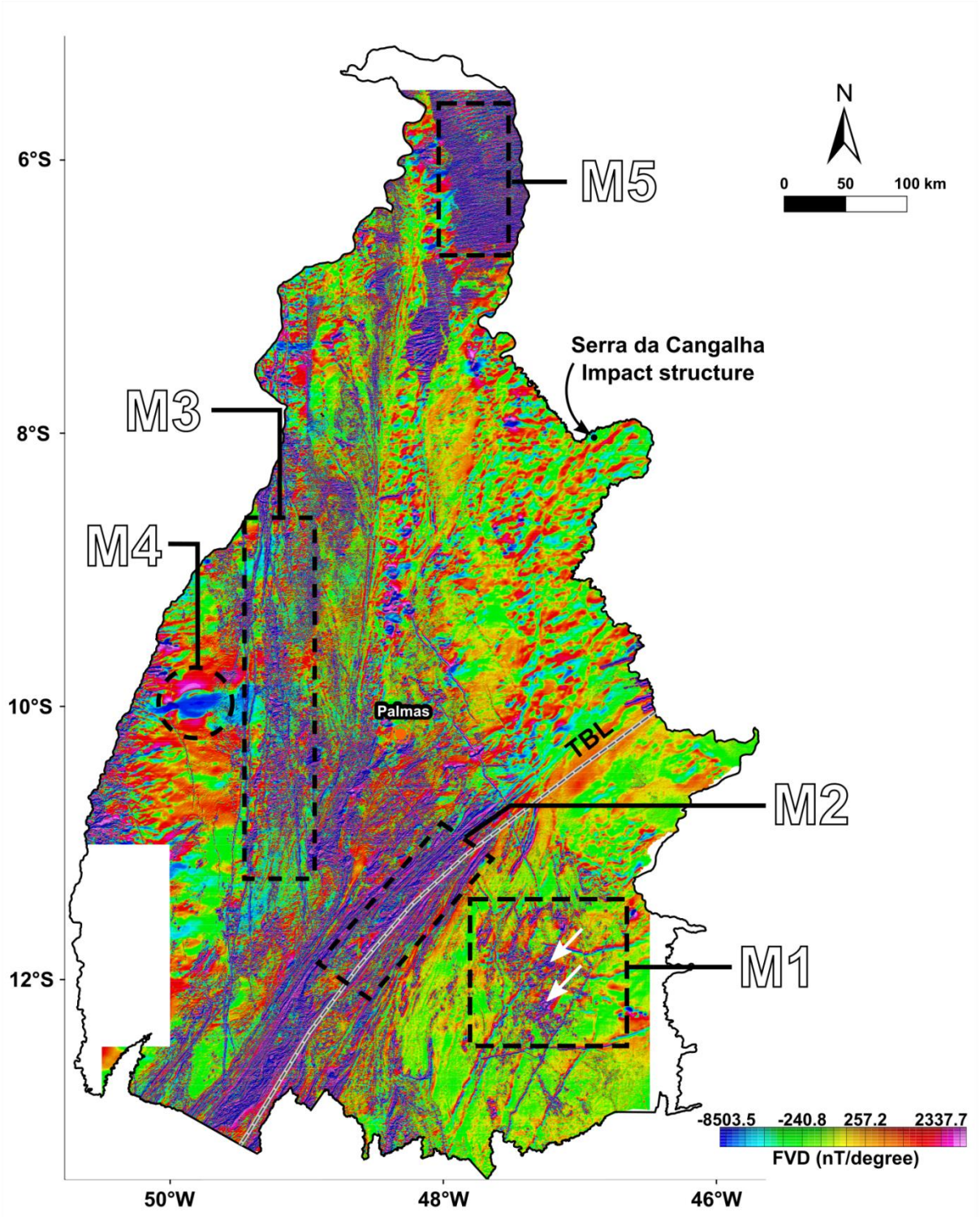

Figure 5: First Vertical Derivative of the Anomalous Magnetic Field (FVD – AMF) map of Tocantins State. M1–M5 corresponds to features whose magnetic signatures can be visualized at regional scales. M1 - magnetic lows of granitic/gneiss/migmatite rocks. The white arrows highlight high-amplitude magnetic anomalies re- lated to the Córrego do Paiol Formation metavolcanics or the Barra do Gameleira mafic intrusions; M2 - linear magnetic anomalies associated with the Transbrasiliano Lineament (TBL); M3 - linear magnetic anomalies as- sociated with dikes and ophiolitic bodies; M4 - unknown circular magnetic anomaly; M5 - Magnetic signatures associated with Mosquito Formation basalts.

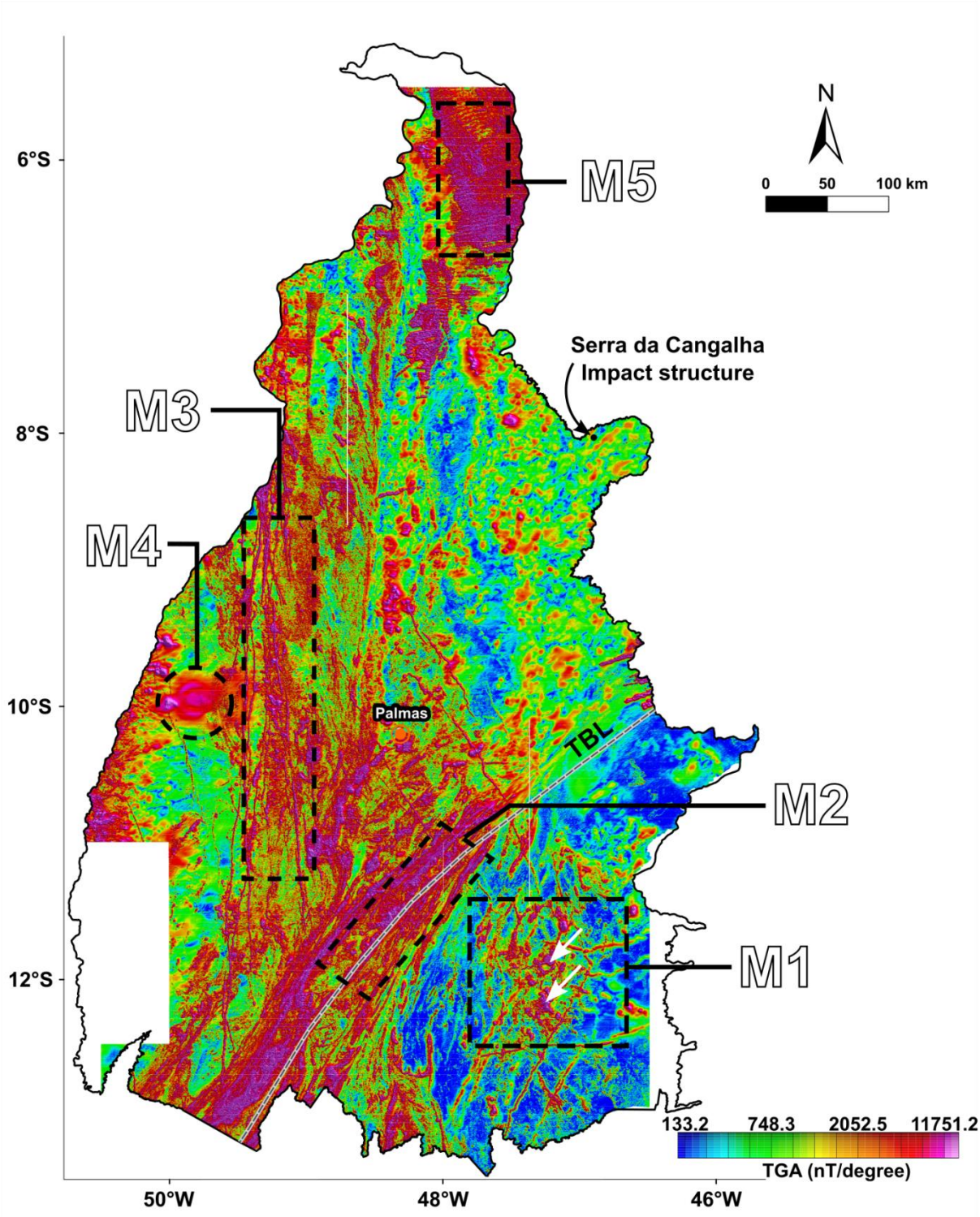

Figure 6: Total Gradient Amplitude of the Anomalous Magnetic Field (TGA – AMF) map of Tocantins State. M1–M5 corresponds to features whose magnetic signatures can be visualized at regional scales. M1 - magnetic lows of granitic/gneiss/migmatite rocks. The white arrows highlight high-amplitude magnetic anomalies re- lated to the Córrego do Paiol Formation metavolcanics or the Barra do Gameleira mafic intrusions; M2 - linear magnetic anomalies associated with the Transbrasiliano Lineament (TBL); M3 - linear magnetic anomalies as- sociated with dikes and ophiolitic bodies; M4 - unknown circular magnetic anomaly.

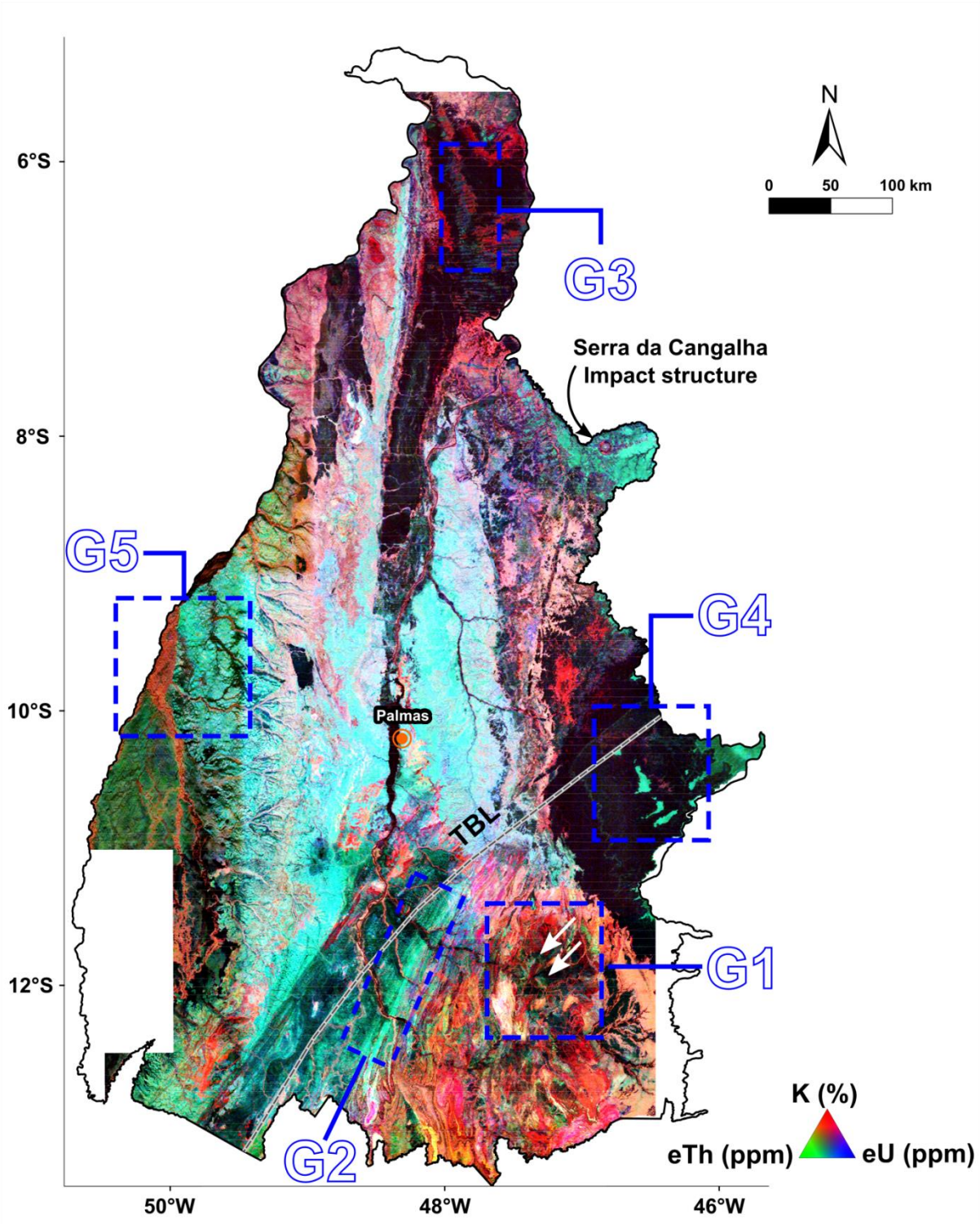

Figure 7: RGB composite color map of the K, eTh and eU concentrations over the territory of Tocantins State. Areas G1–G5 corresponds to features whose radiometric signatures can be distinguished at the regional scale. G1 - radiometric signatures of granitic/gneiss/migmatite terrain. The write arrows highlight low radiometric anomalies associated with mafic intrusions within these terrains; G2 - linear radiometric signatures associated with the Transbrasiliano Lineament (TBL); G3 - low radiometric anomaly due to the presence of Mosquito Formation basalts; G4 - low K, eTh and eU concentrations associated with quartz-rich soils in the Serra Geral do Tocantins region. The residual landforms show comparatively enhanced eTh and eU concentrations; G5 - radiometric signatures of alluvial deposits.

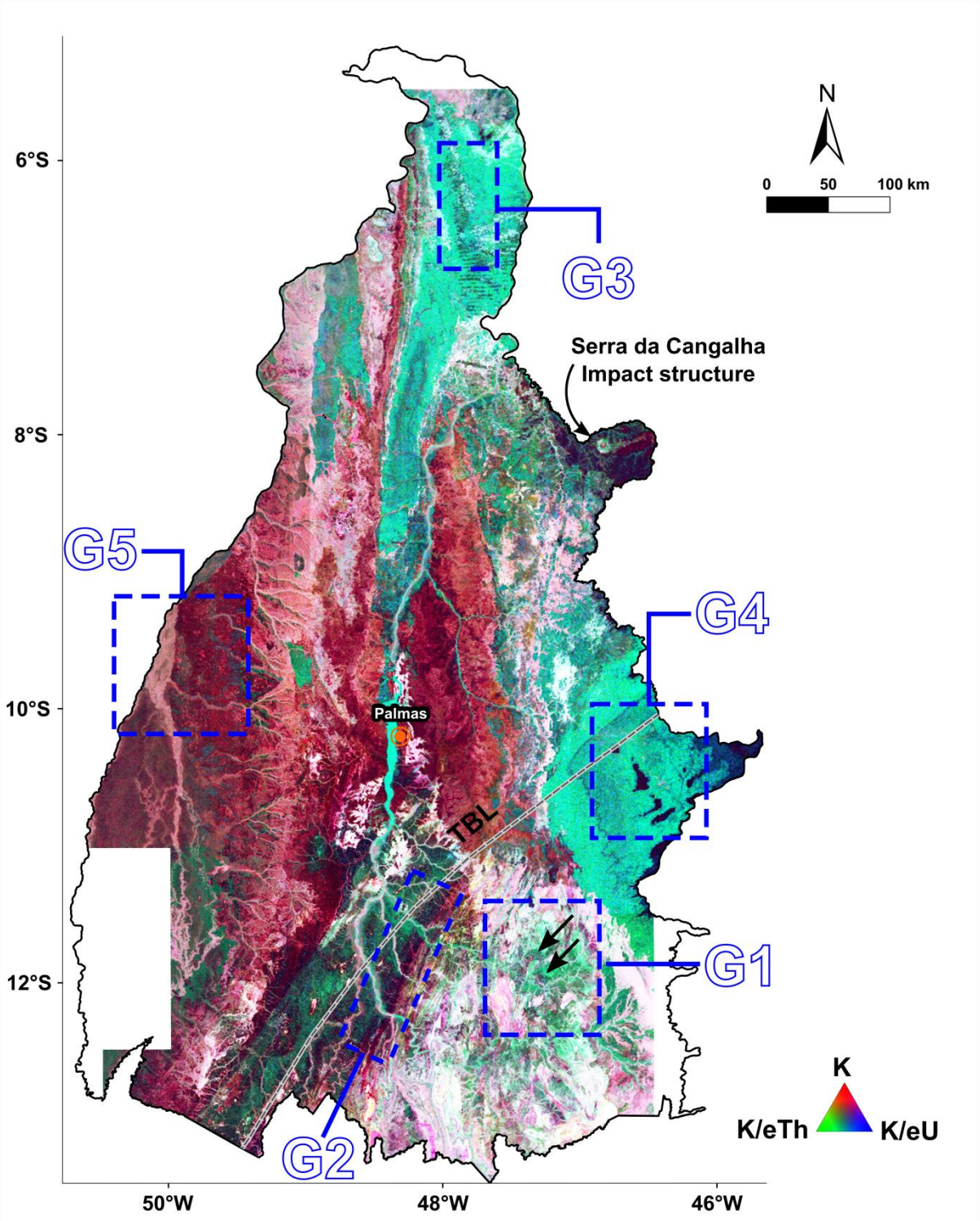

Figure 8: Potassium Inverse Image over the territory of Tocantins State. Areas G1–G5 corresponds to features whose radiometric signatures can be distinguished at the regional scale. G1 - radiometric signatures of granitic/gneiss/migmatite terrains. The black arrows highlight low radiometric anomalies associated with mafic intrusions within these terrains; G2 - linear radiometric signatures associated with the Transbrasiliano Lineament (TBL); G3 - low radiometric anomaly due to the presence of Mosquito Formation basalts; G4 - low K, eTh and eU concentrations associated with quartz-rich soils in the Serra Geral do Tocantins region. The residual landforms show comparatively enhanced eTh and eU concentrations; G5 - radiometric signatures of alluvial deposits.

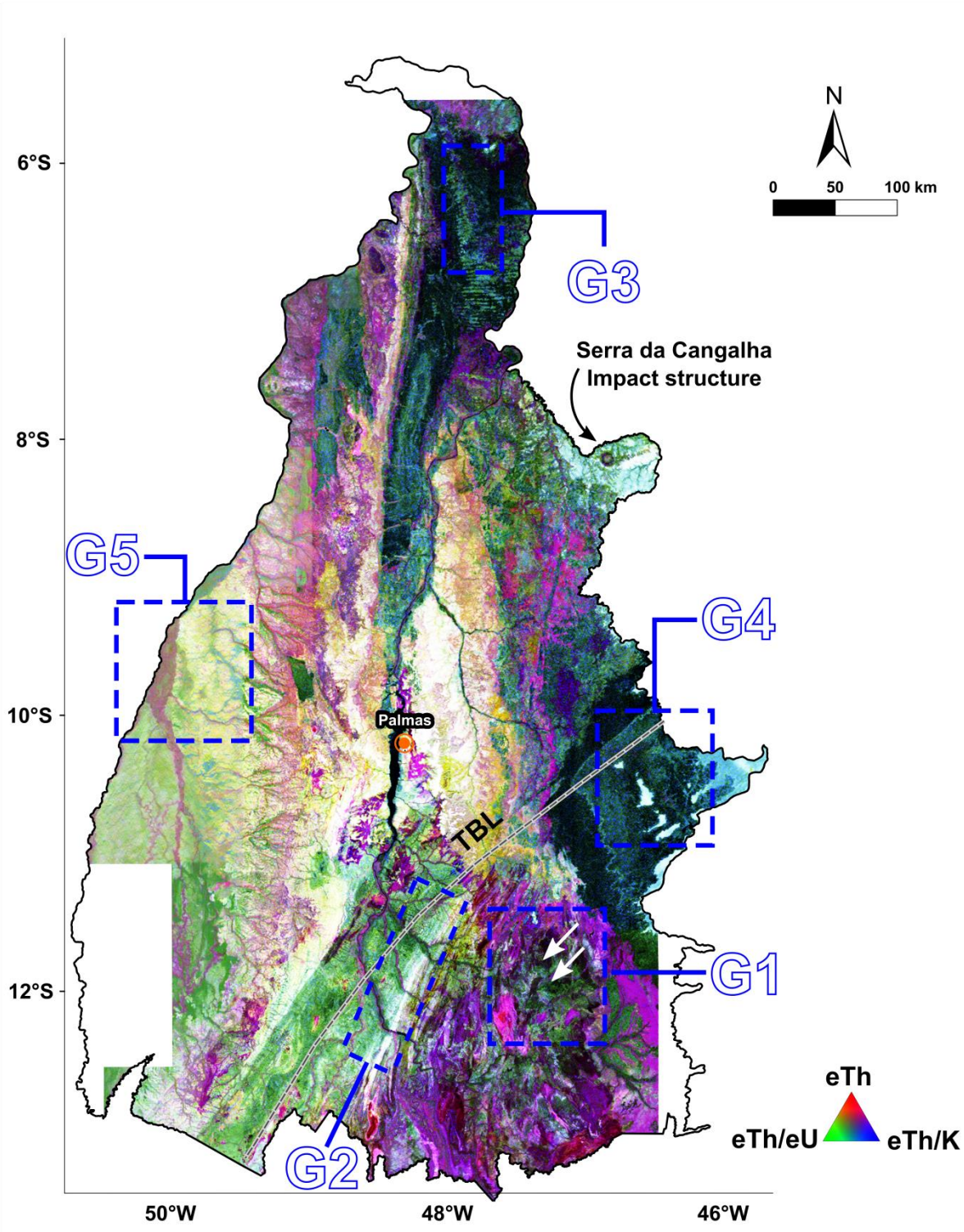

Figure 9: The eTh Inverse Image over the territory of Tocantins State. Areas G1–G5 corresponds to features whose radiometric signatures can be distinguished at the regional scale. G1 - radiometric signatures of granitic/gneiss/migmatite terrains. The black arrows highlight low radiometric anomalies associated with mafic intrusions within these terrains; G2 - linear radiometric signatures associated with the Transbrasiliano Linea- ment (TBL); G3 - low radiometric anomaly due to the presence of Mosquito Formation basalts; G4 - low K, eTh and eU concentrations associated with quartz-rich soils in the Serra Geral do Tocantins region. The residual landforms show comparatively enhanced eTh and eU concentrations; G5 - radiometric signatures of alluvial deposits.

where such high-intensity magnetic anomalies show a linear, E-W directed pattern (Mocitaiba et al., 2017; area M5 in Figures 4, 5 and 6). In the latter case of G4, low K, eTh and eU concentrations may be associated with quartz-rich soils in the Serra Geral do Tocantins region (Silva and Alves, 2022). Residual landforms are represented in green and cyan (Figure 7) and show that weathering may have favored eTh and eU concentrations and K leaching (Taylor et al., 2002; Mello et al., 2021). This idea is corroborated by K and eTh inverse Images: the residual landforms show strong dark hues in K image inverse (G4 in Figure 8), suggesting K leaching, whereas these same residual landforms can be seen as strong bright areas in the eTh Inverse Image (G4 in Figure 9), which suggests eTh concentration. These results suggest that K and eTh Inverse Images can be a useful tool in highlighting products of weathering.

Radiometric signatures seen along large drainage channels, mainly along the Tocantins and Araguaia rivers and their tributaries, are also emphasized on the RGB maps (G5 area in Figures 7, 8 and 9). In western Tocantins (area G5), such anomalies may be derived from alluvial deposits (Bierwirth, 1996). In this case, the color distribution in Figure 7 (area G5) can provide clues about the composition or texture of these deposits. A white color suggests that such deposits are enriched in all 3 radioelements. It can, therefore, be inferred that either these deposits are recent or that their source is close to the place of deposition (Pickup and Marks, 2000; Wilford and Minty, 2007; Rawlins and Webster, 2007; Dent et al., 2013).

On the other hand, a dark color suggests that such deposits are depleted in K, eTh and eU, which may imply that they are dominated by silica-rich minerals, mainly in the sand fraction (Spadoni and Voltaggio, 2013; Mello et al., 2021). Regarding Inverse Images, the path of drainage channels is well-defined in the eTh Inverse Image because there are better contrasts between alluvial deposits and surrounding lithologies (Figure 9).

In the western State of Tocantins, radiometric signatures in the G5 area coincide with a somewhat smooth magnetic relief related to short-wavelength linear magnetic anomalies. However, a large (ca. 32 km wide) magnetic anomaly with an approximately circular shape (area M4 in Figures 4, 5 and 6) seems to be associated with a deep magnetic source, as the magnetic signal is attenuated in the FVD – AMF and TGA maps (Figures 5 and 6). This large circular magnetic anomaly is disturbed by some, previously mentioned, linear magnetic anomalies. The source of this circular magnetic anomaly is unknown, but the existence of circular magnetic anomalies in sedimentary basins may be indicative of mafic intrusions (Gunn, 1997). Alternatively, they may represent the location of a buried impact structure (Pilkington and Grieve, 1992; Gilder et al., 2018).

Radiometric signatures seen along large drainage channels, mainly along the Tocantins and Araguaia rivers and their tributaries, are also emphasized on the RGB maps (G5 area in Figures 7, 8 and 9). In western Tocantins (area G5), such anomalies may be derived from alluvial deposits (Bierwirth, 1996). In this case, the color distribution in Figure 7 (area G5) can provide clues about the composition or texture of these deposits. A white color suggests that such deposits are enriched in all 3 radioelements. It can, therefore, be inferred that either these deposits are recent or that their source is close to the place of deposition (Pickup and Marks, 2000; Wilford and Minty, 2007; Rawlins and Webster, 2007; Dent et al., 2013).On the other hand, a dark color suggests that such deposits are depleted in K, eTh and eU, which may imply that they are dominated by silica-rich minerals, mainly in the sand fraction (Spadoni and Voltaggio, 2013; Mello et al., 2021). Regarding Inverse Images, the path of drainage channels is well-defined in the eTh Inverse Image because there are better contrasts between alluvial deposits and surrounding lithologies (Figure 9).

In the western State of Tocantins, radiometric signatures in the G5 area coincide with a somewhat smooth magnetic relief related to short-wavelength linear magnetic anomalies. However, a large (ca. 32 km wide) magnetic anomaly with an approximately circular shape (area M4 in Figures 4, 5 and 6) seems to be associated with a deep magnetic source, as the magnetic signal is attenuated in the FVD – AMF and TGA maps (Figures 5 and 6). This large circular magnetic anomaly is disturbed by some, previously mentioned, linear magnetic anomalies. The source of this circular magnetic anomaly is unknown, but the existence of circular magnetic anomalies in sedimentary basins may be indicative of mafic intrusions (Gunn, 1997). Alternatively, they may represent the location of a buried impact structure (Pilkington and Grieve, 1992; Gilder et al., 2018).

11.5.2 Radiometric signatures of the Serra da Cangalha impact structure

In the RGB maps (Figures 7, 8 and 9), the radiometric signatures in the area of the SdC impact structure present a circular pattern. Such patterns have been observed for other impact structures (e.g., the Lawn Hill, Mount Toondina, Riachão Ring and Araguainha impact structures; Maziviero et al., 2013; Niang et al., 2022; Leite et al., 2022) and could be the outcome of a number of factors or processes, such as impact-induced K volatilization, impact melt differentiation, hydrothermal alteration, structural deformation, post-impact alteration and distribution of ejecta deposits (Vasconcelos et al., 2012; Baratoux et al., 2019; Niang et al., 2021, 2022). In previous work about the SdC impact structure, it was suggested that the radiometric signatures there

could be related to post-impact alteration, mainly to differential erosion of different lithostratigraphic units (Kenkmann et al., 2011; Vasconcelos et al., 2012, 2013).

Here, we corroborate the results of this previous work with new imagery and observations. We observe an association between the main morphological domains of the SdC impact structure and their radiometric signatures. High K values occur in the area of the central depression and low radiometric values are observed over the area of the annular basin. Outside of the crater rim, we also observe low K values and high eU and eTh values.

New information about the distribution and behavior of radioelements can be extracted from the analysis of radiometric ratio curves across the Serra da Cangalha structure. Figure 10 shows that the innermost depression in the central uplift domain of the structure is indeed characterized by high values of K, eTh and eU, as already observed by Vasconcelos et al. (2012). However, the low values for the eTh/K and eU/K ratio curves over this centralmost area suggest enrichment of K. The K, eTh and eU values in the central part of the annular basin are low, but eU/eTh and eU/K ratio values suggest that eU is enriched in this zone relative to K and eTh.

The low eTh/K and eU/K ratio over the inner part of the central domain can be explained not only by the presence of muscovite, as previously proposed by Vasconcelos et al. (2012), but also by the presence of alluvium containing K-bearing minerals derived from the erosion of the inner walls of the very prominent collar. In the context of impact structures, high K values have been observed to be sometimes correlated with topographic depressions filled by alluvial deposits (e.g.,Niang et al., 2021). Similarly, high eTh and eU concentrations in the inner depression may be associated with Longá Formation shales (Vasconcelos et al., 2012). Furthermore, the presence of accessory minerals derived from erosion of the inner collar should not be ruled out as another possible carrier of radiogenic elements (eU and eTh).

Contrary to the central depression, the annular basin is characterized by low values for the radioelements. Erosion and weathering processes were proposed to explain the radiometric low observed over the annular basin (Vasconcelos et al., 2013). In areas where erosion processes are dominant, the radiometric response may be primarily associated with bedrock minerals or minerals derived from secondary processes (e.g., hydrothermal alteration or weathering; Dickson and Scott, 1997). In places where weathering processes are dominant, high concentrations of eTh can be expected, as Th has a low mobility and, when released, is quickly incorporated into iron oxides or phyllosilicates. In addition, many weathering-resistant minerals are Th-rich (such as monazite, zircon and iron oxides; Dickson and Scott, 1997; Wilford and Minty, 2007; Mello et al., 2021).

In Figure 10, the increments for the annular basin along the eU/eTh and eU/K ratio curves suggest that the annular basin is characterized by generally low K, eTh and eU abundances. If weathering were one of the causes of this radiometric low, an enrichment of eTh relative to eU (that is, decrease along the eU/eTh curves) would be expected, similar to what has been observed over the crater rim zone (see discussion below). Therefore, if weathering contributed to the ra- diometric pattern observed over the annular basin, this contribution could be dominant. On the other hand, the low overall radiometric signature could be related to a lithostratigraphic unit that has been ex- posed by erosion. This unit could be low in K, eTh and eU but could contain U-bearing minerals (e.g.,zircon from aeolian sandstone).

These increments along the eU/eTh and eU/K ratio curves could also be related to intermittent U anomalies, that is, the gamma rays detected during the aerial survey may come from Rn in groundwater discharge zones (Bierwirth, 1996). This is a potentially valid observation, as the annular basin is a focus of drainage channels. It is, thus, recommended to carry out further studies aimed at elucidating the origin of this relative enrichment of eU in the annular basin at SdC. Such studies could include gamma-ray ground surveys, soil sampling for geochemical analysis and petrographic descriptions. Multivariate analysis techniques (e.g., Principal Component Analysis, unsupervised clustering, correlation heatmaps; Ford et al., 2008;Mello et al., 2021) could be applied to such data sets to identify the main contributors to U concentration. Additionally, in situ Rn measurements may be useful to investigate U concentrations derived from groundwater flows.

An interesting aspect of Figure 10 relates to the eU concentrations that are observed at the interface between the outer walls of the inner collar and the center of the annular basin, and which have not been discussed in earlier work. In the NE portion of the profile, at position 12,200 m, an increase in eU concentration is accompanied by a decrease in eTh and K concentrations. This behavior of the radiometric elements is well expressed along the eU/eTh and eU/K ratio curves. Within the region delimited by the inner collar and the center of the annular basin, it is possible to identify areas with local positive maxima on the eU/eTh and eU/K ratio curves, as indicated by black arrows in Figure 10, both to the SW and NE of the central part of the structure. In Figure 10, the center center of the SdC structure is located approximately at position 9,400 m. Consequently, the distance be- tween the peaks and the center of the structure is ap- proximately 2,900 m (SW portion) and 2,800 m (NE portion). Interestingly,

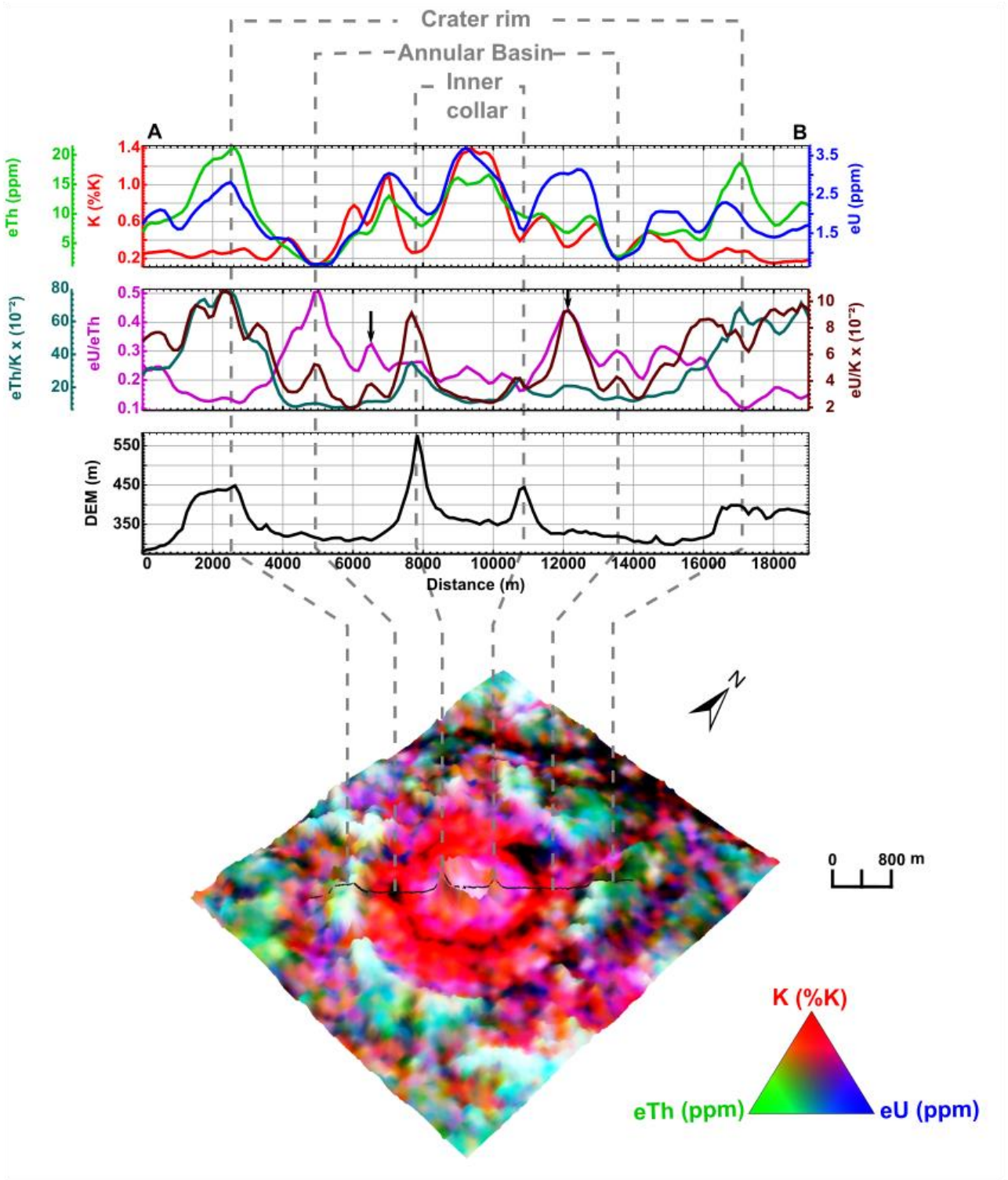

Figure 10: Profile A – B in SW – NE direction (compare with Figure 2) is matched with a 3D visualization of the Serra da Cangalha impact structure based on the RGB composition of radiometric concentrations overlain onto a SRTM digital elevation model. Vertical exaggeration = 5x horizontal scale. The black arrows highlight areas where eU is relatively enriched compared to K and eTh, in the inner zone of the annular basin.

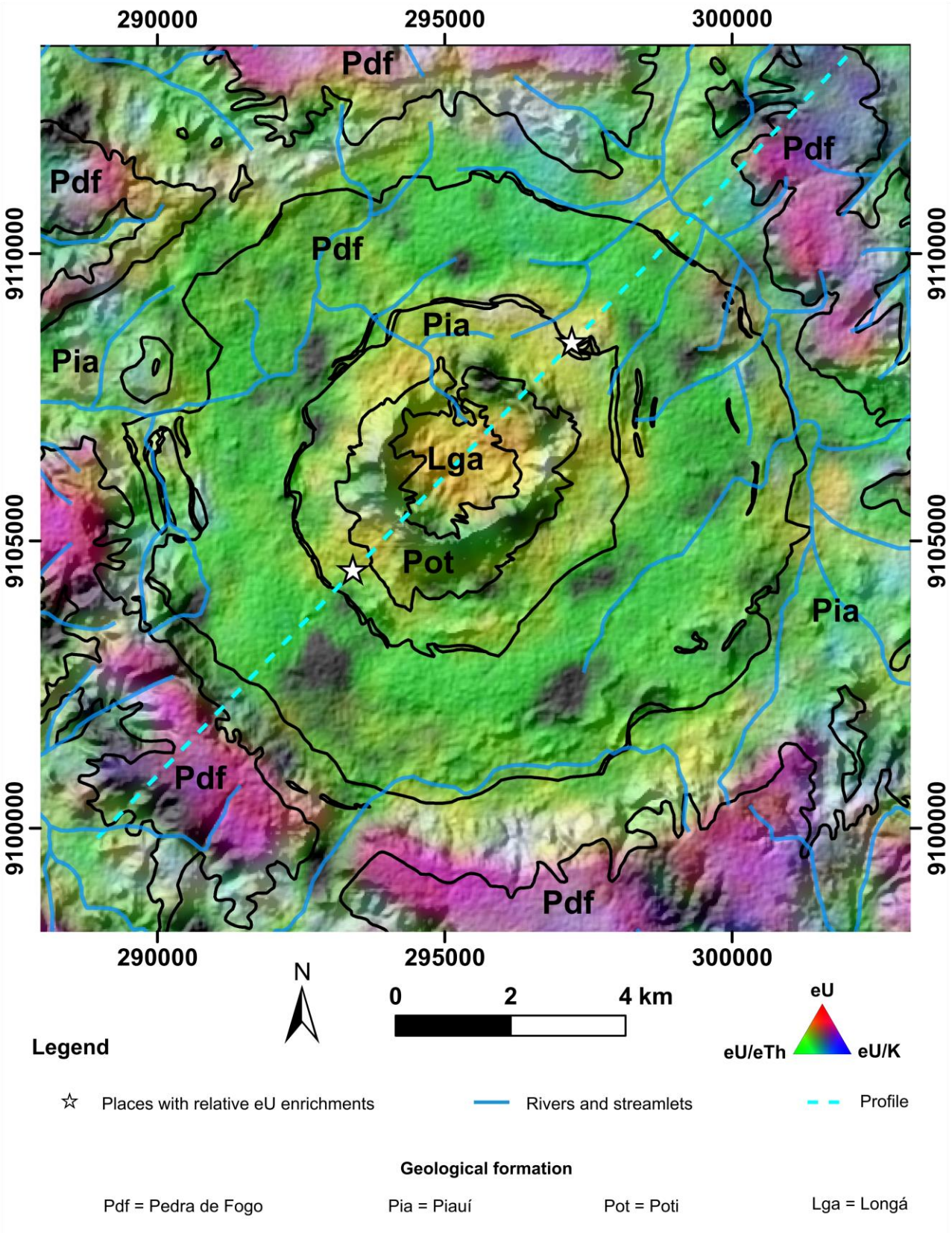

Figure 11: eU Inverse Image map of Serra da Cangalha impact structure. The white stars highlight areas where eU is relatively enriched compared to K and eTh, in the inner zone of the annular basin.

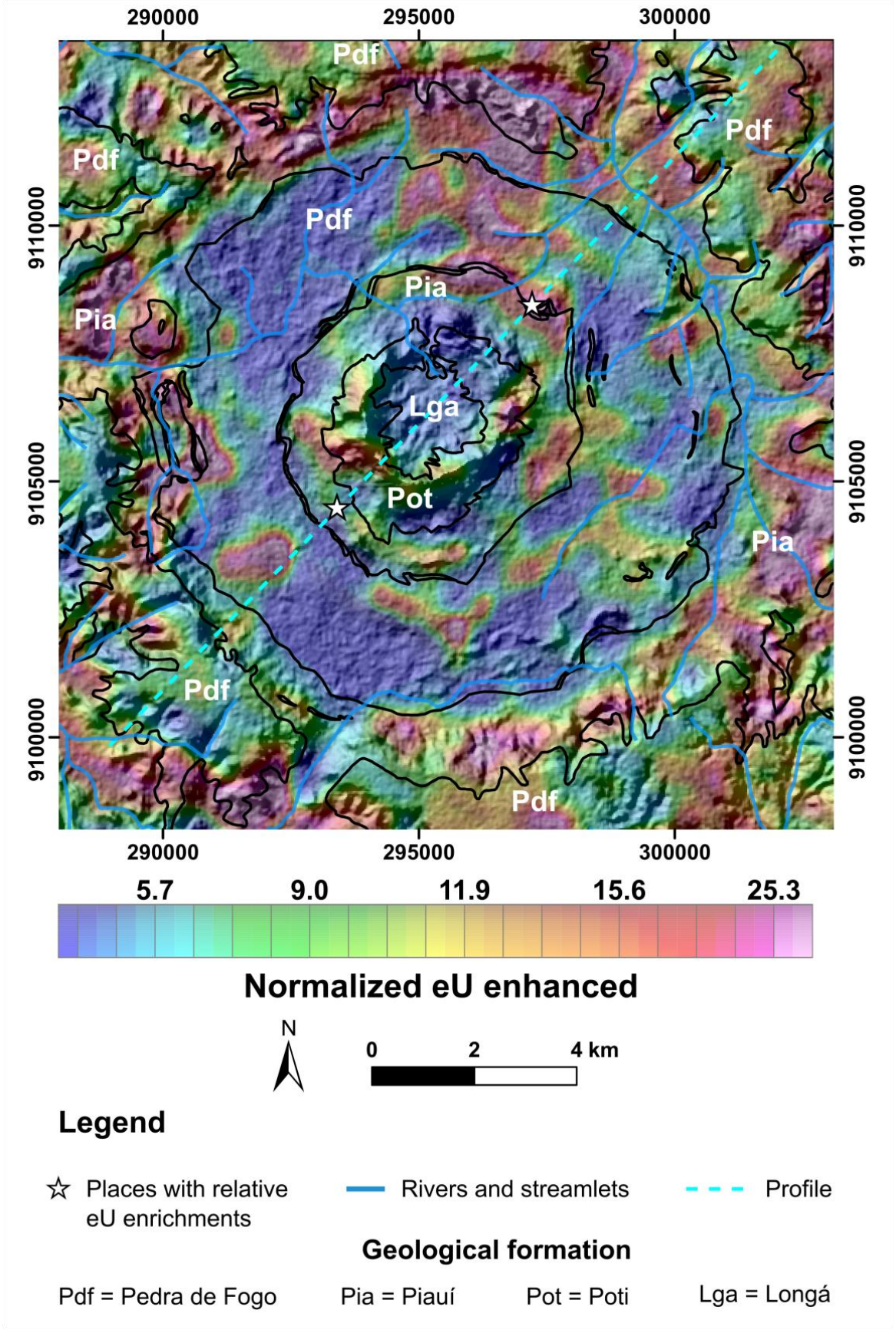

Figure 12: Normalized eU enhancement image (NeU_E) map of Serra da Cangalha impact structure. The white stars highlight areas where eU is relatively enriched compared to K and eTh, in the inner zone of the annular basin.

these distances are similar to those distances (2.8 km) from the center to where the first set of chert ridges occurs. These ridges mark the contact zone between the Piauí Formation and the Pedra de Fogo Formation, and they also mark the outer limit of the central uplift domain.When the local positive maxima on the eU/eTh and eU/K ratio curves are plotted as a point in eU inverse image and NeU_E maps (Figures 11 and 12), the northeasternmost point on profile coincides with Piauí and Pedra de Fogo contact zones and with high NeU_E values (see the white stars in Figures 11 and 12). Otherwise, the southwesternmost point on the profile neither shows high NeU_E nor association with any contact zones. On the one hand, this result suggests that such lithostratigraphic contact zones present relative enrichment of eU and relative depletion of eTh and K abundances, such that we can in- fer that the eU concentrations could stem from brec- ciated chert layers or silicified sandstones. On the other hand, the final word about this enrichment has not yet been spoken and more researches must be done.

Other interesting results derived from radiometric maps in Figure 11 concern mapping of Pedra de Fogo Formation. In the eU Inverse Image (Figure 11), Pedra de Fogo Formation is seen as reddish purple areas whose contours match well those on the geological map as proposed in previous work (Kenkmann et al., 2011; Vasconcelos et al., 2013). Moreover, the central portion of SdC shows yellowish hues, which suggests that the Poti, Piauí and mainly Longá formations can be distinguished from the Pedra de Fogo Formation based on eU and eU/K content.

Finally, the outer zone of the SdC structure is well marked by increases of values on the eTh and eU concentration curves (Figure 10). Both curves then decrease again into the surrounding terrain (outer domain). Abundances of K are low both on the crater rim and over the outer terrain. Increases along the eTh/K and eU/K ratio curves reveal that eTh and eU are relatively enriched with respect to K, whereas a decrease in the eU/eTh curve suggests that eTh is more enriched than eU (Figure 10). Several studies have reported that such a behavior of radioelements could be due to weathering processes that promote eTh and eU concentration in Fe oxides or their adsorption by phyllosilicate minerals – coincident withleaching of K from weathered soils (e.g., Megumi and Mamuro, 1977; Taylor et al., 2002; Wilford and Minty, 2007; Mello et al., 2021). Vasconcelos et al. (2012) suggested that the source of eTh and eU could be Fe-oxide minerals in lateritic crusts that formed in soils of the outer rim.

Potassium, in contrast, may have been leached from the profile. Abundances of eTh may be relatively increased more than abundances of eU, because the latter radioelement could become leached under oxidizing conditions (Lang- muir, 1978; Reinhardt and Hermann, 2018).

11.6 CONCLUSIONS

This work presents a synthesis of the Tocantins State Aerogeophysical Atlas, with special emphasis on the interpretation of the first vertical derivative of anomalous magnetic field (FVD – AMF) and RGB color composition of K, eTh and eU concentration maps. In addition, a special focus was placed onto the aerogeophysical characteristics of the Serra da Cangalha impact structure. Based on visual analysis and previous geological information, we can conclude the following:

- Radiometric and/or magnetic signatures of specific geological units (e.g., Mosquito Formation basalts or granite/gneiss/migmatite terrains), of structural features (e.g. dykes and lineaments), or of related exogenous factors (Serra Geral do Tocantins quartz soils and alluvial deposits on main drainage channels) can be visualized on regional scale magnetic anomaly maps.

- The K and eTh Inverse Images prove to be useful tools for highlighting K-rich Natividade – Cavalcante rocks, weathering products in resid- ual landforms and extents of drainage channels. In the Serra da Cangalha structure, an eU Inverse Image was suitable to outline the Pedra de Fogo Formation contours. Moreover, a normalized eU enhancement map can be a good alternative to map high eU concentrations in the case of SdC.

- Analysis of radiometric ratios over the area of the Serra da Cangalha impact structure has provided new insights, mainly regarding the eU concentrations present in the annular basin. Our preferred interpretation suggests that these eU concentrations could be associ- ated with some lithological unit containing U- bearing minerals (e.g., zircon from aeolian sandstone). Alternatively, eU concentrations could also be related to intermittent U anomalies that come from Rn in groundwater discharge zones.

- For specific areas, such as the Piauí Formation and the Pedra de Fogo Formation contact zones, eU concentrations may be related to unrecognized mechanisms. For example, notable eU concentrations could stem from brecciated chert layers or silicified sandstones.

- We propose that further research about the radiometric signatures of the Serra da Cangalhaimpact structure is required, and we recom- mend that a set of data derived from gamma-ray ground surveys, soil sampling and petrographic descriptions be taken and analyzed by multi- variate data analysis techniques.

11.7 ACKNOWLEDGMENTS

The authors are grateful to the Remote Sensing and Geophysics Division of the Geological Survey of Brazil for providing the airborne geophysical data and software used for this work. The investigation of the Serra da Cangalha impact structure is related to the first author´s MSc project within the Postgraduate Program in Geology at the University of Brasília. The authors are also thankful for reviewers' corrections and recommendations that provided essential improvement of this manuscript. WUR´s contribution was also supported in part by the Coordenação de Aperfeiçoamento de Pessoal de Nível Superior (CAPES), Brazil, under Finance Code 001.

11.8 REFERENCES

Abdallah, S., and P. F. V. Meneghini, 2017, Geologia e recursos minerais da folha arraias – sd.23–v–a: Relatório final: Technical report, CPRM, Goiânia, Brasil. (Access on 05 May 2023).

Airo, M. L., 2002, Aeromagnetic and aeroradio- metric response to hydrothermal alteration: Surveys in Geophysics, **23**, 273–302, doi: 10.1023/A:1015556614694.

Almeida, F. F. M., Y. Hasui, B. B. Brito Neves, and R. A. Fuck, 1981, Brazilian structural provinces: An introduction: Earth-Science Reviews, **17**, 1–29, doi: 10.1016/0012-8252(81)90003-9.

Alvarenga, C. J. S., N. F. Botelho, M. A. Dardenne,O. N. B. Lima, and M. A. Machado, 2007, Nota explicativa das folhas monte alegre de goiás (sd.23–v– c–iii), cavalcante (sd.23–v–c–v) e nova roma (sd.23– v–c–vi). scale 1:100.000: Technical report, Universidade de Brasília/CPRM, Goiás, Brasil. (Access on 05 May 2023).

Alves, F. M., E. R. Silva, and A. B. Silva, 2022, At- las aerogeofísico do estado de goiás: Technical report, Serviço Geológico do Brasil – CPRM, Goiâ- nia, Brasil. (Access on 07 November 2023).

Alves, P. V. F. S., N. F. Botelho, E. L. Dantas, and F. A. Cuadros, 2019, The cambrian peraluminous santa luzia granite suite in the araguaia belt, central Brazil: Evidence for closure of the clymene ocean based on zircon and monazite u–pb data: Journal of South American Earth Sciences, **92**, 116–133, doi: 10.1016/j.jsames.2019.03.007.

Arcanjo, S. H. S., F. A. M. Abreu, and C. A. V. Moura, 2001, Magmatismo alcalino mesoproterozóico na província tocantins – uma evidência de quebramento do supercontinente rodínia?: Pre- sented at the Anais do 7ª Simpósio de Geologia da Amazônia, SBG.

Arcanjo, S. H. S., F. A. M. Abreu, and C. A. V. Moura, 2013, Evolução geológica das sequências do embasamento do cinturão araguaia na região de alto paraíso do tocantins (to), brasil: Brazilian Journal of Geology, **43**, 501–514, doi: 10.5327/Z2317-48892013000300007.

Baratoux, D., C. A. B. Niang, W. U. Reimold,M. S. Sapah, W. Jessell, D. Boamah, G. Faye, S. Bouley, and O. Vanderhaeghe, 2019, Bosumtwi im- pact structure, ghana: Evidence for fluidized em- placement of the ejecta: Meteoritics & Planetary Science, **54**, 2541–2556, doi: 10.1111/maps.13253.

Barros, L. D., and P. S. S. Gorayeb, 2019, Serra do Tapa Ophiolite Suite – Araguaia Belt: Geological Characterization and Neoproterozoic Evolution (Central–Northern Brazil): Journal of South American Earth Sciences, **96**, 102323, doi: 10.1016/j.jsames.2019.102323

Bierwirth, P., 1996, Investigation of airborne gamma–ray images as a rapid mapping tool for soil and land degradation – wagga wagga, nsw: Technicalreport, Australian Geological Survey Organisation, Canberra, Australia. (Access on 05 May 2023).

Brito Neves, B. B., and U. G. Cordani, 1991, Tectonic evolution of south america during the late proterozoic: Precambrian Research, **53**, 23–40, doi: 10.1016/0301-9268(91)90004-T.

Brito Neves, B. B., R. A. Fuck, and M. M. Pimentel, 2014, The brasiliano collage in south america: A review: Brazilian Journal of Geology, **44**, 493–518, doi: 10.5327/Z2317-4889201400030010.

Campos, J. E. G., and M. A. Dardenne, 1997a, Estratigrafia e sedimentação da bacia sanfranciscana: Uma revisão: Revista Brasileira de Geociências, **27**, 269–282. (Access on 05 May 2023).

Campos, J. E. G., and M. A. Dardenne, 1997b, Origem e evolução tectônica da bacia sanfrancis- cana: Revista Brasileira de Geociências, **27**, 283–294. (Access on 05 May 2023).

Cheesman, S., I. MacLeod, and G. Hollyer, 1998, A new, rapid, automated grid stitching algorithm: Exploration Geophysics, **29**, 301–305, doi: 10.1071/EG998301.

Clark, D. A., 1997, Magnetic petrophysics and magnetic petrology: Aids to geological interpretation of magnetic surveys: Journal of Australian Geological and Geophysical, **17**, 83–103. (Access on 05 May 2023).

Cordani, U. G., M. M. Pimentel, C. E. G. Araújo, M. A. S. Basei, R. A. Fuck, and V. A. V. Girardi, 2013, Was there an ediacaran clymene ocean in central brazil?: American Journal of Science, **313**, 517–539, doi: 10.2475/06.2013.01

Crósta, A., W. Reimold, M. Vasconcelos, N. Hausen,G. Oliveira, M. Maziviero, and A. Góes, 2019, Impact

cratering structures: The south american record – part 1: Geochemistry, **79**, 1–61, doi: 10.1016/j.chemer.2018.06.001.

Dardenne, M., 2000, The brasilia fold belt, *in* Tectonic Evolution of South America: 31st International Geological Congress: 231–263. (Available at: rigeo.cprm.gov.br. Access on 05 May 2023).

Delgado, I., J. Souza, N. Silveira Filho, R. Santos, A. Pedreira, J. Guimarães, L. Angelim, A. Vasconcelos, I. Gomes, J. Lacerda Filho, et al., 2003, Geotectônica do escudo atlântico, *in* Geologia, Tectônica e Recursos Minerais do Brasil: Textos, Mapas e GIS: CPRM, 227–334. (Available at: rigeo.cprm.gov.br. Access on 05 May 2023).

Dent, D., R. MacMillan, T. Mayr, W. Chapman, and S. Berch, 2013, Use of airborne gamma radiometrics to infer soil properties for a forested area in british columbia, canada: Journal of Ecosystem and Management, **14**, 1–12, doi: 10.22230/jem.2013v14n1a201.

Dentith, M., and S. Mudge, 2014, Geophysics for the mineral exploration geoscientist, 1st ed.: Cambridge University Press.

Dickson, B., and K. Scott, 1997, Interpretation of aerial gamma-ray surveys adding the geochemicalfactors: Journal of Australian Geology & Geo- physics, **17**, 187–200.

Dietz, R., and B. French, 1973, Two probable astroblemes in brazil: Nature, **244**, 561–562, doi: 10.1038/244561a0.

Duval, J., 1983, Composite color images of aerial gamma-ray spectrometric data: Geophysics, **48**, 722–735, doi: 10.1190/1.1441502.

Figueiredo, A., J. Olímpio, and O. Olivatti, 2001, Conceição do araguaia – folha sb.22–x–b, es- tado do tocantins e pará: Technical report, CPRM/DIEDIG/DEPAT, Brasília, Brazil. (Available at: rigeo.cprm.gov.br. Access on 05 maio 2023).

Ford, K., J. Harris, R. Shives, J. Carson, and J. Buckle, 2008, Remote predictive mapping 2. gamma-ray spectrometry: A tool for mapping canada's north: Geoscience Canada, **35**. (Avail- able at: journals.lib.unb.ca).

Frasca, A., 2015, Amálgamas do w-gondwana na província tocantins: PhD thesis, Universidade de Brasília (UnB), Brasília, DF, Brazil. (Available at: rigeo.cprm.gov.br. Access on 05 May 2023).

Frasca, A., H. Lima, L. Moraes, and P. Ribeiro, 2010, Geologia e recursos minerais da folha gurupi – sc.22–z–d, estado do tocantins: Technical report, CPRM, Goiânia, Brazil. (Available at: rigeo.cprm.gov.br. Access on 05 May 2023).

Frasca, A., P. Ribeiro, J. Lacerda Filho, P. Meneghini, L. Moraes, and H. Lima, 2018, Geologia e recursos minerais da folha alvorada – SC.22–X–B, Estado do Tocantins: Technical report, CPRM, Goiânia, Brazil. (Available at: rigeo.cprm.gov.br. Access on 05 May 2023).

Fuck, R., 1994, A faixa brasília e a compartimentação tectônica na província tocantins: 4º Simpósio de Geologia do Centro-Oeste, SBG, 184–187.

Fuck, R., E. Dantas, M. Pimentel, N. Botelho, R. Armstrong, J. Laux, S. Junges, J. Soares, and I. Praxedes, 2014, Paleoproterozoic crust-formation and reworking events in the tocantins province, central brazil: A contribution for atlantica supercontinent reconstruction: Precambrian Research, **244**, 53–74, doi: 10.1016/j.precamres.2013.12.003.

Galbraith, J., and D. Saunders, 1983, Rock classification by characteristics of aerial gamma-ray measurements: Journal of Geochemical Exploration, **18**, 49–73, doi: 10.1016/0375-6742(83)90080-8.

Gilder, S., J. Pohl, and M. Eitel, 2018, Magnetic signatures of terrestrial meteorite impact craters: A summary, *in* Magnetic Fields in the Solar System: volume **448** *of* Astrophysics and Space Sci- ence Library, 357–382. doi: 10.1007/978-3-319- 64292-5_13.

Gorayeb, P., 1981, Evolução geológica da região de araguacema - pequizeiro, goiás: Master's thesis, Universidade Federal do Pará, Belém, Brazil.

Gunn, P., 1997, Regional magnetic and gravity responses of extensional sedimentary basins: Journalof Australian Geology & Geophysics, **17**, 115–131. (Available at: Geoscience Australia PDF).

Góes, A., and F. Feijó, 1994, Bacia do parnaíba: Boletim de Geociências da Petrobras, **8**, 57–67.

Hasui, Y., C. Tassinari, O. Siga Júnior, W. Teixeira, F. Almeida, and K. Kawashita, 1980, Datações rb- sr e k-ar do centro-norte do brasil e seu significado geológico-geotectônico: Presented at the 31º Congresso Brasileiro de Geologia.

Henkel, H., and M. Guzmán, 1977, Magnetic features of fracture zones: Geoexploration, **15**, 173–181, doi: 10.1016/0016-7142(77)90024-2.

Herz, N., Y. Hasui, J. Costa, and M. Matta, 1989, The araguaia fold belt, brazil: A reactivated brasiliano–pan–african cycle (550 ma) geo- suture: Precambrian Research, **42**, 371–386, doi: 10.1016/0301-9268(89)90020-X.

Hodel, F., R. Trindade, M. Macouin, V. Meira, E. Dantas, M. Paixão, M. Rospabé, M. Castro, G. Queiroga, A. Alkmin, et al., 2018, A neoproterozoic hyper-extended margin associated with rodinia's demise and gondwana's build-up: The araguaia belt, central brazil: Gondwana Research, **66**, 43–62, doi: 10.1016/j.gr.2018.08.010.

International Atomic Energy Agency (IAEA), 2003, Guidelines for radioelement mapping using gamma-ray spectrometry data: Technical report, IAEA, Vienna, Austria.

Johnson, A., S. Cheeseman, and J. Ferris, 1999, Improved compilation of antarctic peninsula magnetic data by new interactive grid suturing and blending methods: Annali Di Geofisica, **42**, 249–259, doi: 10.4401/ag-3717.

Jost, H., F. Chemale Jr, I. Dussin, and C. Tassinari, 2010, Goiás greenstone belts: Archean or paleoproterozoic: 45º Congresso Brasileiro de Geologia, SGB, PAP33.

Jost, H., F. Chemale Jr., R. Fuck, and I. Dussin, 2013, Uvá complex, the oldest orthogneisses of the archean-paleoproterozoic terrane of central Brazil: Journal of South American Earth Sciences, **47**, 201–212, doi: 10.1016/j.jsames.2013.07.002.

Kenkmann, T., M. Vasconcelos, A. Crósta, and W. Reimold, 2011, The complex impact structure serra da cangalha, Tocantins state, brazil: Meteoritics & Planetary Science, **46**, 875–889, doi: 10.1111/j.1945-5100.2011.01199.x.

Langmuir, D., 1978, Uranium solution-mineral equilibria at low temperatures with applications to sedimentary ore deposits: Geochimica et Cosmochimica Acta, **42**, 547–569, doi: 10.1016/0016-7037(78)90001-7.

Leite, E., J. Lambert, M. Vasconcelos, A. Crósta, and A. Batezelli, 2022, Gamma-ray spectrometry of the araguainha impact structure, Brazil: Additional insights into element mobilization due to hydrothermal alteration: Anais da Academia Brasileira de Ciências, **94**, 1–16, doi: 10.1590/0001-3765202220210182.

Li, X., 2006, Understanding 3d analytical sig- nal amplitude: Geophysics, **71**, L13–L16, doi: 10.1190/1.2184367.

Li, Y., and M. Nabighian, 2015, Tools and techniques: Magnetic methods of exploration – principles and algorithms, *in* Treatise on Geophysics, 2nd ed.: Elsevier, 335–391. doi: 10.1016/B978-0-444-53802-4.00196-2.

Mantovani, M., and B. Brito Neves, 2009, The paranapanema lithospheric block: its nature and role in the accretion of gondwana, *in* Neoproterozoic Cambrian Tectonics, Global Change and Evolution: a focus on southwestern Gondwana: Elsevier, volume **16** *of* Developments in Precam- brian Geology, 257–272. doi: 10.1016/S0166-2635(09)01619-3.

Marini, O., and N. Botelho, 1986, Província de granitos estaníferos de goiás: Revista da Sociedade Brasileira de Geociências, **16**, 119–131. (Access: 05 May 2023).

Marini, O., R. Fuck, J. Danni, M. Dardenne, S. Loghercio, and R. Ramalho, 1984, As faixas de dobramentos brasília, uruaçu e paraguai-araguaia e o maciço mediano de goiás, *in* Geologia do Brasil: DNPM, 251–303.

Martins-Ferreira, M., J. Campos, M. Von Huelsen, and B. Neri, 2018a, Paleorift structure constrained by gravity and stratigraphic data: The statherian araí rift case: Tectonophysics, **738–739**, 64–82, doi:10.1016/j.tecto.2018.05.014

Martins-Ferreira, M., F. Chemale, A. Dias, and J. Campos, 2018b, Proterozoic intracontinental basin succession in the western margin of the são francisco craton: Constraints from detrital zircon geochronology: Journal of South American Earth Sciences, **81**, 165–176, doi: 10.1016/j.jsames.2017.11.018.

Martins-Ferreira, M., A. Dias, F. Chemale, J. Campos, M. Seraine, and E. Rodrigues, 2020, Multi–stage crustal accretion by magmatic flare-up and quiescence intervals in the western margin of the são francisco craton: U–pb–hf and geochemical constraints from the almas terrane: Gondwana Research, **85**, 32–54, doi: 10.1016/j.gr.2020.04.005.

Martins-Neto, M., 2009, Sequence stratigraphic framework of proterozoic successions in eastern brazil: Marine and Petroleum Geology, **26**, 163–176, doi: 10.1016/j.marpetgeo.2007.10.001.

Martins-Neto, M., A. Pedrosa-Soares, and S. Lima, 2001, Tectono-sedimentary evolution of sedimentary basins from late paleoproterozoic to late neoproterozoic in the são francisco craton and araçuai fold belt, eastern brazil: Sedimentary Geology, **141-142**, 343–370, doi: 10.1016/S0037-0738(01)00082-3.

Maziviero, M., M. Vasconcelos, A. Crósta, A. Góes, W. Reimold, and C. Carneiro, 2013, Geology and impact features of riachão structure, northern Brazil: Meteoritics & Planetary Science, **48**, 2044–2058, doi: 10.1111/maps.12213.

Megumi, K., and T. Mamuro, 1977, Concentration of uranium series nuclides in soil particles in relation to their size: Journal of Geophysical Research, **10**, 353–356, doi: 10.1029/JB082i002p00353.

Mello, D., J. Demattê, F. Oliveira Mello, R. Poppiel, N. Silveiro, J. Safanelli, A. Barros e Sousa, L. Di Raimo, R. Rizzo, M. Resende, et al., 2021, Ap- plied gamma-ray spectrometry for evaluating tropical soil processes and attributes: Geoderma, **381**, 114736, doi: 10.1016/j.geoderma.2020.114736.

Milligan, P., and P. Gunn, 1997, Enhancement and presentation of airborne geophysical data: AGSO Journal of Australian Geology and Geophysics, **17**, 63–75.

Minty, B., 2011, Short note: on the use of radioelement ratios to enhance gamma-ray spectrometric data: Exploration Geophysics, **42**, 116–120, doi: 10.1071/EG10011.

Mocitaiba, L., D. Castro, and D. Oliveira, 2017, Cartografia geofísica regional do magmatismo mesocenozóico na Bacia do Parnaíba: Geologia USP - Série Científica, **17**, 169–192, doi: 10.11606/issn.2316-9095.v17-455.

Moura, C., and H. Gaudette, 1999, Zircon ages of basement orthogneisses from the northern segment of the Araguaia Belt, Brazil, *in* Basement Tectonics 13: Springer, 155–178. doi: 10.1007/978-94-011-4800-9_10.

Nabighian, M., 1972, The analytical signal of two-dimensional magnetic bodies with polygonal cross-section: its properties and use for automated anomaly interpretation: Geophysics, **37**, 507–517, doi: 10.1190/1.1440276.

Niang, C., D. Baratoux, D. Diallo, P. Rochette, M. Jessell, W. Reimold, S. Bouley, O. Vanderhaeghe, G. Faye, and P. Lambert, 2021, Systematic survey of k, th, and u signatures in airborne radiometric data from australian meteorite impact structures: Possible causes of circular features and implications, *in* Large Meteorite Impacts and Planetary Evolution VI: volume **550** *of* Geological Society of America, Special Paper, 373–405. doi: 10.1130/2021.2550(15).

Niang, C., D. Baratoux, P. Rochette, R. Braucher, W. Reimold, P. Lambert, D. Diallo, V. Regard, S. Carretier, M. Jessell, et al., 2022, The origin of the potassium-rich annular zones at the bosumtwi impact structure, ghana, investigated by field study, radiometric analysis, and first cosmogenic nuclide data: Meteoritics & Planetary Science, **57**, 702–729, doi: 10.1111/maps.13788.

O'Leary, D., C. Brown, and E. Daly, 2022, Digital soil mapping of peatland using airborne radiometric data and supervised machine learning - implication for assessment of carbon stock: Geoderma, **428**,116086, doi: 10.1016/j.geoderma.2022.116086.

Oliveira, A., M. Pimentel, R. Fuck, and D. Oliveira,2018, Petrology of jurassic and cretaceous basaltic formations from the parnaíba basin, ne brazil: correlations and associations with large igneous provinces, *in* Cratonic basin formation: a case study of the Parnaíba Basin of Brazil: volume **472** *of* Geological Society, London, Special Publication, 279–308. doi: 10.6084/m9.figshare.c.3985437.

Oliveira, I., 2000, Zinco, chumbo e cobre de palmeirópolis – estado do tocantins, volume **10** *of* Informe de Recursos Minerais: CPRM.

Oliveira, R., and M. Rodrigues, 2019, Atlas Aerogeofísico do Estado de Pernambuco: Serviço Geológico do Brasil – CPRM. (Available at: https://rigeo.cprm.gov.br/handle/doc/21419. Access on 05 May 2023).

Oliveira, V., 2022, Atlas Aerogeofísico do Estado de Roraima: Serviço Geológico do Brasil – CPRM. (Available at: https://rigeo.sgb.gov.br/handle/doc/22788. Access on 05 May 2023).

Paixão, M., A. Nilson, and E. Dantas, 2008, The neoproterozoic quatipuru ophiolite and the araguaia fold belt, central-northern brazil, compared with correlatives in nw africa, *in* West Gondwana: Pre-Cenozoic Correlations Across the South Atlantic Region: The Geological Society Publishing House, volume **294** *of* Geological Society, Special Publication, 297–318. doi: 10.1144/SP294.16.

Pickup, G., and A. Marks, 2000, Identifying large-scale erosion and deposition process from airborne gamma radiometrics and digital elevation models in a weathered landscape: Earth Surface Processes and Landforms, **25**, 535–557, doi: 10.1002/(SICI)1096-9837(200005)25:5<535::AID-ESP91>3.0.CO;2-N.

Pilkington, M., and R. Grieve, 1992, The geophysical signature of terrestrial impact craters: Reviews of Geophysics, **30**, 161–181.

Pimentel, M., and R. Fuck, 1992, Neoproterozoic crustal accretion in central brazil: Geology, **20**, 375–379, doi: 10.1130/0091-7613(1992)020<0375:NCAICB>2.3.CO;2.

Pimentel, M., R. Fuck, and S. Gioia, 2000, The neoproterozoic goiás magmatic arc, central brazil: a review and new sm-nd data: Revista Brasileira de Geociências, **30**, 35–39. (Available at: https://ppegeo.igc.usp.br/index.php/rbg/article/view/10866. Access on 05 May 2023).

Pinto, L., 2022, Levantamentos aerogeofísicos no serviço geológico do brasil - histórico, produtos e futuro: Presented at the IX Simpósio Brasileiro de Geofísica, SBGf. (Available at: https://sbgf.org.br/mysbgf/resumos_expandidos.php?page=20Aplicada%20%C3%A0%20Cartografia%20Geol% C3%B3gica&sort=sessionarticle. Access on 16 Nov 2023).

Ramos, V., G. Vujovich, R. Martino, and J. Otamendi, 2010, Pampia: a large cratonic block missing in the rodinia supercontinent: Journal of Geodynamics, **50**, 243–255, doi: 10.1016/j.jog.2010.01.019.

Rawlins, B., and R. Webster, 2007, Understandingairborne radiometric survey signals across part ofeastern England: Earth Surface Processes and Landforms, **32**, 1503–1515, doi: 10.1002/esp.1468. Reeves, C., 2005, Aeromagnetic surveys: Principles, practice & interpretation: Geosoft.

Reid, A., 2012, Forgotten truths, myths and sacred cows of potential fields geophysics – ii: SEG Technical Program Expanded Abstracts, 1–3. doi: 10.1190/segam2012-0178.1.

Reimold, W., G. Cooper, R. Romano, D. Cowan, and C. Koeberl, 2006, Investigation of shuttle radar topography mission data of the possible impact structure at erra da Cangalha, Brazil: Meteoritics & Planetary Science, **41**, 237–246, doi: 10.1111/j.1945-5100.2006.tb00207.x.

Reinhardt, N., and L. Hermann, 2018, Gamma-ray spectrometry as a versatile tool in soil science: A critical review: Journal of Plant Nutrition and Soil Science, **182**, 1–19, doi: 10.1002/jpln.201700447.

Ribeiro, P., and C. Alves, 2017, Geologia e recursos minerais da região de Palmas – Folhas Miracema do Norte SC.22–X–D, Porto Nacional SC.22–Z–B e Santa Teresinha SC.22–Z–A: Technical report, CPRM, Goiânia, Brazil. (Available at: https://rigeo.cprm.gov.br/handle/doc/18076. Access on 05 May 2023).

Ribeiro, P., A. Frasca, J. Carneiro, K. Hattingh, E. Rezende, and F. Martins, 2022, Mapa geológico e de recursos minerais do Estado do Tocantins, Scale 1:500.000: Technical report, CPRM, Goiânia, Brazil. (Available at: https://rigeo.sgb.gov.br/handle/doc/22530. Access on 26 Oct 2023).

Roest, W., J. Verhoef, and M. Pilkington, 1992, Magnetic interpretation using the 3–d analytic signal: Geophysics, **57**, 116–125, doi: 10.1190/1.1443174.

Sabóia, A., and P. Meneghini, 2019, Geologia e recursos minerais da Folha Dianópolis – sc.23–y–c, Scale 1:250.000: Technical report, CPRM, Goiânia, Brazil. (Available at: https://rigeo.cprm.gov.br/handle/doc/17734. Access on 05 May 2023).

Santos, J., 2003, Geotectônica dos Escudos das Guianas e Brasil-Central, *in* Geologia, Tectônica e Recursos Minerais do Brasil: CPRM, 169–226.

Schobbenhaus, C., C. Ribeiro, L. Oliva, J. Takanohashi, A. Lindenmayer, J. Vasconcelos, and V. Orlandi, 1975, Folha Goiás (SC-22) Carta Geológica do Brasil ao Milionésimo.: Technical report, DNPM, Brasília, Brazil.

Sgarbi, G., P. Sgarbi, J. Campos, M. Dardenne, and U. Penha, 2001, Bacia Sanfranciscana: O Registro Fanerozóico da Bacia do São Francisco, *in* Bacia do São Francisco: Geologia e Recursos Naturais: SBG-MG, 93–138.

Silva, A., and F. Alves, 2021, Atlas aerogeofísico do Estado do Tocantins: Technical report, Serviço Geológico do Brasil – CPRM, Goiânia, Goiás, Brazil. (Available at: https://rigeo.cprm.gov.br/handle/doc/22566. Access on 05 May 2023).

Silva, A., and F. Alves, 2022, Understanding the Origin of the Airborne Geophysical Signatures of the Jalapão Geomorphological Units, Urucuia Basin, Central–Northern Brazil: Journal of the Geological Survey of Brazil, **5**, 205–220, doi: 10.29396/jgsb.2022.v5.n3.4.

Soares, J., R. Stephenson, R. Fuck, M. Lima, V. Araújo, F. Lima, F. Rocha, and C. Trindade, 2018, Structure of the crust and upper mantle beneath the parnaíba basin, brazil, from wide-angle reflection data, *in* Cratonic Basin Formation: A case study of the Parnaíba Basin of Brazil: Geological Society, London, Special Publication, **472**. doi: 10.1144/SP472.9.

Sousa, F., 2021, Atlas aerogeofísico do estado do ceará: Technical report, Serviço Geológico do Brasil – CPRM, Fortaleza, Ceará, Brazil. (Available at: https://rigeo.sgb.gov.br/handle/doc/22449. Access on 07 Nov 2023).

Sousa, P., R. Borges, and R. Dias, 2012, Atlas do tocantins: subsídios ao planejamento da gestão territorial: Technical report, SEPLAN, Palmas, TO, Brazil.

Spadoni, M., and M. Voltaggio, 2013, Contribution of gamma ground spectrometry to the textural characterization and mapping of floodplain sediments: Journal of Geochemical Exploration, **125**, 20–33, doi: 10.1016/j.gexplo.2012.10.016.

Taylor, M., K. Smettem, G. Pracillo, and W. Verboom, 2002, Relationships between soil properties and high resolution radiometrics, central eastern wheatbelt, western Australia: Exploration Geophysics, **33**, 95–102, doi: 10.1071/EG02095.

Vasconcelos, M., A. Crósta, W. Reimold, A. Góes, T. Kenkmann, and M. Poelchau, 2013, The Serra da Cangalha impact structure, Brazil: Geological, stratigraphic and petrographic aspects of a recently confirmed impact structure: Journal of South American Earth Sciences, **45**, 316–330, doi: 10.1016/j.jsames.2013.03.007.

Vasconcelos, M., E. Leite, and A. Crósta, 2012, Contributions of gamma-ray spectrometry to terrestrial impact crater studies: The example of Serra da Cangalha, northeastern Brazil: Geophysical Research Letters, **39**, L04306, doi: 10.1029/2011GL050525.

Vaz, P., N. Rezende, J. Wanderley Filho, and W. Travassos, 2007, Bacia do Parnaíba: Boletim de Geociências da Petrobras, **15**, 253–263.

Wilford, J., and B. Minty, 2007, The use of airborne gamma-ray imagery for mapping soils and understanding landscape processes, *in* Developments in Soil Science: **31**, 16, 207–218. doi: 10.1016/S0166-2481(06)31016-1.

Table 1: Main characteristics of aerogeophysical projects. The direction of flight and tie lines were N–S and E–W, respectively. Magnetic data were recorded at 0.1 s by using a cesium vapor sensor magnetometer and gamma- ray spectrometric data were recorded using a gamma-spectrometer with sodium iodide (NaI) crystal detectors every 1 s. The following corrections were made: magnetic compensation, parallax, removal of diurnal variation, removal of International Geomagnetic Reference Field (IGRF), leveling and micro-leveling for magnetic data dead time, background removal (aircraft, cosmic and radon), height, Compton Effect and conversion to elemental.

Aerogeophysics Project	**Spacing lines**		**Year**	**Final Report**	**Citation (see the reference list)**
	Flight (m)	**Tie (km)**			
Bacia do Parnaíba	500	4	2006	Marques et al.(2006)	
Tocantins	500	10	2006	CPRM (2006)	
Complemento do Tocantins	500	10	2007	CPRM (2007)	
Conceição do Araguaia	500	10	2012	CPRM (2012)	
Rio Formoso	500	10	2014	CPRM (2014)	
Rio Maria	500	10	2015	CPRM (2015)	

Silva, A.B.: study design/conceptualization, investigation/data acquisition, data interpreta- tion/validation, writing, review/editing; **Silva, M.F.**: writing, review/editing, supervision/project administration; **Reimold, W.U.**: writing, re- view/editing; **Alves, F.M.**: investigation/data acquisition, data interpretation/validation; **Lago, A.L.**: review/editing, supervision/project adminis- tration; **Couto Junior, M.A.**: review/editing, supervision/project administration; **Frasca, A.A.S.**: review/editing, supervision/project ad- ministration; **Ribeiro, P.S.E.**: review/editing, supervision/project administration.

Received on November 20, 2023 / Accepted on July 16, 2024

CHAPTER 12
CONFERENCE ABSTRACTS

12. CONFERENCE ABSTRACTS

The first conference abstract was presented to the 10th Brazilian Symposium on Geophysics, held Octuber 8 – 10, 2024 in Salvador, Bahia, Brazil. The second abstract is accepted to be presented at the Latin American GRSS and ISPRS Remote Sensing Conference (LAGIRS), which will be held on November 10 – 13, 2025, in Foz do Iguaçu, Paraná, Brazil. The full citable references are shown below and the final version of both abstracts can be found in the next pages. Note that the LAGIRS abstract´s final version corresponds to a camera-ready version where reviewers' suggestions have already been incorporated. This camera-ready version will be published in the ISPRS Annals of the Photogrammetry, Remote Sensing and Spatial Information Sciences after presentation.

First abstract:

Silva, A.B., Reimold, W.U. (2024). Airborne magnetic and radiometric signatures of circular structures in Brazil: Insights for mapping of potential targets for impact research. Abstract of the 10th Brazilian Symposium on Geophysics, Retrieved from: https://home.sbgf.org.br/Pages/resumo.php?tipo=simposio&ver=xsimposio#inicio (accessed September 18, 2025).

Second abstract:

Silva, A.B., Reimold, W.U. (2025). Characterization of Brazilian impact structures based on interpretations of Sentinel-1 C-band dual-polarization (VV and VH) data, Abstract accepted to Latin American GRSS and ISPRS Remote Sensing Conference (LAGIRS)

12.1 Airborne magnetic and radiometric signatures of circular structures in Brazil: Insights for mapping of potential targets for impact research.

Adolfo Barbosa da Silva [1,2], Wolf Uwe Reimold[1].

[1]Geological Survey of Brazil.

[2]Postgraduate Program in Geology, Institute of Geosciences of University of Brasilia

12.1.1 Resumo

The geological record of impact cratering on Earth is based on mapping and studying terrestrial impact structures. Such studies have contributed to better understanding of planetary issues, such as formation of the Moon, delivery of metals to Earth, and assessment of future impacts on Earth. To date 210 impact structures are confirmed on Earth, but only eight impact structures have been confirmed so far in Brazil, and another (São Miguel do Tapuio) is essentially confirmed as well. The relatively low number of impact structures known in the Brazilian territory is due to several factors, including only few dedicated studies for impact structures, lack of detailed geological mapping, and older structures having been eroded or they are covered with thick sequences of sedimentary strata. To overcome these challenges, airborne geophysical surveys (mainly magnetics and radiometrics) can be used to map circular landforms potentially formed by impact cratering. This must be, however, followed up by ground truthing. Quite a few studies have reported complete or partially circular magnetic/radiometric signatures in impact structures. Here, we investigate the airborne magnetic and radiometric signatures of five circular structures in Brazil (Bom Jardim – BJD, Sucunduri Dome – SDC, Inajah – INJ, Brejões – BRJ, Itiquira – ITA, and Cardoso – CDS) to verify if they could be good targets for impact. These structures are located in cryistalline (BJD, SDC, INJ, and BRJ) or sedimentary terrain (ITA and CDS), and high-resolution airborne geophysical (magnetic and radiometric) data are available for all of them. We have processed these data and produced several thematic maps (e.g., Anomalous Magnetic Field - AMF and its amplitude gradients; K, eTh, and eU concentration maps, and RGB compositions). We have interpreted these maps considering previous geological information and comparing them with other geophysical signatures of impact structures worldwide. The results show that ITA and CDS have well-defined circular magnetic signatures that disrupt the regional patterns, but their other characteristics resemble mafic or alkaline intrusions. The BRJ structure also shows well-defined circular magnetic and radiometric signatures, but the available geological map suggests that oldest lithostratigraphic units occur in the rim of BRJ, whereas they commonly outcrop in the central parts of complex impact structures. The SDC structure shows an impressive concentric radiometric pattern with an outermost ring reaching a 90 km diameter. Despite that, new geological information obtained by the Geological Survey of Brazil's geological team suggests that these rings have subtle dips, and further analysis is required. Finally, the BJD and INJ structures have well-defined radiometric and magnetic signatures disrupting the regional background fields. Although these structures have been interpreted as magmatic intrusions, the morphology and geophysical signatures make them suitable targets for impact research. However, detailed information about geology and deformation is not available for these structures. Overall, we conclude that airborne geophysical data can be a useful tool in mapping potential targets for impact structures and may provide support for subsequent field research.

12.2 Characterization of Brazilian impact structures based on interpretations of Sentinel-1 C-band dual-polarization (VV and VH) data

Silva, A.B[1, 2], Reimold, W.U.[2]

[1] Geological Survey of Brazil (SGB-CPRM), Goiânia Superintendence, Goiânia, GO, 74170-110, Brazil, [2] University of Brasilia, Institute of Geosciences, Postgraduate Program in Geology, Campus Universitário Darcy Ribeiro, Brasilia, DF 70910-900, Brazil

Keywords: Structural geology, Synthetic Aperture Radar (SAR), Impact cratering research.

12.2.1 Abstract

The known Brazilian impact structures are characterized using C-band Synthetic Aperture Radar (SAR) images from the Sentinel-1 satellites. After acquiring the dual-polarization (VV and VH) Ground Range Detected Dataset from a public repository, we applied standard processing techniques, including calibration, speckle noise reduction, terrain correction, and conversion of backscattering values to linear dB format. RGB visualizations of the polarimetric components were then generated. Our findings indicate that most backscattering in Brazilian impact structures is seemingly influenced by soil properties or vegetation cover. However, first-order structural elements (outer rim, annular basin, or central uplift) of Brazilian impact structures could be completely, or partially, identified in SAR images, including the northern part of the outer rim of Araguainha, the outer rim of Vargeão Dome and Santa Marta, the rim and inner rings on São Miguel do Tapuio, central uplifts in Serra da Cangalha and Riachão Ring, and the annular basin in Riachão Ring. Additionally, certain features, such as silicified sandstones in the central portions of Cerro do Jarau and Serra da Cangalha, as well as structural lineaments in the Santa Marta and Vargeão Dome structures, contribute to backscattering patterns as well. Overall, our results suggest that SAR imagery can be a valuable tool for structural mapping of impact structures. As L-band radar systems (e.g., ALOS PALSAR, JERS-1) have longer wavelength and greater ability to penetrate vegetation, we recommend that the joint use of C- and L-band data could improve geological mapping of impact structures.

12.2.2 Introduction

Terrestrial impact structures form when celestial bodies collide with Earth's surface at hypervelocity, releasing immense energy and causing localized deformation (e.g., French, 1998; Osinski et al., 2022). All confirmed Brazilian impact structures are classified as complex structures, which typically feature an elevated central area (central uplift or the larger ones possibly a peak ring) surrounded by a ring syncline and an outer rim sector (e.g., Kenkmann, 2002, 2014). Secondary structural elements, such as thrust-faulting, folding, and monoclines, may also be present depending on the stratigraphy and properties of the target rock, impact scale, impact angle, and erosion level (Kenkmann et al., 2014).

Spatial imagery, particularly the Synthetic Aperture Radar (SAR), can be a useful tool in structural mapping due to its sensitivity to terrain roughness (e.g., Smith et al., 1999; McHone et al., 2002; Theilen-Willige, 2021). In the context of terrestrial impact structures, previous work has demonstrated that SAR (or derived products such as a Digital Elevation Model - DEM) images have been useful to identify first (e.g., crater-rim faults or crater-rim monocline, ring syncline, and central uplift) or second order (e.g., listric normal faults, folds and thrusts, etc) structural elements in complex impact structures, for example at Araguainha (Theilen - Willige, 1987) and Serra da Cangalha (Reimold et al., 2006), BP and Oasis (McHone et al., 2002; Koeberl et al., 2005; van Gasselt et al., 2017), Spider (McHone et al., 2002), Bosumtwi (Theilen - Willige, 2021), and Manicouagan (Smith et al., 1999). In addition, in hot desert regions, such as the Sahara Desert of Africa, depending on water content in the sands, the electromagnetic wave emitted by SAR instruments can penetrate into the ground and aid to estimate crater diameter or define associated features, like ejecta deposits or impact-induced fracture zones (e.g., Aorounga, BP, and Roter Kamm impact structures - McHone et al., 1996, 2002). On the other hand, flat-surface trench zones (e.g., Spider impact structure) or fine-grained sediments of a post-impact crater fill (e.g., Connolly Basin crater) may decrease the backscattering on SAR images (McHone et al., 2002). Notably, by analysing the strength of backscattering on each polarimetric component, van Gasselt et al. (2017) attempted to distinguish bed rock from unconsolidated cover strata in the Oasis impact structure.

Despite the usefulness of SAR images in impact structure mapping outlined above, few studies (e.g. Crósta et al., 2012) with SAR data have focused on Brazilian impact structures so far, and Sentinel-1 dual polarimetric images have remained essentially unexplored. To close this gap, we characterize these structures using polarimetric images based on band C Sentinel-1 data, to identify structural elements and/or additional features that can improve our understanding of backscattering behaviour at Brazilian impact structures. The following sections provide an overview of the Brazilian impact structures and a description of our methodology. The main findings are then discussed in the context of existing knowledge.

12.2.3 Geological settings of Brazilian impact structures

Eight impact structures have been confirmed in Brazil based on the identification of bona fide shock deformation features (Fig. 1) (Crósta et al., 2019a; Reimold et al., 2022). In addition, São Miguel do Tapuio, although not officially recognized yet, has provided preliminary evidence strongly suggesting an impact

origin (Crósta et al., 2019b), so that we also consider this structure to be of impact origin.

All of the confirmed Brazilian impact structures are located in two Paleozoic intracratonic sedimentary basins, namely the Paraná and Parnaíba basins (Fig. 1). The sedimentary records of these basins have been studied in terms of sedimentary sequences (or supersequences) (Milani and Zalán, 1999). These sequences were formed by major tectono-sedimentary cycles—such as the Late Paleozoic Gondwana glaciation and the opening of the equatorial and southern Atlantic Ocean—and are separated by interregional unconformities (ibid). In summary, the stratigraphic columns of both basins predominantly comprise siliciclastic and carbonate rocks (sandstones, shales, mudstones, carbonates, etc.) deposited during Paleozoic transgressive-regressive cycles, as well as Mesozoic continental deposits with associated igneous rocks.

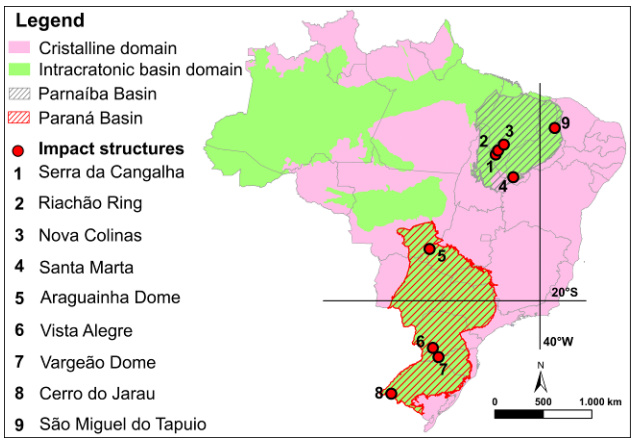

Figure 1. Locations of confirmed Brazilian impact structures 1-8) and São Miguel do Tapuio (9).

12.2.4 Materials and Methodology

The Sentinel-1 mission consists of two satellites, Sentinel-1A and 1B (since 2024, Sentinel-1B was replaced by Sentinel-1C), operating in a sun-synchronous orbit at an altitude of 693 km, phased 180° apart (ESA, 2025). Each satellite is equipped with a C-band instrument that operates at a frequency of 5.405 GHz (wavelength of 5.55 cm) in dual-polarization mode (ESA, 2025). In this study, Sentinel-1 SAR images with VV and VH polarizations were utilized, mainly due to their ready accessibility.

Sentinel-1 images capture backscattering of radiation reflected by the Earth's surface (ESA, 2025). Our images were acquired during the dry season in Interferometric Wide Swath mode and were pre-processed by ESA's Copernicus Space Component Ground Segment before having been made publicly available through the Copernicus Data Space Ecosystem. The datasets correspond to Level-1 Ground Range Detected (GRD) images, which undergo multi-look processing and are projected to ground level, resulting in a final spatial resolution of 12.5 m (ibid). Here, we used Sentinel Application Platform (SNAP) (version 11.0.0) freely available by the European Space Agency (ESA) to carry out the processing described below.

The further processing of Sentinel-1 SAR Level-1 GRD images involved: i) converting pixel values to radar backscattering through radiometric calibration; ii) reducing speckle noise (random interference caused by surface scatter) using a Refined Lee filter (Yommy et al., 2015); iii) correcting geometric distortions through terrain correction; iv) converting the radar backscattering coefficient to linear dB format to enhance visualization and analysis. Following the initial processing, additional bands were derived from the original VV and VH bands:

- Ratio Pol – calculated by dividing VV by VH components.
- Multi Pol – computed as the absolute product of VV and VH components.
- Diff Pol – determined using the absolute difference between VV and VH components.

These original and derived bands were integrated into RGB composite colour visualizations, which were then arranged into maps for further analysis.

12.2.5 Results

The RGB visualizations of impact structures in the Paraná and Parnaíba Basin are displayed in Figures 2-4. Two backscattering patterns seem to be dominant in the most figures. The first pattern (P1) shows dark blue shades and a smoothed texture (see, e.g., feature 1 in Fig. 2). The second pattern (P2) can also be characterized by a smooth texture, but is coloured in light green or cyan shades (Fig. 2). We have noted that the second pattern coincides with vegetation cover, mainly vegetation along drainage channels (e.g., Fig. 2a, 2b, 2c, 2d, and 2c). Despite the dominance of these patterns, it has been possible to identify other backscatter signatures in the SAR images with geological meaning.

12.2.5.1 Backscattering in impact structures of the Paraná Basin

The circular patterns of the Araguainha (40 km diameter), Cerro do Jarau (~13 km diameter) and Vista Alegre (~9.5 km diameter) impact structures commonly seen in optical images (e.g., Crósta et al., 2019a) are less defined in Figures 2a, 2d, and 3a. Even so, some interesting features with geological meaning are noted. In the Araguainha impact structure, such features are represented by: i) a curved feature (feature 1 in the Fig. 2b) in the northern portion of the structure. This portion of Araguainha's rim was also seen in X-band radar images (Theilen-Willige, 1987); ii) several small hill features can be seen in orange colors (feature 2 in Fig. 2b) also in the northern portion of Araguainha; iii) lineaments with NE-SW directions running in the external domain to the north of Araguainha. These lineaments seem to be interrupted by the curved feature described above, but the exact cross-cutting relationships are unclear on Fig. 2b; iv) yellow color zones with rough texture can be seen near the innermost part of Araguainha´s central uplift (feature 4 in Figs. 2a and 2c), mainly in the northeastern sector; and, finally, dark brown features (feature 5 in the Fig. 2a and 2c) occur not only in the central uplift but also in its environs.

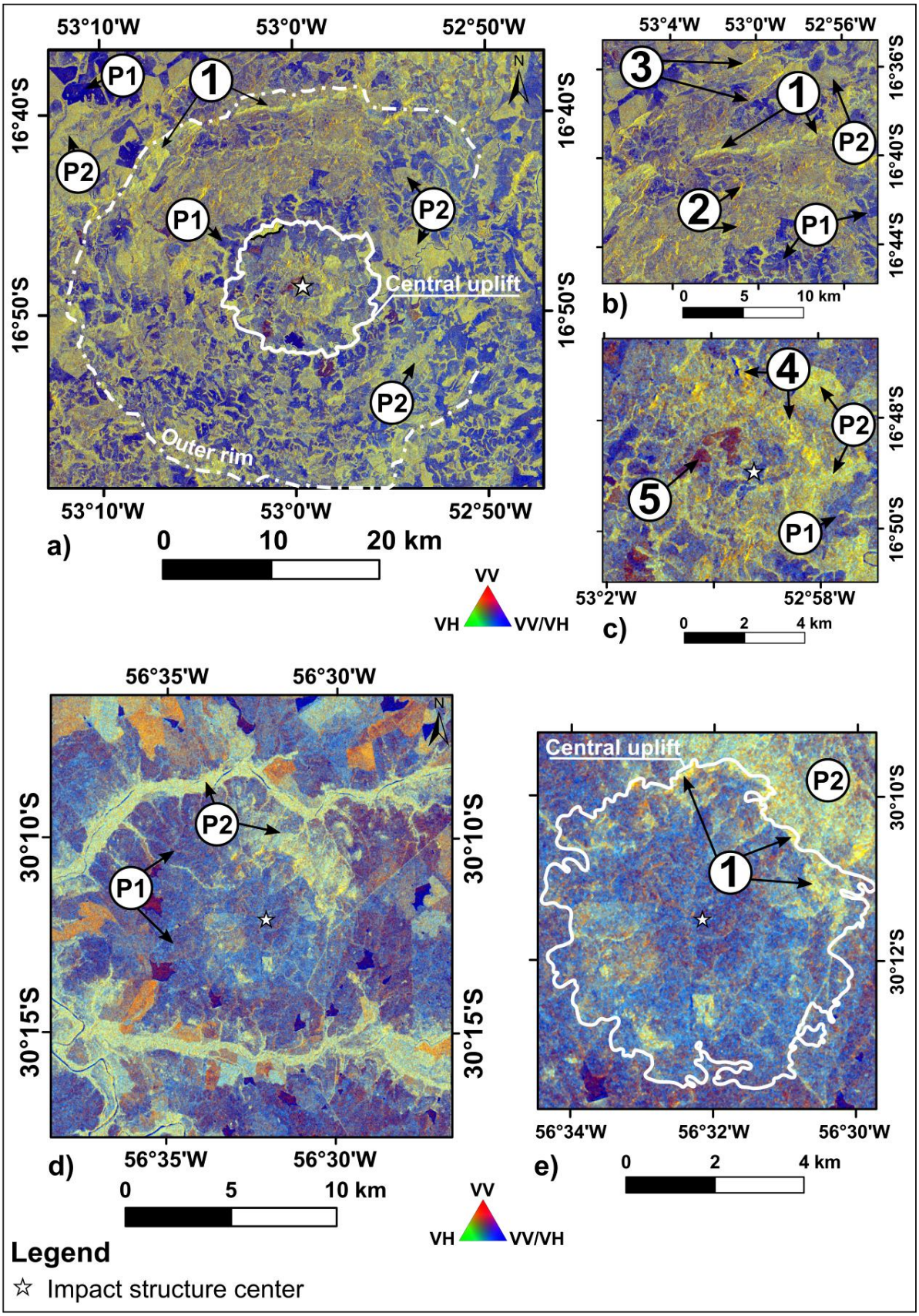

Figure 2. RGB composite colour visualizations of polarimetric components for impact structures in the Paraná Basin. a) Araguainha impact structure. b) Northern portion of Araguainha's rim. c) Araguainha's central uplift. d) Cerro do Jarau impact structure. e) Details of Cerro do Jarau's central uplift. All the numbered features are described in the text.

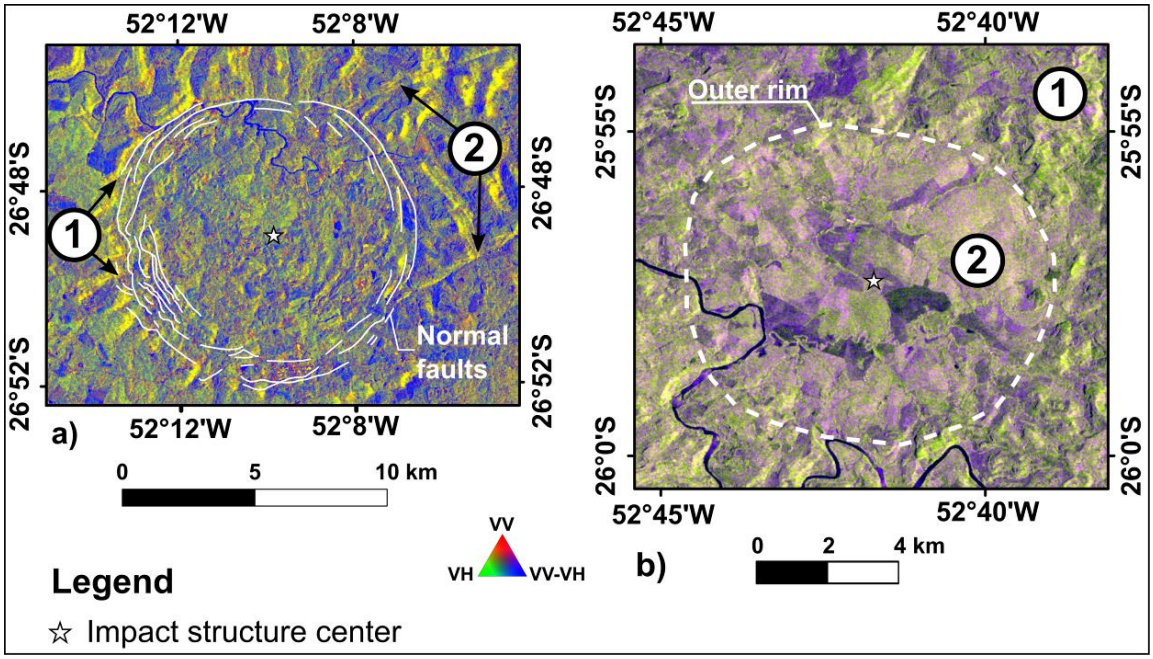

Figure 3. RGB composite colours of polarimetric components of two impact structures in the Paraná Basin. a) Vargeão Dome impact structure. b) Vista Alegre impact structure. The fractured basalt limit separates the interior of the structure from the exterior. All the numbered features are described in the text.

In the Cerro do Jarau impact structure (~13km diameter), light green shades with smooth textures (P2) dominate the northeastern sector of the structure (Fig. 2d and 2e). Another backscattering signature with yellowish shades (feature 1 in Fig. 2e) seemingly surrounds the outer portion of the Cerro do Jarau central uplift.

Unlike these first two impact structures, the circular pattern of the Vargeão Dome impact structure (~12.4 km diameter) is clearly seen in the Sentinel-1 C-band image (Fig. 3a). Structural features along the rim are well-defined, mainly in the western sector (feature 1 in Fig. 3a). In the eastern sector of Vargeão Dome, two NE-SW trending lineaments are evident (feature 2 in Fig. 3a).

The landform relief contrast between the inner and outer portions of the Vista Alegre impact structure (~9.5 km diameter) is represented as different textural patterns in Figure 3b. The textural pattern in the outer portion of the impact structure is rough (feature 1 in Fig. 3b), but inside the structure the pattern becomes smooth (feature 2 in Fig. 3b).

12.2.5.2 Backscattering in impact structures of the Parnaíba Basin

The RGB visualization of polarimetric components of impact structures in the Parnaíba Basin are shown in Figures 4a–e. Serra da Cangalha, Santa Marta, and São Miguel do Tapuio show well-defined circular patterns, whereas for Riachão Ring and Nova Colinas these patterns are subdued.

An area elevated in the inner part of the Serra da Cangalha structure (~13.4 km diameter) (Reimold et al., 2006; Kenkmann et al., 2011; Vasconcelos et al., 2013) appears as a zone of high backscatter showing a rough texture and yellow shades in Figure 4a (feature 1 in Fig. 4a). The western portion of the structure's rim is relatively well-defined (feature 2 in Fig. 4a), but the rim is not well visible in the eastern sector.

Although the circular pattern is subdued at Riachão Ring impact structure (~4 km diameter), it is possible to distinguish two zones within the structure: one area (feature 1 in the Fig. 4b) in the innermost part of the Riachão Ring impact structure characterized by high backscattering signatures, which is surrounded by another low backscatter area (feature 2 in the Fig. 4b). We have noted that this latter area coincides with the annular basin around the small central uplift area. Note that low backscattering signatures also occur outside of Riachão Ring, mainly in the western portion (feature 3 in the Fig. 4b).

Similar to Riachão Ring, a circular pattern is weakly defined at the Nova Colinas impact structure (~7 km diameter) (Fig. 4c). Strong yellow shades occur mainly in the southern portion of the structure (feature 1 in the Fig. 4c), but similar shades are also observed in the northern portion, outside of the impact structure (feature 2 in Fig. 4c). Dark blue zones are noted near the center of the structure (feature 3 in the Fig. 4c) but they are dominant outside of Nova Colinas, mainly to the south (feature 4 in the Fig. 4c).

In the Santa Marta impact structure (~10 km diameter), the outer rim is distinguishable in the eastern portion of SAR images (feature 1 in Fig. 4d). This rim is represented by concentric normal faults (Oliveira et al., 2014). Furthermore, brown shades appear in the northeastern sector, both inside and outside of the impact structure (feature 2 in Fig. 4d). However, this brown pattern seems to be discontinuous and heterogeneous inside of the structure (feature 3 in Fig. 4d). Dark blue shades (P1) are dominant in the northwestern part (feature 4 in Fig. 4d) of the Santa Marta impact structure.

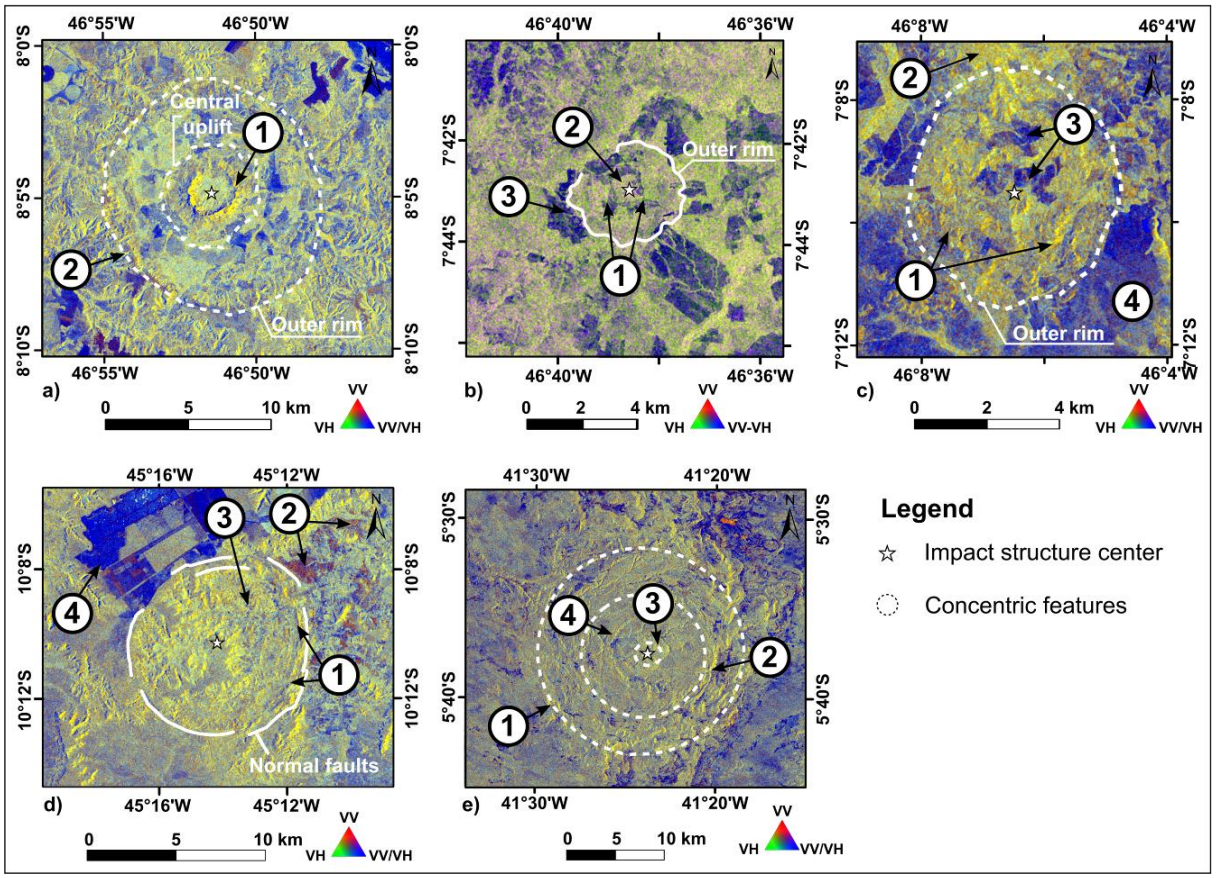

Figure 4: RGB composite colour diagrams of polarimetric components of impact structures in the Parnaíba Basin. a) Serra da Cangalha impact structure. Contour of central uplift and outer rim modified after Vasconcelos et al. (2013). b) Riachão Ring impact structure. Contour of central uplift and outer rim modified after Maziviero et al. (2013). c) Nova Colinas impact structure. Outer rim modified after Reimold et al. (2022). d) Santa Marta impact structure. Normal faults modified after Oliveira et al. (2014, 2017). e) São Miguel do Tapuio impact structure. The black arrows show parts of semi-circular features discussed in the text. Concentric features modified after Martins et al. (2016).

Concentric lineaments are also observed at São Miguel do Tapuio (~23 km diameter) (Fig. 4e). Although it is not clear what the nature of these concentric lineaments is, it is likely that concentric lineaments near the outer rim of the structure are normal faults (see, e.g., feature 1 in Fig. 4e) related to inward rim collapse in the modification stage of cratering.

Semi-circular features are also visible in SAR images inside of São Miguel do Tapuio. Three concentric features at São Miguel do Tapuio were originally proposed by Martins et al. (2016) from digital elevation model imagery, whereas our data seemingly indicate four concentric features. Like Martins et al,'s work, our outermost circular feature (feature 1 in Fig. 4e) seems to be part of the structure's rim. The second outermost ring (feature 2 in Fig. 4e) and the innermost ring (feature 3 in Fig. 4e) can be related to the intermediate and innermost rings suggested by Martins et al. (2016). However, our data suggest a third ring (feature 4 in Fig. 4e) between the intermediate and innermost rings. The nature of this third ring is unclear, but a possible explanation will be given in the next section.

12.2.6 Discussion

Analysis of SAR images of Brazilian impact structure has revealed that, despite their individual peculiarities (e.g., diameter size, locality, erosion level, etc), some commocharacteristics of Brazilian impact structures can be identified in SAR images. For instance: the dark blue shades (first backscattering pattern – P1) seen in the Araguainha, Cerro do Jarau, Serra da Cangalha, Riachão Ring, Nova Colinas, northwestern Santa Marta, and the eastern portions of São Miguel do Tapuio imagery suggest the entire electromagnetic signal returned to the SAR sensor is low but the vertically transmitted/received electromagnetic wave (VV component) is relatively higher than the cross-polarized component (i.e., vertically transmitted and horizontally received—VH). We hypothesize that these signatures are primarily associated with soil properties (e.g., irrigated soil), as VH components tend to exhibit lower intensity in such materials (Guha et al., 2013). The light green or cyan shade patterns (i.e., second backscattering pattern – P2) also occur in areas covered by vegetation (e.g., along the drainage path in the north of Cerro do Jarau impact structure), so that we assume that this backscattering comes from vegetation cover.

We have noted that the dominance of both soil properties and vegetation backscattering signatures hinders the identification of structural elements in Brazilian impact structure somewhat. For instance: Serra da Cangalha, Santa Marta, and São Miguel do

Tapuio display clear structural elements, such as faults and lineaments, whereas other structures, like Araguainha, are less distinct probably due to widespread interference from soil and vegetation. To overcome these shortcomings, further studies should consider geological feature detection in Brazilian impact structures by using L-band instrument data (e.g., ALOS PALSAR 1 and 2, JERS-1, etc.) because the longer wavelength of the L-band radar can penetrate vegetation. Thus, the intermediate to coarse texture variations of surface roughness associated with various geological features (e.g. faults, folds, topographic discontinuities, bedding structures, depressions, and lithological contacts) could be revealed (Pour and Hashim, 2014).

Despite the dominance of vegetation and/or soil property backscattering patterns, this study has also found backscattering signatures that might have geological meaning. For instance: the curved feature (our feature 1 in the Fig. 2b) in the northern portion of the Araguainha impact structure likely is related to Passa Dois Group pelitic rocks that form Araguainha's rim (see Souza et al., 2024). In Vargeão Dome, the structural features (our feature 1 in the Fig. 3a) along the western rim were already interpreted as normal (or listric) faults (Crósta et al., 2012). Similarly, the outer rims of Serra da Cangalha (our feature 2 in the Fig. 4a), Santa Marta (our feature 1 in the Fig. 4d), and São Miguel do Tapuio (our feature 1 in the Fig. 4e) are also well-defined in SAR images. In these cases, the backscattering probably reflects the morphology and structural deformation at the rim.

Beyond observations on outer rims, this work has found other backscattering signatures that could be related to first-order structural elements, such as annular basins or central uplifts. The first case is exemplified by orange colour hill features (our feature 2 in the Fig. 2b) seen in the northern portion of the Araguainha impact structure and low backscattering zones surrounding the center of the Riachão Ring structure (our feature 1 in the Fig. 4b). According to the most recent geological map of Araguainha (Souza et al., 2024), these small hill features likely correspond to prominent Aquidauana Formation sandstone outcrops. This formation is the dominant stratigraphic unit in the annular basin of the Araguainha structure. In Riachão Ring, the low backscattering zones surrounding the structure's center can be thought to arise from the flattish surfaces with fine-grained sediments from drainage channels that occur in the annular basin of the structure. Low backscattering zones related to flat surfaces with fine-grained sediments or crater fill deposits have also been observed in the annular basins of the Spider and Connolly Basin impact structures (McHone et al., 2002).

The second case is exemplified by a backscattering pattern (with yellow colors and rough texture) that was seen to the northeast of Araguainha´s central uplift (our feature 4 in the Fig. 2c), in the northeastern sector of the Cerro do Jarau central uplift (our feature 1 in the Fig. 2e), and in the inner part of the Serra da Cangalha central uplift (our feature 2 in the Fig. 4a). At Araguainha, this pattern coincides with the Serra da Arnica hills of highly deformed Devonian Furnas Formation sandstone (Souza et al., 2024), whereas silicified sandstones seem to be the source of this pattern at Cerro do Jarau and Serra da Cangalha (Vasconcelos et al., 2013, Sánchez, 2014). These findings demonstrate that the shade and texture patterns observed over silicified (or strongly deformed) sandstones on the Araguainha, Serra da Cangalha, and Cerro do Jarau central uplifts corroborate the idea that strong backscattering of cross-polarized components (here, VH components) may be useful for mapping consolidated materials and rocks exposed at surface (e.g., van Gasselt et al., 2017). Furthermore, because the backscattering patterns of silicified sandstones in the Cerro do Jarau central uplift appear more yellowish and texturally rougher than backscattering patterns from vegetation (i.e., the P2 signature), it can be suggested that both silicified sandstones and vegetation backscatter patterns can be distinguished by polarimetric decomposition analysis. It is also worth noting that the third ring between the intermediate and innermost rings in São Miguel do Tapuio could be related to the central uplift or a collapsed peak ring feature. Unfortunately, it has not been possible to find an explanation for the dark brown features seen in the Araguainha central uplift.

In addition to the backscattering signatures discussed above, the analysis of SAR images of Brazilian impact structure also revealed pre-impact features that may have been affected by the impact event. For instance: the lineaments with NE-SW direction in the northern portion of the Araguainha scene (our feature 3 in the Fig. 2b) likely are pre-impact features that may have constrained the morphology of the Araguainha structure (Bernardes et al., in press). Similarly, the NE-SW trending lineaments in the eastern sector of Vargeão Dome (our feature 2 in the Fig. 3a) have been associated with the regional Lacinha–Cubatão fault system, a pre-impact feature that was disrupted by the impact event in the Vargeão Dome area (Kazzuo-Vieira et al., 2009).

At the Riachão Ring impact structure, flat surfaces (our feature 3 in the Fig. 4b) can account also for low backscattering outside of the structure. Here, such surfaces seem to represent alluvial deposits related to drainage that has been controlled by the presence of the impact structure. At the Santa Marta structure, soil properties derived from Quiricó Formation rocks may be the sources of the brown shaded areas outside of the impact structure (our feature 2 in the Fig. 4d). As these same brown areas are discontinuous and heterogeneous inside of the Santa Marta structure (our feature 3 in the Fig. 4d), it is assumed that this discontinuous pattern may be related to original materials (that is, the brown shades of feature 2) that were fragmented, brecciated, and mixed during the impact event.

Finally, landform relief contrast between the inner and outer portions of the Vista Alegre impact structure arises from the impact event (Crósta et al., 2010), but we interpret that the backscattering behaviour over the interior of the Vista Alegre structure is primarily due to extensive agricultural use. In the Nova Colinas impact structure, the strong yellow shades occurring mainly in the southern portion of the structure (our feature 1 in the Fig. 4c) may be related to a linear to curvilinear hill land system (see Reimold et al., 2022) which, in turn, can be considered as rotated/faulted sandstone blocks formed due to the impact. However, similar shades are probably related to vegetation developed on Corda Formation sandstones that occur in the north, outside of the impact structure (our feature 2 in the Fig. 4c). Dark blue zones near the center of the structure are probably related to a low amplitude/declivity hill land system described by Reimold et al. (2022) (our feature 3 in Fig. 4c), whereas the low backscattering zones (dark blue) in the

southern portion outside the Nova Colinas impact structure may be caused by a sandstone and low declivity terrain (our feature 4 in Fig. 4c).

In summary, Brazilian impact structures can be characterized in SAR images as having a significant portion of backscatter associated with soil and/or vegetation properties. Even so, first-order structural elements can still be identified, and in some cases, the backscatter pattern of stratigraphic units affected by the impact can also be distinguished.

12.2.7 Conclusions

This study was designed to characterize the Brazilian impact structures by using polarimetric images based on band C Sentinel-1 data. From the interpretations carried out on RGB composite colour diagrams of VV and VH polarimetric components, this study was successful in identifying structural elements and additional features that improved our understanding of backscattering behaviour on Brazilian impact structures. Our findings allow us to draw the following conclusions:

- The backscattering patterns that come from soil properties, such as moisture in surface-near materials and texture, and from vegetation cover are dominant in the SAR scenes of all impact structures. Such patterns made the identifications of structural elements in Brazilian impact structure less straightforward in some cases.
- Some impact structures, such as Serra da Cangalha, Santa Marta, and São Miguel do Tapuio, display clear structural elements, such as faults and lineaments, whereas others, like Araguainha, are less distinct probably due to widespread interference from soil and vegetation. Such interferences can possibly be mitigated by using data from sensors with microwaves with better penetration capacity (L- or P-bands) and additional polarimetric components (e.g., HH and HV).
- At least one first order structural element (outer rim, annular basin, or central uplift) of Brazilian impact structures could be completely, or partially, identified in all SAR images, such that our findings demonstrate that C-band Sentinel-1 images can effectively identify structural elements in impact structures (e.g., part of outer rim of northern portion of Araguainha, outer rim of Vargeão Dome and Santa Marta structures, rim and inner rings on São Miguel do Tapuio, central uplifts in Serra da Cangalha and Riachão Ring, and annular basin in Riachão Ring).
- Vegetation and silicified sandstones exhibit similar shades, though silicified sandstones tend to appear more yellow. This suggests that these targets can be distinguished using polarimetric decomposition techniques.

12.2.8 Acknowledgements

This work is part of the first author's MSc project within the Postgraduate Program in Geology at the University of Brasília. The authors are grateful to the Institute of Geosciences of the University of Brasília, and its Programa de Pós-Graduação em Geologia, and the Geological Survey of Brazil for providing the necessary infrastructure for this research. We are also grateful to the European Space Agency for the free access to the Sentinel 1 images. We also extend our thanks to the reviewers whose comments and recommendations have improved this work. This study was financed in part by the Coordenação de Aperfeiçoamento de Pessoal de Nível Superior – Brasil (CAPES) – Finance Code 001.

12.2.9 References

Bernardes, R.B., Reimold, W.U., Gibson, R.L., Hauser, N., Pavanetto, P. New insights into the geology and formation of the Araguainha impact structure, Brazil, from morphological and structural analysis. *Geological Society of America Bulletin* (Accepted manuscript).

Crósta, A. P., Koeberl, C., Furuie, R. A., Kazzuo-Vieira, C. 2010: The first description and confirmation of the Vista Alegre impact structure in the Paraná flood basalts of southern Brazil. *Meteoritics & Planetary Science*, 45(2), 181–194. https://doi.org/10.1111/j.1945-5100.2010.01015.x

Crosta, A. P., Kazzuo-Vieira, C., Pitarello, L., Koeberl, C., Kenkmann, T., 2012: Geology and impact features of Vargeão Dome, southern Brazil. *Meteoritics & Planetary Science*, 47(1), 51-71.

Crósta, A. P., Reimold, W. U., Vasconcelos, M. A. R., Hauser, N., Oliveira, G. J. G., Maziviero, M. V., Góes, A. M., 2019a: Impact cratering: The South American record – Part 1. *Geochemistry*, 79(1), 1–61. https://doi.org/10.1016/j.chemer.2018.06.001

Crósta, A. P., Reimold, W. U., Vasconcelos, M. A. R., 2019b: Cerro do Jarau and São Miguel do Tapuio: two newly confirmed, large impact structures in Brazil. *50th Lunar and Planetary Science Conference*, Houston, abstract#3042 (LPI Contrib. No. 2132).

European Space Agency (ESA), 2025. Overview of Sentinel-1 Mission. SentiWiki Home Page. https://sentiwiki.copernicus.eu/web/s1-mission#Sentinel-1-Mission (16 June 2025)

French, B. M., 1998: Traces of Catastrophe: A Handbook of Shock-Metamorphic Effects in Terrestrial Meteorite Impact Structures. LPI Contribution No. 954, Lunar and Planetary Institute, Houston, p. 17–28.

Gottwald, M., Kenkmann, T., Reimold, W., Fritz, T., Breit, H.. 2021: The TanDEM-X Digital Elevation Model and Terrestrial Impact Structures. *IEEE Journal of Selected Topics in Applied Earth Observations and Remote Sensing*, 14, 4128–4138. https://doi.org/10.1109/jstars.2021.3069640

Guha, A., Ghosh, D., Majumdar, R., Kumar, K. V., 2013: Potential of polarimetric Radarsat-2 data in geological mapping – a case study in parts of Dharwar craton, India. *International Journal of Remote Sensing*, 34(6), 1893-1904.

Kazzuo-Vieira, C., Crósta, A. P., Gamboa, F., Tygel, M., 2009: Caracterização geofísica da estrutura de impacto do domo de Vargeão, Brasil. *Revista Brasileira de Geofísica*, 27(3), 375–388. https://doi.org/10.1590/s0102-261x2009000300006

Kenkmann, T., 2002: Folding within seconds. *Geology*, 30(3), 231.https://doi.org/10.1130/0091-7613(2002)030<0231:fws>2.0.co;2

Kenkmann, T., Vasconcelos, M. A. R., Crósta, A. P., Reimold, W. U., 2011: The complex impact structure Serra da Cangalha, Tocantins State, Brazil. *Meteoritics & Planetary Science*, 46(6), 875–889. https://doi.org/10.1111/j.1945-5100.2011.01199.x

Kenkmann, T., Poelchau, M. H., Wulf, G., 2014: Structural geology of impact craters. *Journal of Structural Geology*, 62, 156–182. https://doi.org/10.1016/j.jsg.2014.01.015

Koeberl, C., Reimold, W.U., Plescia, J., 2005. BP and Oasis impact structures, Libya: remote sensing and field studies. In: Koeberl, C., Henkel, H. (Eds.), *Impact Tectonics*, Impact Studies Series 8. Springer-Verlag, Berlin, Heidelberg, pp. 161–190. https://doi.org/10.1007/3-540-27548-7_6

Martins, J. A., Branco, M. C., De Castro, N. A., Peulvast, J.-P., Lima Junior, S. B., 2016: análise morfológica da estrutura circular de São Miguel do Tapuio, Piauí - Brasil. *Revista Brasileira de Geomorfologia*, 17(4). https://doi.org/10.20502/rbg.v17i4.703

McHone, J. F., Greeley, R., & Blumberg, D. (1996, March 18 - 22). SIR-C/X-SAR radar studies; impact and aeolian features, Borkou region northern Chad. *Abstract of the Lunar and Planetary Science* XXVII, https://ui.adsabs.harvard.edu/abs/1996LPI....27..849M/abstract (17 September 2025)

McHone J.F., Greeley R., Williams K.K., Blumberg D.G., Kuzmin R.O., 2002: Space shuttle observations of terrestrial impact structures using SIR-C and XSAR radars. *Meteoritics & Planetary Science*, 37, 407 - 420.

Maziviero, M. V., Vasconcelos, M. A., Crósta, A. P., Góes, A. M., Reimold, W. U., De C. Carneiro, C., 2013: Geology and impact features of Riachão structure, northern Brazil. *Meteoritics & Planetary Science*, 48(10), 2044-2058.

Milani, E. J., Zalán, P. V., 1999: An outline of the geology and petroleum systems of the Paleozoic interior basins of South America. *Episodes Journal of International Geoscience*, *22*(3), 199-205.

Oliveira, G. J. G., Vasconcelos, M. A. R., Crósta, A. P., Reimold, W. U., Góes, A. M., Kowitz, A., 2014: Shatter cones and planar deformation features confirm Santa Marta in Piauí State, Brazil, as an impact structure. *Meteoritics & Planetary Science*, 49(10), 1915–1928. https://doi.org/10.1111/maps.12368

Oliveira, G. J. G. D., Chamani, M. A. C., Góes, A. M., Crósta, A. P., Vasconcelos, M. A. R., Reimold, W. U., 2017: Geological investigation of the central portion of the Santa Marta impact structure, Piauí State, Brazil. *Brazilian Journal of Geology*, 47, 673-692.

Osinski, G. R., Grieve, R. A. F., Ferrière, L., Losiak, A., Pickersgill, A. E., Cavosie, A. J., Hibbard, S. M., Hill, P. J. A., Bermudez, J. J., Marion, C. L., Newman, J. D., Simpson, S. L., 2022: Impact Earth: A review of the terrestrial impact record. *Earth-Science Reviews*, 232, 104112. https://doi.org/10.1016/j.earscirev.2022.104112

Pour, A. B., Hashim, M., 2014: Structural geology mapping using PALSAR data in the Bau gold mining district, Sarawak, Malaysia. *Advances in Space Research*, 54(4), 644-654.

Reimold, W.U., Cooper, G.R.J., Romano, R., Cowan, D.R., and Koeberl C., 2006: Investigation of Shuttle Radar Topography Mission data of the possible impact structure at Serra da Cangalha, Brazil. *Meteoritics & Planetary Science*, 41(2): 237-246. DOI: https://doi.org/10.1111/j.1945-5100.2006.tb00207.x

Reimold, W. U., Ferrière, L., Crósta, Á. P., Vasconcelos, M. A. R., Gottwald, M., Da Silva Borges, M., De Almeida, T. I. R., Pereira, F. L., Goés, A. M., Hauser, N., Jessell, M., & Baratoux, D., 2022: Nova Colinas, Maranhão State: A newly confirmed, complex impact structure in Brazil. *Meteoritics & Planetary Science*, 57(8), 1519–1541. https://doi.org/10.1111/maps.13833

Sánchez, J. P. (2014). Mapeamento geológico - estrutural do astroblema de cerro do Jarau - RS Brasil. (Doctoral thesis, São Paulo State University, Institute of Geosciences and Exact Sciences). https://repositorio.unesp.br/entities/publication/7a488bef-416d-4c3f-9690-f2bb38b64723 (17 September 2025)

Smith, S. K., Grieve, R. A. F., Harris, J. R., & Singhroy, V., 1999: The Utilization of RADARSAT-1 Imagery for the Characterization of Terrestrial Impact Landforms. *Canadian Journal of Remote Sensing*, 25(3), 218–228. https://doi.org/10.1080/07038992.1999.10874721

Souza, C. D. S. M. D., Hauser, N., Reimold, W. U., Bernardes, R. B., Vieira, L. C., Guimarães, E. M., Gottwald, M., 2024: Araguainha impact structure, Brazil: New insights into the geology of the central uplift. *Meteoritics & Planetary Science*, 59(10), 2577-2607.

Theilen-Willige, B., 1987: The use of airborne and spaceborne radar images for the detection and investigation of impact structures. *Research in Terrestrial Impact Structures* (ed. J. Pohl), Vieweg Publ., Wiesbaden, 115-130.

Theilen-Willige, B., 2021: Morphometric and Structural Evaluations of Satellite Data from the Bosumtwi Impact Structure and Adjacent Areas in Ashanti, Ghana. *European Journal of Environment and Earth Sciences*, 2(3), 7–14. https://doi.org/10.24018/ejgeo.2021.2.3.137

van Gasselt S., Kim J.R., Choi Y-S., Kim J., 2017: The Oasis impact structure, Libya: geological characteristics from ALOS PALSAR-2 data interpretation. *Earth, Planets and Space*, 69 - 35.

Vasconcelos, M. A. R., Crósta, A. P., Reimold, W. U., Góes, A. M., Kenkmann, T., Poelchau, M. H., 2013: The Serra da Cangalha impact structure, Brazil: Geological, stratigraphic and petrographic aspects of a recently confirmed impact structure. *Journal of South American Earth Sciences*, 45, 316–330. https://doi.org/10.1016/j.jsames.2013.03.007

Yommy, A. S., Liu, R.,Wu, S., 2015: SAR image despeckling using refined Lee filter. *In 2015 7th International Conference on Intelligent Human-Machine Systems and Cybernetics* (Vol. 2, pp. 260-265). IEEE.

CHAPTER 13
RESEARCH ARTICLE 2

13. RESEARCH ARTICLE 2: FACTORIAL ANALYSIS APPLIED TO AIRBORNE GAMMA-RAY SPECTROMETRY DATA FOR THREE BRAZILIAN IMPACT STRUCTURES (IN FINAL PREPARATION)

The second paper is currently in the final preparation stage. The most up-to-date version (draft) of article 2 can be found on the following pages. The general structure of the article is already defined, with abstract, introduction, local geology of the impact structures studied, factorial analysis approach, materials and methods, results, discussion, and conclusion sections already written. However, new results from field work will be included, such that additional materials (text, images, and tables) will still be included into the manuscript. Moreover, some corrections will still be applied to already written sections. For instance: it has been considered to insert a figure to improve the reader´s understanding of the factorial analysis approach, and the discussion section will be subdivided into subsections to improve the readability. In the same way, some figures will be changed as well. Recommendations by the examination board will also be considered. After all changes, the final version of the manuscript will be submitted to Meteoritics & Planetary Science (MAPS). Note that the reference list of paper 2 has already been formatted in MAPS reference style.

Factorial Analysis applied to airborne gamma-ray spectrometry data from three Brazilian impact structures

Adolfo Barbosa da Silva[1, 2*]

Wolf Uwe Reimold[1]

Gordon R. J. Cooper[3]

Roger L. Gibson[3]

Natália Hauser[1]

[1] University of Brasília, Institute of Geoscience, Graduate Program in Geology

[2] Geological Survey of Brazil

[3] University of the Witwatersrand

*__Correspondence__

148 Street, Setor Marista, 55 62 3240 – 1400, Goiânia, Goiás, Brasil.

e-mail: adolfo.barbosa@sgb.gov.br

13.1 **Abstract**

We explore the application of Factorial Analysis (FA) to airborne gamma-ray spectrometry (AGRS) data from three Brazilian impact structures: Serra da Cangalha, Riachão, and Nova Colinas. This technique was employed using systematic criteria for factorability and factor extraction, retention, and rotation, followed by analyses of communalities, factor loadings, and factor score maps in relation to geological information. Results demonstrate that a three-factor model effectively explains the variance in these airborne radiometric datasets, enabling dimensionality reduction. The first two factors (F1 and F2) primarily reflect weathering and lithological influences, with depositional processes contributing as well. For Serra da Cangalha, the F2 score map reveals erosional hill-type features linked to lithostratigraphic units, whereas at Riachão the F1 score map highlights radiometric signals of the central uplift. The F2 score map for Nova Colinas delineates a peripheral annular basin, a distinct potassium signature related to residual potassium contents in weathered mafic rocks, and a possible K-enrichment in the central zone that could be related to hydrothermal or alluvial depositional processes. Overall, Factorial Analysis proves itself as a valuable tool for enhancing the interpretation of AGRS data. The method may reveal geological features that are otherwise not readily discernible in conventional radiometric maps.

13.2 **Introduction**

Airborne gamma-ray spectrometry (AGRS) data are based on measurements of gamma-rays that naturally emanate from the uppermost 50 cm over the target area (e.g., Killeen et al., 2015). These measurements are recorded by a spectrometry sensor on board of an aircraft and can be used to estimate percentage values of total potassium (%K), and part per million contents of equivalent thorium (eTh) and equivalent uranium (eU) concentrations, in wide areas (Dentith and Mudge, 2014; Killeen et al., 2015). Furthermore, a large portion of the gamma-ray spectrum, usually from 410 keV to 2810 keV, is recorded by airborne spectrometers as Total Count (TC) values, so that K, eTh, eU, and TC are the

primary variables of AGRS data sets. In addition to these variables, some ratios between them (e.g., eU/eTh, eU/K, and eTh/K) can be computed to highlight subtle variations in the behavior of radioelements (IAEA, 2003; Killeen et al., 2015). Interpretation of radiometric data has been attempted for support of different applications, including geological mapping (Costa et al., 2019), mineral exploration (Costa et al., 2020; Weihermann et al., 2023), analysis of soil properties (Rawlins and Webster, 2007; de Mello et al 2021), and studies of carbon storage (O'Leary et al., 2022). In the last decades, AGRS data interpretation has also made interesting contributions to the study of terrestrial impact structures (e.g., Vasconcelos et al., 2012; Baratoux et al., 2019; Niang et al., 2021, 2022; Silva et al., 2024).

In the study of impact structures, gamma-ray spectrometry data are commonly presented as radioelement concentration maps (either for individual radioelements or in the form of RGB ternary composition maps) and/or profiles (ibid). Alternatively, K deviation maps derived from eTh normalization as an attempt to identify remobilization processes have been used, for example for some Brazilian impact structures (e.g., Vasconcelos et al., 2012; Leite et al., 2022). Recently, Niang et al (2021) analyzed radioelement concentration distribution curves and associated them with lithological units within some Australian impact structures. Although these studies have contributed to the understanding of radioelement distributions in impact structures, multivariate analysis techniques applied on AGRS in impact structures have not yet been used much and, to the best of our knowledge, no work has been published that makes use of Factorial Analysis in the impact cratering context.

Factorial Analysis (FA) is a multivariate statistical technique that is used to explore and model the correlative relationships of manifest variables as a linear combination of one or more latent variables (or factors) (Goretzko et al., 2021; Costelo and Osborne, 2005). In this sense, FA has the potential to reveal underlying structures that are not readily visible on traditional radiometric maps. Our hypothesis is that by extracting factors from an AGRS database composed of radiometric variables (TC, K, eTh, and eU, and the eU/eTh, eU/K, and eTh/K ratios) it may be possible to enhance information that could aid in the understanding of radioelement distribution patterns also for impact structures.

We applied Factorial Analysis to AGRS flight-line data acquired over three (Serra da Cangalha, Riachão, and Nova Colinas) Brazilian impact structures with the aim to obtain new information that might improve the understanding of radioelement distribution patterns for these structures. In order to achieve this, correlation matrices were computed for each AGRS dataset and then the factorability of these matrices was investigated with the Kaiser - Meyer - Olkin (KMO) and Bartlett's test of Sphericity (BtS) methods (Kaiser, 1974; Kaiser and Rice, 1974; Bartlett, 1950). Principal Component Analysis was used to extract the factors, whereas Parallel Analysis and Amount of Explained Variance (Fabrigar et al., 1999; Williams et al. 2010; Gaskin and Happell, 2014) were used to retain them. Factor rotations were made by the Varimax method (Kaiser, 1958). Factor scores were computed for each sample on the flight-line and then interpolated to produce factor score maps. Finally, these maps were integrated with available geological information and, for one impact structure (Nova Colinas), ground-gamma-ray spectrometry data and chemical analysis also were considered. One of our main findings suggests that weathering and lithological factors are essential in determining radiometric distribution patterns in the case of these impact structures. We believe that our study demonstrates how Factorial Analysis can be a useful additional tool to interpret airborne gamma-ray spectrometry data also for impact structures.

13.3 **The Serra da Cangalha, Riachão, and Nova Colinas impact structures.**

Among the confirmed Brazilian impact structures (Crósta et al., 2019) high-resolution airborne gamma-ray spectrometry (AGRS) datasets are available for only three structures: Serra da Cangalha, Riachão, and Nova Colinas. Thus, this study had to be limited to processing and interpreting data for these three impact structures. The target rocks affected by these impact events are predominantly siliciclastic rocks of the Paleozoic intracratonic Parnaíba Basin (Góes and Feijó, 1994; Vaz et al., 2007), but in the Nova Colinas structure, basalt of the regional Mosquito Formation and associated diabase dikes have also been affected by the impact (Reimold et al., 2022; Avona et al., 2025) (Fig. 1).

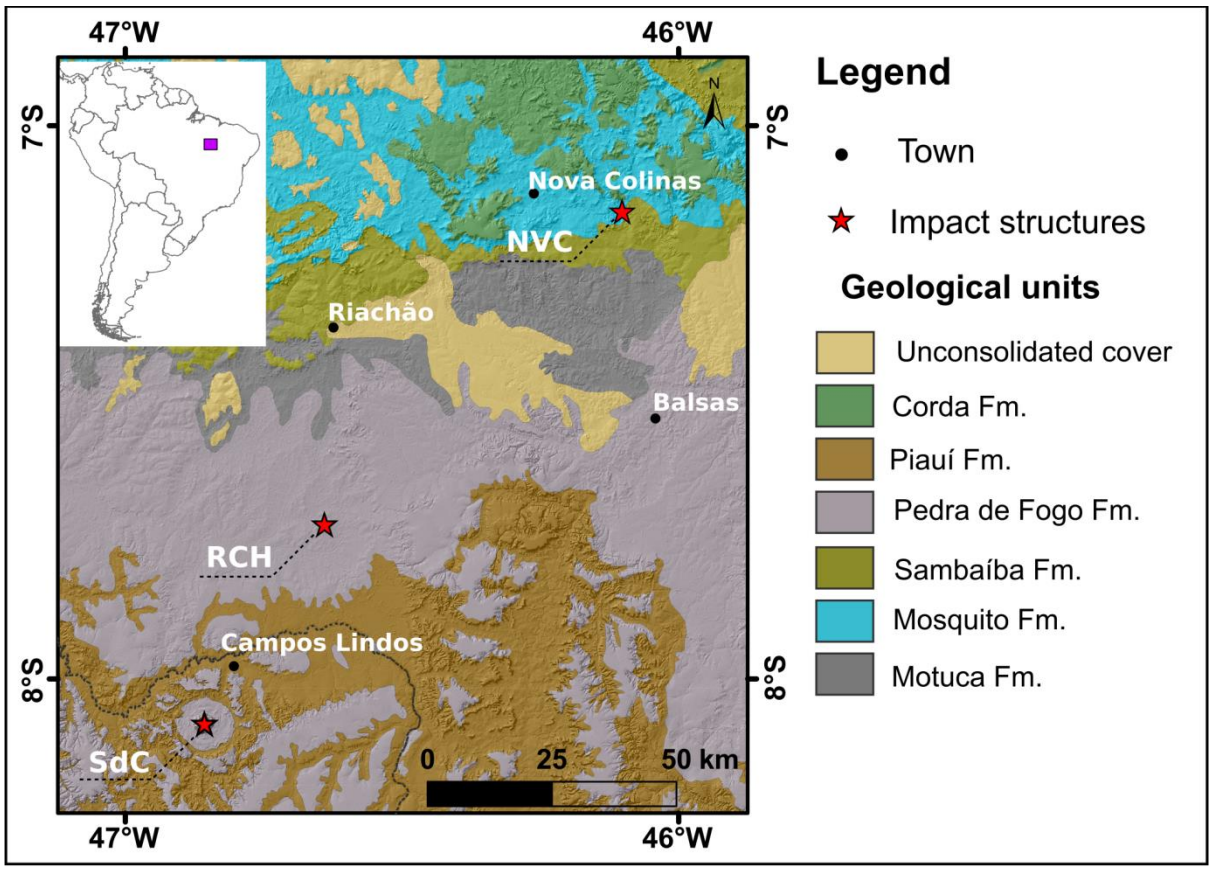

Figure 1: Schematic regional geological map and geographic locations of the Serra da Cangalha (SdC), Riachão (RCH), and Nova Colinas (NVC) impact structures in Brazil. Modified after Ribeiro et al. (2022) and Klein and Sousa (2012).

Serra da Cangalha is a ~13.4 km-diameter, complex impact structure centered at 8°05'S / 46°52'W (Fig. 1), in northeast Tocantins State (see Crósta et al., 2019, for a review; Silva et al., 2024). The origin by impact for Serra da Cangalha had been proposed since the 1970's (Dietz and French, 1973), but bona fide evidence (e.g., shatter cones, Planar Deformation Features (PDF), Planar Fractures (PF) and Feather Features in quartz) were only reported by Kenkmann et al. (2011) and Vasconcelos et al. (2013). Morphologically, Serra da Cangalha comprises a set of concentric rings, whereby the innermost part is characterized by a 2.2-km diameter depressed zone with rare outcrops of Longá Formation black shales and siltstones. This zone is surrounded by a prominent (up to 350 m high)

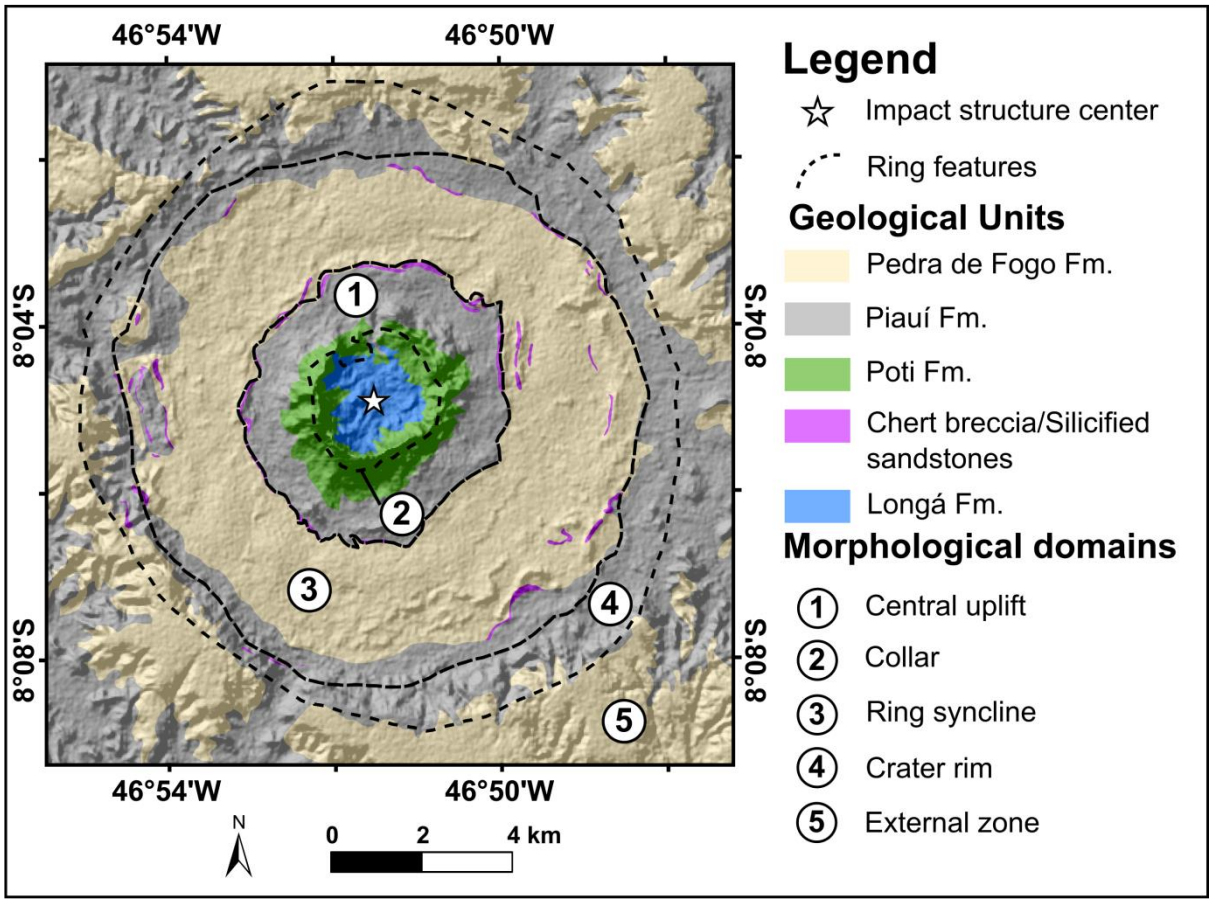

Figure 2: Simplified geological map of the Serra da Cangalha impact structure, modified after Kenkmann et al. (2011) and Vasconcelos et al. (2013). Major morphological domains are also indicated.

collar (which gave the structure its name) supported by silicified Poti Formation sandstones (Fig. 2). Both these zones form the central area that has been interpreted as a differentially eroded central uplift structure (ibid). This central part is surrounded by a 6 km diameter, intermediate ring feature (first ring) composed of Pedra de Fogo brecciated chert and quartzite and then by an 11 km diameter second intermediate ring that comprises Pedra de Fogo Formation silicified chert and sandstones. These intermediate rings occur as elongated hills within the Annular Basin (Reimold et al., 2006; Vasconcelos et al., 2013) (Fig. 2). The outer, apparent size of the Serra da Cangalha structure is represented by a 13.4 km diameter outer ring composed of Pedra de Fogo rocks (mainly sandstones; Vasconcelos et al., 2013). Because impact-generated and possibly datable lithologies have not been found

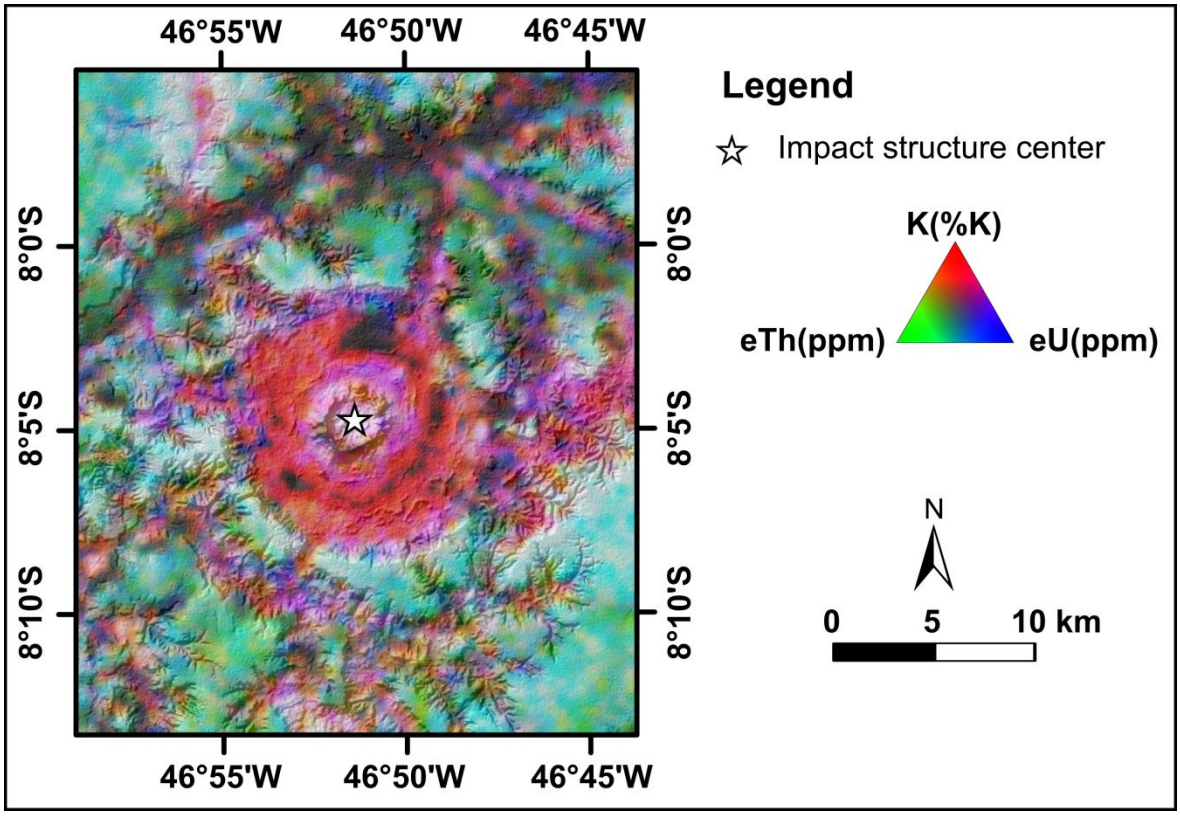

Figure 3: Radiometric signature of Serra da Cangalha impact structure as seen in RGB composite color of K, eTh, and eU radioelement concentrations. Modified after Vasconcelos et al., 2012; Silva et al., 2024.

at Serra da Cangalha, the maximum age for this structure is only constrained by the age of the youngest strata affected by impact - in this case the Pedra de Fogo Formation of ca. 250 Ma age (Vaz et al., 2007). Moreover, structural aspects have suggested that SdC was significantly eroded since its formation, possibly by as much as 500 m (Kenkmann et al., 2011). The differential resistance of the exposed lithologies to erosion has been considered the main reason for the radioelement distribution (Vasconcelos et al., 2012; Silva et al., 2024), which also shows the concentric ring pattern (Compare Fig. 3). Furthermore, previous workers have argued that there might be evidence for possible hydrothermally driven K enrichment in the AGRS data (Vasconcelos et al., 2012).

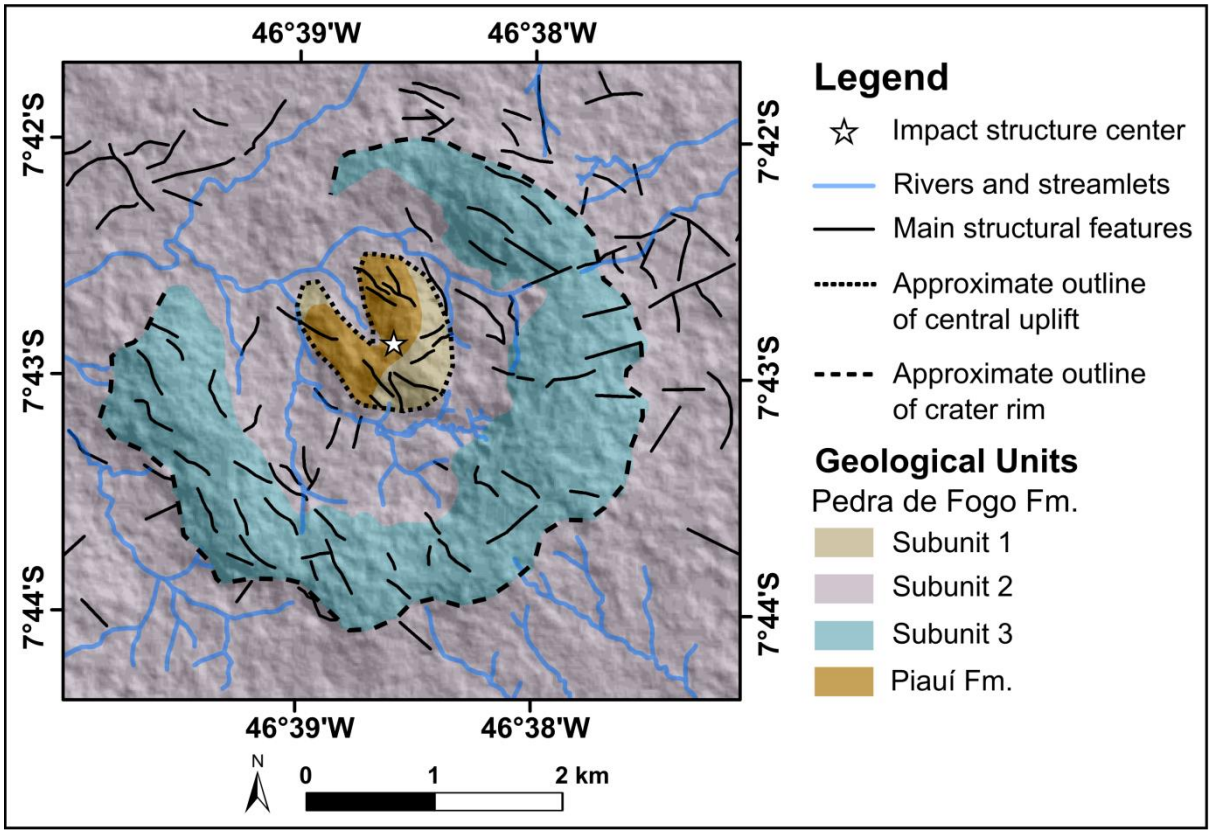

Figure 4: Simplified geological map of the Riachão impact structure. Modified after Maziviero et al. (2013).

Like Serra da Cangalha, the *Riachão* impact structure is also a complex impact structure, but its apparent diameter (~4 km) is much smaller than that of Serra da Cangalha (Crosta et al., 2019). The Riachão structure is centered at 7°42'S and 46°38'W in the southwest of Maranhão State (Fig. 1). The impact origin for Riachão had also been proposed in the 1970's (McHone, 1979; McHone, 1981), but the only quartz grain from Piaui sandstone in Riachão that exhibited a Planar Deformation Feature was reported as bona fide evidence only in 2013 (Maziviero et al., 2013). The central uplift at Riachão is a 1.4 km diameter circular structure that comprises massive Piauí Formation sandstones dipping at 55 to 80 de degrees into several directions (ibid) (Fig. 4). This central uplift is surrounded by an annular depression where outcrops are represented by siltstones and calcilutites. The apparent outer diameter is marked by a 4 km-diameter elevated rim that is open in the NW (Fig. 4). This morphostructural zone has been severely affected by erosion, with few

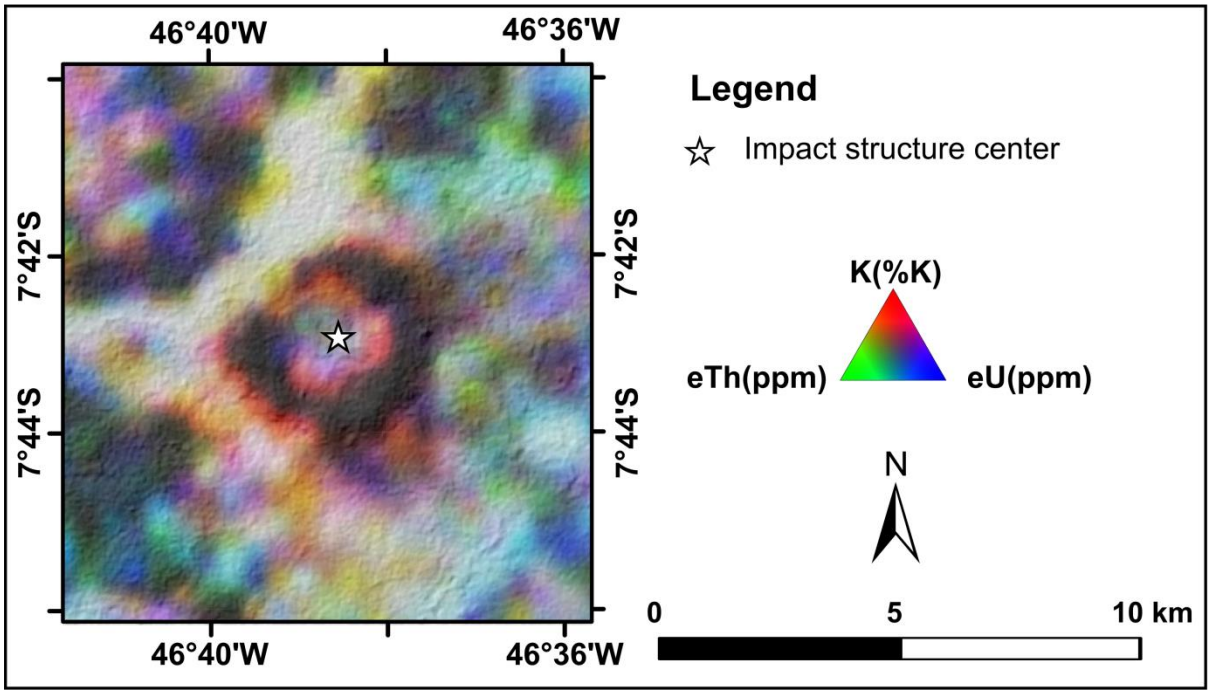

Figure 5: Radiometric signature of Riachão impact structure as seen in RGB composite color of K, eTh, and eU radioelement concentrations. Modified after Maziviero et al. (2013)

outcrops available. The outcrops are composed of sedimentary breccias and lithic sandstones. The former occur mainly in the northern portion of the rim and show a massive texture, with quartz sandstone clasts poorly to moderately sorted and with rounded to angular shapes, all embedded in a sand and silt matrix. The latter occurs in the eastern portion of the RR rim.

The lithic sandstones are composed of quartz grains, possess small-scale cross-bedding, and contain local concentration of sandstone clasts which, in turn, are supported by a matrix that shows similar characteristics as the sedimentary breccia matrix (Maziviero et al., 2012, 2013) (Fig. 4). The gamma-ray signatures of this structure (Fig. 5) have been interpreted to suggest high K concentration in the central part, possibly associated with phyllosilicate in the cement of Piauí sandstone, whereas K, eTh, and eU concentration lows in the crater rim area could be due to weathering-driven remobilization of radioelements (Maziviero et al., 2012 and 2013).

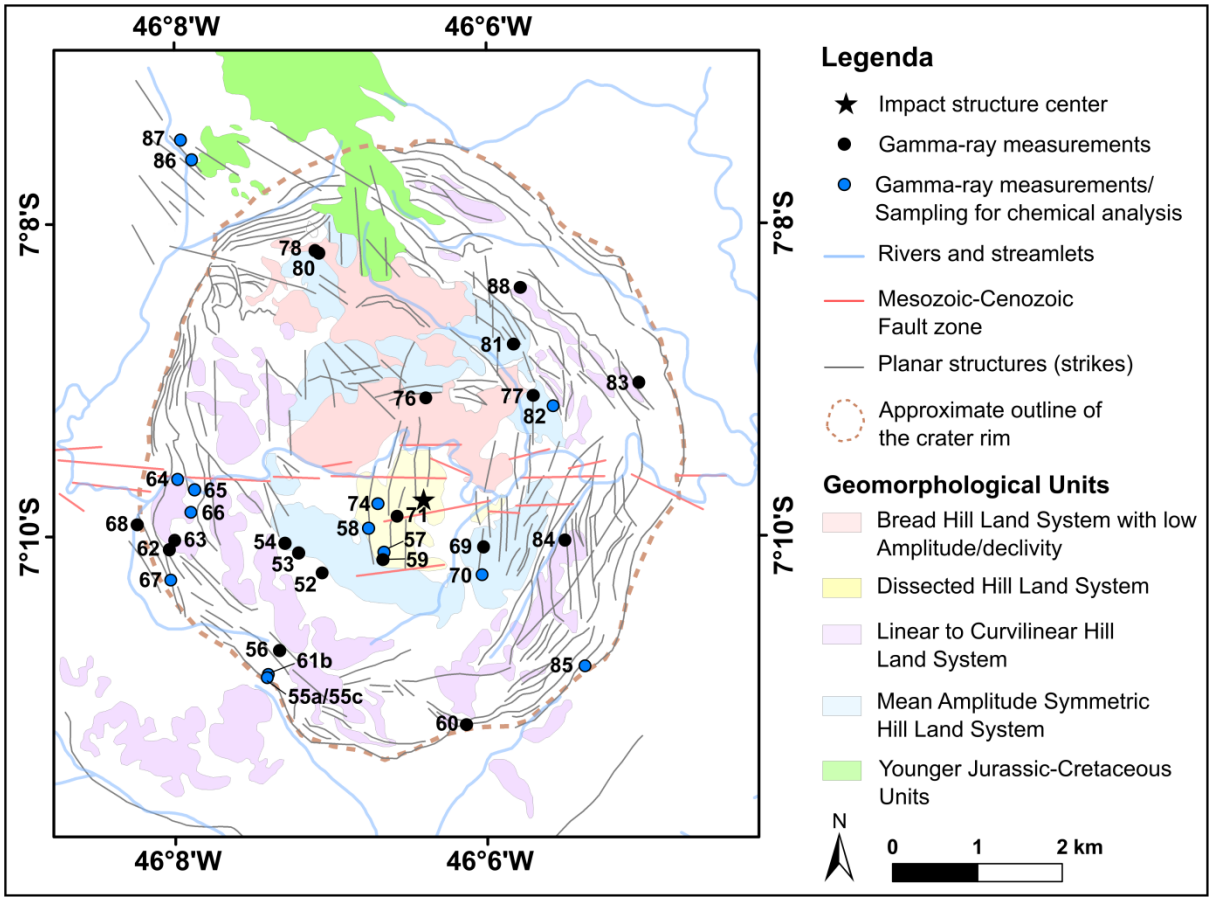

Figure 6: Simplified geomorphological map of the Nova Colinas impact structure. Modified after Reimold et al. (2022 - their figure 3b). The description of gamma-ray measurements and sampling locations will be given in the next section.

Nova Colinas has been more recently confirmed as an impact structure (Reimold et al., 2022). It is also a complex impact structure, with a 7 km wide crater rim. Nova Colinas is centered at 7°09'33''S / 46°06'30''W (Reimold et al., 2022) (Fig. 2). An impact origin for Nova Colinas had been suggested by previous workers (e.g., Silva, 2020), but shock diagnostic features (planar fractures, feather features, and planar deformation features) were first reported by Reimold et al. only in 2022.

A geological map for Nova Colinas was proposed by Avona et al. (2025), but in the present work the morphological unit map of Reimold et al. (2022) and regional geological maps are considered, because: i) the outcrop points visited by Avona et al. (2025) are not available in their map; ii) Avona et al. (2025) proposed that NVC's rim is composed of a

continuum of basalt units. However, as it will be shown in this work, such material occurs only discontinuously along the rim, and iii) silicified sandstone and laterite units are not shown in Avona's geological map.

In regional geological maps, the northern part of the NVC structure is covered by Mosquito Formation basalt and some Corda Formation sandstone (Fig. 1). The central and southern parts of the NVC structure are dominated by siliciclastic units (e.g., Sambaíba sandstones, Pedra de Fogo Formation sandstone, and fine-grained Motuca Formation sandstone), with the Motuca Formation possibly containing some evaporites and the Pedra de Fogo Formation some chert (Fig. 1). The northern and southern areas are well-defined in a color composite map of multitemporal thermal infrared from ASTER scenes and residual magnetic maps (Silva, 2020; Reimold et al., 2022; Pereira et al., 2024). Morphological analysis reported in Reimold et al. (2022) indicates that the relief pattern is essentially moderate within the Nova Colinas structure, with dissected relief of moderate and low slopes (Fig. 6). Greater elevation occurs along the perimeter of the structure and in a small area (up to 0.8 km wide) in the central part of Nova Colinas (Fig. 6). In this central part, the strata are strongly fractured and display variable bedding orientation, from locally subhorizontal to steeply upturned (Reimold et al., 2022).

Monomict sandstone breccia, a few samples of which contain quartz with PDF and FF, are the main impactite facies reported until now from NVC. These monomict breccias consist of very fine-grained, pure quartz sandstone with large rounded grains embedded in a fine-grained groundmass of crushed, splintery fragments (Reimold et al., 2022). Many other sandstone samples from NVC are also strongly cataclased and/or fractured, but they do not show shock features. For instance: near the southeast of the central zone, strongly silicified sedimentary breccia with variably rounded to angular sedimentary clasts has been mapped, but none of these samples displays any diagnostic shock evidence.

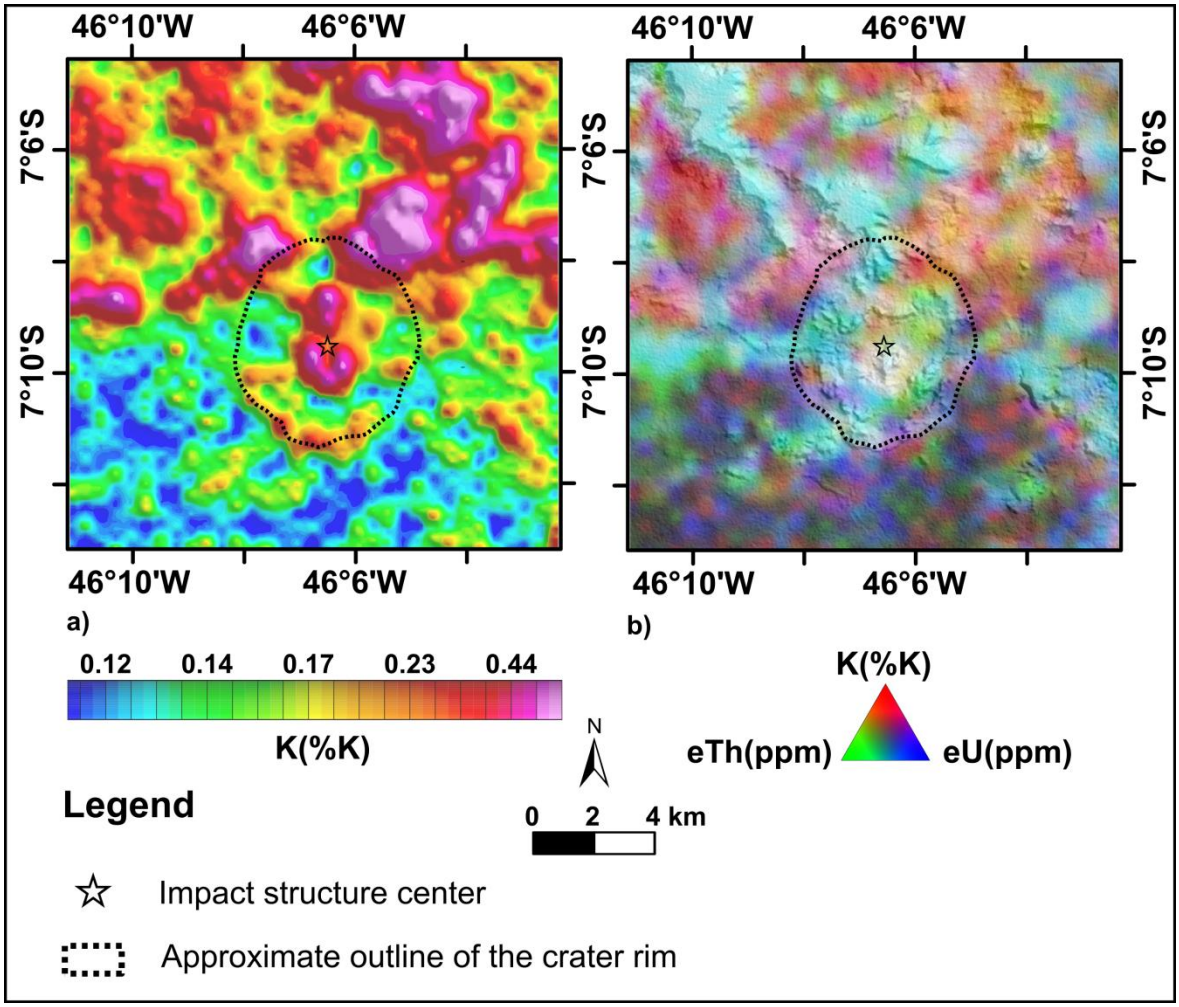

Figure 7: Radiometric signature of Nova Colinas impact structure. a) Percent of total potassium map. b) RGB composite color of K, eTh, and eU radioelement concentrations. Modified after Silva (2020) and Reimold et al. (2022).

Regarding gamma-ray signatures, circular radiometric pattern seen in Serra da Cangalha and Riachão structure is unclear in Nova Colinas impact structure (Compare Figs. 4 and 5 with Fig. 7). However, high K concentration in the northern sector may reflect near-surface materials overlying Mosquito Formation basalts, whereas high-K concentration in the central area could be related to the radiometric signature of a lower stratigraphic unit that was uplifted during collapse and modification of the impact structure (Reimold et al., 2022).

Like at Serra da Cangalha and Riachão, the lack of any impact melt rock or suevite with impact melt clasts has not allowed determining an absolute age of impact, such that the age suggested by Avona et al. (2025), on stratigraphic grounds, is poorly constrained by the

interval from ~ 199 to 130 Mas. The upper limit represents the age of the pre-impact basalt layer of the Mosquito Formation (e.g., Merly et al., 2011), whereas the lower limit represents the depositional interval of the Corda Fm. sandstones, which occur undeformed within the northern rim segment of the impact structure (Fig. 1) (Avona et al., 2025; our own observations).

13.4 **Factorial Analysis**

In Factorial Analysis (FA), the total variance of each variable is partitioned into common, unique, and error variances to reveal underlying factor structures, such that only the common variance appears as a final solution (Costello and Osborne, 2005; Mulaik, 2009). For the purpose of this work, a brief description of the approach will be given in the following, but a more detailed description of the method can be found in Supplementary Material. Mathematical details about FA can be found in several textbooks, such as Mulaik (2009), Fabrigar and Wegener (2012), and Gorsuch (2015).

In a geological context, it is possible to compute a factor score map and integrate it with geological information. The factor scores can be regarded as indices of variables, such that if a given variable has a high load for a given factor, the scores will reflect this variable more strongly. For instance, Asfahani et al. (2005) found that Total Count, eU, eU/eTh, and eU/K are variables with a common factor which they termed, in this case, the first factor (F1). By analyzing the F1 score map, they found that high F1 scores were related with U presence in a phosphate deposit in the Al-Awabed area of Syria. For this reason, they termed F1 the uranium phosphate factor. In another study, F1 was interpreted as the common factor that leads the TC, K, eTh, eU variables to covariance (Hussein et al., 1995). The F1 score reflected the presence of radioelements hosted in felsic rocks, so that F1 was termed the integrated radioactivity factor (ibid). Still in the same study, Hussein et al. (1995) termed a second factor (F2) the ^{40}K index, whereas a third factor (F3) was interpreted as an intra-rock unit differentiation factor. Finally, Factorial Analysis also has been used to reduce the dimensionality of geochemical data (Martins-Ferreira et al., 2017; Ouchchen et al., 2022).

These studies showed that, in order to understand the meaning of factors, it is necessary to understand the correlation structure of an airborne gamma-ray spectrometry dataset and verify how observable radiometric variables are associated with factors. By integrating the factor score maps with geological information, it is possible to interpret the factors in terms of geological processes.

13.5 **Materials and Methods**

13.5.1 Airborne Gamma-ray Spectrometry (AGRS) datasets

The AGRS data for the Serra da Cangalha, Riachão, and Nova Colinas impact structures were acquired for the same Aerogeophysical Project known as the Bacia do Parnaiba project. This project was carried out in 2006 by the Atech/USP institutions, and the AGRS database is freely downloadable from the REATE platform (https://reate.cprm.gov.br/anp/TERRESTRE, code: 0050_MAGGAMA002). The gamma-ray data were measured with a Thallium-activated sodium iodide NaI(Tl) gamma-ray spectrometry sensor along flight lines that were spaced 500 m apart and extended in N-S direction with nominal terrain clearance of 100 m. The radiometric channels were pre-corrected for dead time, background removal (aircraft, cosmic radiation, and radon), height, and Compton Effect, and data were converted to elemental concentrations (Marques et al., 2006). In order to process AGRS data and to perform FA analysis, we used the Seequent's Oasis Montaj and R softwares (RStudio was used as an interface for the R software) (R Core Team, 2021; RStudio Team, 2020). The thematic maps derived from the processing steps given in the next section were produced by using Esri's ArcGis 10.6 software.

13.5.2 Processing

Initially, three AGRS data subsets (named SdC for Serra da Cangalha, RCH for Riachão, and NVC for Nova Colinas) were generated from the Bacia do Parnaiba's AGRS database and then exported as .csv files and imported into the R environment. In the R software, the Factorial Analysis was performed using the "psych" package (Revelle and

Revelle, 2015), as well as other auxiliary packages (“tidyverse”, “corrplot”, and “dplyr”) (Silge and Robinson, 2016; Wei et al., 2017; Wickham et al., 2025). Each .csv file had six columns, the first three of which (line and X and Y coordinates) were kept unchanged during all processing steps. The primary radiometric variables (TC, K, eTh, and eU) were used to compute radiometric ratios (Th/K, eU/K, and eU/eTh). Next, we normalized the primary and ratio radiometric variables by the MIN – MAX method and then computed the correlation matrix.

The Factorial Analysis this study was carried out by following the main recommendations given by previous studies regarding to the key decisions involving factorability analysis, the choice of extraction/retaining/rotation methods, and interpreting/naming the resulting factors (Fabrigar et al., 1999; Williams et al. 2010; Gaskin and Happell, 2014). More detail about such key decisions in the factor Analysis process can be found in the Supplementary Material. In short, factorability of each radiometric data subset was assessed by using Kaiser-Meyer-Olkin (KMO) (Kaiser, 1974; Kaiser and Rice, 1974) and Bartlett’s test of Sphericity (BtS)(Bartlett, 1950) methods (see details in Suppl. Material).

After the factorability analysis step, the factors were extracted from the AGRS data subset by Principal Component Analysis (PCA). Then, the Parallel Analysis (PA) (also known as Horn’s Parallel Analysis) (Horn, 1965) and the Amount of Explained Variance (AEV) method (Fabrigar et al., 1999; Williams et al. 2010; Gaskin and Happell, 2014) were used to support our decision to retain factors. The final solution of the factor model was obtained after rotating the factors using the Varimax rotation method (Kaiser, 1958; Fabrigar et al., 1999). From the final solution of the factor model, we produced three tables to assess the meanings of the factor. These tables contain the loadings, communalities, and radiometric variables. By using regression analysis, factor scores also were estimated for each factor for each sample of the AGRS data subsets (SdC, RCH, or NVC). The scores were interpolated by the Inverse Distance Weighted method with 125 m-cell size and 500 m-search radii. After this procedure, we produced factor score maps for each impact structure.

We also produced conventional radiometric maps (TC, K, eTh, eU, Th/K, eU/K, and eU/eTh) to compare with the factor maps. Finally, we carried out the interpretation of factors and assigned names to them.

13.5.3 Fieldwork

To better understand the meanings of factors, we carried out a field campaign at Nova Colinas. The structure was chosen because the geoscientific knowledge about it is still limited. In addition, one of our factorial score maps (see next section) enhanced subtle features on the rim and central uplift of Nova Colinas that needed to be investigated by ground-truthing. We collected ground gamma-ray spectrometry measurements and sampled rocks for chemical analysis. The places of gamma-ray measurements and/or rocks sampled are indicated on the Nova Colinas geomorphological map in Fig. 6.

13.5.3.1 Ground-based gamma-ray spectrometry data

The gamma-ray readings were obtained with a handheld gamma-ray spectrometer with a large 2" x 2" Bismuth Germanate Oxide (BGO) crystal detector high sensitivity, with a volume of 6.3 in^3 (~103 cm^3), and previously calibrated and stabilized (Radiation Solution Inc., 2025). When placed on rock outcrops, it had been prepared to automatically correct gamma-ray counts for dead time, background, and stripping, and then provides concentrations of percent of potassium total (%K), part per million of equivalent Uranium (eU), and part per million of equivalent thorium (eTh) (Killeen et al., 2015).

For this work, a total of 207 gamma-ray measurements were taken at 33 – mainly in situ - outcrops (see examples in Fig. 6). For each outcrop visited, the following measurement procedure was followed: i) First, an initial reading of 5 min (or 300 s) acquisition time was done on a representative spot of the outcrop. ii) Next, another reading of 2 min (120s) acquisition time was done on the same spot as the first reading. iii) Finally, four more readings of 2 min acquisition time each were obtained at different spots of the outcrop. The distance between spots was generally less than 3 m.

This procedure was adopted because the Nova Colinas impact structure is located in sedimentary target dominantly with very low radiometric signals, such that long acquisition times are needed to reduce the error in the gamma signal counts (see IAEA, 2003; Killeen et al., 2015). However, because reading multiple spots at 5 min acquisition times would result in a lower total number of readings that can be taken in a day (e.g. Killeen et al., 2015), we reduced the reading time for the additional points to 2 min. Then, for each outcrop visited, we calculated the mean value and standard deviation of the radioelement concentrations from the readings taken at the spots with 2 min acquisition time, such that the initial total number of measurements (207) was reduced to 66 with 33 readings taken with 5 min and 33 readings (mean + standard deviation) taken with 2 min. Note that the measurements taken at 5 min possess a lower error count than readings taken for 2 min, but this latter observation may also reflect the spatial variability of the gamma signal for a single outcrop. The ground-based gamma-ray spectrometry data are presented in bivariate diagrams (see the next section). All these plots were produced with software from the R package, like ggplot and dplyr (Wickham, 2016; Wickham et al., 2025).

13.5.3.2 Chemical analysis

A total of fifteen samples were collected at Nova Colinas for chemical analysis. The major element data were obtained by X-ray Fluorescence (XRF) spectrometry, whereas trace element data were obtained by Inductively Coupled Plasma Mass Spectrometry (ICP-MS). The analyses were carried out at the EarthLab of the School of Geosciences at the University of the Witwatersrand in Johannesburg (South Africa).

Initially, the samples were crushed in carbide steel jaw crushers and swing mills. Then, the milled samples were subjected to bulk-rock X-ray Fluorescence (XRF) analysis using a Panalytical PW2404 spectrometer. The chemical analysis by ICP-MS was done with a Thermo Scientific iCAP RQ ICP-MS. With the open-cup method, the sample is placed directly into a Savillex beaker with 3 mL of HF: HNO_3 and heated to 70 °C until evaporation. This process is repeated several times with HNO3 for 72 hours until complete digestion is

achieved Samples are diluted up to 50 mL with 5 % HNO_3. More details about reference materials, detection limits, and repeatability and contamination evaluations can be found in the Supplementary Material.

The quantities of major and trace elements were organized into a table (next section). In an attempt to integrate chemical analyses with ground gamma-ray spectrometry data, some scatterplots for radiometric variables and selected elements were produced. Note that, in this case, only those gamma-ray measurements and chemical analysis could be used for a limited number of outcrops (see Fig. 5).

13.6 **Results**

13.6.1 Factorability and criteria of factor retention

Our results from the factorability analysis are listed in Table 1. All Kaiser-Meyer-Olkin (KMO) values for the Airborne Gamma-Ray Spectrometry datasets (Serra da Cangalha – SdC, Riachão – RCH, and Nova Colinas – NVC) are > 0.5. This suggests that all datasets have an acceptable level of correlation among the radiometric variables. Moreover, the Bartlett's test of Sphericity (BtS) analysis yields high values for Chi-squares and p-values equal to zero for all AGRS datasets. This indicates that the correlation matrices for radiometric variables from the three AGRS datasets are statistically different from the identity matrix (i.e., a matrix where each variable is only correlated with itself). As the p-values are much less than 0.05 for the three AGRS datasets, the Bartlett's test of Sphericity analysis also suggests that these datasets are factorable. Note that p-values are not exactly zero, but they were likely very low numbers that were rounded to zero due to precision or computational limitations.

Figure 8 presents an example for the Serra da Cangalha dataset, in the form of a heat correlation chart computed for the radiometric dataset. The remaining charts (Riachão and Nova Colinas datasets) can be found in the Supplementary Materials. The main results are: i) K is practically uncorrelated with the eTh, eU, and eU/eTh variables in the Serra da Cangalha (Fig. 8) and Nova Colinas (Suppl. Material) cases, but it reaches a positive and

Table 1: Results of factorability analysis of the airborne gamma-ray spectrometry datasets for the three Brazilian impact structures.

Dataset	KMO (Overall MSA)	BtS (χ^2/p. value)
SdC	0.58	197613.6/0.00
RCH	0.61	24510.95/0.00
NVC	0.54	59459.16/0.00

KMO = Kaiser-Meyer-Olkin; MSA = Measure of Sampling Adequacy; BtS = Bartlett's test of Sphericity; χ^2 = Chi square (see the explanation in Supplementary Material;

moderate correlation level (0.63) with eTh for the RCH impact structure (Suppl. Material). ii) K is negatively correlated (-0.7 to -0.5) with the eTh/K and eU/K variables for all three datasets. These radiometric ratios are positively and strongly to moderately (> 0.6) related to each other. iii) For the RCH and NVC datasets (Suppl. Material), Total Count (TC) values are positively and strongly to moderately correlated with the K, eTh, eU, and eTh/K variables. The three latter variables are also positively and strongly correlated with TC for the SdC dataset, but K only shows a weak correlation (< 0.2).

Despite the differences between the different AGRS datasets, analysis of correlation matrices suggests that there are common variances among the radiometric variables, such that at least one factor can be extracted from the AGRS datasets.

To determine how many factors must be retained, we carried out Parallel Analysis (PA) and Amount of Explained Variance (AEV) analyses. Figure 9 shows the results of Parallel Analysis for the three AGRS datasets. For each of these images, Principal Component and Factorial Analysis of actual data are marked by blue lines, whereas Principal Component and Factorial Analysis computed by simulated data are shown in green and with red dashed lines.

All three AGRS datasets show that the first three eigenvalues of Factorial Analysis computed from actual data are higher than the eigenvalues of Factorial Analysis computed from simulated data. These results suggest that three factors must be retained. When

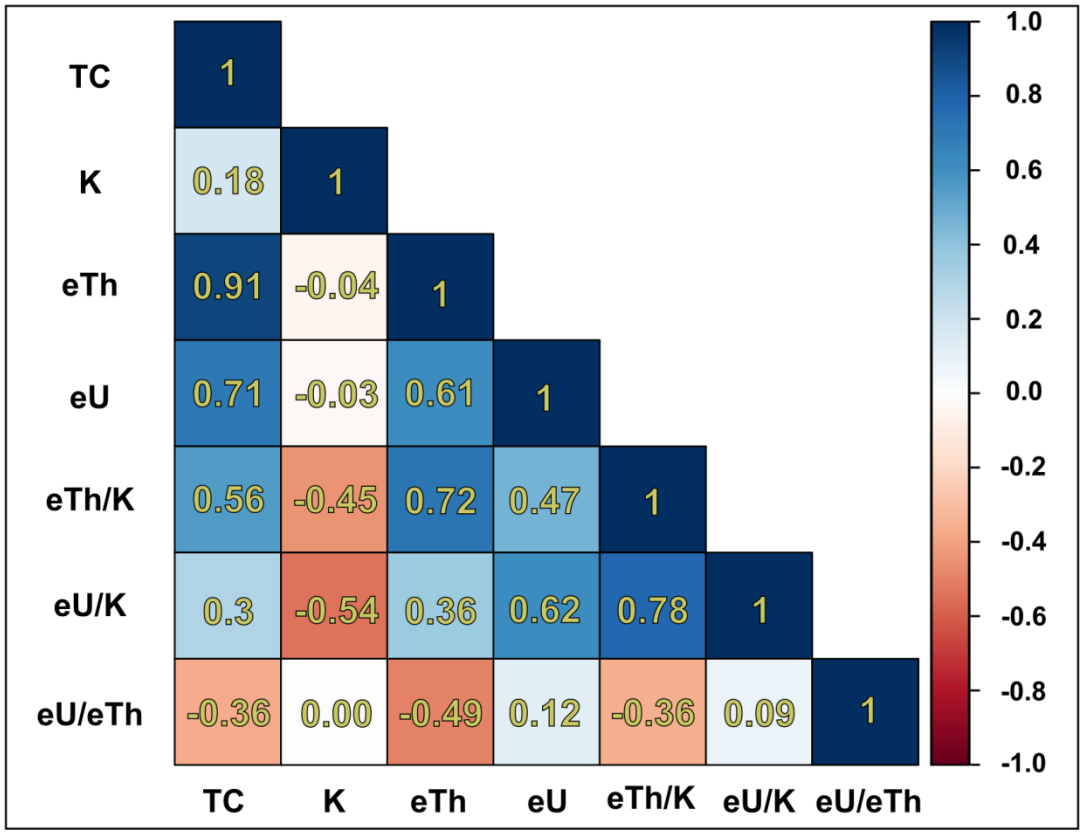

Figure 8: Heat correlation chart computed for the airborne gamma-ray spectrometry dataset for the Serra da Cangalha impact structure.

Principal Component eigenvalues computed from actual data are compared with the results for simulated data only two Principal Components would be suitable to explain the variance in the Nova Colinas dataset. This may suggest that a two-factor model would be appropriate for the Nova Colinas dataset. However, according to the amount of explained variance shown in Figure 10, a two-factor model for the Nova Colinas dataset can explain 70 % of the variance, whereas a three-factor model can explain > 80 % of the variance not only for the Nova Colinas dataset, but also for the other two datasets. Therefore, three factors have been retained in our Factorial Analysis. It is worth mentioning that, when considering the Kaiser-Guttam rule (i.e., to retain only eigenvalues > 1 - Guttman, 1954; Kaiser, 1960, 1992) (see the dashed black line in Fig. 9), the number of factors to be retained decreases to a single one (Serra da Cangalha and Nova Colinas datasets) and to two factors (Riachão dataset).

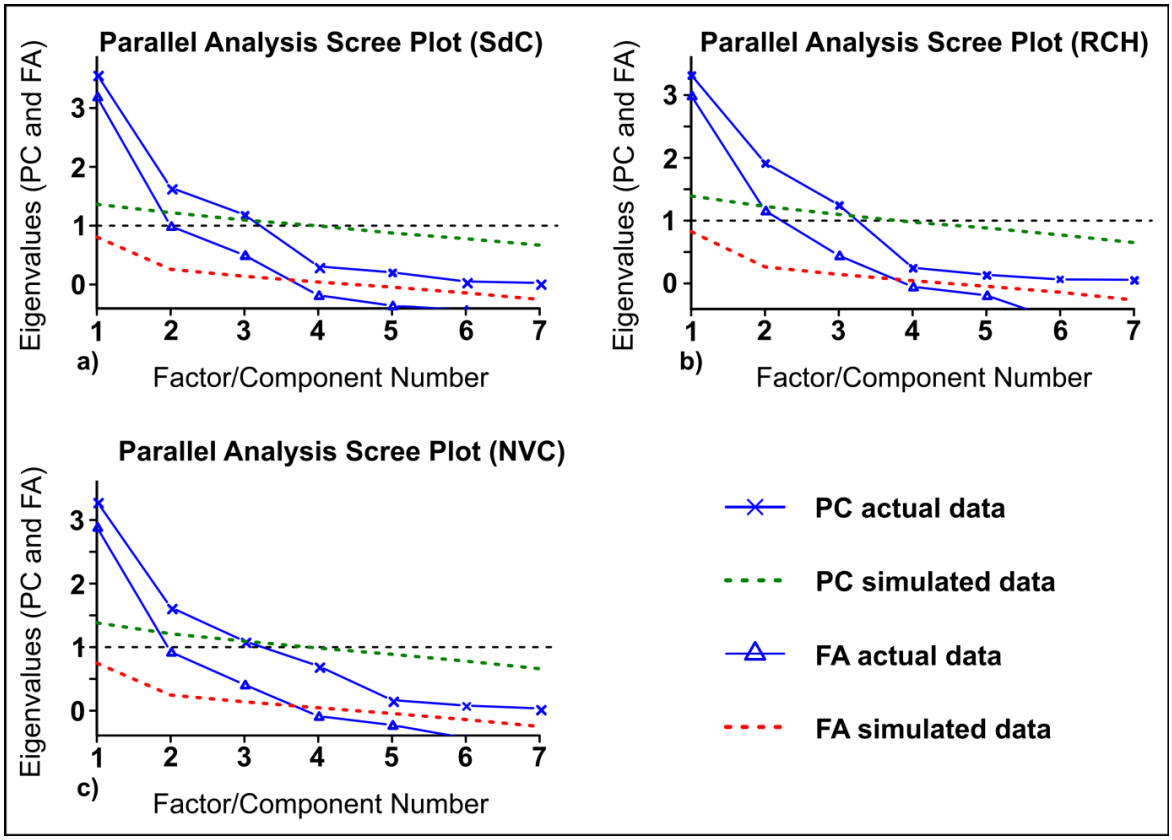

Figure 9: Parallel Analysis for the airborne radiometric datasets. a) Serra da Cangalha dataset. b) Riachão dataset. c) Nova Colinas dataset. The dashed black line refers to the commonly adopted threshold (e.g., eigenvalues > 1) for the Kaiser-Guttman rule.

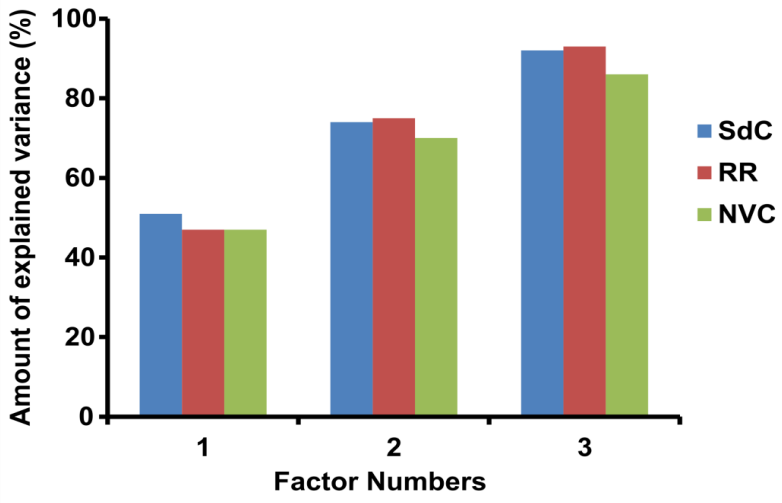

Figure 10: Amount of Explained Variance. The value refers to cumulative variance computed considering one, two, or three factors (as described in the previous section). SdC = Serra da Cangalha dataset; RR = Riachão dataset; NVC = Nova Colinas dataset.

13.6.2 Radiometric variables and latent factor relationships

After the factor retention step, we carried out the Factorial Analysis (FA) itself and calculated the factor loadings and communalities for each radiometric variable for the three AGRS datasets. The results of factor loadings and communalities computed for each

These tables show that a three-factor model yields high to very high (> 0.8) communalities for the majority of radiometric variables, except for eU and eU/eTh for the Nova Colinas dataset, for which the communalities are 0.77 and 0.78, respectively. Even so, communalities > 0.7 are expected when Factorial Analysis is successfully applied (Fabrigar et al., 1999; Costello and Osborne, 2005). Moreover, high communalities corroborate that a three-factor model is suitable to explain almost the totality of variance in each of the three AGRS datasets.

As factor loadings express correlation between factors and radiometric variables, the symbols (+) and (-) indicate the direction of correlation, that is, positive values indicate direct correlation, whereas negative values indicate inverse correlation. In short, the absolute value of factor loadings expresses the extent to which the variable is related to a given factor. Here, we have considered high factor loadings, i.e., loadings with absolute values > 0.7, and moderate factor loadings with absolute values between 0.3 and 0.7. Factor loadings with absolute values < 0.3 were interpreted as low and suggestive of non-correlation. In the following we are focusing on factor loadings > 0.3, because they are more significant for FA.

Table 2 shows that the first factor (F1) has positive and high loadings (> 0.8) for TC, eU, and eTh in the SdC dataset, but it shows low loading for K, suggesting that there is no correlation between F1 and K. On the other hand, relatively high and positive correlation (0.72) is observed between F1 and K in the RR dataset (Table 3) besides positive and high loadings for the TC, eTh, and eU variables. In the NVC AGRS dataset, F1 has positive and high loadings for these variables but also for eTh/K (0.82) (Table 4). In the NVC datasets, F1 also shows low loadings for K. For the RR dataset, F1 is practically uncorrelated (low loadings) with the eU/K and eTh/K variables, but for the SdC dataset F1 has positive and

moderate loadings for eU/K (0.47) and eU/K (0.55). For the NVC dataset, F1 has a positive and moderate loading for eU/K (0.58).

The second factor (F2) has strongly negative (-0.91) and positive (0.95) loadings for K in the Serra da Cangalha and Nova Colinas datasets, and the correlation between F2 and K is moderately negative (-0.58) for the Riachão dataset. F2 also has negative and moderate correlation for eU/K and eTh/K for the Nova Colinas dataset, and these correlations are higher and positive (>0.69) for the SdC and RR datasets. Finally, strongly positive loadings are noted between F3 and the eU/eTh ratio for all three datasets, and moderate correlation between F3 and eTh (-0.48) (SdC dataset), F3 and eU or eU/K (RR dataset), and F3 and eU (NVC dataset) are also evident.

Table 2: Factor loadings and communalities computed for each radiometric variable for the Serra da Cangalha AGRS dataset.

Radiometric Variables	**Factor loadings**			**Communalities**
	F1	F2	F3	
TC	0.93	-0.06	-0.30	0.95
K	0.20	-0.91	0.04	0.86
eTh	0.83	0.15	-0.48	0.93
eU	0.89	0.20	0.29	0.92
eU/eTh	-0.11	0.00	0.96	0.93
eU/K	0.47	0.81	0.19	0.91
eTh/K	0.55	0.69	-0.35	0.90

13.6.3 Factorial score maps and conventional radiometric maps

In order to understand the spatial relationship between factors and original radiometric variables, we produced several maps displaying radiometric concentrations, radiometric ratios, and the first three factor scores retained in our analysis. Figure 9 shows an example of such maps for the Serra da Cangalha dataset. The remaining maps for the

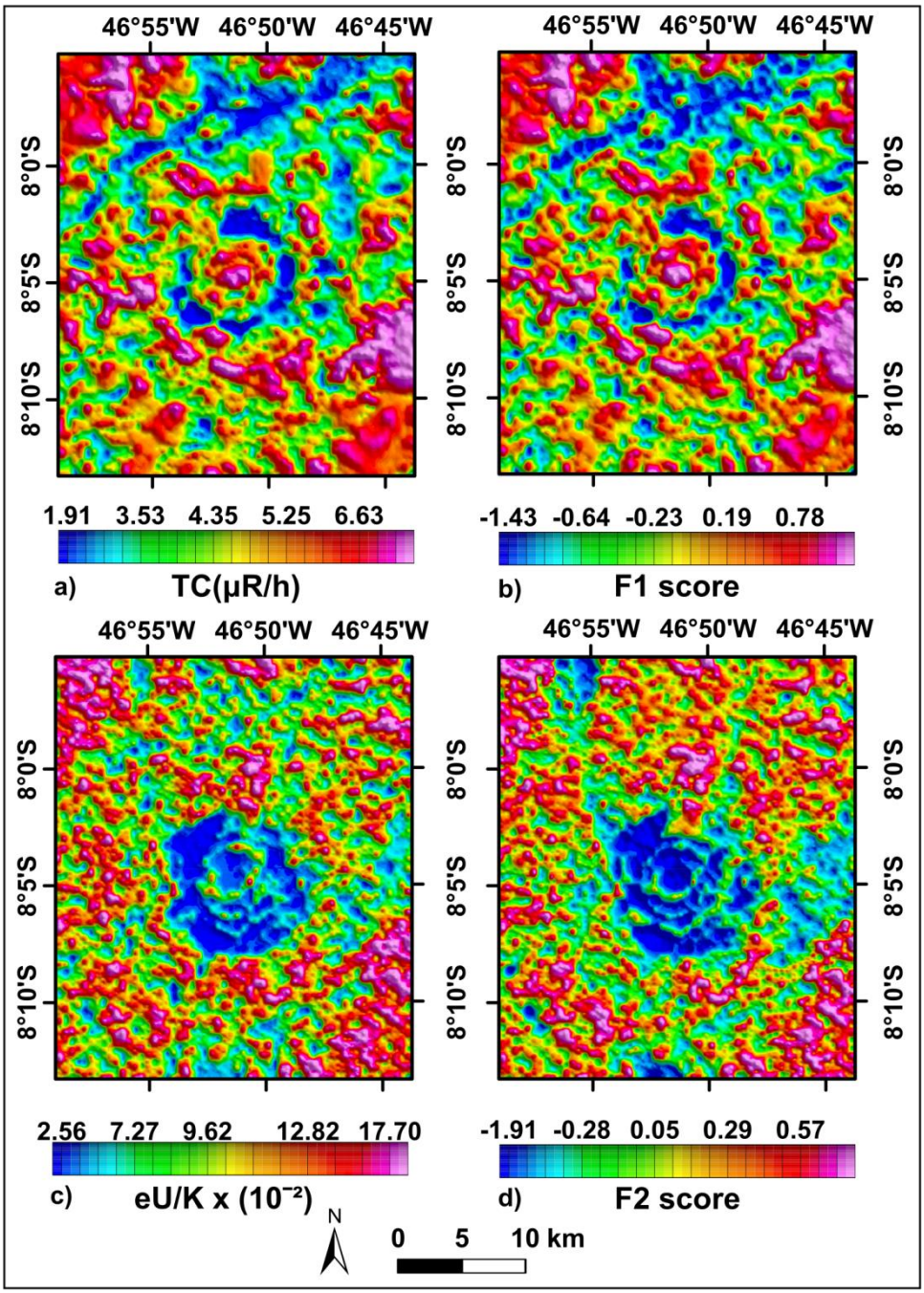

Figure 11: Thematic radiometric maps for the SdC impact structure. a) The Total Count (TC). b) F1 score map. c) eU/K radiometric ratio. d) F2 score map.

Serra da Cangalha, Riachão and Nova Colinas datasets can be found in the Supplementary Material.

The Figures 11 shows that Serra da Cangalha has concentric distribution patterns. This pattern also can be seen in other radiometric maps (e.g. K, eTh, and eU; see the Supplementary Material). Overall, this concentric pattern is characterized by high values for

TC, eTh, and eU in the SdC surrounded by an area of low values that, in turn, is surrounded by discontinuous zones rich in eTh, eU, and TC (Fig. 11a and maps in Supplementary Material). The F1 score map shows very similar concentric distribution patterns for TC, eTh, and eU (e.g., Compare Fig. 11a and 11b). Such similarities between F1 and TC, eTh, and eU maps are also observed for the Nova Colinas and Riachão impact structures (Supplementary Material). The F1 map is also very similar to the K map for the Riachão impact structure, but the concentric distribution patterns are not evident for Nova Colinas (Supplementary Material). These results corroborate that TC, eTh, and eU have a common factor (F1) for the Serra da Cangalha and Nova Colinas datasets. For the Riachão dataset, K also has a common factor with TC, eTh, and eU.

Considering the F2 score maps for Serra da Cangalha, we have observed that high values in the eU/K (and eTh/K, see Supplementary Material) map are also seen as high values in the F2 score map (e.g. Compare Fig. 11c and 11d). Otherwise, high values in the K map can be seen as low values in the F2 map, suggesting that F2 can be considered an inverse map to the K map (Supplementary Material). For the Riachão structure, the F2 score map is practically identical to the eTh/K map, and some features seen in the eU/K map also appear in the F2 map. The F2 score map is also practically identical to the K map for the Nova Colinas structure, but in contrast to the Serra da Cangalha case, high values in the K map are also high values in the F2 score map for Nova Colinas. These results suggest that eU/K, eTh/K, and inverse K have a common factor (F2) in the case of Serra da Cangalha, whereas for Riachão and Nova Colinas, F2 only reflects one variable, which is either eTh/K in the case of the Riachão structure, or K at Nova Colinas. Finally, we observe that the F3 map is essentially the same as the eU/eTh map for all three impact structures.

In summary, the results from radiometric variables and factor maps suggest that the radiometric information contained in seven radiometric variables (TC, K, eTh, eU, eU/eTh, eU/K, and eTh/K) can be reduced to only three latent variables (i.e., factors F1-F3), so that the Factorial Analysis has worked as a condenser of dimensionality for all three AGRS datasets. Additionally, interpretation based on individual factor score maps may reveal

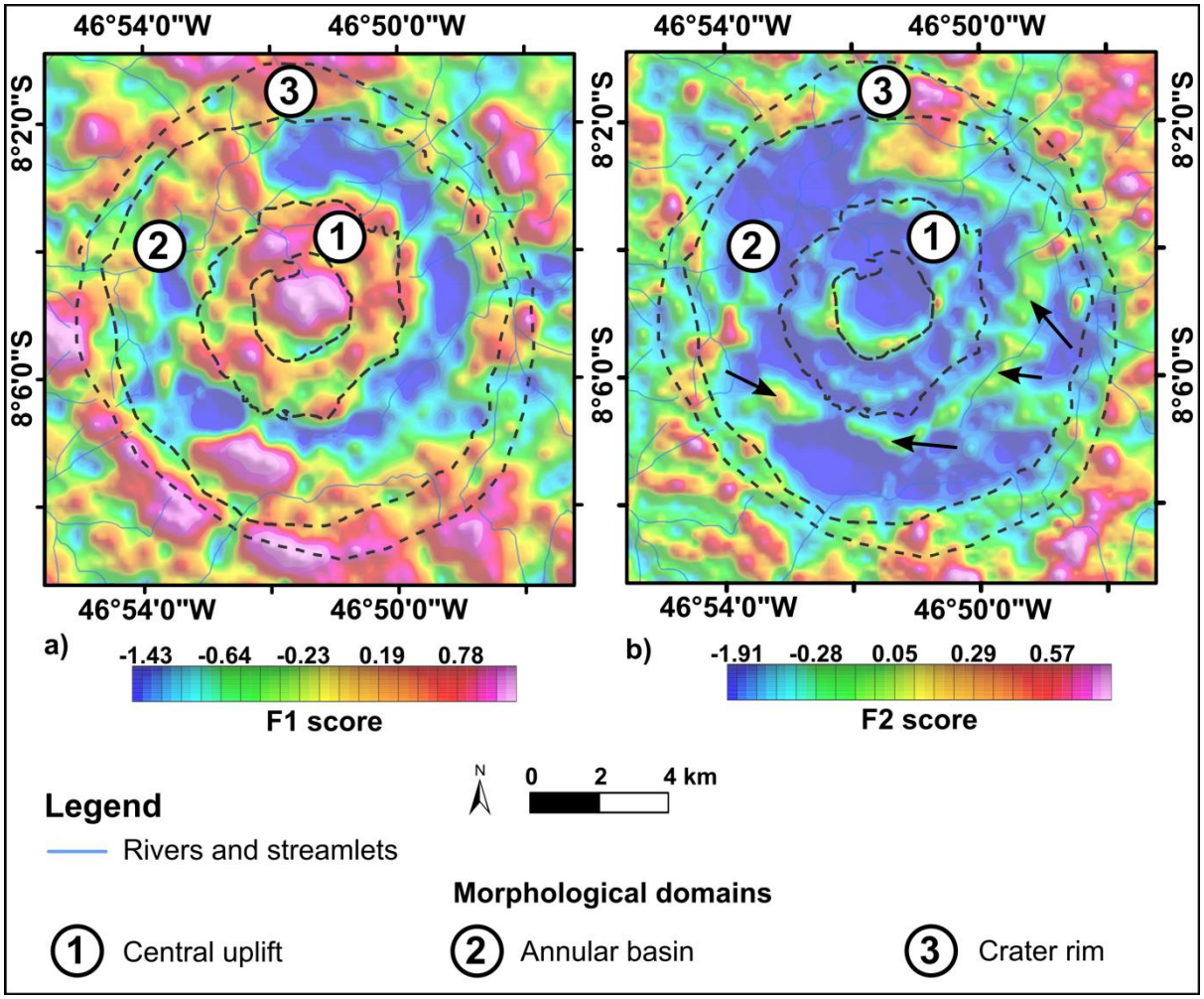

Figure 12: Factor score maps for the Serra da Cangalha impact structure. a) First factor score map. b) Second factor score map. The black arrows indicate hill-like features discussed in the text.

valuable information that is not readily visible in traditional radiometric concentration and ratio maps. This is illustrated in Figures 12-14, where we have analyzed the factor score maps taking into account the morphological limits of the three impact structures. We have focused on the F1 and F2 score maps, because F3 does not show interesting features.

The F1 and F2 score maps for the Serra da Cangalha impact structure is shown in Fig. 12. From the center to the periphery of the structure, the following observations can be made: i) The innermost part of the central uplift is characterized by high scores in the F1 map and low scores in the F2 map (Figures 12a and 12b); ii) The collar of the central uplift is

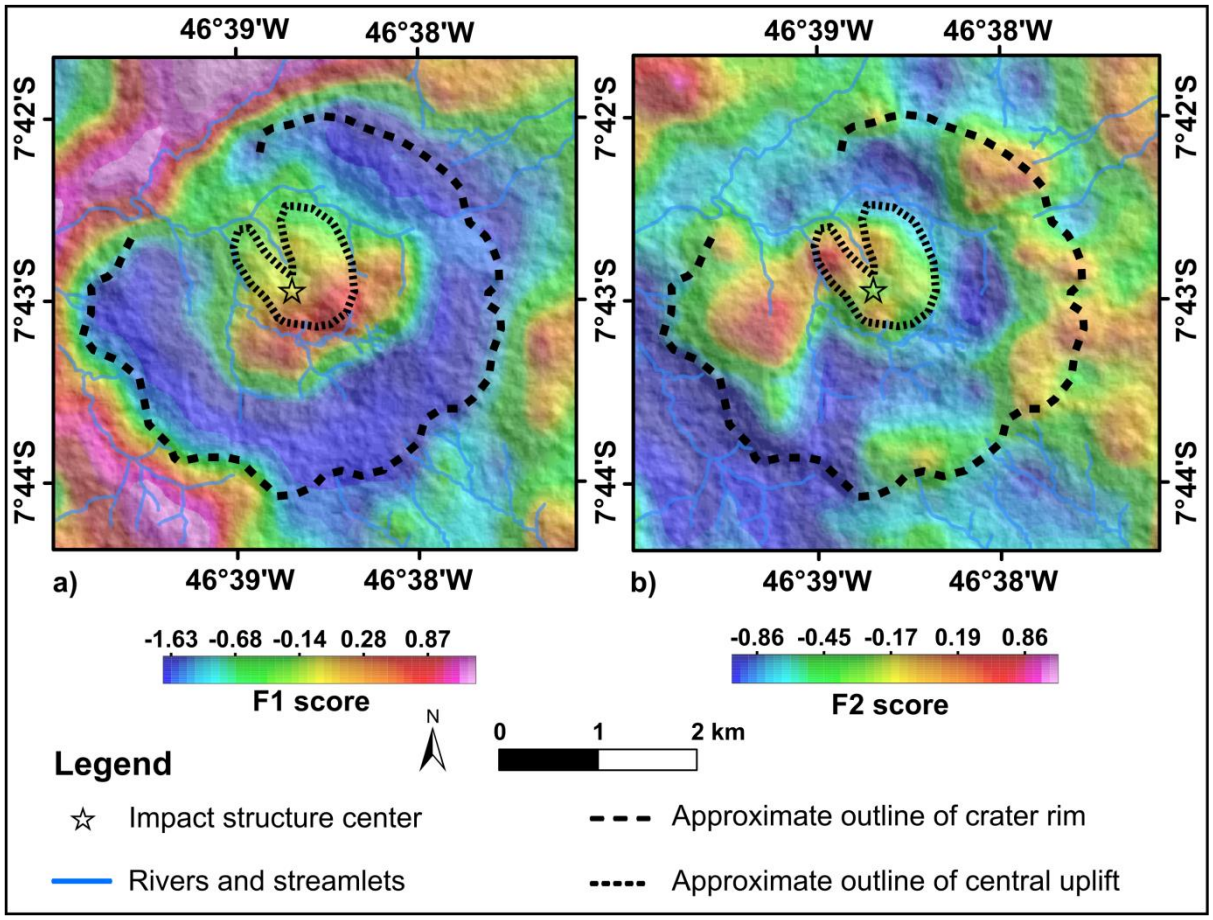

Figure 13: Factor score maps for the Riachão impact structure. a) First factor (F1) score map. b) Second factor (F2) score map.

better outlined in the F2 map than in the F1 map, whereas the outermost part of the central uplift (beyond the collar) is marked by high scores in the F1 map (Fig. 12a). iii) The annular basin area is characterized by low F1 scores, but several hill-like features with moderate values for F2 score are emphasized in this domain, mainly in the southern and eastern sectors (black arrows in Fig. 12b). v) The outermost part of Serra da Cangalha, the craterrim area, is characterized by high F1 scores. Note that the concentric radiometric distribution pattern shown in the F1 score map is similar to what was reported previously (e.g., Vasconcelos et al., 2012; Silva et al, 2024) (Compare Fig. 3 with Fig. 12) based on traditional radiometric concentration and ratio maps. However, the hill-like features seen in the F2 score map had not been identified with such traditional maps.

For Riachão, low F1 scores highlight the crater rim zone, whereas the central part of Riachão is characterized by high to moderate F1 scores, mainly in the southern/southeastern zone (Fig. 13a). The entire western sector of Riachão is marked by a curved segment with high F1 scores, which follows approximately the main streamlet in this sector (Fig. 13a). High and moderate F2 scores also occur within the Riachão impact structure, but the circular pattern seen in the F1 score map is not as clear in the F2 score map (Fig. 13a-b). When compared with a previously published radiometric map (Maziviero et al., 2013), which was based on RGB color composition of K, eTh, and eU concentrations only (Compare Fig. 5 and Fig. 13), our Factorial Analysis approach was useful in highlighting the radiometric signature of the central uplift.

The circular pattern around the rim of the Nova Colinas structure, as indicated on the geomorphological map (Fig. 4), is not noticeable in the F1 and F2 score maps (Fig. 14a and 14b). However, some other interesting information can be extracted from them: For instance, in the northern sector, several plateaus are noted with high F1 scores (e.g., black arrow in Fig. 14a). Also, high F1 scores are seemingly following drainage channels (see white arrows in Figure 14a), and some isolated zones with high scores are seen in Figure 14a (see blue arrows in Fig. 14a). In the F2 score map, the central zone of the NVC impact structure is characterized by high F2 scores (black arrows in Figure 14b), whereas a peripheral, approximately circular zone in the immediate environs of this central zone is characterized by low F2 scores (see white arrows in Figure 14b). In the SW sector, a part of the crater rim is marked by moderate F2 scores (see red arrow in Fig. 14b), whereas the surroundings are characterized by low F2 scores. High F2 scores also occur in the NW and NE sectors of the NVC impact structure. Finally, it is worth mentioning that, although some of these radiometric signatures was already visible in the previous maps (Compare Fig. 7 and Fig. 14), our F2 score map apparently highlighted the radiometric contrast in Nova Colinas, mainly in relation to the annular basin sector.

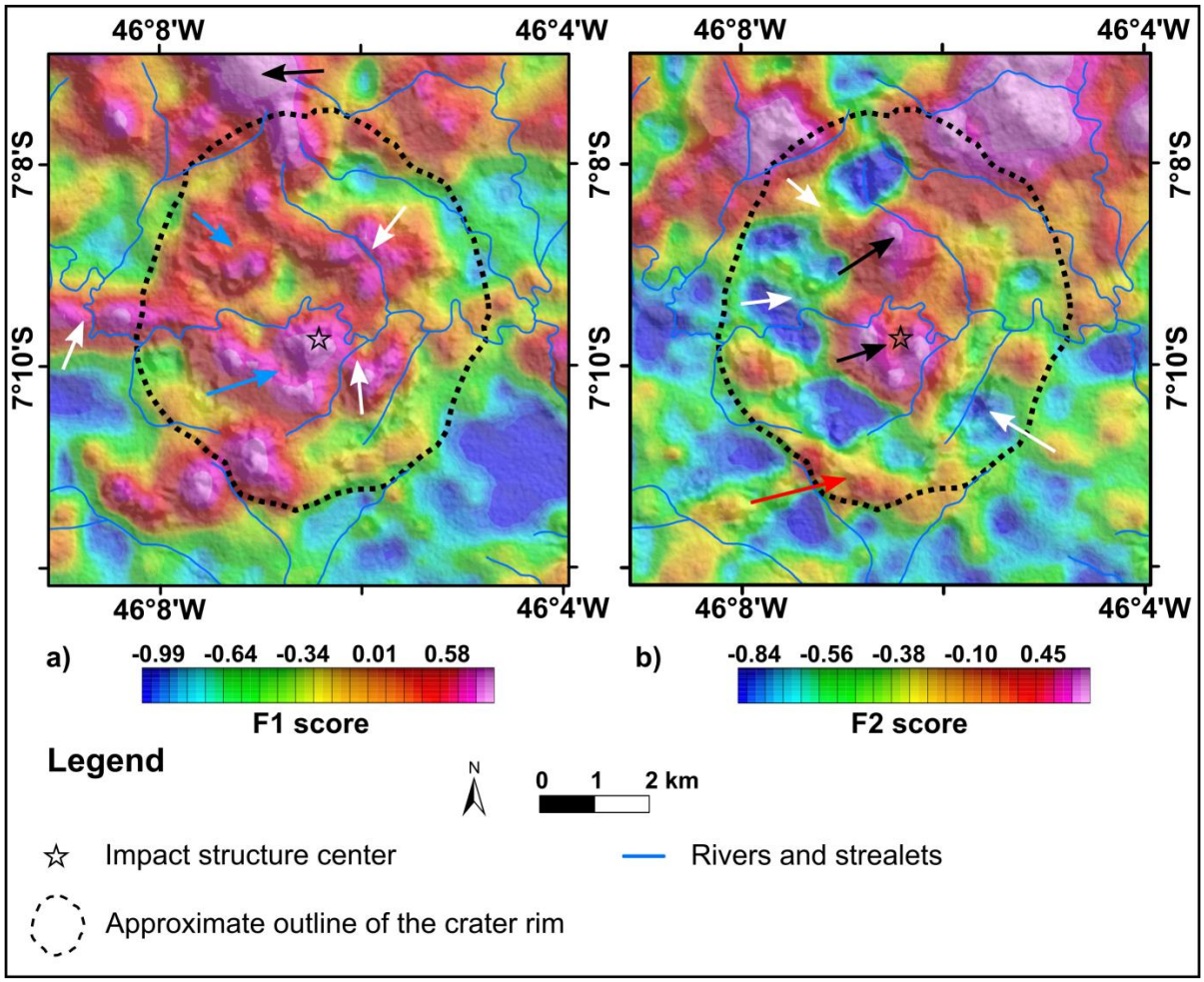

Figure 14: Factor score maps for the Nova Colinas impact structure. a) First factor (F1) score map. b) Second factor (F2) score map. The different colored arrows emphasize some particular effects discussed in the text.

13.6.4 Ground-based gamma-ray spectrometry data compared with chemical analyses

The results derived from ground-gamma ray spectrometry and chemical analysis for the Nova Colinas structure are presented in Figures 15 and 16 and in the Tables 3 and 4. Figure 15 shows that basalts outside of the Nova Colinas structure (sample NC86, see location Fig. 6) are the most K-rich lithological group. On the other hand, the silicified sandstones and other sandstones form the lithological groups with the lowest radioactivity, mainly in terms of K content (K < 0.5 %) (Fig. 15a). The only exception is a sandstone from the central uplift (NC57) that has a K content > 1 % (Fig. 15a).

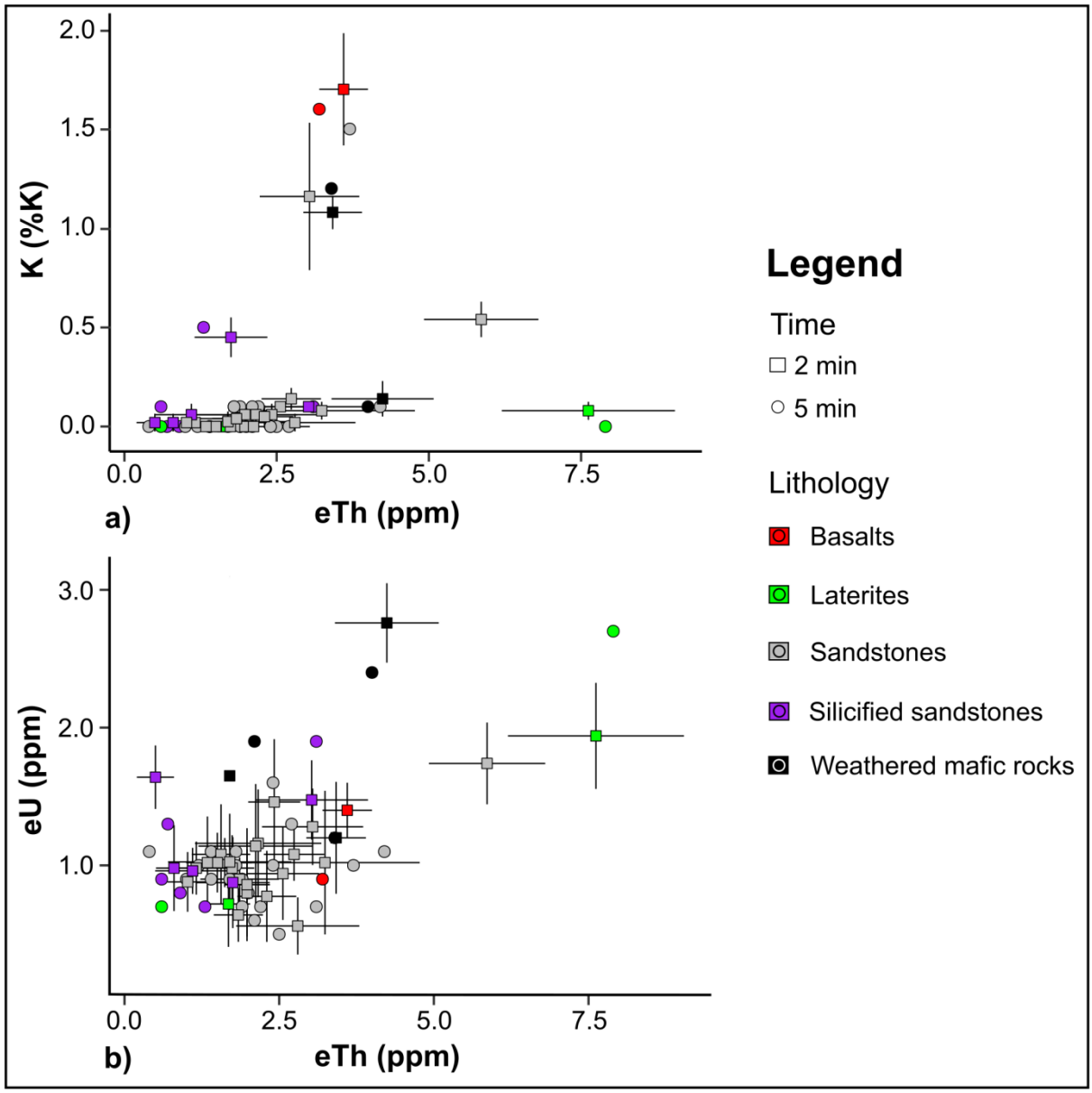

Figure 15: Ground-gamma-ray measurements taken with two acquisition time on the Nova Colinas impact structure. a) Scatterplot of percent of total potassium and equivalent thorium concentration. b) Scatterplot of equivalent uranium and thorium concentrations. The light grey lines in the squares refer to error bar (standard deviations) of the measures taken in 2 min.

Table 3: Results of chemical analysis showing the major and trace elements of Nova Colinas impact structure samples. Abbreviations: WMR = Weathered mafic rocks; SDE = Sandstones; SS = Silicified sandstones; BST = Basalts.

Sample	NC55a	NC55c	NC57	NC58	NC61b	NC64	NC65	NC66	NC67	NC70	NC74	NC82	NC85	NC86	NC87
Lithology	WMR	SDE	SDE	SDE	WMR	SS	SS	SDE	SDE	SDE	SDE	SDE	SDE	BST	SDE
SiO_2	36.16	95.04	92.73	95.19	51.66	98.26	98.11	96.44	95.26	89.33	91.92	98.17	96.37	50.10	88.84
TiO_2	1.84	0.07	0.03	0.04	1.01	0.12	0.00	0.05	0.07	0.23	0.16	0.03	0.05	1.00	0.43
Al_2O_3	29.26	2.48	3.44	2.83	13.94	0.26	0.14	1.65	1.93	5.14	3.23	0.64	1.20	13.78	4.93
Fe_2O_3	19.69	0.29	0.35	0.21	9.99	0.32	0.38	0.27	0.63	1.95	1.96	0.21	0.35	9.91	2.71
MgO	0.00	0.14	0.18	0.15	6.82	0.16	0.17	0.15	0.14	0.13	0.16	0.14	0.14	6.89	0.14
CaO	0.04	0.03	0.04	0.04	9.18	0.06	0.06	0.04	0.03	0.04	0.04	0.02	0.03	9.74	0.04
Na_2O	0.26	0.32	0.35	0.31	2.17	0.32	0.31	0.32	0.31	0.34	0.34	0.36	0.31	2.05	0.32
K_2O	0.01	0.03	1.16	0.08	0.97	0.04	0.02	0.04	0.02	0.13	0.17	0.02	0.04	1.52	0.10
LOI	12.90	1.31	1.18	1.47	4.48	0.42	0.81	1.00	1.22	2.74	2.04	0.43	0.81	5.16	2.74
Sum	100.16	99,71	99,46	100.32	100.22	99.96	100	99.96	99.61	100.03	100.02	100.02	99.3	100.15	100.25
Th	3.27	0.60	1.64	1.13	2.05	0.81	0.08	0.71	0.71	2.07	2.22	0.43	0.53	1.99	2.15
U	1.87	0.18	0.16	0.17	0.33	0.22	2.86	0.22	0.22	0.89	0.49	0.07	0.13	0.35	0.49

Table 4: Ground gamma- ray measurements for samples with chemical analyses.

Sample	Lithology	K (%)		eTh (ppm)		eU (ppm)	
		Acquisition time					
		2 min	5 min	2 min	5 min	2 min	5 min
NC55a	Weathered mafic rocks	0.14±0.9	0.1	4.24±0.84	4.0	2.76±0.28	2.4
NC55c	Sandstones	0.00±0.00	0.0	1.56±0.47	2.0	1.08±0.36	0.8
NC57	Sandstones	1.16±0.37	1.5	3.04±0.82	3.7	1.28±0.28	1.0
NC58	Sandstones	0.00	0.1	2.56±0.58	1.8	0.94±0.34	1.0
NC61b	Weathered mafic rocks	1.08±0.08	1.2	3.42±0.48	3.4	1.2±0.41	1.2
NC64	Silicified sandstones	0.00	0.1	3.2±0.0.91	3.1	1.47±0.29	1.9
NC65	Silicified sandstones	0.06±0.05	0.1	1.1±0.6	0.6	0.96±0.17	0.9
NC66	Sandstones	0.00	0.1	1.98±0.08	2.2	0.8±0.32	0.7
NC67	Sandstones	0.00	0.0	1.5±0.34	1.4	1.02±0.22	1.1
NC70	Sandstones	0.06±0.05	0.0	2.42±0.42	2.7	1.46±0.46	1.3
NC74	Sandstones	0.54±0.08	0.0	5.86±0.93	0.4	1.74±0.3	1.1
NC82	Sandstones	0.025±0.05	0.0	1.7±0.99	2.4	1.02±0.35	1.0
NC85	Sandstones	0.02±0.04	0.0	1.02±0.32	1.2	0.88±0.22	1.0
NC86	Basalts	1.7±0.28	1.6	3.6±0.4	3.2	1.4±0.2	0.9
NC87	Sandstones	0.05±0.05	1.9	2.3±0.48	0.9	0.77±0.33	0.9

A K value > 1 % was also observed in a sample (NC61b) of weathered mafic rock collected on the southwestern outer rim of Novas Colinas. However, another sample (NC55a) of weathered mafic rock collected close to the previous sample has K < 0.1 %. The NC55a sample also has > 2 ppm eU, whereas the other lithological groups (silicified sandstones, sandstones, and basalts) are characterized by eU concentrations < 2 ppm (Fig. 15b). Finally, eTh concentration > 5 ppm was observed in a laterite sample (NC71) from the top of the innermost part of the central uplift. In contrast, laterite (NC62) with low eU (< 1 ppm) and eTh (< 2 ppm) (Fig. 15b) concentrations were obtained at the eastern outer rim.

The results of the chemical analyses are listed in Table 3, and contrasted with the results of ground gamma-ray measurements in the Table 4. A scatter plot integrating the ground gamma-ray spectrometry data and chemical analysis is given in Figure 16.

Samples of weathered mafic rock and basalt samples are characterized by SiO_2 < 55 wt. %, and they have more TiO_2, Al_2O_3, and Fe_2O_3 than sandstones (Table 3). Samples NC55a and NC61b, both of weathered mafic rocks in the southwestern sector of the Nova Colinas outer rim are quite different in composition. The former contains more TiO_2, Al_2O_3, and Fe_2O_3, and less CaO, MgO, K_2O, and Na_2O than the other (Table 3). Ground gamma-ray and X-ray fluorescence results show higher K content in NC61b than in NC55a (Table 4 and Fig. 16a). Sample NC55a has less SiO_2 content and lower thorium and uranium contents than most sandstone (Tables 3 and 4 and Figs. 16 a–f).

Overall, sandstones commonly have SiO_2 > 90 wt. %, but two samples (NC70 and NC87) have < 90 wt. % SiO_2 (Table 3) In addition, their TiO_2 contents are > 0.2 wt. % (Table 3). One sandstone sample from the central uplift (NC57) has ground gamma-ray chemical analytical K contents larger than all other sandstones (Tables 3 and 4 and Figs. 16a and 16b). However, this same sample has thorium and uranium concentrations that are significantly larger in the geophysical analysis than the values by chemical analysis (Table 4 and Figs. 16c and 16e).

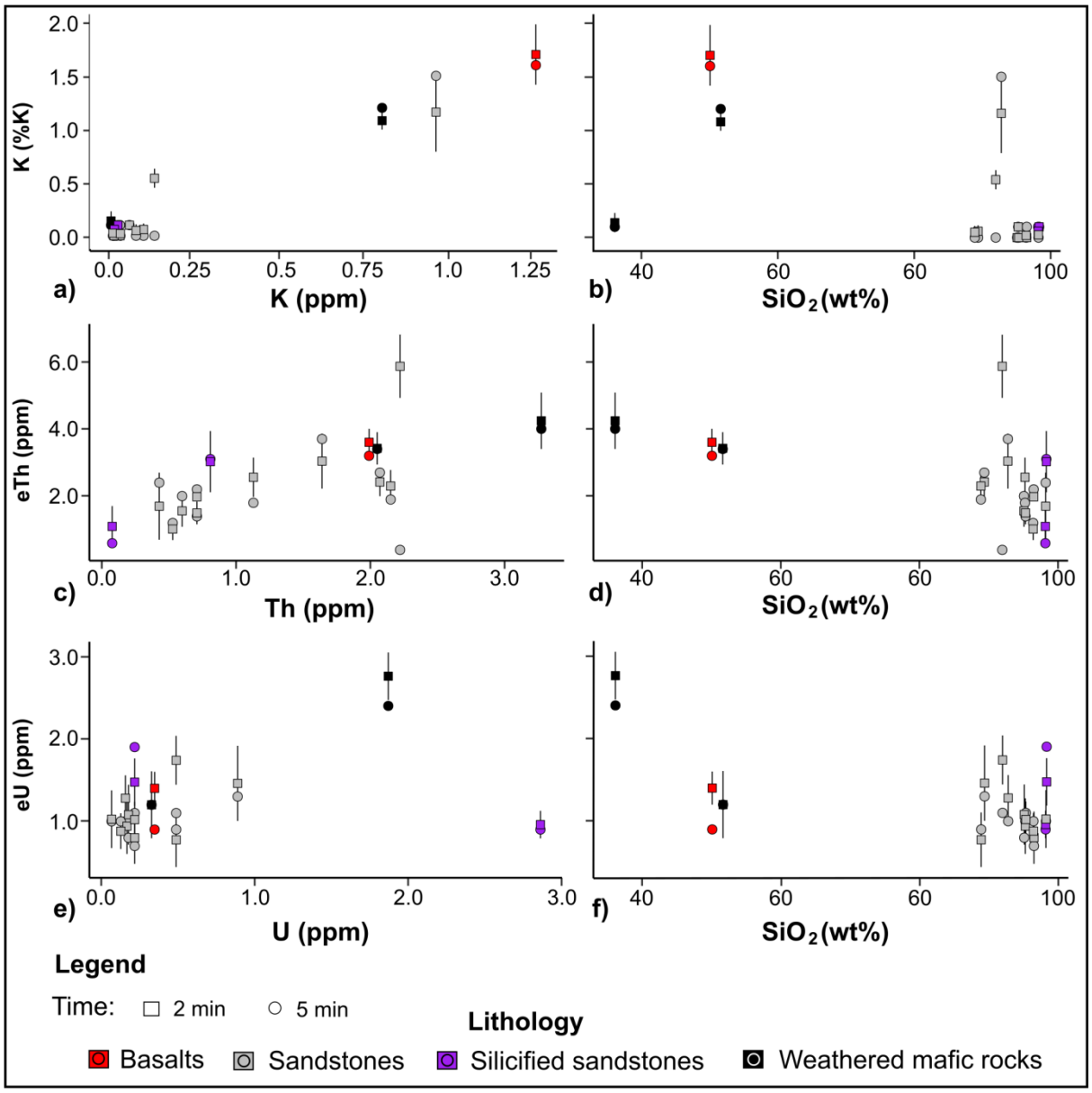

Figure 16: Integration of ground-gamma-ray measurements and chemical analysis for samples from the Nova Colinas impact structure. a) Scatter plot of percent of total potassium and K_2O. b) Scatter plot of percent of total potassium and SiO_2. c) Scatter plot of equivalent thorium and thorium concentration. d) Scatter plot of equivalent thorium and SiO_2. e) Scatter plot of equivalent uranium and uranium concentrations. f) Scatter plot of equivalent uranium and SiO_2. The light grey lines on the data points are 2sigma error bars (standard deviations) for the 2 min measurements.

The silicified sandstones are characterized by very high SiO_2 contents (>98%), and the contents of the major oxides are similar to those of the other sandstones (Table 3). However, the uranium concentrations of silicified sandstones determined by gamma-ray measurement and ICP-MS diverge. For instance: chemical analysis yielded a uranium concentration of 2.8 ppm for the NC65 sample, but the gamma-ray measurements provided concentration < 1 ppm for the same sample (Table 4 and Fig. 16e). On the other hand, gamma-ray measurements provided concentrations between 1.4 and 1.9 ppm for NC64, butICP-MS analysis gave much lower concentration (~0.22 ppm). The exact source of this discrepancy is unknown, but it may be related to the source–detector geometry of handhold gamma-ray instrument which may record gamma-ray signals that come from of areas neighboring the measurement spot (Killeen et al., 2015), so that the ground gamma-ray measurements can be though as averages (regardless of whether they are taken in 2 or 5 min) and, therefore, that can fluctuate above or below a value more well accurate provided by ICP-MS. Whatever the case, these results reveal a possible link between silicification and uranium content. This link can be explored in further studies.

13.7 **Discussion**

13.7.1 Factorial Analysis applied to airborne gamma-ray spectrometry data

Factorial Analysis (FA) is a multivariate technique used to investigate the correlation structure between different input parameters. The method may lead to a reduction of dimensionality, or to construct validation in multivariate datasets (Costello and Osborne, 2005; Suhr, 2005; Goretzko et al., 2021). In order to obtain successful results from Factorial Analysis modelling, some decision-making is required regarding factorability and the extraction, retention, and rotating of factors (Gaskin and Happell, 2014). For this reason, we must evaluate how our respective decisions may have affected the quality of Factorial Analysis modelling for the radiometric datasets of three Brazilian impact structures.

Our airborne gamma-ray spectrometry (AGRS) datasets yielded Kaiser-Meyer-Olkin (KMO) values of ~ 0.5 and Bartlett's test of Sphericity (BtS) p-values numerically equal to zero. According to Kaiser's table, KMO values of ~ 0.5, although acceptable for FA, are considered "miserable", whereas KMO > 0.8 are considered "meritorious" (Kaiser, 1974; Kaiser and Rice, 1974).

The FA fundamentals were based on psychometric studies, such that the KMO values suggested by Kaiser's table (ibid) may not provide good guidance to define the factorability of geoscience data, such as airborne radiometric datasets. Moreover, as several external effects may affect the gamma-ray data (e.g., soil mixture, vegetation, agriculture, eU disequilibrium, statistical noise, inter alia - Killeen et al., 2015), the actual correlation level for our datasets may be lower than calculated. Likewise, the BtS method may be practically insensitive to airborne gamma-ray spectrometry datasets because the number of samples along the flight lines is incredibly high and the different radioelements may have similar behavior (mainly U and Th). Thus, it makes sense that some level of correlation is present in the data and, consequently, BtS values are equal to zero. Based on this discussion and taking into account the high correlation levels demonstrated in the correlation charts (Fig. 6 and Supplementary Material), and that our FA yielded factors with high loadings and high communalities, we may conclude that our datasets for Serra da Cangalha, Riachão, and Nova Colinas are indeed factorable. However, we encourage the development of further studies to quantitatively investigate the factorability of airborne gamma-ray data. Such studies may assess the behavior of BtS p-value (maintaining the significance level constant) as a function of increasing the airborne gamma-ray measurements along the flight lines that cross a specific lithotype (e.g., a granitic intrusion). The goal here would be to investigate the number of data points needed for the correlation level between radiometric variables to become significant, thus allowing the dataset to be factored.

The logical next step is now to discuss the methods for extraction, retention and rotation of factors. Although we have extracted the factors with only a single method

(i.e., Principal Component), our results (i.e., high factor loadings and high communalities) suggest that the process was successful. Regarding retention of factors, this study has corroborated the recommendation of previous work by demonstrating that using at least two retaining methods (i.e., Parallel Analysis - PA and Amount of Explained Variance - AEV) may be suitable to determine how many factors must be retained in the FA (Williams et al., 2010; Gaskin and Happell, 2014). Moreover, our results confirm that the Kaiser-Guttman rule can lead to underestimation of factor numbers, in accordance with previous studies (e.g., Fabrigar et al., 1999; Gaskin and Happell, 2014) that pointed out serious shortcomings of the Kaiser-Guttman rule as a criterion for factor retention. Finally, our results regarding factor retention criteria may be useful for subsequent studies, as factor retention analysis has not been suitably addressed in previous studies of factor analysis applied to AGRS data (e.g., Duval, 1977; Hussein et al., 1995; Asfahani et al., 2005; Alkhateeb et al., 2019).

We have verified that the varimax orthogonal rotation method yields factor solutions with high reliability. The high factor loadings (> 0.8) and high communalities (>0.7) seen for the three AGRS datasets support this reliability (Costello and Osborne, 2005; Williams et al., 2010). Considering everything that has been discussed up to this point, we conclude that Factor Analysis with the AGRS datasets for these three impact structures has been successful.

13.7.2 Interpretation of the main factors controlling the distribution of radioelements

In the previous section, we have shown that Factorial Analysis has worked as a condenser of dimensionality for all three datasets, such that we observed similarities between the individual radiometric maps and the factorial score maps. In the following, we will propose an interpretation of these factors in terms of which geological

phenomena could be responsible for the radioelement correlation observed in these three impact structures.

Serra da Cangalha: the first factor (F1) is a common factor that can explain the TC, eTh, and eU variances, whereas F2 is a common factor that can explain the eU/K, eTh/K, and 1/K variances. One of the geological processes that may lead to mismatch between K, eTh, and eU behavior is chemical weathering.

Weathering processes commonly lead to a concomitant increase of TC, eTh, and eU, whereas K contents may be reduced. These effects arise from U and Th being retained in iron oxides and clay minerals, whereas K may be leached from the system (e.g., Megumi and Mamuro, 1977; Wilford and Minty, 2007; Reinhardt and Hermann, 2018). Regarding TC, previous work has demonstrated that clay contents of soil or rock can be estimated from this value because U and Th contribute to the TC signal (Taylor et al., 2002; Priori et al., 2013). These observations suggest that weathering is a factor that could explain the common variance among TC, eTh, and eU that we are also noting for the surface-near materials in the Serra da Cangalha structure. In fact, high F1 scores for the SdC crater rim would be readily explained by lateritic cover that was also proposed as a source of high eTh and eU content in this area (Vasconcelos et al., 2012). On the other hand, high F1 scores for the innermost area of the central uplift structure could be associated with Longá Formation shales and siltstones, as these lithologies and their weathering products ought to be rich in radioelements, mainly Th and U (ibid). Alternatively, and as Serra da Cangalha's innermost area is a topographically depressed depositional zone, the specific radiometric signature in this zone could come from erosional sediments deposited recently and whose source area is nearby (Wilford and Minty, 2006). The strongly elevated collar zone formed by sandstone is the likely source for such recent accumulation of sediment (Silva et al., 2024). We, thus, conclude that F1 is dominantly a weathering factor, but it probably also contains some TC, eTh, and eU variances due to depositional and lithological aspects.

Although the increased values of eU/K, eTh/K and 1/K could also arise from weathering processes, as discussed regarding F1, there may be another explanation for the regional F2 distribution. Considering the spatial distribution of F2 scores (our Fig. 12b) and that the Serra da Cangalha collar is well defined by moderate F2 scores, it becomes plausible to interpret F2 as an erosion factor because the collar is a residual landform. However, as soil formation is incipient in areas where erosion is active, the radiometric signature in such areas probably relates to bedrock (Wilford et al., 1997). Thus, we consider F2 as a residual lithological factor in the Serra da Cagalha case. In this sense, the hill-type features with moderate F2 scores within the annular basin that are identified in this study (see the black arrows in our Fig. 12b) could be related to a lithostratigraphic unit that has been exposed by erosion, as already proposed by Silva et al. (2024). However, we recommend additional field studies to investigate these F2 related hill-type features.

Riachão: The F1 is a common factor that can be utilized to explain the TC, eTh, eU, and K variances, whereas F2 is a common factor that explains mainly the eU/eTh and eTh/K variances. Mazivieiro et al. (2013) suggested that the high K concentration in the central part of Riachão could be associated with the phyllosilicate cement of Piauí sandstone, whereas low values of K, eTh, and eU along the crater rim could be due to weathering-driven remobilization of radioelements. We note that both the topographically subdued central uplift and the crater rim zones of the Riachão impact structure are marked by high and low F1 scores, respectively. Considering the factor loadings, we prefer to regard F1 as a lithological factor in this case. Our reasons are: i) if weathering were the main mechanism for the K, eTh, and eU distribution, the correlation structure should be similar to F1 in SdC, that is TC, eU, eTh should not be correlated with K. ii) Although correlation between K, Th, and U for sedimentary rock is less marked than for igneous rock, it may still be noticeable (Galbraith and Saunders, 1983; Dentith and Mudge, 2014). Some correlation could be expected when first order factors (e.g., a lithological one) drive the K, U, Th distribution (Saunders et al., 1994),

even when the source is relatively poor in radioelements (e.g., sandstones). The low F1 scores over the Riachão crater rim are clearly related to the low abundances in radiometric elements in these sandstones. Similarly, the phyllosilicate cement of the Piauí sandstone in the inner part of the structure is relatively enriched in K, Th, and U. Therefore, the small central uplift area at Riachão is characterized by high to moderate F1 scores.

A third observation at Riachão is that the radiometric signature that indicates the curved segment with high F1 scores in the western portion of the structure (Fig. 12a) may be related to surficial material deposited along streamlets, so that F1 would also account for variances related to depositional processes. The zone separating areas with high and low F1 scores in the western sector of Riachão helps in the delimitation of the northwestern crater rim. Finally, eTh/K and eU/K ratios are also indicative of weathering. Thus, we propose that F2 is a weathering factor at Riachão. In this case, weathering-driven remobilization of radioelements along the crater rim zone, as proposed by Mazivieiro et al. (2012), would be associated with high F2 scores.

Nova Colinas: The correlation structure for the Nova Colinas data is similar to that for Serra da Cangalha. However, at Nova Colinas the F2 factor basically reflects the spatial K distribution. Similar to Serra da Cangalha, the F1 scores probably reflect weathering because this factor is loaded by the TC, eTh, and eU variables. The laterites/latosols on the top of plateaus in the northern sector of Nova Colinas are characterized by high F1 scores (black arrow in Fig. 14a), which support our interpretation. Furthermore, ground-based gamma-ray measurements with two different acquisition times show that the laterites are rich in eTh and eU, but poor in K. The results for strongly weathered sample NC55a (mafic rock) revealed typical characteristics of chemical weathering: concentration of resistant elements such as Fe, Ti, Th, and U, and leaching of more mobile elements such as K, Ca, and Na. The low amount of SiO_2 and high amount of Al_2O_3 observed in this sample NC55a further emphasizes how intense this process has been. Note that, like at Serra da Cangalha

and Riachão, F1 scores also account for variances of depositional processes because high F1 scores seem to follow main drainage channels (such as the east-west trending bed of the Macapá River) (compare Fig. 15a).

Previous work suggested that high eTh and eU in the innermost portion of Nova Colinas central zone could be related to lateritic cover (Silva, 2020). As high F1 scores also occur in this central zone, the present study corroborates that eTh and eU concentrations are related to laterites on top of the innermost Nova Colinas central uplift. One of our ground gamma-ray measurements on a laterite outcrop (NC71) (see Figs. 6 and 15a) confirmed that such laterite covers are indeed quite rich in eTh and eU, but very poor in K.

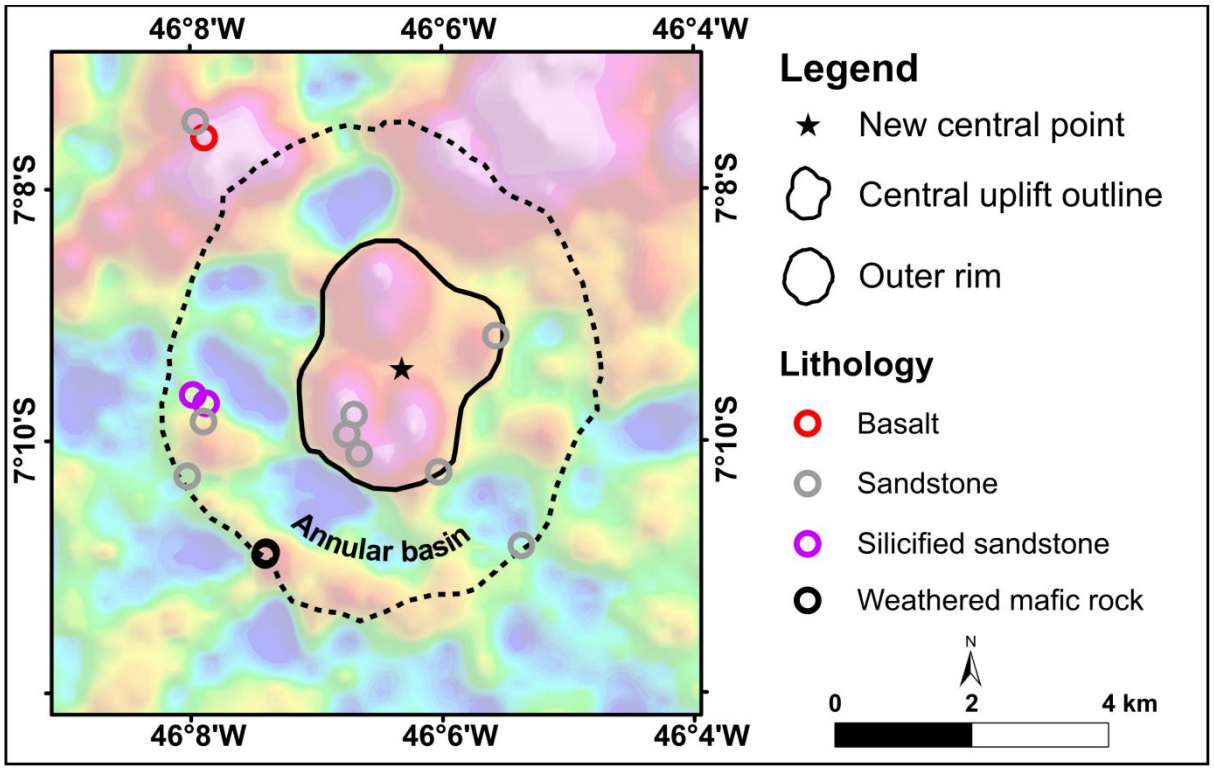

Figure 17: Second factor (F2) score map with the locations of samples containing ground gamma-ray measurements and chemical analysis.

Previous work has suggested that K concentration in the central zone at Nova Colinas could be related to the radiometric signature of a lower stratigraphic unit that was uplifted during collapse of the transient cavity (Silva, 2020; Reimold et al., 2022).

However, our F2 score map, ground-based gamma-ray measurements, and chemical analyses show that the K distribution is more complex than previously thought (compare Fig. 15b).

To better understand the K distribution at Nova Colinas, we prepared the map in Fig. 17, where analytical data from chemical analyses and ground gamma-ray measurements are superimposed onto the F2 score map. This map shows a concentric pattern of K distribution in the Nova Colinas structure, with a central zone characterized by high F2 scores, surrounded by a zone of low F2 score, and then further out, a discontinuous zone of high F2 scores (Fig. 17). This discontinuous zone appears to be better represented in the southwestern part of the outer rim. In our interpretation, the high F2 scores in the southwestern portion of the Nova Colinas outer ring are likely related to the K content still present in the intensely weathered mafic rock. Because the content of major elements in samples NC61b (weathered mafic rock) and NC86 (basalt) are similar, we interpret that the bedrock of the weathered mafic rock would be basalt of the Mosquito Formation, for which fresh outcrop occurs to the north of Nova Colinas. This interpretation is consistent with previous work that has claimed to have discovered impact-generated shatter cones in basalt in the southwestern rim zone (Avona et al., 2025). However, instead of featuring a continuous outer rim of basalt as proposed by Avona et al. (2025; see their geological map, their fig. 4a), the outer rim cover at Nova Colinas is intensely weathered and eroded, so that several wide breaches are evident in the F2 map. Note that the intensity of weathering is also suggested by the concentrations of resistant elements and loss of mobile elements, for example from sample NC55a discussed early.

The low F2 score zone can be interpreted as an annular basin with a cover of sandstones and silicified sandstones (Fig. 17). Since such lithologies show very low K contents, they appear as low F2 scores.

Identifying the cause of the relative K enrichment in the central zone is more challenging. On the one hand, the Nova Colinas central area is composed of sandstones that are generally poor in K. On the other hand, K concentrations as, for example, seen in the NC57 sandstone sample are significant and they could suggest some kind of K enrichment process (e.g., hydrothermal alteration). Alternatively, this effect could be related to mobilization and deposition of K at the bottom of hills topped by laterite. Uplift of strata comparatively enriched in K-feldspar during the collapse of the transient crater could also be a plausible alternative explanation. However, because only one of our samples yielded a significant amount of K, the possibilities listed above for the K source in the central zone should be investigated in more detail in subsequent studies (chemical analysis and ground gamma-ray data acquisition). Despite the uncertainty regarding the K source in the Nova Colinas central zone, our results show progress with respect to the dimension of the central uplift. Here, we assume a diameter of 3.1 – 3.6 km for the Nova Colinas central uplift (Fig. 17). Note that in this new configuration, the central point of Nova Colinas is slightly (by ~670 m) shifted towards the NNE, so that the structure is now centered at 7°09'23" S / 46°06'19 W (Fig. 17).

Based on what has been discussed so far, we interpret F2 at Nova Colinas as a residual lithological factor as concluded for Serra da Cangalha. In summary, weathering and residual lithological effects seem to be the main mechanisms that determine the radiometric distribution patterns over the impact structures investigated here. Our interpretations of these factors corroborate the findings of previous studies (e.g., Kenkmann et al., 2011) that argued in favor of differential resistance to erosion and weathering of the main lithologies responsible for the differential radioelement distribution within the Serra da Cangalha structure. We can extend this argument to Riachão and Nova Colinas, which were formed in the same lithostratigraphic setting of the southern Parnaiba Basin as Serra da Cangalha.

Finally, based on the presence of an open sector or outer rim with discontinuous aspect, lack of ejecta deposits and within-crater impactite deposits, quasi-vertical loss to erosion has been estimated for these impact structures (e.g., 500 m for Serra da Cangalha and Riachão - Kenkmann et al., 2011; Maziviero et al., 2013), this study has corroborate the hypothesis that weathering has played a strong role in modifying or erasing structural features or impactite deposits at these three impact structures.

13.7.3 Factorial Analysis as validation of K or eU deviation maps

Although this study is focused on the correlation structures of airborne gamma-ray spectrometry (AGRS) data for three impact structures, our findings transcend the theme of this study and are applicable to other AGRS datasets and to other interpretative techniques, such as K and/or eU deviation maps (also known as K and/or eU “anomalous” maps) (Saunders et al., 1987; Saunders et al., 1994; Pires, 1995).

The idea behind deviation maps is basically to subtract a background from the original K or eU concentrations such that the resulting residuals can be used to indicate seemingly anomalous concentrations of K or eU (Saunders et al., 1987; Saunders et al., 1994; Pires, 1995). In order to estimate the background, it is assumed that first-order processes such as lithology, detector geometry, and soil mixing tend to simultaneously change K, eTh, and eU concentrations, whereas second order processes (e.g., hydrothermal alteration) tend to selectively change individual radioelement concentrations. As Th is less mobile than K and U, and considering there are approximately linear relationships between K and eTh and between eU and eTh (Galbraith and Saunders, 1983; Saunders et al., 1994), it is possible to estimate K or eU concentrations from eTh concentrations, that is, to estimate “ideal” values of K or eU that would be expected if only first-order factors would be operative (Saunders et al., 1994). By subtracting such “ideal” values from original measurements of radioelement concentrations, the residual values, or deviations, can be utilized as

indicators of selective remobilization. For instance, hydrothermal alteration may result in an increase of the concentration of K without a corresponding increase in the concentration of Th (the so-called “K/eTh antagonism”, Ostroviskiy, 1975; Shives et al., 2000; Dutra et al., 2023). Similarly, in potential areas for sedimentary phosphate or oil/gas prospecting, eU concentrations may increase without concomitant increase in eTh (e.g., Saunders et al., 1994; Curto et al., 2012). In practice, the background estimation in such approaches assumes that there are correlations between K and eTh and/or eU and eTh.

Particularly in relation to Brazilian impact structures, “anomalous K” maps have been used as indicator of remobilization processes, for example at the Serra da Cangalha and Araguainha impact structures (Vasconcelos et al., 2012; Leite et al., 2022). However, none of these published works analyzed the correlation matrix of radiometric data acquired for these impact structures and they also did not discuss which mineral or rock types would be the source of alleged anomalous radiometric signals.

As demonstrated in this study, there is no correlation between K and eTh in the Serra da Cangalha and Nova Colinas datasets, and the Factorial Analysis model suggests that there are no common variances between K and eTh in these datasets either. In such cases, interpretations based only on K deviation maps may be statistically erroneous. On the other hand, the K deviation map approach could be applied to the Riachão dataset, because, and as we have shown, there is reasonable correlation between K and eTh, allowing estimating a suitable background. Consequently, we recommend that the correlation matrix must be analyzed prior to computation of a background. If significant statistical correlation is present in a given dataset, background removal can be used to compute K or eU deviation maps, regardless of the context studied.

13.8 **Conclusions**

This study was carried out to investigate how Factorial Analysis (FA) could be applied to explore the correlation structures of airborne gamma-ray spectrometry (AGRS) data acquired for the Serra da Cangalha – SdC, Riachão – RR, and Nova Colinas impact structres in Brazil. We applied Factorial Analysis to these AGRS datasets by following clear decision-making criteria regarding factorability and extraction, retaining, and rotation of factors. We analyzed communalities and factor loadings, generated factor score maps, and considered the previous and new geological information. Thus, we can conclude:

- A three-factor model can explain the totality of explained variance of the AGRS dataset for each impact structure, such that the FA allows dimensionality reduction.
- Overall, two first factors (F1 and F2) dominantly express weathering and lithology effects, but depositional processes seem to have contributed to the variances explained by these factors.
- In the SdC impact structure, the F2 score map reveals hill-type features that could be associated with a lithostratigraphic unit that has been exposed by erosion.
- In Riachão, the F1 score map is useful to highlight the radiometric contribution that comes from the central uplift.
- For Nova Colinas, the F2 score map is useful to identify a circular zone at the periphery of the central uplift that is characterized by low F2 scores that might represent the annular basin of this structure. Furthermore, the F2 score map also reveals a zone in the SW sector of the crater rim with a radiometric signature that can be attributed to residual K content in weathered mafic rock. For the central zone, the source of K is unknown, but hydrothermal, depositional, or compositional aspects could be responsible.

- Our results emphasize how FA can be useful to highlight spatial features that may not be readily visible on traditional radiometric maps.

13.9 **Acknowledgement**

The authors are grateful to the Brazilian National Agency of Petroleum, Natural Gas and Biofuels and to the Remote Sensing and Geophysics Division of the Geological Survey of Brazil for having made the airborne geophysical data used here available. This work is part of the first author´s MSc thesis within the Postgraduate Program in Geology of the Institute of Geosciences at the University of Brasília. This work was carried out with the partial support of the Coordenação de Aperfeiçoamento de Pessoal de Nível Superior – Brasil (CAPES) – under Finance Code 001. W.U.R.´s research is partially supported by a the Brazilian National Council for Scientific and Technological Development (CNPq) (grant no 305761/2019-6).

13.10 **Data Availability**

The airborne gamma-ray spectrometry data used in this work are available freely on the REATE database website cited in the text. Data can also be requested from the first author upon request. The R code used for the application of the Factorial Analysis is available is available upon request.

13.11 **References**

Alkhateeb S. A., Hossny A. A., Ashami A. S., and Zaeimah M. A. 2019. Ground follow-up of the airborne gamma-ray spectrometric survey data, ramlet HOMAYYER area, east abu-zeneima, southwestern Sinai, Egypt. *Applied Radiation and Isotopes* 151:129–139. https://doi.org/10.1016/j.apradiso.2019.05.036

Asfahani J., Aissa M., and Al-Hent R. 2005. Statistical factor analysis of aerial spectrometric data, Al-Awabed area, Syria: a useful guide for phosphate and uranium exploration. *Applied radiation and isotopes* 62:649–661. 10.1016/j.apradiso.2004.08.050

Avona, P. D., Crósta, A. P., Vasconcelos, M. A. R., Bjonnes, E., Pereira, F. L., & Góes, A. M. (2025). Geology, gravity, and numerical modeling of the Nova Colinas impact

structure, Parnaíba Basin, Brazil. *Meteoritics & Planetary Science 60 (2): 286 – 307. https://doi.org/10.1111/maps.14306*

Bai A., Hira S., and Deshpande P. S. 2015. An application of factor analysis in the evaluation of country economic rank. *Procedia Computer Science* 54:311–317. https://doi.org/10.1016/j.procs.2015.06.036

Baratoux D., Niang C. A. B., Reimold W. U., Sapah M. S., Jessell M. W., Boamah D., Faye G., Bouley S., and Vanderhaeghe O. 2019. Bosumtwi impact structure, Ghana: Evidence for fluidized emplacement of the ejecta. *Meteoritics & Planetary Science* 54: 2541–2556. https://doi.org/10.1111/maps.13253

Bartlett M. S. 1950. Tests of significance in factor analysis. *British journal of psychology*, 77 – 85. https://doi.org/10.1111/j.2044-8317.1950.tb00285.x

Costa I. S. L., Tavares F. M., and Oliveira J. K. M. de. 2019. Predictive lithological mapping through machine learning methods: a case study in the Cinzento Lineament, Carajás Province, Brazil. *Journal of the Geological Survey of Brazil* 2: 26–36. https://doi.org/10.29396/jgsb.2019.v2.n1.3.

Costa I. S. L., Serafim I. C. C. D. O., Tavares F. M., and Polo H. J. D. O. 2020. Uranium anomalies detection through Random Forest regression. *Exploration Geophysics* 51: 555–569. https://doi.org/10.1080/08123985.2020.1725387

Costello A. B., and Osborne J. 2019. Best practices in exploratory factor analysis: Four recommendations for getting the most from your analysis. *Practical assessment, research, and evaluation* 10: 7. https://doi.org/10.7275/jyj1-4868

Crósta A. P., Reimold W. U., Vasconcelos M. A. R., Hauser N., Oliveira G. J. G., Maziviero M. V., and Góes A. M. 2019. Impact cratering: the south American record–Part 1. *Geochemistry* 79: 1–61. https://doi.org/10.1016/j.chemer.2018.06.001

Curto J. B., Pires A. C. B., Silva A. M., and Crósta Á. P. 2012. The role of airborne geophysics for detecting hydrocarbon microseepages and related structural features: The case of Remanso do Fogo, Brazil. *GEOPHYSICS* 77: B35–B41. https://doi.org/10.1190/geo2011-0098.1

Dentith M., and Mudge S. T. 2014. *Geophysics for the Mineral Exploration Geoscientist:* 1st ed. Cambridge University Press, p. 454. https://doi.org/10.1017/CBO9781139024358

Dietz R. S., and French B. M. 1973. Two Probable Astroblemes in Brazil. *Nature* 244:561–562. https://doi.org/10.1038/244561a0

Dutra L. F., Louro V. H. A., and Monteiro L. V. S. 2023. The southern IOCG and hydrothermal nickel mineralization trend of the Carajás Mineral Province: Airborne geophysical and remote sensing evidences for structural controls and hydrothermal signature. *Journal of Applied Geophysics* 213: 105016. https://doi.org/10.1016/j.jappgeo.2023.105016

Duval J. S. 1977. HIGH SENSITIVITY GAMMA-RAY SPECTROMETRY—STATE OF THE ART AND TRIAL APPLICATION OF FACTOR ANALYSIS. *GEOPHYSICS* 42: 549–559. https://doi.org/10.1190/1.1440726

Fabrigar L. R., Wegener D. T., MacCallum R. C., and Strahan E. J. 1999. Evaluating the use of exploratory factor analysis in psychological research. *Psychological methods* 4: 272. https://doi.org/10.1037/1082-989X.4.3.272

Fabrigar L. R., and Wegener D. T. 2012. *Exploratory factor analysis*, Oxford University Press, USA. P. 176 .

Ferguson E., and Cox T. 1993. Exploratory Factor Analysis: A Users'Guide. *International Journal of Selection and Assessment* 1: 84–94. https://doi.org/10.1111/j.1468-2389.1993.tb00092.x

Galbraith J. H., and Saunders D. F. 1983. Rock classification by characteristics of aerial gamma-ray measurements. *Journal of Geochemical Exploration* 18: 49–73. https://doi.org/10.1016/0375-6742(83)90080-8

Gaskin C. J., and Happell B. 2014. On exploratory factor analysis: A review of recent evidence, an assessment of current practice, and recommendations for future use. *International journal of nursing studies* 51: 511–521. 10.1016/j.ijnurstu.2013.10.005

Góes A. M., and Feijó F. J. 1994. Parnaiba Basin; Bacia do Parnaiba. *Boletim de Geociências da PETROBRAS* 8.

Goretzko D., Pham T. T. H., and Bühner M. 2021. Exploratory factor analysis: Current use, methodological developments and recommendations for good practice. *Current Psychology* 40: 3510–3521. https://doi.org/10.1007/s12144-019-00300-2

Gorsuch R. L. 2014. *Factor analysis: Classic edition*, 2nd Edition, Routledge. 464 p.

https://doi.org/10.4324/9781315735740

Guttman L. 1954. Some necessary conditions for common-factor analysis. *Psychometrika* 19: 149–161. https://doi.org/10.1007/BF02289162

Horn J. L. 1965. A rationale and test for the number of factors in factor analysis. *Psychometrika* 30: 179–185. https://doi.org/10.1007/BF02289447

Hussein H. A., Rabie S. I., and Abdel Nabi S. H. 1995. Regional remapping of the basement complex outcrops, using factor analysis to spectrometric data, of the Gabal Eteiqa, Eastern Desert, Egypt. *International Journal of Remote Sensing* 16: 811–823. https://doi.org/10.1080/01431169508954445

Kaiser H. F. 1960. The application of electronic computers to factor analysis. *Educational and Psychological Measurement* 20: 141–151.https://doi.org/10.1177/001316446002000116

Kaiser H. F. 1974. An index of factorial simplicity. *Psychometrika* 39: 31–36. https://doi.org/10.1007/BF02291575

Kaiser H. F., and Rice J. 1974. Little Jiffy, Mark IV. *Educational and Psychological Measurement* 34: 111–117. https://doi.org/10.1177/001316447403400115

Kaiser, H. F. (1958). The varimax criterion for analytic rotation in factor analysis. Psychometrika 23: 187–200. https://doi.org/10.1007/BF02289233

Kaiser H. F. 1992. On Cliff's Formula, the Kaiser-Guttman Rule, and the Number of Factors. *Perceptual and Motor Skills* 74: 595–598. https://doi.org/10.2466/pms.1992.74.2.595

Kenkmann T., Vasconcelos M. A. R., Crósta A. P., and Reimold W. U. 2011. The complex impact structure Serra da Cangalha, Tocantins State, Brazil. *Meteoritics & Planetary Science* 46: 875–889. https://doi.org/10.1016/j.jsames.2013.03.007

Killeen P. G., Mwenifumbo C. J., and Ford K. L. 2015. Tools and Techniques: Radiometric Methods, Treatise on Geophysics. https://doi.org/10.1016/B978-0-444-53802-4.00209-8

Klein E. L., and Sousa C. S. de. 2012. *Geologia e recursos minerais do estado do Maranhão*, CPRM. https://rigeo.cprm.gov.br/handle/doc/17861(Accessed August 15, 2024).

Leite E. P., Lambert J., Vasconcelos M. A. R., Crosta A. P., and Batezelli A. 2022. Gamma-ray spectrometry of the Araguainha impact structure, Brazil: Additional insights into element mobilization due to hydrothermal alteration. *Anais da Academia Brasileira de Ciências* 94: e20210182. https://doi.org/10.1590/0001-3765202220210182

Marques R.P., Kassab Jr F., Molina E.C., Andrade F.A.R. (org.) 2006. Levantamentos aerogeofísicos para a identificação de áreas com ocorrência potencial de petróleo e gás na Bacia do Parnaíba – Tomo II: área Parnaíba – Aerolevantamento magnético e gamaespectrométrico: São Paulo, Convênio ANP – USP, 109 p.

Martins-Ferreira M. A. C., Campos J. E. G., and Pires A. C. B. 2017. Near-mine exploration via soil geochemistry multivariate analysis at the Almas gold province, Central Brazil: A study case. *Journal of Geochemical Exploration* 173: 52–63. https://doi.org/10.1016/j.gexplo.2016.11.011

Maziviero M.V., Vasconcelos M.A.R., Góes A.M., , Crósta, A.P., Reimold W.R. 2012. The Riachão ring impact structure, northeastern Brazil: Re-evaluation of its stratigraphy and evidence for impact: *43rd Lunar and Planetary Science Conference*, Abstract 1511.

Maziviero M. V., Vasconcelos M. A. R., Crósta A. P., Góes A. M., Reimold W. U., and De C. Carneiro C. 2013. Geology and impact features of Riachão structure, northern Brazil. *Meteoritics & Planetary Science* 48: 2044–2058. https://doi.org/10.1111/maps.12213

McHone Jr J. F. 1981. Verified impact structures in Brazil. In *Large Body Impacts and Terrestrial Evolution: Geological, Climatological, and Biological Implications*. p. 31.

McHone J. F. 1977. Riachao Ring, Brazil: A possible meteorite crater discovered by the Apollo astronauts. *Apollo-Soyuz Test Project: Summary Science Report* 1:193.

Megumi K., and Mamuro T. 1977. Concentration of uranium series nuclides in soil particles in relation to their size. *Journal of Geophysical Research* 82: 353–356. https://doi.org/10.1029/JB082i002p00353

de Mello D. C. et al. 2021. Applied gamma-ray spectrometry for evaluating tropical soil processes and attributes. *Geoderma* 381: 114736. https://doi.org/10.1016/j.geoderma.2020.114736

Mulaik S. A. 2009. *Foundations of factor analysis*, 2nd edition, CRC press, p. 548.

Niang C. A. B. et al. 2021. Systematic survey of K, Th, and U signatures in airborne radiometric data from Australian meteorite impact structures: Possible causes of circular features and implications. In *Large Meteorite Impacts and Planetary Evolution VI*, edited by Reimold W. U., and Koeberl C. Geological Society of America. https://doi.org/10.1130/2021.2550(15)

Niang C. A. B. et al. 2022. The origin of the potassium-rich annular zones at the Bosumtwi impact structure, Ghana, investigated by field study, radiometric analysis, and first cosmogenic nuclide data. *Meteoritics & Planetary Science* 57: 702–729. https://doi.org/10.1111/maps.13788

International Atomic Energy Agency (IAEA). 2003. Guidelines for radioelement mapping using gamma ray spectrometry data. IAEA, Vienna, 179 p.

O'Leary D., Brown C., and Daly E. 2022. Digital soil mapping of peatland using airborne radiometric data and supervised machine learning–Implication for the assessment of carbon stock. *Geoderma* 428: 116086. https://doi.org/10.1016/j.geoderma.2022.116086

Oliveira D. C. 2018. Petrology of Jurassic and Cretaceous basaltic formations from the Parnaíba Basin, NE Brazil: correlations and associations with large igneous provinces. *Geological Society, London, Special Publications*, 472(1), 279-308.

Ostrovskiy E. Ya. 1975. Antagonism of radioactive elements in wallrock alterations fields and its use in aerogamma spectrometric prospecting. *International Geology Review* 17: 461–468. https://doi.org/10.1080/00206817509471687

Ouchchen M. et al. 2022. Exploration targeting of copper deposits using staged factor analysis, geochemical mineralization prospectivity index, and fractal model (Western Anti-Atlas, Morocco). *Ore Geology Reviews* 143: 104762. https://doi.org/10.1016/j.oregeorev.2022.104762

Pires A. C. B. 1995. Identificação geofísica de áreas de alteração hidrotermal, Crixás-Guarinos, Goiás. *Brazilian Journal of Geology* 25: 61–68. 10.25249/0375-7536.19956168

Priori S., Bianconi G., Fantapié M., Pellegrini S., Ferrigno G., Guaitoli F., and Costantini E. A. C. 2013. THE POTENTIAL OF γ-RAY SPECTROSCOPY FOR SOIL PROXIMAL SURVEY IN CLAYEY SOILS. *EQA - International Journal of Environmental Quality* 29-38. https://doi.org/10.6092/issn.2281-4485/4086

Rawlins B. G., Lark R. M., and Webster R. 2007. Understanding airborne radiometric survey signals across part of eastern England. *Earth Surface Processes and Landforms* 32: 1503–1515. https://doi.org/10.1002/esp.1468

Reimold W. U., Cooper G. R. J., Romano R., Cowan D. R., and Koeberl C. 2006. Investigation of Shuttle Radar Topography Mission data of the possible impact structure at Serra da Cangalha, Brazil. *Meteoritics & Planetary Science* 41: 237–246. 10.1111/j.1945-5100.2006.tb00207.x

Reimold W. U. et al. 2022. Nova Colinas, Maranhão State: A newly confirmed, complex impact structure in Brazil. *Meteoritics & Planetary Science* 57: 1519–1541. https://doi.org/10.1111/maps.13833

Reinhardt N., and Herrmann L. 2019. Gamma-ray spectrometry as versatile tool in soil science: A critical review. *Journal of Plant Nutrition and Soil Science* 182: 9–27. https://doi.org/10.1002/jpln.201700447

Revelle W., and Revelle M. W. 2015. Package 'psych.' *The comprehensive R archive network* 337: 161–165. https://personality-project.org/r/psych-manual.pdf (Accessed August 15, 2024).

Ribeiro P. S. E., Frasca A. A. S., Carneiro J. de S. M., Hattingh K., Rezende E. S. de, and Martins F. R. 2022. Mapa geológico e de recursos minerais do Estado do Tocantins. http://rigeo.sgb.gov.br/jspui/handle/doc/22530 (Accessed August 15, 2024).

Santana A. de. 2005. Elementos de economia, agronegócio e desenvolvimento local. *Belém: GTZ* 133–142.

R Core Team, 2021, R: A language and environment for statistical computing: R Foundation for Statistical Computing. https://www.R-project.org/(Accessed August 15, 2024).

RStudio Team, 2020, RStudio: Integrated Development for R: RStudio. http://www.rstudio.com/(Accessed August 15, 2024).

Saunders D. F., Terry S. A., and Thompson C. K. 1987. Test of National Uranium Resource Evaluation gamma-ray spectral data in petroleum reconnaissance. *GEOPHYSICS* 52: 1547–1556. https://doi.org/10.1190/1.1442271

Saunders D. F., Branch J. F., and Thompson C. K. 1994. Tests of Australian aerial

radiometric data for use in petroleum reconnaissance. *GEOPHYSICS* 59: 411–419. https://doi.org/10.1190/1.1443603

Shives R. B. K., Charbonneau B. W., and Ford K. L. 2000. The detection of potassic alteration by gamma-ray spectrometry—Recognition of alteration related to mineralization. *GEOPHYSICS* 65: 2001–2011. https://doi.org/10.1190/1.1444884

Silge J., and Robinson D. 2016. tidytext: Text Mining and Analysis Using Tidy Data Principles in R. *The Journal of Open Source Software* 1:37. DOI: doi:10.21105/joss.00037

Silva A. B. da. 2020. Identification of impact cratering-related similarities based on airborne geophysical data and satellite images: the Cabeça de Sapo Structure, Parnaíba Basin, Northeast Brazil. *Journal of the Geological Survey of Brazil* 3: 97–111. https://doi.org/10.29396/jgsb.2020.v3.n2.4

Silva A. B. da, Silva M. F. da, Reimold W. U., Alves F. da M., Lago A. L., Jr M. A. C., Frasca A. A. S., and Ribeiro P. S. E. 2024. The Aerogeophysical Atlas of Tocantins State: Synthesis of Magnetic Anomaly and Radioelement Maps with emphasis on regional signatures and the Serra Da Cangalha Impact Structure. *Brazilian Journal of Geophysics* 42 (2): 1 – 29. 10.22564/brjg.v42i2.2316

Suhr D. D. 2005. Principal component analysis vs. exploratory factor analysis. *SUGI 30 proceedings* 203: 1–11.

Taylor M. J., Smettem K., Pracilio G., and Verboom W. 2002. Relationships between soil properties and high-resolution radiometrics, central eastern Wheatbelt, Western Australia. *Exploration geophysics* 33: 95–102. https://doi.org/10.1071/EG02095

Thurstone L. L. 1947. *Multiple factor analysis*, University of Chicago Press: Chicago.

Vasconcelos M. A. R., Leite E. P., and Crósta A. P. 2012. Contributions of gamma-ray spectrometry to terrestrial impact crater studies: The example of Serra da Cangalha, northeastern Brazil. *Geophysical Research Letters* 39. https://doi.org/10.1029/2011GL050525

Vasconcelos M. A. R., Crósta A. P., Reimold W. U., Góes A. M., Kenkmann T., and Poelchau M. H. 2013. The Serra da Cangalha impact structure, Brazil: Geological, stratigraphic and petrographic aspects of a recently confirmed impact structure. *Journal of South American Earth Sciences* 45: 316–330.

https://doi.org/10.1016/j.jsames.2013.03.007

Vaz P. T., Wanderley Filho J. R., and Travassos W. A. S. 2007. Bacia do parnaíba. *Boletim de Geociências da PETROBRAS* 15: 253–263.

Wei T., Simko V., Levy M., Xie Y., Jin Y., and Zemla J. 2017. Package 'corrplot.' *Statistician* 56: e24. https://peerj.com/articles/9945/Supplemental_Data_S10.pdf (Accessed August 15, 2024).

Weihermann J. D., Oliveira S. P., Li Y., Silva A. M., and Ferreira F. J. F. 2023. Two-dimensional inversion of airborne radiometric data for source concentrations: Application to Cu–Au targeting at Mara Rosa Magmatic Arc, Brazil. *Geophysical Prospecting* 71: 876–888. https://doi.org/10.1111/1365-2478.13349

Wickham H. et al. 2019. Welcome to the Tidyverse. *Journal of Open Source Software* 4:1686. https://doi.org/10.21105/joss.01686

Wilford J. R., Bierwirth e, and Craig M. A. 1997. Application of airborne gamma-ray spectrometry in soil/regolith mapping and applied geomorphology. *AGSO Journal of Australian Geology and Geophysics* 17(2): 201 – 216.

Wilford J., and Minty B. 2006. The use of airborne gamma-ray imagery for mapping soils and understanding landscape processes. *Developments in soil science* 31: 207–610. https://doi.org/10.1016/S0166-2481(06)31016-1

Williams B., Onsman A., and Brown T. 2010. Exploratory Factor Analysis: A Five-Step Guide for Novices. *Australasian Journal of Paramedicine* 8: 1–13. https://doi.org/10.33151/ajp

13.12 **Supplementary Material**

13.12.1 Details of Factorial Analysis approach

In order to understand how Factorial Analysis works, it is important to keep in mind the common factor model (Thurstone, 1947). This model proposes that the original variables in a given dataset can be decomposed into a part that contains common variance and other parts that contain unique variance (Gorsuch, 2015; Goretzko et al., 2021). In the common factor model, for a dataset $\boldsymbol{X}_i$ containing *i* (*i* = 1, 2,..., *p*) standardized variables and *j* (*j* = 1, 2, 3,... *m*) common factors, the expression of the basic FA model can be described as:

$$X_i = \sum_{i=1}^{p} l_{i\,j} \,.\, f_j + \; e_i \quad (1)$$

where $l_{i\,j}$ are the factor loadings, f_j are the common factors, and e_i are the specific factors. In the FA model, it is assumed that (Gorsuch, 2015): i) common and specific factors have a mean equal to zero; ii) common factors have unit variance and are uncorrelated with each other and with specific factors; and iii) the variance of specific factors is called specific variance. Under these assumptions, the covariance matrix of equation (1) can be given by:

$$var\,(X_i) = var\,(\sum_{j=1}^{p} l_{i\,j} \,.\, f_j) + \; var(\,e_i) = \; {h_i}^2 + \; {u_i}^2 \qquad (2)$$

The ${h_i}^2$ terms in equation (2) are called communalities of the variables and represent the portion of the total variance that is common, whereas the ${u_i}^2$ terms represent the portion of the total variance that is unique or specific (Gorsuch, 2015; Santana, 2005). In FA, it is necessary that the ${h_i}^2$ term is greater than the ${u_i}^2$ term, such that most of the total variance can be explained mainly by the common variance. This common variance derives from the interrelationship of original variables and this

interrelationship can be evidenced in a correlation matrix. Therefore, the first step to properly apply FA is to check whether the level of correlation between the original variables is significant and not null. This step is known as factorability analysis and it can be done using two well-known parameters: Kaiser – Meyer – Olkin (KMO) criterion and the Bartlett's test of Sphericity (BtS) (Ferguson and Cox, 1993).

Basically, KMO indicates whether the relationships between variables in the correlation matrix can be explained by a smaller set of factors (Kaiser and Rice, 1974; Ferguson and Cox, 1993), whereas Bartlett's test of Sphericity (BtS) is a chi-square statistical test, in which the correlation matrix is compared with an identity matrix of the same dimension (Ferguson and Cox, 1993; Mulaik, 2009). The KMO provides an overall measure of “sampling adequacy” (Overall MSA) for the complete set of variables, and BtS calculates the probability (p-value) that the correlation matrix of the observed data has correlations that are statistically similar to an identity matrix (null hypothesis) at a given confidence level, commonly taken to be 0.05 (Ferguson and Cox, 1993; Williams et al., 2010). To be factorable, a correlation matrix of a given dataset must return MSA values > 0.5 and p-values of less than 0.05 (Kaiser and Rice, 1974; Williams et al., 2010).

After the factorability analysis step, the next step is to estimate the numerical values of the factor loadings ($l_{i\ j}$) and the communalities ($h_i{}^2$). This step is known as factor extraction from correlation matrix. Although there are other methods to extract factors (e.g,. Maximum Likelihood, Generalized Least Squares, Alpha Factorization, and others - Fabrigar et al., 1999; Williams et al., 2010, Gaskin and Happell, 2014), extraction by PCA has been recommended for non-normal distribution data (Fabrigar et al., 1999), which is commonly the case for AGRS data.

The next is making a decision how much factors need to be retained in the analysis. This decision can be based on different methods, but here, we chosen two methods: Parallel Analysis (PA) (also known as Horn’s Parallel Analysis) (Horn, 1965) and

Amount of Explained Variance (AEV) method (Fabrigar et al., 1999; Williams et al. 2010; Gaskin and Happell, 2014). The former approach compares the scree of eigenvalues of the observed data with that of a random data matrix of the same size as the actual data, whereas the latter takes account of the amount of variance that can be explained by the linear combination of factors (Fabrigar et al., 1999; Williams et al. 2010; Revelle and Revelle, 2015). In PA, factors are chosen when eigenvalues from actual data are greater than eigenvalues from random data (Williams et al. 2010). When using AEV, factors must be retained when 95% of the variance is explained (Williams et al. 2010). We retained the factor by using these criteria and then rotated them.

The next step after retention is factor rotation. The main purpose of rotation is to simplify the factor solution by maximizing items with high loading and minimizing items with low loadings (Fabrigar et al., 1999; Costello and Osborne, 2005; Williams et al., 2010). The most common rotation method is Varimax, which is an orthogonal method that assumes that factors are uncorrelated (Fabrigar et al., 1999). However, oblique methods (e.g., Oblimin and Promax) can be useful to allow correlation between factors. Following Fabrigar et al.´s (1999) suggestion, an oblique method (Oblimin) was used to rotate the factors in the first instance. It was observed that the oblique method yields a solution where factors were practically uncorrelated. So, we ruled out the oblique rotation solution and carried out a new rotation by using the Varimax rotation method to obtain the final factor model solution.

Finally, since that loads has been estimated, we compute the numerical values of factor score (i.e., the f_j in the equation 1) for each observation (i.e., each data point in the flight line) by using regression method. In general terms, the factors can be thought like new variables added in the dataset. However, these new variables can be thought like grouping of original variables and the scores of these new variables correspond to its actual numerical value. Finally, the interpreter can name these new variables (or factors)

by analyzing their effects on the directly measured variables. For instance, the economic development of a given country is a variable that may be difficult to measure directly, but it can be estimated by exploring the correlation structure involving other variables that can be directly measured, such as total investment, volume of imports of goods, rate of employment, etc (e.g., Bai, 2015). In this case, the factor (economic development) controls the variance of observable variable variables (total investment, volume of imports, employment), such that it leads these variables to covariance.

13.12.2 Details of chemical analysis

Reference materials used for XRF analysis were: NIM-P, NIM-D, W2, NIM-S, GSP2, BCR2, NIM-N, NIM-G, PCC1, BHVO2, AGV2, G2, DTS1. The detection limits in wt% for the main element oxides were SiO_2 0.01, Al_2O_3 0.01, Fe_2O_3 0.01, MgO 0.01, CaO 0.01, Na_2O 0.01, K_2O 0.01, TiO_2 0.01, MnO 0.01, Cr_2O_3 0.01, and P_2O_5 0.002. The data were automatically processed by a laboratory information management system, ensuring traceability and quality control.

Internal standards used in trace element data were Re and Rh at 100 ppb, and In and Bi at 50 ppb Calibration were performed with five standard concentrations (10, 30, 50, 75, and 100 ppb) based on several certified reference materials. The equipment was optimized to maximize the In signal. Formation of oxides and double-charged ions was limited to less than 2 %. Measurements were done in triplicate and averaged. If the deviation between replicates exceeds 2 %, the data were marked. In addition, Certified Reference Materials BCR-1, BHVO-2, and BIR-1 were analyzed, which must yield deviations of less than 10 % (generally less than 5 %) from the recommended values. A Procedural Total Blank was measured that includes the entire digestion process to evaluate possible contamination. Final data were ultimately corrected by subtracting Total Blank values.

Table 1: Factor loadings and communalities computed for each radiometric variable for the Riachão AGRS dataset.

Variables	**Factor loadings**			**Communalities**
	F1	F2	F3	
TC	0.94	-0.26	-0.08	0.95
K	0.72	-0.58	-0.12	0.86
eTh	0.92	0.02	-0.28	0.93
eU	0.80	0.15	0.50	0.90
eU/eTh	-0.13	0.04	0.97	0.95
eU/K	-0.07	0.84	0.47	0.93
eTh/K	-0.07	0.97	-0.15	0.96

Table 2: Factor loadings and communalities computed for each radiometric variable for the Nova Colinas AGRS dataset.

Variables	**Factor loadings**			**Communalities**
	F1	F2	F3	
TC	0.88	0.43	0.00	0.95
K	0.05	0.95	0.05	0.91
eTh	0.93	0.00	-0.16	0.88
eU	0.69	-0.25	0.48	0.77
eU/eTh	-0.12	0.03	0.87	0.78
eU/K	0.58	-0.62	0.38	0.86
eTh/K	0.82	-0.42	-0.13	0.86

13.12.3 Heat correlation charts computed for Riachão and Nova Colinas impact structures.

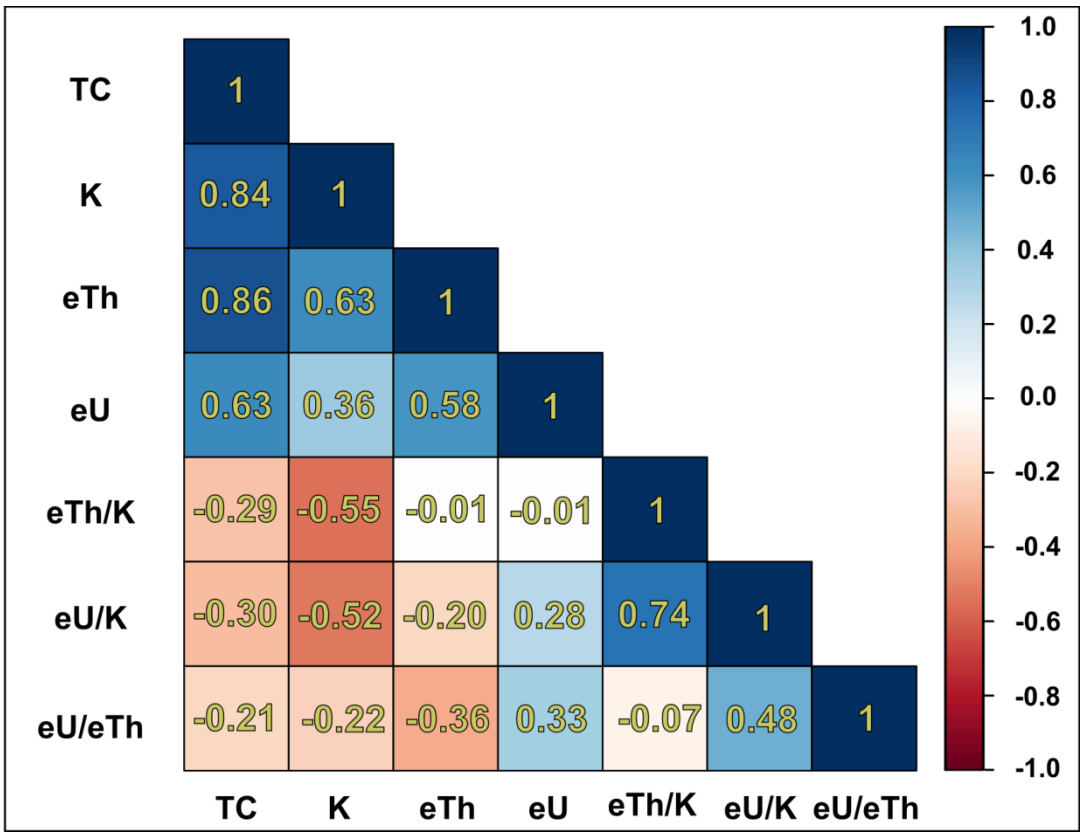

Figure 1: Heat correlation chart computed for the spell out (AGRS) dataset for the Riachão (RR) impact structure. The correlations have been computed using the Pearson Correlation Coefficient.

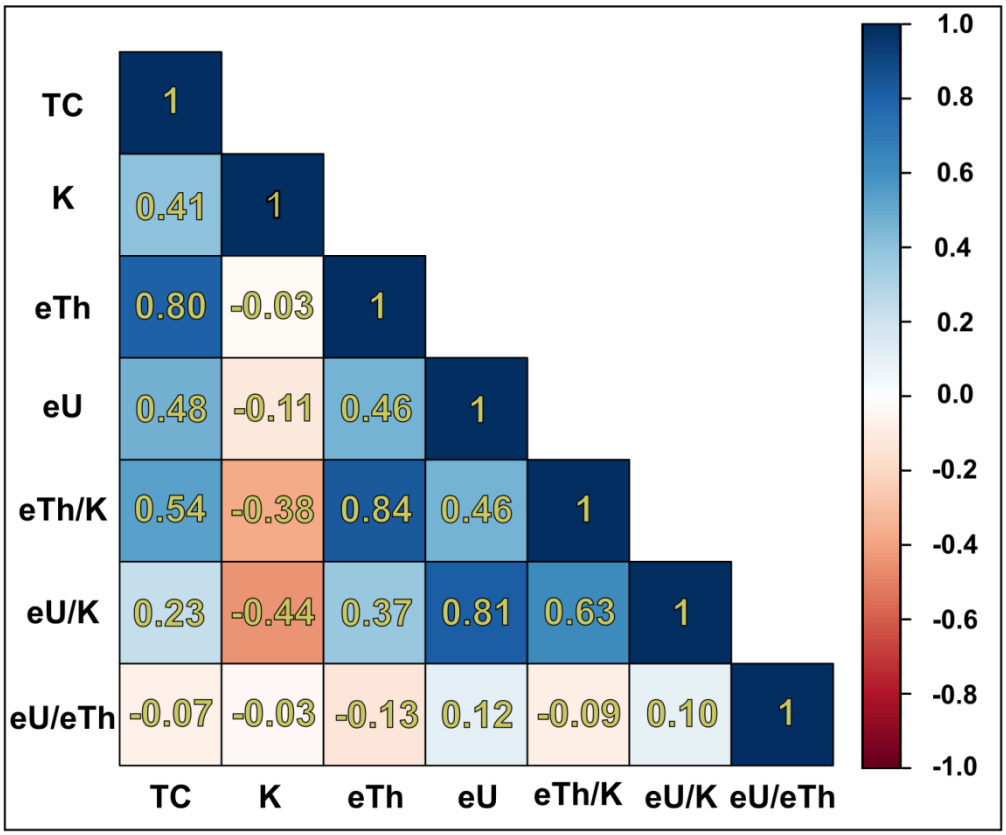

Figure 2: Heat correlation chart computed for the AGRS dataset for the Nova Colinas (NVC) impact structure. The correlations have been computed using the Pearson Correlation Coefficient.

13.12.4 Factorial score maps and the original radiometric maps computed for Riachão and Nova Colinas.

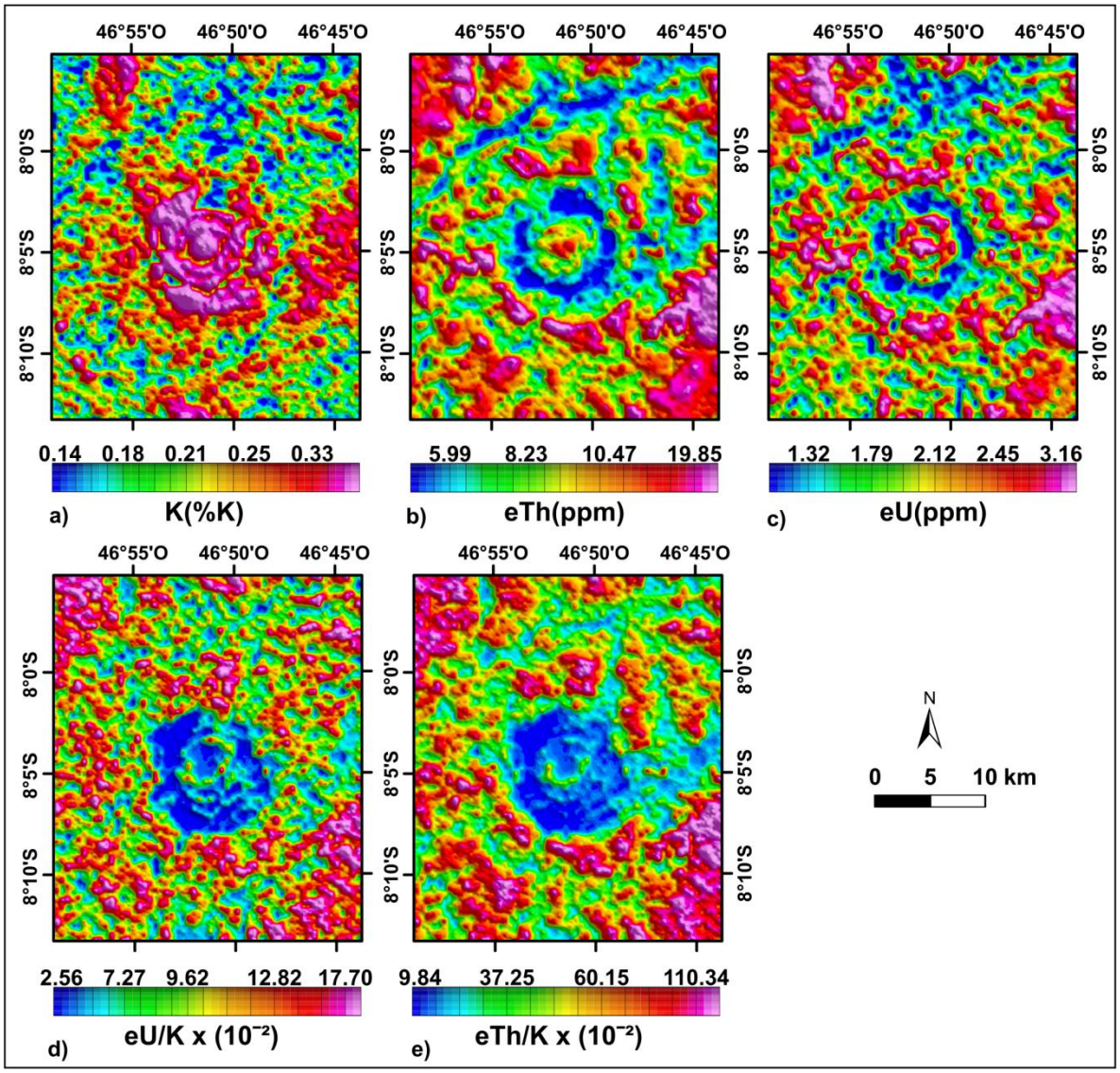

Figure 3: Thematic radiometric maps for the Serra da Cangalha impact structure. Concentration maps: a) Percent of total potassium (K); b) Part per million of equivalent thorium (eTh); c) Part per million of equivalent uranium (eU). Ratios: d) eU/K ratio; e) eTh/K ratio.

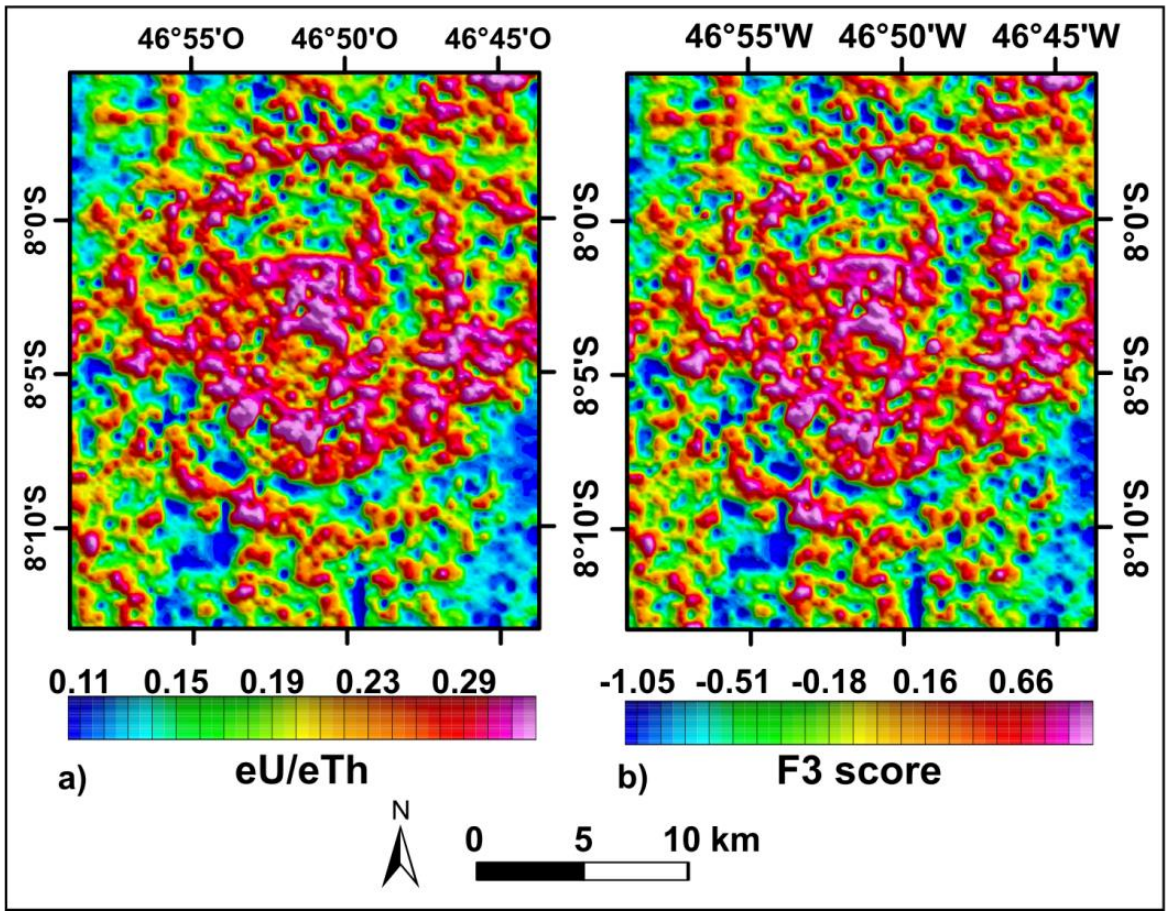

Figure 4: Thematic radiometric maps for the Serra da Cangalha impact structure. a) eU/eTh ratio. b) Third (F3) factor score.

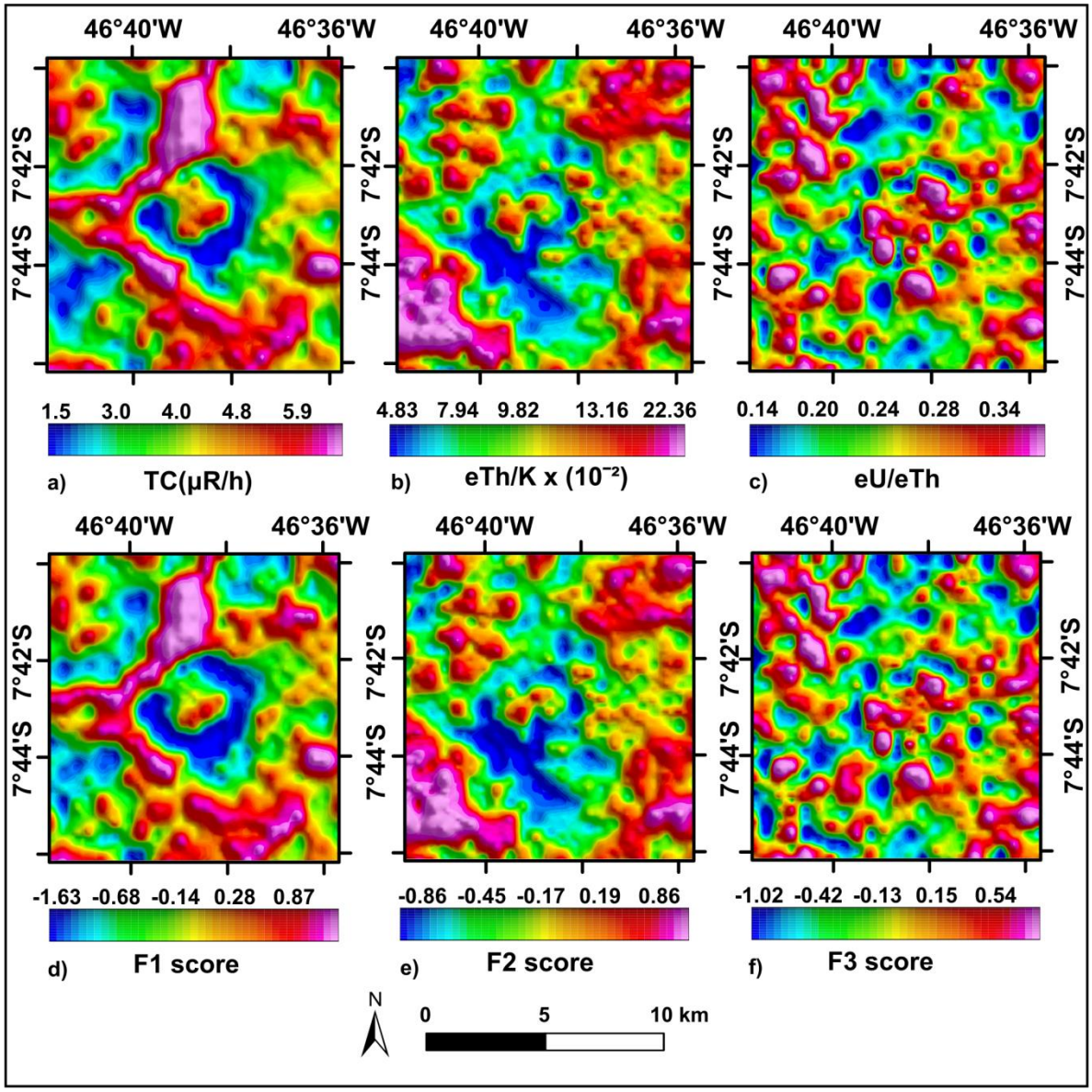

Figure 5: Thematic radiometric maps for the Riachão (RR) impact structure. Original radiometric variable maps: a) Total count; b) eTh/K ratio; c) eU/eTh ratio. ; d) Factor scores: d) First (F1) Factor scores; e) Second (F2) factor scores; f) Third (F3) factor score.

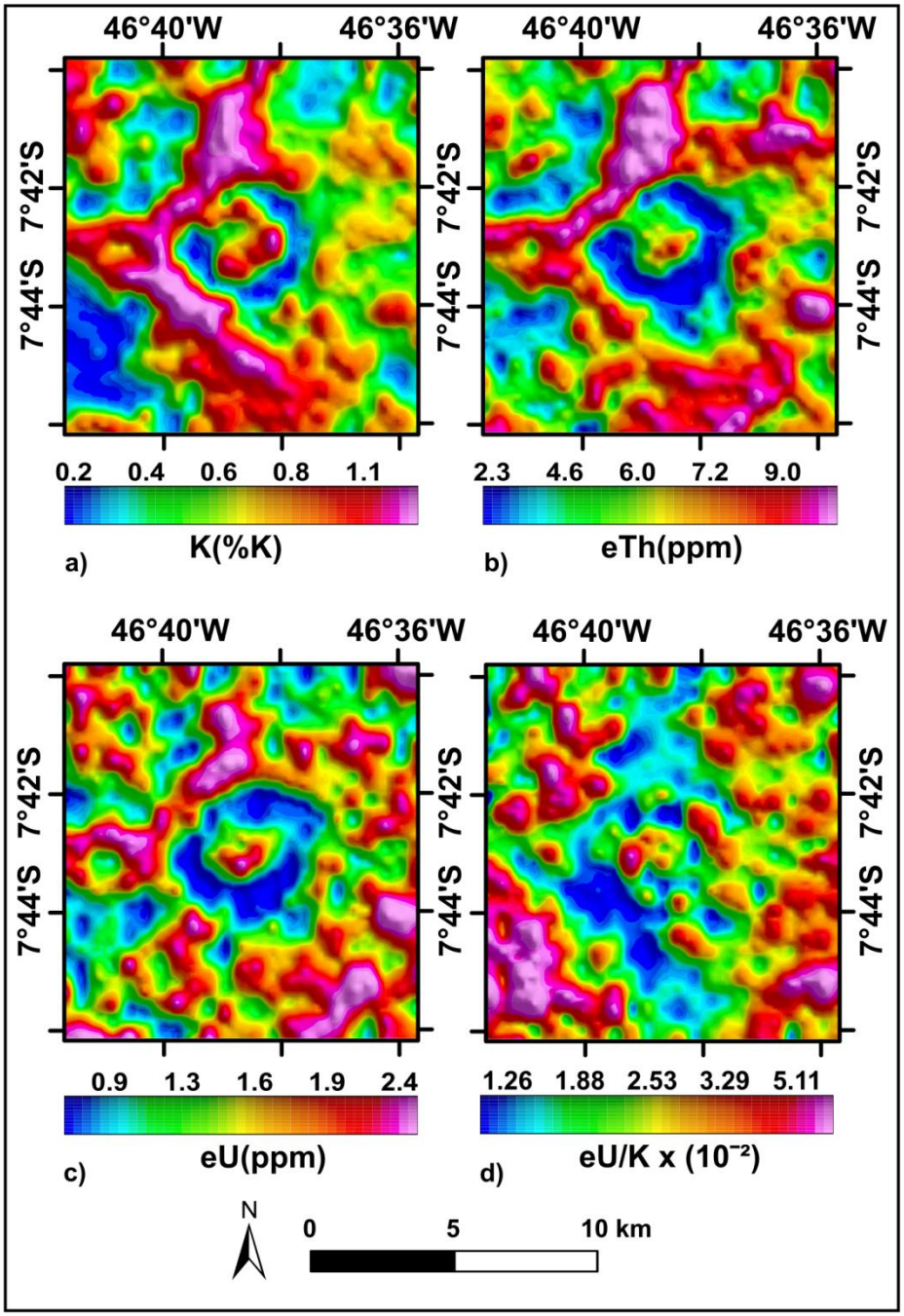

Figure 6: Thematic radiometric maps for the Riachão impact structure. Original radiometric variable maps: a) Percent of total potassium (K); b) Part per million of equivalent thorium (eTh); c) Part per million of equivalent uranium (eU). d) eU/K ratio; e) eTh/K ratio.

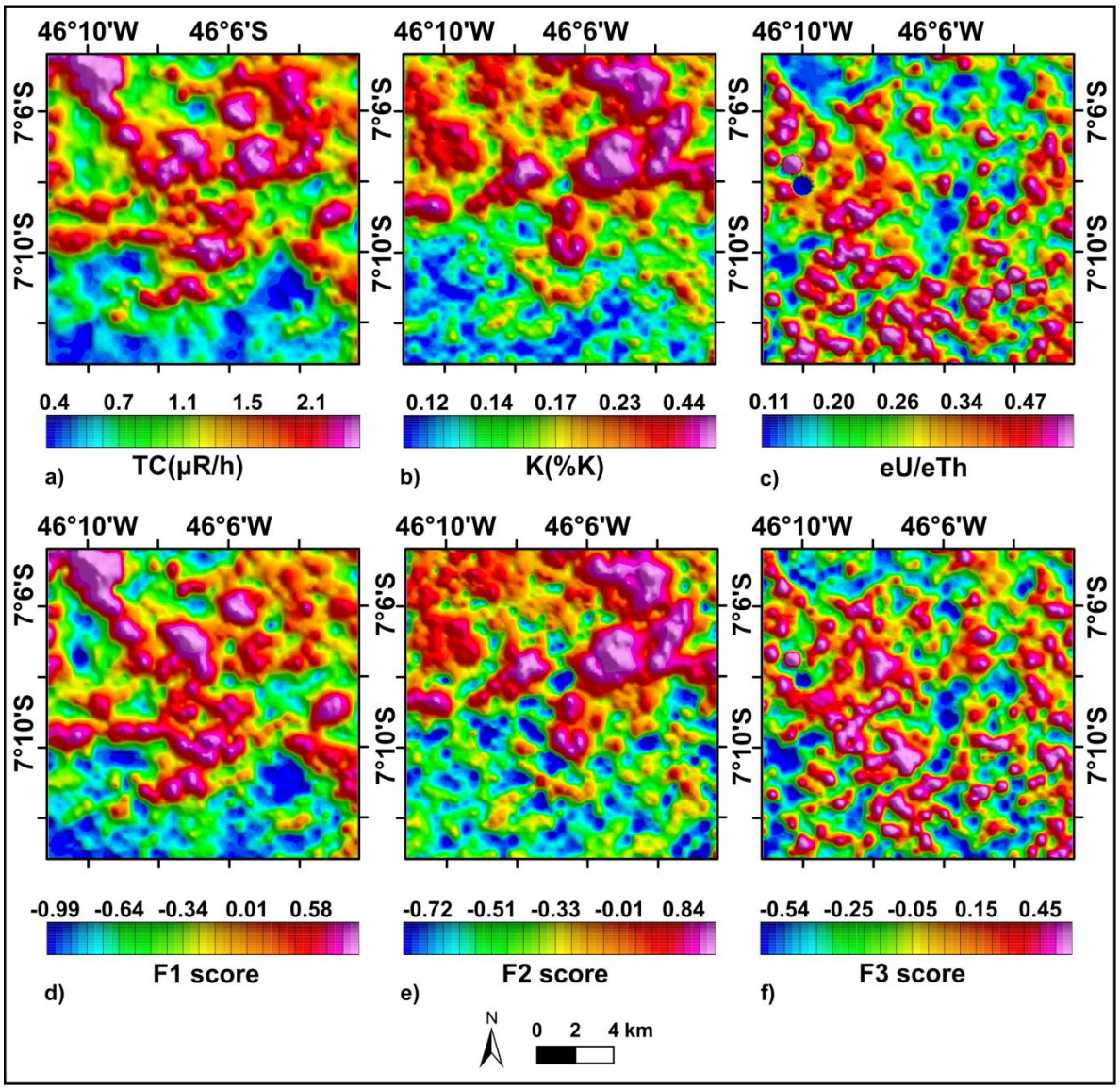

Figure 7: Thematic radiometric maps for the Nova Colinas impact structure. Original radiometric variable maps: a) Total count; b) Percent of total potassium (K); c) eU/eTh ratio. Factor score maps: d) First (F1) Factor scores; e) Second (F2) factor scores; f) Third (F3) factor score.

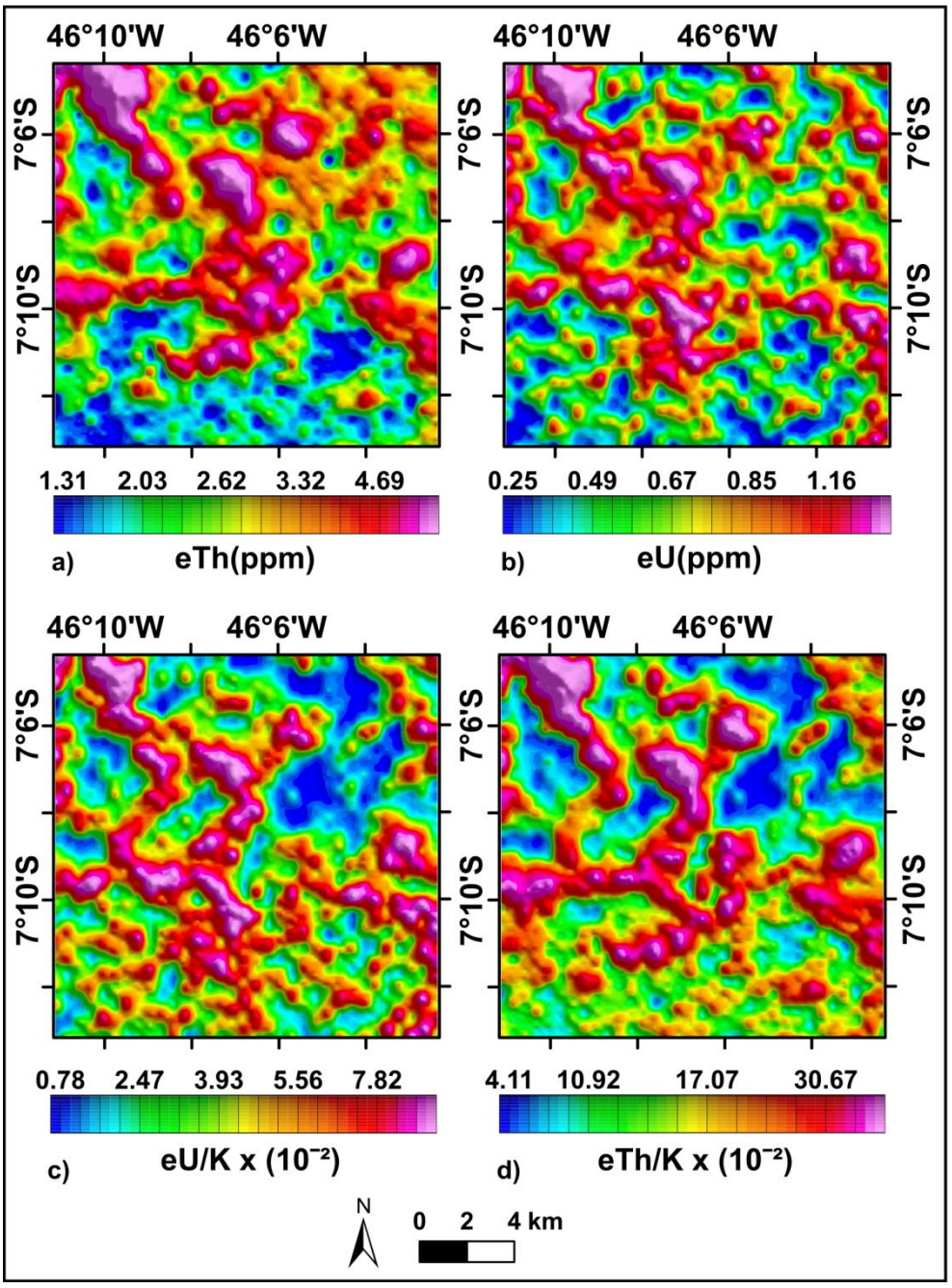

Figure 8: Thematic radiometric maps for the Nova colinas impact structure. Original radiometric variable maps: a) Part per million of equivalent thorium (eTh); b) Part per million of equivalent uranium (eU); c) eU/K ratio; e) eTh/K ratio.

CHAPTER 14
RESULTS

14. RESULTS

In order to comprehend the different types of results derived from the application of the methodology previously described, all results are grouped here into two main sections. The first one is dedicated to the results for Brazilian impact structures and the second to the results for potential targets. For each of these sections, the geological, geophysical, and spaceborne features of each structure were organized into subsections. Indeed, because a detailed analysis of the huge amount of images derived from processing of airborne geophysical data and spaceborne images for the considerable number of structures, which would have required a very large amount of time far beyond that available for the present project, it was decided to provide only some examples to demonstrate the main features of impact structures and of the potential targets as seen in geophysical or satellite images, by choosing the most instructive cases.

14.1 Main geological, geophysical and spaceborne features of Brazilian impact structures

14.1.1 Main geological features

Some of the main geological features of Brazilian impact structures are summarized in Table 3. Shatter cones have not been reported for the CJU, RR, and SMT impact structures. In this latter structure, possible shatter cones were allegedly identified in the center of SMT, but analysis is still ongoing (Crósta et al., 2019b and c). Regarding microscopic shock features, except from the VGD impact structure, samples from all other Brazilian impact structures have shown PDFs in quartz grains. Unambiguous impact melt rock has only been reported from the AGD impact structure (Crósta et al., 2019; Souza et al., 2024), but thin melt layers on shatter cones from VGD have been discussed as possible product of shock unloading after passage of shock waves through the rock (Pittarello et al., 2015). Planar fractures (PF) and FF in quartz are present in most Brazilian impact structures. No meteoritic component has been reported from Brazilian impact structures to date.

Table 3: Main geological features of Brazilian impact structures. The informations were compiled from the previous work listed in the table 1 (Chapter 10). Abbreviations: AGD – Araguainha; CJU – Cerro do Jarau; VGD – Vargeão Dome; VTA – Vista Alegre; SdC – Serra da Cangalha; RR – Riachão Ring; NVC – Nova Colinas; SM – Santa Marta; SMT – São Miguel do Tapuio.

Impact structure	Center position	Size (km)	Age (Ma)	Shock deformation feature	Impactites	Morphstructural elements
AGD	16°48'45''S 52°59'02''W	~40	~250	Shatter cones in metasedimentary rocks; kink bands in biotite and muscovite; PF and PDF in K-feldspar and quartz, impact melt rocks; shocked zircon.	Polymict impact breccias (suevite and lithic breccia). Clasts (>1 cm) derived from metasedimentary and sedimentary sources, less frequently from granite, and groudmass composed of fine-grained materials from the same sources; melt particles mostly highly silicious. Impact melt rocks.	Central peak, annular basin, and crater rim are visible. Oldest stratigraphic units strongly deformed/fractured outcrops in the central zone. The central uplift shows abrupt tectonic contacts, with rotated, faulted, and upturned strata. Concentric inner rim affected by faults and slumps into annular basin. In the innermost rim, strata dipping at high angles both outward and inward of the crater. The rim shows kilometer-scale blocks cut by radial faults.
CJU	30°12'S 56°32'W	~13.5	<134**	PF, FF, and PDF in quartz of sandstones located in the central parts.	Basaltic monomict breccias, sandstone monomict breccias, and lithic polymict breccias. They show sandstone and/or basalt clasts and a groundmass commonly composed of clay and, sometimes, Fe-oxide.	Central uplift is prominent, but crater rim is not well-defined around the entire structure. Some sandstone is strongly silicified and cataclased in the central uplift; these rocks show subvertical dip and tectonic contacts with basalts, or even stratigraphic inversion. Within the entire structure, basalts are intensely fractured.
VGD	26°49'S 52°10'W	~12.4	< 134 Ma	Shatter cones in sandstones and basalts, and rare PF and FF in quartz of monomict sandstone breccia. Thin apparent melt films on some shatter cones.	Monomict sandstone breccias (sandstone fragments supported by a groundmass predominantly composed of submillimeter quartz clasts without oxides) and polymict breccias (angular, millimetric volcanic clasts, with smaller amounts of sandstone and calcite, all supported by red, fine-grained, and strongly oxidized groundmass that is composed of comminuted basalt and rhyodacite, quartz, and calcite clasts)	A central uplift has been inferred due to the presence of strongly deformed sandstone. Some sandstone outcrops appear as failures of large blocks in abrupt tectonic contact with basalts or polymict breccias. Towards the center of the structure, the rocks (basalts, rhyolites, and sandstones) become more intensely brecciated, fractured and locally melted. Normal faults occur in the rim.
VTA	25°57'S 52°41'W	~9.5	<134**	Shatter cones on basaltic clasts in polymict impact breccia and PDF in quartz grains.	Polymict impact breccias with millimeter to decimeter sized, angular clasts, embedded in a groundmass of fine-grained material supposedly derived from Serra Geral Formation basalts.	The rim is elevated up to 150 m above the interior and shows steep slopes that separate the practically flat surface of the interior of the crater from rougher surrounding terrain. The central zone has been supposed to feature deformed sandstone blocks.
SdC	8°05'S 46°52'W	~13.4	<250**	Shatter cones in sandstone, PF, FF, and PDF in quartz.	Polymict lithic breccias (angular and subrounded quartz and claystone fragments in a matrix of small angular quartz and feldspar grains with large amount of iron oxide cement) and monomict impact breccias (fragments of sandstones with grains commonly angular and sometimes embedded into a matrix with iron oxide cement)	There is a prominent central uplift, annular basin and well-defined crater rim. The central uplift is composed of the regionally oldest stratigraphic units and its innermost part is surrounded by a notable collar of silicified sandstones. The annular basin contains two inner rings of chert and high-silica sedimentary rock. The strata at the crater rim seem to be intersected by radial faults. Impact-related deformation increases from the rim toward the center.

RR	7°42’S 46°38’W	~4	< 250**	Rare PDF in quartz of Piaui Formation sandstone.	Brecciated cherts - microcrystalline silica commonly crosscut by silica and/or iron oxide hydroxide veins, at the transition from central-uplift to annular depression.	A central zone is composed of chaotically arranged blocks and folded beds of sandstones containing high proportions of comminuted and sharp-edged quartz grains. The rim is not very prominent and open in the NW sector.
NVC	7°09’33’’S 46°06’30’’W	~7	199 to 130**	Shatter cones in basalts, and a few sandstone samples with PF, FF, and PDF in quartz.	Monomict sandstone breccia of very fine-grained, pure quartz sandstone with large rounded grains embedded into a fine-grained groundmass of crushed, often splintery fragments.	The structure is quite degraded but still shows a somewhat notable crater rim and elevation in the central part. This central zone is supposed to be composed of Pedra de Fogo sandstones. The internal zones of the annular basin show a moderate relief pattern, with dissected relief of moderate and low slopes. The crater rim is best defined in the SW sector.
SM	10°10’S 45°14’W	~10	< 93-100**	Shatter cones in sandstones and boulders from conglomerate, PF and PDF in quartz grains in polymict lithic brecca.	Monomict breccias (clasts of coarse-grained, poorly sorted sandstones, with some clasts exhibiting shock deformation features) near the central uplift. Polymict lithic breccias (clasts with mostly angular shapes, coarse-grained, poorly sorted of different types of sedimentary rocks within a silty to sandy groundmass) may in part represent impact breccia, but similar materials have been described as likely Cenozoic cover over the southwestern sector.	The central uplift zone is formed of strongly deformed Devonian sandstones and pelites of the Pimenteiras and Cabeças formations. There are several structural elements, such as concentric normal faults and lateral thrust ramps. The rim is well-defined along several sectors of the structure, mainly in the eastern/southern parts.
SMT (*)	5°37.6’S 41°23.3’W	20 - 21	Undefined.	FF, PF, and PDF in quartz grains in rare samples of monomict sandstone breccia.	A few samples of monomict sandstone breccia found near the center; results have not been fully published yet.	A prominent topographic “central uplift”, annular zone containing concentric rings, and a notable rim has been identified. The intensity of deformation tends to increase from the rim towards the center, such that the dip of strata becomes steeper, the sandstones become more deformed, and comminution of quartz grains becomes more evident. The rim shows steep escarpments.

* Still not formally accepted. **Based on stratigraphic relationships (youngest strata affetected by impact or age of basalt layers affected by impact).

It can be seen from Table 3 that, despite the peculiarities of the different targets of the Brazilian impact structures, some overall characteristics regarding impactites are noted. Brecciated materials commonly are formed by angular to subrounded, poorly sorted, or crushed clasts which, in turn, are derived from local rocks. The clasts are embedded into a groudmass composed of fine-grained materials also derived from the target rocks. In some cases, this groundmass can also contain iron oxide cements of likely secondary origin. The minerals of breccias are commonly fractured, cataclased, comminuted, and sometimes recrystallized. Fluidal structures with intensely silicified parts have also been reported in injected polymict breccias in the central uplift of the SM impact structure (Oliveira et al., 2014). Additionally, deformation features related to, but not exclusively, impact events, like dislocations, twinning, kink bands, mosaicism, and/or undulatory extinction (Langenhorst and Deutsch, 2012; Deutsch, 2015) also occur in some minerals of breccias from Brazilian impact structures (e.g., AGD, NVC, and CJU)(Crósta et al., 2019; Reimold et al., 2018 and 2022).

Brazilian impact structures also show specific morphostructural elements that can not be generalized (Table 3). For instance: at least one first-order structural element (central uplift, annular basin, or crater rim) can be identified in all Brazilian impact structures. All Brazilian impact structures show increase of deformation from outward to inward. This tendency is consistent with the fact that shock pressures decrease hemispherically outward from the impact point (e.g., Kenkmann et al., 2014). The oldest lithostratigraphic units crop out in the central uplifts, and in the Brazilian impact structures they commonly represent siliciclastic materials. Such materials commonly are intensely silicified, fractured, and/or folded, such that the primary sedimentary structures may be unrecognizable in some cases.

The lithostratigraphic contact zones in the central uplifts commonly are abrupt, so that overturned, thickened, thrusted, and/or rotated strata are second-order structural features common in Brazilian impact structures (e.g., Araguainha, Cerro do Jarau, Santa Marta). Inner rings in annular basins seem to be present at least in four impact structures (SdC, SM, SMT, VGD), whereas at NVC, which is smaller than the aforementioned ones, such inner rings have not been identified. Inner rings apparently do not occur in the CJU and VTA

impact structures. The outer rims (i.e., the limit between inside and outside zones of Brazilian impact structures) are visible for most impact structures. However, some rims are intersected by radial faults and some of them are also intensely eroded, providing more linear, discontinuous aspect (e.g. AGD, SdC, VGD) and/or open zones (RR, NVC, and CJU). Listric-faults, strata dipping outwards, concentric normal faults, fractured kilometer-scale blocks are some second-order structural elements that can also be found in the rim zones of some Brazilian impact structures.

14.1.2 Airborne gamma-ray spectrometry and magnetic signatures

The main geophysical signatures of Brazilian impact structures are summarized in Table 4. This table shows that some radiometric signatures are always present in those impact structures, for which airborne gamma-ray spectrometry data are available. Araguainha, Serra da Cangalha, and Riachão Ring show clear circular radiometric partterns, whereas at Nova Colinas and Santa Marta this pattern is more subdued.

In terms of geological implications, the Total Count (TC) map of the Araguainha impact structure shows that total counts greater than 300 cps coincide with lithostratigraphic units containing pelitic and organic materials (e.g., Passa Dois Group and Ponta Grossa Fm.) or with the Serra Negra Suite porphyritic alkali granite (Fig. 24). In this latter case, our results are corroborated by previous works which suggested that this granite has high K (4% K), eTh (3-8 ppm), and eU (6-10 ppm) concentrations (Leite et al., 2022). On the other hand, low TC values (TC < 200 cps) can be associated with sandy rocks (e.g., Aquidauana or Furnas Fm.).

The way in which airborne gamma-ray spectrometry data are analyzed can also impact the results generated. For example: the circular radiometric patterns in Serra da Cangalha and Riachão Ring can be easily seen on conventional maps (e.g., figures 3 and 6 of Vasconcelos et al., 2012, figure 10 of Silva et al., 2024 (Chapter 14), and figure 9a of Maziviero et al., 2013, respectively). However, the use of statistical analysis techniques, such as Principal Component Analysis and Factorial Analysis, can reveal subtle variations and/or latent patterns that are not readily noticeable on conventional maps.

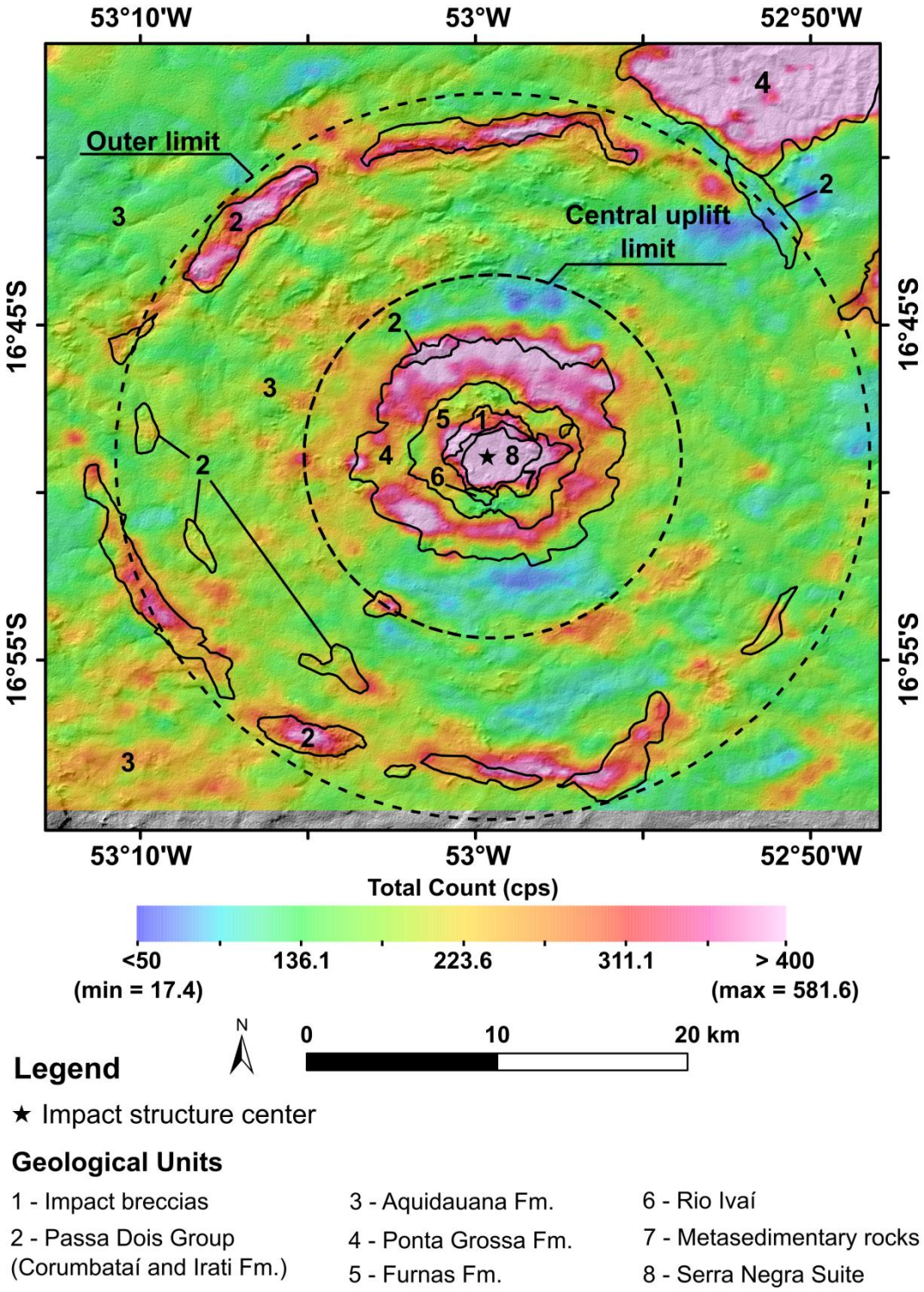

Figure 24: Total Count (TC) radiometric map of the Araguainha impact structure. Geological map after Sousa et al. (2024) and Borges et al. (in press).

Table 4: Airborne gamma-ray spectrometry and spaceborne images / signatures of Brazilian impact structures. Abbreviations: AGD – Araguainha; CJU – Cerro do Jarau; VGD – Vargeão Dome; VTA – Vista Alegre; SdC – Serra da Cangalha; RR – Riachão Ring; NVC – Nova Colinas; SM – Santa Marta; SMT – São Miguel do Tapuio.

Impact structure	Gamma-ray spectrometry signatures	Magnetic signatures	Main features in spaceborne images
AGD	Lithostratigraphic units containing pelitic and organic materials (Passa Dois Group and Ponta Grossa Fm.) and granite rocks (Serra Negra Suite) show high TC values, whereas quartzose sedimantary rocks (e.g., Aquidauana and Furnas sandstones) show low radiometric signatures (Fig. 24)	Two small magnetic anomalies relatively well-isolated, with normal polarities, and relatively deep (750 - 1200 m) in the area of the Araguainha central uplift (black arrows in Figs. 33 and 34). The innermost part of the central uplift of the Araguainha impact structure (Serra Negra Suite Granite) is non-magnetic. Note that this granite seems to be enclosed by a magnetic halo that, turn in, encompasses the two normal dipole magnetic anomalies described earlier (Fig. 34b). Other magnetic anomalies occur between the central uplift and outer rim, including several linear NE-SW magnetic anomalies (inferred lineaments in the Fig. 33) and a long-wavelength magnetic anomaly seated in eastern portion of AGD's rim (white arrow in the Fig. 33).	The Passa Dois Group and Ponta Grossa Fm. are clearly outlined with light green color, such that the outer rim and outermost central uplift boundaries can be seen (feature #1 in the Fig. 36a). In the annular basin, features with a rough texture and strong pink tones (feature #1 in the Fig. 36a) and smooth texture and cyan tones (feature #3 in the Fig. 36a) can be seen. The first signature occurs in the northern portion of the central uplift, whereas the second is more common in the southern portion of the annular basin.
CJU	Data not available	Data not available	The central uplift can be seen as an ellipsoidal area of light green color (i.e., high B4/B3 ratio) (Fig. 36b). The major axis with north-south direction has been estimated at 7.5 km. Silicified sandstones in the external portion of the central uplift show high backscattering of VH and VV polarimetric components (see conference paper, Chapter 12).
VGD	Data not available	There is a circular magnetic anomaly with inverted polarity close to the center of Vargeão Dome (Fig. 35a). Its depth estimates range from 556 m (central-northern portion) to 1380 m (western portion) (Fig. 35b). Outside of the impact structure, two linear ENE-WSW trending magnetic anomalies can be seen in the eastern sector (features #1 and #2 in the Fig. 35b). The SED solutions yield a 580 m depth for one of these (feature #2) linear magnetic anomalies	Two linear features trending WSW-ENE can be seen in the eastern portion of the Vargeão Dome structure in SAR images (feature #1 in the Fig. 36c). Other structural features, like the outer rim and inner ring features seem to be well visualized in the elevation map (features #2 and #3 in the Fig. 36c).
VTA	Data not available	The inside portion of Vista Alegre seems to be non-magnetic, but a linear magnetic anomaly trending WNW ESE can be seen running across the entire eastern portion of the structure and ending nearits center (see the black arrow in the Fig. 29c).	The difference in the textural pattern of the internal (feature #2 in the Fig. 36d) and external (feature #1 in the Fig. 36d) portion of the Vista Alegre impact structure is a feature that can be seen in images from different sensors (e.g., Fig. 36d).
SdC	The first PC (PC1) practically has isolated the radiometric contribution of the annular basin (ring syncline), whereas PC2 scores isolate the radiometric contribution of the central basin and an area in the southwest sector of the annular basin where previous works identified anomalous K abundance (black arrow in the Fig. 25). Additionally, Factorial Analysis revealed a semi-circular feature within the annular basin (see research paper, Chapter 14).	There is a linear magnetic anomaly with NE-SW trend that practically crosses the SdC structure (feature #2 in the Fig. 29a). The Structural Index (SI) computed for this linear magnetic anomaly (SI < 1.00) suggests that magnetic contrast can be modeled as a contact-type. The magnetic source depths show different values depending on the different sectors of the impact structure (Fig. 29a).	The collar of the central uplift and the central basin are characterized by high backscattering zones, but the ormer shows a rough texture, whereas the second is more smooth-textured (see conference paper, Chapter 12). An intriguing semi-circular Thermal Infrared (TIR) spectral signature (red colors) (black arrows in the Fig. 37a) suggests that the radiance in band 13 (10.25 – 10.95 μm) is larger than that of bands 12 (8.925–9.275) μm and 10 (8.125–8.475 μm). Inherently, these TIR semi-circular signatures match well with the semi-circular feature revealed by Factorial Analysis (see research paper in Chapter 14).

RR	Outer rim is characterized by very low PC1 scores, whereas moderate PC1 scores seem to enhance the southeast portion of the Riachão Ring central uplift. The annular basin seems to be well-defined in PC4 scores (black arrow in the Fig. 26b).	Linear long-wavelength magnetic anomalies do not cross the Riachão Ring impact structure (see the black arrows in the Fig. 29b). From west to east, a linear magnetic anomaly trends NW-SE; it has a shallow depth (370 m), and then it gradually deflects towards NE–SW and reaches great depth (~ 1000 m). The SI = 1.5 suggests a complex magnetic source (dike or vertical cylinder) for this linear magnetic anomaly at RR.	On SAR images (see conference paper, Chapter 12), the central uplift and outer rim show high backscattering signatures, whereas the annular basin shows low backscattering signatures. On optical images (Fig. 37b), the central uplift and outer rim show strong green shades (i.e., strong reflectance in band 8)(features #1 and #2 in the Fig. 37b).
NVC	The F2 score map can be used to distinguish the K contributions that come from the rim and the central uplift (Fig. 27)	A well-defined ring-shaped magnetic anomaly coincides with the Nova Colinas crater rim. The magnetic sources are essentially < 750 m and the SI values (2.5-3.75) suggest such sources at Nova Colinas may have complex geometries (cylinder or sphere) (Fig. 37b), mainly in the northern sector. No magnetic anomaly was observed at Nova Colinas' center. Additionally, the polarity of magnetic anomaly in the northern sector is composed of a minimum surrounded by two maxima (see the black arrows in the Fig. 31a). Note that some parts of the magnetic ring-shape seem to be subduced.	The difference between the northern and southern portions is well defined in the TIR images (see the features #1 and #2 in the Fig. 37c). High and low backscattering zones inside of Nova Colinas structure are well defined in Sentinel-1 SAR Dual-Pol images (see conference paper, Chapter 12).
SM	Circular radiometric source(s) of eTh and eU seem to be present near the western slope of the Central Elevated Plateau (CEP) (black arrows in the Fig. 28c and d)	A long-wavelength magnetic anomaly can be related to the central part of the structure. The polarity of magnetic anomaly is composed of a minimum surrounded by two maxima (Fig. 32a). The magnetic source in the structure's center can be modeled as a sphere (SI = 3.36) at 2,035 m depth (Fig. 4d), whereas the magnetic source along the structure's rim can be modeled as a contact (SI = 0.42) at 880 m depth (Fig. 32b).	Structural elements (e.g., Central Elevated Plateau - CEP, concentric inner rings, and outer rim) can be seen in optical and radar images (e.g., feature #1 in the Fig. 37d). On Sentinel-2 band ratio images, a circular feature surrounding the center of Santa Marta can be seen due to its light green shade (e.g., high band 4/band 3 ratio) and smoother textural pattern(feature #2 in the Fig. 37d). It is slightly elongated in the north-south direction, with a main axis of 3.6 km (Fig. 37d).
SMT	Data not available	A linear magnetic anomaly crosses the entire structure in the southeast (feature #1 in the Fig. 30). Related magnetic sources are dominantly deep seated (> 1000m); the shallowest magnetic sources (500 – 100 m) seem to be present just on the outer rim (Fig. 30). In the NE sector, other linear magnetic anomalies seem to arise from deep magnetic source (> 1500 m) feature #2 in Fig. 30, but their magnetic signal seems have to be interrupted near the central zone (feature #3 in the Fig. 30).	All optical and radar images corroborate the strong circular pattern seen for São Miguel do Tapuío (see the conference paper, Chapter 12). An interesting TIR spectral signature suggests that an area closest to the center of São Miguel do Tapuio is characterized by low radiance, thus yielding a dark-colored area (feature #1 in the Fig. 38).

Figures 25, 26, and 27 illustrate this idea. By analyzing Figures 25-27 and Table 4, it becomes clear that PCA analysis applied to airborne gamma-ray spectrometry data for Serra da Cangalha and Riachão Ring is useful to analyze the radiometric contributions of first (outer rim, ring synclines, central uplift) or second order (central basin and collar) structural elements (Fig. 25). In the case of the Serra da Cangalha impact structure, PC1 represents the total variance that comes from K/eTh, eU/K, and eTh, such that the radiometric signature represented by the PC1 score map probably reflects different radiometric sources in the annular basin (Fig. 25a). On the other hand, PC2 represents the total variance that comes primarily from K, such that the central basin and an area in the southwest sector of the annular basin (Fig. 25b) probably are enriched in this radioelement.

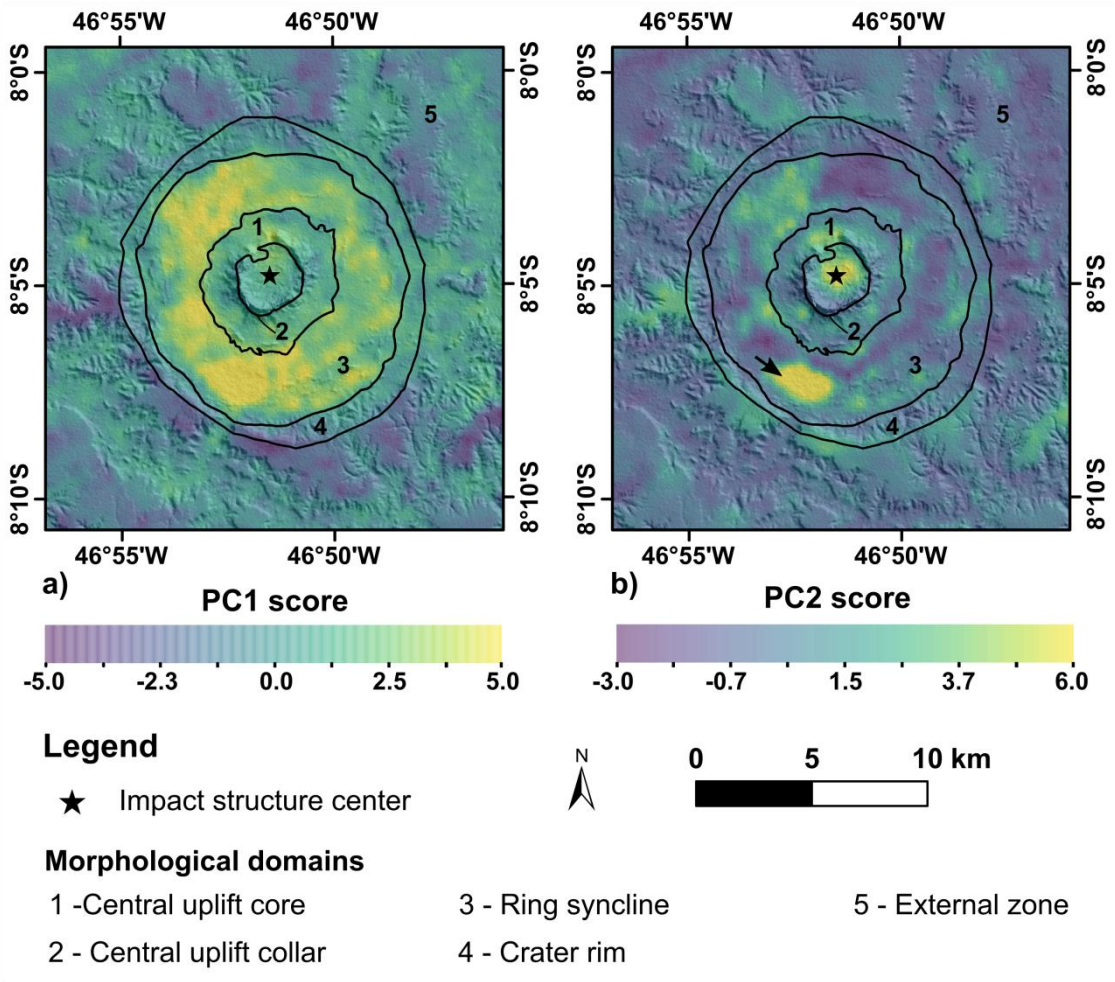

Figure 25: Principal Component (PC) score maps of the Serra da Cangalha impact structure. a) The PC1 score map. b) The PC2 score map. The black arrow highlights the K-rich zone.

For Riachão Ring, the PC1 map represents the total variance that comes primarily from K, such that very low PC1 scores are equivalent to very low K values. This means that, whereas the rim is characterized by low K, the central uplift shows moderate K values (Fig. 26a). In the case of PC4, total variance comes practically from the eU/K ratio. In this way, the PC4 score map shows eU is relatively more abundant than K in the annular basin and outside of the Riachão Ring structure (Fig. 26b). Note that some areas with elevated PC4 score also occur in drainage channels outside of the structure (Fig. 26b).

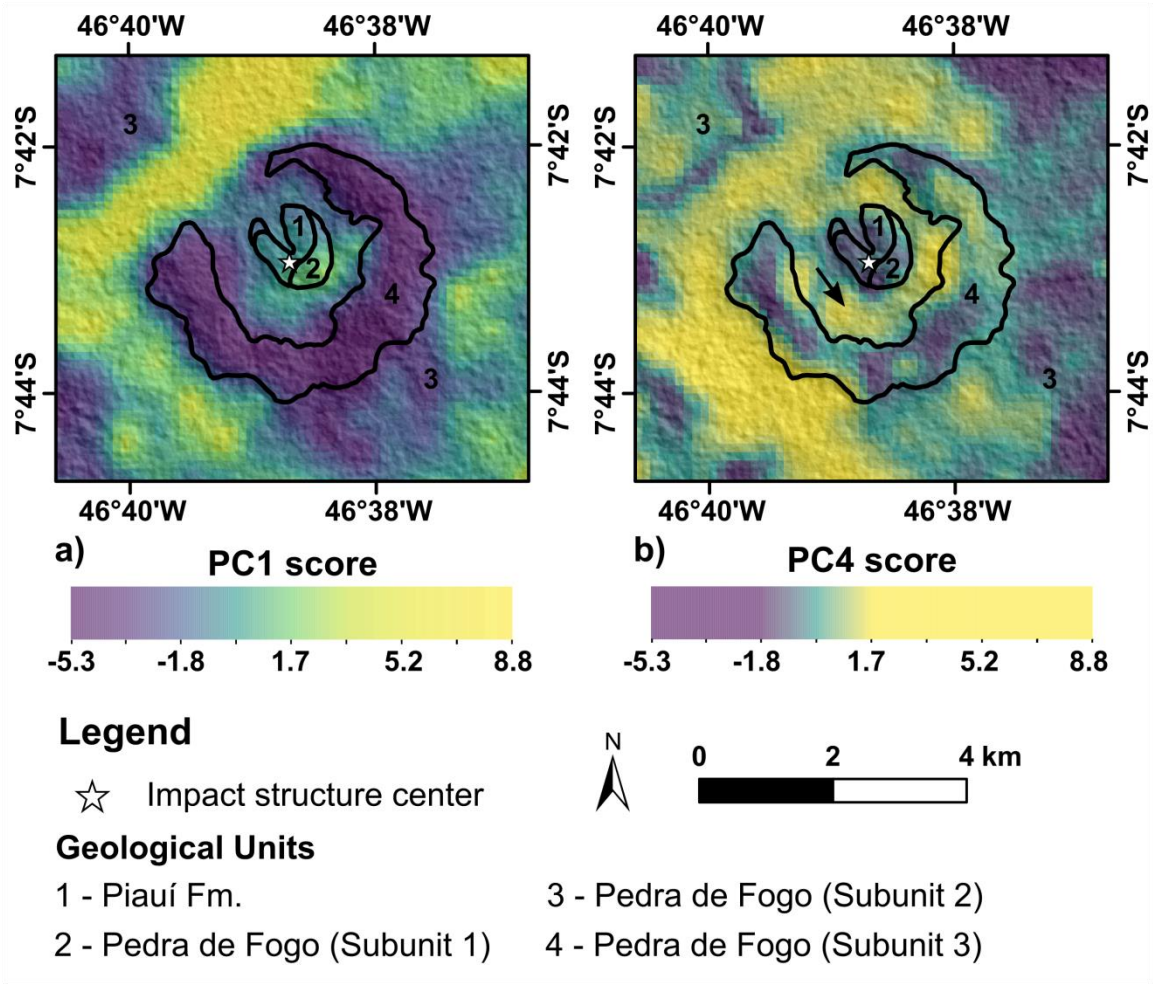

Figure 26: Principal Component (PC) score maps for the Riachão Ring impact structure. a) The PC1 score map. b) The PC2 score map. The black arrow highlights the annular basin. Geological units after Maziviero et al. (2013).

The PCA approach did not reveal a circular pattern at Nova Colinas. However, by using Factorial Analysis, it has been possible to delineate parts of the central uplift, annular basin, and outer rim (Fig. 27). Details of the Factorial

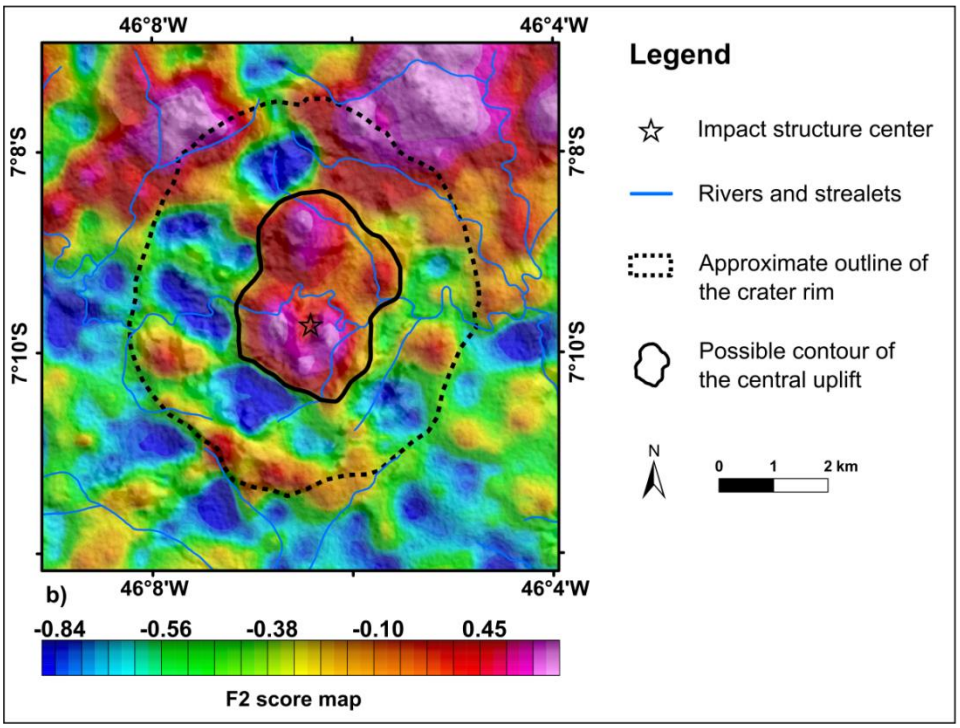

Figure 27: Second-factor (F2) score map for the Nova Colinas impact structure. For more detail see the research paper in Chapter 14.

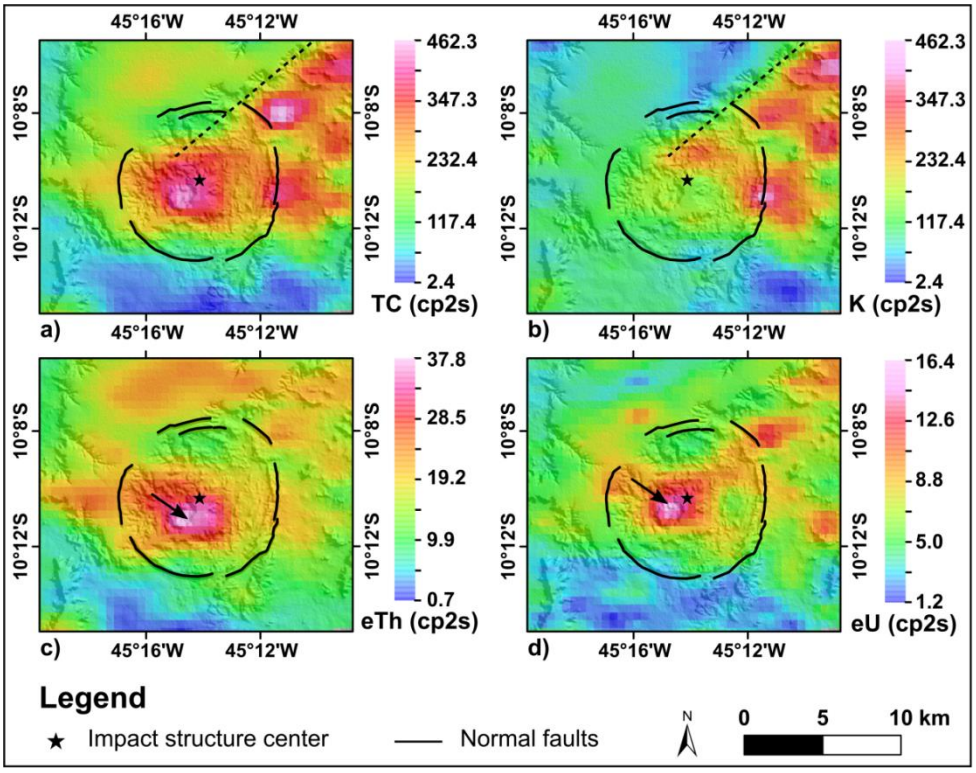

Figure 28: Gamma-ray spectrometry maps for the Santa Marta impact structures. Because the data were not calibrated, the measurements are given as count per two second values (cp2s). The NE-SW trending radiometric signature (dashed line) referred in the text is well-defined in the total count (a) and potassium (b) maps. A circular radiometric signature can be seen in thorium (c) and uranium (d) maps.

Analysis approach can be found in the research paper (Chapter 14). In short, Factorial Analysis applied to airborne gamma-ray spectrometry data acquired over the Nova Colinas impact structure suggest that K variance can be modeled as being derived from a single factor (namely F2). When analyzing the F2 score map, it was possible to identify different high score zones in the SW portion of the rim, near the central uplift, and in the NW and NE sectors outside of the Nova Colinas structure (Fig. 27).

The PCA approach has not provided new information when compared to outcomes from conventional maps for the Santa Marta impact structure (Fig. 28). Even so, interesting features could be identified, including a clear NE-SW trending radiometric signature that apparently ends against the central zone of the Santa Marta impact structure and a circular radiometric signature that is prominent in the eTh and eU maps (Fig. 28 a – d). This radiometric signature is closed on the western side of the slope of the Central Elevated Plateau (CEP) defined by Oliveira et al. (2014). As erosion tends to be dominant in elevated slope areas, this radiometric signature may be related to bedrock, as soil is barely developed in such areas (Wilford et al., 1997). This gamma-ray signature was not reported previously (e.g., Oliveira et al., 2014). Possible reasons for this will be discussed in the next section.

Regarding airborne magnetic signatures of Brazilian impact structures, it is possible to define two groups: magnetic signatures whose associations with the impact event are unclear and magnetic signatures where some association with the impact events can be inferred. The first cases emcompass Serra da Cangalha, Riachão Ring, São Miguel do Tapuio, and Vista Alegre (Figs. 29 and 30), whereas the second case refers to Nova Colinas, Santa Marta, Araguainha, and Vargeão Dome (Figs. 31-35).

Linear magnetic anomalies are present in the Serra da Cangalha, Riachão Ring, and Vista Alegre impact structures, and in São Miguel do Tapuio magnetic anomaly maps. There are no isolated magnetic anomalies at the center of these impact structures, nor are there any ring-shaped anomalies that could be related to these circular structures. Furthermore, the presence of magnetic lows or strongly weakened magnetic relief is also not observed over these impact structures (Figs. 29a, 29b, and 29c, and 30).

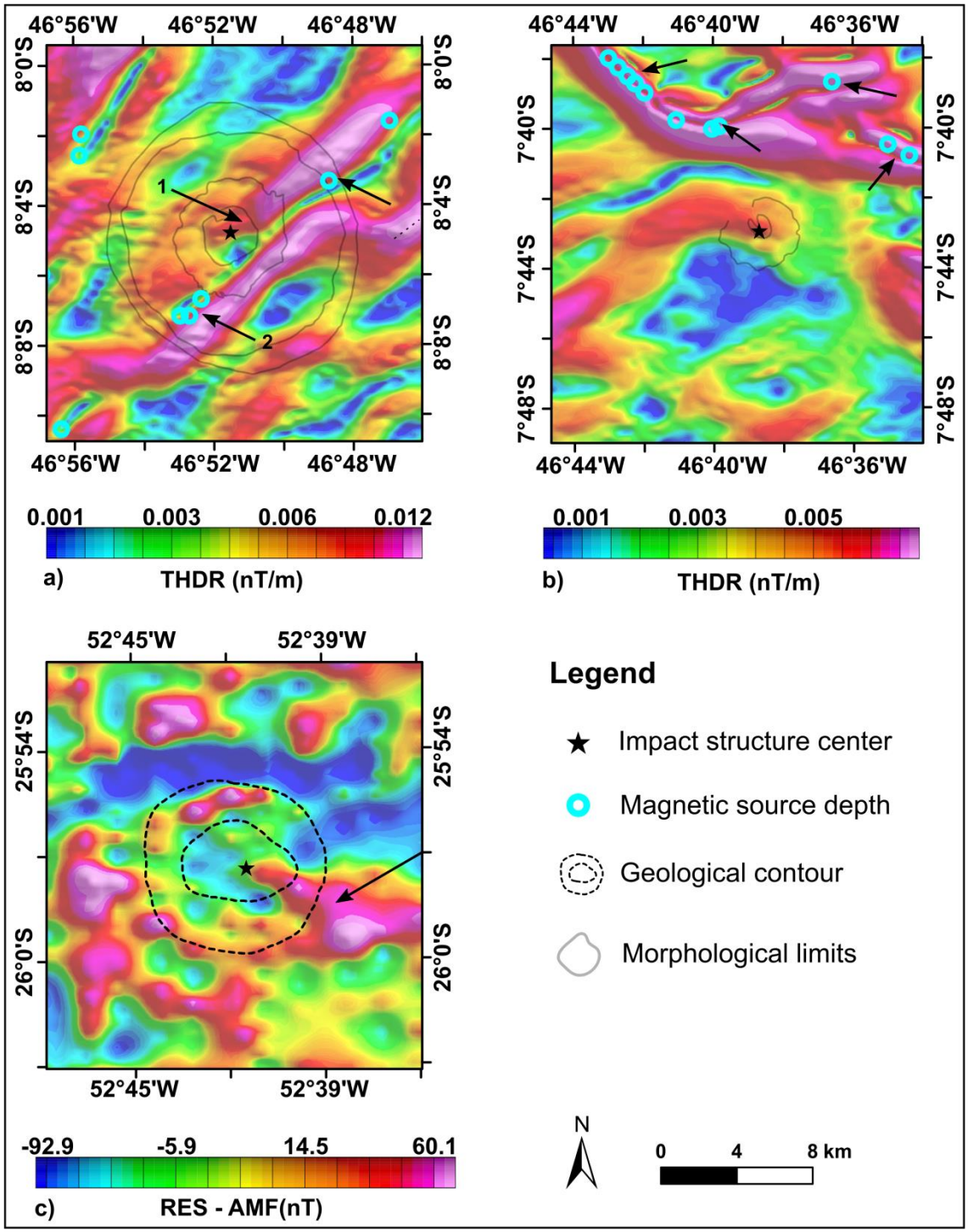

Figure 29: Magnetic anomaly maps of impact structures. a) The THDR map of Serra da Cangalha. The black arrows and labels 1 and 2 denote linear magnetic anomalies discussed in the text. b) The THDR map of Riachão Ring. The black arrows indicate linear magnetic anomalies discussed in the text. c) Anomalous Magnetic Field (AMF) map for the Vista Alegre impact structure. The black arrows indicate linear magnetic anomalies discussed in the text.

At the Serra da Cangalha structure, a linear magnetic anomaly with NE-SW trend seems to cross the impact structure, and becomes terminated against the center (Fig. 29a). In the NE sector far outside of Serra da Cangalha, this

magnetic anomaly reaches a maximum depth of 1899 m depth, which then becomes more shallow (938 m depth) at the NE outer rim. In Serra da Cangalha's central uplift, the northernmost lineament (black arrow #1 in Fig. 29a) seems to disappear, whereas the southernmost lineament (black arrow #2 in Fig. 29a) crosses the entire eastern portion of the central uplift and continues to the SW outer rim. Then it becomes deflected towards an E–W direction. In the SW portion of the outer rim, the magnetic source depth estimates range from ~859 m to 1112 m. Interestingly, these magnetic source depth estimations relate to the area close to a prominent K occurrence described in the previous subsection.

Linear magnetic anomalies can also be noted at the Riachão impact structure, but these anomalies do not cross it (Fig. 29b). At Vista Alegre, a linear magnetic anomaly trending WNW–ESE can be seen extending across the entire eastern portion of the structure and ending near its center. However, as the noise level is high, no magnetic source depth could be estimated (Fig. 29c).

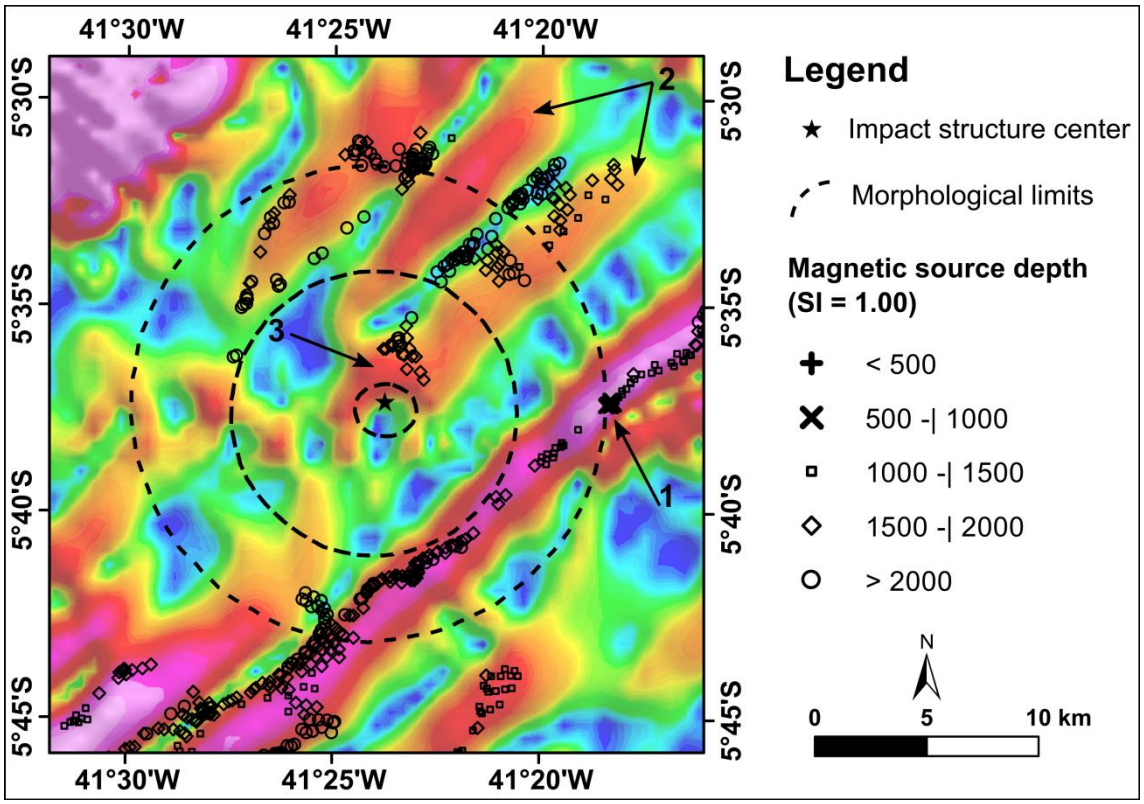

Figure 30: Anomalous Magnetic Field map for the São Miguel do Tapuio (SMT) impact structure. The magnetic signatures of linear magnetic anomalies (black arrows) are described in the text and in Table 4.

At São Miguel do Tapuio, a linear magnetic anomaly trending NE-SW crosses the entire structure in the southeastern part of the structure, against the intermediate ring (black arrow #1 in the Fig. 30). On the other side, other linear magnetic anomalies extend from the NE to the central zone of São Miguel do Tapúio (black arrows #2 in Fig. 30). Except for the linear magnetic anomalies in the NE sector of São Miguel do Tapuio, with shallow magnetic source depth (500 – 100m m), all other linear magnetic anomalies have source depths estimated at > 1 km.

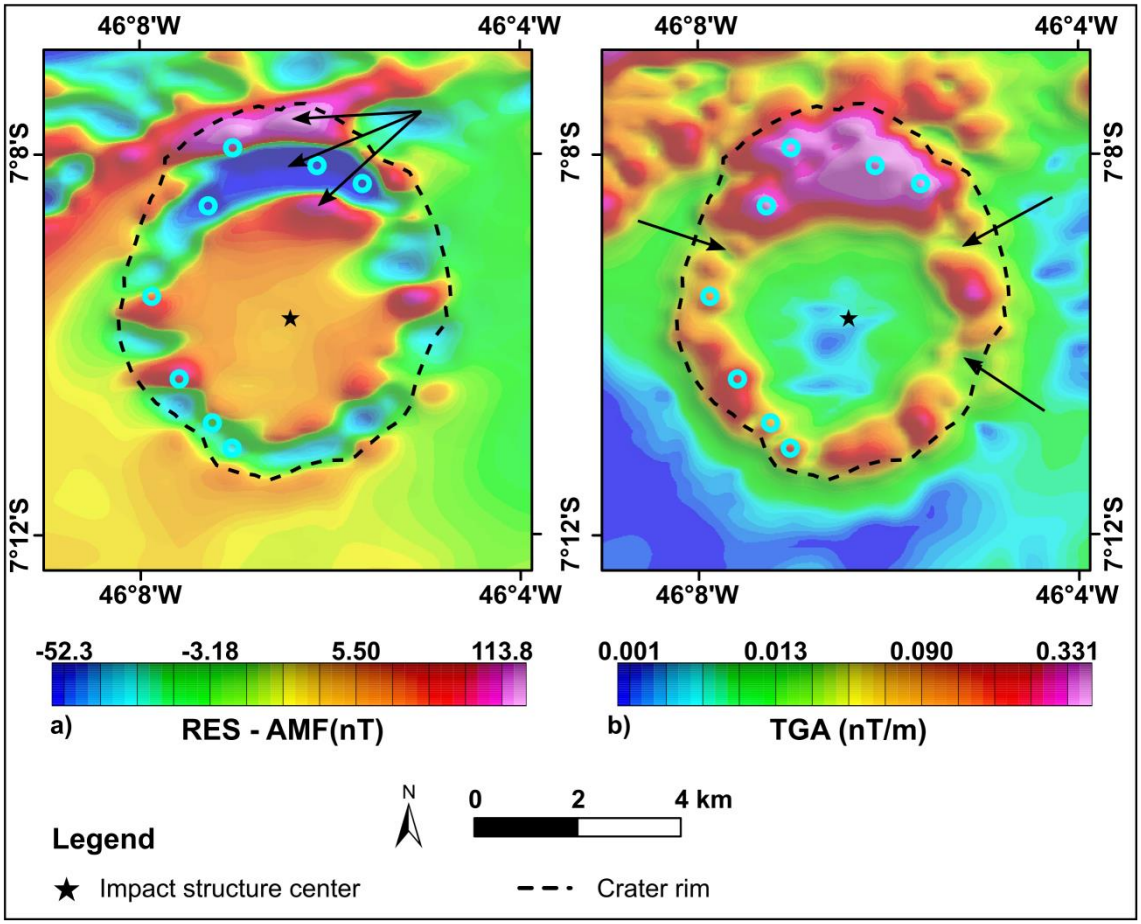

Figure 31: Magnetic anomaly maps for the Nova Colinas (NVC) impact structure. a) Residual Anomalous Magnetic Field (RES – AMF). Note the polarity (black arrows) of the magnetic anomaly in the northern portion of the NVC structure is characterized by a negative part surrounded by two positive parts. b) Total Gradient Amplitude of the map shown in a). The black arrows indicate part of the ring-shaped magnetic anomaly where the magnetic signal is relatively weaker.

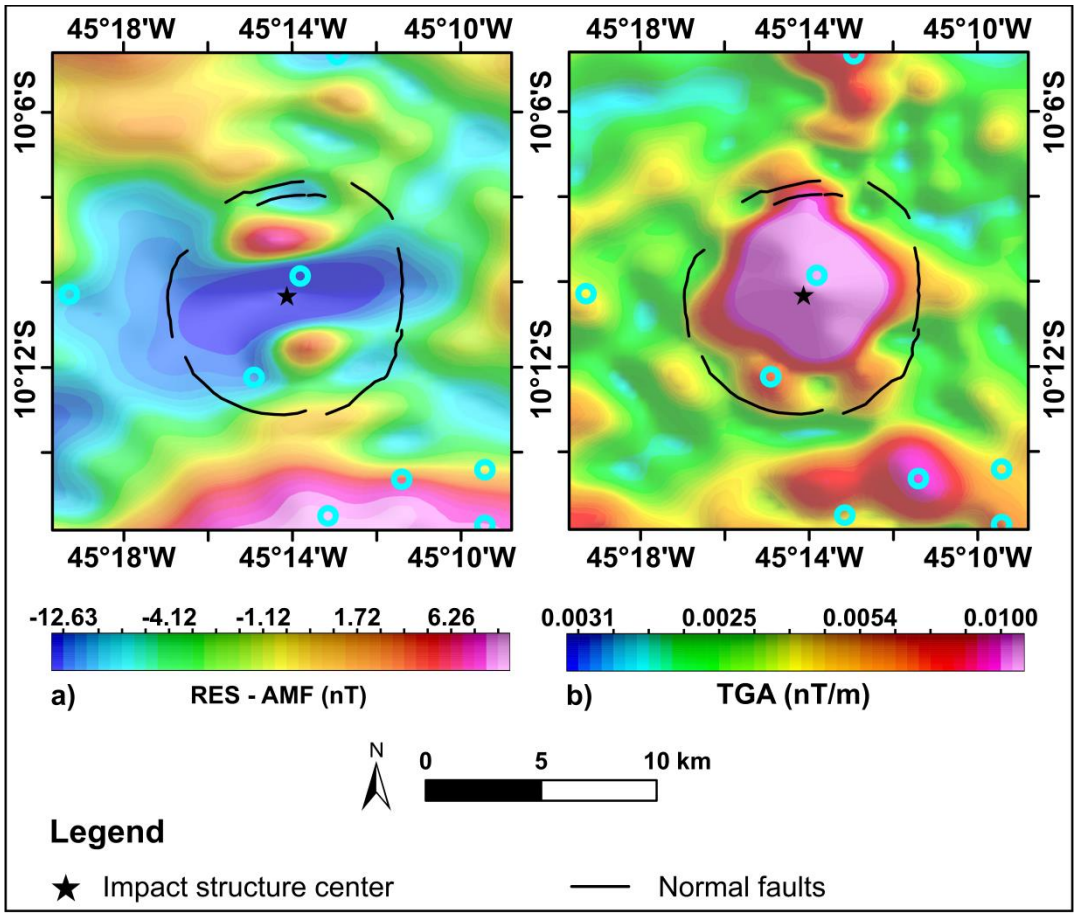

Figure 32: Magnetic anomaly maps for the Santa Marta (SM) impact structure. a) Residual Anomalous Magnetic Field (RES – AMF). b) Total Gradient Amplitude (TGA) of the anomaly shown in a).

Among the magnetic anomalies that may have a relationship with an impact event, the Nova Colinas and Santa Marta impact structures are the more noticeable examples. A well-defined ring-shape magnetic anomaly coincides with the rim of the Nova Colinas structure (Fig. 31a and b). This ring shows interruptions (black arrows in Fig. 31a). The magnetic sources are at depths < 750 m and their shapes are complex. In the Santa Marta impact structure, the magnetic anomalies have a long wavelength and cover the entire impact structure (Fig. 32). This long-wavelength magnetic anomaly can be modeled as a sphere (SI = 3.36) at 2,035 m depth (Fig. 4d), whereas the magnetic source along the structure's rim can be modeled as a contact feature (SI = 0.42) at 880 m depth.

Note that the magnetic anomaly amplitude in the northern part of Nova Colinas is three times greater (0.9 nT/m) than in the south (~0.3 nT/m) (e.g., Silva, 2020). To the north of Nova Colinas, the polarity of magnetic anomaly is

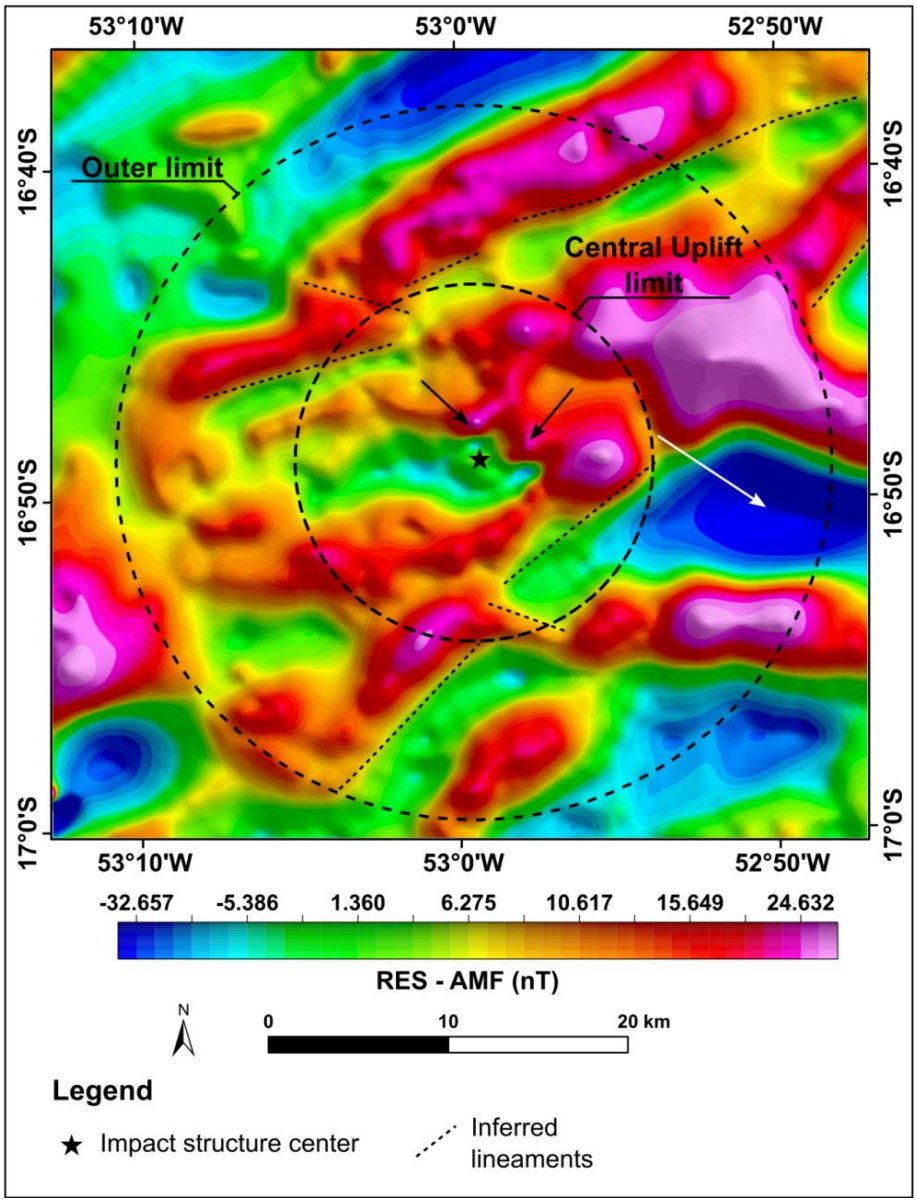

Figure 33: Residual Anomalous Magnetic Field (RES – AMF) of the Araguainha impact structure. The black arrows, white arrow, and dashed lines are magnetic anomalies mentioned in Table 4.

composed of a minimum surrounded by two maxima, suggesting a kind of polarity that would be expected for magnetic anomalies near the magnetic equator (Reid, 2010; Beard, 2012; Dentith and Mudge, 2014). A similar polarity can be seen for the magnetic anomaly in the Santa Marta structure. Indeed, a brief search on the Magnetic Field Calculator website (NOAA, 2025) showed that the magnetic inclinations during formation times for both impact structures were less then -15° (-10.7° for Nova Colinas and -6.1° for Santa Marta). In the next section, it will be discussed how the polarity of these magnetic anomalies could be reinterpreted differently from the proposal by Pereira et al. (2024).

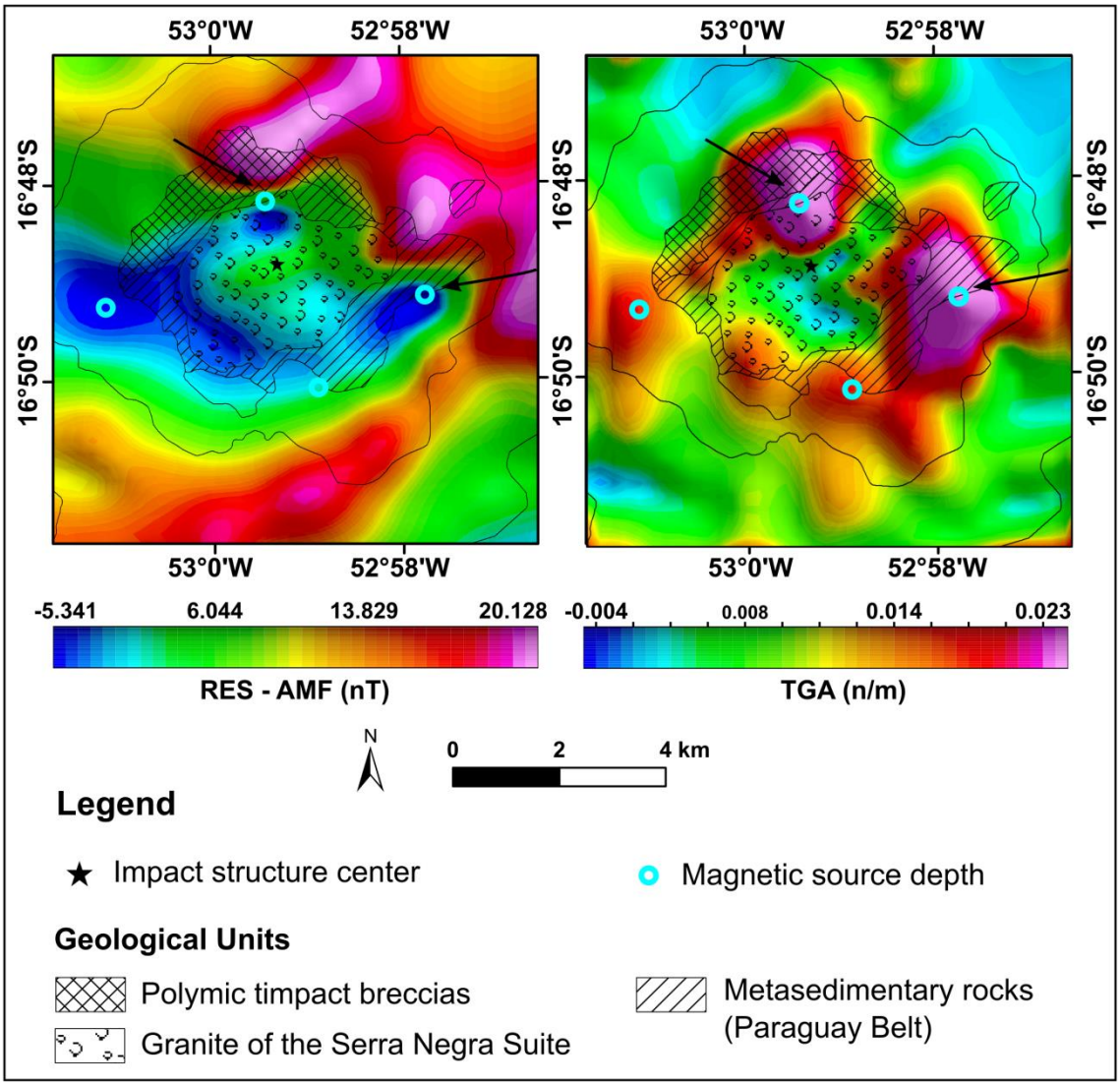

Figure 34: Magnetic anomaly maps for the Araguainha (AGD) central uplift. a) Residual Anomalous Magnetic Field (RES – AMF). Note the polarity of the magnetic anomaly in the NNW and NE of the AGD structure. b) Total Gradient Amplitude for the map shown in a). The black arrows indicate two small but distinct magnetic anomalies in the central uplift area.

Questions about the polarities of magnetic anomalies have also been raised in the context of the Araguainha and Vargão Dome impact structures. Regarding Araguainha, magnetic signatures are listed in Table 4 and shown in the anomaly map of Fig. 33. There are two very prominent but small magnetic anomalies relatively well-isolated in the Araguainha central uplift (black arrows in Fig. 34). Interestingly, they show normal polarities (i.e., the negative part faces south and a positive part facies north) (Fig. 34a), and they are relatively deep seated (750 - 1200 m). Their magnetic peak coincides with metasedimentary rocks of the basement that are in contact with the Serra Negra Suite Granite in the center of the structure (Fig. 34). The Serra Negra

Granite, in turn, does not shows magnetic anomalies. Note that this granite seems to be enclosed by a magnetic halo that encompasses the two normal dipole magnetic anomalies described above (Fig. 34b). The origin of these magnetic anomalies will be discussed in the next section. Regarding the magnetic signatures of Vargeão Dome, there are magnetic lineaments and an approximately circular magnetic anomaly close to the center of Vargeão Dome (Fig. 35). The linear magnetic anomalies are trending ENE–WSW and have been interpreted as magnetic signatures related to the regional Lacinha Cubatão fault system (Kazzuo-Vieira et al., 2009) (black arrow #1 in Fig. 35b). As these lineaments are truncated by the rim of Vargeão Dome (Fig. 35b), they were considered pre-impact features (ibid). In the southeastern survey area, outside the VGD structure, SED solutions calculed yield a 580 m depth for one of these linear magnetic anomalies (black arrow #2 in the Fig. 35b). This magnetic source depth estimate is substantially less than values presented in previous work (1000 m) (Kazzuo-Vieira et al., 2009).

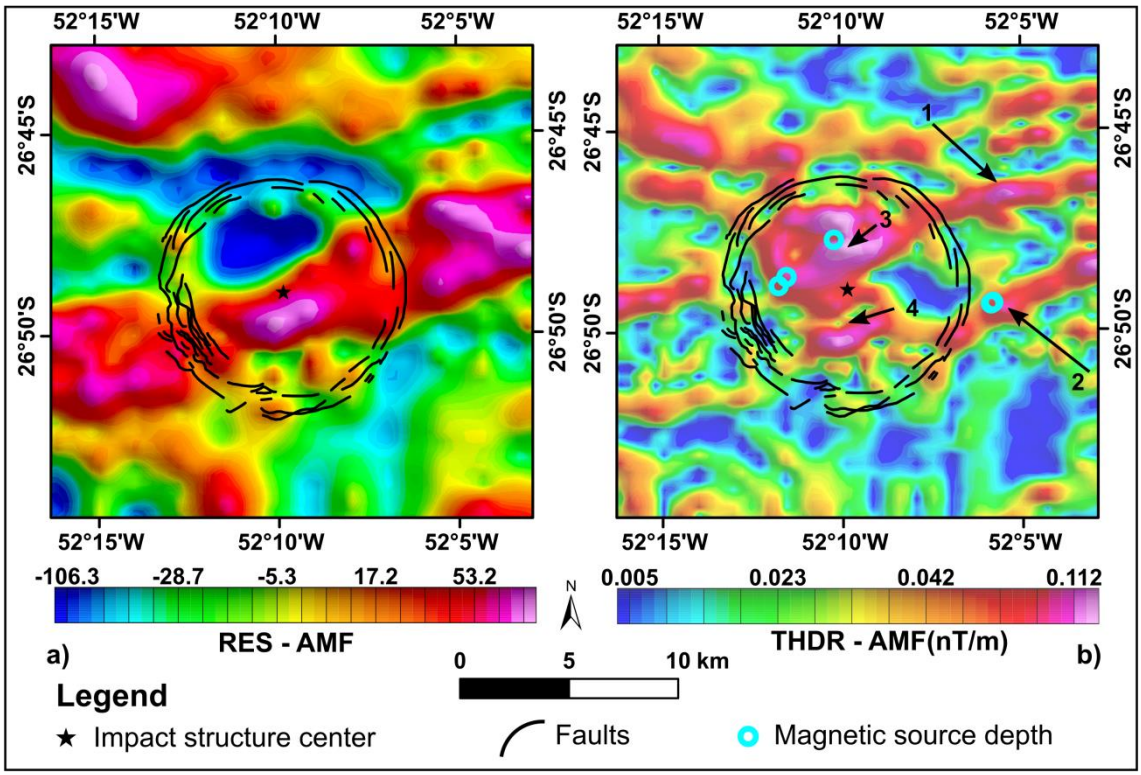

Figure 35: Magnetic anomaly maps for the Vargeão Dome (VGD) impact structure. a) Residual Anomalous Magnetic Field (RES – AMF). b) Total Gradient Amplitude for the map shown in a). The black arrows indicate the magnetic anomalies described in the text.

The circular magnetic anomaly close to the center of Vargeão Dome was also observed by Kazzuo-Vieira et al. (2009). They introduced this circular anomaly as a strong magnetic (~0.324 nT/m) anomaly, which they interpreted as being related to impact breccias, which, in turn, could represent a remnant of a central uplift. However, the map shown in Fig. 35b suggests that this circular magnetic anomaly is actually formed by two sources: one located towards the north (black arrow #3 in Fig. 35b) and another more to the south (black arrow #4 in Fig. 35b) of the center of the Vargeão Dome impact structure. The former has a circular shape and magnetic source depth estimates of 556 m (central-north portion) to 1380 m (western portion) (Fig. 35b), whereas the second anomaly has a linear shape, but no depth estimates were obtained for it because no Standard Euler Deconvolution Solutions (SEDS) were found. Figure 35a shows that the interaction between these two anomalies with the magnetic signal from the linear pre-impact structures mentioned above results in a linear magnetic anomaly with an ENS-WSW direction. Despite this superposition, it is clear that the magnetic anomalies within the impact structure show an inverted polarity (Fig. 35a), that is, the positive part is facing south and the negative part is facing north. Again, a quick search on the NOAA website shows that the magnetic data for Vargeão Dome were acquired at mid-magnetic latitudes (magnetic inclination of -27.3°). At such latitudes, if only induced magnetization is present, the shape of the magnetic anomaly is expected to have a positive part facing north and a negative part facing south (i.e., normal polarity), just the opposite of what is observed at Vargeão Dome. The possible explanation for these observations will be explored.

14.1.3 Main features seen in spaceborne images.

The main features of Brazilian impact structures seen in spaceborne images also have been summarized in Table 4. This subsection is focused on results derived from multispectral images. The results derived from SAR images have been accepted for presentation at the 2025 Latin American GRSS and ISPRS Remote Sensing Conference (see Chapter 12). Here, some of these results will be discussed.

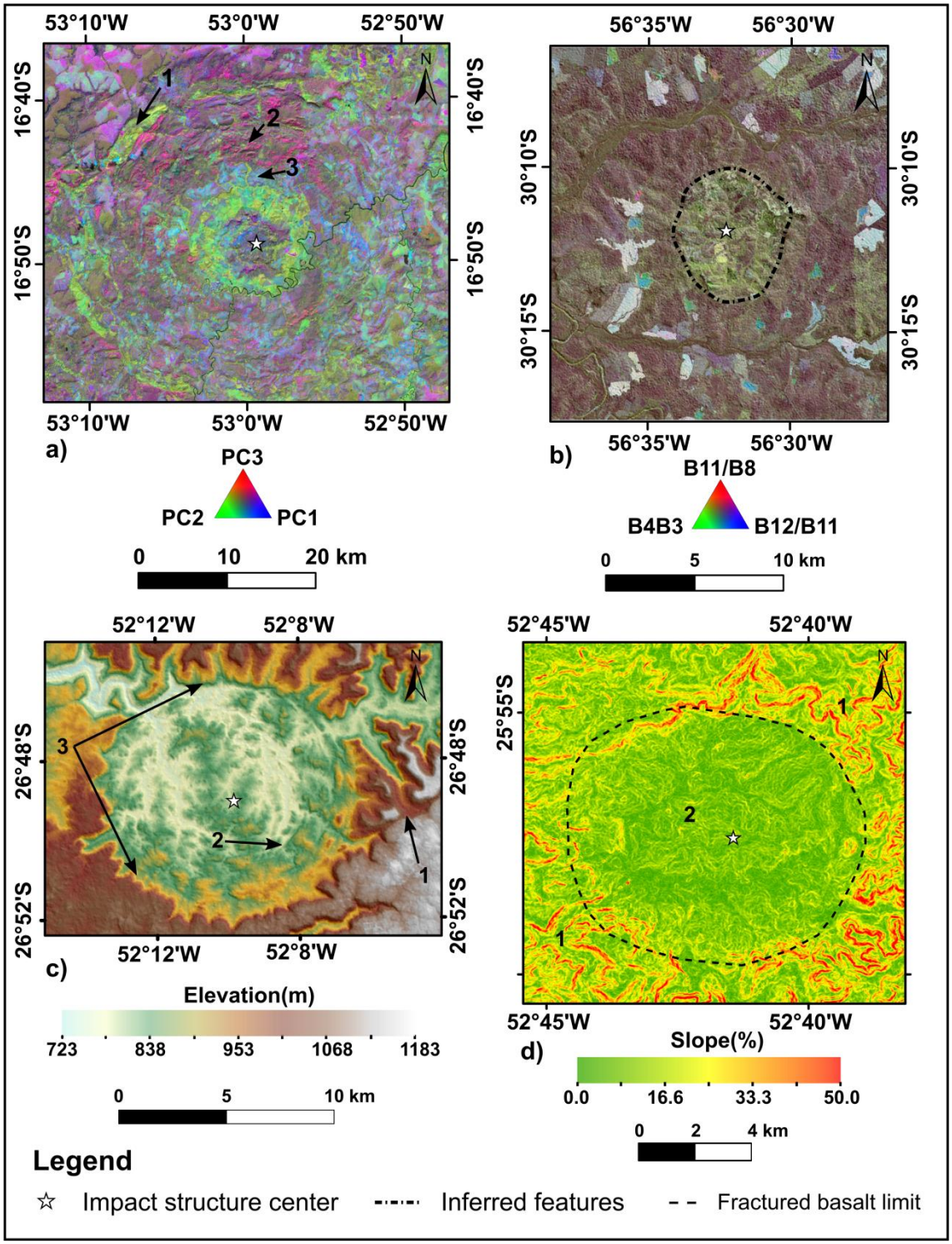

Figure 36: Examples of spaceborne images of impact structures in the Paraná Basin. a) Principal Component score maps from ASTER scenes for the AGD structure. Features 1, 2, and 3 are described in Table 4. b) Sentinel-2 band ratio map of the CJU structure. c) Elevation map of the Vargeão Dome impact structure. Features 1, 2, and 3 are described in Table 4. d) Slope map for the Vista Alegre impact structure. Features 1 and 2 are described in Table 4.

Regarding impact structures in the Paraná Basin, Table 4 and Fig. 36 show that the approach of using images from more than one sensor was a good strategy, as some first-order elements of impact structures (outer rim, ring syncline, or central uplift) are better visualized by one given sensor, but not by others. For instance: the spectral contrast when using PCA applied to ASTER scenes clearly outlines the Araguainha outer rim and outermost part of its central uplift (Fig. 36a). On the other hand, an elliptical feature in the Cerro do Jarau impact structure is well-defined in Sentinel-2 band ratios (Fig. 36b). Second order structural elements (normal faults, concentric faults, etc) in Vargeão Dome and the contrast between internal and external portions of the Vista Alegre scene are emphasized in elevation maps derived from Digital Elevation Models (DEM's) (Fig. 36c and d).

In the Parnaíba basin, the use of imagery from different sensors was also essential to enhance first-order features. A few prominent examples include: i) the decorrelated TIR-ASTER bands revealed a semi-circular feature in the Serra da Cangalha annular basin (black arrows in Fig. 37a); ii) The Riachão Ring's central uplift and outer rim are well-defined in RGB composite color of Sentinel-2 bands (features #1 and #2 in the Fig. 37b); iii) the north and south sectors of the Nova Colinas impact structure are distinguished in the TIR-ASTER bands (features #1 and #2 in the Fig. 37c); iv) an approximately circular feature is identified in Santa Marta's central zone through the RGB composite color map for Sentinel-2 band ratios (feature #2 in the Fig. 37d), and v) an intriguing Thermal Infrared (TIR) signature is seen in the São Miguel do Tapuio central uplift area (feature #1 in the Fig. 38).

Regarding Sentinel-1 Dual Pol images, most backscatter signatures of Brazilian impact structures are dominant results of soil properties, flat surfaces, and vegetation. However, part of the backscatter signatures may be related (directly or indirectly) to features that arise from impact events. This may be the case for the high VV and VH backscatter that can be associated with silificied sandstones in the Serra da Cagalha and Cerro do Jarau central uplifts, the high and low backscatter zones in the Nova Colinas impact structure, low backscatter zones in the Riachão Ring annular basin, and a semicircular feature between the intermediate ring and the central high of São Miguel do Tapuio

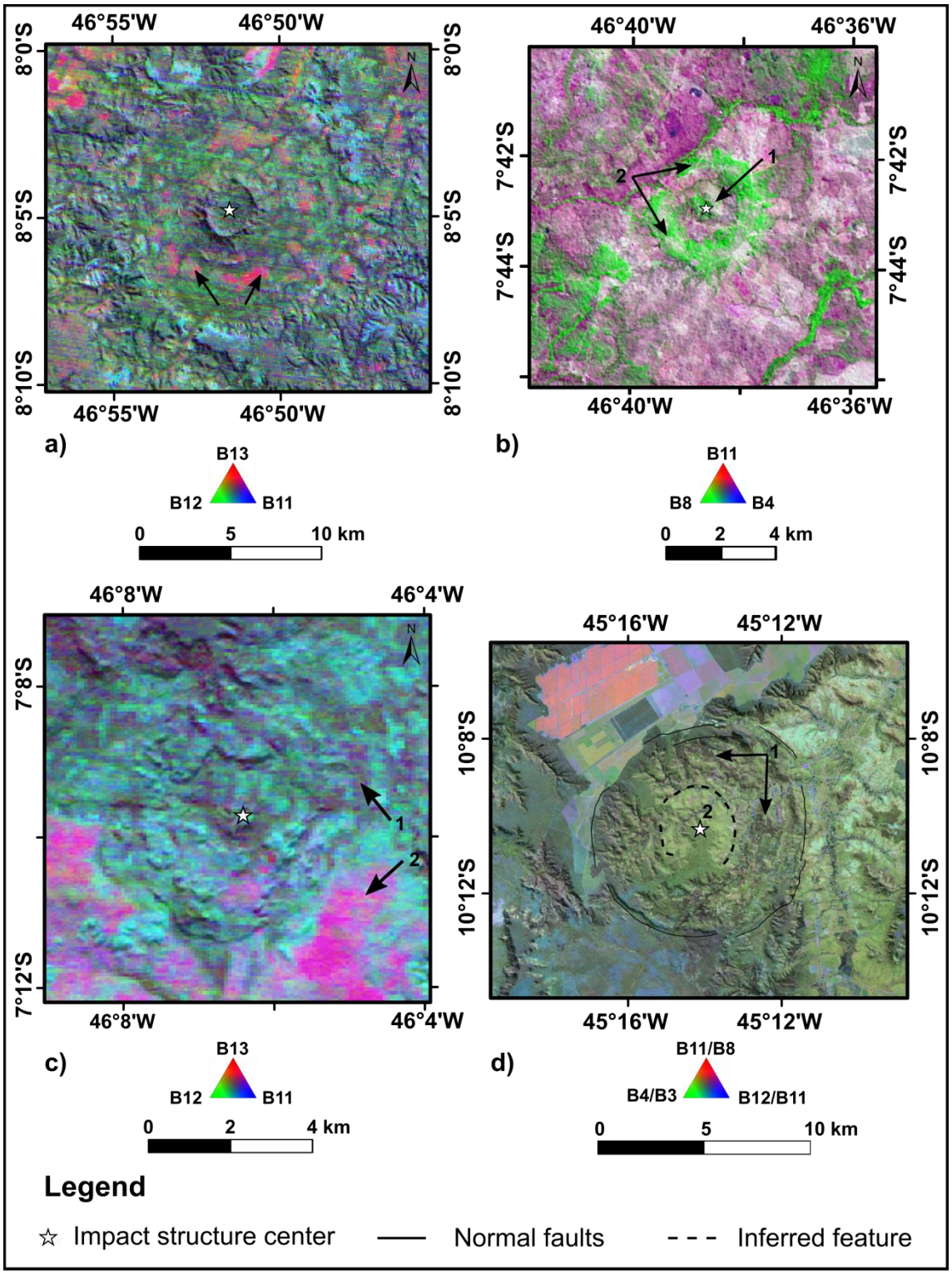

Figure 37: Examples of spaceborne images of impact structures in the Parnaíba Basin. All the features indicated by numbered black arrows on the maps are described in Table 4 and in the text. a) RGB composite color map of decorrelated TIR-ASTER bands for the Serra da Cangalha impact structure. b) RGB composite color map of Sentinel-2 bands of the Riachão Ring impact structure. c) RGB composite color map for decorrelated TIR-ASTER bands for the Nova Colinas impact structure. d) RGB composite color map for Sentinel-2 band ratios for the Santa Marta impact structures.

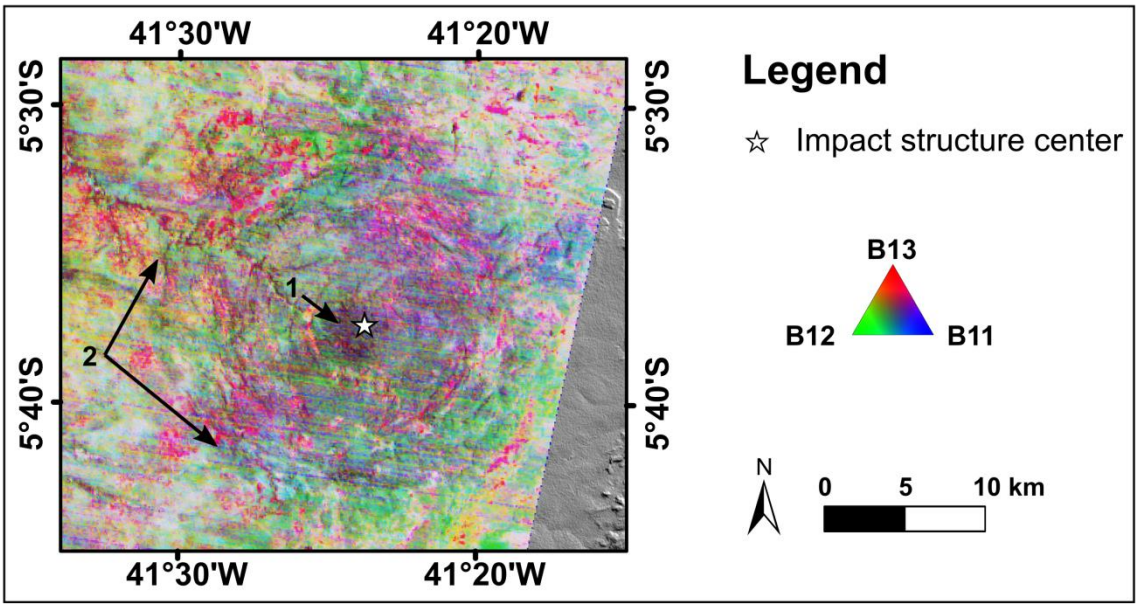

Figure 38: RGB composite color map for decorrelated TIR-ASTER bands for the São Miguel do Tapuio impact structure. The features indicated by numbered black arrows are described in Table 4 and in the text.

structure. All these SAR features are described in the conference paper (Chapter 12).

Finally, it is worth to mention that several spaceborne image signatures described above, especially those related to morpho-structural compartments, had also been indicated in previous works (e.g., see Crósta et al., 2019a and references therein). However, some findings derived from optical and SAR images reported here (e.g., the TIR signatures of the São Miguel do Tapuio and Serra da Cangalha structures, elliptical features found over the Cerro do Jarau and Santa Marta central uplifts, and high VV and VH backscatter from silificied sandstones in the Serra da Cagalha and Cerro do Jarau central uplifts) reveal that there is an avenue to still study the spectral signatures of impact structures in more detail.

14.2 Main geological, geophysical and spaceborne features of potential targets

14.2.1 Main geological features

The main geological features of potential targets selected in this work are summarized in Table 5. This table demonstrates a large discrepancy in terms of available geological information between the structures on sedimentary and

crystalline target rocks. Even for potential targets in crystalline terrain, detailed geological maps (scales ~ 1:100,000) are only available for two potential targets (Inajáh and Brejões), and only one of them (Brejões) has been effectively studied in more detail (e.g., Barbosa et al., 1998 and 2006). Detailed geological and geophysical information is available only for the Colônia target. Much work has been done here in the past (see Chapter 9). In addition, the Colônia structure is located close to major universities, which has facilitated access, and Colônia was evaluated as a target for an ICDP drilling project.

The lack of geological information of potential targets in sedimentary terrain arises from the fact that geological mapping efforts in Brazil have generally focused on Precambrian terrains, which apparently have a greater mineralization potential (Costa et al., 2023). Although recent geological maps of Brazilian intracratonic sedimentary basins have been published (e.g., Bacia do Paraná - Horn et al. 2022), the regional scale of such maps (commonly 1:1,000,000 or 1:500,000) does not allow the identification of the geological units associated with limited size potential targets in sedimentary terrain, such as those studied here.

In an attempt to work around this problem, information was obtained from either personal communication or mining activity recorded by the Brazilian National Mineral Agency. Depending on the type of mining activity being carried out in a given region, it is possible to obtain lithological information. For instance, the regional geological map available for Itiquira (ITA) shows an area dominated by siliciclastic materials, but, interestingly, recent requests (e.g., mining process numbers 860635/2022, search data: July 19, 2025) from mining companies have focused on research for industrial minerals, such as Rare Earth Elements, and gold. Although the source of such minerals may be secondary, it is equally possible that they derive from a primary source (e.g.,

Table 5: Main geological features of potential target structures. The information was compiled from the previous work listed in Table 1 (Chapter 10) and from results of this work. Abbreviations: ITA – Itiquira; CDS – Cardoso; BJD – Bom Jardim; SCD – Sucunduri Dome; INJ – Inajáh; BRJ – Brejões; SFM – São Francisco do Maranhão; CNB – Caraíbas; CLA – Colônia.

Potential Targets	Central point	Diameter (km)	Age (Ma)	Outcrop descriptions	Description of structural elements.	Petrographic observations
ITA	54°22'W / 17°21'S	~17.5*	Undefined	Not available.	Not available.	Not available.
CDS	50°34'W / 14°06'S	~5.25*	Undefined	Not available.	Not available.	Not available.
SFM	43°02'W / 6°11'S	8.5	Undefined	Supposedly strongly fractured or recrystallized monocrystalline quartz pebbles and breccia with fluidal texture inside the northeastern part of the structure.	Not available.	Not available.
CNB	43°10'W / 7°12'S	~1.85*	Undefined	Not available.	Not available.	Not available.
INJ	50°58'W / 8°40'S	~6.2*	1985±6**	Medium- to coarse-grained meta-sandstones (Mururé Fm.), strongly silicified rocks, and alumosilicate metasedimentary hornfels occurs near the rim, whereas rock fragments with fine-grained phaneritic to aphanitic texture thought to be derived from diabase dikes occur within the structure. Vertical fractures and vertical quartz veins seem to occur locally in the INJ structure.	Shows a depressed circular basin surrounded by a ring of strongly weathered silicified rocksthat seems to be elevated by several meters above the surrounding terrain. No distinct central zones or intermediate features. A small circular structure occurs in the SW of the INJ structure and several other 2 - 4.5 km diameter circular bodies occur in the vicinity.	The monzogranites of the Tarumã Suite exhibit a hypidiomorphic granular texture. The main constituent minerals are quartz, plagioclase, K-feldspar, and biotite. Deformation features were not visible in the figures presented by Silva et al. (2021)
SDC	59°07'W / 8°07'S	~90	Undefined	Brecciated materials and silicified rocks have been mapped within the structure. Some breccias derived from rhyolites are characterized with red color, mineral fragments, and strong cataclasis. These breccias, and other rocks, are commonly strongly hydrothermally altered. Brecciated quartzite was mapped in fault zones at the northeast rim.	Impressive semi-circular features with lithostratigraphic units becoming younger toward the outer rim structure. However, the youngest alkaline rocks seem to be present in the north-central part. The rim is well-defined in the east, whereas in the northwest and west sectors the outer rim is open. There is an apparent NE-SW trending inversion at the SW terminus of the rim. Other dome-like features occur close to the SDC structure.	Not available.
BJD	63°27'W / 9°57'S	~9*	995 – 1005**	Granites show textural variation towards the center, changing from coarse-grained to medium- or even fine-grained textures. Microgranite dykes with 20 cm width and trending NW and NE are common around the central zone of the structure. Tobocas syenites also show textural variation with granular, microgranular, and porphyritic types commonly observed.	The contact zones between Massangana and Bom Jardim facies are abrupt and interpenetrative, with numerous enclaves of Massangana granitoids, with some enclaves having meter-size. The intrusion of the Bom Jardim facies overprinted an intense fracturing event in the Massagana facies.	Perthitic orthoclase is dominant, with biotite, quartz, and plagioclase being the most common other minerals. These assemblages are commonly surrounded by finer-grained minerals (e.g., quartz, biotite, plagioclase, and fluorite and biotite halos). Quartz occurs in idiomorphic crystals and mainly as a constituent of finer-grained masses, in the interstices between larger crystals (mainly orthoclase).

BRJ	39°46'W / 13°07'S	~19.5*	2.061±6**	Overall, the oldest lithostratigraphic rocks seem to occur outside of the structure (e.g., heterogeneous granulites) and along the rim (metabasalts). Inside the structure, charnockites are alleged to be heterogeneously deformed and include angular xenoliths of the surrounding rocks.	Has a complex structural pattern. Foliations dip outwards in the east, west, and north sectors, but dips are toward the center in the southern portion. The inner parts show high strain deformation with typically vertical structures, whereas in the core, foliations have subhorizontal dips. Radial faults are abundant in the rim zone, whereas in the core seems to exist an approximately N-S trending fault.	Porphyroblasts (2 - 4.3 mm) and xenomorphic (0.3 - 1.2 mm) quartz crystals display undulatory extinction, deformation bands, development of sub-grains with serrated to lobate boundaries to other quartz grains, and microstructures that bulge into neighbouring deformed (elongate and almond-shaped) garnet porphyroblasts.
CLA	46°42'20'' / 23°52'S	3.6	Undefined	The structure is filled by sediments and there are no outcrops of them in the swampy deposits at surface. Samples recovered from boreholes into the structure with supposed impact facies have not been available to the academic community.	Shows crater-lake morphology with the outer ring reaching up to 125 m above the inner depression. No other crater-like structure occurs near CLA.	Supposed PDF, mosaicism, undulatory extinction, and other impact-related features in quartz grains have been claimed by previous works, but bona fide confirmation of impact dagnostic features is missing.

*Diameter size estimated by this work. **Age of target rock.

intrusion). Similarly, the regional geological map of the Cardoso target shows only Cenozoic deposits, but this target was investigated for ilmenite occurrence approximately three years ago (mining process number 860635/2022, search data: July 19, 2025). Unfortunately, it was not possible to obtain information on whether ilmenite was actually found, or the type(s) of rock occurring in the area.

Unlike the ITA and CDS targets, no mining process request at or close to the São Francisco do Maranhão (SFM) and Carnaíba (CNB) targets has been recorded by the Brazilian National Mineral Agency websites. However, a few pieces of information could be recovered from previous work and personal communication for at least the SFM structure.

As metioned, the SFM (formerly called Amarante) circular structure was identified by Lima et al. (1990), who associated it with Mesozoic magmatism. However, this association has not been supported by geological or petrographic evidence yet. More recently, a research team from the Maranhão Astronomy Society and Astrobiology Laboratory of the Federal University of Maranhão State found some unusual features in rock samples, including strongly fractured or recrystallized sandstones and monocrystalline quartz pebbles and breccias with alleged fluidal texture (pers. comm. S.L.A. Brenha, São Luis) (Fig. 39). This team proposed an impact origin for SFM. However, bona fide evidence for impact based on unequivocal shock deformation features (PF, FF, PDF, diaplectic glass, etc) has not been published for SFM yet. Finally, the only information that can be inferred for the Caraíbas (CNB) structure from the regional geological map is that unconsolidated materials probably include sandstones, siltstones and shales of the upper Poti Formation.

Among the potential targets located in crystalline terrain, Colônia shows several features of potential interest for impact research including brecciated materials with angular and poorly sorted clasts and several minerals with alleged planar microdeformation features (Velázquez et al., 2013). However, the impact origin for Colônia is still unresolved because it has not been proven that these planar features are unambiguous impact evidence (see Reimold et al., 2014).

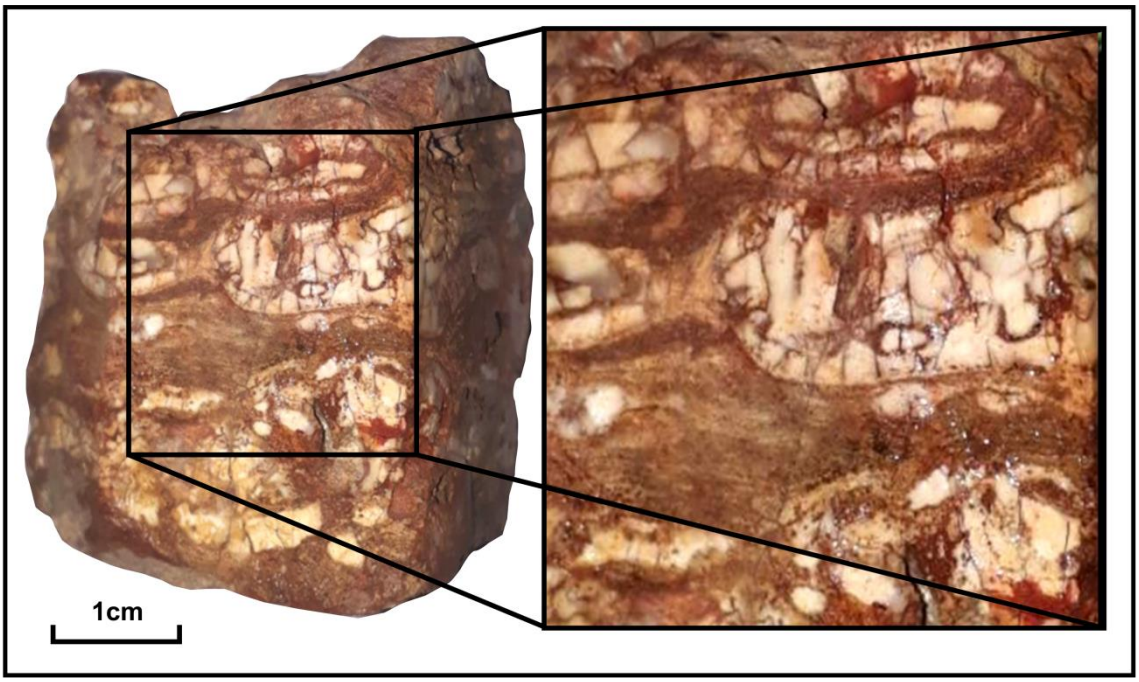

Figure 39: Example of supposedly recrystallized sandstone from São Francisco do Maranhão. Image courtesy of S.L.A. Brenha.

Brejões (BRJ) is another target in crystalline terrain that is relatively well-studied. For the purpose of the present study, it is important to note that the main deformation features in BRJ (e.g., quartz crystals with undulatory extinction, deformation bands, sub-grains with serrated to lobate boundaries to other quartz grains, and deformed garnet porphyroblasts) (Table 5) do not occur in samples from BRJ's central zone, but from alleged contact zones against heterogeneous granulites or supracrustal rocks (Barbosa et al., 2006). Such zones occur in the rim zone where vertical, radial faults are alleged. Otherwise, the BRJ central zone displays features with subhorizontal dips and the rocks are more homogeneous and younger than the heterogeneous granulites and other supracrustal rocks that surround the structure (Table 5). There are other dome-like features near the BRJ structure that also show deformation features similar to what has been seen at BRJ.

A geological map at a relatively small scale (1: 100,000) is also available for Inajáh (INJ), but in contrast to BRJ, INJ has not been extensively studied, such that geological information about it is sparse. Among the few geological descriptions obtained in this work, the presence of strongly silicified rocks, alumosilicate metasedimentary horfels, and granular minerals (quartz, feldspars, and/or cordierite) associated with elongated poikiloblasts (andalusite,

biotite, and fibrous sillimanite) along the edge of INJ were considered most relevant. Again, other circular bodies also have been mapped close to INJ. They are smaller than the INJ structure, but they have been considered coeval with it.

Regarding the Sucunduri Dome potential target, advance in the knowledge of this structure has been hindered mainly because outcrops are in difficult-to-reach areas (e.g., a few outcrops can only be accessed by small boat). However, a recent investigation carried out by a geologist of the Geological Survey of Brazil has shed some light on this structure. For instance: the plateau near the center of SDC seems to be supported by alkaline rocks that are strongly radioactive (I.P. Marques, pers. commun.). Inside of the SDC structure, some breccias containing rhyolite fragments occur, but in general, such breccias are predominately composed of phenocrysts of K-feldspar and strongly hydrothermally altered (ibid).

Some possibly significant geological features of the Bom Jardim (BJD) target include (Table 5): abrupt contact zones between Bom Jardim facies and Massangana facies containing meter-size blocks of country rock (i.e. Massangana granites), textural variation towards the BJD center, presence of microgranite dikes near the BJD central zone, and presence of quartz of well-formed grains and as main constituent of finer-grained masses. As will be seen in the next section (Chapter 15), all these geological features could be interpreted in an impact origin context for the BJD structure.

14.2.2 Airborne gamma-ray spectrometry and magnetic signatures

Of the potential targets in sedimentary terrain, only the Cardoso structure shows a significant radiometric signature. This signature is characterized by a K concentration of only 1.5 %, but it is high enough to make this structure distinct from its surroundings (Fig. 41a). No circular radiometric signatures are seen at Itiquira (ITA) (Fig. 41b), and airborne gamma-ray spectrometry data are not available for the São Francisco do Maranhão (SFM) and Caraíbas (CBN) potential targets. In contrast, circular or partially circular airborne gamma-ray spectrometry signatures are evident at all potential targets in crystalline terrain. The rim of Brejões (BRJ) is well characterized by low radioelement content (Fig. 42a). This signature is particularly evident in the eastern sector, where two

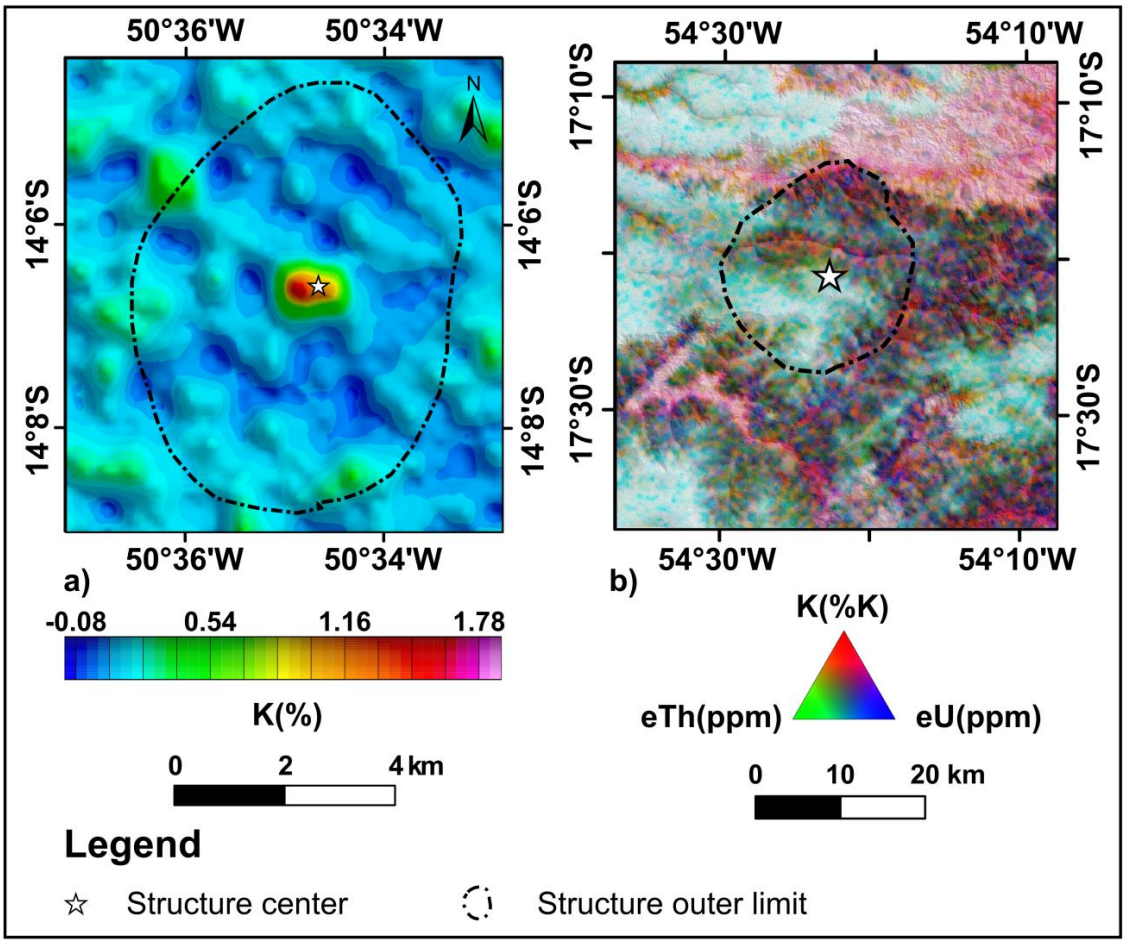

Figure 41: Radiometric maps for the Cardoso and Itiquira circular targets. a) K concentration map for the Cardoso potential target. b) RGB composite color of radioelement concentrations at the Itiquira potential target.

separate eU and eTh rich zones (colored in cyan on Fig. 42a) occur. Zones enriched in eU and eTh also occur in the Colônia (CLA) structure, but here, these zones are emphasized in the eU/K and eTh/K ratio maps (e.g., Fig. 42b), suggesting that both eU and eTh are relatively more abundant than K. Note that the center of this radiometric signature is shifted northward relative to the CLA geometric center. The airborne gamma-ray spectrometry signature of Sucunduri Dome (SDC) represents the most impressive result amongst the potential targets on the Amazonian Craton. There are several concentric features in the eastern and southern portions of the structure (feature #1 in the Fig. 43), whereas in the northwestern portion (feature #2 in the Fig. 43) the SDC structure is open and no concentric features can be seen. Interestingly, there is a turning point in the SW sector of the apparent rim (feature #3 in the Fig. 43), that is, the curvature

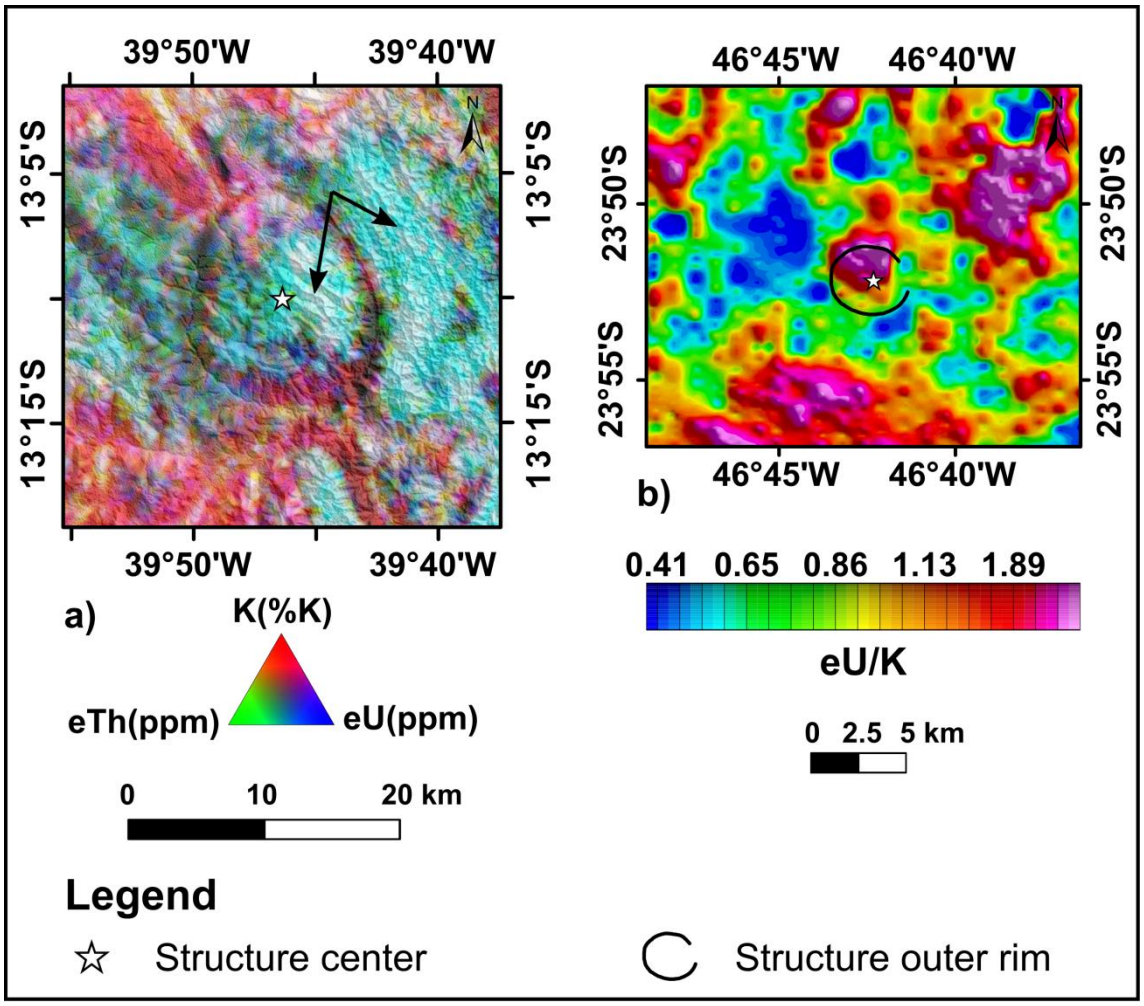

Figure 42: Radiometric maps of the Brejões and Colônia circular targets. a) RGB composite color of radioelement concentrations for the Brejões potential target. The black arrows are described in the text. b) The U/K radiometric ratio for the Colônia potential target.

of the rim appears to change, so that the concentric features in the rim do not continue towards the north, but they go towards the southwest. Another interesting feature is the strong positive radiometric signature near the center of SDC (feature #4 in the Fig. 43). It is characterized by rather high eTh and eU concentrations up to 200 ppm and 30 ppm, respectively. Note that SDC´s circular gamma-ray signature matches its geological map (compare geological map of Fig. 19, Chapter 8). However, the complex color scheme in Figure 43 suggests that different types of sources are present in the structure.

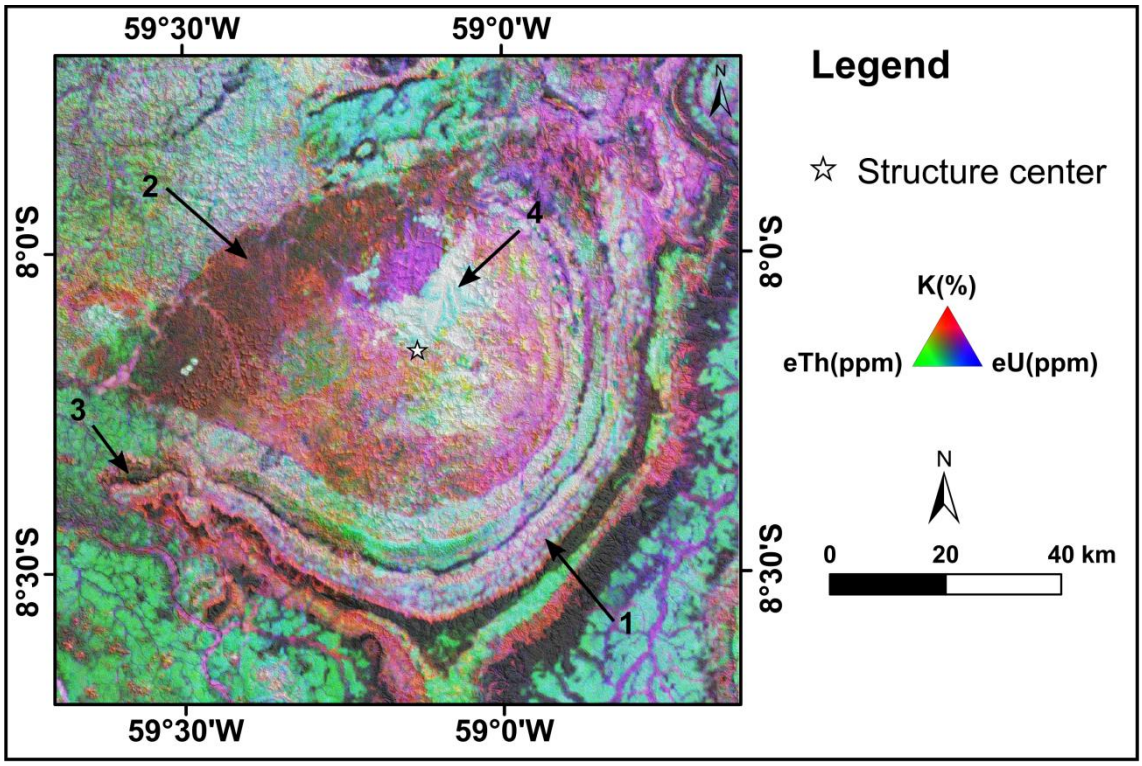

Figure 43: RGB composite color map of radioelement concentrations over Sucunduri Dome. The radiometric signatures indicated by black arrows are described in the text.

Concentric radiometric features are also indicated at the Bom Jardim potential target (Fig. 44a). Although the circular pattern of BJD is well-defined in the eU concentration map (Fig. 44a), RGB composite color of radioelement contents shows at least four signatures (Fig. 44b): i) an external region in red (high K content); ii) a bright peripheral internal region (high K, eTh, and eU content) close to BJD´s rim; iii) a flat-surface internal zone with high eTh and eU contents (cyan colors inside BJD), and iv) an innermost part with purple color denoting high K and eU contents. Figure 44b also shows that some of these radiometric signatures are subject to discontinuities, suggesting the presence of faults or fractures.

The Inajáh (INJ) target also shows a well-defined circular radiometric signature (Fig. 44c and d). This signature is characterized by low radioelement concentrations (dark zones within INJ). It clearly disrupts the background, which is characterized by bright areas (high radioelement contents) (Fig. 44d). The eU concentration map (Fig. 44c) suggests that eU-bearing sources occur along drainage channels that cut through the structure. Outside the structure, some lineaments terminate sharply against the structure's rim, mainly in the western sector.

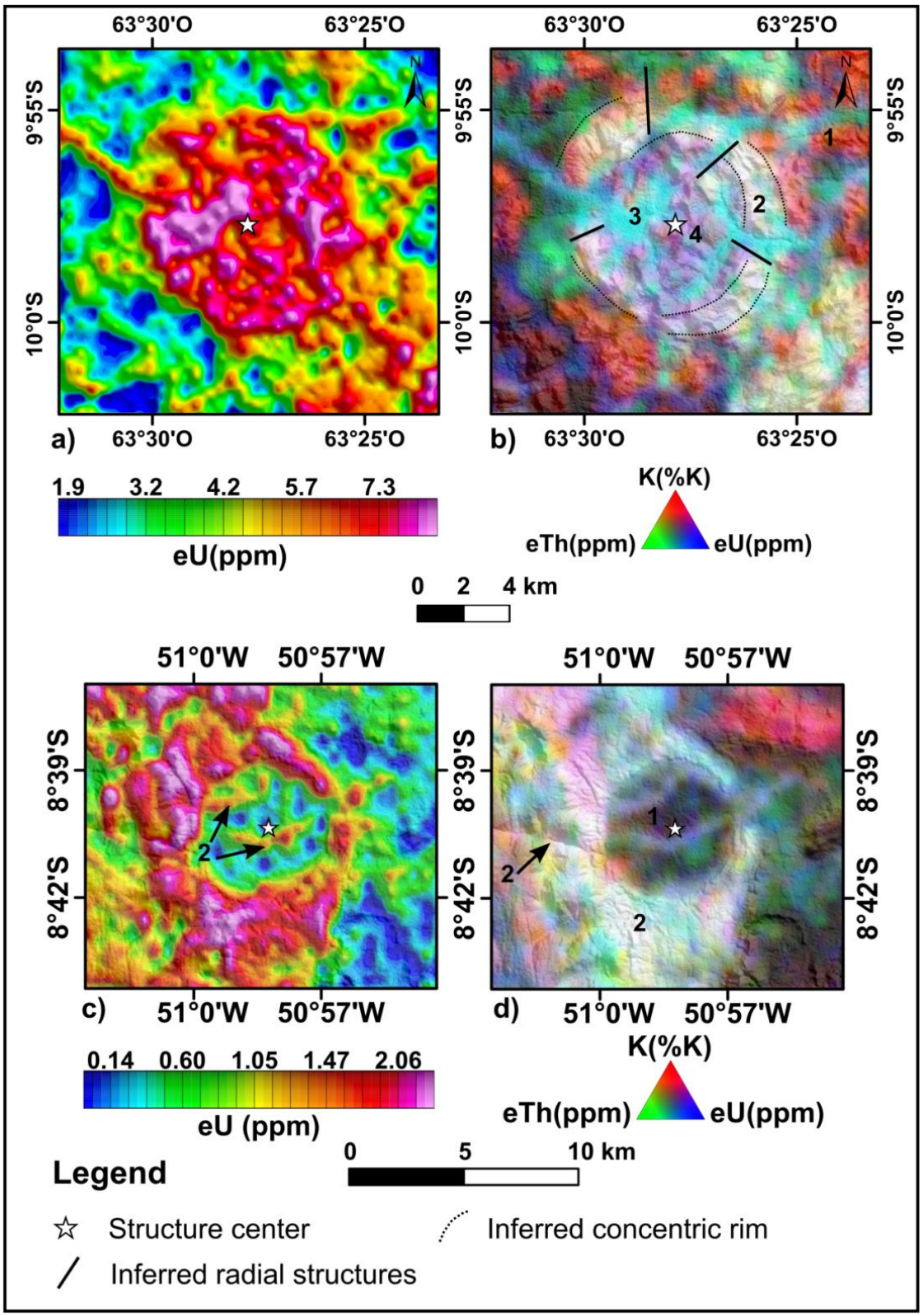

Figure 44: Radiometric maps for the Bom Jardim (a, b) and Inajáh (c, d) circular targets. The eU concentration map (a) and RGB composite color map of radioelement concentrations (b) for the Bom Jardim target. Similarly, eU concentration map and RGB composite color of radioelement concentrations for the Inajáh target are shown in (c) and (d).

Magnetic signature maps for SFM and CNB were not produced, as interpolation yielded a noisy grid (in the case of SFM) or no flight lines crossed the target (at CNB). Moreover, no relevant magnetic anomalies were observed in the Colônia (CLA) structure. Thus, no magnetic maps will be presented for SFM, CNB, and CLA.

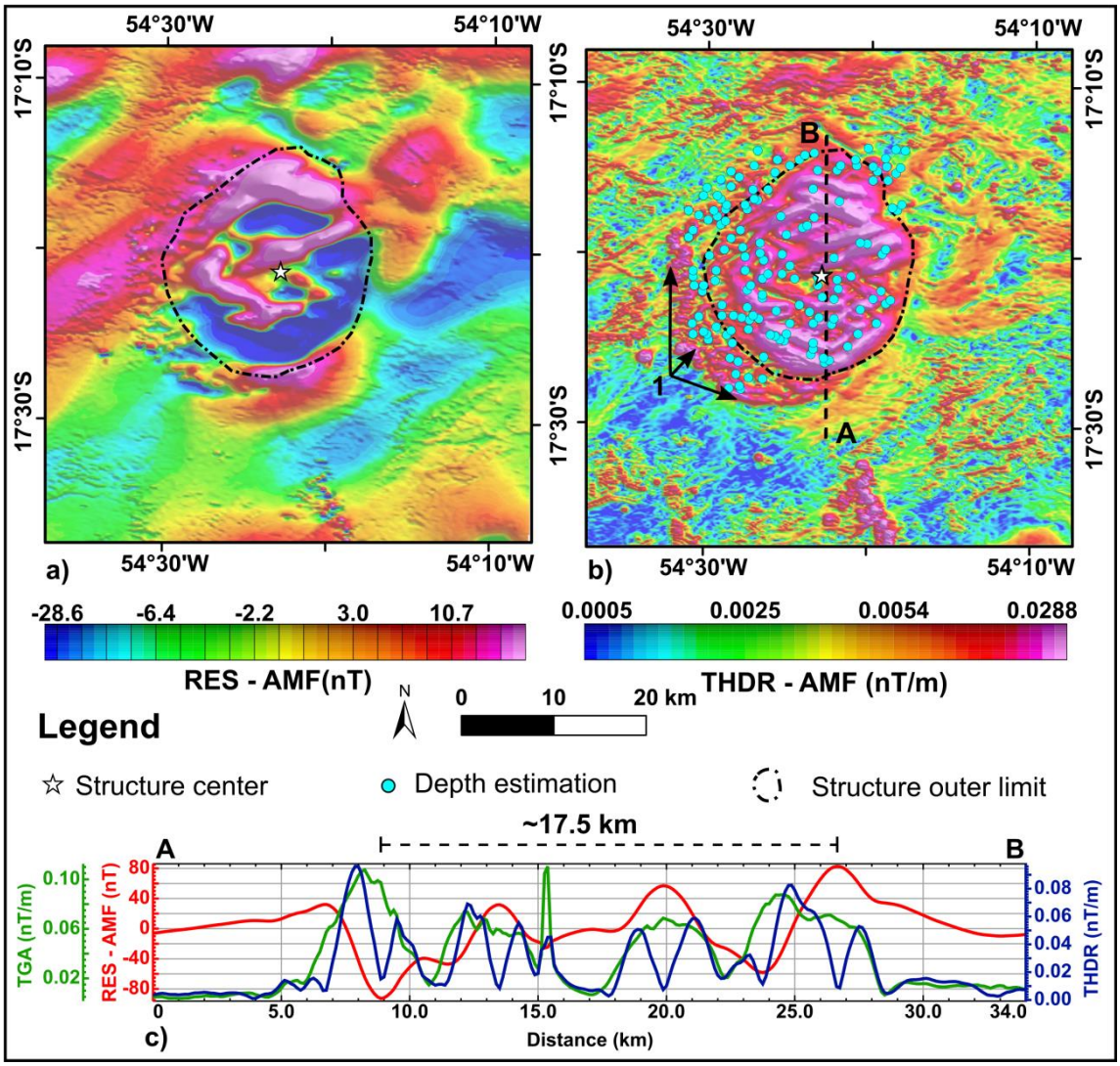

Figure 45: Magnetic maps and magnetic profile for the Itiquira target. a) Residual Anomalous Magnetic Field (RES – AMF). b) Total Horizontal Derivative of RES – AMF. Feature #1 is described in the text. c) Magnetic curves for the A-B profile shown in (b). The RES-AMF, THDR, and TGA (Total Gradient Amplitude) curves are shown in red, dark blue, and green, respectively.

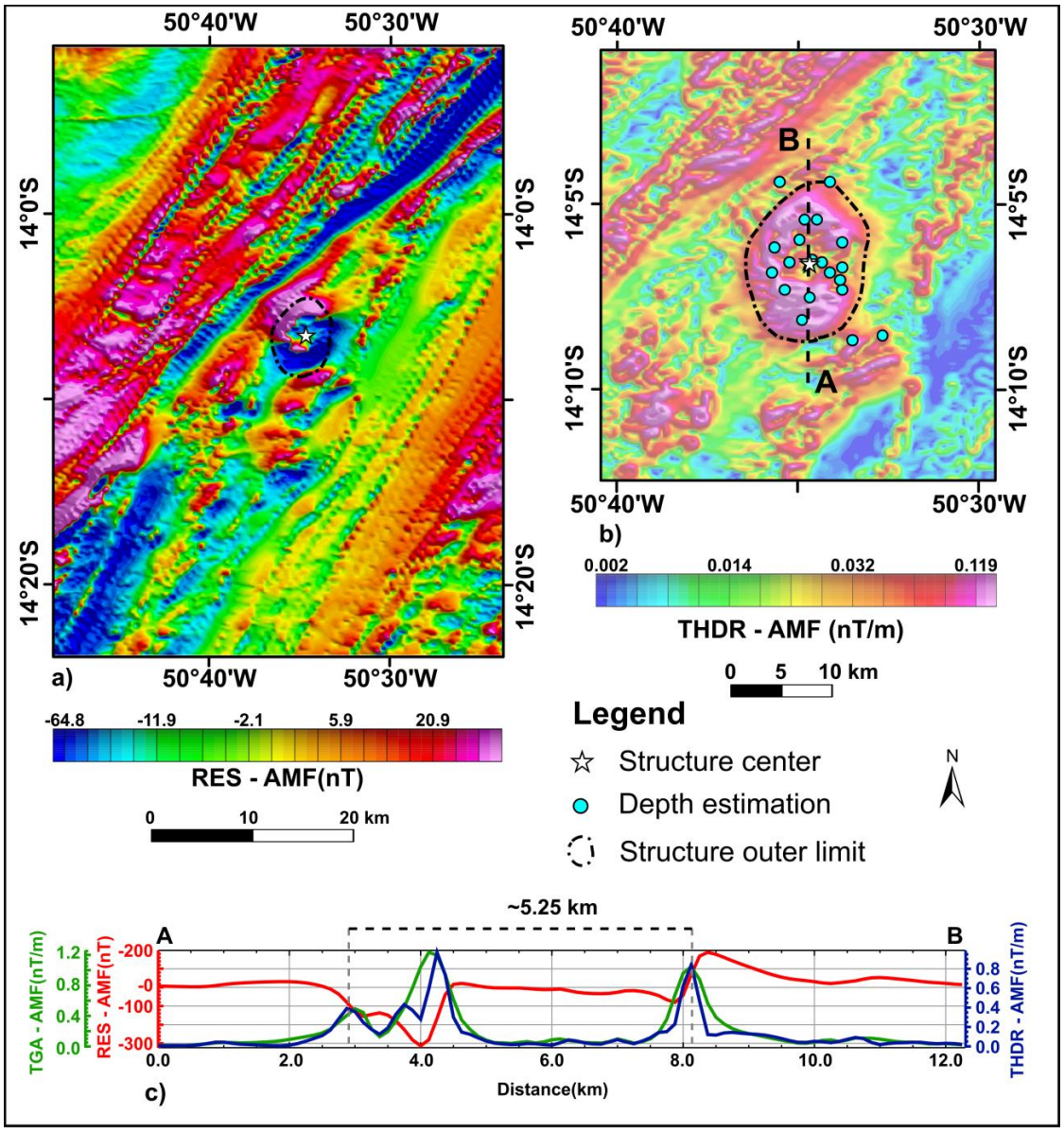

Figure 46: Magnetic maps and magnetic profile for the Cardoso target. a) Residual Anomalous Magnetic Field (RES – AMF). b) Total Horizontal Derivative of RES - AMF. c) Magnetic curves along the A-B profile shown in (b). The RES-AMF, THDR, and TGA (Total Gradient Amplitude) curves are shown in red, dark blue, and green, respectively.

In sedimentary terrain, only Cardoso (CDS) and Itiquira (ITA) show clear magnetic signatures (Fig. 45 and 46), but they are not completely circular in shape. For instance: the magnetic signature of the ITA target seems to be alongated in its SW portion. In this portion, the outline of the ITA structure may be imprecise because of presence of several short wavelegth magnetic anomalies (feature #1 in the Fig. 45b).

The outline of the ITA structure was drawn based on the Residual Magnetic Anomaly Field (RES-AMF) map because the interferences of these

short wavelegth magnetic anomalies were less pronounced in this representation. Based on analysis of the N – S magnetic profile (Fig. 45c), the diameter of the ITA structure can be estimated at ~17.5 km. Within the ITA structure, the magnetic pattern is characterized by interposition of magnetic signals from different sources (Fig. 45b and c), with average and maximum depths of 168.4 m and 729 m. Note that the ITA magnetic signature clearly disrupts the quiet background magnetic pattern.

Like at the ITA structure, the magnetic anomaly of the Cardoso (CDS) structure is more elliptical than circular in shape (Fig. 46). The analysis of a magnetic profile suggests that the major axis of this elliptical shape is N - S in direction and approximately 5.25 km long (Fig. 46b). The CDS internal magnetic pattern shows strongly subdued anomaly amplitudes and gradients (Fig. 46c), whereas the rim exhibits magnetic anomalies with amplitudes up to 300 nT (Fig. 46c). The magnetic sources within the CDS structure are shallow, with average and maximum depths of 125.5 m and 1140 m, respectively. The external portion of CDS is marked by several long linear magnetic anomalies, especially in its NW sector (Fig. 46a and 46b).

A subdued magnetic signal zone is also seen within the Brejões (BRJ) target (Fig. 47). This zone seems to be delimited by two main magnetic anomalies: one in the north (feature #1 in Fig. 47a) and another in the south (feature #2 in Fig. 47a). Both these anomalies are separated by ~14.2 km distance (Fig. 47b). Part of the northern magnetic anomaly coincides with the rim of BRJ but the southern magnetic anomaly occurs inside of the rim. When considering the distance between the magnetic anomalies that mark the rim (see magnetic profile on Fig. 47b), the diamenter of the structure can be estimated at ~19.5 km. Like at CDS and ITA, the magnetic sources in BRJ are essentially shallow, with average and maximum depths of 220.2 m and 952 m.

The magnetic signatures of potential targets on the Amazonian Craton show some interesting features. A partially circular magnetic signature can be seen for Sucunduri Dome (SDC) (feature #1 in the Fig. 48). This circular magnetic anomaly is also open in the northwest sector (feature #2 in the Fig. 48). The anomaly is smaller than the diameter of the circular radiometric signature described earlier in section 14.1.2. Inside of SDC, there are several

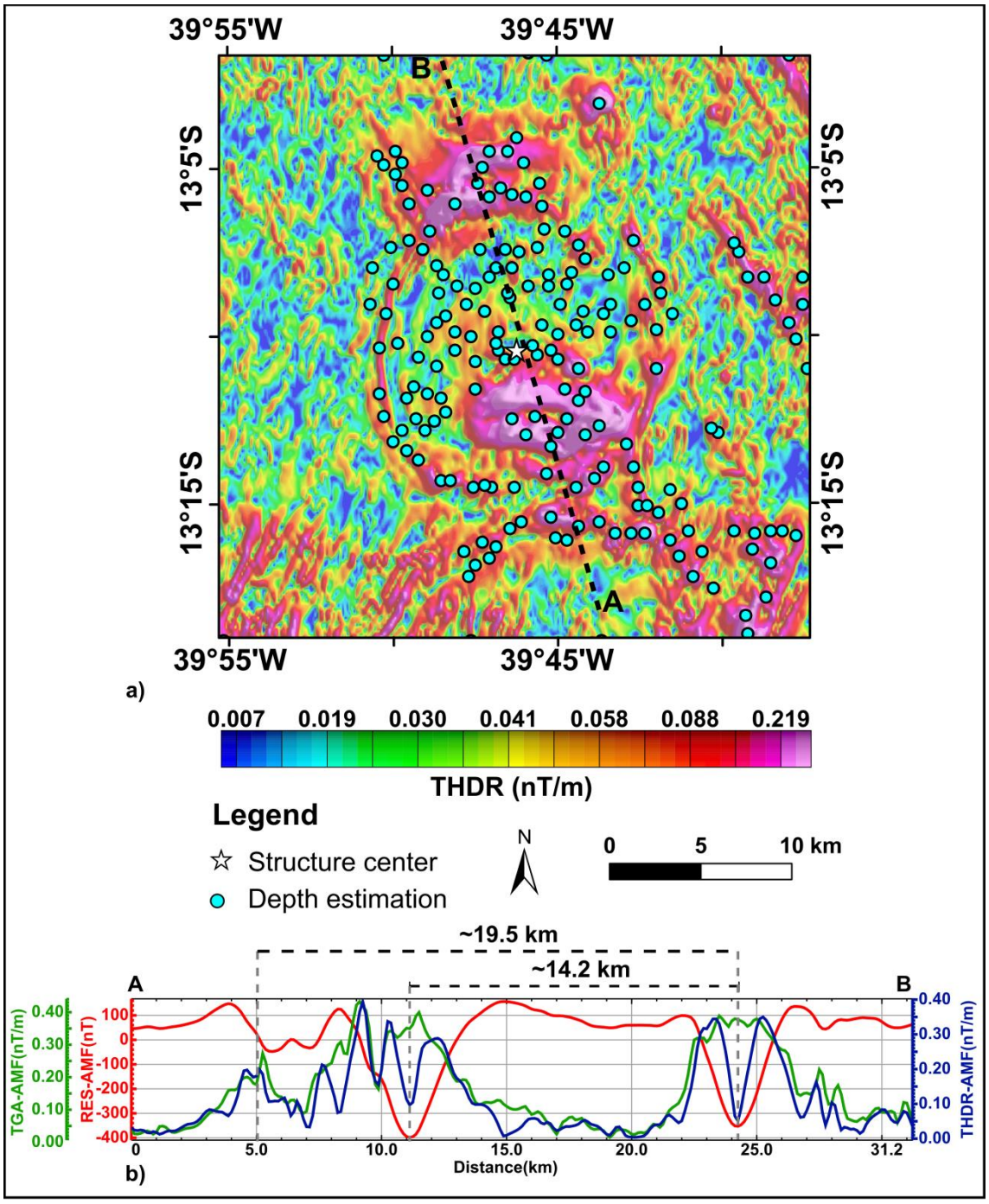

Figure 47: Magnetic results for the Brejões target. a) Total Horizontal Derivative of the Residual Anomalous Magnetic Field (THDR). Magnetic curves along the A-B profile shown in (b). The RES-AMF, THDR, and TGA (Total Gradient Amplitude) curves are shown in red, dark blue, and green, respectively.

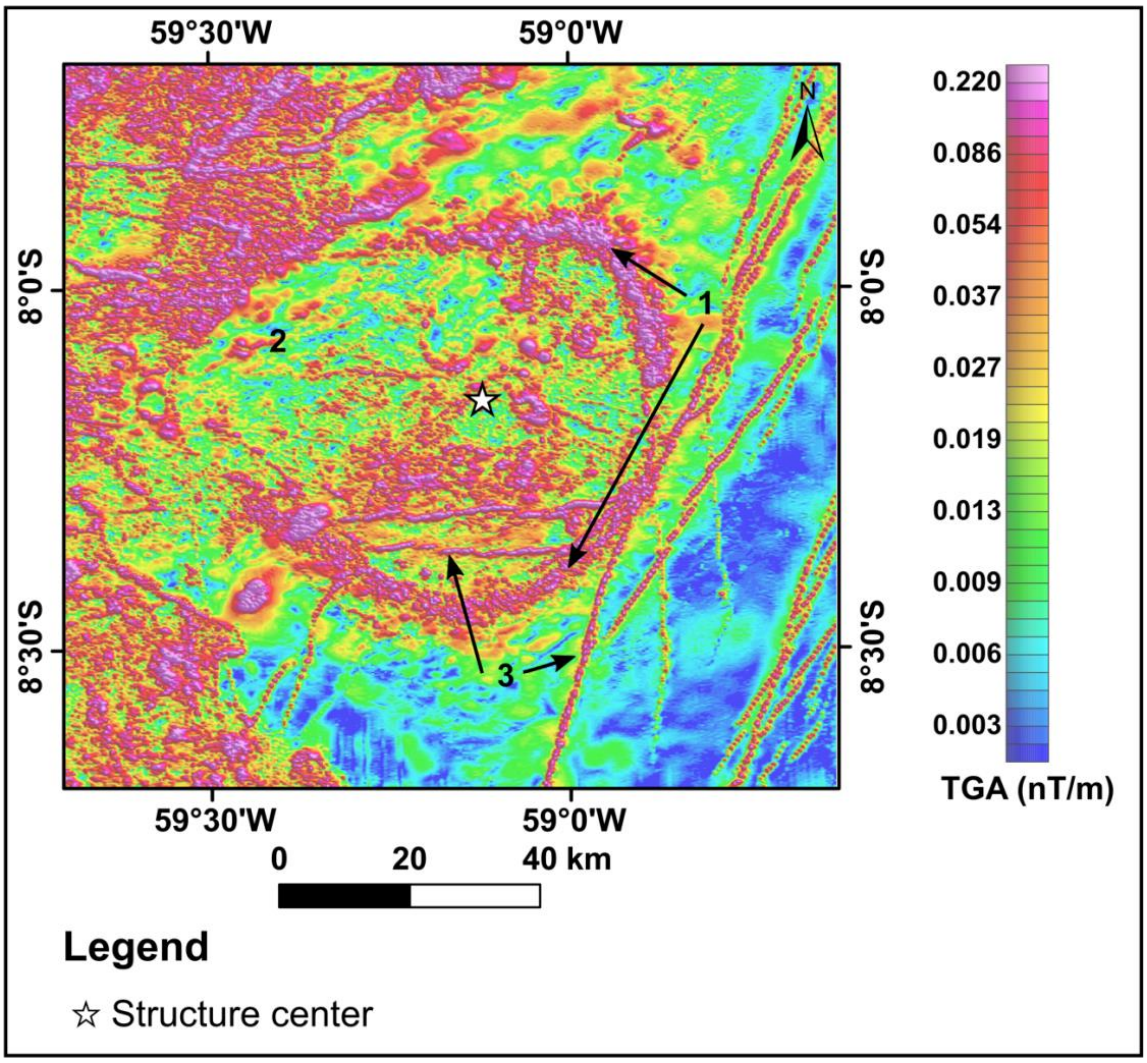

Figure 48: Total Gradient Amplitude of the Residual Anomalous Magnetic Field of the Sucunduri Dome circular structure. The black arrows and numbers refer to magnetic signatures described in the text.

other magnetic anomalies, especially some linear magnetic anomalies with high amplitude (feature #3 in the Fig. 48).

Inajáh (INJ) and Bom Jardim (BJD) show magnetic anomalies that clearly mark the rims of both structures (Fig. 49a and 50a). The difference between them is the TGA peak (compare the TGA curves in Figs. 49b and 50b): the magnetic anomaly related to BJD's rim shows TGA peaks that are less intense (~0.08 nT/m) than the TGA peaks (~0.3 nT/m) observed at INJ's rim. Based on TGA peaks of magnetic profiles (Figs. 49b and 50b), the diameter of BJD can be estimated at ~9 km, whereas INJ's diameter is estimated at ~6.2 km. Note that the anomaly amplitudes and gradients of the internal portions of both BJD and INJ are strongly subdued, but isolated magnetic anomalies with

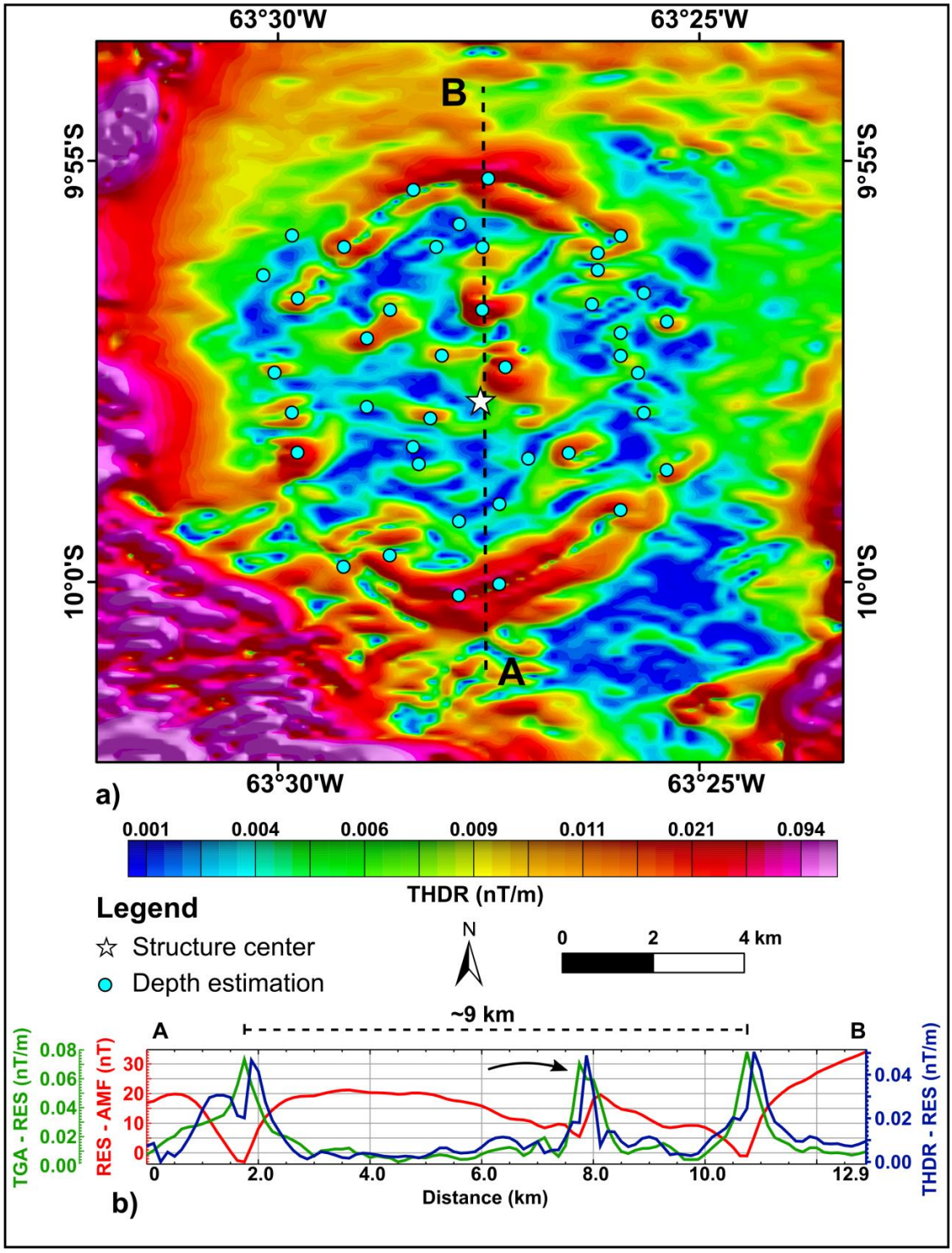

Figure 49: Total Horizontal Derivative of the Residual Anomalous Magnetic Field of the Bom Jardim target. Magnetic curves along the A-B profile shown in (b). The RES-AMF, THDR, and TGA (Total Gradient Amplitude) curves are shown in red, dark blue, and green, respectively.

high amplitude and short wavelength can be seen on the magnetic maps (Figs. 49a and 50a). For instance, several high amplitude and short wavelength anomalies occur in the BJD structure, and some of them have a TGA peak comparable to that seen in the ring structure (e.g., black arrow in Fig. 49b). The

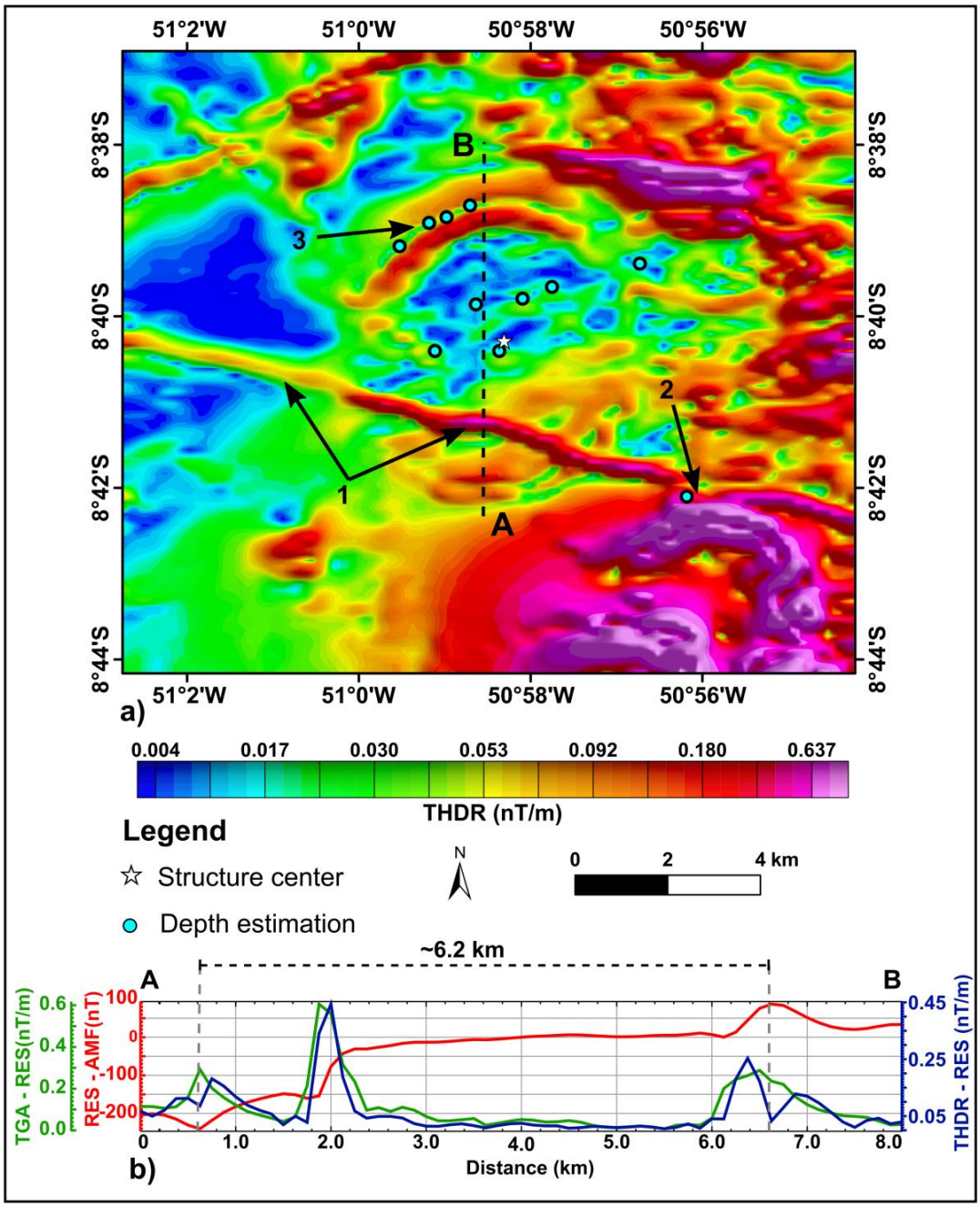

Figure 50: Total Horizontal Derivative of the Residual Anomalous Magnetic Field of the Inajáh target. Magnetic curves along the A-B profile shown in (b). The RES-AMF, THDR, and TGA (Total Gradient Amplitude) curves are shown in red, dark blue, and green, respectively.

sources of magnetic anomalies within and at the rim of BJD are shallow (average depth of 111.8 m and maximum depth of 435 m) and their structural indeces (commonly less then 1.00) suggest they can be modeled as contact-types (Reid et al., 1990).

There is a linear NW–SE trending magnetic anomaly at INJ that crosses the SE sector of the rim, but it is strongly attenuated after crossing the NW rim (feature #1 in the Fig. 50a). Unfortunately, no depth estimate could be obtained

because of the linear magnetic anomaly in the inner portion of the INJ, but outside the structure, a depth of ~500 m has been estimated in the SE portion of the linear magnetic anomaly (feature #2 in the Fig. 50a). The structural index (~2.38) suggests this linear magnetic source can be modeled as a horizontal cylinder-type anomaly. Inside of INJ, the magnetic anomalies are shallowest, with depths of less than 180 m and a structural index less then 1.00 (contact-type)(Reid et al., 1990) (Fig. 50a). In the northern portion of the INJ rim, the depths of the magnetic sources have been estimated at ~500 m, and structural indices (~1.9) suggest that the sources can be modeled as vertical cylinder-type (feature #3 in the Fig. 50a).

14.2.3 Main features seen in spaceborne images

This Results section emphasizes the main features seen in space imagery. No circular morphological pattern was found for Itiquira (ITA), such

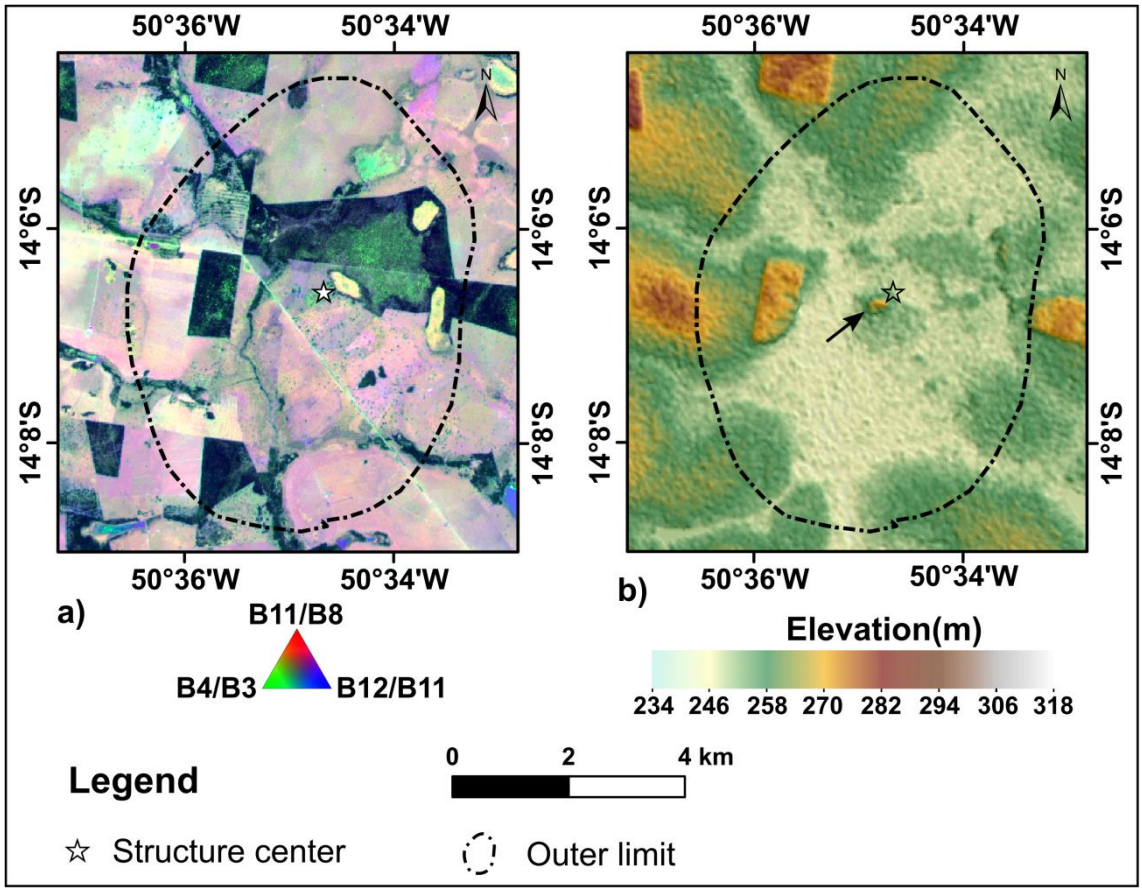

Figure 51: Spaceborne images of the Cardoso circular target. a) RGB composite color Sentinel-2 band ratio map. b) Elevation map. The black arrow points at the hill-type feature mentioned in the text.

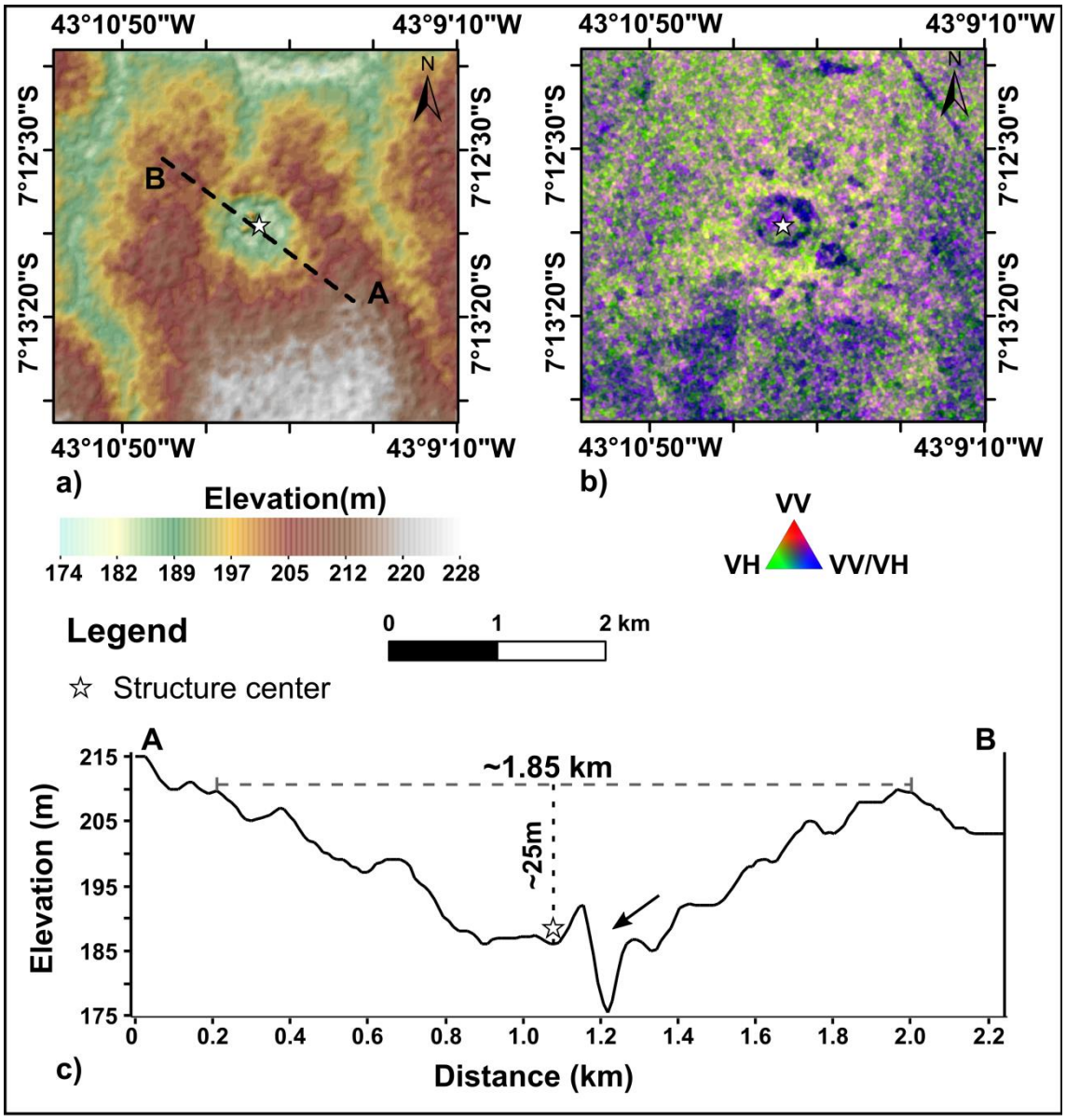

Figure 52: Spaceborne images and topographic profile A-B for the Caraíbas target. a) Elevation map. The topographic profile is shown at the bottom of the figure. b) RGB composite color Sentinel-1 bands. The black arrow on the profile highlights the hill-valley feature near the structure's center.

that no optical or radar maps are presented here for this structure. No circular morphological pattern was observed for the Cardoso target, but a subtle hill-type feature occurs close to its center. On the RGB composite color Sentinel-2 band ratio plot (black arrow in Fig. 51), this little hill shows light green shade (high B4/B3 ratio), indicating the possible presence of ferric iron-bearing minerals (Van der Meer et al., 2014).

A little hill-type feature also seems to be present near the center of Caraíbas (CNB) (Fig. 52a and c). It has relatively steep slopes, shows

predominantly a VV backscattering component, and is surrounded by a crater-like form that is characterized by very low backscattering signals (Fig. 52b). Based on the topographic profile (Fig. 52c), the diameter of the crater-like feature has been estimated at 1.85 km, whereas its depth is estimated at 25 m. The hill-type feature near the center of CDS seems to be a hill/valley pair with amplitude of some 16 m and width of 187 m (black arrow in the Fig. 52c). Finally, the crater-like form seems to contain a small lake.

Circular patterns over the São Francisco do Maranhao (SFM) target are more difficult to see in radar and DEM images, but they can be inferred from optical images. From the RGB composite color of Sentinel-2 bands (Fig. 53), it is possible to infer the presence of some structural features, such as a set of NW-SE trending lineaments in the NW sector; an external circular feature that is well-defined in the SW sector, and an innermost circular feature that emcompasses the SFM center. This central area seems to be dominated by flat-topped plateaus (Fig. 53b).

Among the potential targets in the crystalline domain, Colônia (CLA), Brejões (BRJ), Inajáh (INJ), and Sucunduri Dome (SDC) show a clear circular pattern in optical, SAR, and/or DEM images (Figs. 54, 55, and 57). The BRJ structure also shows a somewhat circular pattern, but this structure is

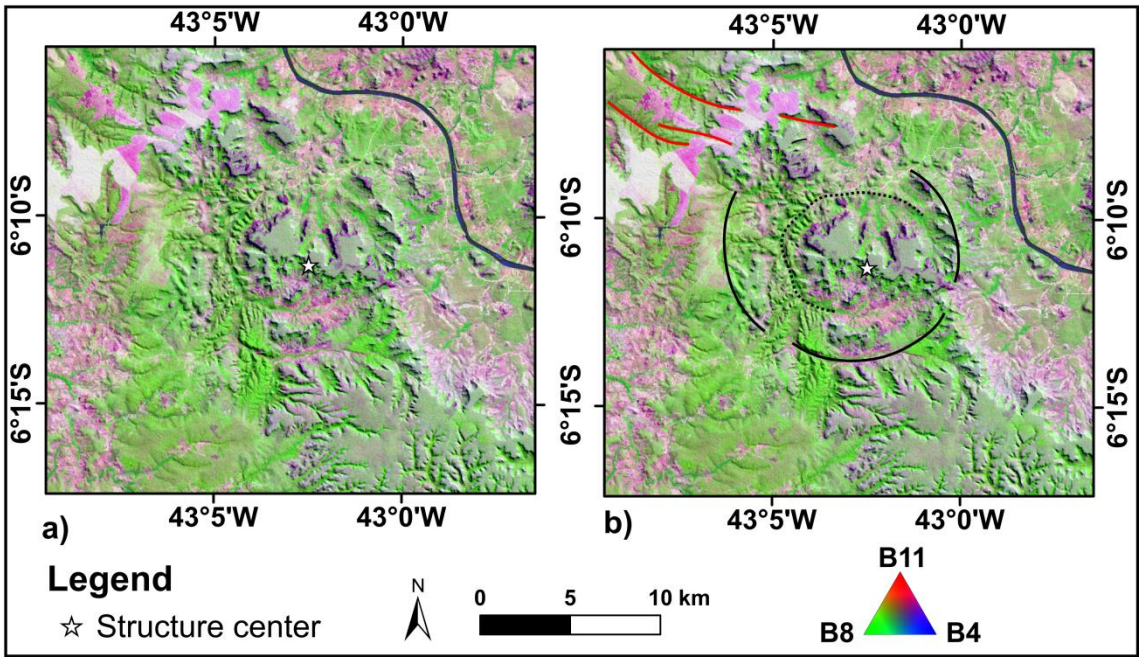

Figure 53: RGB composite color Sentinel-2 band mage of the São Francisco do Maranhão target. The uninterpreted (a) and interpreted (b) images.

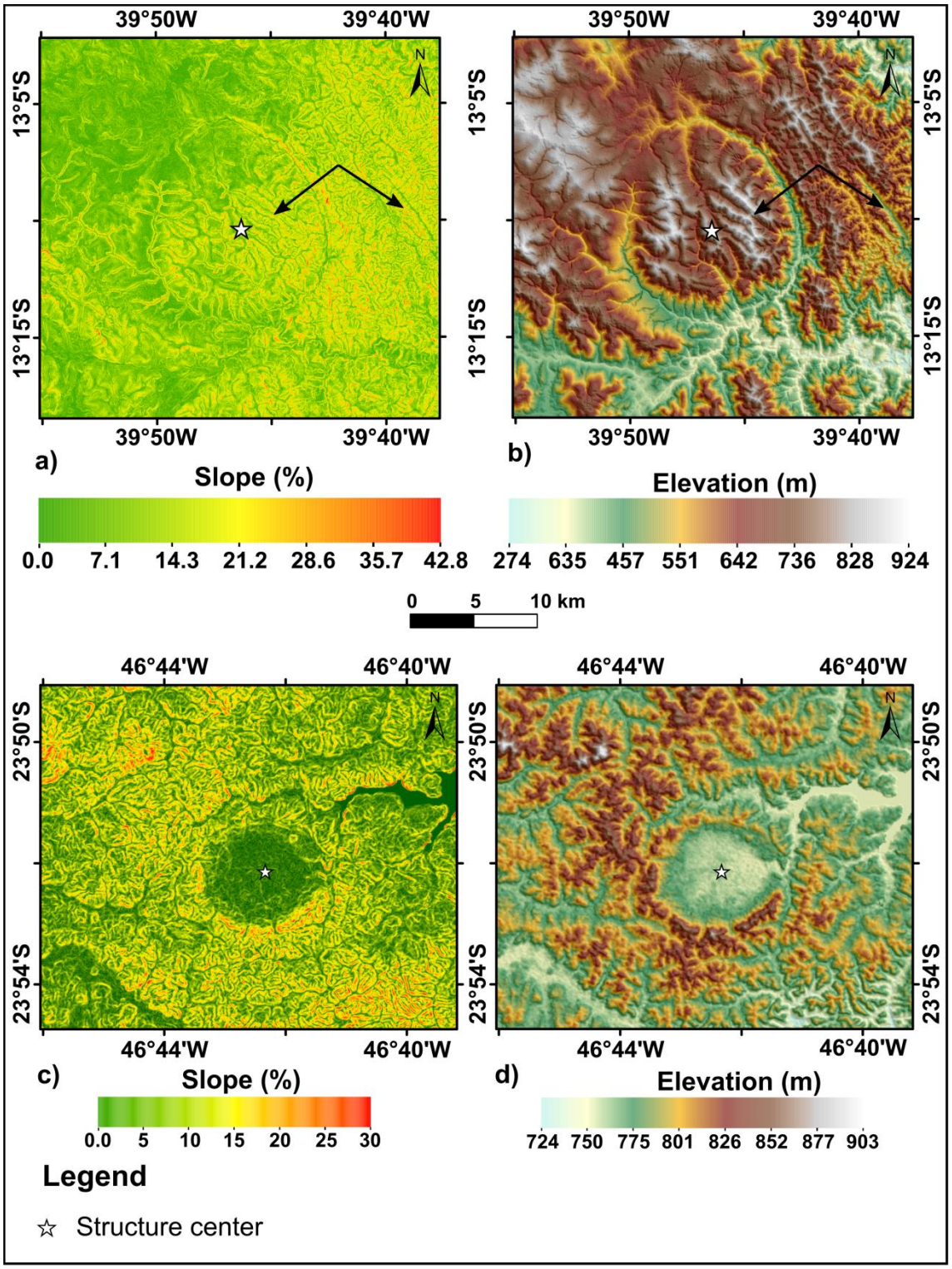

Figure 54: Spaceborne images of the Brejões and Colônia targets. Slope (a) and elevation (b) maps of the Brejões circular target. The black arrows show linear features mentioned in the text. Slope (c) and elevation (d) maps of the Colônia target.

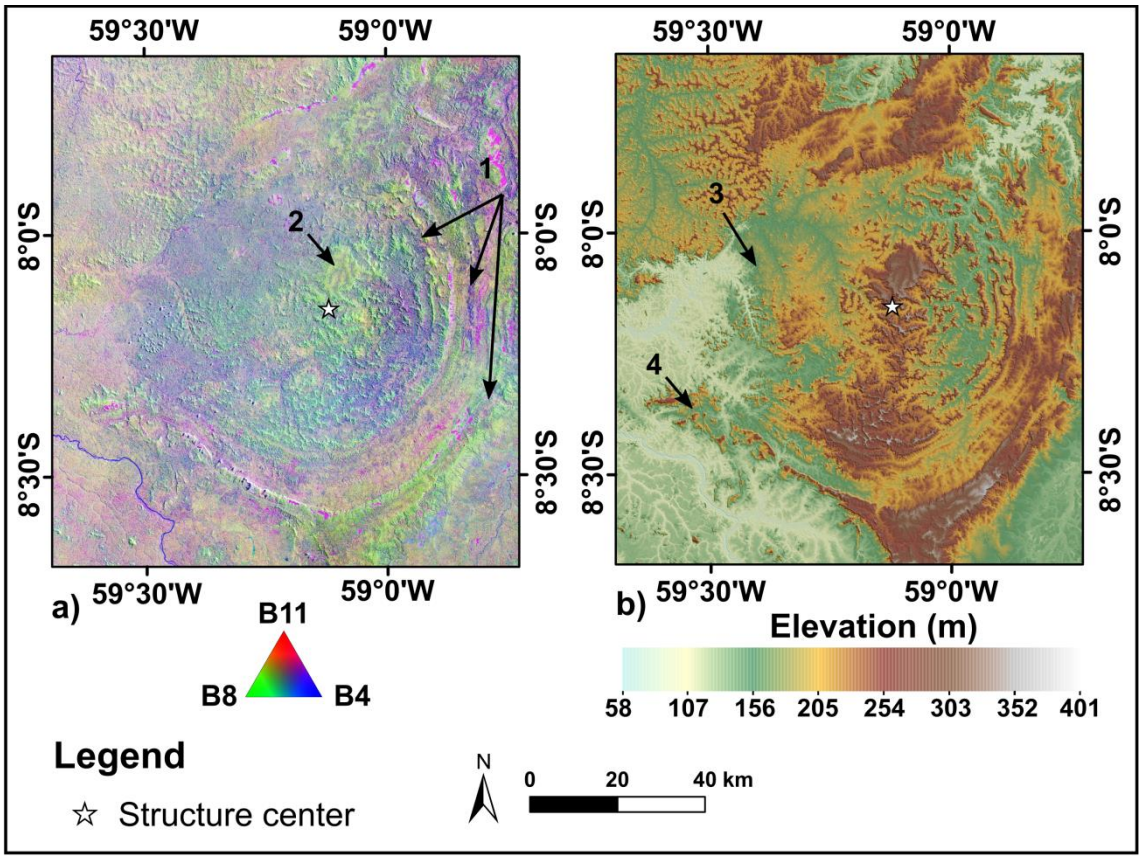

Figure 55: Spaceborne images of the Sucunduri Dome. a) RGB composite color Sentinel-2 bands. b) Elevation map. The black arrows with numbers highlight features described in the text.

more elliptical than circular, with the main axis trending in NNW-SSE direction (Figs. 54a and b). The length of the main axis has been measured at 17.3 km, a value very close (~17.6 km) to the diameter that was estimated from magnetic data in the previous subsection. Note that the BRJ rim is depressed and there is no landform relief contrast against the surrounding terrain (Fig. 54a). Additionally, some NNW–SSE trending linear features occur in the east, outside of the BRJ structure (black arrows in Figs. 54a and 54b), nearly parallel to the main axis.

It has been reported in previous work on Colônia (e.g., Riccomini et al., 2011), that it can be characterized as a 3.6 km diameter crater that is well-defined in DEM and Slope maps (Fig. 54c and d). The CLA structure seems to be open in its eastern sector. Note that there is a clear landform relief contrast between CLA and its surrounding terrain (Fig. 54c and d). Indeed, the crater basin is surrounded by a very prominent ring of up to 125 m high hills (Crósta et al., 2019b; Plaso et al., 2019).

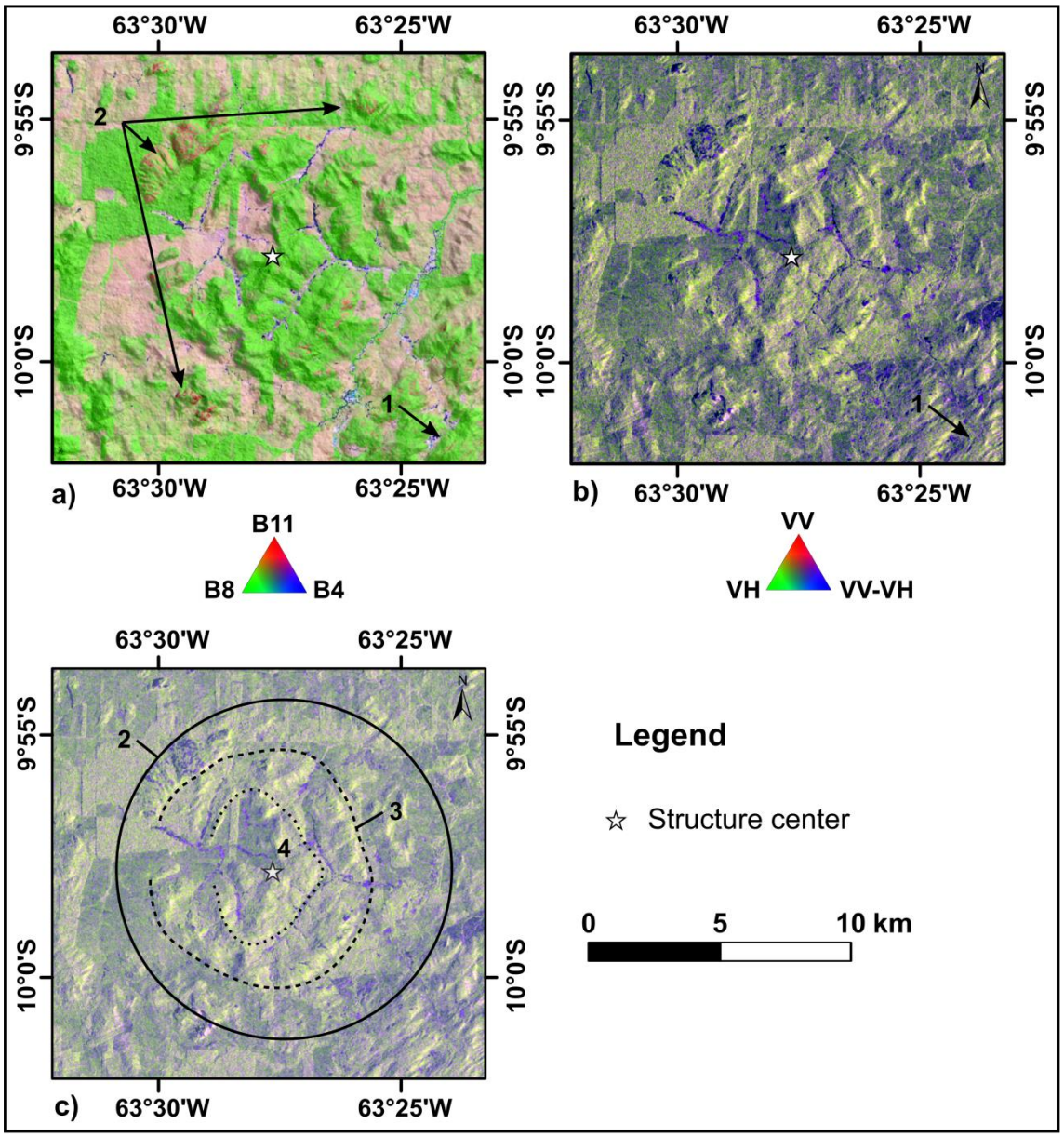

Figure 56: Optical and SAR images of the Bom Jardim structure. a) RGB composite color Sentinel-2 bands. b) RGB composite color Sentinel-1 bands. c) Interpreted image from the maps shown in (a) and (b). Features 1, 2, 3 and 4 are described in the text.

On the Amazonian Craton, the Sucunduri Dome (SDC) shows similar features that were seen in its radiometric data, including: several concentric rings in the eastern and southern sectors (black arrow #1 in the Figs. 55a and b); a region with flat-surface close to the center (black arrow #2 in Fig. 55a and b); a ring open to the northwest and west (black arrow #3 in the Fig. 55b), and an apparent ENE-WSW inflection of the outermost ring (black arrow #4 in the Fig. 55b). Note that inner rings are practically continuous with a few features cutting them.

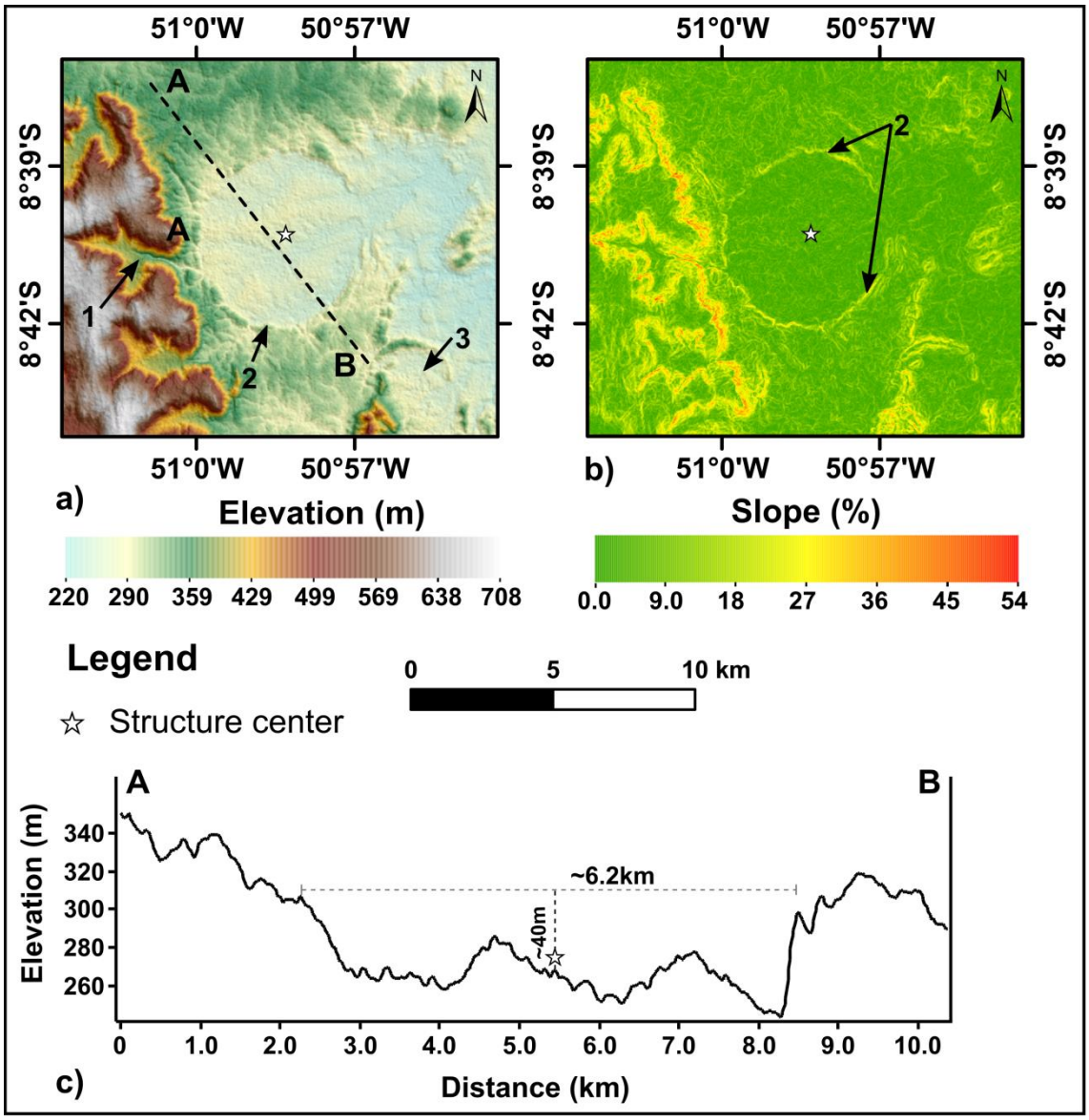

Figure 57: Elevation (a) and slope (b) maps for the Inajáh target. Features 1, 2, and 3 are described in the text. c) Topographic profile derived from the map shown in (a) from A to B.

Inner ring-like features also seem to occur in the Bom Jardim (BJD) target, but they are less evident than those seen at SDC (Fig. 56). Based on Sentinel 1 and 2 images, the following features (see Fig. 56c) can be interpreted: an external area in the SE sector of the BJD structure, which is characterized by several NE-SW trending lineaments (black arrow #1 in Fig. 56a and b); and ii) an outer ring seemingly confined to the NW, NNE, and SE sectors (black arrow #2 in the Fig. 56a and feature 2 in the Fig. 56c). In the NW sector, some lineaments with directions apparently pointing to the center of the structure seem to cut this outer ring. Then there is iii) an inner ring practically around the entire BJD structure (feature 3 in the Fig. 56c); and iv) an elliptical

innermost elevated area that separates drainage channels on the eastern and western sides (feature 4 in the Fig. 56c). Overall, the discontinuous aspects of these features suggest that the BJD structure has been strongly eroded. The diameters of outer rim and inner ring have been estimated at ~12.5 km and ~8.8 km, respectively. Note that the ~8.8 km diameter for the inner ring is close to that of the circular magnetic anomaly given above (~9 km).

Finally, a limited rim height and flat inner surface suggest that the Inaják (INJ) structure has also been considerably eroded. An extraordinary circular appearance and significant relief contrast can be seen on spaceborne images (Fig. 57). This pattern was already noted by previous workers (e.g., Cicco and Zucoloto, 2002). Disruption of the background landform relief is illustrated by an ESE-WNW trending lineament in the western portion of INJ that clearly is interrupted by the circular structure (black arrow #1 in the Fig. 57a). A topographic profile (Fig. 57c) across the INJ structure shows that it has a ~6.2 km diameter crater-like form, with steep rims and some internal features (Fig. 57c). The rim rises up to approximately 40 m above the level of the structure´s center, which, in turn, appears to coincide with a depressed region (black arrow #2 in Fig. 57a-c). An apparently circular structure with raised edges and a flat inner surface occurs about 6.8 km southeast of the center of the Inaják structure (black arrow #3 in Fig. 57a). This smaller circular structure also seems to disrupt the background landform relief like the INJ structure does.

CHAPTER 15
DISCUSSION

15. DISCUSSION

The results described in the previous sections provide the ground for a wide-ranging and diverse discussion, and addressing all possible topics is well beyond the scope of this research. Because of the prime objective of the present study "provide potential targets for impact research", the discussion of the results from this work will be focused on three main aspects: i) the influence of lithology on the characteristics of Brazilian impact structures seen in multispectral, SAR, and gamma-ray images; ii) review of interpretation of magnetic anomalies of Brazilian impact structures, and iii) screening of circular structures potentially formed by impact for a future prioritization for ground-truthing efforts. The first two topics of the discussion will be useful for understanding the sources of the features seen in geophysical and spaceborne images of Brazilian impact structures. This understanding can provide a guide to discuss (the final topic) which of the potential targets studied here may be of greatest interest for future ground-truthing campaigns.

15.1 Influence of lithology and differential erosion on the characteristics of confirmed Brazilian impact structures as seen in multispectral, SAR, and gamma-ray spectrometry images.

When studying the geological context of all confirmed Brazilian impact structures, a question that naturally arises is why have all Brazilian impact structures been discovered in sedimentary terrains where systematic geological mapping is still deficient? Obviously, answering this question requires additional data far beyond what was collected, processed, and interpreted in this study. However, some of the results reported in this study help shed light on this issue.

Sedimentary processes may work as a protector of impact structures from erosion or even enhance some of their morphostructural features, but they can also remove them from direct observation or detection in imagery of spaceborne data (Pilkington and Grieve, 1992; Gottwald et al., 2021). Furthermore, erosion can facilitate the mapping of structural elements in impact structures, especially in complex impact structures (Pilkington and Grieve, 1992; McCall, 2009; Kenkmann, 2021). However, deep erosion can erase the entire impact structure, including perhaps some of its geophysical signatures (Pilkington and Grieve, 1992; Plado et al, 1999).

Particularly regarding complex impact structures, the most favorable scenario for recognition of such structures in sedimentary terrain is when the structure is pristine or when the structure was buried soon after its formation and, subsequently, erosion exposed it at the present surface. Thus, despite some level of erosion, the main first and second order structural features can still be identified. In this scenario, the differential degrees of erosion (resistance to erosion) of steeply dipping strata in parts of complex impact structures, especially in the central uplift, may be particularly responsible for enhancement of eye-catching parts of impact structures (Abels et al., 2005). Thus, combined lithological variability and differential erosion may favor the development or exhumation of morphostructural features, landform relief contrasts, or condition secondary indicators, such as vegetation patterns, drainage, and deposition of weathered material (Abels et al., 2005). Then, all these elements can be identified from remote sensing images, especially on multispectral, SAR, or gamma-ray images, such that if one circular structure possesses these characteristics, it may pass the same characteristics to other geological targets, irrespective of whether geological mapping is incipient or advanced in the survey area. As will be seen in the following, this scenario seems to be the case for all Brazilian impact structures.

Table 6 summarizes the interpretations given for the most prominent radiometric and spaceborne image signatures that were described in the previous section. Although many of these interpretations must be verified by fieldwork, they should be considered as possible causes of the radiometric and spaceborne signatures identified in this work.

Overall, Table 6 shows that most of the features found in airborne gamma-ray spectrometry and/or spaceborne data may be related to disposition of geological units, weathering products, or unconsolidated sediment cover (e.g., alluvium). Furthermore, morphological compartments and/or first-order structural elements of Brazilian impact structures that are reported here or were given in previous studies (i.e., Araguainha – Theilen-Willige, 1987; Cerro do Jarau - Crósta et al., 2010a, Vista Alegre –Crósta et al., 2010b; Vargeão Dome – Kazzuo-Vieira et al., 2009; Serra da Cangalha – Almeida-Filho et al., 2005; Reimold et al., 2006; Riachão Ring – Maziviero et al., 2013; Nova Colinas – Reimold et al., 2022; Santa Marta – Oliveira et al., 2014, 2017; and São Miguel

do Tapuio – Martins, 2016; Martins et al., 2016) are commonly seen in at least one spaceborne sensor. As all target rocks of confirmed Brazilian impact structures involve more than one lithostratigraphic unit, it appears possible that parts of these radiometric and/or spaceborne signatures are derived from lithological compositional variations and/or differences of erosion resistance of different target rocks.

Compositional variation of sedimentary strata seems to be of prime importance in the case of airborne gamma-ray spectrometry signatures. In fact, radiometric signatures, especially circular ones, seem to be influencied by radiometric contrast between pelitic rocks and sandstones. This contrast is well-demostrated in Araguainha's Total Count (TC) map with respect to the strata rich in phyllosilicate minerals or organic matter (Passa Dois Group and Ponta Grossa Fm.) that commonly show strong radiometric signatures, mainly due to their eU and eTh contents, whereas quartzose (e.g., Aquidauana and Furnas) formations tend to have weak radiometric signatures.

It is worth mentioning that the TC map shown here (see Figure 24) is more uniform and has smoother radiometric contours, without a "bull-eye" or flight line artifacts, than the TC map published in previous work (e.g., see Leite et al., 2022 and their fig. 2). This difference is due to different processing approaches. The TC map presented by Leite et al. (2022) was interpolated using the minimum curvature method and no filter was applied to suppress directional trends, whereas the approach used here was the Inverse Distance Weighted (IDW) interpolation method, and filters to suppress directional trends and spurious peaks were applied, providing a map with a distribution of total count measurements more consistent with the geology. These results corroborate the studies of Grant (1998) and Silva et al. (2023), in which the authors suggested that IDW interpolation tends to produce better radiometric grids. Additionally, although the Directional Cosine filter is applied commonly to airborne magnetic data, this study suggests this filter can also successfully suppress flight-line artefacts on airborne radiometric data that are poorly leveled.

Likewise, phyllosilicate mineral or organic material-rich rocks in the Serra da Cangalha (e.g., Longá Fm.) and Santa Marta (likely Pimenteiras Fm.) impact structures could contribute to a strong radiometric signal observed, whereas

silicified rocks (e.g., inner collar of the Serra da Cangalha central uplift or the annular basin of Nova Colinas) tend to have weak radiometric signatures. In fact, the modeling of the correlation structure by applying a Factorial Analysis approach (Research paper 2, Chapter 13) on airborne gamma-ray spectrometry data of Serra da Cangalha, Riachão Ring, and Nova Colinas has demonstrated that lithology is one of the main factors that control the variance of radioelements in these impact structures, corroborating that compositional variation of sedimentary strata seems to be of prime importance on radioelement distribution. However, the Factorial Analysis approach also has indicated that weathering is another factor that plays an essential role on the control of the variance of radioelement abundances in the Serra da Cangalha, Riachão Ring, and Nova Colinas impact structures. This result is in accordance with the fact that these structures also show other signals of deep erosion, such as rims with open sectors (e.g., Riachão Ring and Nova Colinas) or discontinuous aspect (e.g., Serra da Cangalha), as well as lack of ejecta deposits. Moreover, the quasi-vertical loss to erosion has been estimated based on field studies and/or numerical modeling of impact simulation (e.g., 500 m for Serra da Cangalha and Riachão Ring - Kenkmann et al., 2011; Maziviero et al., 2013). These observations clearly demonstrate that this parameter may play a strong role in modifying or erasing structural features or impactite deposits not only at Serra da Cangalha, Riachão Ring, and Nova Colinas impact structures, but at the other Brazilian impact structures as well.

In a similar way, the target rocks with differences in grain size or organic matter or carbonate content will respond differently to erosion and weathering processes, and this may favor the development of contrasts in morphological features. For instance: the Serra Grande Group rudaceous rocks are more resistant to erosive, and, thus, they support the tops of elevations and separate Paleozoic units from Mesozoic units in the Santa Marta impact structure (Oliveira et al., 2017). Similarly, silicification of sandstones increases the resistance to erosion, thus making it possible to form high hills in the central areas of impact structures (e.g., inner collar in Serra da Cagalha, external portion of Cerro do Jarau central uplift, and possibly inner rings of São Miguel do Tapuio). The latter case needs to be investigated in the field.

Table 6: Interpretations of airborne gamma-ray spectrometry and spaceborne image signatures of Brazilian impact structures. Abbreviations: AGD – Araguainha; CJU – Cerro do Jarau; VGD – Vargeão Dome; VTA – Vista Alegre; SdC – Serra da Cangalha; RR – Riachão Ring; NVC – Nova Colinas; SM – Santa Marta; SMT – São Miguel do Tapuio.

Impact structure	Gamma-ray spectrometry and spaceborne image signatures	Interpretation (potential sources of the signatures)
AGD	1 - High TC values in pelitic strata and granites; 2 – low TC values in quartzose sedimentary rocks; 3 - rough texture/pink shades and smooth texture/cyan shades in annular basin.	1 – eTh and eU relate clays and/or organic matter rich strata; 2 – quartz/quartzite is commonly poor in radioelementcontents; 3 - rough texture/pink shades can be related to Aquidauna Fm. sandstone outcrops, whereas smooth texture/cyan shades probably reflect soils, some of which are derived from Aquidauna Fm.
CJU	1 - Ellipsoidal area with high B4/B3 ratio in the apparent central uplift; 2 – silicified sandstones in the outer central uplift show high backscattering of VH and VV polarimetric components.	1 - The B4/B3 band ratio can be regarded as a proxy for Fe^{3+} (Van der Meer et al., 2014), thus this signature may be related to different materials including oxidized materials from sandstone matrix or soils derived from them; 2 - This can be due to diffuse scattering that arises from hilly terrain on these silicified sandstones.
VGD	1 - Outer rim and inner ring features seen in elevation map.	1 – This probably arises from differential erosion.
VTA	1 – Landform relief contrast of internal and external portions.	1 – This probably arises from differential erosion.
SdC	High PC1 scores (i.e., K/eTh, eU/K, and eTh contents) in annular basin; 2 – High PC2 scores (i.e., K content) in central basin and SW portion of the rim; 3 – Semi-circular Thermal Infrared signature (high radiance in band 13).	1 – May result from different radiometric sources (rocks or soils derived from them; 2 – central basin: may reflect the content of K contained in Longa Formation shale and/or alluvium (eroded collar material deposited in the central basin (Vasconcelos et al., 2012; Silva et al., 2024). SW portion of rim: unclear. Previous work Vasconcelos et al., 2012 have pointed out that K anomalies in the inner sectors of SdC could arise from remobilization of hydrothermal fluids during the late stages of crater formation (Vasconcelos et al., 2012). However, petrograpphic evidence supporting this proposition has not been reported yet. Here, such K-rich zones also could be related to a depositional zones because spaceborne images shows this area with several drainage channels; 3 – unclear. Because quartzose sedimentary rocks show low radiance in band 10 and 12, but not in band 13 (Ninomiya and Fu, 2016), it is possible that this semi-circular TIR spectral signature may be due to such rocks (e.g., chert or silicified sandstones).
RR	1 – Very low PC1 score (i.e., low K values) in outer rim area; 2 – Moderate PC1 score in SE part of the central uplift; 3 – High PC4 scores (i.e., high eU/K ratio) in annular basin and outside of structure; 4 – central uplift and outer rim show strong green shades (i.e., strong reflectance in band 8); 5 - annular basin has low backscattering signatures.	1 - Sandstones supporting the outer ring would already be naturally poor in radioelements, but chemical weathering may have augmented this deficit (also see Maziviero et al., 2013); 2 - According to the geological map of these authors, the K content represented by PC1 scores over the central uplift may relate to lithic particles and/or muscovite traces; 3 – bcause organic material can favor Uranium concentration (e.g. Dentith and Mudge, 2014), the peloids and bioclast carbonate grains in the annular basin and outside of the structure (Maziviero et al., 2013) could explain the high PC4 score (high eU in relation to K) in these areas. However, alluvial deposits in drainage channels also contribute for this radiometric signature. 4 – This signature may relate to a spectral vegetation signature. 5 – May be related to fine-grained materials deposited in the annular basin. Similar low backscattering zones have also been reported for the annular basins of the Spider and Connolly Basin impact structures (McHone et al., 2002).
NVC	1 - TIR spectral signatures emphasizing the difference between the northern and southern portions of NVC impact structure; 2 - High and low backscattering zones inside of the structure.	1 – May reflect areas dominated by basalt and related soils in the north and sandstone-dominated areas in the south (Reimold et al., 2022); 2 - maybe related to linear to curvilinear features of the hill land system and low amplitude/declivity hill land system described by Reimold et al. (2022), respectively.

SM	1 - Circular radiometric source(s) of eTh and eU near the western side of the steep slope of the Central Elevated Plateau (CEP); 2 – circular feature seen as light green shades (e.g., high band 4/band 3 ratios) and a smoother texture pattern in the central zone of Santa Marta.	1 - It is likely that this radiometric signature may arise from Th and U contents of pelitic units (e.g., Pimenteiras Fm. that is radioactive and organic-matter rich - Góes and Feijo, 1994; Vaz et al., 2007; Oliveira et al., 2017) and that were uplifted in the central zone. 2 – Again, the B4/B3 band ratio can be regarded as a proxy for Fe^{3+} (Van der Meer et al., 2014), and it can be assumed that the signature resulting from weathering products are usually poor in ferric minerals, because the Santa Marta central uplift is essentially formed of sandstones, conglomerates and shales. Note that this circular feature does not coincide with the eU and eTh signature described earlier, which would be expected if its sources were distinct.
SMT	1 - TIR spectral signatures (low radiance) close to São Miguel do Tapuio's center.	1 – Unclear. The impact-induced brecciation and fracturing of sandstones quartzitic monomict breccias of the São Miguel do Tapuio center could account for greater internal scattering of the radiance, generating a decrease in radiance as recorded in TIR bands. However, such effects were reported for visible and near-infrared regions, not for the TIR region of the spectrum (Johnson and Hörz, 2003). Therefore, the origin of this intriguing TIR signature remains open and further field observations are required to support resolving this problem.

These observations suggest that diversity of lithology and differential erosion and weathering play an essential role in the development of morphostructures of the confirmed Brazilian impact structures seen in multispectral, SAR, and gamma-ray spectrometry images. Clearly, such signatures have been favorable in identifying Brazilian impact structures in such sedimentary environments, even if comprehensive, systematic geological mapping is still lacking. On the other hand, the greater resistance to deformation and more homogeneous composition of crystalline target terrains may result in less contrasts, e.g., in radiometric imagery. In fact, this is a main constraint in this study, as it is necessary to compare the signatures of structures formed in sedimentary basin fill with target structures that do, or could, contain crystalline rocks. However, rheological contrasts, for example due to brecciation, silicification, and erosion (especially in areas of central uplifts) may still be present in the crystalline target (Abels et al., 2005; Collins et al., 2008), which may make such targets identifiable in remote sensing images.

15.2 Review of interpretations of magnetic anomalies of Brazilian impact structures.

The results regarding magnetic signatures of Brazilian impact structures show that analysis of polarities of magnetic anomalies plays an important role in the interpretations of their magnetic sources. In the present work some possible errors in the interpretation of magnetic anomalies in Brazilian impact structures reported in previously published work were identified. The previous interpretations given for sources of magnetic anomalies in the Nova Colinas and Santa Marta impact structures are in this regard the most prominent cases.

A recent publication argued that a dipole anomaly was evident at the center of the Nova Colinas structure after residual/regional separation processing by analysis of the radially averaged power spectrum (Pereira et al., 2023, their figure 4c). Note that this dipole was identified in the regional magnetic anomaly field, from which the average depth of all magnetic sources was estimated at 3500 m by those authors. According to them, this dipole was likely related to deeper magnetic sources (e.g., a possible diabase sill – see Horizon II identified by Pereira et al., 2023) that would have been uplifted during the modification stage of crater formation. Here, this dipole feature is

considered irrealistic because: i) as this dipole was identified based on regional field expression and, considering that the average depth of magnetic sources that contribute to these regional magnetic signals is 3500 m, this supposed dipole would have to be at the same depth as the basement (~ 2200m) (see horizon IV in Pereira et al. (2024) and their fig. 8). However, according to seismic data shown by Pereira et al. (2023), impact-driven crustal deformation was constrained to the uppermost 1000 m, such that it is unlikely that this dipole feature is related to deeper magnetic sources. ii) This supposed dipole feature should be present in other magnetic thematic maps (e.g., TGA or THDR), but no magnetic anomaly at the center of Nova Colinas is notable in such maps (see Fig. 2 of Silva 2020, fig. 6 of Reimold et al., 2022, and fig. 4d of Pereira et al., 2023), and in maps of this work (Figs. 31a and 31b, Chapter 14). iii) As shown in this work, the polarity of the magnetic anomaly to the north of Nova Colinas is composed of a minimum surrounded by two maxima, which represents the kind of polarity that would be expected for magnetic anomalies at the magnetic equator (e.g., Reid, 2010; Beard, 2012; Dentith and Mudge, 2014; Betts et al., 2024). However, Pereira et al. (2023) interpreted this magnetic anomaly as if it were composed of a minimum and only one maximum (that is, only two of three black arrows in the Fig. 31a, Chapter 14), thus suggesting the presence of a dipole. Considering that the magnetic inclination during magnetic survey times at Nova Colinas was approximately -10.7°, that is very close to the magnetic equator, the shape of a magnetic anomaly with a minimum and two positive sides would be more consistent than a dipole, which is expected in mid-latitudes (i.e., for inclination of ~45°) (Beard, 2012; Betts et al., 2024).

It is worth noting that the magnetic anomaly to the south of Nova Colinas also has the same shape as a magnetic anomaly that would be expected near the magnetic equator (Silva, 2022). The difference between total gradient amplitudes observed in the northern and southern portions of the ring-shaped magnetic anomaly at Nova Colinas can be explained as follows: In the southern portion, the outward movement during the excavation stage may have promoted a local thickening of diabase sills, thus enabling a contrast in lateral magnetic susceptibility that would otherwise be observed only at the crater rim. This lateral magnetic susceptibility contrast has been evocated to explain the ring-shaped magnetic anomalies seen in other impact structures, such as Glikson

(Macdonald et al., 2005) and Foelsche (Haines and Rawlings, 2002) in Australia. In the northern portion, magnetic sources have more complex shapes (structural indices from 2.5 to 3.75 - this work) and have variable depths (from 250 m to 1000 m) (Silva, 2020; Reimold et al., 2022; Pereira et al., 2023). This suggests that, in addition to lateral magnetic contrast arising from the thickening effect, a thicker and deep magnetic source may be present there. Here, it is interpreted that this thicker and deep source may result from contact between the regionally occurring diabases and sandstones. Finally, it is worth to mention that the ring-shaped magnetic anomaly in the NVC structure is not continuous, but shows some weak zones (the black arrows in Fig. 31b, Chapter 14). Although the origins of these zones are unknown, they can be related to radial faults in the NVC's outer rim or can represent oxidation of magnetite in fractured target rocks (Henkel and Guzman, 1977). Furthermore, the top of a locally thickened diabase layer may outcrop at surface, so that even though it is strongly weathered, this top shows relatively higher K concentrations than the surrounding sandstones (as seen in F2 score map showed in the Fig. 27). As that F2 score map (that is, K concentration variance) is also not a complete circle (i.e., it shows several open zones probably due to heavly erosion), it can be suggested that the outline of Mosquito Fm. basalts on the geological map of the NVC impact structure proposed by Avona et al. (2024) may be imprecise.

The magnetic anomaly polarity problem has also lead to misinterpretation of magnetic sources in the Santa Marta impact structure. As described in a previous section (Chapter 14), the Santa Marta long-wavelength magnetic anomaly is characterized by a central minimum value surrounded by positive shoulders (compare Figs. 31a and 32a) as in the northern part of Nova Colinas. Although impact structures do not have a distinct magnetic signature pattern, impact structures of similar size to Santa Marta generally exhibit a low magnetic anomaly pattern (compare Cowan and Cooper 2012; Pilkington and Grieve 1992; Grieve and Pesonen 1992).

Before Santa Marta was actually confirmed as an impact structure by Oliveira et al. (2014), Vasconcelos et al. (2010) proposed it as a potential impact structure based on similarity between the low magnetic pattern observed at Santa Marta in comparison to features at similar sized impact structures (ibid). As introduced in a previous section (Chapter 6, subsection 6.2), this low

magnetic pattern could be caused by shock demagnetization, dissociation of Si and Fe in magnetic minerals, or by oxidation of magnetite in the fractured target rocks, promoting a contrast with undeformed/less shocked surrounding terrain (Henkel, 1997; Henkel and Pesonen, 1992; Henkel and Guzman, 1977; Henkel and Reimold, 2002; Gilder et al., 2018). But in the Santa Marta impact structure, the magnetic inclinations during magnetic survey times (-6.1°) suggest that the magnetic equator was much closer to the structure. Thus, the long-wavelength magnetic anomaly in Santa Marta is not a magnetic low due to shock demagnetization as proposed by Vasconcelos et al. (2010), it only has the character of a magnetic anomaly expected at the magnetic equator (Dentith and Mudge 2014, Betts et al., 2024). This is confirmed by analyzing the TGA map (Fig. 32b) that shows that, unlike demagnetization features, the Santa Marta magnetic anomaly has a positive magnetization contrast, so that it could be characterized as a strongly magnetized, approximately circular magnetic feature, similar to magnetic anomalies derived from other magnetic sources (e.g., kimberlite) (Keating and Sailhac 2004).

The actual source of the magnetic anomaly in the core of Santa Marta is still unclear, but the long-wavelength and estimate of depth for this source (~2000 m) suggest that this feature might be related to uplifted basement. This proposition is consistent with magnetotelluric data, although the estimates by that method for the depth to basement were shallower (~1 km) (Ferreira et al., 2019b).

In addition to the Nova Colinas and Santa Marta cases discussed above, other Brazilian impact structures also exhibit magnetic anomalies, whose interpretations for magnetic sources should be revisited. A comparison between previous interpretations and those proposed in this work is summarized in Table 7. Overall, magnetic anomaly polarity issues for Araguainha and Vargeão Dome remain unresolved, so that new studies are needed. For instance: new profiles from electrical resistivity tomography (similar to what was done by Tong et al., 2010) and/or from a ground-based magnetic gradiometer could be useful to better constrain the source geometry of the airborne magnetic anomaly. The problems involving the sources of magnetic anomalies at Serra da Cangalha, Nova Colinas, and Santa Marta could be adressed by reflection seismic studies.

Table 7: Comparison between interpretations (previous and this study) for magnetic sources in some Brazilian impact structures. Abbreviations: AGD – Araguainha; VGD – Vargeão Dome; SdC – Serra da Cangalha; SMT – São Miguel do Tapuio.

Impact structure	Magnetic anomaly(is) observed	Previous interpretation	This study
AGD	1 – Linear magnetic anomalies with NE-SW trends mainly in the northern portion of the impact structure; 2 - Two small magnetic anomalies relatively well-isolated occurring in the Araguainha central uplift; 3 – long-wavelength magnetic anomaly in the eastern portion of the structure.	1 – Such linear magnetic anomalies may relate to the Transbrasiliano Lineament (Vasconcelos, 2007); 2 – By analyzing Analytical Signal Amplitude (now known as Total Gradient Amplitude – TGA), Vasconcelos (2007) suggested that magnetic contrast observed at Araguainha's center (see the 16.8°S and -53°W coordinates in his figure 4.22) comes from the granitic core.	1 – Likewise; 2 – Unclear. Both small magnetic anomalies over the Araguainha central uplift show normal dipole configurationwhich is unexpected for the magnetic latitude at the time of data acquisition. As the magnetic inclination was less than -10° (Vasconcelos, 2007), the magnetic anomalies near the magnetic equator are expected to have a U-shape (e.g., long-wavelength magnetic anomaly in the eastern portion of the Araguainha structure). Because magnetic source depth estimated at 750-1200 m) for these small magnetic anomalies are close to basement depth (1000 m) (Masero et al.,1994; Vasconcelo, 2007), their sources may be related to basement features. However, considering that the magnetic modeling carried out by Vasconcelos (2007) required strong remanent magnetization and taking into account that Yokoyama et al. (2014) found stable characteristic remanent magnetizations (derived from samples of impact melt rock and granite) with normal polarities, the relationship of these small anomalies with blocks of impact melt rock (suggested by Tong et al., 2010) at depth cannot be completely ruled out; 3 – This anomaly has not been mentioned in previous works. Here, it is interpreted as an intrusion into the basement.
VGD	1 - Linear magnetic anomalies with ENE-WSW trends; 2 - circular magnetic signature near the center of VGD.	1 – May be related to pre-impact features such as the Lacinha - Cubatão fault zone (Kazzuo-Vieira et al. (2009); 2 – Kazzuo-Vieira et al.(2009) suggested that this circular magnetic signature is composed of high and low magnetic zones. They argued that high magnetic zones could be related to presence of impact breccias, whereas low magnetic zones could be related to Chapecó acid volcanic rock.	1 – Likewise. Additionally, magnetic source depth for a lineament in the southern part has been estimated at ~580 m. As it is well-defined in SAR images, it is possible that this lineament has a continuity that goes from the surface to a depth of 580 m. Although Kazzuo-Vieira et al. (2009) have linked Lacinha - Cubatão fault zone as a source of this linear magnetic anomaly, they also could be derived from diabase dikes. 2 – The magnetic source depth estimation for this anomaly is 556 m (central-north portion) to 1380 m (west portion). Taking into account the height of the investigation (~500 m), it is unlikely that the magnetic anomaly in the center of Vargeão Dome is due to magnetization contrasts of rocks occurring at shallow levels, such as breccias and felsic rocks. Interestingly, Yokoyama et al. (2015) reported a zone of coherent magnetization in the Vargeão Dome, with higher Natural Remanent Magnetization (NRM) values occurring between 2 and 4 km from the center. According to them, this strong NRM may have resulted from the impact formation of new magnetic iron oxides (e.g., hematite and magnetite). However, it is unclear if these new magnetic carrier would be at depth as well.
SdC	1 – Long wavelength linear magnetic anomaly with NE-SW trend that practically crosses the SdC structure. A clear and isolated magnetic anomaly in the SdC's central uplift not has been observed in this study.	1 - Adepelumi et al. (2005) has claimed that there is a magnetic anomaly in the Serra da Cangalha's central uplift. They suggested that the oval-shape magnetic anomaly observed by them at the center of SdC could be the result of shock remagnetization, Vasconcelos et al. (2012b) also observed a long wavelength linear magnetic anomaly with NE-SW trend that practically crosses the SdC structure, but according to them, this linear magnetic anomaly was modified near to SdC's central uplift due to basement uplift during the impact event.	1 – First of all, Apedelumi et al. (2005) seem to have segmented the linear long wavelength magnetic anomaly, given them the impression of an oval-shape. Note that SdC is a deeply eroded structure and an impact-induced melt layer or even impact-melt bearing breccia has not been found. Thus, shock remagnetization is unlikely to explain this linear magnetic anomaly. Following Vasconcelos et al. (2012b), the present work has interpreted the long wavelength linear magnetic anomaly as a magnetic signal derived from sources linked to the Transbrasilian Lineament. However, whereas Vasconcelos et al. (2012b) claimed that the source of the linear magnetic anomaly may have been modified by impact-induced basement uplift, this work suggest that the interpretation of this linear magnetic anomaly should be more complex because easternmost segments cross the eastern portion of the central uplift, whereas another segment seems to be interrupted at the western portion of the central uplift. Note that Vasconcelos et al. (2012b) based their interpretation on Analytical Signal Amplitude (named TGA in this study), which has lower definition than the Total Horizontal Derivative (THDR) used in the present study (Betts et al., 2024). In short, there is no evidence that this linear long wavelength magnetic anomaly has been modified due to impact-induced basement uplift in the central portion of the SdC, such that it is not possible to state that the basement was affected by the impact based on the airborne magnetic data currently available.

SMT	A linear magnetic anomaly uninterruptedly crosses the entire structure in the southeast, whereas another linear structure seems to be interrupted in the western portion of the structure. All magnetic sources are essentially deep seated (>1000m), but a shallower magnetic source (500 – 100 m) seems to be present just on the outer rim.	Mariano et al. (2004) claimed that a semi-circular magnetic pattern is evident at SMT with spatial distribution of magnetic highs coinciding with morphologic characteristics of SMT. They suggested that this pattern reflects the iron-rich sandstone beds of the Cabeças Formation. Using these same low resolution airborne magnetic data, Martins (2016) suggested that the long wavelength magnetic signatures at SMT show a NE-SW trend compatible with the general tectonic framework of the Precambrian basement to the Parnaíba Basin and related this trend to the Transbrasiliano Lineament.	1 – Considering the depth estimates and trends of these linear magnetic anomalies, the present work also has associated these linear signatures to the regional Transbrasiliano Lineament. Otherwise, high magnetic anomalies are unclear, and could even be due to the noise level.

In this case, investigations using an acquisition arrangement similar to what was done at the Ries impact structure (McCall et al., 2023) might result in good imaging of the central uplifts of these structures.

15.3 Screening of circular structures potentially formed by impact for suitability for ground-truthing.

In order to investigate the origin of crater-form structures in Fennoscandia and adjacent areas, Henkel and Pesonen (1992) used several criteria (e.g., historical records of the observation of meteorite impacts; meteorite fragments, shock features, impactites, topographic features, geophysical signatures, etc) to classify sixty-two circular structures. Unfortunately, the lack of geological information and even geophysical data for some potential targets studied here hindered an application similar to Henkel and Pesonen's (1992) approach to assess the possibility of impact origin for such targets. On the other hand, results obtained in this study allow us to at least identify which of these potential targets have a set of characteristics that could favor a meteoritic impact scenario, such that a prioritization of candidates for ground-truthing can be done. Based on this approach and considering the shortcomings of direct comparison between Brazilian impact structures in sedimentary environments and potential targets in crystalline terrains discussed above, beyond the main geological, geophysical, and morphological characteristics of Brazilian impact structures, this study also has considered additional features that have been reported for other impact structures around the world, as described in the initial sections of this work (see chapters 5, 6, and 7).

Starting with potential targets in sedimentary terrains, the lack of geological information represented the main shortcoming that constrained the interpretations of airborne geophysical and spaceborne images for targets in the sedimentary domain. Even so, the results obtained here suggest that a rough prioritization of candidates for ground-truthing can be done for such targets.

In an ascending order of prioritization for ground-truthing surveys for impact research, the ITA target can be regarded as being of lower priority among the targets in the sedimentary terrain because: i) the results (radiometric or morphological signatures) reported here suggest that the ITA target is

probably a buried structure, so that to finding outcrops of these sources in a ground-truth survey may be difficult; ii) the lack of a central zone, where the probability of finding supposed shocked rocks would be greater, makes it difficult to pinpoint places for sample collection; iii) although the magnetic anomaly associated with ITA shows an approximately circular pattern that disrupts the regional magnetic field, a typical feature seen in impact structures, other magnetic patterns commonly seen in impact structures (e.g., low and/or subdued magnetic, ring-shaped, or isolated magnetic high in the central zone) (Henkel, 1997; Henkel and Pesonen, 1992; Henkel and Reimold, 2002; Haines and Rawlings, 2002; Hawke, 2003; MacDonald et al., 2005; Cowan and Cooper, 2012; Gilder et al., 2018) are missing within ITA ; iv) taking into account that mining companies have focused on research for industrial minerals, such as Rare Earth Elements and gold, in the ITA structure, its origin may be by an endogenous process, possibly a magmatic intrusion. This idea is supported by regional geological understanding, whereby alkaline intrusions (e.g., Goiás Alkaline Province) occur approximately 320 km northeast of ITA and also show some circular magnetic anomalies (see Alves et al., 2022).

The CDS target can also be regarded as having lower priority because of the following reasons: i) the center of the structure appears to emerge on surface, but the outer limit is practically not exposed; ii) a magnetic anomaly suggests the shape of the CDS structure to be more elliptical than circular, which is unusual for impact structures but not impossible, as seen by Matt Wilson impact structure in Australia (Kenkmann and Poechau, 2008; Dunster et al., 2014). iii) The K and ferric iron-rich strata and subdued magnetic anomaly areas in the central magnetic high could suggest that CDS could be a strongly eroded impact structure. However, if this were the case, the magnetic anomaly in the CDS rim would be expected to be strongly reduced due to erosion (Plado et al., 1999), but it shows strong amplitude (~300 nT) over the CDS rim. iv). As the CDS area has been investigated for ilmenite exploration, it is possible that it represents a magmatic intrusion. In this scenario, the linear magnetic lineaments of the CDS area can be interpreted as related to Transbrasiliano Lineament faults that may have provided a conduit for a magmatic intrusion.

In the case of the Caraíbas (CNB) target, the spaceborne results show that CNB is indeed a noticable, completely circular structure. Due to its small

diameter (~1.85 km), it would make sense to compare it with simple rather than complex impact structures, so that the features seen at the complex Brazilian impact structures can not be used as a guide in this case.

When compared with known simple bowl-shape impact structures, it is noted here that diameter (~1.85 km) and apparent depth (~25 m) of the CDS structure yield an apparent depth/diameter ratio of 0.012, whereas the apparent depth/diameter relationship given by Grieve and Pesonen (1992) yields a ratio of 0.25 for a simple impact crater of similar size. Additionally, because simple craters in sedimentary targets commonly have a flat floor (Melosh, 1989; French, 1998), the 182 m-wide hill-type feature near the CNB center does not support an impact origin. On the other hand, other crater forming processes, such as sinkhole formation, do not seem to provide an alternative explaination for the formation of CNB because such processes commonly create craters with diameters smaller than 1.5 km (e.g., Nel and Haarhorff, 2011). Based on these observations, this study considers that the origin of the CNB structure is currently entirely unknown and further studies are needed to investigate its origin. These studies may include analysis of high spatial resolution digital elevation models (e.g., TanDEM-X data) and analysis of time series of satellite images. Further analysis of the regional geology is clearly also demanded.

For the last, i.e., the São Francisco do Maranhão – SFM, target in sedimentary terrain, the presence of alleged breccias and strongly fractured sandstones (pers. comm., S.L.A. Brenha, São Luis) may encourage a ground-truth survey. Moreover, the interpretations of optical images carried out for this work suggests that the SFM structure has a prominent outer rim surrounding a broad central area. The delimitation of the supposed central zone is important because, as has been seen in Brazilian impact structures, the most strongly deformed areas, with possible presence of impactites with shocked minerals, occur in the central zone of the structures. However, a ground-truth survey in SFM's central zone may be a difficult task because this central zone seems to be dominated by flat-topped plateaus which may cover the potential original level of shocked rocks (see the Fig. 53b). As the distance between SFM and CNB is approximately 150 km, both structures could be investigated in the same field campaign. This possibility gives to SFM and CNB a relatively higher priority among the targets in sedimentary domain.

When considering targets in the crystalline domain, a first prioritization of targets for ground-truthing can also be done. Starting with the lowest priority target, results from this study supports that an endogenous origin is likely the cause of the Brejões (BRJ) structure because i) unlike impact structures, where older units occur strongly deformed in the center of the structure, older, strongly deformed units occur in BRJ's rim area; ii) the magnetic ring anomaly in the BRJ structure is likely related to the metabasalt layer occurring in the structure's rim, not related to impact-driven outward movement related magnetic contrast (e.g., truncations or thickening of magnetic horizons in Foelsche and Glikson, as argued by Hawke,2003, Macdonald et al., 2005, and Haines and Rawlings, 2002 - and possibly Nova Colinas – this work); iii) the textural pattern of the inner zone of BRJ seen in spaceborne images is consistent with that observed in the external portion of the structure, including the presence of linear features (faults or fractures) trending in the same direction. This means that there is no disruption of regional background typically seen at impact structures; iv) areas rich in eU and eTh occur similarly in the inner and outer portions of the BRJ structure, suggesting that the internal and regional background radiometric patterns are similar; v) the presence of other dome-like features near the BRJ structure with similar deformation features suggests that the formation of BRJ was not an isolated event. All these observations favor a magmatic intrusion.

Another potential target in the crystalline domain that may be considered a low priority for field investigation is Sucunduri Dome. Although the presence of brecciated rhyolite, the impressive concentric radiometric pattern, and a partially circular magnetic signature could hint at a possible impact origin, access to the interior of the structure to look for possible evidence (impactites) seemingly is an extremely difficult task due to presence of vegetation. Furthermore, some factors might support an endogenous origin. For instance, one could think that SDC resulted from an alkaline intrusion, similar to the Richat structure in Mauritania (see Matton et al., 2005). The factors that favor this idea include: i) breccias are predominately composed of phenocrysts of K-feldspar and are strongly hydrothermalized; ii) several volcanic products (e.g., tuffs, basalts, volcanic breccias – mainly rhyolitic breccias, rhyolites, and ignimbrite) seem to predominate the dome's geology; iii) similar to Richat, inner rings of SDC can be seen in radiometric, spaceborne, and magnetic data (see Abdeina et al., 2021);

and ; iv) very high concentrations of eU (~30 ppm) and eTh (200 ppm) corroborate the presence of alkaline rocks supporting the plateau near the SDC center (I.P. Marques, pers. commun.),

Another observation in the SDC structure that also does not support an impact origin is the apparent change in the curvature of the SDC's outer limit (the turning point in the SW sector). This curvature change suggests that the SDC structure already was naturally open during its formation. The outer limits of Impact structures, on the other hand, are naturally closed features and then may have been truncated due to erosion of the rim (e.g., Riachão Ring, Nova Colinas, and Cerro do Jarau impact structures, see Table 3, Chapter 14). It has been postulated that the entire SDC structure was formed due to the different rheological behaviors of lithostratigraphic units in the face of regional folding (I.P. Marques, pers. commun.). However, the formation mechanism for SDC is unclear and new data are required to investigate this structure in more depth. Further studies could use the airborne gravity data that were used to produce the Brazilian gravity map (see Santos, 2022) and verify whether any Bouguer anomaly is associated with the SDC structure in a similar way to what has been seen at impact structures of comparable size.

From a morphological point of view, Inaján (INJ) is very similar to the Vista Alegre impact structure. Like this latter structure, INJ shows very circular shape, with landform relief contrast in relation to regional background, flat inner surface, raised rim, and a 6.2 km diameter crater-like form. Other indicators that could favor an origin by impact include: i) raised rim, flat inner surface, extraordinary circular appearance, and landform relief contrast as morphological features seen in the Inaján target and at the Vista Alegre impact structure; ii) geophysical (gamma-ray and magnetic) and spaceborne signatures clearly show the INJ structure has disrupted the regional pattern in a similar way than some impact structures. iii) INJ has a 6.2 km diameter crater-like form. iv) INJ's rim is well-defined by magnetic anomalies, whereas the inner portions show a subdued magnetic relief. The diameter of the magnetic anomaly (~6.2 km) coincides with the diameter estimated from a topographic profile. v) Inside of INJ, the shallow (< 200 m) and weak magnetic anomalies may be of the contact-type, for instance representing faults, fracture zones, or even pods of impact melt-bearing breccias. vi) The low radiometric signature of INJ is

apparently inconsistent with the locally occurring lithological types (biotite-granites, monzonite, alkali-granites, and hornblende-biotite granite) that would be expected to be rich in radioelement contents, mainly K (Dentith and Mudge, 2014). Indeed, because INJ is heavily eroded, low K content would be expected, but eTh content could be high due to the limited mobility of this element in soils (Wilford and Minty 2007; Dentith and Mudge, 2014). It could be considered that crater-fill sediments may cover the radiometric signature of target rock. Moreover, crater-fill sediments could explain why the superficial expression of a linear NW–SE trend is masked within the INJ structure, whereas magnetic data suggest that this lineament continues at depth within the structure and then approaches the surface again in its western portion.

Regarding geology, the INJ structure itself has been barely studied, such that outcrop descriptions are still incipient. Even so, whereas the geophysical and morphological signatures could be interpreted as possibly derived from impact, the presence of strongly silicified rocks and alumosilicate metasedimentary hornfels near the rim and and granular minerals (quartz, feldspars, and/or cordierite) associated with elongated poikiloblastic minerals (andalusite, biotite, and fibrous sillimanite) could be an indicator of contact metamorphism. In this case, the circular magnetic anomaly could arise from new magnetic carriers related to the emplacement of an intrusive body. Additionally, the presence of a smaller structure with similar features to INJ, the volcanic environment, and possible magnetic carriers formed during contact metamorphism could provide support for an endogenous origin of INJ. Although the northern portion of the INJ structure is heavily vegetated, which would hinder fieldwork, the southern portion of the structure is accessible, with several dirt roads running within the structure. Thus, a ground-truth campaign can be recommended to investigate if INJ was derived from an impact event or from a magmatic intrusive event involving contact metamorphism.

The Bom Jardim (BJD) target shows geological, geophysical, and spaceborne signatures that might support a meteorite impact context. For instance: abrupt contact zones containing meter-size enclaves of country rocks in the BJD’s rim could be derived from outward movement during the excavation stage of impact cratering (e.g., Osinski et al., 2022). The textural variation (from coarse-grained to medium- or even fine-grained granite)

observed from the outer parts towards the BJD center could result from heterogeneous cooling of a magma, or melting with uneven distribution of water in a magma chamber - as proposed by Romanini (1981). Alternatively, because the fragmentation degree seemingly increases inward to the center of an impact structure (e.g., Kenkmann et al., 2014), this textural variation could also be explained by differential impact deformation. Note this tendency of increase of deformation towards the interior has been observed in all Brazilian impact structures studied here.

Similarly, an impact event could also be responsible for the presence of microgranite dikes in the BJD central zone because impact melt dykes can be emplaced in the crater floor during the impact (e.g., Osinski et al., 2008 and 2022). In the same way, the presence of quartz as idiomorphic crystals and at the same time as main constituent of finer-grained fine-grained Bom Jardim biotite granite may result from a magmatic process (Romanini, 1991), but this could also be interpreted as a result of brecciation, fracturing, faulting, and grain comminuation that might be impact-induced. Structurally, the lineaments with directions apparently pointing to the center of the structure, the discontinuities of the circular radiometric signatures, the inner ring, and the innermost elevated area that separate the drainage channels on the eastern and western sides could be interpreted as first- or second-order structural elements of an impact structure, like radial faults, ring syncline, folding, and central uplift formation (Kenkmann, 2002, 2014).

The magnetic signatures in the BJD structure can also be related to impact. The BJD outer rim is well-defined on magnetic maps, the related sources are shallow (average depth of 111.8 m and maximum depth of 435 m), and they can be modeled as contact-type sources. Impact structures of similar size as BJD (~10 km) are essentialy shallow and the magnetization contrast on impact structure rims may come from rocks that are strongly rotated or overturned due to outward movement during the excavation stage (Hawke, 2003; Kenkmann et a., 2014). Amplitudes and gradients in the internal portion of BJD are strongly subdued, but isolated magnetic anomalies with high amplitude and short wavelength can be seen on the magnetic maps. This strongly subdued magnetic relief could arise from shock demagnetization, dissociation of Si and Fe in magnetic minerals, or from oxidation of magnetite in

the fractured target rocks, promoting a contrast with undeformed/less shocked surrounding terrain. In contrast, isolated magnetic anomalies with high amplitude and short wavelength could be related to impact products (e.g., impact-melt pods or impact melt-bearing breccias) (Henkel, 1997; Henkel and Pesonen, 1992; Henkel and Guzman, 1977; Henkel and Reimold, 2002; Gilder et al., 2018).

The main counterargument to an impact origin for the BJD structure is the existence of other intrusions (e.g., the São Domingo facies - Romanini, 1982; Bettencourt et al., 1997) near the BJD structure. Although these intrusions do not show circular geophysical signatures like the BJD structure, but they also entail Massangana facies granites and also show abrupt contacts between these granites and those of the São Domingos or Tabocas facies. Furthermore, the regional geological context in which the BJD is embedded is predominantly volcanic, so an endogenous origin for the BJD cannot be ruled out at this point. Taking into account that the entire BJD structure is accessible and that it is in relative proximity to Arequimes town (less then 100 km), the BJD structure can be regarded as a relatively high priority target for future ground-truthing surveys.

Regarding the Colônia (CLA) circular structure, the presence of brecciated materials and possible minerals with planar microfeatures (e.g. Velázquez et al., 2018), the geophysical signatures (e.g., Plado et al., 2019 and references therein), a distinct 3.6 km diameter crater form, and well-defined landform relief contrast between the CLA crater form and its surrounding terrain (this and previous works) support CLA as a strong candidate for impact origin. Additionally, U and Th rich zones seen in eU/K and eTh/K ratio maps likely arise from phyllosilicate and organic matter rich materials, as these radioelements are more easily adsorbed in clays or tend to be accumulated in the presence of organic complexes (Megumi and Mamuro 1977; Dickson and Scott, 1997; Taylor et al. 2002; Wilford and Minty 2007; Dentith and Mudge, 2014). The existing drilling products need to be reexamined for proof of shock metamorphic materials. The seemingly currently abandoned plan to drill the structure should be reconsidered – drilling will possibly be the only way to obtain proof to satisfactorily resolve the question about Colônia's origin. In addition, the sedimentary record from a long closed basin has great potential to improve the

paleo-environmental knowledge about this critical Atlantic rainforest region (Riccomini et al., 1991 and 2011).

After the discussion presented above, this work proposes that the Colônia, Bom Jardim, and Inajáh circular structures can be regarded as high-priority targets for field campaigns at possible impact structures on crystalline basement, whereas the São Francisco do Maranhão and Caraíbas circular structures seems to be good targets in sedimentary basins. The remaining targets (e.g. Cardoso, Itiquira, Brejões, and Sucunduri Dome) show less potential as possible impact structures, but they could be of strong interest for mineral exploration.

CHAPTER 16
CONCLUSIONS

16. CONCLUSIONS

Integrated analysis of data from different remote sensors (multispectral, synthetic aperture, magnetic, and radiometric) and geological information have been useful to map the main characteristics of confirmed Brazilian impact structures and use these fndings to evaluate circular targets as potentially formed by meteorite impact, with a view of subsequently selecting promising targets for future ground-truth surveys. By applying several processing techniques and making interpretations based on the available geological knowledge, the main findings of this study allow us to establish the following conclusions:

- The confirmed Brazilian impact structures occur in sedimentary intercontinental basins and the structures settings are dominated by sedimentary strata (besides some volcanic deposits in two structures).
- The diversity of sedimentary strata, affected to differing degrees by differential erosion, play an essential role in the capability of geophysical datasets, and multispectral, SAR, and, sometimes, airborne radiometric images to characteize first (central uplift, ring syncline, and/or crater rim) or second (listric faults, upturned strata, thrusting, etc) order attributes of impact structures.
- The analysis of magnetic anomalies for the Araguainha, Vargeão Dome, Nova Colinas, and Santa Marta impact structures revealed that alternative interpretations to published material may have to be considered to explain the sources of such anomalies.
- By comparing the main (geological, geophysical, and spaceborne) features seen in impact structures (including the Brazilian ones), this study was successful in evaluating other circular structures of putative impact origin, such that a priorization for future ground-truth surveys could be established. On crystalline rocks, the Colônia circular target remains the prime candidate for impact origin. In addition, this study has revealed that two targets (Bom Jardim and Inajáh) may be promising, with some results that could be interpreted to suggest an impact origin. However, because these two

targets occur in ancient volcanic environments of the Amazonian Craton, endogenous processes cannot be ruled out for these structures either. On sedimentary rocks, the São Francisco do Maranhão and Caraíbas circular structures have top priority for ground-truthing the possible impact origin for these structures.

- The other circular tagets studied here (Cardoso, Itiquira, Brejões, and Sucunduri Dome) show less potential for impact research, but they could be of interest for mineral exploration.

17. REFERENCES

Abdeina, E. H., Bazin, S., Chazot, G., Bertrand, H., Le Gall, B., Youbi, N., Sabar, M.S., Bensalah, M.K., & Boumehdi, M. A. (2021). Geophysical modelling of the deep structure of the Richat magmatic intrusion (northern Mauritania): insights into its kinematics of emplacement. Arabian Journal of Geosciences, 14(22), 2315. https://doi.org/10.1007/s12517-021-08734-4

Abels, A., Zumsprekel, H., & Bischoff, L. (2005). Basic remote sensing signatures of large deeply eroded impact structures. In Impacts and the Early Earth (pp. 309-326). Berlin, Heidelberg: Springer Berlin Heidelberg.

Acevedo, R. D., Rocca, M. C., Ponce, J. F., & Stinco, S. G. (2015). Impact Craters in South America. Springer International Publishing. Pg. 45 – 53. https://doi.org/10.1007/978-3-319-13093-4_4

Ackermann, H. D., Godson, R. H., & Watkins, J. S. (1975). A seismic refraction technique used for subsurface investigations at Meteor Crater, Arizona. Journal of Geophysical Research, 80(5), 765-775.

Adepelumi, A. A., Fontes, S. L., Schnegg, P. A., & Flexor, J. M. (2005). An integrated magnetotelluric and aeromagnetic investigation of the Serra da Cangalha impact crater, Brazil. Physics of the Earth and Planetary Interiors, 150(1-3), 159-181.

Ahern, J. L. (2003). The potential of potential fields for detecting buried impact structures: Earth and Mars. The Leading Edge, 22(8), 776–778. https://doi.org/10.1190/1.1605080

Almeida, J. D. A. C., de Oliveira, V. E. S., Rocha, J. L. S., de Lima Feio, G. R., Rocha, M. C., & da Rocha, K. P. P. (2020). Caracterização geológica, geoquímica e aerogeofísica dos granitoides arqueanos da porção sul do Domínio Rio Maria. Geologia USP. Série Científica, 20(2), 61-85.

Almeida-Filho, R., Moreira, F. R. S., & Beisl, C. H. (2005). The Serra da Cangalha astrobleme as revealed by ASTER and SRTM orbital data. International Journal of Remote Sensing, 26(5), 833–838. https://doi.org/10.1080/01431160310001618815

Almeida V.V., Guerra G.I.T., Oliveira A.A., Marques I.P., Loreti-Junior R., Ribeiro L.M.A.L., Azevedo E.J.H.C.B.P. Mapa Geológico Integrado da Região Metropolitana de São Paulo. Mapa. São Paulo: CPRM, 2019, mapa colorido. Escala 1:250.000. Projeto Materiais de Construção na Região Metropolitana de São Paulo.

Alsemgeest, J., Brouwer, F. M., & Cluster, G. (2006). Thermodynamic Modelling of Hydrothermal Alteration in the Vista Alegre Impact Structure (Brazil) to Distinguish Between Different Alteration Stages. Philosophical. Transactions of the Royal Society of London. B: Bilogical Sciences, 361, 1474.

Alsemgeest, J., Brouwer, F. M., Auqué, L. F., Hauser, N., & Reimold, W. U. (2021). Hydrothermal alteration at the basalt-hosted Vista Alegre impact structure, Brazil. Meteoritics & Planetary Science, 56(12), 2155–2174. https://doi.org/10.1111/maps.13763

Alsemgeest, J., & Brouwer, F. M. (2022). Impact-reactivation of a hydrothermal system at Vargeão Dome, Brazil. Abstracts of the 85th Annual Meeting of The Meteoritical Society 2022. Lunar and Planetary Institute Contrib. No. 2695, p.6052... https://www.hou.usra.edu/meetings/metsoc2022/pdf/6052.pdf

Alsemgeest, J. (2024). Impact-generated hydrothermal systems in terrestrial basalt as analogues for lifesupporting environments on Mars. (PhD Thesis - Research and graduation internal, Vrije Universiteit Amsterdam). https://doi.org/10.5463/thesis.763

Anderson, R.R., Hartung, J.B. 1991. The Structural Configuration of the Manson Impact Structure, Iowa, as Interpreted from Seismic Data and Confirmed by Drill Samples. Abstracts of the 22nd Lunar and Planetary Science Conference, volume 22, page 25. https://www.lpi.usra.edu/meetings/lpsc1991/pdf/1013.pdf

Antoine, L. A. G., Nicolaysen, L. O. & Niccol, S. L. (1990). Processed and enhanced gravity and magnetic images over the Vredefort structure and their interpretation. Tectonophysics, 171(1-4), 63-74.

Armour, M., Boyce, J. I., Shulman, Z., & Zilkey, D. R. (2024). 3-D geophysical modeling of a buried, simple impact crater: Holleford impact structure, Ontario, Canada. Meteoritics & Planetary Science, 59(1), 171–192. https://doi.org/10.1111/maps.14113

Alaska Satellite Facility Distributed Active Archive Center (ASF-DAAC). (2014). ALOS PALSAR High Resolution Radiometric Terrain Corrected Product [Data set]. NASA Alaska Satellite Facility Distributed Active Archive Center. https://doi.org/10.5067/Z97HFCNKR6VA Date Accessed: 2025-08-20.

Assine, M. L., Piranha, J. M., & Carneiro, C. D. R. (2004). Os paleodesertos Pirambóia e Botucatu. Geologia do Continente Sul-Americano: Evolução da Obra de Fernando Flávio Marques de Almeida, Editora Beca, São Paulo, pp. 77 – 92..

Alves, F.M., Silva, E.R., Silva, A.B., & (2022). Atlas Aerogeofísico do Estado de Goiás. Levantamentos Geológicos e de Potencial Mineral de Novas Fronteiras, SGB-CPRM, Goiânia, GO, Brazil. https://rigeo.sgb.gov.br/handle/doc/23325

Avona, P. D., Crósta, A. P., Vasconcelos, M. A. R., Bjonnes, E., Pereira, F. L., & Góes, A. M. (2025). Geology, gravity, and numerical modeling of the Nova Colinas impact structure, Parnaíba Basin, Brazil. Meteoritics & Planetary Science, 60(2), 286–307. https://doi.org/10.1111/maps.14306

Baratoux, D. & Reimold, W. U. (2016). The current state of knowledge about shatter cones: Introduction to the special issue. Meteoritics & Planetary Science, 51(8), 1389–1434. https://doi.org/10.1111/maps.12678

Baratoux, D., Niang, C. A. B., Reimold, W. U., Sapah, M. S., Jessell, M. W., Boamah, D., Faye, G., Bouley, S., & Vanderhaeghe, O. (2019). Bosumtwi impact structure, Ghana: Evidence for fluidized emplacement of the ejecta. Meteoritics & Planetary Science, 54(10), 2541–2556. https://doi.org/10.1111/maps.13253

Barbosa, J. S. F., da Silva, F. A., Sapucaia, N. S., & Iyer, S. S. (1998). Petrological and Geochemical Characteristics of the Granulitic Terrain of Brejões, Bahia, Brazil. Gondwana Research, 1(3-4), 343-356. https://doi.org/10.1016/S1342-937X(05)70850-9

Barbosa, J., Martin, H., & Peucat, J. J. (2004). Palaeoproterozoic dome-forming structures related to granulite-facies metamorphism, Jequié block, Bahia, Brazil: petrogenetic approaches. Precambrian Research, 135(1-2), 105-131. https://doi.org/10.1016/j.precamres.2004.08.002

Barbosa, V. C., & Silva, J. B. (2005). Deconvolução de Euler: passado, presente e futuro – um tutorial. Revista Brasileira de Geofísica, 23, 243-250. https://doi.org/10.1590/S0102-261X2005000300004

Barbosa, J., Nicollet, C., Leite, C., Kienast, J. R., Fuck, R. A., & Macedo, E. P. (2006). Hercynite–quartz-bearing granulites from Brejões Dome area, Jequié Block, Bahia, Brazil: Influence of charnockite intrusion on granulite facies metamorphism. Lithos, 92(3-4), 537-556. https://doi.org/10.1016/j.lithos.2006.03.064

Beard, L. P. (2012). Magnetic Anomalies of Impact Craters at Low Magnetic Latitudes. Symposium on the Application of Geophysics to Engineering and Environmental Problems 2012, 92–100. https://doi.org/10.4133/1.4721703

Bettencourt, J. S., Leite Junior, W. B., Payolla, B. L., Scandolara, J., Muzzolon, R., & Vian, J. A. (1997). The rapakivi granites of the Rondônia Tin Province, northern Brazil. In Excursions Guide. Second International Symposium on Granites and Associated Mineralizations, Salvador, Bahia, Brazil. https://repositorio.usp.br/item/000947992

Bettencourt, J. S., Tosdal, R. M., Leite Jr, W. B., & Payolla, B. L. (1999). Mesoproterozoic rapakivi granites of the Rondônia Tin Province, southwestern border of the Amazonian craton, Brazil—I. Reconnaissance U–Pb geochronology and regional implications. Precambrian Research, 95(1-2), 41-67. https://doi.org/10.1016/S0301-9268(98)00126-0

Betts, P. G., Moore, D., Aitken, A., Blaikie, T., Jessell, M., Ailleres, Armit, R., McLean, M., Munukutla, R., & Chukwu, C. (2024). Geology from aeromagnetic data. Earth-Science Reviews, 258, 104958. https://doi.org/10.1016/j.earscirev.2024.104958

Bishop, J.L. (2019) Visible and Near-Infrared Reflectance Spectroscopy: Laboratory Spectra of Geologic Materials. In: Bishop J.L, Bell III J.F., Moersch J.E., eds. Remote Compositional Analysis: Techniques for Understanding Spectroscopy, Mineralogy, and Geochemistry of Planetary Surfaces. Cambridge Planetary Science. Cambridge University Press : 68-101. https://doi.org/10.1017/9781316888872.006

Blakely, R. J., & Simpson, R. W. (1986). Approximating edges of source bodies from magnetic or gravity anomalies. Geophysics, 51(7), 1494-1498. https://doi.org/10.1190/1.1442197

Brito Neves, B. B., Fuck, R. A., & Cordani, U. G. (1984). Influence of basement structures on the evolution of the major sedimentary basins of Brazil: a case of tectonic heritage. Journal of Geodynamics, 1(3-5), 495-510. https://doi.org/10.1016/0264-3707(84)90021-8

Brito Neves, B. B. (2002). Main stages of the development of the sedimentary basins of South America and their relationship with the tectonics of supercontinents. Gondwana Research, 5(1), 175-196. https://doi.org/10.1016/S1342-937X(05)70901-1.

Brito Neves, B. B , Fuck, R. A., & Pimentel, M. M. (2014). The Brasiliano collage in South America: a review. Brazilian Journal of Geology, 44(3), 493-518. https://doi.org/10.5327/Z2317-4889201400030010

Bernardes, R.B., Reimold, W.U., Gibson, R.L., Hauser, N., & Pavanetto, P. (2025). New insights into the geology and formation of the Araguainha impact structure, Brazil, from morphological and structural analysis. Geological Society of America Bulletin (Accepted manuscript).

Bruckenthal, E. A., & Pieters, C. M. (1984, March 12 – 16). Spectral effects of natural shock on plagioclase feldspar. Abstract of the XV LUNAR AND PLANETARY SCIENCE Conference, 15, pp. 96-97), Houston, TX, US. https://articles.adsabs.harvard.edu/pdf/1984LPI....15...96B

Buch, T., Dall'Igna, L. G., Graça, M. C., & Silva, D. R. V. D. (2019). Áreas de relevante interesse mineral: reavaliação da província estanífera de Rondônia. Provincias Minerais do Brasil, CPRM, Porto Velho, Brazil. https://rigeo.sgb.gov.br/handle/doc/20938

Campos J.E.G., Dardenne M.A. 1997a. Estratigrafia e sedimentação da Bacia Sanfranciscana: uma revisão. Revista Brasileira de Geociências, 27(3), 269-282. https://doi.org/10.25249/0375-7536.1997269282

Campos J.E.G., Dardenne M.A. 1997b. Origem e evolução tectônica da Bacia Sanfranciscana. Revista Brasileira de Geociências, 27(3), 283-294. https://doi.org/10.25249/0375-7536.1997283294

Campos-Enriquez, J. O., Morales-Rodríguez, H. F., Domínguez-Mendez, F., & Birch, F. S. (1998). Gauss's theorem, mass deficiency at Chicxulub crater (Yucatan, Mexico), and the extinction of the dinosaurs. Geophysics, 63(5), 1585-1594. https://doi.org/10.1190/1.1444455

Canup, R. M. (2012). Forming a Moon with an Earth-like composition via a giant impact. Science, 338(6110), 1052-1055.DOI: 10.1126/science.1226073

Castro, D. L., Bezerra, F. H., Fuck, R. A., & Vidotti, R. M. (2016). Geophysical evidence of pre-sag rifting and post-rifting fault reactivation in the Parnaíba basin, Brazil. Solid Earth, 7(2), 529-548. https://doi.org/10.5194/se-7-529-2016

COMPANHIA DE PESQUISA DE RECURSOS (CPRM). (1981). Projeto prospecção de carvão energético nas bordas norte e oeste da Bacia do Paraná-áreas I, II, III. CPRM, Goiânia, Brazil. https://rigeo.sgb.gov.br/handle/doc/4262

Catchings, R. D., Powars, D. S., Gohn, G. S., Horton, J. W., Goldman, M. R., & Hole, J. A. (2008). Anatomy of the Chesapeake Bay impact structure revealed by seismic imaging, Delmarva Peninsula, Virginia, USA. Journal of Geophysical Research: Solid Earth, 113(B8). https://doi.org/10.1029/2007jb005421

Cicco, M. A., & Zucolotto, M. E. (2002). Appraisal of Brazilian astroblemes and similar structures. Meteoritics & Planetary Science, vol. 37, Supplement, p. A40, 37, Avaliable in (accessed Ago 22, 2025): https://articles.adsabs.harvard.edu/pdf/2002M%26PSA..37R..40D

Collins, G. S., Melosh, H. J., & Osinski, G. R. (2012). The Impact-Cratering Process. Elements, 8(1), 25–30. https://doi.org/10.2113/gselements.8.1.25

Collins, G. S., Kenkmann, T., Osinski, G. R., & Wünnemann, K. (2008). Mid-sized complex crater formation in mixed crystalline-sedimentary targets: Insight from modeling and observation. Meteoritics & Planetary Science, 43(12), 1955–1977. https://doi.org/10.1111/j.1945-5100.2008.tb00655.x

Correa, R.T. (2019a). Mapa da anomalia magnética do Brasil (terceira edição). Escala: 1:500.000, Serviço Geológico do Brasil, Brasília, Brazil. https://rigeo.sgb.gov.br/handle/doc/21299

Correa, R.T. (2019b). Mapa da anomalia radiométrica do Brasil (terceira edição). Escala: 1:500.000, Serviço Geológico do Brasil, Brasília, Brazil. https://rigeo.sgb.gov.br/handle/doc/21296

Correia, G. A., de Menezes, J. R. C., Bueno, G. V., & Marques, E. J. J. (2005). Identificação de uma estrutura de impacto no Cretáceo Superior da Bacia de Santos em sísmica de reflexão 3D. Boletim de Geociências da Petrobras, 13(1), 123-127. https://bgp.petrobras.com.br/bgp/article/view/478

Cowan, D. R., & Cooper, G. R. (2005). Enhancement of magnetic signatures of impact structures. In. Kenkmann, T., Hörz, F., Deutsch, A. (eds). Large Meteorite Impact III. Geological Society of America. https://doi.org/10.1130/0-8137-2384-1.51

Creech, J. B., Moynier, F., & Koeberl, C. (2019). Volatile loss under a diffusion-limited regime in tektites: Evidence from tin stable isotopes. Chemical Geology, 528, 119279.

Crósta, Á. P., Gaspar, J. C., & Cândia, M. Â. F. (1981). Feições de metamorfismo de impacto no Domo de Araguainha. Revista Brasileira de Geociências, 11(3), 139-146. https://repositorio.usp.br/item/002172362

Crósta, A. P., (1982). Mapeamento geológico do Domo de Araguainha utilizando tecnicas de sensoriamento remoto. MSc dissertation, Instituto de Pesquisas Espaciais (INPE), São José dos Campos, 108p.

Crósta, A.P. (1987). Impact Structures in Brazil. In: Pohl, J. (eds) Research in Terrestrial Impact Structures. Earth Evolution Sciences. Vieweg+Teubner Verlag, Wiesbaden. https://doi.org/10.1007/978-3-663-01889-6_2

Crosta, A. P., De Souza Filho, C. R., Azevedo, F., & Brodie, C. (2003). Targeting key alteration minerals in epithermal deposits in Patagonia, Argentina, using ASTER imagery and principal component analysis. International journal of Remote sensing, 24(21), 4233-4240. https://doi.org/10.1080/0143116031000152291

Crosta,A.P.; Kazzuo-Vieira,C.; Choudhuri,A.; Schrank,A. 2005. Vargeão Dome, State of Santa Catarina - A meteoritic impact record on volcanic rocks of the Paraná Basin. In: Winge,M.; Schobbenhaus,C.; Berbert-Born,M.; Queiroz,E.T.; Campos,D.A. (Edit.) Sítios Geológicos e Paleontológicos do Brasil. https://sigep.eco.br/sitio044/sitio044english.pdf

Crósta, A. P., Lourenço, F. S., & Priebe, G. H. (2010a). Cerro do Jarau, Rio Grande do Sul: A possible new impact structure in southern Brazil., Large Meteorite Impacts and Planetary Evolution IV. Geological Society of America. https://doi.org/10.1130/2010.2465(12)

Crósta, A. P., Koeberl, C., Furuie, R. A., & Kazzuo-Vieira, C. (2010b). The first description and confirmation of the Vista Alegre impact structure in the Paraná flood basalts of southern Brazil. Meteoritics & Planetary Science, 45(2), 181–194. https://doi.org/10.1111/j.1945-5100.2010.01015.x

Crósta, A. P., Kazzuo-Vieira, C., Pitarello, L., Koeberl, C., & Kenkmann, T. (2012). Geology and impact features of Vargeão Dome, southern Brazil. Meteoritics & Planetary Science, 47(1), 51–71. https://doi.org/10.1111/j.1945-5100.2011.01312.x

Crósta, A. P., Reimold, W. U., Vasconcelos, M. A. R., Hauser, N., Oliveira, G. J. G., Maziviero, M. V., & Góes, A. M. (2019a). Impact cratering: The South American record – Part 1. Geochemistry, 79(1), 1–61. https://doi.org/10.1016/j.chemer.2018.06.001

Crósta, A. P., Reimold, W. U., Vasconcelos, M. A. R., Hauser, N., Oliveira, G. J. G., Maziviero, M. V., & Góes, A. M. (2019b). Impact cratering: The South American record—Part 2. Geochemistry, 79(2), 191–220. https://doi.org/10.1016/j.chemer.2018.09.002

Crósta A.P., Reimold W.U., Vasconcelos M.A.R. (2019c 18 – 22 March). CERRO DO JARAU AND SÃO MIGUEL DO TAPUIO: TWO NEWLY CONFIRMED, LARGE IMPACT, Abstract of the 50th Lunar and Planetary Science Conference 2019 (LPI Contrib. No. 2132), The Woodlands, TX. US. https://ui.adsabs.harvard.edu/abs/2019LPI....50.3042C/abstract

Crósta, A. P. (2024). Geological Records of Meteoritic Impacts in Brazil: Evolution and Current Knowledge. Derbyana, 45, e818. DOI:10.14295/derb.v45.818.

Cunha, B. C. C.; Potiguar, L. A. T.; Ianhez, A. C.; Bezerra, P. E. L.; Pithan, J. H. L.; Souza Júnior, J. J.; Montalvão, R. M. G.; Souza, A. M. S.; Hildred, P. R.; Tassinari, C. C. G.1981. Geologia. In: Projeto RADAMBRASIL. Folha SC. 22 - Tocantins: geologia, geomorfologia, pedologia, vegetação e uso potencial da terra. Rio de Janeiro, RJ, Brazil. p. 110-114. (Levantamento de Recursos Naturais, 22). https://biblioteca.ibge.gov.br/index.php/biblioteca-catalogo?view=detalhes&id=219603

Cruz, S. C. P., Leal, A. B. D. M., Damasceno, G. C., & Palmeira, D. D. S. (2009). Carta geológica: folha Amargosa-SD. 24-VD-II. Salvador, BA, Brazil. https://rigeo.sgb.gov.br/handle/doc/18290

Daly, M. C., Andrade, V., Barousse, C. A., Costa, R., McDowell, K., Piggott, N., & Poole, A. J. (2014). Brasiliano crustal structure and the tectonic setting of the Parnaíba basin of NE Brazil: results of a deep seismic reflection profile. Tectonics, 33(11), 2102-2120. https://doi.org/10.1002/2014TC003632

Dentith, M., & Mudge, S. T. (2014). Geophysics for the mineral exploration geoscientist. Cambridge University Press. https://doi.org/10.1017/CBO9781139024358

Deutsch, A., Poelchau, M. H., & Kenkmann, T. (2015). Impact metamorphism in terrestrial and experimental cratering events. In. Lee, M.R., Leroux, H. (eds). Planetary Mineralogy. Mineralogical Society of Great Britain and Ireland. https://doi.org/10.1180/emu-notes.15.4

Dickson, B. L., & Scott, K. M. (1997). Interpretation of aerial gamma-ray surveys-adding the geochemical factors. AGSO Journal of Australian Geology and Geophysics, 17. https://ecat.ga.gov.au/geonetwork/srv/api/records/fae9173a-71bb-71e4-e044-00144fdd4fa6

Dieperink, D., Alsemgeest, J., van Ruitenbeek, F., & Brouwer, F. M. (2024, March 11 – 15). SWIR Data from Brazilian Impact Structures for Understanding Impact-Generated Hydrothermal Systems on Mars. In 55th Lunar and Planetary Science Conference (Vol. 3040, p. 1247). The Woodlands, TX, US. https://ui.adsabs.harvard.edu/abs/2024LPICo3040.1247D/abstract

Dietz, R. S. (1960). Meteorite Impact Suggested by Shatter Cones in Rock: Three cryptoexplosion structures yield new evidence of natural hypervelocity shocks. Science, 131(3416), 1781–1784. https://doi.org/10.1126/science.131.3416.1781

Dietz, R. S., & French, B. (1973). Araguainha Dome and Serra da Cangalha, Brazil: probable astroblemes. Meteoritics, Vol. 8, p. 345-347, 8, 345-347. https://ui.adsabs.harvard.edu/abs/1973Metic...8..345D/abstract

Duda, K., Daucsavage, J., Siemonsma, D., Brooks, B., Oleson, R., Meyer, D., & Doescher, C. (2015). Advanced spaceborne thermal emission and reflection radiometer (aster) level 1 precision terrain corrected registered at-sensor radiance product (ast_l1t). US Geological Survey, USA. https://lpdaac.usgs.gov/documents/1401/ASTER_L1T_Product_Specification_v1.pdf

Dunster, J. N., Haines, P. W., & Munson, T. J. (2014). Meteorites and impact structures in the Northern Territory. Northern Territory Geological Survey, Darwin, AU. https://geoscience.nt.gov.au/gemis/ntgsjspui/handle/1/82468

Elbra, T., Kontny, A., & Pesonen, L. J. (2009). Rock-magnetic properties of the ICDP-USGS Eyreville core, Chesapeake Bay impact structure, Virginia, USA. In. Gohn, G.S., Koeberl, C., Miller, K.G., Reimold, W.R. The ICDP-USGS Deep Drilling Project in the Chesapeake Bay impact structure: Results from the Eyreville Core Holes. Geological Society of America. https://doi.org/10.1130/2009.2458(06)

Emmanuel, H., Yu, J., Wang, L., Choi, S. H., & Rwatangabo, D. E. R. (2023). Object-Oriented Remote Sensing Approaches for the Detection of Terrestrial Impact Craters as a Reconnaissance Survey. Remote Sensing, 15(15), 3807. https://doi.org/10.3390/rs15153807

Engelhardt, W. V., Pohl, J., & Walzebuck, J. (1985). Araguainha Impact Structure, Mato Grosso, Brazil. Meteoritics, Vol. 20, p. 640, 20, 640. https://ui.adsabs.harvard.edu/abs/1985Metic..20Q.640E/abstract

Engelhardt, W. V., Matthäi, S. K., & Walzebuck, J. (1992). Araguainha impact crater, Brazil. I. The interior part of the uplift. Meteoritics, 27(4), 442–457. https://doi.org/10.1111/j.1945-5100.1992.tb00226.x

European Space Agency (ESA). 2025a. Sentinel-2 SentiWiki chapter. https://sentiwiki.copernicus.eu/web/sentinel-2 (accessed in Ago 21 ,2025)

European Space Agency (ESA). 2025b. Sentinel-1 SentiWiki chapter. https://sentiwiki.copernicus.eu/web/sentinel-1 (accessed in Ago 21 ,2025)

Fabrigar, L. R., Wegener, D. T., MacCallum, R. C., & Strahan, E. J. (1999). Evaluating the use of exploratory factor analysis in psychological research. Psychological methods, 4(3), 272. https://doi.org/10.1037/1082-989X.4.3.272

Fabrigar, L. R., & Wegener, D. T. (2012). Exploratory factor analysis. Oxford University Press. Oxford, UK. https://doi.org/10.1093/acprof:osobl/9780199734177.003.0002

Ferreira, J. C., Leite, E. P., Vasconcelos, M. A. R., & Crósta, A. P. (2015). 3D GRAVITY MODELING OF IMPACT STRUCTURES IN BASALTIC FORMATIONS IN BRAZIL: PART I – VARGEÃO, SANTA CATARINA. Revista Brasileira de Geofísica, 33(2). https://doi.org/10.22564/rbgf.v33i2.723

Ferreira, J. C., Leite, E. P., Vasconcelos, M. A. R., & Crósta, A. P. (2019a). 3D GRAVITY MODELING OF IMPACT STRUCTURES IN BASALTIC FORMATIONS IN BRAZIL: PART II - VISTA ALEGRE, PARANÁ. Brazilian Journal of Geophysics, 37(1), 69. https://doi.org/10.22564/rbgf.v37i1.980

Ferreira, E. F., Vasconcelos, M. A. R., Batista, J. C., Santos-Matos, A., Crósta, A. P., Sena, S., & Alves, A. O. (2019b, October 30 – November 3). Geoelectric Signatute of the Santa Marta Impact Structure, Brazil. Abstract of the Large Meteorite Impacts and Planetary Evolution VI Conference (No. LPI-Contrib-2136), Brasília, Brazil. https://ui.adsabs.harvard.edu/abs/2019LPICo2136.5031F/abstract

Fischer-Gödde, M., Tusch, J., Goderis, S., Bragagni, A., Mohr-Westheide, T., Messling, N., Elfers, B.-M., Schmitz, B., Reimold, W. U., Maier, W. D., Claeys, P., Koeberl, C., Tissot, F. L. H., Bizzarro, M., & Münker, C. (2024). Ruthenium isotopes show the Chicxulub impactor was a carbonaceous-type asteroid. Science, 385(6710), 752–756. https://doi.org/10.1126/science.adk4868

French, B. M. (1998). Traces of catastrophe: A handbook of shock-metamorphic effects in terrestrial meteorite impact structures (No. LPI-Contrib-954). Lunar and Planetary Institute, Houston, US, 120pp. https://ui.adsabs.harvard.edu/abs/1998trca.book.....F/abstract

Ford, K., Harris, J. R., Shives, R., Carson, J., & Buckle, J. (2008). Remote predictive mapping 2. Gamma-ray spectrometry: A tool for mapping Canada's North. Geoscience Canada, 35(3), 109-126. https://ostrnrcan-dostrncan.canada.ca/handle/1845/182004

Garcia, D. D., Leite, E. P., Vasconcelos, M. A. R., Christou, E., & Crósta, A. P. (2024). Distribution of gamma-ray elements in Cerro do Jarau impact structure and a proposal of geothermal modeling. Anais Da Academia Brasileira de Ciências, 96(1). https://doi.org/10.1590/0001-3765202420230005

Garvin, J. B., Schnetzler, C. C., & Grieve, R. A. F. (1992). Characteristics of large terrestrial impact structures as revealed by remote sensing studies. Tectonophysics, 216(1–2), 45–62. https://doi.org/10.1016/0040-1951(92)90155-y

Gebhardt, A. C., Niessen, F., & Kopsch, C. (2006). Central ring structure identified in one of the world's best-preserved impact craters. Geology, 34(3), 145. https://doi.org/10.1130/g22278.1

Giacomini, B. B., Leite, E. P., & Crósta, A. P. (2017). 3D gravimetric investigation of the Cerro do Jarau structure, Rio Grande do Sul, Brazil. Meteoritics & Planetary Science, 52(4), 565–583. https://doi.org/10.1111/maps.12813

Gilder, S. A., Pohl, J., & Eitel, M. (2018). Magnetic signatures of terrestrial meteorite impact craters: A summary. In Magnetic fields in the solar system: Planets, moons and solar wind interactions (pp. 357-382). Cham: Springer International Publishing. https://doi.org/10.1007/978-3-319-64292-5_13

Glass, B. P., & Simonson, B. M. (2012). Distal Impact Ejecta Layers: Spherules and More. Elements, 8(1), 43–48. https://doi.org/10.2113/gselements.8.1.43

Glikson, A., & Uysal, I. T. (2013). Geophysical and structural criteria for the identification of buried impact structures, with reference to Australia. Earth-Science Reviews, 125, 114-122. https://doi.org/10.1016/j.earscirev.2013.07.002

Glikson, A. (2018). Structure and origin of Australian ring and dome features with reference to the search for asteroid impact events. Tectonophysics, 722, 175–196. https://doi.org/10.1016/j.tecto.2017.11.003

Gottwald, M., Kenkmann, T., Reimold, W., Fritz, T., & Breit, H. (2021). The TanDEM-X Digital Elevation Model and Terrestrial Impact Structures. IEEE Journal of Selected Topics in Applied Earth Observations and Remote Sensing, 14, 4128–4138. https://doi.org/10.1109/jstars.2021.3069640

Grant, J. A. (1998). Ten things the textbooks don't tell you about processing and archiving airborne gamma-ray spectrometric data. Current research, 83-87.

Grauch, V. J. S., & Cordell, L. (1987). Limitations of determining density or magnetic boundaries from the horizontal gradient of gravity or pseudogravity data. Geophysics, 52(1), 118-121. https://doi.org/10.1190/1.1442236

Green, R. W., & Chetty, P. (1990). Seismic refraction studies in the basement of the Vredefort structure. Tectonophysics, 171(1–4), 105–113. https://doi.org/10.1016/0040-1951(90)90092-m

Grieve, R. A. (1987). Terrestrial impact structures. Annual Review of Earth and Planetary Sciences, vol. 15, 245-270. Book Chapter., 15. https://doi.org/10.1146/annurev.ea.15.050187.001333

Grieve, R. A., Wood, C. A., Garvin, J. B., McLaughlin, G., & McHone Jr, J. F. (1988). Astronaut's guide to terrestrial impact craters (No. LPI-TRN-88-03). NASA, Houston, TX, US. https://ntrs.nasa.gov/citations/19900014482

Grieve, R. A. F. (1990). Impact Cratering on the Earth. Scientific American, 262(4), 66–73. https://doi.org/10.1038/scientificamerican0490-66

Grieve, R. A. F., & Pesonen, L. J. (1992). The terrestrial impact cratering record. Tectonophysics, 216(1-2), 1-30. https://doi.org/10.1016/0040-1951(92)90152-V

Góes, A. M., & Feijó, F. J. (1994). Bacia do Parnaiba. Boletim de Geociências da PETROBRAS, 8. https://bgp.petrobras.com.br/bgp/article/view/581

Goetz, A. F., & Rowan, L. C. (1981). Geologic remote sensing. Science, 211(4484), 781-791. DOI: 10.1126/science.211.4484.781

Gulick, S. P. S., Christeson, G. L., Barton, P. J., Grieve, R. A. F., Morgan, J. V., & Urrutia-Fucugauchi, J. (2013). GEOPHYSICAL CHARACTERIZATION OF THE CHICXULUB IMPACT CRATER. Reviews of Geophysics, 51(1), 31–52. https://doi.org/10.1002/rog.20007

Haines, P. W., & Rawlings, D. J. (2002). The Foelsche structure, Northern Territory, Australia: An impact crater of probable Neoproterozoic age. Meteoritics & Planetary Science, 37(2), 269–280. https://doi.org/10.1111/j.1945-5100.2002.tb01109.x

Hauser, N., Reimold, W. U., Cavosie, A. J., Crósta, A. P., Schwarz, W. H., Trieloff, M., Da Silva Maia De Souza, C., Pereira, L. A., Rodrigues, E. N., & Brown, M. (2019). Linking shock textures revealed by BSE, CL, and EBSD with U-Pb data (LA-ICP-MS and SIMS) from zircon from the Araguainha impact structure, Brazil. Meteoritics & Planetary Science, 54(10), 2286–2311. https://doi.org/10.1111/maps.13371

Hawke, P. J. (2003, August 5 – 7). SOME RING-LIKE MAGNETIC ANOMALIES IN IMPACT STRUCTURES AND THEIR POSSIBLE. Abstract of the Large Meteorite Impacts Conference, Nördlingen, Germany ((No. LPI-Contrib-4064). https://ui.adsabs.harvard.edu/abs/2003lmim.conf.4064H/abstract

Hawke, P. J., Buckingham, A. J., & Dentith, M. C. (2006). Modelling Source Depth and Possible Origin of Magnetic Anomalies Associated with the Yallalie Impact Structure, Perth Basin, Western Australia. Exploration Geophysics, 37(2), 191–196. https://doi.org/10.1071/eg06191

Henkel, H., & Guzmán, M. (1977). Magnetic features of fracture zones. Geoexploration, 15(3), 173-181. https://doi.org/10.1016/0016-7142(77)90024-2

Henkel, H. (1992). Geophysical aspects of meteorite impact craters in eroded shield environment, with special emphasis on electric resistivity. Tectonophysics, 216(1-2), 63-89. https://doi.org/10.1016/0040-1951(92)90156-Z

Henkel, H. (1997). The magnetism of impact structures. Meteoritics & Planetary Science, 32(2), 154–154. https://doi.org/10.1111/j.1945-5100.1997.tb01255.x

Henkel, H., & Reimold, W. U. (1998). Integrated geophysical modelling of a giant, complex impact structure: anatomy of the Vredefort Structure, South Africa. Tectonophysics, 287(1-4), 1-20. https://doi.org/10.1016/S0040-1951(98)80058-9

Henkel, H., & Pesonen, L. J. (1992). Impact craters and craterform structures in Fennoscandia. Tectonophysics, 216(1–2), 31–40. https://doi.org/10.1016/0040-1951(92)90153-w

Henkel, H., & Reimold, W. U. (2002). Magnetic model of the central uplift of the Vredefort impact structure, South Africa. Journal of Applied Geophysics, 51(1), 43–62. https://doi.org/10.1016/s0926-9851(02)00214-8

Henkel, H., & Aaro, S. (2005). Geophysical investigations of the Siljan impact structure—a short review. Impact tectonics, 247-283. https://doi.org/10.1007/3-540-27548-7_9

Henkel, H., Hietala, S., Plado, J., & Ekneligoda, T. C. (2022). The 20 km diameter Dellen impact structure, central Sweden. Report Research Gate ISBN, 978-91.

Hergarten, S., & Kenkmann, T. (2015). The number of impact craters on Earth: Any room for further discoveries?. Earth and Planetary Science Letters, 425, 187-192. https://doi.org/10.1016/j.epsl.2015.06.009

Hietala, S., Kreitsmann, T., Plado, J., Nenonen, J., Lerssi, J., & Pesonen, L. J. (2020,August 10 – 12). Summanen Impact Structure — New Geological and Preliminary Geophysical Studies. Abstract of the 11th Planetary Crater Consortium Meeting (LPI Contr-2251), Boulde, CO/ held virtually. https://ui.adsabs.harvard.edu/abs/2020LPICo2251.2048H/abstract

Hietala, S., Jokinen, J., Lerssi, J., Niskanen, M., Pesonen, L. J., & Plado, J. (2023). Summanen structure: Further geological and geophysical evidence of a meteorite impact event in Central Finland. Meteoritics & Planetary Science, 58(7). 1002–1017. https://doi.org/10.1111/maps.14033

Hietala, S., Moilanen, J., & Plado, J. (2022). Keurusselkä impact structure, Finland—Overview, new observations, and renewed interpretation of the size. Meteoritics & Planetary Science, 57(11), 2063–2080. https://doi.org/10.1111/maps.13920

Hippertt, J. P., Lana, C., Weinberg, R. F., Tohver, E., Schmieder, M., Scholz, R., Gonçalves, L., & Hippertt, J. F. (2014). Liquefaction of sedimentary rocks during impact crater development. Earth and Planetary Science Letters, 408, 285–295. https://doi.org/10.1016/j.epsl.2014.09.045

Horn, B. L. D.; Oliveira, A. A.; Simões, M. S.; Besser, M. L.; Araújo, L. L. 2022. Projeto Geologia e Potencial Mineral da Bacia do Paraná. Mapa Geológico. Serviço Geológico do Brasil, Porto Alegre, RS. Available in: https://rigeo.sgb.gov.br/handle/doc/23037

Hunt, G. R. (1977). Spectral signatures of particulate minerals in the visible and near infrared. Geophysics, 42(3), 501-513. https://doi.org/10.1190/1.1440721

Hunt, G. R. (1979). Near-infrared (1.3-2.4 mu m) spectra of alteration minerals; potential for use in remote sensing. Geophysics, 44(12), 1974-1986. https://doi.org/10.1190/1.1440951

Isles, D. J., & Rankin, L. R. (2013). Geological interpretation of aeromagnetic data. Society of Exploration Geophysicists and Australian Society of Exploration Geophysicists, 365p. https://library.seg.org/doi/book/10.1190/1.9781560803218

Innes, M. J. S. (1961). The use of gravity methods to study the underground structure and impact energy of meteorite craters. Journal of Geophysical Research, 66(7), 2225–2239. https://doi.org/10.1029/jz066i007p02225

Iwanuch, W. (1981). Geologia da região do o do domo do Sucunduri (Doctoral dissertation, University of São Paulo). https://repositorio.usp.br/item/000712075

Iza, E. R. H. D. F., Santos, R. S. V. D., & Cruz Filho, B. E. D. (2020). Integration of multisource data to support the identification of lateritic regolith in Eastern-Bahia, northeastern Brazil. Journal of the Geological Survey of Brazil 3 (1):1-24. https://doi.org/10.29396/jgsb.2020.v3.n1.1

Jessell, M.W. (2002). The Atlas of Structural Geophysics II. Journal of the Virtual Explorer. Vol. 5. http://virtualexplorer.com.au.

Jiang, Y., Chen, H., Fegley Jr, B., Lodders, K., Hsu, W., Jacobsen, S. B., & Wang, K. (2019). Implications of K, Cu and Zn isotopes for the formation of tektites. Geochimica et Cosmochimica Acta, 259, 170-187.

Johnson, J. R., & Hörz, F. (2003). Visible/near-infrared spectra of experimentally shocked plagioclase feldspars. Journal of Geophysical Research: Planets, 108(E11). https://doi.org/10.1029/2003je002127

Johnson, J. R., Hörz, F., & Staid, M. I. (2003). Thermal infrared spectroscopy and modeling of experimentally shocked plagioclase feldspars. American Mineralogist, 88(10), 1575–1582. https://doi.org/10.2138/am-2003-1020

Johnson, J. R., Staid, M. I., & Kraft, M. D. (2007). Thermal infrared spectroscopy and modeling of experimentally shocked basalts. American Mineralogist, 92(7), 1148–1157. https://doi.org/10.2138/am.2007.2356

Jolliffe, I. T., & Cadima, J. (2016). Principal component analysis: a review and recent developments. Philosophical Transactions of the Royal Society A: Mathematical, Physical and Engineering Sciences, 374(2065), 20150202. https://doi.org/10.1098/rsta.2015.0202

Juhlin, C., & Pedersen, L. B. (1987). Reflection seismic investigations of the Siljan impact structure, Sweden. Journal of Geophysical Research: Solid Earth, 92(B13), 14113-14122. https://doi.org/10.1029/JB092iB13p14113

Kalinowski, A., & Oliver, S. (2004). ASTER mineral index processing manual. Remote Sensing Applications, Geoscience Australia, 37(36), 36-37. https://ecat.ga.gov.au/geonetwork/srv/api/records/a05f7892-da28-7506-e044-00144fdd4fa6

Kearey, P., Brooks, M. and Hill, I. (2002) An Introduction to Geophysical Exploration. Blackwell Science Ltd., Oxford.

Keating, P., & Sailhac, P. (2004). Use of the analytic signal to identify magnetic anomalies due to kimberlite pipes. Geophysics, 69(1), 180-190. https://doi.org/10.1190/1.1649386

Kazzuo-Vieira, C., Crósta, A. P., Gamboa, F., & Tygel, M. (2009). Caracterização geofísica da estrutura de impacto do domo de Vargeão, Brasil. Revista Brasileira de Geofísica, 27(3), 375–388. https://doi.org/10.1590/s0102-261x2009000300006

Kenkmann, T. (2002). Folding within seconds. Geology, 30(3), 231. https://doi.org/10.1130/0091-7613(2002)030<0231:fws>2.0.co;2

Kenkmann, T., & Poelchau, M. H. (2008, March 10 - 14). Matt Wilson: an elliptical impact crater in Northern Territory, Australia. Abstract of 39th Annual Lunar and Planetary Science Conference, League City, TX, US. (No. 1391, p. 1027). https://ui.adsabs.harvard.edu/abs/2008LPI....39.1027K/abstract

Kenkmann, T., Poelchau, M. H., & Wulf, G. (2014). Structural geology of impact craters. Journal of Structural Geology, 62, 156–182. https://doi.org/10.1016/j.jsg.2014.01.015

Kenkmann, T., Afifi, A. M., Stewart, S. A., Poelchau, M. H., Cook, D. J., & Neville, A. S. (2015). Saqqar: A 34 km diameter impact structure in Saudi Arabia. Meteoritics & Planetary Science, 50(11), 1925-1940. https://doi.org/10.1111/maps.12555

Kenkmann, T., Vasconcelos, M. A. R., Crósta, A. P., & Reimold, W. U. (2011). The complex impact structure Serra da Cangalha, Tocantins State, Brazil. Meteoritics & Planetary Science, 46(6), 875–889. https://doi.org/10.1111/j.1945-5100.2011.01199.x

Kenkmann, T. (2021). The terrestrial impact crater record: A statistical analysis of morphologies, structures, ages, lithologies, and more. Meteoritics & Planetary Science, 56(5), 1024-1070. https://doi.org/10.1111/maps.13657

Killeen, P. G., Mwenifumbo, C. J., & Ford, K. L. (2015). Tools and techniques: radiometric methods. Treatise on geophysics, 447-524. DOI: 10.1016/B978-0-444-53802-4.00209-8

Klein E.L., Sousa C.S. (2012). Geologia e recursos minerais do Estado do Maranhão: Sistema de Informações Geográficas – SIG: texto explicativo dos mapas geológico e de recursos minerais do Estado do Maranhão. Escala 1:750. 000. Belém, Serviço Geológico do Brasil – CPRM. ttp://rigeo.cprm.gov.br/xmlui/handle/doc/17861?show=full

Koeberl, C. (2004). Remote sensing studies of impact craters: How to be sure? Comptes Rendus. Géoscience, 336(11), 959–961. https://doi.org/10.1016/j.crte.2004.05.001

Koeberl, C., Reimold, W.U., Plescia, J., 2005. BP and Oasis impact structures, Libya: remote sensing and field studies. In: Koeberl, C., Henkel, H. (Eds.), Impact Tectonics, Impact Studies Series 8. Springer-Verlag, Berlin, Heidelberg, pp. 161–190. https://doi.org/10.1007/3-540-27548-7_6

Koeberl, C., Claeys, P., Hecht, L., & McDonald, I. (2012). Geochemistry of Impactites. Elements, 8(1), 37–42. https://doi.org/10.2113/gselements.8.1.37

Koeberl, C. (2014). The geochemistry and cosmochemistry of impacts. In H. D. Holland & K. K. Turekian (Eds.), Treatise on geochemistry (2nd ed., Vol. 2, pp. 73–118). Planets, Asteroids, Comets and the Solar System. Elsevier. https://doi.org/10.1016/B978-0-08-095975-7.00130-3

Kollert, R., Bjornberg, A., & Davino, A. (1961). Estudos preliminares de uma depressão circular na região de Colônia: Sto. Amaro, São Paulo. Boletim da Sociedade Brasileira de Geologia, 10, 57-77.

Korenaga, J., & Marchi, S. (2023). Vestiges of impact-driven three-phase mixing in the chemistry and structure of Earth's mantle. *Proceedings of the National Academy of Sciences*, *120*(43), e2309181120. https://doi.org/10.1073/pnas.2309181120

Kuzmicheva, M. Yu., & Ivanov, B. A. (2021). Modeling the Magnetic Anomaly of the Bosumtwi (Ghana) Complex Meteorite Crater by Taking Into Account the Impact Demagnetization and Morphological Features. Izvestiya, Physics of the Solid Earth, 57(5), 795–804. https://doi.org/10.1134/s1069351321050128

Lacerda Filho, J. V. D., Abreu-Filho, W., Valente, C. R., Oliveira, C. C. D., & Albuquerque, M. C. D. (2004). Geologia e recursos minerais do Estado de Mato Grosso. CPRM; Secretaria de Estado de Indústria, Comércio, Minas e Energia do Estado de Mato Grosso (SICME-MT), Cuiabá, Mato Grosso, Brazil. 252p. https://rigeo.sgb.gov.br/handle/doc/4871

Lana, C., Romano, R., Reimold, U., & Hippertt, J. (2006). Collapse of large complex impact craters: Implications from the Araguainha impact structure, central Brazil. Geology, 34(1), 9. https://doi.org/10.1130/g21952.1

Lana, C., Filho, C. R. S., Marangoni, Y. R., Yokoyama, E., Trindade, R. I. F., Tohver, E., & Reimold, W. U. (2007). Insights into the morphology, geometry, and post-impact erosion of the Araguainha peak-ring structure, central Brazil. Geological Society of America Bulletin, 119(9–10), 1135–1150. https://doi.org/10.1130/b26142.1

Lana, C., Filho, C. R. S., Marangoni, Y. R., Yokoyama, E., Trindade, R. I. F., Tohver, E., & Reimold, W. U. (2008). Structural evolution of the 40 km wide Araguainha impact structure, central Brazil. Meteoritics & Planetary Science, 43(4), 701–716. https://doi.org/10.1111/j.1945-5100.2008.tb00679.x

Langenhorst, F. (2002). Shock metamorphism of some minerals: Basic introduction and microstructural observations. Bulletin of the Czech Geological Survey, 77(4), 265-282. http://www.geology.cz/bulletin/contents/art2002.04.265

Langenhorst, F., & Deutsch, A. (2012). Shock Metamorphism of Minerals. Elements, 8(1), 31–36. https://doi.org/10.2113/gselements.8.1.31

Le Ber, E., Loggia, D., Denchik, N., Lofi, J., Kring, D. A., Sardini, P., Siitari-Kauppi, M., Pezard, P., Olivier, G., & IODP-ICDP Expedition 364 Science Party. (2022). Petrophysics of Chicxulub

Impact Crater's Peak Ring. Journal of Geophysical Research: Solid Earth, 127(5). https://doi.org/10.1029/2021jb023801

Laurencelle, J., Logan, T., & Gens, R. (2015). ASF radiometrically terrain corrected ALOS PALSAR products (Product Guide, Revision, 1). https://asf.alaska.edu/wp-content/uploads/2019/03/rtc_product_guide_v1.2.pdf

Leite, E. P., Lambert, J., Vasconcelos, M. A. R., Crósta, A. P., & Batezelli, A. (2022). Gamma-ray spectrometry of the Araguainha impact structure, Brazil: Additional insights into element mobilization due to hydrothermal alteration. Anais Da Academia Brasileira de Ciências, 94(3). https://doi.org/10.1590/0001-3765202220210182

Li, X. (2006). Understanding 3D analytic signal amplitude. Geophysics, 71(2), L13-L16. https://doi.org/10.1190/1.2184367

Li, X. (2003). On the use of different methods for estimating magnetic depth. The Leading Edge, 22(11), 1090-1099. https://doi.org/10.1190/1.1634912

Li, Y., & Nabighian, M. (2015). Tools and techniques: magnetic methods of exploration–principles and algorithms. In. Schubert G. Treatise on Geophysics (2nd ed), Elsevier, https://doi.org/10.1016/B978-0-444-53802-4.00196-2

Lima, M. I. C., Monteiro, N., Silva, L. D., & Marinho, D. (1990, June 24 – 29). Identificação de morfoestruturas anômalas na porção centro-oriental da bacia do Maranhão (Brasil), através de imagens SLAR e Landsat-TM. VI Simpósio Brasileiro de Sensoriamento Remoto, 6, 663-670.

Lima, R. P., & Marfurt, K. J. (2018). Principal component analysis and K-means analysis of airborne gamma-ray spectrometry surveys. In SEG Technical Program Expanded Abstracts 2018 (pp. 2277-2281). Society of Exploration Geophysicists. https://doi.org/10.1190/segam2018-2996506.1

Lowrie, W. 2007. Fundamentals of Geophysics (2nd), Cambridge University Press, New York, US, 381pp. https://doi.org/10.1017/CBO9780511807107

Luchetti, A. C. F., Nardy, A. J., & Madeira, J. (2018). Silicic, high-to extremely high-grade ignimbrites and associated deposits from the Paraná Magmatic Province, southern Brazil. Journal of Volcanology and Geothermal Research, 355, 270-286. https://doi.org/10.1016/j.jvolgeores.2017.11.010

Martini PR, Liu CC (1997) Acahay and Inajah: two possible Astroblemes in South America. Memories of VIII Latin America remote sensing symposium. Merida, Venezuela, Nov 1997.

Masero, W. C. B., & Fontes, S. L. (1991, October). Audiomagnetotelluric Investigation of the Colonia Depression, São Paulo-Brazil. In 2nd International Congress of the Brazilian Geophysical Society (pp. cp-316). European Association of Geoscientists & Engineers.

Masero, W., Schnegg, P. A., & Fontes, S. L. (1994). A magnetotelluric investigation of the Araguainha impact structure in Mato Grosso-Goiás, central Brazil. Geophysical Journal International, 116(2), 366-376. https://doi.org/10.1111/j.1365-246X.1994.tb01803.x

Masero, W., Fischer, G., & Schnegg, P. A. (1997). Electrical conductivity and crustal deformation from magnetotelluric results in the region of the Araguainha impact, Brazil. Physics of the Earth and Planetary Interiors, 101(3-4), 271-289. https://doi.org/10.1016/S0031-9201(96)03267-0

MaCdonald, F. A., Wingate, M. T. D., & Mitchell, K. (2005). Geology and age of the Glikson impact structure, Western Australia. Australian Journal of Earth Sciences, 52(4–5), 641–651. https://doi.org/10.1080/08120090500170419

Mantovani, M. S., & de Brito Neves, B. B. (2009). The Paranapanema lithospheric block: its nature and role in the accretion of Gondwana. Developments in Precambrian Geology, 16, 257-272. https://doi.org/10.1016/S0166-2635(09)01619-3

Marangoni, Y. R., Santon, D. S., Vasconcelos, M. A., Molina, E. C., Vieira, C. D., de Sá, N. C., Trandade, R.F.I., Lana, C., & Filho, C. R. S. (2007, November, 19 - 23). Gravity at Araguainha Impact Structure: Preliminary Results. In 10th International Congress of the Brazilian Geophysical Society & EXPOGEF 2007, Rio de Janeiro, Brazil, pp. 1852-1857. Society of Exploration Geophysicists and Brazilian Geophysical Society. https://doi.org/10.1190/sbgf2007-360

Martins, J. A. (2016). Estudo geológico, geofísico e morfológico da estrutura circular de São Miguel do Tapuio, Piauí - Brasil. [Doctoral dissertation, Federal University of Ceara]. http://repositorio.ufc.br/handle/riufc/59993

Martins, J. A., Branco, M. C., De Castro, N. A., Peulvast, J.-P., & Lima Junior, S. B. (2016a). ANÁLISE MORFOLÓGICA DA ESTRUTURA CIRCULAR DE SÃO MIGUEL DO TAPUIO, PIAUÍ - BRASIL. Revista Brasileira de Geomorfologia, 17(4). https://doi.org/10.20502/rbg.v17i4.703

Martins, J. A., de CASTRO, N. A., Gomes, R. M., & Branco, C. (2016b). A MORFOLOGIA SUPERFICIAL DA ESTRUTURA CIRCULAR DE SÃO MIGUEL DO TAPUIO (PIAUÍ-BR) E CASOS SIMILARES NO TERRITÓRIO BRASILEIRO. Geociências, 35(2), 183 – 202. https://www.periodicos.rc.biblioteca.unesp.br/index.php/geociencias/article/view/11375

Mariano, R., Branco, G. C., de Castro, D. L., & Cunha, L. S. (2004, August, 2 - 6). Geological, geophysical, and imaging data of São Miguel do Tapuio (SMT) astrobleme, Brazil. Abstract of the 67th Annual Meteoritical Society Meeting (No Contr. 5229), Rio de Janeiro, RJ, Brazil. https://www.lpi.usra.edu/meetings/metsoc2004/pdf/5229.pdf

Matton, G., Jébrak, M., & Lee, J. K. (2005). Resolving the Richat enigma: doming and hydrothermal karstification above an alkaline complex. Geology, 33(8), 665-668. https://doi.org/10.1130/G21542AR.1

Maziviero, M. V., Vasconcelos, M. A. R., Góes, A. M., Crósta, A. P., & Reimold, W. U. (2012, March 19 - 23). The Riachão Ring impact structure, Northeastern Brazil: re-evaluation of its stratigraphy and evidence for impact. Abstract of the 43rd Annual Lunar and Planetary Science Conference (No. 1659, p. 1511), The Woodlands, TX, US. https://www.lpi.usra.edu/meetings/lpsc2012/pdf/1511.pdf

Maziviero, M. V., Vasconcelos, M. A. R., Crósta, A. P., Góes, A. M., Reimold, W. U., & De C. Carneiro, C. (2013). Geology and impact features of Riachão structure, northern Brazil. Meteoritics & Planetary Science, 48(10), 2044–2058. https://doi.org/10.1111/maps.12213

Mazur, M. J., Hildebrand, A. R., Hladiuk, D., Schafer, A., & Pilkington, M. (2002, March 11 - 15). The Steen River crater seismic refraction project. Abstract of the XXXIII Lunar and Planetary Science Conference, (No Cront. p. 1736), Houston, TX, US. https://ui.adsabs.harvard.edu/abs/2002LPI....33.1736M/abstract

McCall, G. J. H. (2009). Half a century of progress in research on terrestrial impact structures: A review. Earth-Science Reviews, 92(3–4), 99–116. https://doi.org/10.1016/j.earscirev.2008.11.004

McCall, N., Gulick, S. P. S., Karro, K., Jõeleht, A., Wilk, J., & Pösges, G. (2024). Understanding the Ries impact structure subsurface from high-resolution seismic data. Geology, 52(1), 39–44. https://doi.org/10.1130/g51503.1

McHone, J. F. (1979). Riachão Ring, Brazil: A possible meteorite crater discovered by the Apollo astronauts. In. Farouk El-Baz, D M Warner (ed.). Apollo-Soyuz Test Project Summary Science Report — NASA Special Publication 412 2, p. 193-202, National Aeronautics and Space Administration (NASA), Washington, DC, US.

McHone Jr, J. F. (1981, Octuber 19 - 22). Verified impact structures in Brazil. Abstract of the Large Body Impacts and Terrestrial Evolution: Geological, Climatological, and Biological Implications (No. Contr. 449, p. 31), Snowbird, Utan, US. https://ui.adsabs.harvard.edu/abs/1981LPICo.449...31M/abstract

McHone, J. F., Greeley, R., & Blumberg, D. (1996, March 18 - 22). SIR-C/X-SAR radar studies; impact and aeolian features, Borkou region northern Chad. Abstract of the Lunar and Planetary Science XXVII, 27, p. 849, Houston, TX, US. https://ui.adsabs.harvard.edu/abs/1996LPI....27..849M/abstract

McHone, J. F., Greeley, R., Williams, K. K., Blumberg, D. G., & Kuzmin, R. O. (2002). Space shuttle observations of terrestrial impact structures using SIR-C and X-SAR radars. Meteoritics & Planetary Science, 37(3), 407-420. https://doi.org/10.1111/j.1945-5100.2002.tb00824.x

Megumi, K., & Mamuro, T. (1977). Concentration of uranium series nuclides in soil particles in relation to their size. Journal of geophysical research, 82(2), 353-356. https://doi.org/10.1029/JB082i002p00353

Melero-Asensio, I., Ormö, J., Sturkell, E., Stockmann, G., & Mansfeld, J. (2018). Geophysical signature of Målingen, the minor crater of the Lockne–Målingen doublet impact structure. Meteoritics & Planetary Science, 53(7), 1456–1475. https://doi.org/10.1111/maps.13090

Meloni, R.E.; Benevides Filho, P.R.R.; Simões, M.S.; Lisboa, T.de M.; Ramos, M.N.; Oliveira, A.C.S.; Silva, A.R.da C.; Queiroz, L.C. 2021. Mapa Geológico: ARIM Sudeste do Amazonas. Escala 1:500.000 Programa de Gestão Estratégica da Geológia, Mineração e Transformação Mineral: Ação Áreas de Relevante Interesse Mineral (ARIM), SGB-CPRM, Manaus, Amazonas, Brazil. https://rigeo.sgb.gov.br/handle/doc/18952

Melosh, H. J. (1989) Impact Cratering: A Geologic Process. Oxford Monographs on Geology and Geophysicsm Series, n. 11. Oxford University Press, New York, NY. 245 pp.

Melosh, H. J., & Ivanov, B. A. (1999). IMPACT CRATER COLLAPSE. Annual Review of Earth and Planetary Sciences, 27(1), 385–415. https://doi.org/10.1146/annurev.earth.27.1.385

Meneses P.R. 2012: Sensor radar de abertura sintética, In: Meneses P.R., Almeida T., Introdução ao Processamento de Imagens de Sensoriameto Remoto. Universidade de Brasília, Brasília, pp. 57 – 76.

Meneses P.R. & Sano E.E 2012: Príncipios de sensoriamento remote, In: Meneses P.R., Almeida T., Introdução ao Processamento de Imagens de Sensoriameto Remoto. Universidade de Brasília, Brasília, pp. 1 – 31.

Mescher, P., Schultz, D. J. (1995, March 28 – 29) Gamma ray marker in Arbuckle dolomite, Wilburton Field, Oklahoma – A widespread event associated with the Ames Hole impact crater. Abstract of the Ames Structure and Similar Features - A Workshop, pp. 35. Norman, Oklahoma, US. http://ogs.ou.edu/docs/circulars/C100.pdf

Michel, P., Küppers, M., Bagatin, A. C., Carry, B., Charnoz, S., De Leon, Fitzsimmons, A., Gordo, P., Green, S.F., Hénrique, A., Juzi, M., Karatekin, Ö, Kohout, T., Lazzarin M., Naomi, M., Okada, T., Palomba, E., Praved, T., Snodgrass, C., Tortora, P., Tsiganis, K., Ulamec, S., Vicent, J-B., Wünnemann, K., Zhang, Y., Raducan, S.D., Dotto, E., Chabot, N., Cheng, A.F., Rivkin, A., Barnouin, O., Ernst, C., Stickle, A., Richardson, D.C., Thomas, C., Asphaug, E., Ballouz, R-L., Bottke Jr., W.F., J., Lauretta, D.S., Walsh, K.J., Martino, P., & Carnelli, I. (2022). The ESA Hera mission: detailed characterization of the DART impact outcome and of the binary asteroid (65803) Didymos. The Planetary Science Journal, 3(7), 160. https://doi.org/10.3847/PSJ/ac6f52

Milani, E. J., & Zalán, P. V. (1999). An outline of the geology and petroleum systems of the Paleozoic interior basins of South America. Episodes Journal of International Geoscience, 22(3), 199-205. https://doi.org/10.18814/epiiugs/1999/v22i3/007

Milani, E.J. & Thomaz-Filho, A. (2000). Sedimentary basins of South America. In: Cordani, U.G.; Milani, E.J.; Thomaz-Filho, A.; and Campos, D.A. (dds.), Tectonic evolution of South America. Rio de Janeiro, 31st International Geological Congress, Rio de Janeiro, RJ, Brazil. 389 – 449. https://rigeo.sgb.gov.br/handle/doc/19419

Milligan, P.R. and Gunn, P.J. (1997) Enhancement and Presentation of Airborne Geophysical Data. Journal of Australian Geology & Geophysics, 17, 63-75. https://dev.ecat.ga.gov.au/geonetwork/srv/api/records/fae9173a-71b2-71e4-e044-00144fdd4fa6

Milton, D. J., Barlow, B. C., Brown, A. R., Moss, F. J., Manwaring, E. A., Sedmik, E. C. E., Young, J.A., & Son, J. V. (1996). Gosses Bluff-a latest Jurassic impact structure, central Australia. Part 2: seismic, magnetic, and gravity studies. AGSO Journal of Australian Geology and Geophysics, 16(4), 487-528. https://ecat.ga.gov.au/geonetwork/srv/api/records/fae9173a-7190-71e4-e044-00144fdd4fa6

Miura, G. C. M., Santos, R. P. Z., & Marangoni, Y. R. (2015, August 3 - 6). Investigação geofísica da cratera de Colônia. Abstract of the 14th International Congress of the Brazilian Geophysical Society & EXPOGEF, Rio de Janeiro, RJ, Brazil, 2015, 735–740. https://doi.org/10.1190/sbgf2015-144

Miyazaki, M. R., Leite, E. P., Vasconcelos, M. A. R., Wünnemann, K., & Crósta, A. P. (2021). Bouguer anomaly inversion and hydrocode modeling of the central uplift of the Araguainha impact structure. Anais Da Academia Brasileira de Ciências, 93(suppl 4). https://doi.org/10.1590/0001-3765202120210081

Moon, W. M., & Jiao, L. X. (1998). Sudbury meteorite-impact structure modeling with LITHOPROBE high-resolution seismic refraction results. Geosciences Journal, 2(1), 26–36. https://doi.org/10.1007/bf02910201

Moreira, M. L. O., Moreton, L. C., Araújo, V. A. D., Lacerda Filho, J. V. D., & Costa, H. F. D. (2008). Geologia do Estado de Goiás e Distrito Federal. CPRM - SIC-FUNMINERAL, Goiânia, GO, Brazil. https://rigeo.sgb.gov.br/handle/doc/10512

Morgan, J. V., Warner, M. R., Collins, G. S., Melosh, H. J., & Christeson, G. L. (2000). Peak-ring formation in large impact craters: Geophysical constraints from Chicxulub. Earth and Planetary Science Letters, 183(3–4), 347–354. https://doi.org/10.1016/s0012-821x(00)00307-1

Morgan, J., Rebolledo-Vieyra, M., Osinski, G. R., & Pierazzo, E. (2013). Geophysical studies of impact craters. In: Osinski, G. R., & Pierazzo, E. Impact cratering: Processes and products, 211-222. https://doi.org/10.1002/9781118447307.ch14

Motta, U. S., & Flexor, J. M. (1991, October 27 – November 01). Estudo Gravimétrico da Depressão Circular de Colônia, São Paulo, Brasil. Abstract of the 2nd International Congress of the Brazilian Geophysical Society, (pp. cp-316), Salvador, BA, Brazil. https://doi.org/10.3997/2214-4609-pdb.316.28.

Moynier, F., Beck, P., Jourdan, F., Yin, Q. Z., Reimold, U., & Koeberl, C. (2009). Isotopic fractionation of zinc in tektites. Earth and Planetary Science Letters, 277(3-4), 482-489. https://doi.org/10.1016/j.epsl.2008.11.020

Moynier, F., Koeberl, C., Beck, P., Jourdan, F., & Telouk, P. (2010). Isotopic fractionation of Cu in tektites. Geochimica et Cosmochimica Acta, 74(2), 799-807.

Naumov, M. V. (2005). Principal features of impact-generated hydrothermal circulation systems: Mineralogical and geochemical evidence. Geofluids, 5(3), 165-184. https://doi.org/10.1111/j.1468-8123.2005.00092.x

Nédélec, A., Paquette, J., Yokoyama, E., Trindade, R. I. F., Aigouy, T., & Baratoux, D. (2013). In situ U/Pb dating of impact-produced zircons from the Vargeão Dome (Southern Brazil). Meteoritics & Planetary Science, 48(3), 420–431. https://doi.org/10.1111/maps.12066

Nel, D. T., & Haarhoff, J. (2011). The failure probability of welded steel pipelines in dolomitic areas. Journal of the South African Institution of Civil Engineering= Joernaal van die Suid-Afrikaanse Instituut van Siviele Ingenieurswese, 53(1), 9-21.

Neves, F. A. (1998). Estudo da depressão circular de Colônia-SP pelo método sísmico. Brazilian Journal of Geology, 28(1), 03-10. https://repositorio.usp.br/item/001016961

Niang, C. A. B., Baratoux, D., Diallo, D. P., Rochette, P., Jessell, M. W., Reimold, W. U., Bouley, S., Vanderhaeghe, O., Faya, G., & Lambert, P. (2021). Systematic survey of K, Th, and U signatures in airborne radiometric data from Australian meteorite impact structures: Possible causes of circular features and implications. In. Reimold, W.R., Koeberl, C. (eds). Large Meteorite Impacts and Planetary Evolution VI, Geological Society of America, 373 – 405. https://doi.org/10.1130/2021.2550(15)

Niang, C. A. B., Baratoux, D., Rochette, P., Braucher, R., Reimold, W. U., Lambert, P., Diallo, D. P., Regard, V., Carretier, S., Jessell, M. W., Faye, G., & Koeberl, C. (2022). The origin of the potassium-rich annular zones at the Bosumtwi impact structure, Ghana, investigated by field study, radiometric analysis, and first cosmogenic nuclide data. Meteoritics & Planetary Science, 57(3), 702–729. https://doi.org/10.1111/maps.13788

Niang, C. A. B., Baratoux, D., Rochette, P., Quesnel, Y., & Reimold, W. U. (2025). The impact record of West Africa: Confirmed impact structures and potential impact sites. Journal of African Earth Sciences, 228, 105627. https://doi.org/10.1016/j.jafrearsci.2025.105627

Ninomiya, Y., & Fu, B. (2019). Thermal infrared multispectral remote sensing of lithology and mineralogy based on spectral properties of materials. Ore Geology Reviews, 108, 54-72. https://doi.org/10.1016/j.oregeorev.2018.03.012

Nicholson, U., Bray, V. J., Gulick, S. P. S., & Aduomahor, B. (2022). The Nadir Crater offshore West Africa: A candidate Cretaceous-Paleogene impact structure. Science Advances, 8(33). https://doi.org/10.1126/sciadv.abn3096

National Oceanic and Atmospheric Administration (NOAA). 2025. Magnetic field calculator. https://www.ngdc.noaa.gov/geomag/calculators/magcalc.shtml (acessed in Ago 21, 2025)

Oliveira, G. (2015). Caracterização geológica da estrutura de impacto meteorítico de Santa Marta (PI) [MSc Dissertation, Universidade Estadual de Campinas]. https://doi.org/10.47749/t/unicamp.2015.956856

Oliveira, G. J. G., Vasconcelos, M. A. R., Crósta, A. P., Reimold, W. U., Góes, A. M., & Kowitz, A. (2014). Shatter cones and planar deformation features confirm Santa Marta in Piauí State, Brazil, as an impact structure. Meteoritics & Planetary Science, 49(10), 1915–1928. https://doi.org/10.1111/maps.12368

Oliveira, G. J. G. D., Chamani, M. A. C., Góes, A. M., Crósta, A. P., Vasconcelos, M. A. R., & Reimold, W. U. (2017). Geological investigation of the central portion of the Santa Marta impact structure, Piauí State, Brazil. Brazilian Journal of Geology, 47(4), 673–692. https://doi.org/10.1590/2317-4889201720160095

Oliveira, A. L., Pimentel, M. M., Fuck, R. A., & Oliveira, D. C. (2018). Petrology of Jurassic and Cretaceous basaltic formations from the Parnaíba Basin, NE Brazil: correlations and associations with large igneous provinces. In. M. C. Daly, R. A. Fuck, J. Julià, D.I.M. MacDonald, A. B. Watts (eds). Cratonic Basin Formation: A Case Study of the Parnaíba Basin of Brazil. Special Publications of Geological Society of London, 472, 279 – 308. https://doi.org/10.1144/SP472.21

Oliveira, J. R. D., Vasconcelos, M. A. R., Crósta, A. P., & Sena, F. (2019, September 30 – Octuber 3). Gravity Forward Modeling of the Santa Marta Impact Structure. Abstract of the Large Meteorite Impacts and Planetary Evolution VI (No Contr. 2136), Brasília, DF, Brazil. https://ui.adsabs.harvard.edu/abs/2019LPICo2136.5028O/abstract

Osinski, G. R., Grieve, R. A. F., Collins, G. S., Marion, C., & Sylvester, P. (2008). The effect of target lithology on the products of impact melting. Meteoritics & Planetary Science, 43(12), 1939–1954. https://doi.org/10.1111/j.1945-5100.2008.tb00654.x

Osinski, G.R., Pierazzo, E. (2012). Impact cratering: processes and products, In: Osinski, G.R., Pierazzo, E. Impact cratering: Process and Products, First. Edition, Blackwell Publishing Ltd. https://doi.org/10.1002/9781118447307.ch1

Osinski, G. R., Tornabene, L. L., Banerjee, N. R., Cockell, C. S., Flemming, R., Izawa, M. R., McCutcheon, J., Parnell, J., Preston, L., Pickersgill, A., Pontefract, A., Sapers, H.M., & Southam, G. (2013). Impact-generated hydrothermal systems on Earth and Mars. Icarus, 224(2), 347-363. https://doi.org/10.1016/j.icarus.2012.08.030

Osinski, G. R., Cockell, C. S., Pontefract, A., & Sapers, H. M. (2020). The role of meteorite impacts in the origin of life. Astrobiology, 20(9), 1121-1149. https://doi.org/10.1089/ast.2019.22

Osinski, G. R., Grieve, R. A. F., Ferrière, L., Losiak, A., Pickersgill, A. E., Cavosie, A. J., Hibbard, S. M., Hill, P. J. A., Bermudez, J. J., Marion, C. L., Newman, J. D., & Simpson, S. L. (2022). Impact Earth: A review of the terrestrial impact record. Earth-Science Reviews, 232, 104112. https://doi.org/10.1016/j.earscirev.2022.104112

Oufella, A., Quesnel, Y., & Godard, V. (2024, July 2 – August 2). MORPHOLOGICAL AND GEOPHYSICAL EVOLUTION OF IMPACT CRATERS. Abstract of the 86th Annual Meeting of the Meteoritical Society Meeting (Vol. 59, No. SP1, p. 6120). Brussels, Belgium. https://ui.adsabs.harvard.edu/abs/2024LPICo3036.6120A/abstract

Ould Mohamed Navee, E., Baratoux, D., Chennaoui Aoudjehane, H., Si Mhamdi, H., & Raji, M. (2024). Systematic search of circular structures using satellite imagery to identify potential new impact structures in Mauritania. Journal of African Earth Sciences, 216, 105303. https://doi.org/10.1016/j.jafrearsci.2024.105303

Palmeira, A, L. C. M.; Carvalho, J. M. A. 2018. Carta geológica da Folha Ariquemes S C.20-V-D (Escala 1:250.000). Programa Geologia do Brasil–PGB, Projeto Geologia e Recursos Minerais da Folha Ariquemes SC.20-V-D, Porto Velho, RO, Brazil. https://rigeo.sgb.gov.br/handle/doc/17243

Parfenova, O. V., & Iakovlev, O. I. (1977, September 13 - 17). Some peculiarities of selective evaporation in target rocks after meteoritic impact. Abstract of the Impact and Explosion Cratering: Planetary and Terrestrial Implications (pp. 843-859), Proceedings of the Symposium on Planetary Cratering Mechanics, Flagstaff, AZ, US. https://ui.adsabs.harvard.edu/abs/1977iecp.symp..843P/abstract

Passos, G. F., & Shukowsky, W. (1997, September 28 – Octuber 2). Inversão Gravimétrica 3D para Superfície entre Dois Meios Homogęneos, com Aplicação à Depressão Circular de Colônia (São Paulo/SP). Abstract of the 5th International Congress of the Brazilian Geophysical Society, São Paulo, SP, Brazil. (pp. cp-299).

Pereira, F. L., Crósta, A. P., Avona, P. D., Vasconcelos, M. A. R., & Goés, A. M. (2024). Magnetometric and seismic investigation of the Nova Colinas impact structure, Parnaíba Basin, Brazil. Journal of South American Earth Sciences, 149, 105215. https://doi.org/10.1016/j.jsames.2024.105215

Pesonen, L. J., Jarvela, J., Sarapaa, O., & Pietarinen, H. (1996). The Iso-Naakkima meteorite impact structure: physical properties and paleomagnetism of a drill core. Meteoritics & Planetary Science, vol. 31, page A105, 31. https://ui.adsabs.harvard.edu/abs/1996M%26PSA..31S.105P/abstract

Pesonen, L. J., Lehtinen, M., Deutsch, A., Elo, S., & Lukkarinen, H. (1996b, March 18 – 22). New geophysical and petrographic results of the Suvasvesi N impact structure, Finland. Abstract of Lunar and Planetary Science XXVII, page 1021, Houston, TX, US. https://ui.adsabs.harvard.edu/abs/1996LPI....27.1021P/abstract

Pesonen, L. J., Abels, A., Lehtinen, M., & Tuukki, P. (1998). Lake Saarijarvi: A new impact structure in northern Finland. Meteoritics & Planetary Science, vol. 33, p. A121, 33, A121. https://ui.adsabs.harvard.edu/abs/1998M%26PSA..33Q.121P/abstract

Pesonen, L. J., Elo, S., Lehtinen, M., Jokinen, T., Puranen, R., & Kivekäs, L. (1999). Lake Karikkoselka impact structure, central Finland: New geophysical and petrographic results. In. L. J. Pesonen, S. Elo, M. Lehtinen, T. Jokinen, R. Puranen, & L. Kivekäs, Large meteorite impacts and planetary evolution; II. Geological Society of America. https://doi.org/10.1130/0-8137-2339-6.131

Pierazzo, E., & Artemieva, N. (2012). Local and Global Environmental Effects of Impacts on Earth. Elements, 8(1), 55–60. https://doi.org/10.2113/gselements.8.1.55

Pilkington, M., & Grieve, R. A. F. (1992). The geophysical signature of terrestrial impact craters. Reviews of Geophysics, 30(2), 161–181. https://doi.org/10.1029/92rg00192

Pittarello, L., Nestola, F., Viti, C., Crósta, A. P., & Koeberl, C. (2015). Melting and cataclastic features in shatter cones in basalt from the Vista Alegre impact structure, Brazil. Meteoritics & Planetary Science, 50(7), 1228–1243. https://doi.org/10.1111/maps.12466

Pirajno, F., Hawke, P., Glikson, A. Y., Haines, P. W., & Uysal, T. (2003). Shoemaker impact structure, Western Australia. Australian Journal of Earth Sciences, 50(5), 775-796. https://doi.org/10.1111/j.1440-0952.2003.01027.x

Pirajno, F. (2005). Hydrothermal processes associated with meteorite impact structures: evidence from three Australian examples and implications for economic resources. Australian Journal of Earth Sciences, 52(4-5), 587-605. https://doi.org/10.1080/08120090500170468

Plado, J., Pesonen, L. J., & Puura, V. (1999). Effect of erosion on gravity and magnetic signatures of complex impact structures: Geophysical modeling and applications.. https://doi.org/10.1130/0-8137-2339-6.229

Plado, J., Pesonen, L. J., Koeberl, C., & Elo, S. (2000). The Bosumtwi meteorite impact structure, Ghana: A magnetic model. Meteoritics & Planetary Science, 35(4), 723–732. https://doi.org/10.1111/j.1945-5100.2000.tb01456.x

Plescia, J. B., Daniels, D. L., & Shah, A. K. (2009). Gravity investigations of the Chesapeake Bay impact structure. In. Gohn, G.S., Koeberl, C., Miller, K.G., Reimold, W.R. The ICDP-USGS Deep Drilling Project in the Chesapeake Bay impact structure: Results from the Eyreville Core Holes. Geological Society of America. https://doi.org/10.1130/2009.2458(09)

Poelchau, M. H., & Kenkmann, T. (2011). Feather features: A low-shock-pressure indicator in quartz. Journal of Geophysical Research: Solid Earth, 116(B2). https://doi.org/10.1029/2010JB007803

Popov, Y., Mayr, S., Romushkevich, R., Burkhardt, H., & Wilhelm, H. (2014). Comparison of petrophysical properties of impactites for four meteoritic impact structures. Meteoritics & Planetary Science, 49(5), 896–920. https://doi.org/10.1111/maps.12299

Prado, R. L., Espin Fenoll, I. C., Ullah, I., Miura, G. C. M., Crósta, A. P., Zanon dos Santos, R. P., ... & Diogo, L. A. (2019). Geophysical investigation of the Colônia structure, Brazil. Meteoritics & Planetary Science, 54(10), 2357-2372. https://doi.org/10.1111/maps.13292

Quesnel, Y., Bezaeva, N. S., Kuzina, D. M., Rochette, P., Gattacceca, J., Uehara, M., Badyukov, D. D., Nasyrtdinov, B. M., Chareev, D. A., & Champollion, C. (2022). The Karla impact structure (Russia) explored by potential-field investigations. Meteoritics & Planetary Science, 57(5), 989–1003. https://doi.org/10.1111/maps.13806

Quesnel, Y., Gattacceca, J., Osinski, G. R., & Rochette, P. (2013). Origin of the central magnetic anomaly at the Haughton impact structure, Canada. Earth and Planetary Science Letters, 367, 116–122. https://doi.org/10.1016/j.epsl.2013.02.032

R Core Team (2021). R: A language and environment for statistical computing. R Foundation for Statistical Computing, Vienna, Austria. URL https://www.R-project.org/.

RStudio Team (2019). RStudio: Integrated Development for R. RStudio, Inc., Boston, MA URL http://www.rstudio.com/.

Ramsey, M. S. (2002). Ejecta distribution patterns at Meteor Crater, Arizona: On the applicability of lithologic end-member deconvolution for spaceborne thermal infrared data of Earth and Mars. Journal of Geophysical Research: Planets, 107(E8). https://doi.org/10.1029/2001je001827

Reeves, C. (2005). Aeromagnetic surveys: principles, practice and interpretation, Geosoft, Washington – DC, US, 155p.

Reid, A. B., Allsop, J. M., Granser, H., Millett, A. T., & Somerton, I. W. (1990). Magnetic interpretation in three dimensions using Euler deconvolution. Geophysics, 55(1), 80-91. https://doi.org/10.1190/1.1442774

Reid, A. (2010). Forgotten truths, myths and sacred cows of Potential Fields Geophysics. Abstract of the SEG Technical Program Expanded Abstracts, Society of Exploration Geophysicists, Houston, TX, US1198 – 1201. https://doi.org/10.1190/1.3513058

Reimold, W. U. (1998). Exogenic and endogenic breccias: a discussion of major problematics. Earth-Science Reviews, 43(1-2), 25-47. https://doi.org/10.1016/S0012-8252(97)00037-8

Reimold, W. U. (1995). Pseudotachylite in impact structures—Generation by friction melting and shock brecciation?: A review and discussion. Earth-Science Reviews, 39(3–4), 247–265. https://doi.org/10.1016/0012-8252(95)00033-x

Reimold, W. U., Cooper, G. R., Romano, R., Cowan, D. R., & Koeberl, C. (2006). Investigation of Shuttle Radar Topography Mission data of the possible impact structure at Serra da Cangalha, Brazil. Meteoritics and Planetary Science, 41(2), 237-246. https://doi.org/10.1111/j.1945-5100.2006.tb00207.x

Reimold, W. U., Crósta, A. P., Hasch, M., Kowitz, A., Hauser, N., Sanchez, J. P., Simões, L. S. A., De Oliveira, G. J., & Zaag, P. T. (2019). Shock deformation confirms the impact origin for the Cerro do Jarau, Rio Grande do Sul, Brazil, structure. Meteoritics & Planetary Science, 54(10), 2384–2397. https://doi.org/10.1111/maps.13233

Reimold, W. U., Ferrière, L., Crósta, Á. P., Vasconcelos, M. A. R., Gottwald, M., Da Silva Borges, M., De Almeida, T. I. R., Pereira, F. L., Goés, A. M., Hauser, N., Jessell, M., & Baratoux, D. (2022). Nova Colinas, Maranhão State: A newly confirmed, complex impact structure in Brazil. Meteoritics & Planetary Science, 57(8), 1519–1541. https://doi.org/10.1111/maps.13833

Reimold, W. U., & Koeberl, C. (2014). Impact structures in Africa: A review. Journal of African Earth Sciences, 93, 57-175. https://doi.org/10.1016/j.jafrearsci.2014.01.008

Reimold, W. U., Ferrière, L., Deutsch, A., & Koeberl, C. (2014). Impact controversies: Impact recognition criteria and related issues. Meteoritics & Planetary Science, 49(5), 723-731. https://doi.org/10.1111/maps.12284

Reimold, W. U., & Jourdan, F. (2012). IMPACT! - BOLIDES, CRATERS, AND CATASTROPHES. Elements, 8(1), 19–24. https://doi.org/10.2113/gselements.8.1.19

Reimold, W.U., Hauser, N., Crósta, A.P. (2018). The Impact Record of Southwest Gondwana. In: Siegesmund, S., Basei, M., Oyhantçabal, P., Oriolo, S. (eds) Geology of Southwest Gondwana. Regional Geology Reviews. Springer, Cham. https://doi.org/10.1007/978-3-319-68920-3_24

Romanini, S. J. (1982). Geologia e geoquímica do complexo granitóide de Massangana e sua relação com as mineralizações de estanho. (MSc dissertation, Federal University of Bahia) https://rigeo.sgb.gov.br/handle/doc/13661

Riccomini, C., Tucrq, B., Martin, L., Moreira, M. Z., & Lorscheitter, M. L. (1991). The Colônia astrobleme, Brasil. Revista do Instituto Geológico, 12(1-2), 87-94. https://doi.org/10.5935/0100-929X.19910007

Riccomini, C., Crosta, A. P., Prado, R. L., Ledru, M. P., Turcq, B. J., Sant'anna, L. G., Ferrari, J.A., & Reimold, W. U. (2011). The Colônia structure, São Paulo, Brazil. Meteoritics & Planetary Science, 46(11), 1630-1639. https://doi.org/10.1111/j.1945-5100.2011.01252.x

Roest, W. R., Verhoef, J., & Pilkington, M. (1992). Magnetic interpretation using the 3-D analytic signal. Geophysics, 57(1), 116-125. https://doi.org/10.1190/1.1443174

Roest, W. R., & Pilkington, M. (1993). Identifying remanent magnetization effects in magnetic data. GEOPHYSICS, 58(5), 653–659. https://doi.org/10.1190/1.1443449

Rosa-Costa, L. T., dos Santos, P. A., de Medeiros, V. C., Sobrinho, V. R. S., & Klein, E. (2023). Overview of the geological mapping in Brazil: historical analysis until 2022. Journal of the Geological Survey of Brazil, 6(1), 91-105. https://doi.org/10.29396/jgsb.2023.v6.n1.6

Rossman GR, Ehlmann BL. Electronic Spectra of Minerals in the Visible and Near-Infrared Regions. In: Bishop JL, Bell III JF, Moersch JE, eds. Remote Compositional Analysis: Techniques for Understanding Spectroscopy, Mineralogy, and Geochemistry of Planetary Surfaces. Cambridge Planetary Science. Cambridge University Press; 2019:3-20. https://doi.org/10.1017/9781316888872.003

Salem, A., & Ravat, D. (2003). A combined analytic signal and Euler method (AN-EUL) for automatic interpretation of magnetic data. Geophysics, 68(6), 1952-1961. https://doi.org/10.1190/1.1635049

Salminen, J., Pesonen, L. J., Reimold, W. U., Donadini, F., & Gibson, R. L. (2009). Paleomagnetic and rock magnetic study of the Vredefort impact structure and the Johannesburg Dome, Kaapvaal Craton, South Africa—implications for the apparent polar wander path of the Kaapvaal Craton during the Mesoproterozoic. Precambrian Research, 168(3-4), 167-184. https://doi.org/10.1016/j.precamres.2008.09.005

Sánchez, J. P. (2014). Mapeamento geológico - estrutural do astroblema de cerro do Jarau - RS Brasil. (Doctoral thesis, São Paulo State University, Institute of Geosciences and Exact Sciences). https://repositorio.unesp.br/entities/publication/7a488bef-416d-4c3f-9690-f2bb38b64723

Sánchez, J. P., Simões, L. S. A., & Martins, L. E. B. (2014). Estratigrafia e estrutura do Cerro do Jarau: nova proposta. Brazilian Journal of Geology, 44(2), 265-276.

Santos, J.O.S, 2003, Geotectônica dos Escudos das Guianas e Brasil-Central: In: Bizzi, L.A., Schobbenhaus, C., Vidotti, R.M., Gonçalves, J.H., Geologia, Tectônica e Recursos Minerais do Brasil: CPRM, Brasília, Brazil: 169 - 226.

Santos, R. P. Z., Marangoni, Y. R., Chaves, C. A. M., & Marotta, G. S. A. (2022). New free-Air and Bouguer Gravity Anomalies Maps of Brazil. Brazilian Journal of Geophysics, 40(6), 19-28. http://dx.doi.org/10.22564/brjg.v40i6.2195

Schobbenhaus C., Ribeiro C.L., Oliva L.A., Takanohashi J.T., Lindenmayer A.G., Vasconcelos J.C., and Orlandi V, 1975, Folha Goiás (SC-22) Carta Geológica do Brasil ao Milionésimo. Texto Explicativo. DNPM, Brasília, Brazil, p. 99-113.

Shepard, D. (1968, August 27 - 29). A two-dimensional interpolation function for irregularly-spaced data. Abstract of the Proceedings of the 1968 23rd ACM national conference, Association for Computing Machinery, New York, NY, US, pp. 517-524).

Soares, J. E., Stephenson, R., Fuck, R. A., Lima, M. V. A.G., Araújo, V.C.M, Lima, Lima, F.T., Rocha, F.A.S., & Trindade, C.R. (2018). Structure of the crust and upper mantle beneath the Parnaíba Basin, Brazil, from wide-angle reflection–refraction data. In. M. C. Daly, R. A. Fuck, J. Julià, D.I.M. MacDonald, A. B. Watts (eds). Cratonic Basin Formation: A Case Study of the Parnaíba Basin of Brazil. Special Publications of Geological Society of London, 472, 67 - 82. https://doi.org/10.1144/SP472.

Silva, A. D., Lopes, R. D. C., Vasconcelos, A. M., & Bahia, R. B. (2003). Bacias sedimentares paleozóicas e meso-cenozóicas interiores. Geologia, Tectônica e Recursos Minerais do Brasil. Brasília. In: Bizzi, L.A., Schobbenhaus, C., Vidotti, R.M., Gonçalves, J.H., Geologia, Tectônica e Recursos Minerais do Brasil: CPRM, Brasília, Brazil: 55 – 85.

Silva, A.B. (2020). Identification of Impact Cratering-Related Similarities Based on Airborne Geophysical Data and Satellite Images: The Cabeça De Sapo Structure, Parnaíba Basin, Northeast Brazil". Journal of the Geological Survey of Brazil 3 (2):97-111. https://doi.org/10.29396/jgsb.2020.v3.n2.4

Silva, R. C. S., Sabóia, A. M., & Polo, H. J. O. (2021). Projeto integração geológica-geofísica-metalogenética das sequências de Greenstone Belts do Domínio Rio Maria–Novas Fronteiras Rio Maria. Levantamentos Geológicos e de Potencial Mineral de Novas Fronteiras, CPRM, Belém, PA, Brazil. https://rigeo.sgb.gov.br/handle/doc/22379

Silva, A. B., Pires de Lima, R., & La Marca, K. (2023). Decomposing and recovering airborne radiometric data through principal component analysis applied on flight-line data: An alternative to reduce noise. Interpretation, 11(3), T523-T535. https://doi.org/10.1190/INT-2022-0110.1

Silva, A.B., & Alves, F.M. (2023). Atlas aerogeofísico do Estado de Mato Grosso. Levantamentos Geológicos e de Potencial Mineral de Novas Fronteiras, SGB-CPRM, Goiânia, GO, Brazil. https://rigeo.sgb.gov.br/handle/doc/24566

Silva, A.B., Silva, M. F., Reimold, W. U., Alves, F. M., Lago, A. L., Couto Jr, M. Frasca, A.A.S., & Ribeiro, P.S.E. (2024). The aerogeophysical atlas of Tocantins state: synthesis of magnetic anomaly and radioelement maps with emphasys on regional signatures and the Serra da

Cangalha impact structure. Brazilian Journal of Geophysics, 42(2), 1 – 29. http://dx.doi.org/10.22564/brjg.v42i2.2316

Schmieder, M., & Kring, D. A. (2020). Earth's impact events through geologic time: a list of recommended ages for terrestrial impact structures and deposits. *Astrobiology*, *20*(1), 91-141. https://doi.org/10.1089/ast.2019.2085

Smith, S. K., Grieve, R. A. F., Harris, J. R., & Singhroy, V. (1999). The Utilization of RADARSAT-1 Imagery for the Characterization of Terrestrial Impact Landforms. Canadian Journal of Remote Sensing, 25(3), 218–228. https://doi.org/10.1080/07038992.1999.10874721

Sousa, C.S., Silva, R.C.S., Polo, H.J.O., Saboia, A. M., Paula, R.R., Barbosa, J.P.O., & Costa, U.A. (2020). Mapa Geológico da Folha SC.22-X -A-IV Rio Inajá. Escala 1:100.000. Projeto integração geológica-geofísica-metalogenética das sequências de Greenstone Belts do Domínio Rio Maria–Novas Fronteiras Rio Maria. Levantamentos Geológicos e de Potencial Mineral de Novas Fronteiras, CPRM, Belém, PA, Brazil. https://rigeo.sgb.gov.br/bitstream/doc/20441/5/carta_geologica_rio_inaja.pdf

Souza, C. D. S. M. D., Hauser, N., Reimold, W. U., Bernardes, R. B., Vieira, L. C., Guimarães, E. M., & Gottwald, M. (2024). Araguainha impact structure, Brazil: New insights into the geology of the central uplift. Meteoritics & Planetary Science, 59(10), 2577–2607. https://doi.org/10.1111/maps.14236

Spudis PD. The Geology of Multi-Ring Impact Basins: The Moon and Other Planets. Cambridge University Press; 1993. https://doi.org/10.1017/CBO9780511564581

Stewart, S. A., & Allen, P. J. (2002). A 20-km-diameter multi-ringed impact structure in the North Sea. Nature, 418(6897), 520-523. https://doi.org/10.1038/nature00914

Stewart, S. A. (2003). How will we recognize buried impact craters in terrestrial sedimentary basins? Geology, 31(11), 929. https://doi.org/10.1130/g19853.1

Stöffler, D., & Langenhorst, F. (1994). Shock metamorphism of quartz in nature and experiment: I. Basic observation and theory. Meteoritics, 29(2), 155-181. https://doi.org/10.1111/j.1945-5100.1994.tb00670.x

Stöffler, D., & Grieve, R. A. F. (2007). Impactites, Chapter 2.11, In. Fettes, D. and Desmons, J.(eds.) Metamorphic rocks: A classification and glossary of terms, recommendations of the International Union of Geological Sciences – Subcommission on the Systematics of Metamorphic Rocks, 82 – 92.

Stöffler, D., Hamann, C., & Metzler, K. (2018). Shock metamorphism of planetary silicate rocks and sediments: Proposal for an updated classification system. Meteoritics & Planetary Science, 53(1), 5-49. https://doi.org/10.1111/maps.12912

Suhr, D. D. (2005). Principal component analysis vs. exploratory factor analysis. SUGI 30 proceedings, 203(230), 1-11.

Talwani, P., Wildermuth, E., & Parkinson, C. D. (2003). An impact crater in northeast South Carolina inferred from potential field data. Geophysical Research Letters, 30(7). https://doi.org/10.1029/2003gl017051

Tada, T., Kurosawa, K., Tomioka, N., Nagaya, T., Isa, J., Hamann, C., Ono, H., Niihara, T., Okamoto, T., & Matsui, T. (2024). Detailed occurrence of feather features in quartz in experimentally shocked granite. Journal of Geophysical Research: Planets, 129(11), e2024JE008409.

Taylor, M. J., Smettem, K., Pracilio, G., & Verboom, W. (2002). Relationships between soil properties and high-resolution radiometrics, central eastern Wheatbelt, Western Australia. Exploration geophysics, 33(2), 95-102. https://doi.org/10.1071/EG02095

Teixeira, W. (1990). The Proterozoic mafic dyke swarms and alkaline intrusions in the Amazonian craton, South America, and their tectonic evolution based on Rb – Sr, K – Ar and ^{40}Ar-^{39}Ar geochronology. In. Parker, A.J., Rock, P.C., Tucker, D.H. (eds)., Mafic Dykes and Emplacement Mechanism. A.A. Balkema, Rotterdam, pp. 285 – 293.

Theilen-Willige, B. (1982). The Araguainha astrobleme/Central Brazil. Geologische Rundschau, 71(1), 318–327. https://doi.org/10.1007/bf01825044

Theilen-Willige, B. (2021). Morphometric and Structural Evaluations of Satellite Data from the Bosumtwi Impact Structure and Adjacent Areas in Ashanti, Ghana. European Journal of Environment and Earth Sciences, 2(3), 7–14. https://doi.org/10.24018/ejgeo.2021.2.3.137

Theilen-Willige, B. (2023a). Detection of Ring Structures and Their Surrounding Tectonic Pattern in South-Algeria, North-Mali and North- Niger based on Satellite Data. Energy and Earth Science, 6(2). https://doi.org/10.22158/ees.v6n2p1

Theilen-Willige, B. (2023b). Inventory of Ring Structures in N- and W-Morocco based on Satellite Data. European Journal of Environment and Earth Sciences, 4(1), 34–45. https://doi.org/10.24018/ejgeo.2023.4.1.364

Thompson, D. T. (1982). EULDPH: A new technique for making computer-assisted depth estimates from magnetic data. Geophysics, 47(1), 31-37. https://doi.org/10.1190/1.1441278

Tohver, E., Lana, C., Cawood, P. A., Fletcher, I. R., Jourdan, F., Sherlock, S., Rasmussen, B., Trindade, R. I. F., Yokoyama, E., Souza Filho, C. R., & Marangoni, Y. (2012). Geochronological constraints on the age of a Permo–Triassic impact event: U–Pb and 40Ar/39Ar results for the 40km Araguainha structure of central Brazil. Geochimica et Cosmochimica Acta, 86, 214–227. https://doi.org/10.1016/j.gca.2012.03.005

Torquato, J. R. F. (1981). O astroblema de São Miguel do Tapuio (PI). Ciências da Terra, 1(1), 37.

Tong, C. H., Lana, C., Marangoni, Y. R., & Elis, V. R. (2010). Geoelectric evidence for centripetal resurge of impact melt and breccias over central uplift of Araguainha impact structure. Geology, 38(1), 91–94. https://doi.org/10.1130/g30459.1

Tornabene, L. L., Moersch, J. E., Osinski, G. R., Lee, P., & Wright, S. P. (2005). Spaceborne visible and thermal infrared lithologic mapping of impact-exposed subsurface lithologies at the Haughton impact structure, Devon Island, Canadian High Arctic: Applications to Mars. Meteoritics & Planetary Science, 40(12), 1835–1858. https://doi.org/10.1111/j.1945-5100.2005.tb00149.x

Tsikalas, F. (2005). Mjølnir Crater as a Result of Oblique Impact: Asymmetry Evidence Constrains Impact Direction and Angle. In: Koeberl, C., Henkel, H. (eds) Impact Tectonics. Impact Studies. Springer, Berlin, Heidelberg. https://doi.org/10.1007/3-540-27548-7_10

Uchôa, E. B., Vasconcelos, M. A. R., & Crósta, A. P. (2013, March 18 - 22). Santa Marta crater: Macroscopic and petrographic evidences of a new confirmed impact structure in northeastern Brazil. Abstract of the 44th Annual Lunar and Planetary Science Conference (No. 1719, p. 1316), The Woodlands, TX, US. https://www.lpi.usra.edu/meetings/lpsc2013/pdf/1316.pdf

Ugalde, H. A., Artemieva, N., & Milkereit, B. (2005). Magnetization on impact structures—Constraints from numerical modeling and petrophysics. In. Kenkmann, T., Hörz, F., Deutsch, A. Large Meteorite Impact III, Geological Society of America, 25 – 42. https://doi.org/10.1130/0-8137-2384-1.25

Urbini, S., Nicolosi, I., Zeoli, A., El Khrepy, S., Lethy, A., Hafez, M., El Gabry, M., El Barkooky, A., Barakat, A., Gomaa, M., Radwan, A. M., El Sharkawi, M., D'orazio, M., & Folco, L. (2012). Geological and geophysical investigation of Kamil crater, Egypt. Meteoritics & Planetary Science, 47(11), 1842–1868. https://doi.org/10.1111/maps.12023

Van Zyl J, Elachi C, Kim Y (2019). Radar Remote Sensing: Theory and Applications. In: Bishop J.L., Bell III J.F., Moersch J.E. (eds). Remote Compositional Analysis: Techniques for Understanding Spectroscopy, Mineralogy, and Geochemistry of Planetary Surfaces. Cambridge Planetary Science. Cambridge University Press; 239-258. https://doi.org/10.1017/9781316888872.012

Van der Meer, F. D., Van der Werff, H. M. A., & Van Ruitenbeek, F. J. A. (2014). Potential of ESA's Sentinel-2 for geological applications. Remote sensing of environment, 148, 124-133. https://doi.org/10.1016/j.rse.2014.03.022

Van Gasselt, S., Kim, J. R., Choi, Y. S., & Kim, J. (2017). The Oasis impact structure, Libya: geological characteristics from ALOS PALSAR-2 data interpretation. Earth, Planets and Space, 69(1), 35. https://doi.org/10.1186/s40623-017-0620-8

Van Lopik, J. R., & Geyer, R. A. (1963). Gravity and Magnetic Anomalies of the Sierra Madera, Texas, “Dome.” Science, 142(3588), 45–47. https://doi.org/10.1126/science.142.3588.45

Vasconcelos, M.A.R. (2007). Caracterização geofísica da estrutura de impacto de Araguainha, MT/GO . (MSc dissertation, University of São Paulo). https://doi.org/10.11606/d.14.2007.tde-17052007-105856

Vasconcelos, M. A. R., Crósta, A. P., & Molina, E. C. (2010). Geophysical characteristics of four possible impact structures in the Parnaíba Basin, Brazil: Comparison and implications. In. Gibson, R.L., Reimold, W.U. (eds). Large Meteorite Impacts and Planetary Evolution IV, Geological Society of America, 201 – 217. https://doi.org/10.1130/2010.2465(14)

Vasconcelos, M. A. R., Leite, E. P., & Crósta, A. P. (2012a). Contributions of gamma-ray spectrometry to terrestrial impact crater studies: The example of Serra da Cangalha, northeastern Brazil. Geophysical Research Letters, 39(4). https://doi.org/10.1029/2011gl050525

Vasconcelos, M. A. R., Crósta, A. P., Reimold, W. U., Góes, A. M., Kenkmann, T., & Poelchau, M. H. (2013). The Serra da Cangalha impact structure, Brazil: Geological, stratigraphic and petrographic aspects of a recently confirmed impact structure. Journal of South American Earth Sciences, 45, 316–330. https://doi.org/10.1016/j.jsames.2013.03.007

Vasconcelos, M. A. R., Rocha, F. F., Crósta, A. P., Wünnemann, K., Güldemeister, N., Leite, E. P., Ferreira, J. C., & Reimold, W. U. (2019). Insights about the formation of a complex impact structure formed in basalt from numerical modeling: The Vista Alegre structure, southern Brazil. Meteoritics & Planetary Science, 54(10), 2373–2383. https://doi.org/10.1111/maps.13298

Vasconcelos, M. A. R., Wünnemann, K., Crósta, A. P., Molina, E. C., Reimold, W. U., & Yokoyama, E. (2012b). Insights into the morphology of the Serra da Cangalha impact structure from geophysical modeling. Meteoritics & Planetary Science, 47(10), 1659–1670. https://doi.org/10.1111/maps.12001

Vaz, P. T., Wanderley Filho, J. R., & Travassos, W. A. S. (2007). Bacia do parnaíba. Boletim de Geociências da PETROBRAS, 15(2), 253-263. https://bgp.petrobras.com.br/bgp/article/view/308.

Velázquez, V. F., Riccomini, C., Azevedo Sobrinho, J. M., Pletsch, M. A., Sallun, A. E. M., Sallun Filho, W., & Hachiro, J. (2013). Evidence of shock metamorphism effects in allochthonous breccia deposits from the Colônia Crater, São Paulo, Brazil. International Journal of Geosciences, 4(1A), 274-282. DOI:10.4236/ijg.2013.41A025

Velázquez, V. F., Lucena, R.F.D., & Sallun, A.E.M. (2018). Petrographic investigation of target rock transformation under high shock pressures from the Colônia impact crater, Brazil. Earth Science Research, 7(1), 13-24. DOI: 10.5539/esr.v7n1p13

Wihanto, L., & Kenkmann, T. (2023). Geophysical and structural analyses of the Middlesboro impact structure, Kentucky, USA: Reactivation of a thrust detachment of the Appalachian

foreland fold-and-thrust belt. Meteoritics & Planetary Science, 58(12), 1848–1871. https://doi.org/10.1111/maps.14107

Wilford, J. R., Bierwirth, P. E., & Craig, M. A. (1997). Application of airborne gamma-ray spectrometry in soil/regolith mapping and applied geomorphology. AGSO Journal of Australian Geology and Geophysics, 17. 201 – 216.

Wilford, J., & Minty, B. (2006). The use of airborne gamma-ray imagery for mapping soils and understanding landscape processes. Developments in soil science, 31, 207-610. https://doi.org/10.1016/S0166-2481(06)31016-1

Williams, Q., & Jeanloz, R. (1988). Spectroscopic Evidence for Pressure-Induced Coordination Changes in Silicate Glasses and Melts. Science, 239(4842), 902–905. https://doi.org/10.1126/science.239.4842.902

Wright, S. P., Johnson, J. R., & Christensen, P. R. (2004, March 15 – 19). THERMAL EMISSION SPECTRA OF IMPACT GLASS AND SHOCKED DECCAN BASALT FROM LONAR CRATER, INDIA AND IMPLICATIONS FOR REMOTE SENSING OF MARS. Abstract of the 35th Annual Lunar and Planetary Science Conference (No Contr. 1786), League City, TX, US. https://www.lpi.usra.edu/meetings/lpsc2004/pdf/2072.pdf

Wright, S. P., Christensen, P. R., Sharp, T. G., & Wright, S. P. (2006, March 13 - 17). Thermal emission spectroscopy of shocked basalt from the Earth and Mars: A review plus new insights. Abstract of the 37th Annual Lunar and Planetary Science Conference (No Contr. 1786), League City, TX, US. https://ui.adsabs.harvard.edu/abs/2006LPI....37.1786W/abstract

Wright, S.P., Tornabene, L.L. and Ramsey, M.S. (2012). Remote Sensing of Impact Craters. In. Osinski, G.R., Pierazzo, E. (eds). Impact Cratering. https://doi.org/10.1002/9781118447307.ch13

Yamaguchi, Y., Kahle, A. B., Tsu, H., Kawakami, T., & Pniel, M. (1998). Overview of advanced spaceborne thermal emission and reflection radiometer (ASTER). IEEE Transactions on Geoscience and Remote Sensing, 36(4), 1062-1071. DOI: 10.1109/36.700991

Yokoyama, E., Trindade, R. I. F., Lana, C., Filho, C. R. S., Baratoux, D., Marangoni, Y. R., & Tohver, E. (2012). Magnetic fabric of Araguainha complex impact structure (Central Brazil): Implications for deformation mechanisms and central uplift formation. Earth and Planetary Science Letters, 331–332, 347–359. https://doi.org/10.1016/j.epsl.2012.01.005

Yokoyama, E., Brandt, D., Tohver, E., & Trindade, R. I. F. (2014). Palaeomagnetism of the Permo-Triassic Araguainha impact structure (Central Brazil) and implications for Pangean reconstructions. Geophysical Journal International, 198(1), 154–163. https://doi.org/10.1093/gji/ggu125

Yokoyama, E., Nédélec, A., Baratoux, D., Trindade, R. I. F., Fabre, S., & Berger, G. (2015). Hydrothermal alteration in basalts from Vargeão impact structure, south Brazil, and implications

for recognition of impact-induced hydrothermalism on Mars. Icarus, 252, 347–365. https://doi.org/10.1016/j.icarus.2015.02.001

Yommy, A. S., Liu, R., & Wu, S. (2015, August 26 - 27). SAR image despeckling using refined Lee filter. Abstract of the 7th International Conference on Intelligent Human-Machine Systems and Cybernetics, 2, 260-265. DOI: 10.1109/IHMSC.2015.236.

Zhang, P., Rasmussen, T. M., & Pedersen, L. B. (1988). Electric resistivity structure of the Siljan impact region. Journal of Geophysical Research: Solid Earth, 93(B6), 6485-6501. https://doi.org/10.1029/JB093iB06p06485

Zumsprekel, H., & Bischoff, L. (2005). Remote sensing and GIS analyses of the Strangways impact structure, Northern Territory. Australian Journal of Earth Sciences, 52(4–5), 621–630. https://doi.org/10.1080/08120090500181077

18. APPENDIX I – PRINCIPAL COMPONENT ANALYSIS IN R CODE.

The R script below is an example of Principal Component Analysis applied to airborne gamma-ray spectrometry data. Note that the input file needs to be already grided, converted to .tiff format (e.g. K.tif file below), and placed on folder (in this exemple, named as “your_folder”) together with R project.

```
################## Start of script

############## Instaling and charging the package

install.packages(RStoolbox)

install.packages(ggplot2)

install.packages(factoextra)

########## Data import

K <- raster("C:\\your_folder\\K.tif")

eTh <- raster("C:\\your_folder\\eTh.tif")

eU <- raster("C:\\your_folder\\eU.tif")

eUeTh <- raster("C:\\your_folder\\eUeTh.tif")

eUK <- raster("C:\\your_folder\\eUK.tif")

KeTh <- raster("C:\\your_folder\\KeTh.tif")

########## Stacking the raster files

gama_map <- stack(K, eTh, eU, eUeTh, eUK, KeTh, layer=NULL)

########## Normalizing and applying the PCA approach

pcamap<-rasterPCA(gama_map, spca = TRUE)

#########Contributions of variables into PC (1, 2, and so on).

fviz_contrib(pcamap$model,choice = "var", axes = 1, top = 10)

fviz_contrib(pcamap$model,choice = "var", axes = 2, top = 10)

######### Getting the explained variance

pca_numbers <- get_eig(pcamap$model)

#Exporting PCA raster file.

saveRSTBX(pcamap, filename = "PCA_GAMA_SdC", format = "GTiff", overwrite=TRUE)
```